energies

Special Issue Reprint

Exploration and Development of Unconventional Oil and Gas Resources

Latest Advances and Prospects: 2nd Edition

Edited by
Shu Tao, Wei Ju, Shida Chen, Zhengguang Zhang and Jiang Han

mdpi.com/journal/energies

MDPI

Exploration and Development of Unconventional Oil and Gas Resources: Latest Advances and Prospects: 2nd Edition

Exploration and Development of Unconventional Oil and Gas Resources: Latest Advances and Prospects: 2nd Edition

Guest Editors

Shu Tao
Wei Ju
Shida Chen
Zhengguang Zhang
Jiang Han

MDPI

Basel • Beijing • Wuhan • Barcelona • Belgrade • Novi Sad • Cluj • Manchester

Guest Editors

Shu Tao
Department of Energy and Environment
China University of Geosciences
Beijing
China

Wei Ju
School of Resources and Geosciences
China University of Mining and Technology
Xuzhou
China

Shida Chen
School of Energy
China University of Geosciences (Beijing)
Beijing
China

Zhengguang Zhang
General Prospecting Institute of China National Administration of Coal Geology
Beijing
China

Jiang Han
School of Vehicle and Energy
Yanshan University
Qinhuangdao
China

Editorial Office
MDPI AG
Grosspeteranlage 5
4052 Basel, Switzerland

This is a reprint of the Special Issue, published open access by the journal *Energies* (ISSN 1996-1073), freely accessible at: https://www.mdpi.com/journal/energies/special_issues/5BRQ6539U8.

For citation purposes, cite each article independently as indicated on the article page online and as indicated below:

Lastname, A.A.; Lastname, B.B. Article Title. *Journal Name* **Year**, *Volume Number*, Page Range.

ISBN 978-3-7258-5781-4 (Hbk)
ISBN 978-3-7258-5782-1 (PDF)
https://doi.org/10.3390/books978-3-7258-5782-1

Contents

energies

MDPI

Article

Impacts and Countermeasures of Present-Day Stress State and Geological Conditions on Coal Reservoir Development in Shizhuang South Block, Qinshui Basin

Xinyang Men, Shu Tao *, Shida Chen, Heng Wu and Bin Zhang

School of Energy Resources, China University of Geosciences (Beijing), Beijing 100083, China
* Correspondence: taoshu@cugb.edu.cn

Abstract: This study investigates the reservoir physical properties, present-day stress, hydraulic fracturing, and production capacity of No. 3 coal in the Shizhuang south block, Qinshui Basin. It analyzes the control of in situ stress on permeability and hydraulic fracturing, as well as the influence of geo-engineering parameters on coalbed methane (CBM) production capacity. Presently, the direction of maximum horizontal stress is northeast–southwest, with local variations. The stress magnitude increases with burial depth, while the stress gradient decreases. The stress field of strike-slip faults is dominant and vertically continuous. The stress field of normal faults is mostly found at depths greater than 800 m, whereas the stress field of reverse faults is typically found at depths shallower than 700 m. Permeability, ranging from 0.003 to 1.08 mD, is controlled by in situ stress and coal texture, both of which vary significantly with tectonics. Hydraulic fracturing design should consider variations in stress conditions, pre-existing fractures, depth, structural trends, and coal texture, rather than employing generic schemes. At greater depths, higher pumping rates and treatment pressures are required to reduce fracture complexity and enhance proppant filling efficiency. The Shizhuang south block is divided into five zones based on in situ stress characteristics. Zones III and IV exhibit favorable geological conditions, including high porosity, permeability, and gas content. These zones also benefit from shorter gas breakthrough times, relatively higher gas breakthrough pressures, lower daily water production, and a higher ratio of critical desorption pressure to initial reservoir pressure. Tailored fracturing fluid and proppant programs are proposed for different zones to optimize subsequent CBM development.

Keywords: Qinshui Basin; Shizhuang south block; present-day stress; description of CBM reservoir; hydraulic fracture

1. Introduction

The capacity of coalbed methane (CBM) wells is a crucial indicator for evaluating CBM projects. Geological factors, such as in situ stress, reservoir properties, sedimentary conditions, burial depth, and hydrological conditions, significantly influence CBM productivity [1–6]. Engineering factors, including completion techniques, well placement, hydraulic fracturing design, drilling, and production regulation, also play vital roles [7–11]. Among these, reservoir properties, tectonic stress, and hydraulic fracturing design are paramount for CBM production [12].

In China, the complex tectonic movements across various coal-bearing basins result in diverse in situ stress distributions and CBM reservoir properties [13–17]. This complexity necessitates distinct hydraulic fracturing schemes for effective development. In situ stress comprises overburden pressure and tectonic stress. While vertical stress gradients remain relatively constant due to gravity, tectonic stresses are variable and spatially heterogeneous [18]. Different stress states—normal fault, reverse fault, and strike-slip fault—are distinguished by the magnitudes of horizontal and vertical stresses [19]. Regional plate movements typically dictate the dominant stress state and orientation [20].

The orientation, state, and magnitude of stress vary across geological units [21–24]. Researchers employ borehole measurements, geophysical surveys, and tectonic–geological studies to examine present-day stresses [25–28]. Identifying in situ stress distributions is critical for assessing coal permeability variations and CBM zonation [29–31]. Present stress regimes, magnitudes, and orientations affect in situ permeability by influencing the connectivity, length, and width of natural fracture systems [32]. In CBM gas development, horizontal stress differentials and orientations are crucial for configuring hydraulically induced fractures and ensuring borehole stability [33]. Higher horizontal stress differentials lower breakdown pressure, leading to simpler hydraulic fracture shapes, while lower stress differentials favor complex fracture networks [34,35]. Natural fractures in coal reservoirs can also impact hydraulic fracture propagation under varying stress conditions [36,37].

The Shizhuang south block in the Qinshui Basin, China, with over 1300 production wells, provides substantial data for analyzing the present-day stress state and coal reservoir characteristics and their impacts on CBM development and hydraulic fracturing [38–40]. This study comprehensively collects geological, engineering, and production data from the Shizhuang south block. Inversion models are used to systematically analyze the distribution of in situ stress and coal reservoir parameters. The study discusses how these factors influence coal reservoir properties and hydraulic fracturing in the context of tectonic trends. Finally, it offers engineering optimization suggestions for the Shizhuang south block.

2. Geological Settings

Situated in northern China, the Qinshui Basin is a sizable syncline basin with a symmetrical, double-sided structure, encompassing an area of 23,500 km^2 [41] (Figure 1a). The Shizhuang south blockis located in the southern part of the Qinshui Basin and can be divided into five structural units, and the data used for the modeling in this study came primarily from Zones 2, 3, and 5 (Figure 1b). The primary coal-bearing strata are the Taiyuan Formation of the Upper Carboniferous and the Shanxi Formation of the Lower Permian, consisting mainly of coal seams, mudstone, limestone, sandstone, and siltstone [38] (Figure 1c). The most consistent recoverable coal seams in the basin are coal seam No. 3 (3–9 m) from the Shanxi Formation and coal seam No. 15 (2–8 m) from the Taiyuan Formation, which are the main focus for CBM exploration and extraction. This study analyzes the Shizhuang south block, an area that has been extensively explored with comprehensive data available.

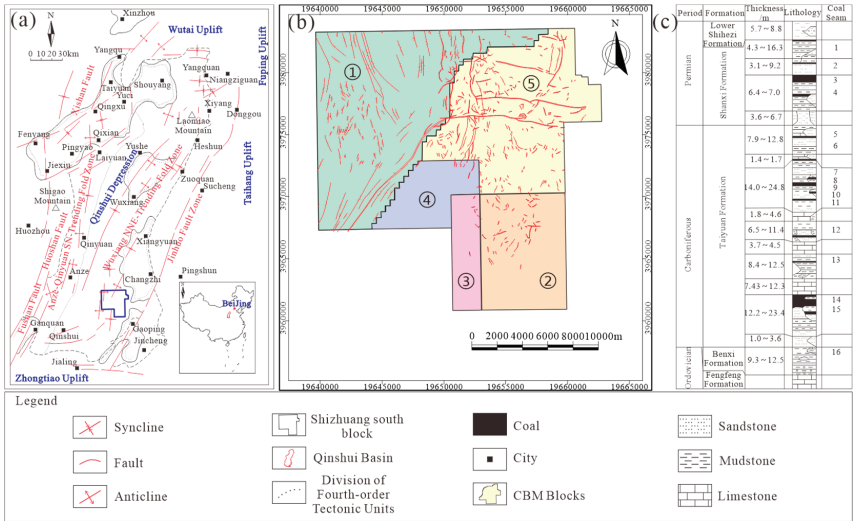

Figure 1. Comprehensive geologic map of Shizhuang south block in Qinshui Basin. (**a**) Qingshui Basin, China, and the location of the Shizhuang south block; (**b**) Tectonic outline map of Shizhuang south block; (**c**) Stratigraphic histogram of Shizhuang south block.

The basin has experienced various tectonic movements since the Carboniferous–Permian period, including the Indosinian, Yanshanian, and Himalayan phases [42]. During the Indosinian movement, the basin underwent north–south tectonic compression without significant geological structures forming. In the Yanshanian period, a SEE-NWW compression stress field caused broad, flat folds and a set of small-scale normal faults oriented NE-NNE. In the early Himalayan period, the tectonic stress shifted from a reversed to a tension stress field in the SEE-NWW orientation, later transitioning to compression in the NEE-SWW direction during the mid–late Himalayan period, resulting in a series of faults [43].

Since the Quaternary neotectonic period, the strata have been under a horizontal compressive force oriented NE-SW, aligning with the Taihang and Huoshan Mountains. This tectonic stress pattern remains constant today. The prevailing stress influencing the Qinshui Basin mainly originates from the Pacific Plate subducting beneath Western Eurasia and the Philippine Plate subducting under the Eurasian landmass. Consequently, the orientation of the maximum horizontal stress (σ_H) in the basin (NE 40~70°) aligns with the principal stress trajectory of China [44] (Figure 2).

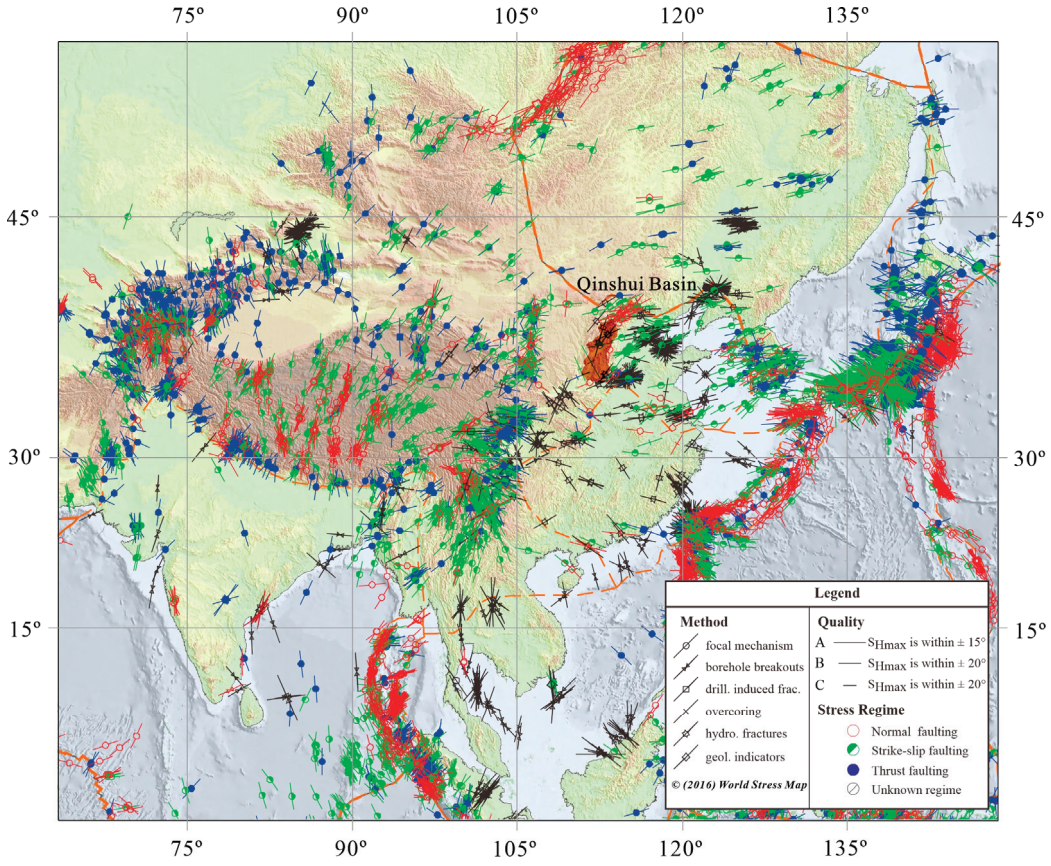

Figure 2. Maximum horizontal stress trajectory in China, based on data from the World Stress Map (WSM) Database [45]. The stress map was generated using data from WSM available at http://www.world-stress-map.org/casmo/ (accessed on 10 May 2024).

3. Methodology

Data on gas content, in situ stress, core samples, hydraulic fracturing, 3D seismic information, production data, porosity, permeability, fracture monitoring, and logging curves were obtained from CBM wells in the region, courtesy of the China United Coalbed Methane Corporation. According to China National Standard GB/T 24504-2009 [46], 16 pore pressure and 16 permeability data points were measured at depths of 558 to 1227 m using the injection/fall-off well test. Multi-loop hydraulic fracturing, following China

Industry Standard DB/T 14-2018 [47], was performed on 95 CBM wells to obtain shut-in pressure (p_s) and breakdown pressure (p_f) data in megapascals. Additionally, 53 porosity data points were measured at depths of 451 to 1154 m according to China National Standard GB/T 29172-2012 [48]. A total of 447 gas content data points, measured using the natural desorption method, were collected at depths of 451 to 1349 m according to China National Standard GB/T 19559-2021 [49]. Coal texture discrimination was conducted on 428 core samples from 28 wells, following China National Standard GB/T 30050-2013 [50]. Since the number of data points was insufficient to cover the entire work area, inversion of coal reservoir parameters is required for comprehensive modeling.

The water injection/well drop test recorded the change in bottomhole pressure over time, and parameters such as initial reservoir pressure and permeability were calculated using linear analysis and plate matching methods. Four cycles of in situ stress measurements were performed, recording the p_f in each cycle, and the pressure drop data were obtained by shutting down the well and calculating p_s using the square root of time method.

Stress regimes are commonly represented by σ_H, with the minimum stress (σ_h) and the vertical stress (σ_v). The p_s denotes the minimum bottomhole pressure necessary to maintain the openness of pre-existing fractures, analogous to the normal stress exerted on the vertical fracture surface of rocks [51]:

$$\sigma_h = p_s \tag{1}$$

For a vertical borehole, the estimation of σ_H can be achieved through the following equation, assuming the rocks demonstrate impermeability, homogeneity, isotropy, and elasticity [52]:

$$\sigma_H = 3p_s - p_f - p_o \tag{2}$$

where p_o represents the reservoir pressure.

Multi-loop hydraulic fracturing is an effective approach for assessing in situ stress within deep rock formations [53]. The Kaiser effect is also a reliable technique for identifying stress conditions through acoustic emission (AE) tests and uniaxial compression conducted on drilling cores [54,55]. Chen et al. demonstrated that multi-loop hydraulic fracturing yields outcomes comparable to Kaiser effect stress tests, verifying the method's reliability [1]. The σ_v is influenced by the thickness and density of overlying layers, with a nearly linear relationship between its magnitude and depth:

$$\sigma_v = \int_0^H \rho(H) g d_H \tag{3}$$

where ρ represents the density, kg/m^3 and g represents the gravitational acceleration, m/s^2.

If density logging data are unavailable, a vertical stress gradient of 0.025 MPa/m can approximate σ_v in the Qinshui Basin, aligning with findings from stress relief measurements in underground coal mines in China [56].

Data on hydraulic fracturing from 95 CBM production wells at depths of 549 to 891 m were gathered from the Shizhuang south block. This information includes details on p_f, p_s, fracturing fluid volume, proppant concentration, and displacement, along with data on coal depth and thickness:

$$\sigma_h = \frac{v}{1-v}(\sigma_v - \alpha P_o) + \frac{E\xi_h}{1-v^2} + \frac{vE\xi_H}{1-v^2} + \alpha P_o \tag{4}$$

$$\sigma_H = \frac{v}{1-v}(\sigma_v - \alpha P_o) + \frac{E\xi_H}{1-v^2} + \frac{vE\xi_h}{1-v^2} + \alpha P_o \tag{5}$$

$$\xi_h = \frac{\sigma_h - \alpha P_o - v(\sigma_H + \sigma_v - 2\alpha P_o)}{E} \tag{6}$$

$$\xi_H = \frac{\sigma_H - \alpha P_o - v(\sigma_h + \sigma_v - 2\alpha P_o)}{E} \tag{7}$$

where v represents the Poisson's ratio; α represents the Biot coefficient; ξ_H represents the maximum horizontal tectonic strain; ξ_h represents the minimum horizontal tectonic strain factor; and E represents the Young's modulus.

Based on the measured horizontal principal stress, the horizontal tectonic strain is determined. The findings indicate a positive relationship between the horizontal tectonic strain factor and burial depth (Figure 3). A linear conversion equation between burial depth and the horizontal tectonic strain factor is established to calculate in situ stress values for each well in the study area.

$$\xi_H = 0.000\,003 \times Depth - 0.000\,6 \tag{8}$$

$$\xi_h = 0.000\,000\,6 \times Depth - 0.000\,4 \tag{9}$$

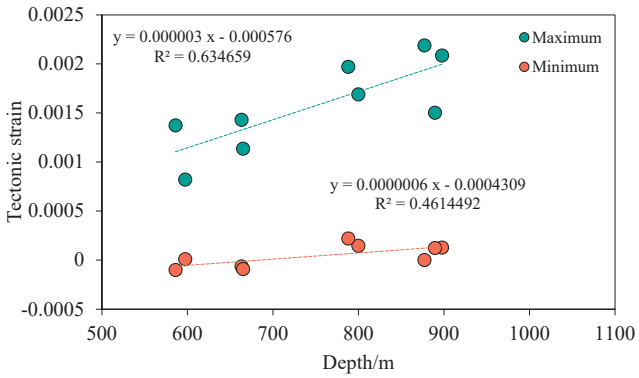

Figure 3. Variation law of tectonic strain with depth in the Shizhuang south block.

Micro-seismic monitoring was conducted on eight wells, ranging in depth from 672 to 982 m, to observe hydraulic fracturing development. Prior to fracturing operations, six high-sensitivity seismic sensors were positioned around the well to detect and capture micro-seismic wave signals generated by fractures within the coal seam. These signals were transformed and used to determine the fracture source's position, with the fracture patterns, directions, and sizes characterized by analyzing the spatial arrangement of seismic source locations.

Fractured coal reservoirs can be classified into three ideal models: a collection of sheets (Model I, Figure 4a), a bundle of matchsticks (Model II, Figure 4b), and a collection of cubes (Model III, Figure 4c) [57]. Model I is particularly suitable for depicting high-rank coals, such as anthracite [58]. The fracture permeability of Model I can be calculated using the equation proposed by Hou [59]:

$$k_f = 8.50 \times 10^{-4} w^2 \varphi_f \tag{10}$$

where k_f represents fracture permeability; w represents fracture width; φ_f represents fracture porosity.

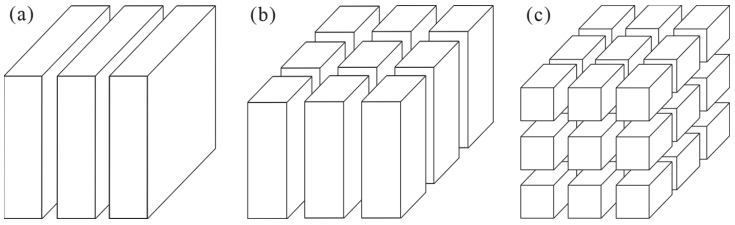

Figure 4. Model evaluating coal reservoir permeability. (**a**) Sheet model; (**b**) Matchstick model; (**c**) Cube model.

Using logging data, permeability inversion of the coal reservoir in the Shizhuang south block was conducted. The fracture width calculation utilized the improved formula introduced by Li et al. [60]:

$$\frac{1}{R_{LLS}} - \frac{1}{R_{LLD}} = \left(\frac{w}{\pi}\right)^m \left[\frac{1}{R_{mf}(d_1 + r_w)^m} - \frac{1}{R_w(d_2 + r_w)^m}\right] \tag{11}$$

where R_{LLS} and R_{LLD} represent shallow and deep lateral resistivity, respectively; m represents the cementation index; R_{mf} and R_w represent the resistivity of mud and formation water, respectively; d_1 and d_2 represent the investigation radius of shallow and deep lateral logs, respectively; r_w represents the radius of the wellbore.

The fracture porosity is calculated using Archie's law and the method proposed by Chatterjee and Pal, with a cementation index of 1.6 and R_{mf} set at 0.65 Ω·m [61]:

$$\varphi_f = \left(\frac{R_{mf}}{R_{LLS}}\right)^{\frac{1}{m}} = \left(\frac{0.65}{R_{LLS}}\right)^{\frac{1}{1.6}} \tag{12}$$

The overall bulk density of coal is determined by the coal skeleton density and the presence of fluids such as water and hydrocarbons. The impact of fluids on the total density is directly linked to coal porosity. Thus, the density (DEN) log response can measure coal porosity. The effective porosity can be determined using the formula provided by Asquith et al. [62]:

$$\varphi_D = \frac{\rho_{ma} - \rho_b}{\rho_{ma} - \rho_{fl}} \tag{13}$$

where φ_D represents the density-derived porosity; ρ_{ma} represents the matrix density; ρ_b represents the formation bulk density; ρ_{fl} represents the fluid density.

Various physical properties display distinct characteristics in logging responses. For instance, low DEN, high caliper (CAL), and high acoustic time difference (AC) typically indicate fracture development, while high gamma (GR) usually indicates high clay content [63–65]. Generally, GR and DEN measurements decline as coal deforms, whereas LLD increases [66,67]. The correlation between logging curves and coal texture is utilized to establish a discriminant equation based on the Fisher discrimination criterion of IBM SPSS Statistics version 26.0 software:

$$F_{undeformed} = 205.502 \times DEN - 0.069 \times GR + 0.002 \times LLD - 155.346 \tag{14}$$

$$F_{cataclastic} = 195.953 \times DEN - 0.119 \times GR + 0.003 \times LLD - 143.129 \tag{15}$$

$$F_{granulated} = 182.551 \times DEN - 0.103 \times GR + 0.003 \times LLD - 120.767 \tag{16}$$

$$F_{cataclastic} = 266.255 \times DEN - 0.037 \times GR + 0.002 \times LLD - 265.722 \tag{17}$$

Geological, property, and geomechanical models of the coal reservoir in the Shizhuang south block were developed using Schlumberger's Petrel software (version 2021). Detailed steps for software modeling and parameter settings are referenced [68].

4. Results

4.1. Stress Magnitudes

The No. 3 coal seam in the Shizhuang south block ranges from 491 m to 1175 m in depth. The σ_v (or p_f) ranges from 10.02 to 31.72 MPa, with a gradient of 2.00 to 3.16 MPa/100 m. The σ_h (or p_s) ranges from 5.29 to 18.47 MPa, exhibiting a gradient of 0.89 to 3.14 MPa/100 m. The σ_H ranges from 8.43 to 30.81 MPa, with a gradient of 1.46 to 5.14 MPa/100 m. These stress parameters (p_o, σ_H, and σ_h) increase linearly with depth. Notably, significant stress gradient values are observed around 550 m depth, where the σ_h

gradient surpasses the vertical stress gradient, indicating substantial tectonic stress in the horizontal direction.

The stress regimes, influenced by both the magnitudes and gradients of change, lead to varying stress distributions across different depths. In the Shizhuang south block, the predominant stress regime is characterized by a strike-slip fault, accounting for 66.4% of the total and spanning depths from 491 m to 1175 m. The normal fault stress regime represents 26.1% and is primarily observed at depths greater than 800 m. The reverse fault stress regime, comprising 7.5%, is predominantly observed at depths shallower than 600 m. Shallow depths (<600 m) exhibit a lack of a normal fault stress regime, suggesting high structural stress. A small amount of data (14%) indicates a normal fault stress regime at depths between 600 m and 800 m, dominated by a strike-slip fault stress regime (78%). Beyond 800 m, the magnitudes of horizontal stress diminish, with a minority of data suggesting a reverse fault stress regime and the majority (52%) indicating a normal fault stress regime. The lateral pressure coefficient (k), defined as the ratio of the average of σ_H and σ_h to σ_v, ranges from 0.48 to 1.63, with 40% of the values exceeding 1 (Figure 5e). As depth increases, changes in σ_H/σ_v, σ_h/σ_v, and k typically correspond to shifts in stress regimes, with an overall decreasing trend.

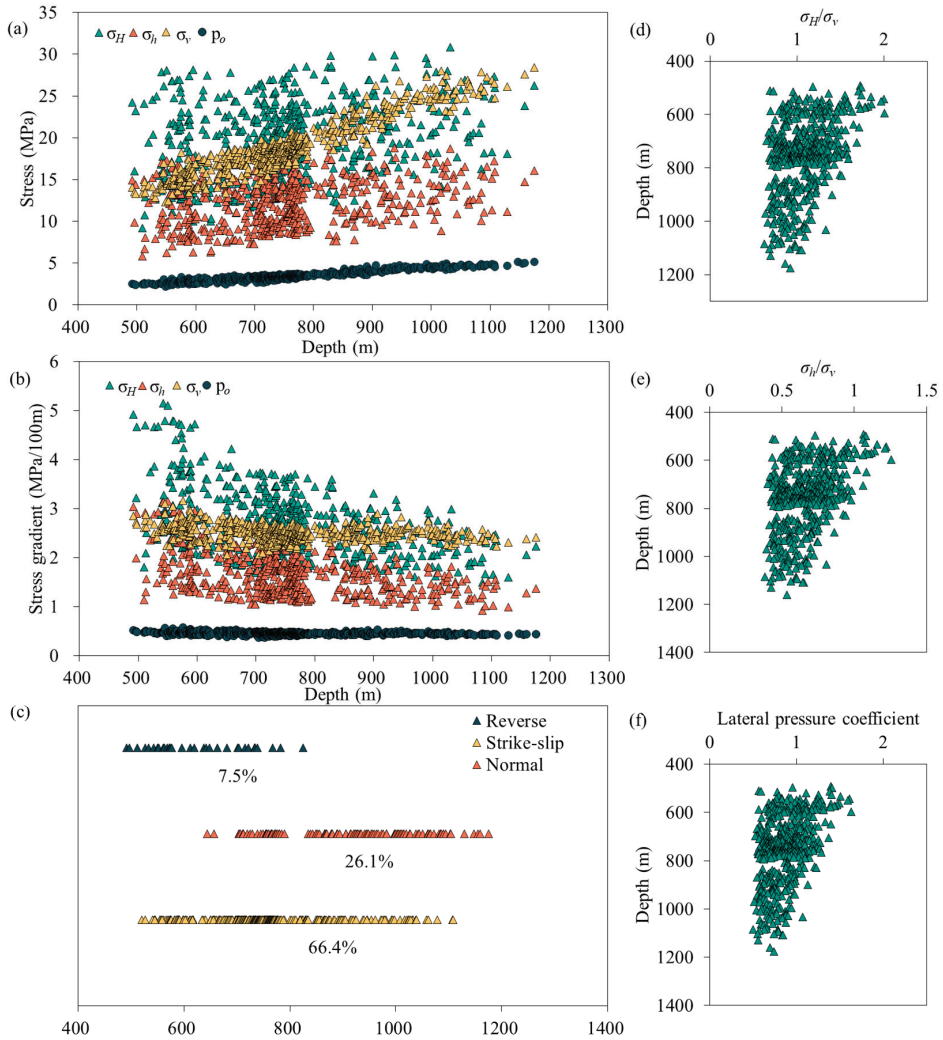

Figure 5. Scatter plot of in situ stress vs. depth. (**a**) Stress magnitudes vs. depth; (**b**) Stress gradient magnitudes vs. depth; (**c**) Stress regimes vs. depth; (**d**) σ_H/σ_v vs. depth; (**e**) σ_h/σ_v vs. depth; (**f**) Lateral pressure coefficient vs. depth.

Horizontal stress differentials are crucial for hydraulic fracturing of unconventional reservoirs and are influenced by stress regime variations [69]. Horizontal stress differences in coals, ranging from 5.8 to 13.0 MPa, generally increase with depth (Figure 6a). However, these differences vary significantly across stress regimes. The reverse fault stress regime demonstrates the greatest horizontal stress disparities (7.26 to 13.03 MPa) at the same depth, followed by the strike-slip fault stress regime (6.00 to 12.68 MPa). The normal fault stress regime displays the lowest values (5.83 to 10.32 MPa), indicating the strength of tectonic stress.

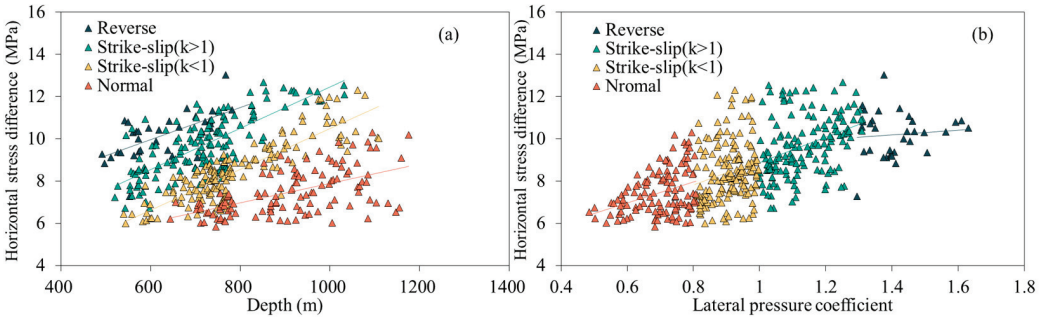

Figure 6. (**a**) The horizontal stress differential vs. depth; (**b**) Plot of horizontal stress difference vs. lateral pressure coefficient for different stress regimes.

In the Shizhuang south block, reservoir pressure ranges from 1.92 to 5.62 MPa, averaging 3.51 MPa. The pressure gradient of the coal reservoirs is 0.34 to 0.57 MPa/100 m, classifying it as an under-pressure reservoir (<0.9 MPa/100 m). Based on fault stress regimes, the Shizhuang south block is divided into five in situ stress zones, all dominated by the strike-slip fault stress type (Figure 7). The fault stress regimes of the CBM wells in each zone show that zones I (Figure 8a) and IV (Figure 8d) have the distribution characteristics of strike-slip fault stress type > normal fault stress type > reverse fault stress type. Zone II (Figure 8b) shows strike-slip fault stress type ≈ normal fault stress type > reverse fault stress type. Zones III (Figure 8c) and V (Figure 8e) are characterized by strike-slip fault stress type > reverse fault stress type > normal fault stress type.

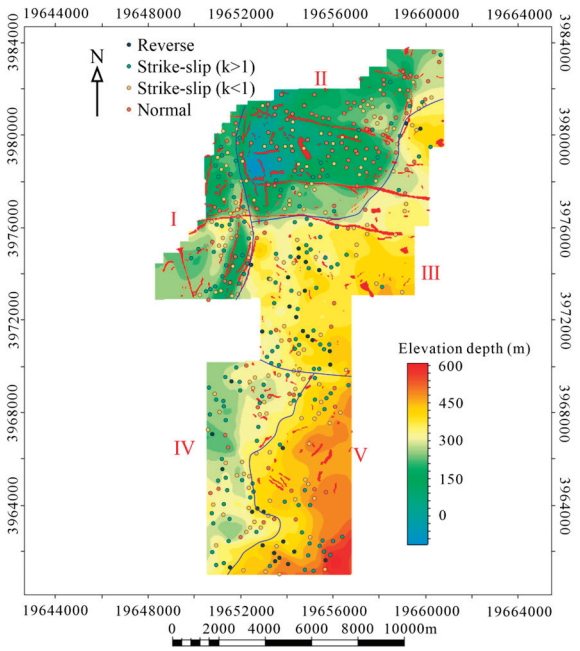

Figure 7. Map of the distribution of fault stress types in Shizhuang south block.

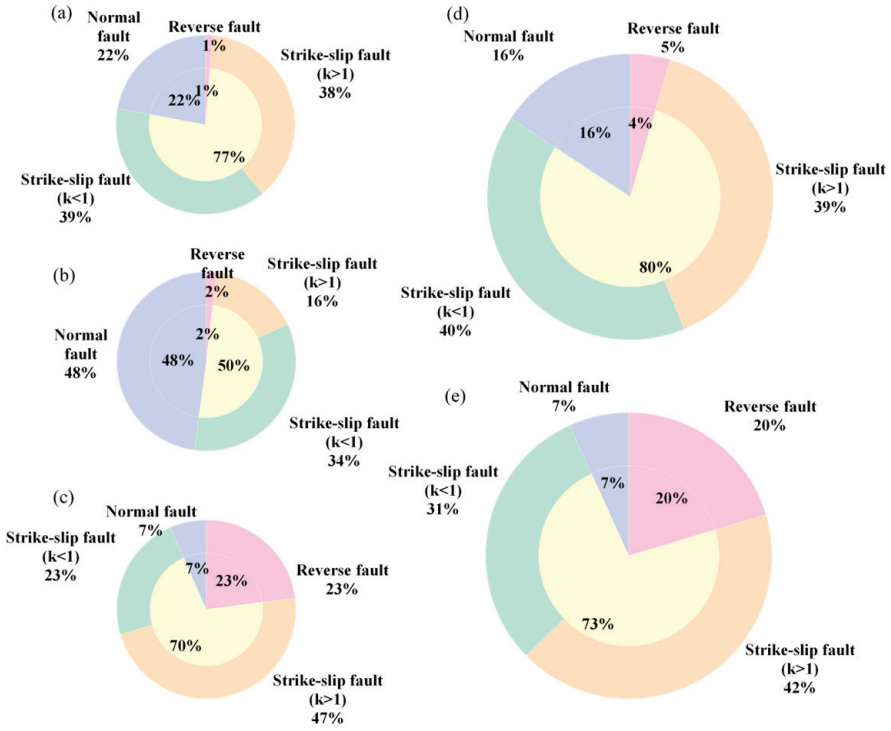

Figure 8. Pie chart of the percentage of fault stress types in the Shizhuang south block. (**a**) In situ stress zone I; (**b**) In situ stress zone II; (**c**) In situ stress zone III; (**d**) In situ stress zone IV; (**e**) In situ stress zone V.

4.2. Geological Parameters

4.2.1. Coal Permeability and Porosity

Figure 9 illustrates the in situ permeability of coal in the Shizhuang south block, which varies between 0.003 and 1.08 mD, with an average of 0.40 mD. Approximately 11.2% of the values are less than 0.1 mD, with a lower limit of about 0.01 mD. Typically, coal in situ permeability decreases with increasing depth. Within the depth range of the coal seams in the Shizhuang south block, permeability varies widely from 0.01 mD to 1 mD (Figure 9c). At depths less than 700 m, permeability rapidly decreases with increasing horizontal stress. Between 800 m and 1200 m, coal seam permeability remains low due to the stress mechanism of highly stressed strike-slip faults. Beyond 1000 m, permeability becomes highly variable with no discernible trend, likely due to the stress-release mechanism of normal faults. The porosity ranges from 2% to 12% (Figure 9b,d), with an average of 7.3%. At burial depths less than 800 m, porosity values exhibit a wider distribution, indicating strong heterogeneity in the coal rock. Beyond 800 m, porosity values become more concentrated, generally falling below 8%, likely due to compaction from increased σ_v. Overall, porosity decreases with increasing burial depth.

4.2.2. Coal Texture

Regionally, coal texture is influenced by both stress and tectonics. In the northwestern part of the Shizhuang south block, where burial depth is large and tectonic activity is significant, granulated coal is highly developed, especially near faults (Figure 10b). The central part of the block, with shallow burial depth and weak tectonic structure, shows a smaller proportion of granulated coal development. Undeformed coal is developed throughout the block and remains relatively stable (Figure 10a). Vertically, as burial depth and tectonic development increase, coal texture transitions from undeformed, cataclastic coal to cataclastic, granulated coal, resulting from increased stress and tectonic deformation (Figure 10c,d).

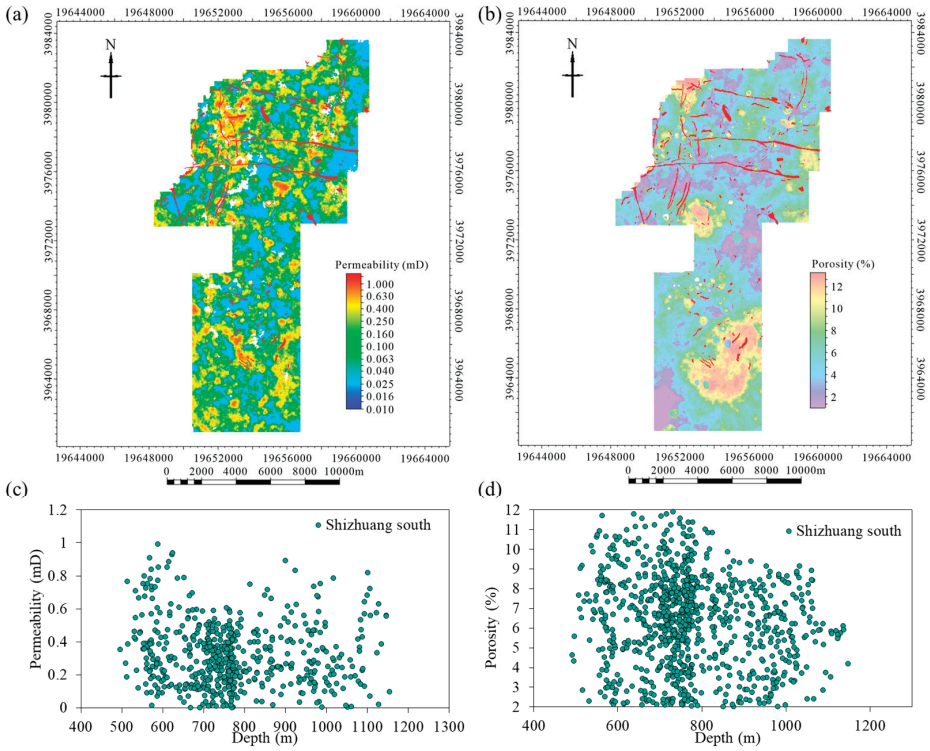

Figure 9. Spatial distribution and measurement points of permeability and porosity. (**a**) Spatial distribution of permeability (mD); (**b**) Spatial distribution of porosity (%); (**c**) Measurement points of permeability; (**d**) Measurement points of porosity.

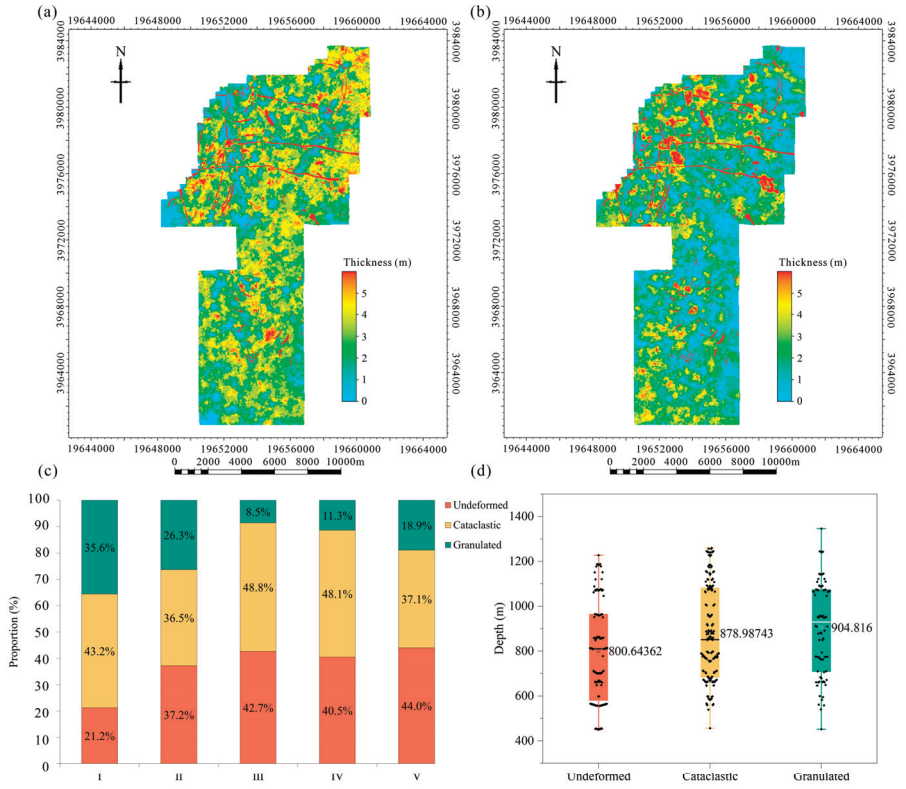

Figure 10. Map of coal texture distribution. (**a**) Undeformed coal; (**b**) Granulated coal; (**c**) Percentage of coal texture in the in-situ stress zones; (**d**) Coal texture vs. depth.

5. Discussion

5.1. Effects of In Situ Stress and Coal Texture on Porosity and Permeability of Coal Reservoirs

Permeability and porosity in coal reservoirs are significantly influenced by in situ stress, with coal texture also playing a critical role [70–73]. Higher stress typically leads to compaction of the coal seam and closure of macroscopic pores and fractures, resulting in reduced porosity and permeability. At the same depth, compressive stresses under reverse and strike-slip faults lead to fault closure, which reduces pore spaces and fractures in coal reservoirs, decreasing coal seam permeability. Conversely, normal faults, formed under gravity and horizontal tension, are more conducive to the formation of highly permeable coal reservoirs.

Tectonic deformation macroscopically leads to structural fragmentation of coal texture and microscopically affects the macromolecular structure of coal, leading to the development of micropores and microfractures, which in turn affects porosity and permeability [74]. Coal seams located at tectonic high points experience tensile stresses, resulting in a fragile coal texture, whereas those at tectonic low points are influenced by extrusion stresses, resulting in a compact coal texture and reduced porosity and permeability. The coal reservoir in the Shizhuang south block is governed by various factors, as indicated by the limited correlation observed among permeability, porosity, and in situ stress (Figure 11).

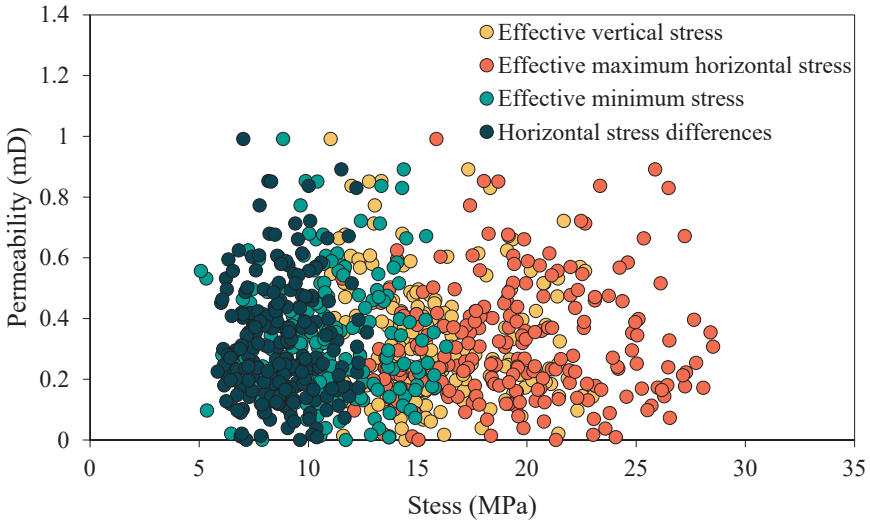

Figure 11. Map of effective stresses vs. permeability.

The structural topographic map of coal seam No. 3 in the Shizhuang south block (Figure 12) shows the region on a slope dipping toward the northwest, with higher elevations in the southeast and lower elevations in the northwest. In the northwestern part of the block, near-north–south- and near-east–west-trending normal faults are well developed.

Figure 13 presents a cross-sectional view of seven testing wells in the Shizhuang south block, demonstrating variations in stress levels and permeability across various tectonic settings. These wells, less than 800 m deep, belong to shallow coal seams. Although some wells are located at tectonic high points (e.g., TS-1 and TS-5), the degree of tectonic deformation in the southeastern part is much smaller than in the northwestern part, resulting in slight or no deformation of the coal reservoirs. Thus, natural fractures are poorly developed, and the coal texture remains undeformed, leading to low in situ permeability. Conversely, wells TS-2 and TS-4, affected by nearby faults, exhibit cataclastic and granulated coal textures, with a well-developed natural fracture network, resulting in high in situ permeability.

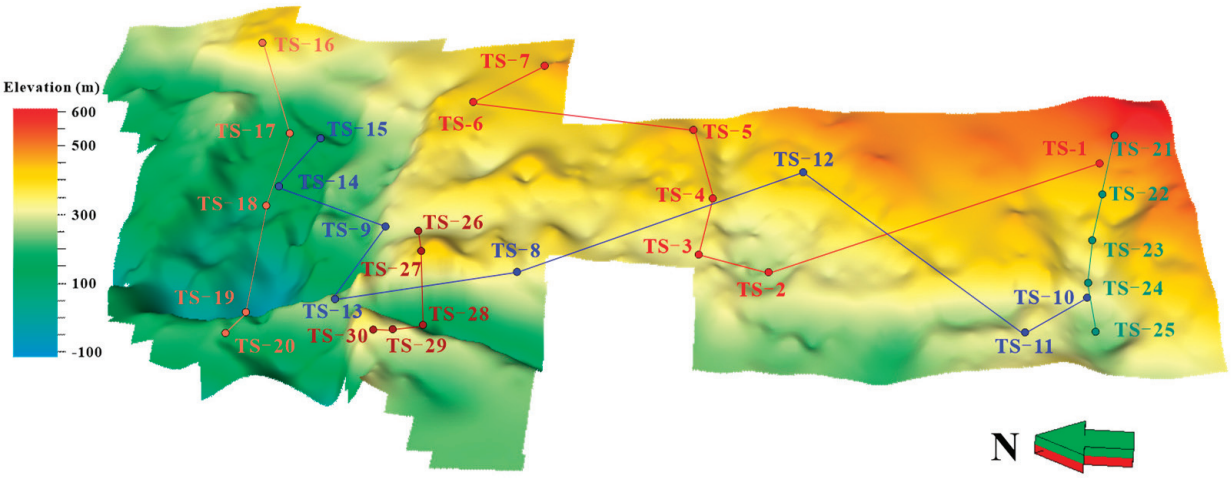

Figure 12. Three-dimensional visualization of the geological formations of coal seam No. 3 within the Shizhuang south block.

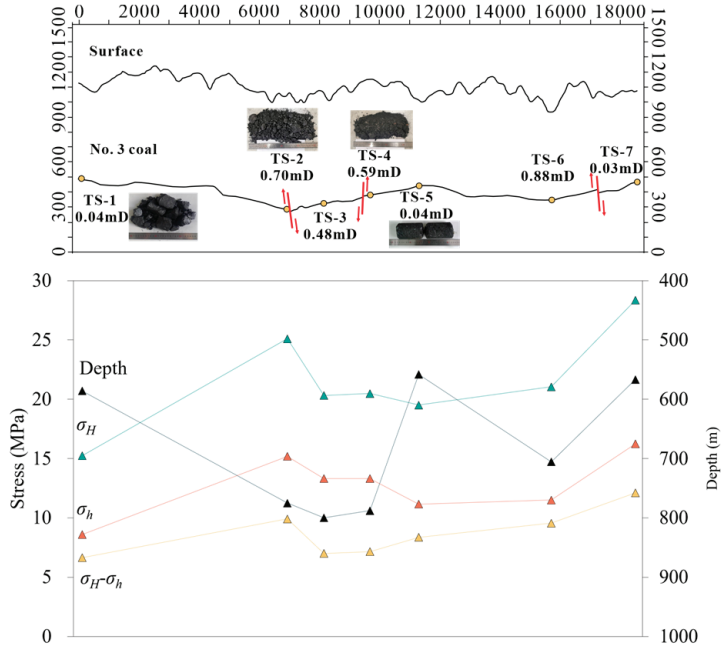

Figure 13. The cross-sectional diagram and parameters (permeability, coal quality, burial depth, and stress magnitude) of test wells in Shizhuang south block.

This research examines the impact of tectonics on in situ stress by characterizing vertical in situ stress within the stratigraphy of the study area. The variation in in situ stress with burial depth in the study block can be categorized into three groups: stable increasing, stable–rapid–stable increasing, and stable–rapid increasing. As burial depth increases from shallow to deep, stress variations occur across different tectonic units. In the tectonic slope zone with shallow burial depth, in situ stress increases steadily with minimal fluctuations (Figure 14). At the microtectonic high point with shallow burial depth, stress increases insignificantly due to limited tectonic deformation (Figure 15). At greater burial depths and in areas of intense tectonic deformation, in situ stresses exhibit rapid increases and significant fluctuations (Figure 16).

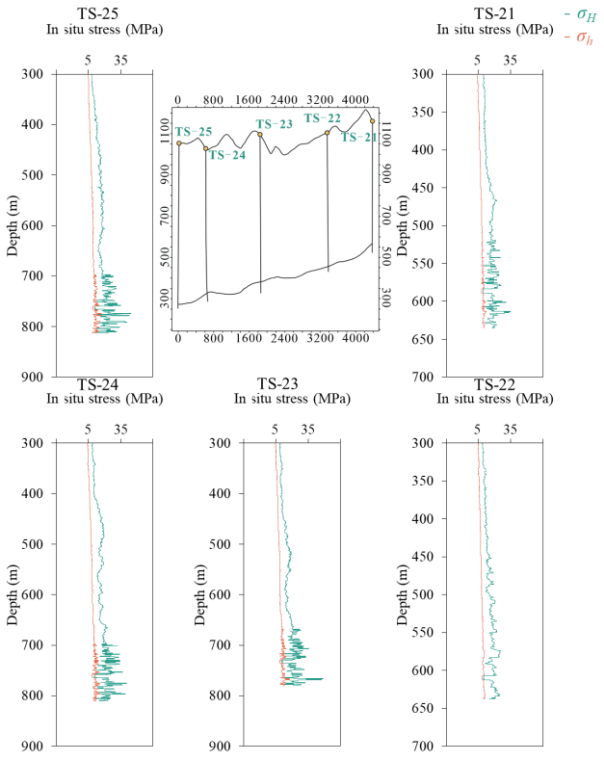

Figure 14. Vertical distribution of well profiles and in situ stresses in the slope zone connecting wells in the Shizhuang south block.

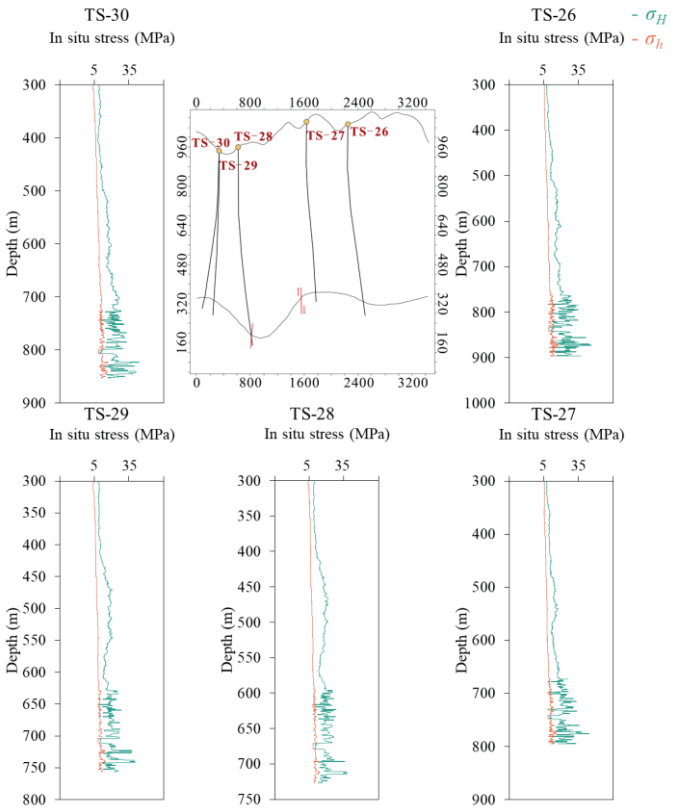

Figure 15. Vertical distribution of microtectonic connecting well profiles and in situ stresses in the Shizhuang block.

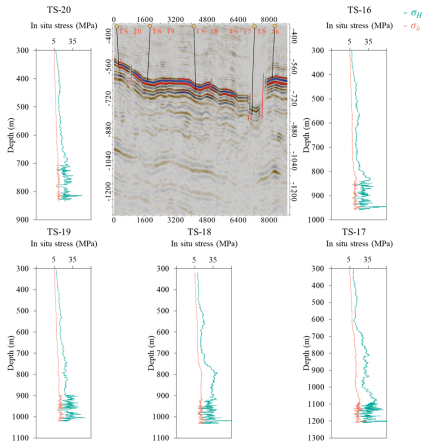

Figure 16. Well section and vertical distribution of in situ stress in the Shizhuang south block.

5.2. The Effect of In Situ Stress on Hydraulic Fracturing of CBM

The Qinshui Basin exhibits lower coal permeability than other coal-bearing basins, necessitating hydraulic fracturing to enhance reservoir flow capacity [75]. Understanding present-day stress magnitudes and regimes is crucial for effective hydraulic fracturing. Data from 95 CBM production wells revealed consistent construction parameters—sand-adding volume, fracturing fluid volume, sand concentration, and displacement rates—across different depth intervals (Figure 17). These findings indicate a standardized fracturing scheme, neglecting variations in depth and in situ stresses. This oversight in depth-related stress variations appears to be a significant technical factor contributing to the decline in gas productivity with increasing depth. Additionally, well fracture pressure and shut-in pressure are influenced by the in situ stress regime during fracturing, aligning with the trend of horizontal stress changes with depth (Figure 17d,e).

Micro-seismic monitoring data from eight wells were analyzed to evaluate the orientation and geometry of hydraulic fractures. Predominantly, fractures are oriented northeast to southwest, with some variations northwest to southeast and east to west, as shown in Table 1 and Figure 18. This orientation, consistent with the maximum principal stress trace in China, suggests that the current maximum horizontal stress orientation is primarily northeast–southwest, resulting from the combined action of the Pacific and Philippine plate subduction under the Eurasian plate. The effect of horizontal stress variations on hydraulic fracture morphology in fracture-developed reservoirs has been elucidated [76]. A high stress magnitude discrepancy generally leads to simple hydraulic fractures, while minimal discrepancy facilitates hydraulic fracture networks [77,78]. In coal cleats, parallel alignment of face cleats with the σ_H orientation results in longer hydraulic fractures under high stress difference conditions [79]. Fracture lengths in the study area decrease with increasing burial depth, as measured by micro-seismic monitoring wells. This indicates that increased vertical stress limits fracture expansion, making the same fracturing scheme unsuitable for areas with significant burial depth variation.

Table 1. Statistical table of micro-seismic event parameters.

Well Name	Fracture Length (m)	Fracture Width (m)	Fracture Height (m)	Azimuth	Depth (m)
TS-8	290	160	56	N51° E	672.38
TS-9	310	180	42	N70° E	774.76
TS-10	250	180	50	N55° W	758.81
TS-11	300	110	66	N55° W	737.14
TS-12	400	65	35	N57° E	764.92
TS-13	280	240	42	N48° E	691.73
TS-14	155	125	46	N40° E	978.23
TS-15	180	140	32	N42° E	982.38

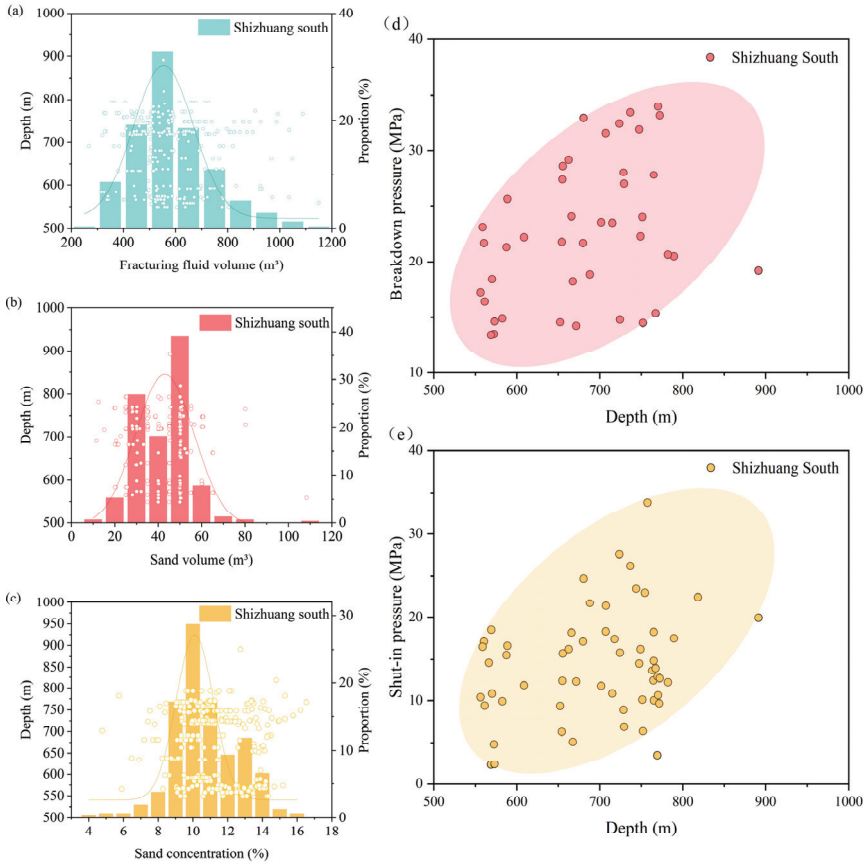

Figure 17. Fracturing construction parameters vs. depth. (**a**) Fracturing fluid volume; (**b**) Sand volume; (**c**) Sand concentration; (**d**) Breakdown pressure; (**e**) Shut-in pressure.

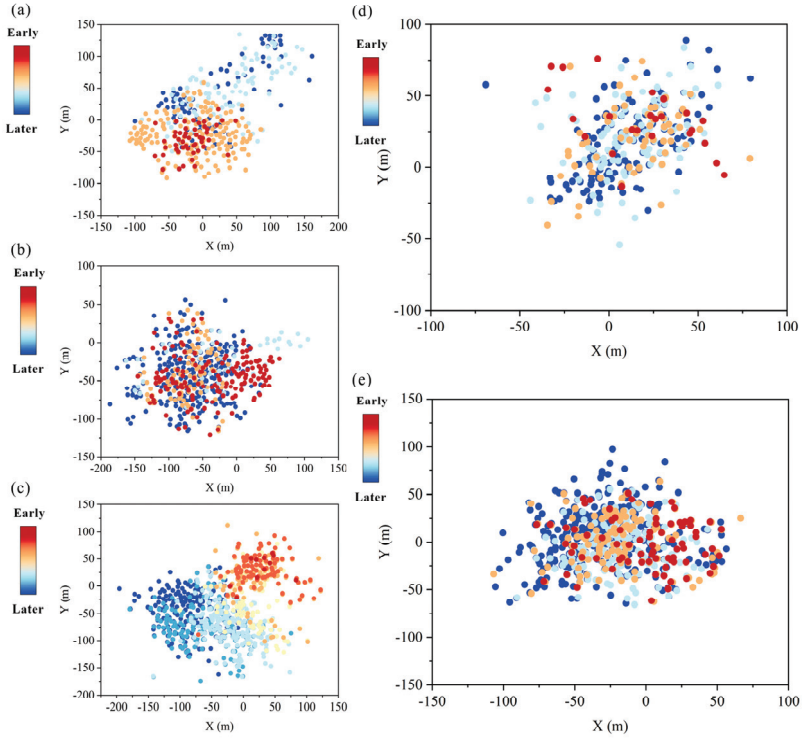

Figure 18. Statistical map of micro-seismic events for parameter wells. (**a**) TS-8; (**b**) TS-9; (**c**) TS-13; (**d**) TS-14; (**e**) TS-15.

Hydraulic fracture morphology is contingent upon prevailing stress conditions and pre-existing fractures, influenced by structural trends and coal texture [80–82]. Coal texture distribution is strongly associated with structural characteristics. An analysis of a cross-section featuring four wells with coal core images obtained from drilling reveals that cataclastic and granulated coal are predominantly found near fault planes (e.g., TS-2 and TS-4), whereas undeformed coal is observed within folds (e.g., TS-1 and TS-5) [83] (Figure 13). In hydraulic fracturing, there is notable dispersion in micro-seismic events, with no discernible correlation between these events' distribution and the dominant fracture orientation or maximum horizontal stress. Fracture geometry in cataclastic coals supports this observation. Hydraulic fractures in these circumstances are influenced by a combination of stress and existing fractures, resulting in fractures forming at various angles and orientations (Figure 19).

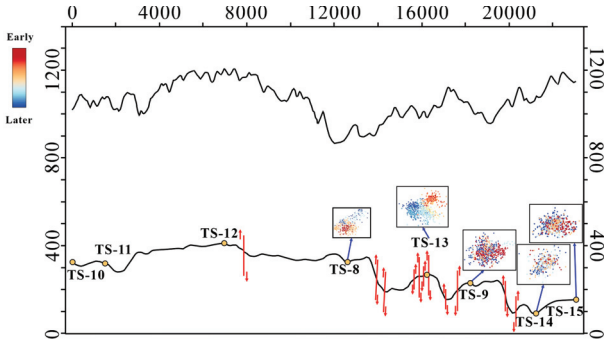

Figure 19. The cross-sectional diagram and micro-seismic parameters of test wells in Shizhuang south block.

In wells like TS-13, located near fault planes, micro-seismic data sets exhibit a discontinuous and extensively distributed pattern. The primary fracture exhibits significant angles with its branches, along with parallel fractures. In contrast, in structurally low areas, predominant fracture and branch propagation occur along the maximum horizontal orientation due to elevated differential stresses, leading to a nearly straight arrangement of micro-seismic data, as observed in examples like TS-8 and TS-14. It is crucial to consider various fracturing schemes based on factors, such as burial depth, stress regimes, coal textures, and structural trends, rather than relying on standardized construction parameters. Deeper coal seams exhibit a higher propensity for intricate fractures, posing greater difficulties in sand filling. Mitigating complex fracture geometries in these regions requires higher pumping rates and treatment pressures compared to structural lows.

According to the CBM exploration and development theories during China's "13th Five-Year Plan" and "14th Five-Year Plan," the fracturing process for CBM has shifted from conventional fracturing to ultra-large-scale extreme volume fracturing. This transition has seen the operational scale evolve from medium–small displacement rates (7 to 12 m^3/min), medium–small fluid volumes (<10,000 m^3/well), and medium–small proppant volumes (30 to 70 m^3/stage) to large displacement rates (14 to 18 m^3/min), large fluid volumes (>20,000 m^3/well), and large proppant volumes (300 to 450 m^3/stage). The daily gas production from vertical and directional wells increased from 300–2000 m^3/d to 3000–20000 m^3/d, while the production from horizontal wells increased from 3000–10,000 m^3/d to 30,000–100,000 m^3/d [84]. In the Ordos Basin, CNPC has experienced a progression in deep CBM development from conventional fracturing (30 to 70 m^3/stage of proppant, 7 to 12 m^3/min displacement) to large-scale fracturing (170 to 300 m^3/stage of proppant, 8 to 14 m^3/min displacement), and finally to ultra-large-scale extreme volume fracturing (300 to 450 m^3/stage of proppant, 14 to 18 m^3/min displacement), with operational pressure increasing from 30 MPa to 60 MPa [85]. The average initial daily gas production per well in the Ordos Basin is 11 $\times$ 10^4 m^3. For example, in the Daning–Jixian Block of deep coalbed methane, the average proppant scale in large-scale volume fracturing

of vertical cluster wells is six times that of conventional fracturing wells. The average gas production and estimated ultimate recovery are 2.7 times and twice that of conventional fracturing wells, respectively. The Jishen 6–7 Ping 01 horizontal well, which underwent large-scale extreme volume fracturing with a single-stage fluid volume of 3000 m^3, a proppant volume of 350 m^3, and a displacement rate of 18 m^3/min, achieved an average daily gas production of 5.82 × 10^4 m^3, with a peak daily production of 10.1 × 10^4 m^3. In the Zhengzhuang North-Qinnan West Block, where coal seam depths range from 650 to 1500 m and are similar to those in the study area, the fracturing fluid volume in vertical wells was increased from 500–800 m^3 to 1300–2000 m^3, the displacement rate was increased from 4–6 m^3/min to 10–14 m^3/min, and the proppant concentration was increased from 8% to 12–15%, resulting in an average single-well production increase of 1190 m^3/d. In horizontal wells, large-scale, high-displacement fracturing technology was employed, increasing the single-stage fluid volume from 450–600 m^3 to 2000 m^3, the single-stage proppant volume from 30–50 m^3 to 150 m^3, and the displacement rate from 6 m^3/min to 15 m^3/min, leading to an average daily gas production increase from 8000 m^3/d to 18,000 m^3/d [86].

5.3. Statistics of Geo-Engineering Parameters in Different Stress Zones and Development Recommendations

Figure 20 highlights the influence of hydraulic fracturing and coal reservoir pore permeability on production capacity. In the Shizhuang south block, the No. 3 coal seam contains 731 vertical CBM production wells and 490 directional CBM production wells, collectively producing an average daily gas production rate of 299 m^3/d per well. In contrast, single-branch horizontal wells exhibit a higher average production rate of 1892 m^3/d. Horizontal wells are preferred for CBM production due to their ability to significantly alter coal reservoirs, establish intricate fracture networks, stimulate seeps, and ultimately enhance overall coal reservoir permeability.

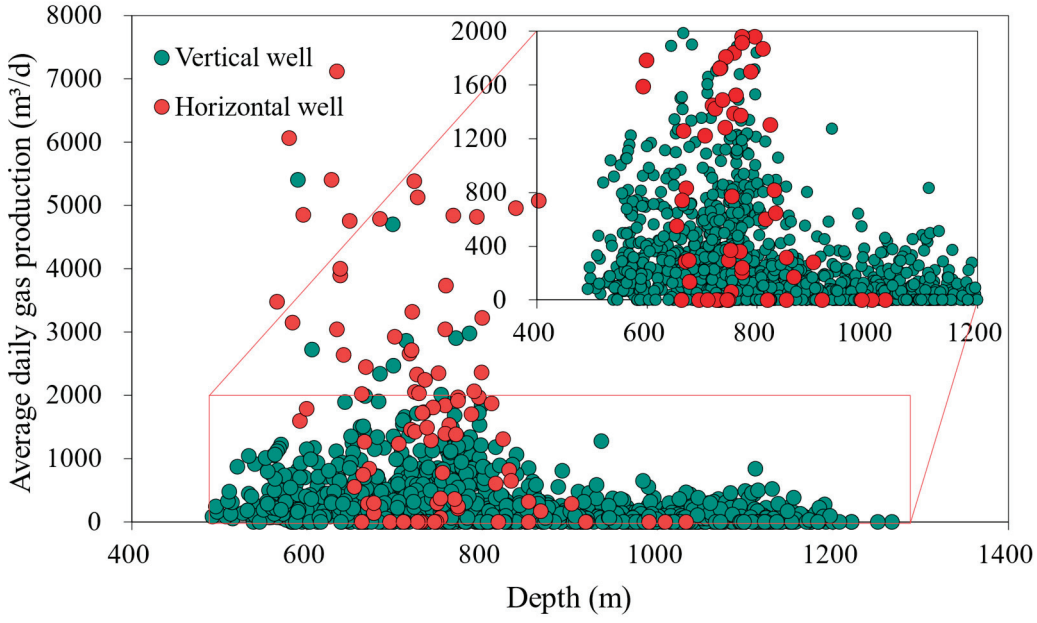

Figure 20. Average daily gas production versus depth for different types of wells in the Shizhuang south block.

High-producing wells are primarily found at depths below 800 m. These wells are situated in coal reservoirs with excellent porosity and permeability. In contrast, CBM wells at greater depths show minimal to no methane production, reflecting deteriorating geological conditions. Statistical results indicate that CBM wells in in situ stress zones III and IV have higher average daily gas production (Figure 21) and wells exceeding 1000 m^3/d account for 13.2% and 19.4%, respectively. These wells are characterized by shorter gas breakthrough

times, relatively higher gas breakthrough pressures, lower daily water production, and higher ratio of critical desorption pressure to initial reservoir pressure. The proportion of coalbed methane wells with gas breakthrough times less than 60 days in in situ stress zones III and IV reaches 33.5% and 31.3%, respectively.

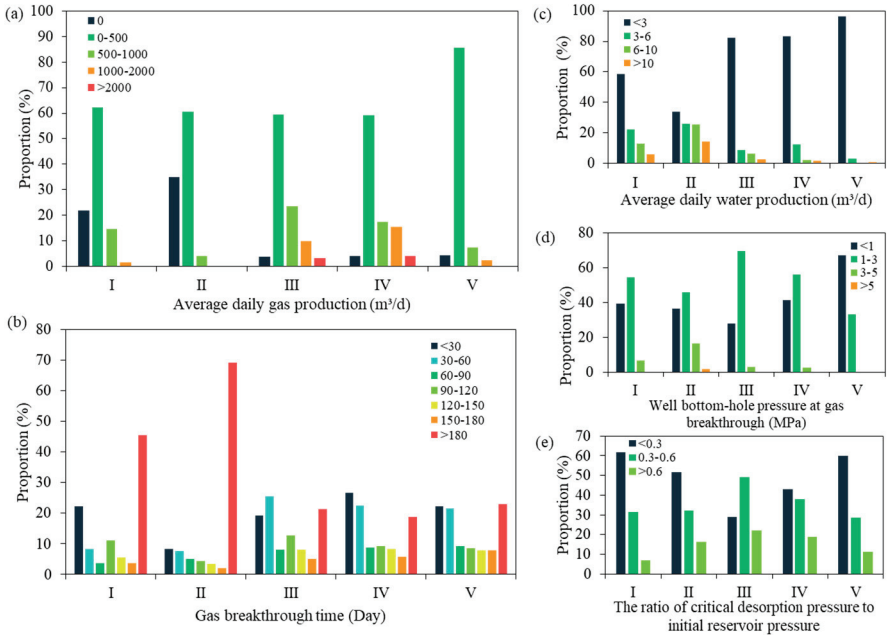

Figure 21. Statistical map of engineering parameters of production wells within the tectonic unit. (**a**) Average daily gas production; (**b**) Gas breakthrough time; (**c**) Average daily water production; (**d**) well bottom pressure at gas breakthrough; (**e**) The ratio of critical desorption pressure to initial reservoir pressure.

The percentage of daily water production of CBM wells in in situ stress zones III and IV below 3 m^3/d stand at 82.2% and 83.4%, while the percentage of gas breakthrough pressures ranging from 1 to 3 MPa are 69.3% and 56.0%. Additionally, the percentage of critical desorption pressure to initial reservoir pressure exceeding 0.6 are 22.1% and 19.0%. A high ratio of critical desorption pressure to initial reservoir pressure accelerates coalbed methane desorption by requiring a smaller reduction in coal reservoir pressure to reach critical desorption pressure. Low water production during drainage and pressure reduction indicates efficient pressure transfer in coal reservoirs, benefiting CBM production. Reduced water content in the coal reservoir enhances stability during the gas production phase.

In terms of geological parameters, in situ stress zones III and IV exhibit higher porosity, permeability, and gas content, with coal textures dominated by undeformed and cataclastic coals (Figure 22). High permeability indicates strong gas transmission capability, while high gas content suggests significant resource potential. The primary and fractured coal structures indicate that the coal reservoirs can be effectively fractured to increase permeability at later stages.

For zones I and II, characterized by high in situ stress and relatively broken coal texture, selecting fracturing fluids with low friction resistance is crucial to improving sand-carrying capacity. Viscoelastic surfactant clean fracturing fluid can prevent reservoir damage during hydraulic fracturing. Alternatively, variable-viscosity slickwater, combining the high bearing capacity of high-viscosity slickwater with the drag-reduction performance of traditional slickwater, can form an extensive proppant fracturing network and enhance production.

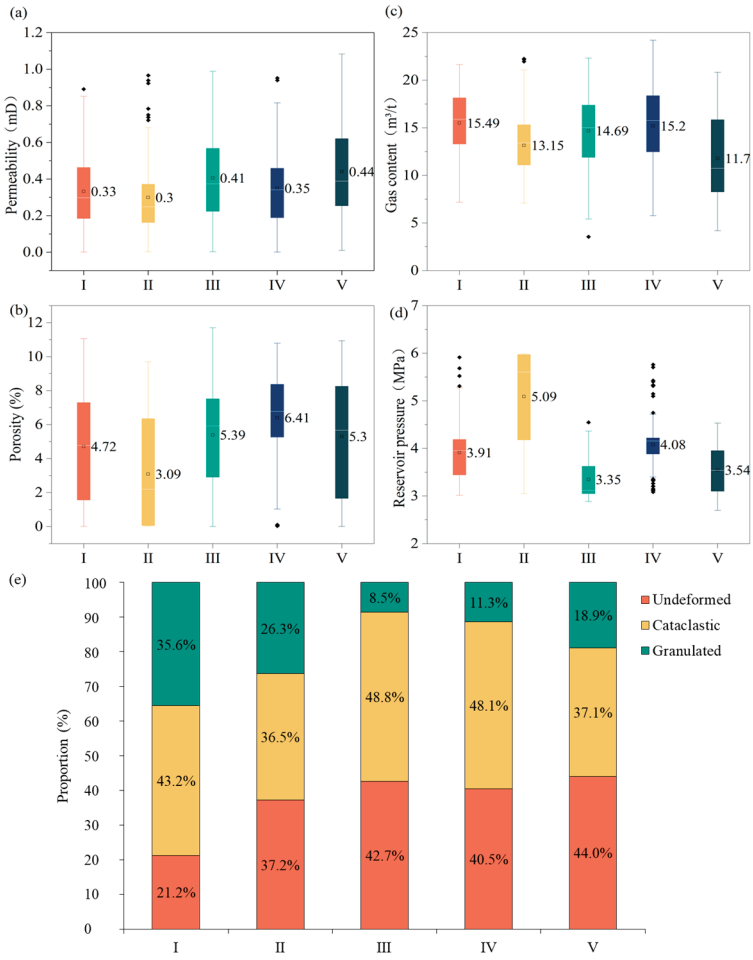

Figure 22. Statistical map of geological parameters of production wells within the tectonic unit. (**a**) Permeability; (**b**) Gas content; (**c**) Porosity; (**d**) Reservoir pressure; (**e**) Coal texture.

Regarding proppant selection, coal, as a low-permeability reservoir, typically has natural microfractures and the potential for additional microfractures during fracturing. Traditional proppants often fail to keep these small fractures open. Injecting nanosized proppant into the reservoir can fill microfractures along the main fracture before injecting conventional fracturing proppant, effectively supporting the microfractures. For zones III and IV, low-density proppants with decreased density or hollow structures can be used to enhance fracture creation. Zone V, with lower gas content, is less economical to develop but can be considered a potential future development area.

6. Conclusions

In the southern section of the Shizhuang area within the Qinshui Basin, in situ stresses within coal deposits increase in magnitude with depth, while the gradient and lateral pressure coefficients decrease. Due to the large depth range of the coal seams, complex stress regimes exist. In the Shizhuang south block, the strike-slip fault stress regime is predominant, with normal fault stress regimes mainly distributed at depths greater than 800 m and reverse fault stress regimes at depths less than 600 m. Horizontal stress differences vary by stress regime, being largest for reverse fault stress, followed by strike-slip fault stress, and smallest for normal fault stress. The horizontal stress difference is positively correlated with burial depth. Coal permeability ranges from 0.003 to 1.08 mD, averaging 0.4 mD, while porosity ranges from 2% to 12%, averaging 7.3%. Both porosity and permeability generally decrease with increasing stress but are enhanced by coal texture and tectonics (faulting).

Micro-seismic occurrences associated with hydraulic fracturing indicate that the primary orientation of σ_H in the Shizhuang south block is northeast–southwest, with some localized variations in the northwest–southeast and east–west directions. The formation of fractures through hydraulic fracturing is influenced by tectonic strike, coal quality, and pre-existing fractures. Conventional small-scale fracturing techniques are less effective in deep-seated CBM development or tectonic low points, as proppant-supported profiles are inadequate. Fracture length, width, and height measured by micro-seismic monitoring wells decrease with increasing burial depth, indicating that the same fracturing scheme is not applicable across areas with significant depth variation. Enhancing proppant dosage and pumping rate has proven successful in CBM development. The study area is divided into five stress zones, with geo-engineering parameters for each zone documented and recommendations for fracturing fluids and proppants provided.

Author Contributions: Conceptualization, X.M. and S.C.; methodology, X.M.; software, X.M.; validation, B.Z., H.W., and S.T.; formal analysis, S.C.; investigation, X.M.; resources, H.W.; data curation, B.Z.; writing—original draft preparation, X.M.; writing—review and editing, S.C.; visualization, X.M.; supervision, S.T.; project administration, S.T.; funding acquisition, S.T. All authors have read and agreed to the published version of the manuscript.

Funding: This research was supported by China United Coalbed Methane Co., Ltd. Seven-Year Action Plan Technology Project: Research on Coalbed Methane Storage and Transportation Technology (CNOOC-KJ135ZDXM 40 ZL01), the National Natural Science Foundation of China (42272200), and Tackling applied science and technology projects of China National Petroleum Corporation (2023ZZ18).

Data Availability Statement: The data presented in this study are available upon request from the corresponding author due to privacy restrictions.

Acknowledgments: The authors are grateful to the editor and anonymous reviewers for their careful reviews and detailed comments, which helped to substantially improve the manuscript.

Conflicts of Interest: The authors declare no conflicts of interest.

References

1. Chen, S.; Tao, S.; Tang, D. In situ coal permeability and favorable development methods for coalbed methane (CBM) extraction in China: From real data. *Int. J. Coal Geol.* **2024**, *284*, 104472. [CrossRef]
2. Huang, Q.; Du, Z.; Liu, H.; Niu, Q.; Fang, H.; Yang, J.; Lou, M. Investigation of cleat and micro-fracture and its aperture distribution in the coals of different ranks in North China: Relative to reservoir permeability. *Front. Earth Sci.* **2023**, *10*, 1048042. [CrossRef]
3. Li, R.; Jin, L.; Wang, S.; Liu, H.; Cui, Z.; Xiang, W. A new mode of visible fracture system in coal seams and its implications for coalbed methane seepage. *Geofluids* **2023**, *2023*, 2455954. [CrossRef]
4. Ren, F.; Zhou, F.; Jeffries, M.; Beaney, S.; Sharma, V.; Lai, W. Affecting Factors on History Matching Field-Level Coal Seam Gas Production from the Surat Basin, Australia. *Energy Fuels* **2024**, *38*, 3131–3147. [CrossRef]
5. Wang, W.; Liu, S.; Sang, S.; Du, R.; Liu, Y. A Study on the Production Simulation of Coal–Shale Interbedded Coal Measure Superimposed Gas Reservoirs under Different Drainage Methods. *Processes* **2023**, *11*, 3424. [CrossRef]
6. Zhou, D.; Wang, J.; Wang, B.; Gao, D.; Zhao, J. Physical characteristics and controlling factors of coal gas reservoir in Pingdingshan No. 10 coal mine. *Processes* **2023**, *11*, 3130. [CrossRef]
7. Ma, T.; Liu, J.; Fu, J.; Wu, B. Drilling and completion technologies of coalbed methane exploitation: An overview. *Int. J. Coal Sci. Technol.* **2022**, *9*, 68. [CrossRef]
8. Tao, S.; Pan, Z.; Tang, S.; Chen, S. Current status and geological conditions for the applicability of CBM drilling technologies in China: A review. *Int. J. Coal Geol.* **2019**, *202*, 95–108. [CrossRef]
9. Zhang, R.; Wang, P.; Cheng, Y.; Shu, L.; Liu, Y.; Zhang, Z.; Zhou, H.; Wang, L. A new technology to enhance gas drainage in the composite coal seam with tectonic coal sublayer. *J. Nat. Gas Sci. Eng.* **2022**, *106*, 104760. [CrossRef]
10. Danesh, N.N.; Zhao, Y.; Teng, T.; Masoudian, M.S. Prediction of interactive effects of CBM production, faulting stress regime, and fault in coal reservoir: Numerical simulation. *J. Nat. Gas Sci. Eng.* **2022**, *99*, 104419. [CrossRef]
11. Pan, J.; Du, X.; Wang, X.; Hou, Q.; Wang, Z.; Yi, J.; Li, M. Pore and permeability changes in coal induced by true triaxial supercritical carbon dioxide fracturing based on low-field nuclear magnetic resonance. *Energy* **2024**, *286*, 129492. [CrossRef]
12. Yang, R.; Chen, J.; Qin, X.; Huang, Z.; Li, G.; Liu, L. Stress evolution and permeability enhancement mechanism of multistage cavity completion in coalbed methane horizontal wells. *SPE J.* **2023**, *28*, 2767–2789. [CrossRef]
13. Yao, Y.; Liu, D.; Qiu, Y. Variable gas content, saturation, and accumulation characteristics of Weibei coalbed methane pilot-production field in the southeastern Ordos Basin, China. *AAPG Bull.* **2013**, *97*, 1371–1393. [CrossRef]

14. Liu, D.; Jia, Q.; Cai, Y.; Gao, C.; Qiu, F.; Zhao, Z.; Chen, S. A new insight into coalbed methane occurrence and accumulation in the Qinshui Basin, China. *Gondwana Res.* **2022**, *111*, 280–297. [CrossRef]
15. Chen, S.; Zhang, Y.; Tang, D.; Tao, S.; Pu, Y.; Chen, Z. Present-day stress regime, permeability, and fracture stimulations of coal reservoirs in the Qinshui Basin, North China. *AAPG Bulletin* 2024, (20,240,401). Available online: https://archives.datapages.com/data/bulletns/aop/2024-04-01/aapgbltn22056aop.html (accessed on 15 May 2024).
16. Xia, Y.; Yang, X.; Hu, C.; Lin, H.; Li, H. Sedimentary infill of Early-Middle Jurassic in the southeastern Tarim Basin and its constraints on the evolution of the Altyn Tagh Fault in the Northeast Tibet Plateau. *Mar. Pet. Geol.* **2024**, *161*, 106657. [CrossRef]
17. Liu, G.; Li, J.; Qi, X.; Zhu, M. Geochemistry of High-Maturity Crude Oil and Gas from Deep–Ultradeep Reservoirs and Their Geological Importance in a Foreland Basin: A Case Study of the Southern Thrust Belt, Junggar Basin, Northwest China. *J. Energy Eng.* **2024**, *150*, 04023051. [CrossRef]
18. Bott, M.H.P. The mechanics of oblique slip faulting. *Geol. Mag.* **1959**, *96*, 109–117. [CrossRef]
19. Jones, O.T. The Dynamics of Faulting and Dyke Formation: With Applications to Britain. *Nature* **1942**, *149*, 651–652. [CrossRef]
20. Salmachi, A.; Rajabi, M.; Wainman, C.; Mackie, S.; McCabe, P.; Camac, B.; Clarkson, C. History, geology, in situ stress pattern, gas content and permeability of coal seam gas basins in Australia: A review. *Energies* **2021**, *14*, 2651. [CrossRef]
21. Han, J.; Zhang, H.; Liang, B.; Rong, H.; Lan, T.; Liu, Y.; Ren, T. Influence of large syncline on in situ stress field: A case study of the Kaiping Coalfield, China. *Rock Mech. Rock Eng.* **2016**, *49*, 4423–4440. [CrossRef]
22. Pu, Y.; Li, S.; Tang, D.; Chen, S. Effect of magmatic intrusion on in situ stress distribution in deep coal measure strata: A case study in Linxing Block, eastern margin of Ordos Basin, China. *Nat. Resour. Res.* **2022**, *31*, 2919–2942. [CrossRef]
23. Yu, G.; Liu, K.; Xi, K.; Yang, X.; Yuan, J.; Xu, Z.; Zhou, L.; Hou, S. Variations and causes of in-situ stress orientations in the Dibei-Tuziluoke Gas Field in the Kuqa Foreland Basin, western China. *Mar. Pet. Geol.* **2023**, *158*, 106528. [CrossRef]
24. Zeng, L.; Song, Y.; Liu, G.; Tan, X.; Xu, X.; Yao, Y.; Mao, Z. Natural fractures in ultra-deep reservoirs of China: A review. *J. Struct. Geol.* **2023**, *175*, 104954. [CrossRef]
25. Ganguli, S.S.; Sen, S. Investigation of present-day in-situ stresses and pore pressure in the south Cambay Basin, western India: Implications for drilling, reservoir development and fault reactivation. *Mar. Pet. Geol.* **2020**, *118*, 104422. [CrossRef]
26. Rajabi, M.; Tingay, M.; Heidbach, O.; Hillis, R.; Reynolds, S. The present-day stress field of Australia. *Earth-Sci. Rev.* **2017**, *168*, 165–189. [CrossRef]
27. Rajabi, M.; Esterle, J.; Heidbach, O.; Travassos, D.; Fumo, S. Characterising the contemporary stress orientations near an active continental rifting zone: A case study from the Moatize Basin, central Mozambique. *Basin Res.* **2022**, *34*, 1292–1313. [CrossRef]
28. Zhang, Z.; Qin, Y.; You, Z.; Yang, Z. Distribution characteristics of in situ stress field and vertical development unit division of CBM in Western Guizhou, China. *Nat. Resour. Res.* **2021**, *30*, 3659–3671. [CrossRef]
29. Burra, A.; Esterle, J.S.; Golding, S.D. Horizontal stress anisotropy and effective stress as regulator of coal seam gas zonation in the Sydney Basin, Australia. *Int. J. Coal Geol.* **2014**, *132*, 103–116. [CrossRef]
30. Ren, P.; Wang, Q.; Tang, D.; Xu, H.; Chen, S. In situ Stress–Coal Structure Relationship and Its Influence on Hydraulic Fracturing: A Case Study in Zhengzhuang Area in Qinshui Basin, China. *Nat. Resour. Res.* **2022**, *31*, 1621–1646. [CrossRef]
31. Zou, G.; Zhang, Q.; Peng, S.; She, J.; Teng, D.; Jin, C.; Che, Y. Influence of geological factors on coal permeability in the Sihe coal mine. *Int. J. Coal Sci. Technol.* **2022**, *9*, 6. [CrossRef]
32. Mou, P.; Pan, J.; Wang, K.; Wei, J.; Yang, Y.; Wang, X. Influences of hydraulic fracturing on microfractures of high-rank coal under different in-situ stress conditions. *Fuel* **2021**, *287*, 119566. [CrossRef]
33. Huang, J.; Morris, J.P.; Fu, P.; Settgast, R.R.; Sherman, C.S.; Ryerson, F.J. Hydraulic-Fracture-Height Growth Under the Combined Influence of Stress Barriers and Natural Fractures. *SPE J.* **2018**, *24*, 302–318. [CrossRef]
34. Fu, H.; Wang, X.; Zhang, L.; Gao, R.; Li, Z.; Zhu, X.; Xu, W.; Li, Q.; Xu, T. Geological controls on artificial fracture networks in continental shale and its fracability evaluation: A case study in the Yanchang Formation, Ordos Basin, China. *J. Nat. Gas Sci. Eng.* **2015**, *26*, 1285–1293. [CrossRef]
35. Rajabi, M.; Tingay, M.; Heidbach, O. The present-day stress field of New South Wales, Australia. *Aust. J. Earth Sci.* **2016**, *63*, 1–21. [CrossRef]
36. Rajabi, M.; Tingay, M.; King, R.; Heidbach, O. Present-day stress orientation in the Clarence-Moreton Basin of New South Wales, Australia: A new high density dataset reveals local stress rotations. *Basin Res.* **2017**, *29*, 622–640. [CrossRef]
37. Li, S.; Qin, Y.; Tang, D.; Shen, J.; Wang, J.; Chen, S. A comprehensive review of deep coalbed methane and recent developments in China. *Int. J. Coal Geol.* **2023**, *279*, 104369. [CrossRef]
38. Qin, Y. Research progress of symbiotic accumulation of coal measure gas in China. *Nat. Gas Ind. B* **2018**, *5*, 466–474. [CrossRef]
39. Tao, S.; Chen, S.; Pan, Z. Current status, challenges, and policy suggestions for coalbed methane industry development in China: A review. *Energy Sci. Eng.* **2019**, *7*, 1059–1074. [CrossRef]
40. Ni, X.; Zhao, Z.; Wang, Y.; Wang, L. Optimisation and application of well types for ground development of coalbed methane from no. 3 coal seam in shizhuang south block in Qinshui basin, Shanxi province, China. *J. Pet. Sci. Eng.* **2020**, *193*, 107453. [CrossRef]
41. Su, X.; Lin, X.; Zhao, M.; Song, Y.; Liu, S. The upper Paleozoic coalbed methane system in the Qinshui basin, China. *AAPG Bull.* **2005**, *89*, 81–100. [CrossRef]
42. Ni, X.; Jia, Q.; Wang, Y. The Relationship between Current Ground Stress and Permeability of Coal in Superimposed Zones of Multistage Tectonic Movement. *Geofluids* **2019**, *2019*, 9021586. [CrossRef]

43. Cao, L.; Yao, Y.; Cui, C.; Sun, Q. Characteristics of in-situ stress and its controls on coalbed methane development in the southeastern Qinshui Basin, North China. *Energy Geosci.* **2020**, *1*, 69–80. [CrossRef]
44. Yang, S.; Yao, R.; Cui, X.; Chen, Q.; Huang, L. Analysis of the characteristics of measured stresses in Chinese mainland. *Chin. J. Geophys.* **2012**, *55*, 708–718. [CrossRef]
45. Heidbach, O.; Rajabi, M.; Cui, X.; Fuchs, K.; Müller, B.; Reinecker, J.; Reiter, K.; Tingay, M.; Wenzel, F.; Xie, F.; et al. The World Stress Map database release 2016: Crustal stress pattern across scales. *Tectonophysics* **2018**, *744*, 484–498. [CrossRef]
46. *GB/T 24504-2009*; The Method of Injection/Falloff Well Test for Coalbed Methane Well. National Coal Standardization Technical Committee: Beijing, China, 2009.
47. *DB/T 14-2018*; Specification of Hydraulic Fracturing and Overcoring Method for In-Situ Stress Measurement. National Seismological Standardization Technical Committee: Beijing, China, 2018.
48. *GB/T 29172-2012*; Practices for Core Analysis. National Oil & Gas Standardization Technical Committee: Beijing, China, 2012.
49. *GB/T 19559-2021*; Method of Determining Coalbed Methane Content. National Coal Standardization Technical Committee: Beijing, China, 2021.
50. *GB/T 30050-2013*; Classification of Coal-Body Structure. National Coal Standardization Technical Committee: Beijing, China, 2013.
51. Haimson, B.; Cornet, F. ISRM Suggested Methods for rock stress estimation—Part 3: Hydraulic fracturing (HF) and/or hydraulic testing of pre-existing fractures (HTPF). *Int. J. Rock Mech. Min. Sci.* **2003**, *40*, 1011–1020. [CrossRef]
52. Haimson, B. The hydrofracturing stress measuring method and recent field results. *Int. J. Rock Mech. Min. Sci. Geomech. Abstr.* **1978**, *15*, 167–178. [CrossRef]
53. Kang, H.; Zhang, X.; Si, L.; Wu, Y.; Gao, F. In-situ stress measurements and stress distribution characteristics in underground coal mines in China. *Eng. Geol.* **2010**, *116*, 333–345. [CrossRef]
54. Li, C.; Nordlund, E. Experimental verification of the Kaiser effect in rocks. *Rock Mech. Rock Eng.* **1993**, *26*, 333–351. [CrossRef]
55. Cerfontaine, B.; Collin, F. Cyclic and Fatigue Behaviour of Rock Materials: Review, interpretation and Research Perspectives. *Rock Mech. Rock Eng.* **2017**, *51*, 391–414. [CrossRef]
56. Kang, H.; Gao, F.; Xu, G.; Ren, H. Mechanical behaviors of coal measures and ground control technologies for China's deep coal mines—A review. *J. Rock Mech. Geotech. Eng.* **2023**, *15*, 37–65. [CrossRef]
57. Reiss, L.H.; Creusot, M.; Du Pétrole Et Des Moteurs, E.N.S. *The Reservoir Engineering Aspects of Fractured Formations*; Editions Technip: Paris, France, 1980; Available online: https://ci.nii.ac.jp/ncid/BA90642290 (accessed on 15 May 2024).
58. Harpalani, S.; Chen, G. Influence of gas production induced volumetric strain on permeability of coal. *Geotech. Geol. Eng.* **1997**, *15*, 303–325. [CrossRef]
59. Hou, J.S. *Logging Evaluation Technologies and Its Applications For Coalbed Methane Reservoirs*; Metallurgical Industry Press: Beijing, China, 2000.
60. Li, J.; Liu, D.; Yao, Y.; Cai, Y.; Qiu, Y. Evaluation of the reservoir permeability of anthracite coals by geophysical logging data. *Int. J. Coal Geol.* **2011**, *87*, 121–127. [CrossRef]
61. Chatterjee, R.; Pal, P. Estimation of stress magnitude and physical properties for coal seam of Rangamati area, Raniganj coalfield, India. *Int. J. Coal Geol.* **2010**, *81*, 25–36. [CrossRef]
62. Asquith, G.; Krygowski, D.; Henderson, S.; Hurley, N. *Basic Well Log Analysis*; American Association of Petroleum Geologists eBooks: Tulsa, OK, USA, 2004. [CrossRef]
63. Teng, J.; Yao, Y.; Liu, D.; Cai, Y. Evaluation of coal texture distributions in the southern Qinshui basin, North China: Investigation by a multiple geophysical logging method. *Int. J. Coal Geol.* **2015**, *140*, 9–22. [CrossRef]
64. Ghosh, S.; Chatterjee, R.; Paul, S.; Shanker, P. Designing of plug-in for estimation of coal proximate parameters using statistical analysis and coal seam correlation. *Fuel* **2014**, *134*, 63–73. [CrossRef]
65. Chen, S.; Liu, P.; Tang, D.; Tao, S.; Zhang, T. Identification of thin-layer coal texture using geophysical logging data: Investigation by Wavelet Transform and Linear Discrimination Analysis. *Int. J. Coal Geol.* **2021**, *239*, 103727. [CrossRef]
66. Fu, X.; Qin, Y.; Wang, G.G.; Rudolph, V. Evaluation of coal structure and permeability with the aid of geophysical logging technology. *Fuel* **2009**, *88*, 2278–2285. [CrossRef]
67. Zhao, Z.; Tao, S.; Tang, D.; Chen, S.; Ren, P. A mathematical method to identify and forecast coal texture of multiple and thin coal seams by using logging data in the Panguan syncline, western Guizhou, China. *J. Pet. Sci. Eng.* **2020**, *185*, 106616. [CrossRef]
68. Wang, Z.; Tang, S.; Yan, Z.; Zhang, S.; Xi, Z.; Zhang, K.; Wang, K.; Zhang, Q.; Yang, X. Three-Dimensional geological modeling of coal reservoirs and analysis of sensitivity factors for combined mining capacity. *Processes* **2023**, *11*, 3448. [CrossRef]
69. Bashmagh, N.M.; Lin, W.; Radwan, A.E.; Manshad, A.K. Comprehensive analysis of stress magnitude and orientations and natural fractures in complex structural regimes oil reservoir: Implications for tectonic and oil field development in the Zagros suture zone. *Mar. Pet. Geol.* **2024**, *160*, 106615. [CrossRef]
70. Somerton, W.H.; Söylemezoğlu, I.M.; Dudley, R.C. Effect of stress on permeability of coal. *Int. J. Rock Mech. Min. Sci. Geomech. Abstracts.* **1975**, *12*, 129–145. [CrossRef]
71. Palmer, I.; Mavor, M.; Gunter, B. Permeability changes in coal seams during production and injection: 2007 International Coalbed Methane Symposium: Tuscaloosa. *Ala. Univ. Ala. Pap.* **2007**, *713*, 20.
72. Gao, Q.; Liu, J.; Huang, Y.; Li, W.; Shi, R.; Leong, Y.; Elsworth, D. A critical review of coal permeability models. *Fuel* **2022**, *326*, 125124. [CrossRef]

73. Lin, Y.; Qin, Y.; Ma, D.; Wang, S.; Qiao, J. In situ stress variation and coal reservoir permeability response of the Jurassic Yan'an formation in the southwestern Ordos basin, China: Its impact on coalbed methane development. *Geoenergy Sci. Eng.* **2023**, *222*, 211444. [CrossRef]
74. Pan, J.; Zhao, Y.; Hou, Q.; Jin, Y. Nanoscale pores in coal related to coal rank and deformation structures. *Transp. Porous Media* **2015**, *107*, 543–554. [CrossRef]
75. Yang, G.; Hu, W.; Tang, S.; Zhou, Z.; Song, Z. Impacts of vertical variation of coal seam structure on hydraulic fracturing and resultant gas and water production: A case study on the Shizhuangnan Block, Southern Qinshui Basin, China. *Energy Explor. Exploit.* **2023**, *42*, 52–64. [CrossRef]
76. Temizel, C.; Canbaz, C.H.; Palabiyik, Y.; Hosgor, F.B.; Atayev, H.; Ozyurtkan, M.H.; Aydin, H.; Yurukcu, M.; Narendra, B. A review of hydraulic fracturing and latest developments in unconventional reservoirs. In Proceedings of the Offshore Technology Conference, Houston, TX, USA, 2 May 2022. [CrossRef]
77. Gong, X.; Ma, X.; Liu, Y. Analysis of geological factors affecting propagation behavior of fracture during hydraulic fracturing shale formation. *Geomech. Geophys. Geo-Energy Geo-Resour.* **2024**, *10*, 102. [CrossRef]
78. Song, J.; Qiao, Q.; Chen, C.; Zheng, J.; Wang, Y. Numerical Analysis of the Stress Shadow Effects in Multistage Hydrofracturing Considering Natural Fracture and Leak-Off Effect. *Water* **2024**, *16*, 1308. [CrossRef]
79. Mukherjee, S.; Rajabi, M.; Esterle, J.; Copley, J. Subsurface fractures, in-situ stress and permeability variations in the Walloon Coal Measures, eastern Surat Basin, Queensland, Australia. *Int. J. Coal Geol.* **2020**, *222*, 103449. [CrossRef]
80. Qiu, G.; Chang, X.; Li, J.; Guo, Y.; Zhou, Z.; Wang, L.; Wan, Y.; Wang, X. Study on the interaction between hydraulic fracture and natural fracture under high stress. *Theor. Appl. Fract. Mech.* **2024**, *130*, 104259. [CrossRef]
81. Huang, L.; Li, B.; Wu, B.; Li, C.; Wang, J.; Cai, H. Study on the extension mechanism of hydraulic fractures in bedding coal. *Theor. Appl. Fract. Mech.* **2024**, *131*, 104431. [CrossRef]
82. Zhao, X.; Wang, T.; Elsworth, D.; He, Y.; Zhou, W.; Zhuang, L.; Zeng, J.; Wang, S. Controls of natural fractures on the texture of hydraulic fractures in rock. *J. Pet. Sci. Eng.* **2018**, *165*, 616–626. [CrossRef]
83. Wang, Y.; Liu, D.; Cai, Y.; Yao, Y.; Pan, Z. Constraining coalbed methane reservoir petrophysical and mechanical properties through a new coal structure index in the southern Qinshui Basin, northern China: Implications for hydraulic fracturing. *AAPG Bull.* **2020**, *104*, 1817–1842. [CrossRef]
84. Wu, Y.; Men, X.; Lou, Y. New progress and prospect of coalbed methane exploration and development in China during the 14th Five-Year Plan period. *China Pet. Explor.* **2024**, *29*, 1–13.
85. Xu, F.; Nie, Z.; Sun, W.; Xiong, X.; Xu, B.; Zhang, L.; Shi, X.; Liu, Y.; Liu, S.; Zhao, Z.; et al. Theoretical and technological system for Highly efficient development of deep coalbed methane in the Eastern edge of Erdos Basin. *J. China Coal Soc.* **2023**, *49*, 528–544.
86. Zhang, C.; Li, M.; Hu, Q.; Jia, H.; Li, K.; Wang, Q.; Yang, R. Moderately deep coalbed methane reservoirs in the southern Qinshui Basin: Characteristics and technical strategies for exploitation. *Coal Geol. Explor.* **2024**, *52*, 122–133.

energies

MDPI

Review

Research Progress on Characteristics of Marine Natural Gas Hydrate Reservoirs

Jiajia Yan [1,2,3,4], Kefeng Yan [1,2,3,4,5,*], Ting Huang [1], Minghang Mao [1,2,3,4], Xiaosen Li [1,2,3,4,5,*], Zhaoyang Chen [1,2,3,4,5], Weixin Pang [1], Rui Qin [1] and Xuke Ruan [1,2,3,4,5]

[1] State Key Laboratory of Offshore Natural Gas Hydrates, Beijing 100028, China; jj_3342@tju.edu.cn (J.Y.)
[2] Key Laboratory of Gas Hydrate, Guangzhou Institute of Energy Conversion, Chinese Academy of Sciences, Guangzhou 510640, China
[3] School of Energy Science and Technology, University of Science and Technology of China, Hefei 230026, China
[4] Guangdong Key Laboratory of New and Renewable Energy Research and Development, Guangzhou 510640, China
[5] University of Chinese Academy of Sciences, Beijing 100049, China
* Correspondence: yankf@ms.giec.ac.cn (K.Y.); lixs@ms.giec.ac.cn (X.L.); Tel.: +86-20-8704-8054 (K.Y.); +86-20-8705-7037 (X.L.)

Abstract: As one of the most important future clean energy sources, natural gas hydrate (NGH) is attracting widespread attention due to the vast reserves available and high energy density. How to extract this source in a safe, efficient, and environmentally friendly manner has become the key to the commercial utilization of its resources. This paper reviews the recent advances in the study of the fundamental reservoir properties of offshore NGH, summarizing the methods and technologies for testing the sedimentary properties of reservoirs, analyzing the characteristics in reservoir mechanics, electrics, thermodynamics, and fluid dynamics, and discusses the influence of reservoir fundamental properties on NGH exploitation. The aim is to provide guidance and reference for research on the exploitation of NGH in different target exploitation areas offshore.

Keywords: natural gas hydrate; reservoir characteristics; basic physical properties; test method and technology

1. Introduction

Natural gas hydrate (NGH), commonly known as methane hydrates or combustible ice, is a type of ice-like crystalline solid composed of natural gas molecules trapped within a lattice of water molecules. Under conditions of low temperature and high pressure, water molecules form a cage-like structure through hydrogen bonding, enclosing guest molecules (such as methane, ethane, CO_2, and H_2) within their crystalline lattice to create stable hydrate formations. The most prevalent structures of NGH in natural environments are types SI and SII, primarily composed of methane hydrates. One cubic meter of NGH can yield approximately 186 cubic meters of natural gas and 0.8 cubic meters of water, indicating its high energy density. Moreover, the NGH reserves are substantial, estimated to be between 1 and 150 $\times$ 10^{15} cubic meters, which is twice the total conventional fossil fuel reserves and more than ten times [1,2] the total conventional natural gas reserves on Earth. Even if the estimated recoverable reserves range from 17% to 20%, these resources could meet global energy demands for over 200 years [3,4].

Due to the escalating global energy challenges and increasing environmental awareness, there has been a drive towards researching and developing efficient, clean energy sources. NGH resources are characterized by large reserves and high energy density, and are considered potent substitutes for petroleum and natural gas. NGH resources are predominantly found in deep-sea sedimentary layers and terrestrial permafrost, with approximately 27% of land and 90% of seabeds identified as potential NGH reservoirs, with

around 99% of global NGH resources located in marine deposits [5]. Since the accidental discovery of NGH at the Messoyakha gas field in Siberia in the 1960s, countries worldwide have embarked on continuous exploration and development of NGH deposits. The initial attempts to produce natural gas from NGH reservoirs were conducted at the Mallik field in Canada's Mackenzie Delta, with research led by the Geological Survey of Canada and Japan National Oil Corporation, culminating in a second production test in 2007. Subsequent trials have been conducted by Japan, the United States, and China in the Nankai Trough, Alaska, and the Shenhu area of the South China Sea, respectively. Early production trials predominantly employed methods such as thermal stimulation and depressurization, with attempts also made using inhibitor injection methods; however, depressurization has proven technically viable and more stable for production processes [6]. In 2008, the United States conducted CO_2 replacement experiments for NGH production in Alaska, exploring the potential of CO_2 exchanging with methane in reservoirs [7], providing a research direction to address geological stability during direct exploitation. Japan conducted trial exploitations in the Nankai Trough in 2013 and 2017. China conducted its first offshore trial exploitation in the Shenhu area of the South China Sea in 2017, followed by a second trial in 2020 that introduced innovative horizontal well exploitation techniques, setting records for daily gas production and total exploitation volume [8]. Despite the expanding scale and output of NGH mining trials, significant gaps remain in achieving commercial exploitation efficiency. The geological challenges and engineering hurdles must be overcome during the exploitation, particularly in maintaining the stability of hydrate reservoirs and improving exploitation efficiency, which constitute the core challenges of NGH production. The exploitation processes inevitably affect the surrounding operational temperature and pressure conditions, as well as sedimentary states, complicating the maintenance of original conditions and continuous operation. And it will potentially lead to geological hazards such as submarine landslides [9], gas leakage [10], and strata subsidence [11]. Therefore, by studying the characteristics of marine gas hydrate sediments (GHs), and analyzing the mineral composition, particle size distribution, pore structure, and mechanical properties of target exploitation areas, we can improve the understanding and assessment of NGH resource formation and distribution. This research will aid in the exploration and exploitation of NGH resources, effectively improving the development efficiency, reducing the development risks, and providing a scientific basis for the sustainable utilization of NGH.

In this paper, the recent research progress is reviewed on the fundamental physical properties of marine GHs, including summarizing the testing methods and technologies for GH basic properties, analyzing the mechanical, electrical, thermodynamic, and fluidic characteristics of GHs, exploring the impact of GH basic properties on the exploitation of NGH in various target exploitation zones of marine environments, and aiming to provide guidance and reference for the research on NGH exploitation in different target exploitation areas of marine environments.

2. Measurement Methods and Technologies for Reservoir Fundamental Properties

The fundamental property testing of marine NGH reservoirs typically involves stratigraphic exploration prediction and sample analysis, as illustrated in Figure 1. The exploration of marine strata primarily uses geological detection to analyze the information about the stratigraphic distribution, lithologic characteristics, and fault features of the reservoir. The sample analysis employs techniques in spectroscopy, crystallography, thermology, mechanics, and geology to ascertain the basic physical properties of sediments and hydrates within the reservoir samples. Marine NGH reservoir samples are obtained from seabed strata using pressure-preserving coring techniques [12,13]. Due to the limited drilling cases, high sampling costs, and the complexity of maintaining temperature and pressure, the research on measurement methods and technologies for reservoir sample properties is constrained. With the rapid advances in computer technology, emerging visualization testing and analysis methods have gained in popularity in research. These methods integrate and reconstruct data using in situ photoelectric testing technologies,

allowing for the visualization of the microstructure of samples, significantly enhancing the outcomes of instrumental tests and analyses.

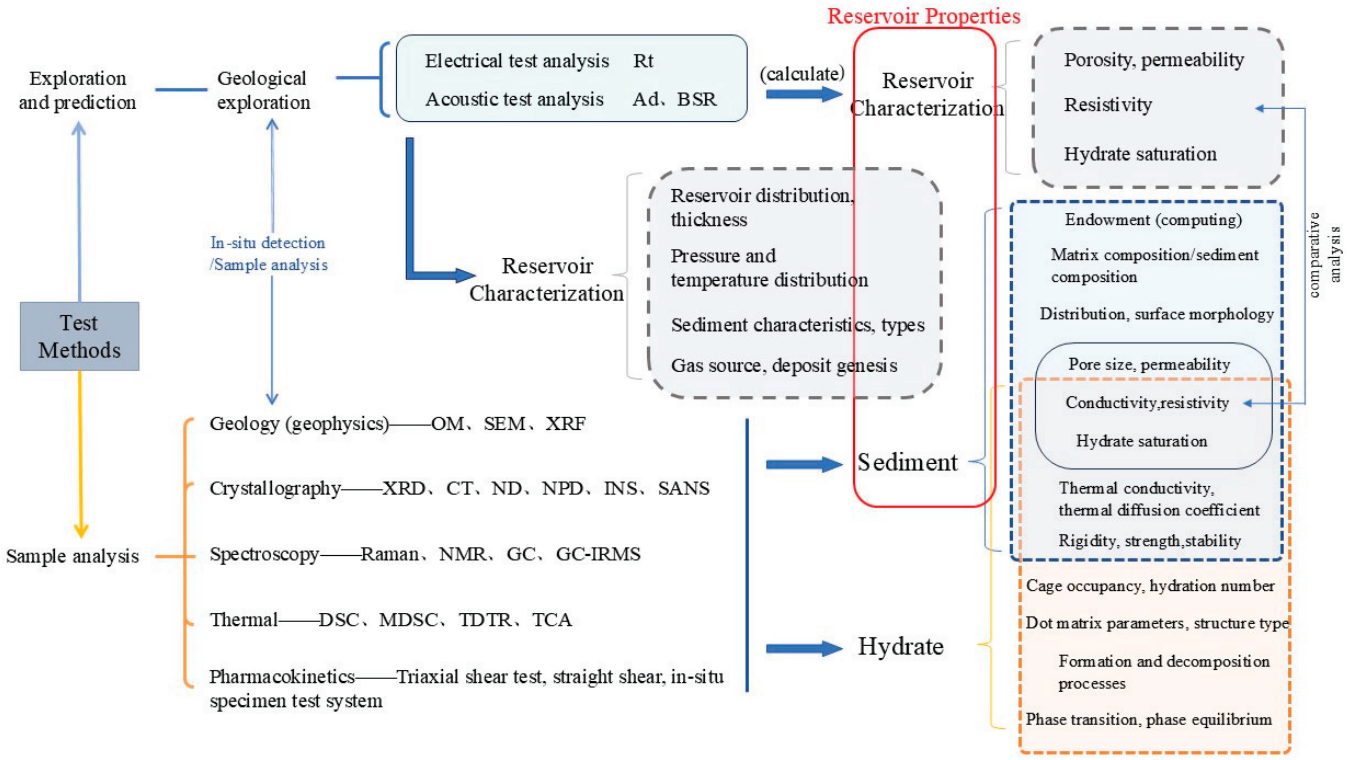

Figure 1. Testing method of reservoir foundation physical properties.

2.1. Geological Analysis

Geological analysis commonly employs acoustic and electrical technologies to obtain information on the stratigraphic distribution of hydrate reservoirs through geological sampling and seismic surveys, thereby characterizing the occurrence forms of hydrates. The bottom simulating reflector (BSR) is a frequently used predictive technique for NGH exploration. It utilizes the reflection of seismic waves between the hydrate layer and underlying rock layers to delineate information about the base interface of the hydrate layer, such as thickness and reflection intensity. This technique is often used to identify and locate NGH layers and assess their physical properties, stability, and the formation conditions. Additionally, geological analysis facilitates the acquisition of reservoir lithological and fault characteristics through the interpretation of core samples and seismic data. Exploratory well logging data are used to calculate the key reservoir properties such as permeability, resistivity, and hydrate saturation [14,15]. Winters et al. [16] compared the porosity measurements from core samples with well log-derived porosities at the Mount Elbert test well, finding a strong correlation that supports the overall accuracy of the well log data. However, due to the limited availability of logging data, the precise in situ assessment of hydrate porosity saturation remains challenging [7,17]. Researchers have elucidated the physical and chemical changes in hydrates under various geological conditions by studying their formation and dissociation processes [18–20]. Furthermore, through geological analysis, we can calculate parameters such as gas production, emissions, and accumulation [21,22], by constructing geological models to simulate the generation and migration characteristics of gases within hydrate reservoirs.

Microscopic imaging techniques, such as optical microscopy (OM) and scanning electron microscopy (SEM), are also commonly used in geological analysis to directly observe the micro-morphological features of GH rock samples. The chemical components and material content in samples are detected through X-ray fluorescence (XRF) and isotope analysis techniques. Currently, the optical microscopes used in the laboratory can achieve

a resolution down to a few micrometers, while some high-precision SEMs can reach imaging at the nanometer level. Advanced techniques based on low-temperature Cryo-SEM can provide surface morphology information of hydrate samples with the highest resolution of up to 1 nanometer [23,24]. Figure 2 shows the drilling platform and pressure-preserving coring device used during the second trial exploitation in the South China Sea. Le et al. [25] utilized high-resolution optical microscopy with a pixel size of 6.5 μm and synchrotron radiation X-ray computed tomography with a voxel size of 0.9 μm to study the growth of methane hydrates at micrometer scales under excess gas conditions. They observed the growth characteristics well below the size of the pores and on time scales shorter than 1 s. This study revealed hydrate forms and growth features that cannot be detected by conventional X-ray computed tomography alone, observing hollow filamentous growth driven by capillary forces. Bai et al. [26], using SEM combined with computed tomography and specific surface area analysis, studied the micro-depositional structure of GHs, observed different pore types, and analyzed the impact of various pores on NGH enrichment, discovering that the microstructure of sediments is a critical control factor for NGH accumulation and elucidating the mechanisms of hydrate formation.

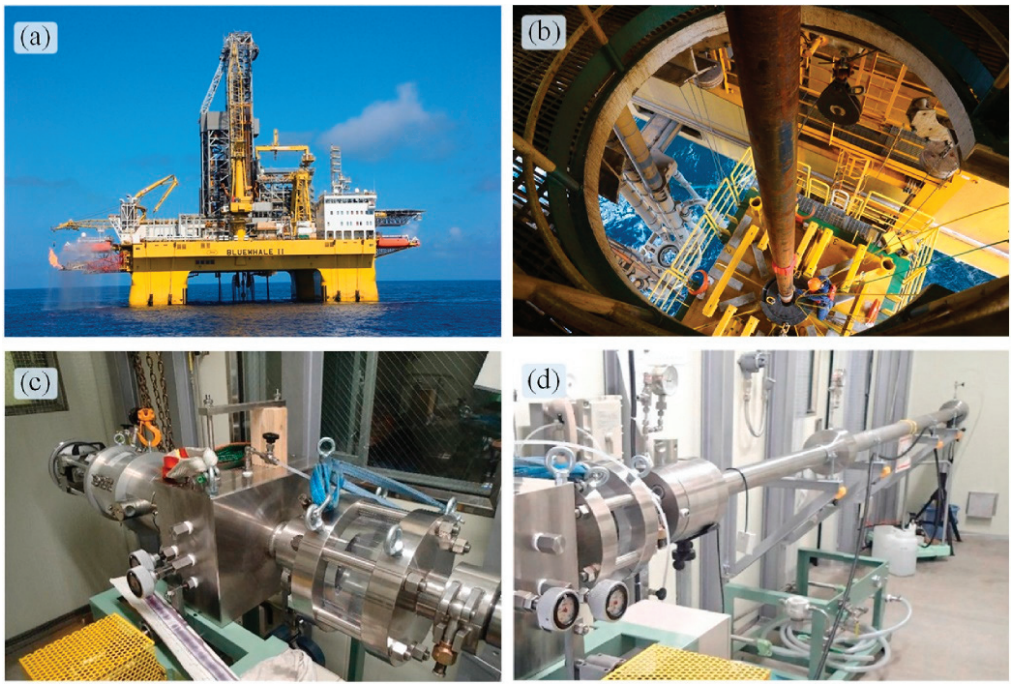

Figure 2. Physical drawing of drilling platform and pressure-retaining coring equipment [27]. (**a**) Platform of Bluewhale II; (**b**) drilling construction; (**c**,**d**) the pressure-core non-destructive analysis tools (PNATs). Copyright (2024), with permission from Elsevier.

Due to the complexity of the forms of hydrate occurrences and reservoir geological conditions, geological analysis requires extensive geological data and samples, hence demanding high standards for exploration and research. Therefore, ship-borne in situ testing and analysis are poised to become the future direction of geological analysis for hydrate reservoirs. The coupling and combined use of different instruments, deployed on research vessels for real-time in situ sample analysis, will play a crucial role in guiding the exploration and development of marine NGH.

2.2. Crystallographic Analysis

Crystallographic analysis is a fundamental technique for analyzing the physical properties of materials with crystalline structures. Techniques involved in crystallographic analysis include X-ray diffraction (XRD), powder X-ray diffraction (PXRD), X-ray computed tomography (X-CT), neutron diffraction (ND), neutron powder diffraction (NPD),

inelastic neutron scattering (INS), and small angle neutron scattering (SANS). XRD is a commonly used method that provides information about the distribution of sediment components, the crystal structure of NGH, lattice parameters, hydration index, and cavity occupancy rates [28,29]. XRD identifies the structural type and composition of hydrates through the positions and intensities of diffraction peaks, and studies their phase transition behaviors and thermodynamic properties [28]. X-CT, a non-destructive technique potentially used for detecting NGH, captures and projects crystal images [30]. It can determine the location of hydrates within sediments and help understand the relationship between NGH and host sediments. This technique can also ascertain local density changes, three-dimensional morphology, pore structure, porosity, and permeability during the formation and dissociation of hydrates by calculating CT numbers or using network models [31–34]. The fundamental principles of X-CT are illustrated in Figure 3 [35]. Micro-computed tomography (μCT) utilizes computational reconstruction to obtain high-resolution three-dimensional images of internal structures. Some high-resolution X-CT systems can achieve sub-micrometer spatial resolution. Paired with specially designed sample cells, these systems can image samples under high-pressure conditions of several tens of megapascals, making them suitable for studying the behavior of hydrates in extreme environments. And in recent years, it has gained popularity in hydrate research [36–38]. Crystallographic research has significant advantages in analyzing the internal structure and deformation of hydrates. However, due to the complex phase transitions and multiphase flow involved in the formation and decomposition of hydrates, resolving phases in multiphase fluids remains challenging. The application of more powerful characterization technologies and equipment, such as μCT and surface-enhanced Raman scattering spectroscopy (SERS), or the coupled use of various detection methods, should be considered for real-time analysis of hydrate formation, decomposition processes, and reservoir changes. Additionally, leveraging advanced computational equipment and modeling algorithms could enhance the clarity and resolution of crystal analysis, improving the accuracy of identification.

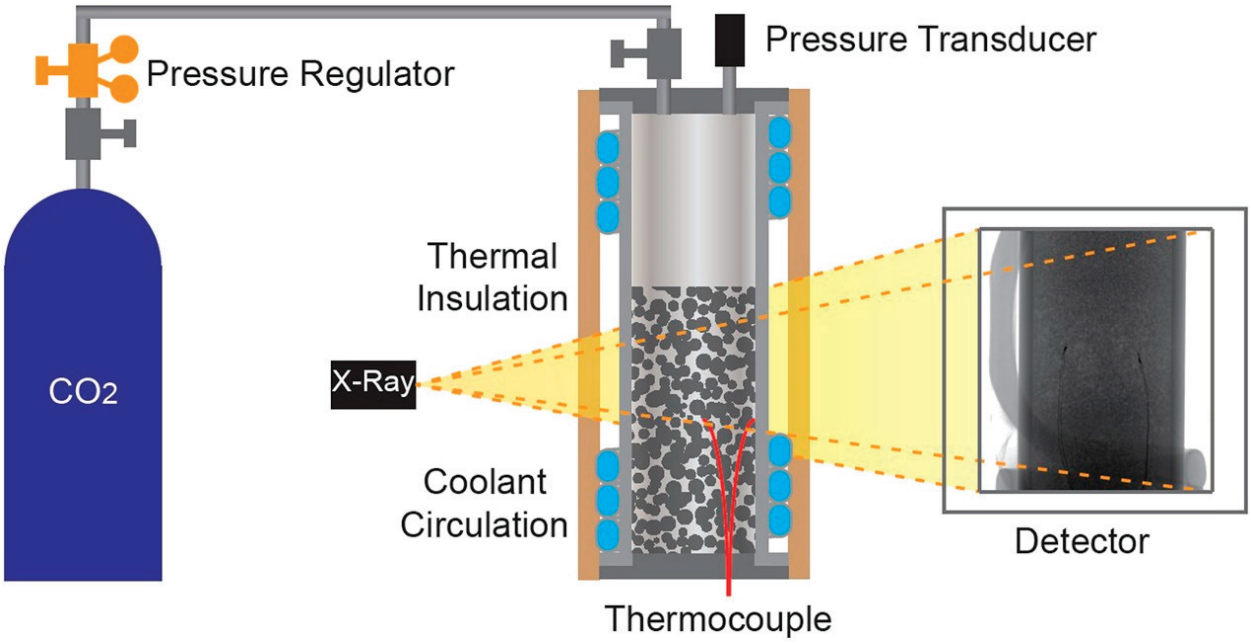

Figure 3. Device of X-ray CT [35]. Copyright (2019), with permission from American Geophysical Union.

2.3. Spectroscopic Analysis

Common spectroscopic analysis methods include infrared spectroscopy (IR), Raman spectroscopy (Raman), nuclear magnetic resonance spectroscopy (NMR), gas chromatography (GC), and gas chromatography-isotope ratio mass spectrometry (GC-IRMS). IR analysis identifies the composition and structure of GHs by studying their absorption characteristics

within the infrared wavelength range [39,40]. Raman analysis determines the molecular vibrational modes and lattice structure of NGH by measuring frequency shifts in Raman scattering, which can provide information about the crystal structure and phase transition behavior of hydrates [41,42]. Some high-performance spectrometers can achieve wavelength resolution at the picometer level, which is very useful for detailed structural analysis and peak separation. Raman spectroscopy testing has a wide range of temperature and pressure conditions, and Raman spectrometers can be used for analysis without affecting the optical path. NMR spectroscopy investigates the molecular structure and dynamic behavior of NGH by detecting signals from nuclear spins [43,44], offering insights into the relative contents of different components within hydrates and their interactions with the surrounding environment. The chemical shift precision of NMR testing can reach 0.01 ppm or even higher, which is significant for the analysis of hydrate crystal structures and the study of dynamic processes. Giovannetti et al. [45] used ice water as a model to study the effects of sediments, salt (NaCl), and temperature on the formation of hydrates. They used Raman spectroscopy to study the stretching vibrations of water molecules in test liquids and ice water, comparing changes induced by sodium chloride, sediments, and temperature under various experimental conditions. Their findings suggest that the presence of a porous medium typically facilitates the formation of hydrates, and it was observed that sand grains could counteract the inhibitory effect of salt molecules. Li et al. [46] employed a low-field nuclear magnetic resonance (LF-NMR) system, as illustrated in Figure 4, combined with a gas/water two-phase system to quantitatively and visually study the heterogeneity of methane hydrate formation/dissociation in two sand samples during thermal intrusion. They discovered that the formation rate of methane hydrates negatively correlates with sediment grain size and occurs heterogeneously within porous media, while the dissociation rate is influenced by both fluid flow resistance and heat supply, accelerating with increasing quartz sand grain size in GHs due to thermal stimulation.

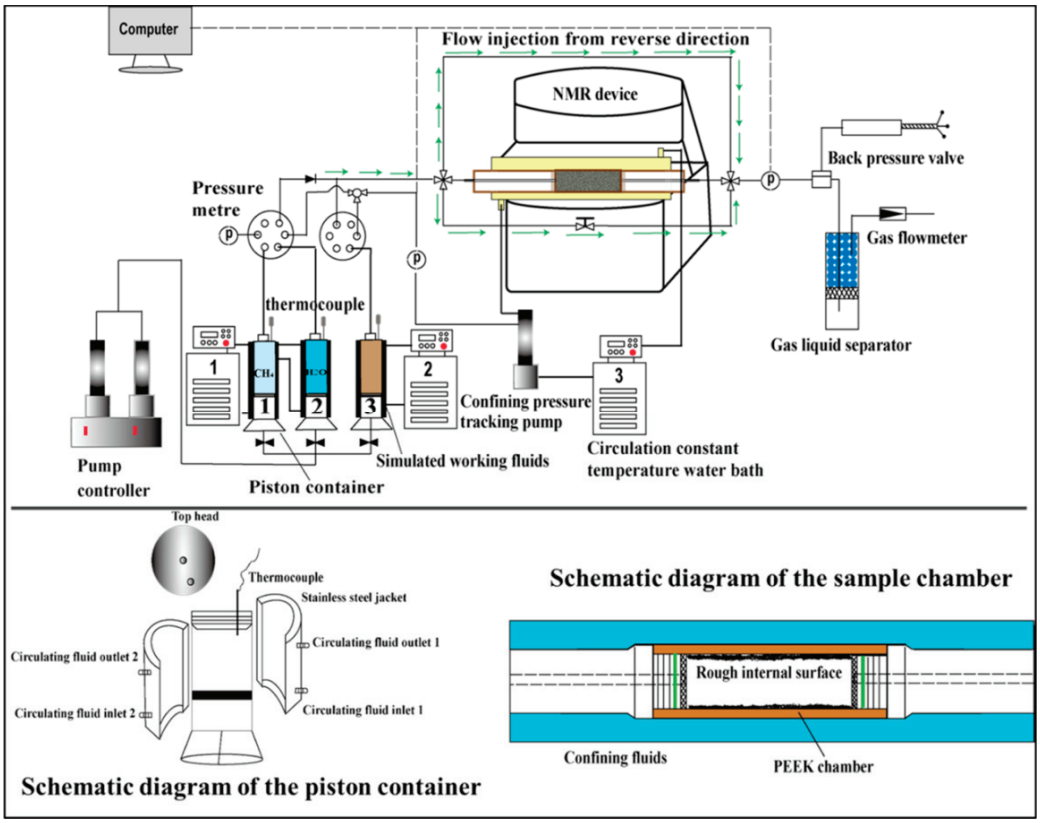

Figure 4. Device diagram of LF-NMR system [46]. Copyright (2024), with permission from American Chemical Society.

Spectroscopic analytical techniques play a crucial role in studying the molecular composition, structural types, and formation and dissociation kinetics of sediments and hydrates. However, these techniques impose specific requirements on the samples and involve issues of sensitivity and resolution differences in the equipment, such as the peak overlapping in IR analysis and artifact differentiation in NMR analysis. Therefore, employing multiple devices and multi-scale considerations for comprehensive analysis is essential to enhance the accuracy of the results.

2.4. Thermal Analysis

The thermal analysis methods operated by controlling temperature programs are used to record changes in the physical properties of substances with temperature variations. The thermal analysis methods used in GH research include differential scanning calorimetry (DSC), thermogravimetric analysis (TGA), time-domain thermal reflectance (TDTA), and thermal conductivity analysis (TCA). These methods facilitate the investigation of thermal properties such as the thermal conductivity, heat capacity, heat flux density, and thermal diffusivity of GHs. DSC is one of the most commonly used thermal analysis methods. It is suitable for obtaining data on the equilibrium properties of NGH during the solid–liquid phase transitions under high pressure [47,48]. Combining thermal analysis with related heat transfer studies also deepens the understanding of the formation, dissociation, and inhibition mechanisms of GHs [48]. TGA is a thermal analysis technique that studies the regularities of sample mass changes with temperature under controlled temperature programs, and is used to investigate material thermal stability and composition [49]. TDTA employs ultrafast laser pulses to generate thermal stimuli on the surface of material samples and measures the time-temperature response of reflected light to infer the sample's thermal conductivity. This method is useful for measuring materials with uneven thermal conductivity distributions, such as rocks and minerals. In GH research, thermal conductivity analysis mainly refers to the measurement of the thermal conductivity of hydrates and their sediments, which is a critical parameter describing the heat transfer characteristics of sedimentary reservoirs.

Thermal conductivity measurements involve determining the heat transfer process through spatial temperature differences, encompassing techniques for measuring heat flux density and effective thermal conductivity. The measurements of heat flux density reflect the changes at different locations or times. The heat exchange during the formation/dissociation of hydrates in vertical or horizontal directions can be analyzed, and heat losses can be calculated. Li et al. [50] analyzed the impact of reservoir heat transfer factors on hydrate dissociation by observing temperature distribution changes during the formation and dissociation of NGH. Effective thermal conductivity measurement methods include the hot-wire method, thermal ribbon method, probe method, and transient plane source method. He et al. [51] used the transient hot-wire method to measure the effective thermal conductivity of quartz sand containing hydrates, analyzing hydrate distribution through resistance changes, and studying changes in effective thermal conductivity with factors such as gas saturation, pressure, water saturation, water pressure, and temperature, with their experimental setup illustrated in Figure 5. Li et al. [52] conducted in situ measurements of the effective thermal conductivity of different water-containing sediment layers, analyzing the effects of temperature, particle size, and sediment type. They emphasized the dominant role of porous media types on the effective thermal conductivity characteristics of water-bearing sediments, noting that the intrinsic thermal conductivity of porous media controls the effective thermal conductivity characteristics of water-bearing sediments. The effective thermal conductivity values of different water-bearing sediment layers in descending order are water-containing silicon carbide sediments > water-containing quartz sand sediments > water-containing clay sediments. During the formation and dissociation of hydrates, the density of hydrate samples and the structure of porous media may change, which could lead to probe or wire damage and measurement failure during measurements using plane sources or hot-wire methods. The temperature field of the samples themselves

may also be affected. Therefore, non-destructive testing methods such as TDTR or ultrasonic tomography [53,54] should be considered for analyzing temperature distributions, or existing temperature detection devices should be improved by using thermistors or point heat source methods to study the temperature field and heat transfer during the hydrate formation and dissociation processes [31,55].

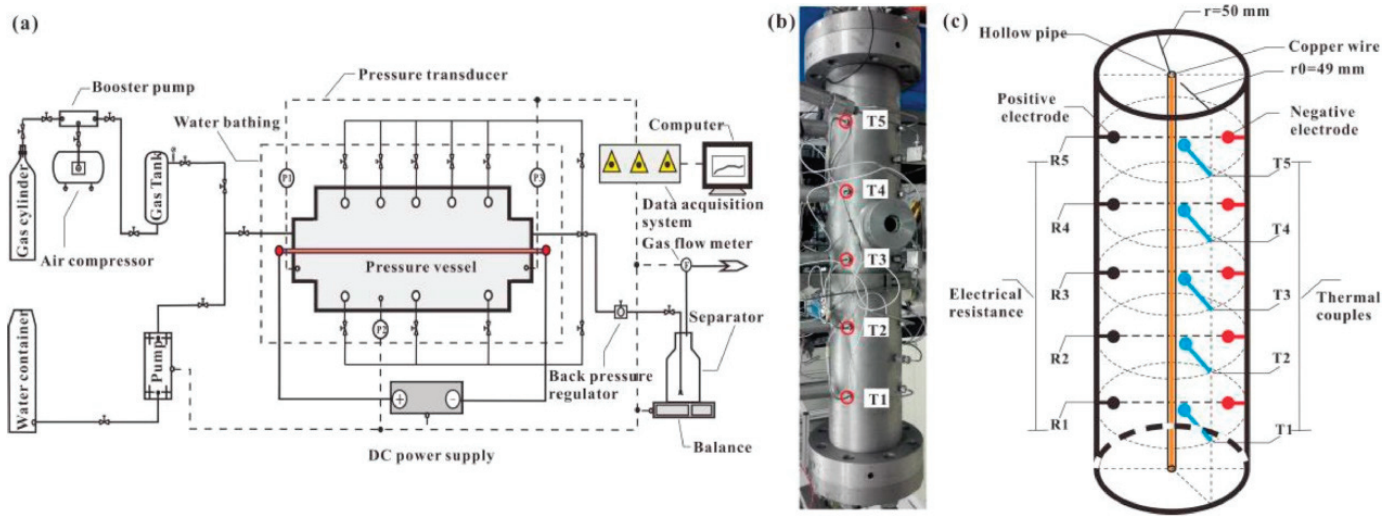

Figure 5. Device diagram for thermal conductivity measurement by transient hot wire method [51]. (**a**) The cylindrical reactor fabricated with 316L stainless steel. (**b**) Five thermal couples which are uniformly distributed along with the axis of the reactor. (**c**) Being fixed in the same circle surface with the thermal couple, two electrodes with a distance of 90 mm are regarded as a measuring point for the electrical resistance. Copyright (2021), with permission from Elsevier.

2.5. Mechanical Analysis

Currently, the main methods used to study the mechanical properties of hydrated sediments are using methods such as triaxial shear tests and direct shear tests. The direct shear test, a commonly used direct testing method in laboratories, can determine the strength of hydrate-bearing sediments under large strain conditions. Zhou et al. [56] conducted a series of direct shear tests to explore the shear strength characteristics of the hydrate-bearing soil. It was shown that the shear strength of the soil can be significantly influenced by pore gas pressure, unhydrated water content, hydrate saturation, and several other factors. A shear strength criterion, which enforces the equilibrium condition of pore hydrate, is developed for hydrate-bearing soil, establishing a link between the equilibrium condition and the shear strength. A combined injection synthesis and direct shear testing system was developed and the results of the research show that the shear strength of hydrate-bearing soil is higher for the cementation habit than for the pore-filling habit, which verifies the reliability of the instrument. [57] Triaxial shear tests, conducted under low-temperature high-pressure conditions, explore the mechanical performance of GHs. These tests demonstrate a stable pattern of residual strength variation. The residual strength is minimally affected by sample uniformity, but it exhibits markedly lower residual strength at low temperatures compared to high temperatures, displaying distinct peak and softening trends. This is entirely different from the hardening trend observed in direct shear tests. Direct shear testing is a common and effective engineering method characterized by low cost, simplicity, and short duration. However, it does not allow control of the pore water pressure and drainage conditions, and the shear plane of the sample is predetermined, which typically does not align with the weak planes of the soil samples. Furthermore, the residual strength in direct shear tests is influenced by the shear rate and temperature. Increases in shear rate and decreases in temperature can enhance the strength of GHs, but the effect of shear rate on residual strength shows irregular trends, potentially leading to significant yielding and softening. The fractures in direct shear tests are greatly influenced by sample uniformity,

while fractures in triaxial tests are less affected. The results of direct shear tests may not represent the true mechanical strength of GHs. Thus, triaxial shear tests are generally used for testing the mechanical properties of NGH reservoir samples. Zhao et al. [58] performed mechanical property tests on hydrate-bearing clayey–silty sediments using a triaxial shear device (as shown in Figure 6), analyzed the compressibility and shear behavior of the hydrate sediments, obtained compressibility parameters (reflecting compressibility characteristics), bonding coefficients (reflecting bonding effects), and dilatancy coefficients (reflecting filling effects), and established a constitutive model that uniformly describes the mechanical behavior of clayey and sandy sediments. Yoneda et al. [13] conducted triaxial or uniaxial compression tests on pressure core samples obtained from drilling in the eastern Nankai Trough, Japan, developed empirical equations for the triaxial compressive strength and deformation modulus as functions of NGH saturation, effectively confining pressure, porosity, and strain rate, and predicted the strength and modulus of the deformation of the sediments based on logging data.

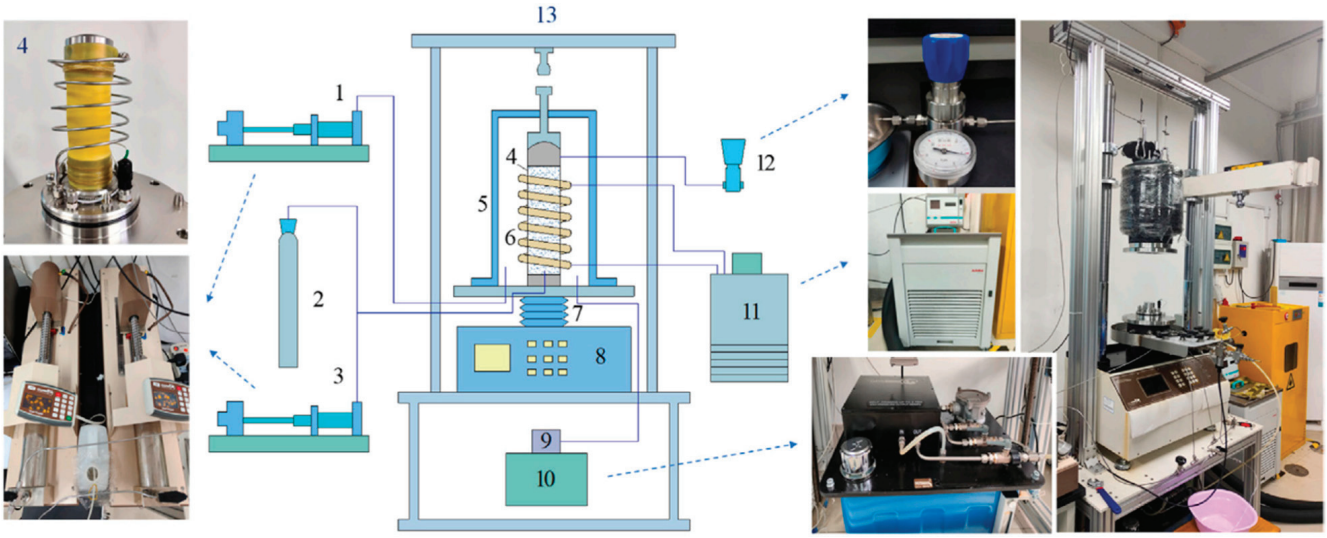

Figure 6. Device diagram of triaxial shear test [58]. (1) Confining pressure controller; (2) methane gas cylinder; (3) pore pressure controller; (4) sample; (5) pressure chamber cover; (6) condenser pipe; (7) telescopic rod; (8) axial load controller; (9) oil pump; (10) hydraulic oil tank; (11) temperature controller; (12) back pressure valve; (13) reaction frame. Copyright (2024), with permission from Elsevier.

The combined use of triaxial shear tests and various microscopic testing techniques offers a comprehensive approach to analyzing the mechanical properties and influencing factors of gas hydrate reservoir sediments. This method has become crucial in recent studies of the mechanical properties of these sediments. As previously mentioned, microscopic techniques can reveal the microstructure and composition of hydrate reservoir sediments, aiding in understanding the impact of hydrate crystals on sediment mechanical properties. Combining these techniques allows researchers to analyze the distribution of hydrate crystals within sediments, pore structure, and interactions with other minerals, leading to a more accurate assessment of sediment sample mechanical behavior and stability. Commonly used combined techniques include computer tomography combined with triaxial shear testing. Yoneda et al. [59] employed micro-focused X-ray computed tomography to analyze the large-strain mechanical behavior of hydrate-bearing sediments at different hydrate saturations (S_h = 0%, 39%, and 62%). The obtained stress–strain relationships indicated strengthening with increasing hydrate saturation and a brittle failure mode of the hydrate-bearing sand. The quantitative analysis of localized deformation through sub-millimeter and micron-scale imaging revealed that the shear band thickness decreased with increasing hydrate saturation. Wu et al. [60] used computed tomography to observe

and analyze the cementation failure behavior (morphology), deformation evolution (quantitative statistics), and localized shear deformation in different regions of the stress–strain curves. They studied the varying behaviors of hydrate cementation clusters in different regions. Figure 7 shows the CT images of the hydrate samples with axial strain increasing, where the Series C and Series D images, respectively, depict the deformation processes in uncemented and cemented regions (clustered hydrate patches).

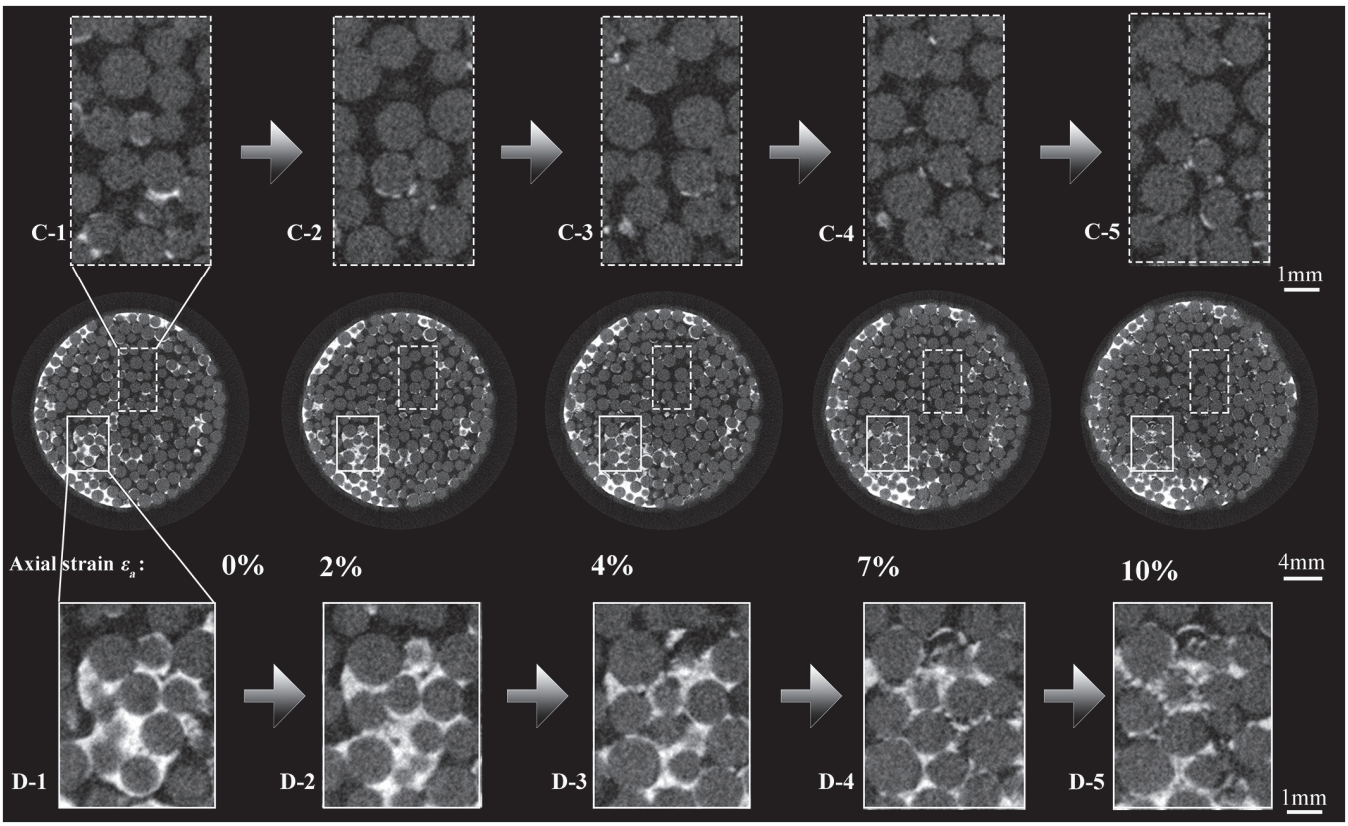

Figure 7. The CT images of the hydrate samples with axial strain increasing [60]. Copyright (2019), with permission from American Geophysical Union.

Both triaxial and direct shear tests cause irreversible damage to the samples, making it impossible to verify the accuracy and reliability of the experimental results. In particular, for naturally extracted hydrate core samples, which are typically non-replicable, there is a need to strengthen the validation and comparison between different testing methods. By standardizing test procedures and parameters, comparability between different methods can be enhanced, providing a more accurate basis for the application of test results. The mechanical performance of GHs is controlled by their internal structure, with microscopic hydrate behavior playing an increasingly significant role in macroscopic mechanical phenomena [27,36]. A measurement, combined with electrical, optical, and acoustic techniques, will aid in the integrated analysis of the mechanical and physical properties of sediments [61–64].

3. Study of Reservoir Basic Physical Properties in Target Exploitation Areas

The current global distribution of identified sources of NGH are illustrated in Figure 8. The complex origins of gases significantly influence the formation of GHs [65–68], combined with complex geological conditions and depositional environments. These are closely related to the formation mechanisms of NGH. Influenced by the GH particle size, pore size, stress strength, and surrounding fluid environment, hydrates in sediments with smaller particles and pore sizes predominantly exist as fracture fillings, known as fracture-filling hydrates, as shown in Figure 8. Due to the difficulty in filling fine-grained sediment pores,

hydrates occupy variously shaped and sized fractures in multiple forms such as massive, vein, and nodular, forming hydrate reservoirs with diverse storage types [36,69,70]. In the sediments with larger particles and higher porosity, the hydrates can be easily filled with pores or cement sand grains, and exist as pore-filling hydrates. These are represented by suspension, contact, and cementation modes of occurrence (as shown in Figure 8). Different occurrence forms of hydrates impact the structural composition and physical properties of GHs, thereby affecting the exploitation process differently. Consequently, the exploration and prediction of hydrates with different storage forms should adopt varied evaluation methods.

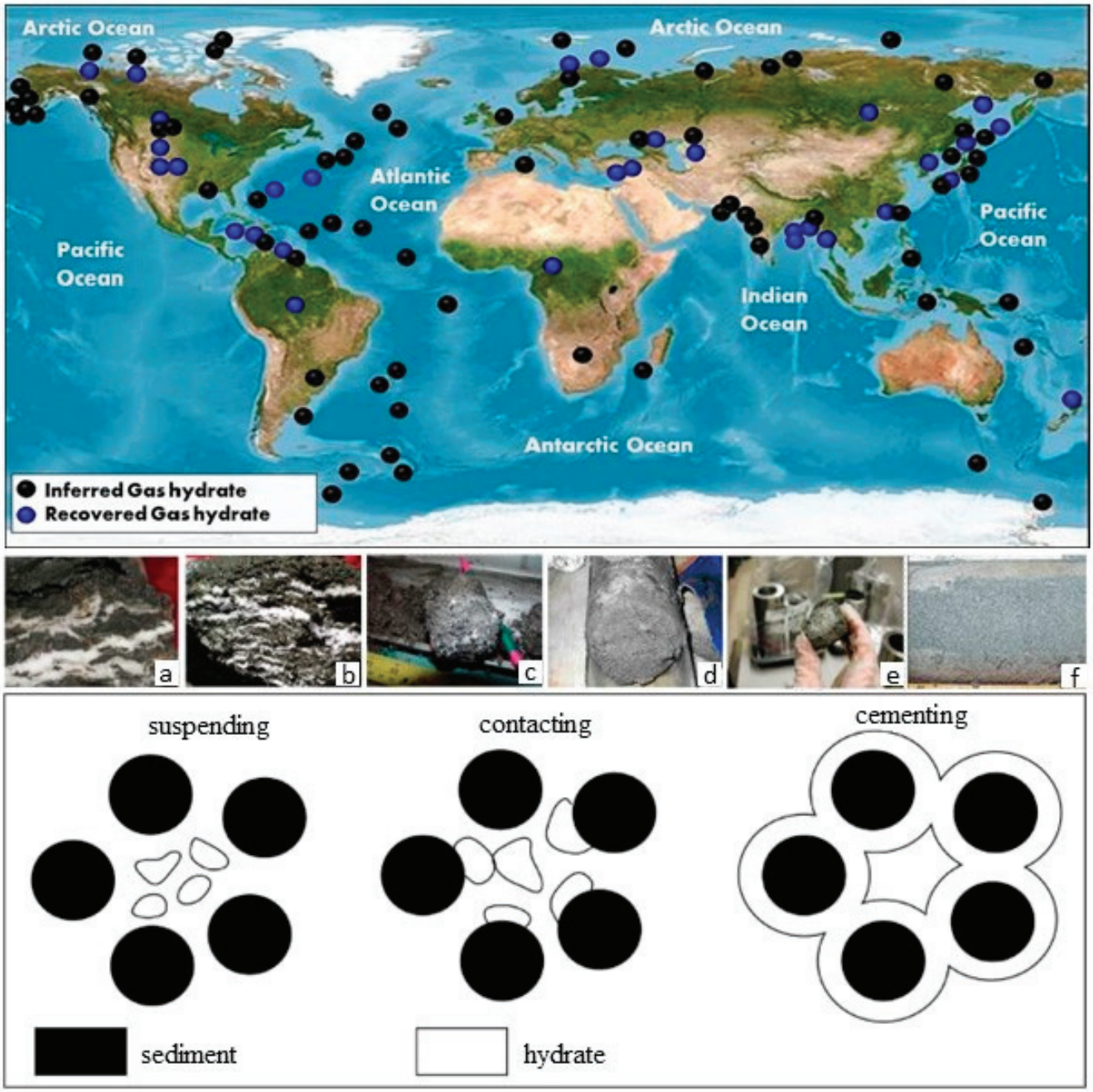

Figure 8. Location distribution and occurrence pattern diagram of NGHs, modified from [36,69,70]. (The middle part: (**a**,**b**) are fissure-filling type, and (**c**–**f**) is pore-filling type). Copyright (2024), with permission from Elsevier; Copyright (2020), with permission from Elsevier.

Global NGH pilot exploitation areas are primarily located in the Malik region of the Mackenzie Delta in Canada, the North Slope of Alaska in the USA, the Qilian Mountains area of the Qinghai–Tibet Plateau in China, the Nankai Trough in Japan, and the Shenhu area in the South China Sea. In the Malik region, hydrates mainly exist in the unconsolidated loose sandstone deposits of the Tertiary Mackenzie Bay and Kugmallit sequences, distributed at depths of approximately 900–1100 m [71]. These rock layers predominantly consist of thickly bedded sandstone interbedded with gravel, and layered sandstone with siltstone. NGH predominantly forms as pore-fillings with saturation levels between 50% and 90%. Extracted core samples primarily include unconsolidated gravelly sandstone, compact sandstone, and shale, also incorporating small amounts of dolomite-cemented sandstone and low-rank coal layers. The hydrates mainly consist of Structure I methane hydrate [5,72,73]. In the North Slope of Alaska, NGH is predominantly distributed in six laterally continuous Lower Tertiary sandstone and gravel units of the Sagavanirktok Formation, covering parts of the Kuparuk River, Prudhoe Bay, and Milne Point oil fields. The lithology of the drilled samples is mainly characterized by thick sandstone, including sandstone, mudstone, and siltstone. Many wells in this area have multiple hydrate-bearing units, each ranging in thickness from 3 to 31 m (0.9 to 9.4 feet) [74,75]. The Qilian Mountains region of the Qinghai–Tibet Plateau, located at a low-latitude mountainous permafrost zone, has relatively shallow permafrost but has yielded unique NGH samples. This permafrost zone is situated along the northern edge of the Qinghai–Tibet Plateau. The drilling area's terrain gradually slopes from higher elevations in the west and south to lower elevations in the east and north. The elevations range between 4026 and 4128 m, with permafrost depths typically between 60 and 80 m [76,77]. Hydrates are primarily found in fine siltstone and mudstone core cracks in the form of icy thin layers or fine impregnations [78]. In Japan's Nankai Trough, hydrate reservoirs mainly contain turbidite channel-type deposits within submarine fan systems, with the primary depositional system being submarine fan turbidites [79,80], comprised of an upper muddy zone, an upper methane hydrate concentration zone (MHCZ), a silt-dominated zone, a lower MHCZ, and a hydrate-bearing zone. The upper MHCZ is alternately composed of fine sands (fine and very fine sands) and fine silts (sandy silt and clayey silt). The silt-dominated zone is similar to the upper MHCZ but with a higher proportion of silt layers. The lower MHCZ also features alternating sand and silt, with the thickest sand layers containing channel sands [81]. Sediment reservoirs in the Shenhu area of the South China Sea are primarily composed of clayey silt rich in foraminiferal and other paleontological fossils, followed by silty clay [82]. The mineral compositions of GHs in various target exploitation areas are shown in Figure 9 (based on the test results of extracted core samples). The mineralogical composition of the GHs in each of the target exploitation areas consists mainly of quartz, illite, calcite, dolomite, glauconite, sodium feldspar, potassium feldspar, pyrite, and minor amounts of amphibole and rock salt. Illite and quartz are generally present in high concentrations in the sediments, followed by glauconite and carbonate minerals, with other minerals being less abundant [83,84]. Hydrate reservoirs in the Shenhu region of China mainly consist of fine-grained clayey silt, characterized by low permeability and challenging exploitation, which contrasts significantly with the hydrate reservoirs in the USA and Canada (predominantly gravel) and Japan (generally coarse sand) [85]. Generally, sandy sediments with larger pore spaces, good connectivity, and high permeability are favorable for the flow of hydrocarbon fluids and the formation and storage of NGH. If silt-dominated sediments contain biogenic carbonates, diatom fossils, and volcanic ash, they can alter the sediment's pore structure, connectivity, and permeability, thus improving the formation and storage environment for hydrates. Clayey sediments have smaller porosities and lower permeability, but due to the tectonic activity, differential compaction, and fluid effects, high-angle faults or fractures often exist within the sediment layers. These faults or fractures can expand the storage space of fine-grained sediments, forming various forms of fracture-filled hydrates [70,86,87].

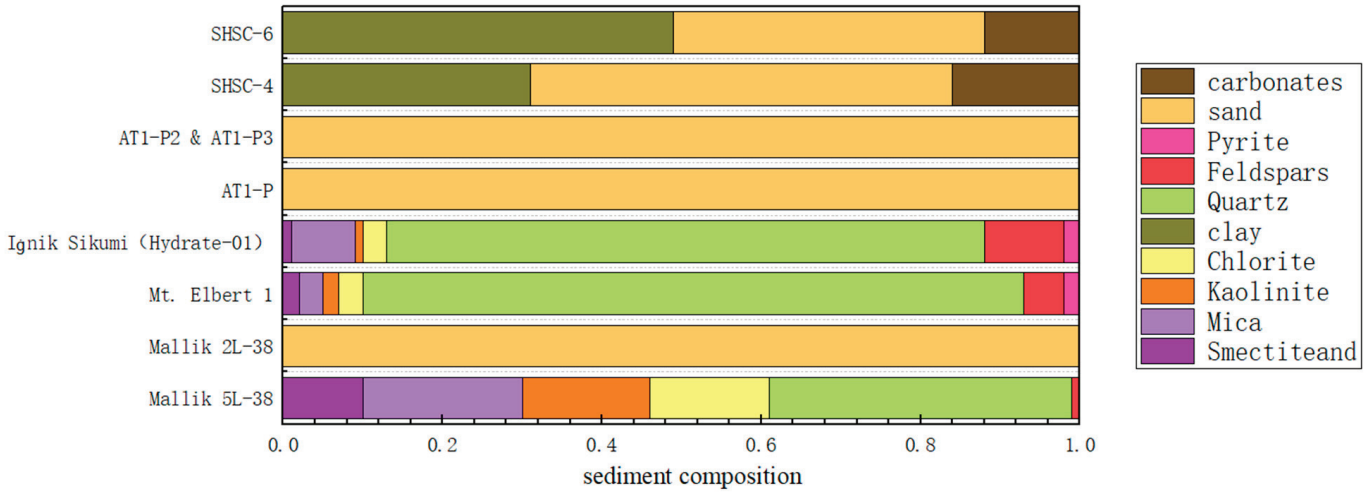

Figure 9. Distribution of mineral composition of hydrate reservoirs in each exploitation.

The foundational physical properties of NGH reservoirs critically influence the hydrate accumulation and exploitation. The saturation of hydrates within the reservoirs is a vital indicator for assessing NGH accumulation. Generally, under suitable environmental conditions and ample gas molecule availability, larger GH particle sizes and greater pore spaces correlate with higher hydrate saturations. This is because hydrate formation and storage require sufficient pore space, and high porosity facilitates the formation and storage of hydrates. For instance, the reservoirs in the Malik area of the Mackenzie Delta, primarily composed of gravelly sediment, exhibit hydrate saturations ranging from 60% to 80%, reaching up to 90% [88]. In contrast, the reservoirs in the North Slope of Alaska and the Nankai Trough area in Japan, which are primarily sandy, have smaller average grain sizes with hydrate saturation ranging from 50% to 80%, with peak saturations recorded at 77.4% [16]. In the Shenhu area of the South China Sea, the reservoirs predominantly consist of muddy siltstone sediments, with notably lower hydrate saturations usually between 10% and 40%. The physical property data from various exploitation efforts are summarized in Table 1. High saturation levels indicate a rich content of hydrates within the reservoirs, which is advantageous for exploitation. However, excessively high hydrate saturations may alter the physical properties of the reservoir rocks, such as reducing their strength, thereby impacting the stability of the reservoirs. Permeability parameters describe the fluid dynamics-related characteristics of hydrate reservoirs. They reflect the ability of fluids to flow through the rock formations. Higher permeability implies that gas can more easily flow through the rock pores, which is beneficial for hydrate exploitation. Conversely, low permeability may hinder gas flow, increasing the difficulty of exploitation.

In the Shenhu area of the South China Sea, GH overall porosity is relatively uniform, predominantly consisting of micro- to nanometer pores, with pore channels appearing as sheet-like and curved lamellar structures [19], and pore diameters ranging from approximately 500 nm to 20 μm, constituting the primary connectivity spaces. Some larger pores exist due to foraminifera, with occasional fractures observed. Overall porosity ranges from 33% to 55%, with capillary pressures between 0.57 and 1.10 MPa [85], and effective permeability ranging from 0.2 to 40 millidarcies [89–92]. Generally, sandy sediments have relatively good permeability, reaching tens or even thousands of millidarcies. However, such sandy layers are typically scarce, as exemplified by the Nankai Trough layers tested in Japan. Most often, the sediment comprises very fine-grained muddy silt with low permeability, sometimes less than a few millidarcies. This characteristic is common across most of the globally explored NGH reservoirs, including the Shenhu area in the South China Sea [93,94].

Table 1. Physical property data of hydrate reservoirs for each exploitation.

Country	Canada	Canada	USA	USA	Japan	Japan	China	China
Location	Mackenzie delta	Mackenzie delta	North Slope in Alaska	North Slope in Alaska	Nankai trough in Japan	Nankai trough in Japan	Shenhu area in South China Sea	Shenhu area in South China Sea
Year	2002	2007	2007	2012	2013	2017	2017	2020
Teat well	Mallik 5L-38	Mallik 2L-38	Mt. Elbert1	Ignik Sikumi	AT1-P	AT1-P2 and AT1-P3	SHSC-4	SHSC-4
Well type	vertical	vertical	vertical	vertical	vertical	vertical	vertical	horizontal
Method of exploitation	Thermal stimulation	Depressurization	Depressurization and CO_2 replacement	Depressurization and CO_2 replacement	Depressurization	Depressurization	Depressurization	Depressurization
Drawdown duration/d	5	6	6–12 h	30	6	12 + 24	60	42
Cumulative gas production/10^4 m^3	0.0516	1.3		2.4	12[4]	3.5 + 20	30.9	149.86
Reason for stopping production	sanding events	sanding events	sanding events	sanding events	sanding events	weather conditions	ESP power cable failure	production off
Reservoir type	class 3	class 3	class 3	class 3	class 3	class 3	class 1	class 1
Sediment type	Sandstone	Sandstone	Sandstone	Sandstone	Sand-silt alternation	Sand-silt alternation	Clayey silt	Clayey silt
Temperature/°C	13.9	11.2	2.3–2.6	5	13.5	13.5	—	—
Pressure/Mpa	11.6	11.3	6.7	6.9	13	13	—	—
Hydrate saturation/%	60–80	60–80	65	72	50–80	60–80	31	31
Intrinsic/initial permeability/md	400/0.5–35	400/0.5–35	500–200/0.2–0.5	<1 (initial)	47–840	47–840	1.5 (Mean effective)	2.38 (Mean effective)
Porosity of sediments	—	0.02–0.04	0.4	0.4	0.4–0.5	0.3–0.5	0.33	0.37

4. Study on the Reservoir Characteristics Measurement and the Influence on NGH Exploitation

4.1. Mechanical Properties

The mechanical properties of GHs are critical for analyzing the potential geological hazards and the stability of mining wells during exploitation processes. The presence of NGH significantly alters the mechanical characteristics of sediments [95]. The mechanical behavior of GHs is primarily determined by factors such as hydrate saturation, effective confining pressure, sediment composition, and temperature. For GHs with lower hydrate saturations, the impact of hydrate saturation on their strength is minimal. As saturation increases, the strength and stiffness of hydrate-bearing sedimentary reservoirs significantly improve, accompanied by increased expansiveness, primarily due to the filling and cementing effects of hydrates. An increase in hydrate saturation reduces the sediment compaction processes while enhancing expansion processes, thereby influencing the mechanical properties of the reservoirs [96]. Furthermore, as hydrate saturation increases, hydrate particles fill the interstitial spaces between the grains, enhancing the interactions among hydrate particles, which can increase the tensile and shear strength of the reservoirs and enhance hydrate stability. Increased effective confining pressure leads to stronger interlocking and bonding between sand and hydrate particles, augmenting the internal friction of the sediment, while also restricting the free movement of sand and hydrate particles, significantly enhancing the mechanical strength of GHs [97]. The relationship between the strength of GHs and hydrate saturation as well as the effective confining pressure are illustrated in Figure 10. The composition of the sediment also has a significant impact on the mechanical performance of hydrates. The proportion of particles in the sediment, their size distribution, and shape can affect the mechanical properties of hydrates. A higher proportion of larger particles increases the strength of the hydrate–sediment composite, while round sand particles enhance the cohesion of the hydrate–sediment composite [98]. An increased proportion of fine particles promotes the formation of larger hydrate cement clusters, thereby strengthening the sedimentary reservoirs [99]. Additionally, changes in temperature and pore pressure also affect the mechanical performance of the hydrate–sediment composite; reductions in temperature and increases in pore pressure enhance the stiffness and strength of the sedimentary reservoirs [96,97,100].

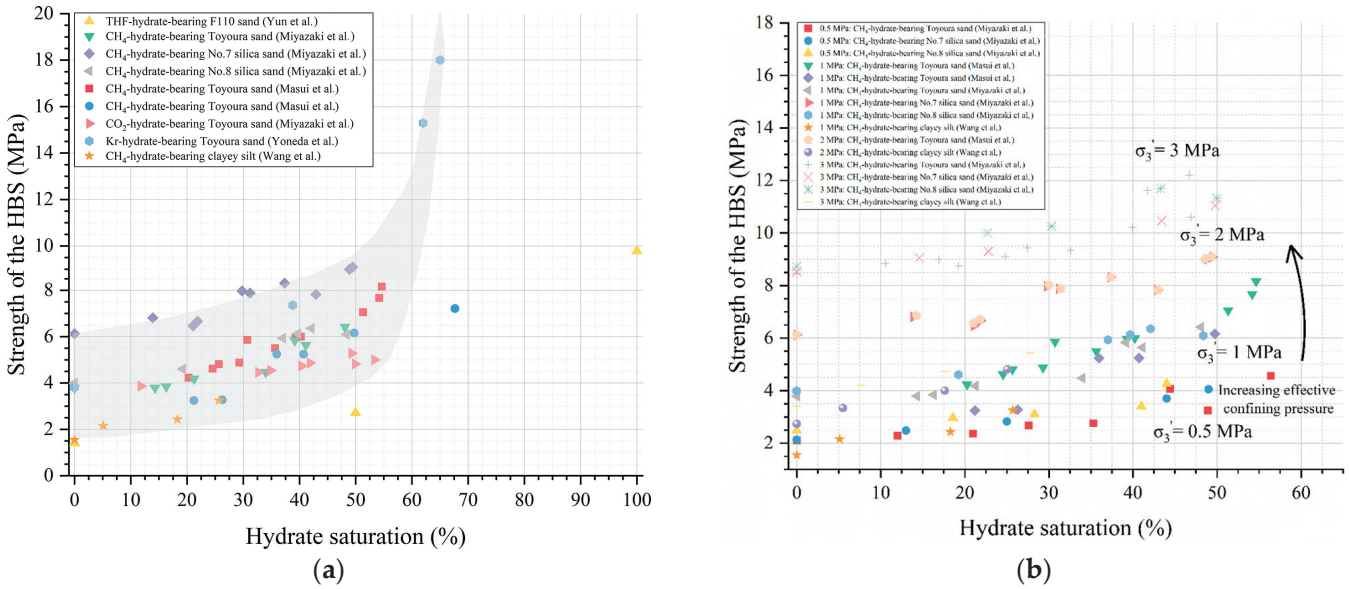

Figure 10. Modified from [96]. (**a**) Relationship between the strength of HBS and hydrate saturation under an effective confining pressure of 1 Mpa [59,101–105]; (**b**) relationship between the strength of HBS and the effective confining pressure under different hydrate saturations [102,103,105]. Copyright (2020), with permission from American Chemical Society.

4.2. Electrical Properties

The volumetric fraction and spatial distribution of sediment components can be characterized by evaluating their overall electrical and electromagnetic properties [106]. Sensitive electromagnetic measurement techniques can complement seismological studies and are used to determine the saturation and distribution of NGH in natural environments [107–110]. The conductivity of GHs is predominantly controlled by the movement of hydrated ions within the pore water and around the mineral surfaces within the electrical double layers, particularly for sediments with high specific surface areas [111]. The resistivity of GHs is influenced by the combined effects of hydrate microstructure and pore architecture. The microstructure of hydrates depends on the distribution and migration of gas and water within the pores, which in turn is controlled by the characteristics of the pore structure [19,39]. Chen et al. [112] utilized X-ray computed tomography (X-CT) and resistivity measurement techniques to study the response characteristics of the resistivity of hydrate-bearing sediments. Their results indicated that when hydrate saturation is below 20%, resistivity is primarily controlled by the salt exclusion effect, and the impact of hydrate content is not significant. However, when hydrate saturation exceeds 20%, the increase in hydrates leads to enhanced pore blockage, causing significant variations in resistivity. Through resistivity–saturation relationship models established based on electromagnetic testing techniques, we can analyze the anomalous resistivity responses in GHs and apply these findings for calculating and evaluating the saturation of hydrate reservoirs.

4.3. Thermal Properties

In the actual hydrate reservoirs, the presence of natural gas, water, hydrates, and mineral particles creates a multiphase coupled system that complicates the heat transfer process, making it challenging to accurately measure and predict the thermal conductivity parameters of the reservoirs. Numerous computational models for heat transfer in GHs have been developed, yet there is still a need for extensive experimental data to further calibrate and optimize these model parameters. Various experimental studies have revealed the complex interactions between porosity, effective stress, grain size, and the pore spaces filled by fluids and hydrates [113–115]. For GHs, their effective thermal conductivity largely depends on the heat transfer processes between particles, including the following: (a) conduction along the mineral; (b) particle–fluid–particle conduction across the fluid near contacts; (c) particle-to-particle conduction across contacts; (d) fluid convection within large pores; (e) particle–fluid conduction; and (f) conduction along the pore fluid within the pore space (hydrostatic and advection pore fluid), as shown in Figure 11 [116,117]. Experimental studies, such as those by Waite et al. [118], have found that with increasing solid hydrate content, the effective thermal conductivity of sand and methane hydrate mixtures initially increases and then decreases, reaching a maximum when the solid hydrate proportion is 33%. The increase in thermal conductivity is due to hydrates in the pores enhancing particle contacts, thereby strengthening heat transfer [116]. As hydrates fill the pores and gradually replace sand grains, the overall thermal conductivity decreases because the thermal conductivity of hydrates is lower than that of mineral particles [116,119]. Furthermore, confining the stress and phase transition processes also affects the thermal conductivity of hydrate-bearing sediments. Effectively confining stress can increase the number and quality of particle contacts, raising the thermal conductivity; during hydrate dissociation, the migration of water improves contact quality, also increasing thermal conductivity [120]. Thus, the effective thermal conductivity of GHs under multiphase coupling conditions in hydrate reservoirs is not only related to the thermal conductivity of the components, but should also consider contributions from sediment particles and pore fluids.

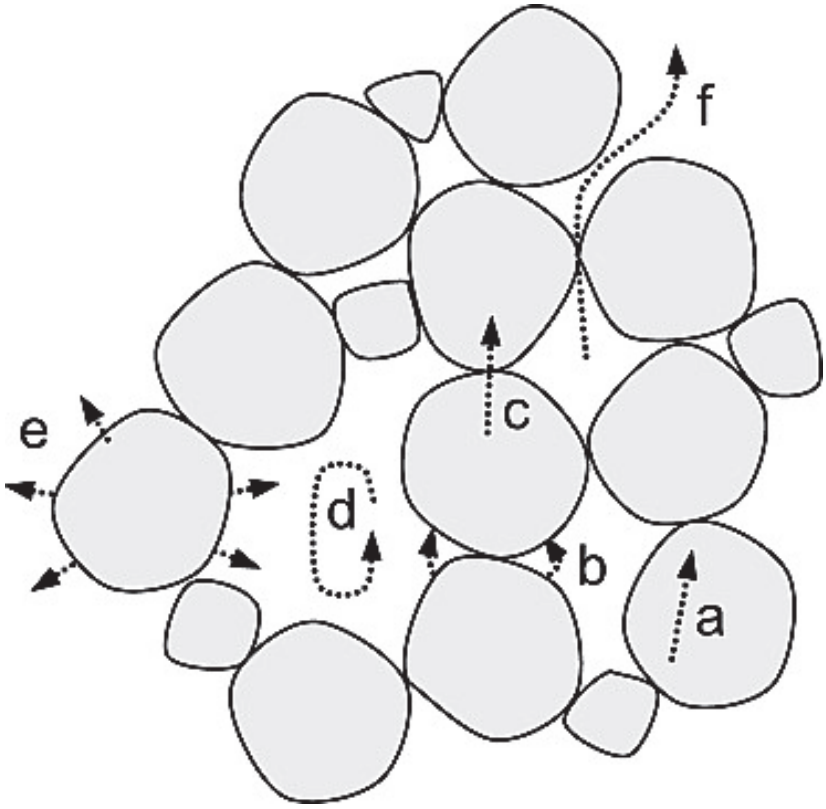

Figure 11. Primary particle-level heat transport processes in granular materials [116]. Copyright (2009), with permission from American Geophysical Union.

4.4. Fluid Dynamics Characteristics

Permeability is commonly used to measure the ability of a porous medium to allow fluid passage. The microstructure of the porous medium not only controls the permeability and fluid flow paths, but also influences the saturation and aggregation distribution of the NGH [111]. Besides the mineral composition, shape, and arrangement of sediment particles, as well as the surface area and tortuosity of the pores, the presence of NGH adds complexity to the sedimentary reservoirs. The spatial distribution of hydrates alters the size, shape, and interconnectivity of pores, thereby changing the sediments' permeability [113]. Numerous experimental studies at macroscopic and microscopic scales have investigated fluid flow phenomena in hydrate-bearing porous sediments, exploring the relationship between permeability and the liquid phase flow patterns within GHs. The presence of hydrates affects the permeability by reducing the pore size and altering pore shape. When hydrates form within pore spaces, the fluid transport pathways are diminished, correspondingly reducing permeability [121,122]. Wang et al. [123] combined pore network models with X-ray computed tomography (X-CT) to study the impact of grain size and porosity on the permeability of porous media, finding that larger grain sizes correspond to higher porosity and greater absolute permeability. Fine grains, typically smaller than 100 μm, often coexist with NGH-bearing sediments and are easily mobilized by the flow of water and/or gas during the formation of gas hydrate. The migration of fine grains, involving the generation, movement, and retention of solid particles in porous media, inevitably leads to a reduction in permeability [124]. Furthermore, under identical water saturation conditions in reactors, higher porosity results in greater relative water permeability and lower gas permeability [114]. The research by Jin et al. [125] showed that the absolute permeability of sediments is directly proportional to the number of continuous pores in the vertical direction. The ratio of horizontal to vertical channel numbers also affects absolute permeability [126]. Seol et al. have studied the impact of hydrate saturation on the permeability of sedimentary layers [127]. They found that hydrates initially form in

porous media at low saturations, and when hydrate saturation is below 40%, the impact on sediment permeability is minimal. However, when hydrate saturation exceeds 40%, the permeability of the reservoir sediments significantly decreases.

5. Conclusions and Future Directions

Current laboratory tests, field observations, and sample analyses have extensively studied the physical properties of submarine GHs, revealing critical characteristics such as porosity, permeability, thermal performance, mechanical properties, and the composition and structure of sediments. These studies aid in better understanding how various sediment properties impact hydrate formation and exploitation.

Gas hydrates exist in solid form within reservoirs in marine environments and are present in multiple occurrence forms, complicating the description of reservoir physical properties. The extraction process of NGH involves complex interactions among multiple physical fields within the reservoir, including gas–water two-phase flow, reservoir thermodynamics, phase transition dynamics, and geomechanical deformations, posing significant challenges to the study of GH characteristics. Research on GH properties will increasingly focus on the dynamic changes in fundamental physical property parameters related to the flow field, such as relative permeability and capillary forces of gas–water; dynamic changes in the thermal properties of hydrate-bearing sediments related to the temperature field, including the endothermic nature of hydrate decomposition; studies on the kinetics of hydrate formation/decomposition related to the chemical field, especially considering equations pertinent to porous media; and the mechanical properties of and dynamic changes in hydrate-bearing sediments related to the mechanical field. Thus, further elucidating the coupling relationships among these physical fields, obtaining key coupled parameters and their dynamic characteristics, and advancing foundational research on the physical properties of marine GHs are critical pathways to guide the rational and efficient extraction of hydrates.

Complex environmental and geological conditions can easily trigger multiphase flow obstacles and control risks of safe pressure in hydrate extractions, making the foundational research on the physical properties of marine GHs crucial for the safe regulation of NGH resource exploitation and geological risk management. Integrating stratigraphic exploration predictions with sample analyses, and establishing a bridge between "deep-sea in-situ laboratories" and "onshore simulation experimental systems", the creation of "in-situ experimental stations" that examine the interplay between natural gas hydrate extraction processes and deep-sea environmental changes will likely be a future trend in GHs foundational physical property research. This approach will aid in uncovering the complex environmental dynamics of and overall macroscopic changes in the hydrate system, further advancing hydrate extraction technologies, reducing geological risks in engineering, and addressing the challenges of sustainable development in the hydrate industry.

Author Contributions: Conceptualization, J.Y.; methodology, K.Y.; validation, J.Y. and K.Y.; writing—original draft preparation, J.Y.; writing—review and editing, X.L., M.M. and X.R.; supervision, K.Y.; project administration, X.L. and Z.C.; funding acquisition, T.H., W.P., and R.Q. All authors have read and agreed to the published version of the manuscript.

Funding: This work was supported by State Key Laboratory of Offshore Natural Gas Hydrates Open Fund Project (KJQZ-2024-2102).

Data Availability Statement: Data are contained within the article.

Conflicts of Interest: The authors declare no conflicts of interest.

References

1. Buffett, B.A. Clathrate hydrates. *Annu. Rev. Earth Planet. Sci.* **2000**, *28*, 477–507. [CrossRef]
2. Li, X.S.; Xu, C.G.; Zhang, Y.; Ruan, X.K.; Li, G.; Wang, Y. Investigation into gas production from natural gas hydrate: A review. *Appl. Energy* **2016**, *172*, 286–322. [CrossRef]
3. Sain, K.; Gupta, H. Gas hydrates in India: Potential and development. *Gondwana Res.* **2012**, *22*, 645–657. [CrossRef]

4. Makogon, Y.F.; Holditch, S.A.; Makogon, T.Y. Natural gas-hydrates—A potential energy source for the 21st Century. *J. Pet. Sci. Eng.* **2007**, *56*, 14–31. [CrossRef]
5. Collett, T.; Johnson, A.; Knapp, C.; Boswell, R.J. *Natural Gas Hydrates: Energy Resource Potential and Associated Geologic Hazard*; The American Association of petroleum Geologists: Tulsa, OK, USA, 2009.
6. Dallimore, S.; Wright, J.; Yamamoto, K.; Bellefleur, G.J. Proof of concept for gas hydrate production using the depressurization technique, as established by the JOGMEC/NRCan/Aurora Mallik 2007–2008 Gas Hydrate Production Research Well Program. *Bull. Geol. Surv. Can.* **2012**, *601*, 1–15.
7. Boswell, R.; Schoderbek, D.; Collett, T.S.; Ohtsuki, S.; White, M.; Anderson, B.J. The Iġnik Sikumi Field Experiment, Alaska North Slope: Design, Operations, and Implications for CO2–CH4 Exchange in Gas Hydrate Reservoirs. *Energy Fuels* **2016**, *31*, 140–153. [CrossRef]
8. Ye, J.L.; Qin, X.W.; Xie, W.W.; Lu, H.L.; Ma, B.J.; Qiu, H.J.; Liang, J.Q.; Lu, J.A.; Kuang, Z.G.; Lu, C.; et al. The second natural gas hydrate production test in the South China Sea. *China Geol.* **2020**, *3*, 197–209. [CrossRef]
9. Jiang, M.; Sun, C.; Crosta, G.B.; Zhang, W. A study of submarine steep slope failures triggered by thermal dissociation of methane hydrates using a coupled CFD-DEM approach. *Eng. Geol.* **2015**, *190*, 1–16. [CrossRef]
10. Wallmann, K.; Riedel, M.; Hong, W.L.; Patton, H.; Hubbard, A.; Pape, T.; Hsu, C.W.; Schmidt, C.; Johnson, J.E.; Torres, M.E.; et al. Gas hydrate dissociation off Svalbard induced by isostatic rebound rather than global warming. *Nat. Commun.* **2018**, *9*, 83. [CrossRef]
11. McConnell, D.R.; Zhang, Z.; Boswell, R. Review of progress in evaluating gas hydrate drilling hazards. *Mar. Pet. Geol.* **2012**, *34*, 209–223. [CrossRef]
12. Liu, L.; Liu, C.; Wu, N.; Ruan, H.; Zhang, Y.; Hao, X.; Bu, Q. Advances in pressure core transfer and testing technology of offshore hydrate-bearing sediments. *Geol. Bull. China* **2021**, *40*, 408–422.
13. Yoneda, J.; Suzuki, K.; Oshima, M.; Muraoka, M.; Jin, Y.S.K. Empirical evaluation of the strength and deformation characteristics of natural and synthetic gas hydrate-bearing sediments with different ranges of porosity, hydrate saturation, effective stress, and strain rate. *Prog. Earth Planet. Sci.* **2024**, *11*, 3. [CrossRef]
14. Tamaki, M.; Fujii, T.; Suzuki, K. Characterization and Prediction of the Gas Hydrate Reservoir at the Second Offshore Gas Production Test Site in the Eastern Nankai Trough, Japan. *Energies* **2017**, *10*, 1678. [CrossRef]
15. Haines, S.S.; Collett, T.S.; Yoneda, J.; Shimoda, N.; Boswell, R.; Okinaka, N. Gas Hydrate Saturation Estimates, Gas Hydrate Occurrence, and Reservoir Characteristics Based on Well Log Data from the Hydrate-01 Stratigraphic Test Well, Alaska North Slope. *Energy Fuels* **2022**, *36*, 3040–3050. [CrossRef]
16. Winters, W.; Walker, M.; Hunter, R.; Collett, T.; Boswell, R.; Rose, K.; Waite, W.; Torres, M.; Patil, S.; Dandekar, A. Physical properties of sediment from the Mount Elbert Gas Hydrate Stratigraphic Test Well, Alaska North Slope. *Mar. Pet. Geol.* **2011**, *28*, 361–380. [CrossRef]
17. Fujii, T.; Suzuki, K.; Takayama, T.; Tamaki, M.; Komatsu, Y.; Konno, Y.; Yoneda, J.; Yamamoto, K.; Nagao, J. Geological setting and characterization of a methane hydrate reservoir distributed at the first offshore production test site on the Daini-Atsumi Knoll in the eastern Nankai Trough, Japan. *Mar. Pet. Geol.* **2015**, *66*, 310–322. [CrossRef]
18. Zhang, Q.; Yang, Z.; He, T.; Lu, H.; Zhang, Y. Growth pattern of dispersed methane hydrates in brine-saturated unconsolidated sediments via joint velocity and resistivity analysis. *J. Nat. Gas Sci. Eng.* **2021**, *96*, 104279. [CrossRef]
19. Li, Y.H.; Song, Y.C.; Yu, F.; Liu, W.G.; Zhao, J.G. Experimental study on mechanical properties of gas hydrate-bearing sediments using kaolin clay. *China Ocean. Eng.* **2011**, *25*, 113–122. [CrossRef]
20. Misyura, S.Y.; Donskoy, I.G.; Manakov, A.Y.; Morozov, V.S.; Strizhak, P.A.; Skiba, S.S.; Sagidullin, A.K. Studying the influence of key parameters on the methane hydrate dissociation in order to improve the storage efficiency. *J. Energy Storage* **2021**, *44*, 103288. [CrossRef]
21. Piñero, E.; Hensen, C.; Haeckel, M.; Rottke, W.; Fuchs, T.; Wallmann, K. 3-D numerical modelling of methane hydrate accumulations using PetroMod. *Mar. Pet. Geol.* **2016**, *71*, 288–295. [CrossRef]
22. Su, P.; Liang, J.; Peng, J.; Zhang, W.; Xu, J. Petroleum systems modeling on gas hydrate of the first experimental exploitation region in the Shenhu area, northern South China sea. *J. Asian Earth Sci.* **2018**, *168*, 57–76. [CrossRef]
23. Falenty, A.; Kuhs, W.F. "Self-Preservation" of CO_2 Gas Hydrates-Surface Microstructure and Ice Perfection. *J. Phys. Chem. B* **2009**, *113*, 15975–15988. [CrossRef] [PubMed]
24. Lu, J.; Lin, D.; Li, D.; Liang, D.; Wen, L.; Wu, S.; Zhang, Y.; He, Y.; Shi, L.; Xiong, Y. Microcosmic Characteristics of Hydrate Formation and Decomposition in the Different Particle Size Sediments Captured by Cryo-SEM. *J. Mar. Sci. Eng.* **2022**, *10*, 769. [CrossRef]
25. Le, T.X.; Bornert, M.; Brown, R.; Aimedieu, P.; Broseta, D.; Chabot, B.; King, A.; Tang, A.M. Combining Optical Microscopy and X-ray Computed Tomography Reveals Novel Morphologies and Growth Processes of Methane Hydrate in Sand Pores. *Energies* **2021**, *14*, 5672. [CrossRef]
26. Bai, C.; Su, P.; Su, X.; Guo, J.; Cui, H.; Han, S.; Zhang, G. Sediment Microstructure in Gas Hydrate Reservoirs and its Association with Gas Hydrate Accumulation: A Case Study From the Northern South China Sea. *Front. Earth Sci.* **2022**, *10*, 876134. [CrossRef]
27. Liu, J.Q.; Kong, L.; Zhao, Y.P.; Sang, S.K.; Niu, G.; Wang, X.R.; Zhou, C.Y. Test research progress on mechanical and physical properties of hydrate-bearing sediments. *Int. J. Hydrogen Energy* **2024**, *53*, 562–581. [CrossRef]

28. Tse, J.S.; McKinnon, W.R.; Marchi, M. Thermal expansion of structure I ethylene oxide hydrate. *J. Phys. Chem.* **2002**, *91*, 4188–4193. [CrossRef]
29. Tse, C.W.; Bishnoi, P.R. Prediction of carbon dioxide gas hydrate formation conditions in aqueous electrolyte solutions. *Can. J. Chem. Eng.* **2009**, *72*, 119–124. [CrossRef]
30. Ma, S.; Zheng, J.-n.; Tang, D.; Li, Y.; Li, Q.; Lv, X. Application of X-Ray Computed Tomography Technology in Gas Hydrate. *Energy Technol.* **2019**, *7*, 1800699.
31. Yang, L.; Zhao, J.F.; Liu, W.G.; Yang, M.J.; Song, Y.C. Experimental study on the effective thermal conductivity of hydrate-bearing sediments. *Energy* **2015**, *79*, 203–211.
32. Li, C.; Hu, G.; Zhang, W.; Ye, Y.; Liu, C.; Li, Q.; Sun, J. Influence of foraminifera on formation and occurrence characteristics of natural gas hydrates in fine-grained sediments from Shenhu area, South China Sea. *Sci. China Earth Sci.* **2016**, *59*, 2223–2230. [CrossRef]
33. Kneafsey, T.J.; Tomutsa, L.; Moridis, G.J.; Seol, Y.; Freifeld, B.M.; Taylor, C.E.; Gupta, A. Methane hydrate formation and dissociation in a partially saturated core-scale sand sample. *J. Pet. Sci. Eng.* **2007**, *56*, 108–126. [CrossRef]
34. Chen, X.Y.; Espinoza, D.N. Ostwald ripening changes the pore habit and spatial variability of clathrate hydrate. *Fuel* **2018**, *214*, 614–622. [CrossRef]
35. Lei, L.; Liu, Z.; Seol, Y.; Boswell, R.; Dai, S. An Investigation of Hydrate Formation in Unsaturated Sediments Using X-ray Computed Tomography. *J. Geophys. Res. Solid Earth* **2019**, *124*, 3335–3349. [CrossRef]
36. Abbasi, G.R.; Arif, M.; Isah, A.; Ali, M.; Mahmoud, M.; Hoteit, H.; Keshavarz, A.; Iglauer, S. Gas hydrate characterization in sediments via x-ray microcomputed tomography. *Earth-Science Reviews* **2022**, *234*, 104233. [CrossRef]
37. Al-Raoush, R.; Hannun, J.; Jarrar, Z.; Alshibli, K.; Jung, J. In Impact of Fines Type on Gas Flow Using 3D Micro-Computed Tomography. In Proceedings of the SPE Kuwait Oil & Gas Show and Conference, Mishref, Kuwait, 13–16 October 2019.
38. Bu, Q.; Xing, T.; Li, C.; Zhao, J.; Liu, C.; Wang, Z.; Zhao, W.; Kang, J.; Meng, Q.; Hu, G. Effect of Hydrate Microscopic Distribution on Acoustic Characteristics during Hydrate Dissociation: An Insight from Combined Acoustic-CT Detection Study. *J. Mar. Sci. Eng.* **2022**, *10*, 1089. [CrossRef]
39. Makogon, Y.F. *Hydrates of Hydrocarbons*; PennWell Publishing Company: Tulsa, OK, USA, 1997; 400p.
40. Vlasic, T.M.; Servio, P.D.; Rey, A.D. Infrared Spectra of Gas Hydrates from First-Principles. *J. Phys. Chem. B* **2019**, *123*, 936–947. [CrossRef]
41. Morita, K.; Nakano, S.; Ohgaki, K. Structure and stability of ethane hydrate crystal. *Fluid Phase Equilibria* **2000**, *169*, 167–175. [CrossRef]
42. Choukroun, M.; Morizet, Y.; Grasset, O. Raman study of methane clathrate hydrates under pressure: New evidence for the metastability of structure II. *J. Raman Spectrosc.* **2006**, *38*, 440–451. [CrossRef]
43. Dec, S.F.; Bowler, K.E.; Stadterman, L.L.; Koh, C.A.; Sloan, E.D. NMR study of methane+ ethane structure I hydrate decomposition. *J. Phys. Chem. A* **2007**, *111*, 4297–4303. [CrossRef] [PubMed]
44. Gupta, A.; Dec, S.F.; Koh, C.A.; Sloan, E. NMR investigation of methane hydrate dissociation. *J. Phys. Chem. C* **2007**, *111*, 2341–2346. [CrossRef]
45. Giovannetti, R.; Maria Gambelli, A.; Castellani, B.; Rossi, A.; Minicucci, M.; Zannotti, M.; Li, Y.; Rossi, F. May sediments affect the inhibiting properties of NaCl on CH_4 and CO_2 hydrates formation? an experimental report. *J. Mol. Liq.* **2022**, *359*, 119300. [CrossRef]
46. Li, X.; Huang, W.; Sun, J.; Wang, Z.; Wang, J.; Liu, Y. NMR Investigation of Methane Hydrate Formation and Dissociation Behavior Induced by Heat Flow in Sandy Porous Media. *Energy Fuels* **2024**, *38*, 5834–5846. [CrossRef]
47. Rueff, R.M.; Dendy Sloan, E.; Yesavage, V.F. Heat capacity and heat of dissociation of methane hydrates. *AIChE J.* **2004**, *34*, 1468–1476. [CrossRef]
48. Yamamoto, Y.; Nagashima, K.; Kornai, T.; Wakisaka, A. Effect of Inhibitor Methanol on the Microscopic Structure of Aqueous Solution. *Ann. N. Y. Acad. Sci.* **2006**, *912*, 797–806. [CrossRef]
49. Tao, Y.; Yan, K.; Li, X.; Chen, Z.; Yu, Y.; Xu, C. Effects of Salinity on Formation Behavior of Methane Hydrate in Montmorillonite. *Energies* **2020**, *13*, 231. [CrossRef]
50. Li, X.Y.; Li, X.S.; Wang, Y.; Li, G.; Zhang, Y.; Hu, H.Q.; Wan, K.; Zeng, H.P. Influence of Particle Size on the Heat and Mass Transfer Characteristics of Methane Hydrate Formation and Decomposition in Porous Media. *Energy Fuels* **2021**, *35*, 2153–2164. [CrossRef]
51. He, J.; Li, X.S.; Chen, Z.Y.; You, C.Y.; Yan, K.F.; Xia, Z.M.; Li, Q.P. Effect of hydrate distribution on effective thermal conductivity changes during hydrate formation in hydrate-bearing quartz sands. *Int. J. Heat Mass Transf.* **2021**, *174*, 121289. [CrossRef]
52. Li, X.X.; Wei, R.C.; Li, Q.P.; Pang, W.X.; Fan, Q.; Chen, G.J.; Sun, C.Y. Experimental investigation on the effective thermal conductivities of different hydrate-bearing sediments. *Pet. Sci.* **2023**, *20*, 2479–2487. [CrossRef]
53. Liu, S.; Liu, S.; Ren, T. Ultrasonic tomography based temperature distribution measurement method. *Measurement* **2016**, *94*, 671–679. [CrossRef]
54. Jia, Y.; Skliar, M. Noninvasive Ultrasound Measurements of Temperature Distributionand Heat Fluxes in Solids. *Energy Fuels* **2016**, *30*, 4363–4371. [CrossRef]
55. Zhao, J.; Wang, B.; Yang, L.; Cheng, C.; Song, Y. A novel apparatus for in situ measurement of thermal conductivity of hydrate-bearing sediments. *Rev. Sci. Instrum.* **2015**, *86*, 085110. [CrossRef]

56. Zhou, Y.; Zhou, J.; Chen, P.; Wei, C. Shear strength degradation of gas hydrate-bearing sediment due to partial hydrate dissociation. *J. Rock Mech. Geotech. Eng.* **2024**, *16*, 2749–2763. [CrossRef]
57. Zhou, Y.; Wei, C.F.; Zhou, J.Z.; Chen, P.; Wei, H.Z. Development and application of gas hydrate injection synthesis and direct shear test system. *Rock Soil Mech.* **2021**, *42*, 2311–2320.
58. Zhao, Y.P.; Kong, L.; Liu, L.L.; Hu, G.W.; Ji, Y.K.; Bu, Q.T.; Bai, C.Y.; Zhao, J.H.; Li, J.; Liu, J.Q.; et al. Mechanical behaviors of natural gas hydrate-bearing clayey-silty sediments: Experiments and constitutive modeling. *Ocean Eng.* **2024**, *294*, 116791. [CrossRef]
59. Yoneda, J.; Jin, Y.; Katagiri, J.; Tenma, N. Strengthening mechanism of cemented hydrate-bearing sand at microscales. *Geophys. Res. Lett.* **2016**, *43*, 7442–7450. [CrossRef]
60. Wu, P.; Li, Y.; Liu, W.; Sun, X.; Kong, X.; Song, Y. Cementation Failure Behavior of Consolidated Gas Hydrate-Bearing Sand. *J. Geophys. Res. Solid Earth* **2020**, *125*, e2019JB018623. [CrossRef]
61. Hyodo, M.; Wu, Y.; Nakashima, K.; Kajiyama, S.; Nakata, Y. Influence of Fines Content on the Mechanical Behavior of Methane Hydrate-Bearing Sediments. *J. Geophys. Res. Solid Earth* **2017**, *122*, 7511–7524. [CrossRef]
62. Sahoo, S.K.; North, L.J.; Marín-Moreno, H.; Minshull, T.A.; Best, A.I. Laboratory observations of frequency-dependent ultrasonic P-wave velocity and attenuation during methane hydrate formation in Berea sandstone. *Geophys. J. Int.* **2019**, *219*, 713–723. [CrossRef]
63. Jin, Y.; Li, S.; Yang, D. Experimental and theoretical quantification of the relationship between electrical resistivity and hydrate saturation in porous media. *Fuel* **2020**, *269*, 117378. [CrossRef]
64. Kumari, A.; Khan, S.H.; Majumder, C.B.; Arora, A.; Dixit, G. Physio-chemical and mineralogical analysis of gas hydrate bearing sediments of Andaman Basin. *Mar. Geophys. Res.* **2021**, *42*, 2. [CrossRef]
65. Zhang, G.; Liang, J.; Lu, J.; Yang, S.; Zhang, M.; Holland, M.; Schultheiss, P.; Su, X.; Sha, Z.; Xu, H.; et al. Geological features, controlling factors and potential prospects of the gas hydrate occurrence in the east part of the Pearl River Mouth Basin, South China Sea. *Mar. Pet. Geol.* **2015**, *67*, 356–367. [CrossRef]
66. Collett, T.S.; Johnson, A.H.; Knapp, C.C.; Boswell, R.; Collett, T.; Johnson, A.; Knapp, C.; Boswell, R. Natural Gas Hydrates: A Review. In *Natural Gas Hydrates—Energy Resource Potential and Associated Geologic Hazards*; American Association of Petroleum Geologists: Tulsa, OK, USA, 2009; Volume 89.
67. Li, J.; Lu, J.A.; Kang, D.; Ning, F.; Lu, H.; Kuang, Z.; Wang, D.; Liu, C.; Hu, G.; Wang, J.; et al. Lithological characteristics and hydrocarbon gas sources of gas hydrate-bearing sediments in the Shenhu area, South China Sea: Implications from the W01B and W02B sites. *Mar. Geol.* **2019**, *408*, 36–47. [CrossRef]
68. Fan, Q.; Li, Q.; Zhou, S.; Li, L.; Zhu, Z.; Lv, X. Source-Reservoir Characteristics and Accumulation of Gas Chimney-Type Gas Hydrates in Qiongdongnan Basin, Northern South China Sea. *Front. Earth Sci.* **2022**, *10*, 880471. [CrossRef]
69. Ren, X.; Guo, Z.; Ning, F.; Ma, S. Permeability of hydrate-bearing sediments. *Earth-Sci. Rev.* **2020**, *202*, 103100. [CrossRef]
70. Liu, C.H.; Sun, Y. B, Characteristics of marine gas hydrate reservoir and its resource evaluation methods. *Mar. Geol. Quat. Geol.* **2021**, *41*, 44–57.
71. Dallimore, S.; Collett, T. Regional gas hydrate occurrences, permafrost conditions, and Cenozoic geology, Mackenzie Delta area. *Bull.-Geol. Surv. Can.* **1999**, *544*, 31–44.
72. Dallimore, S.; Collett, T. *Scientific Results from the Mallik 2002 Gas Hydrate Production Research Well Program, Mackenzie Delta, Northwest Territories, Canada*; Geological Survey of Canada: Vancouver, BC, Canada, 2005.
73. Zhang, X.H.; Lu, X.B.; Liu, L.L. Advances in natural gas hydrate recovery methods. *Prog. Geophys.* **2014**, *29*, 858–869.
74. Yoneda, J.; Jin, Y.; Muraoka, M.; Oshima, M.; Suzuki, K.; Walker, M.; Otsuki, S.; Kumagai, K.; Collett, T.S.; Boswell, R.; et al. Multiple physical properties of gas hydrate-bearing sediments recovered from Alaska North Slope 2018 Hydrate-01 Stratigraphic Test Well. *Mar. Pet. Geol.* **2021**, *123*, 104748. [CrossRef]
75. Anderson, B.; Boswell, R.; Collett, T.S.; Farrell, H.; Ohtsuki, S.; White, M.; Zyrianova, M. Review of the findings of the Iġnik Sikumi CO2-CH4 gas hydrate exchange field trial. In Proceedings of the 8th International Conference on Gas Hydrates (ICGH8-2014), Beijing, China, 28 July–1 August 2014.
76. Lu, Z.; Zhu, Y.; Zhang, Y.; Wen, H.; Li, Y.; Liu, C. Gas hydrate occurrences in the Qilian Mountain permafrost, Qinghai Province, China. *Cold Reg. Sci. Technol.* **2011**, *66*, 93–104. [CrossRef]
77. Lu, Z.; Zhu, Y.; Liu, H.; Zhang, Y.; Jin, C.; Huang, X.; Wang, P. Gas source for gas hydrate and its significance in the Qilian Mountain permafrost, Qinghai. *Mar. Pet. Geol.* **2013**, *43*, 341–348. [CrossRef]
78. Liu, C.L.; Meng, Q.G.; He, X.L.; Li, C.F.; Ye, Y.G.; Lu, Z.Q.; Zhu, Y.H.; Li, Y.H.; Liang, J.Q. Comparison of the characteristics for natural gas hydrate recovered from marine and terrestrial areas in China. *J. Geochem. Explor.* **2015**, *152*, 67–74. [CrossRef]
79. Noguchi, S.; Shimoda, N.; Takano, O.; Oikawa, N.; Inamori, T.; Saeki, T.; Fujii, T. 3-D internal architecture of methane hydrate-bearing turbidite channels in the eastern Nankai Trough, Japan. *Mar. Pet. Geol.* **2011**, *28*, 1817–1828. [CrossRef]
80. Saeki, T.; Fujii, T.; Inamori, T.; Kobayashi, T.; Hayashi, M.; Nagakubo, S.; Takano, O. In Extraction of Methane Hydrate Concentrated Zone for Resource Assessment in the Eastern Nankai Trough, Japan. In Proceedings of the Offshore Technology Conference, Houston, TX, USA, 5–8 May 2008.
81. Konno, Y.; Fujii, T.; Sato, A.; Akamine, K.; Naiki, M.; Masuda, Y.; Yamamoto, K.; Nagao, J. Key Findings of the World's First Offshore Methane Hydrate Production Test off the Coast of Japan: Toward Future Commercial Production. *Energy Fuels* **2017**, *31*, 2607–2616. [CrossRef]

82. Wei, J.; Liang, J.; Lu, J.; Zhang, W.; He, Y. Characteristics and dynamics of gas hydrate systems in the northwestern South China Sea—Results of the fifth gas hydrate drilling expedition. *Mar. Pet. Geol.* **2019**, *110*, 287–298. [CrossRef]
83. Zhang, H.; Lu, H.; Wu, N.; Liang, J. The methane hydrate accumulation controlled compellingly by sediment grain at Shenhu, northern South China Sea. *Chin. Sci. Bull.* **2016**, *61*, 388–397. [CrossRef]
84. Jiang, H.; Su, M.; Wu, D.; Sha, Z.; Kuang, Z.; Wu, N.; Lei, X.; Liu, J.; Yang, R.; Cong, X.; et al. Fine-grained turbidites in GMGS01 of the Shenhu Area, northern South China Sea and its significance. *Mar. Geol. Quat. Geol.* **2017**, *37*, 131–140.
85. Li, J.F.; Ye, J.L.; Qin, X.W.; Qiu, H.J.; Wu, N.Y.; Lu, H.L.; Xie, W.W.; Lu, J.A.; Peng, F.; Xu, Z.Q.; et al. The first offshore natural gas hydrate production test in South China Sea. *China Geol.* **2018**, *1*, 5–16. [CrossRef]
86. Horozal, S.; Kim, G.Y.; Bahk, J.J.; Wilkens, R.H.; Yoo, D.G.; Ryu, B.J.; Kim, S.P. Core and sediment physical property correlation of the second Ulleung Basin Gas Hydrate Drilling Expedition (UBGH2) results in the East Sea (Japan Sea). *Mar. Pet. Geol.* **2015**, *59*, 535–562. [CrossRef]
87. Winters, W.J.; Wilcox-Cline, R.W.; Long, P.; Dewri, S.K.; Kumar, P.; Stern, L.; Kerr, L. Comparison of the physical and geotechnical properties of gas-hydrate-bearing sediments from offshore India and other gas-hydrate-reservoir systems. *Mar. Pet. Geol.* **2014**, *58*, 139–167. [CrossRef]
88. Henninges, J.; Huenges, E.; Burkhardt, H. In situ thermal conductivity of gas-hydrate-bearing sediments of the Mallik 5L-38 well. *J. Geophys. Res. Solid Earth* **2005**, *110*, B11206. [CrossRef]
89. Wu, N.; Huang, L.; Hu, G.; Li, Y.; Chen, Q.; Liu, C. Geological controlling factors and scientific challenges for offshore gas hydrate exploitation. *Mar. Geol. Quat. Geol.* **2017**, *37*, 1–11.
90. Sun, J.; Zhang, L.; Ning, F.; Lei, H.; Liu, T.; Hu, G.; Lu, H.; Lu, J.; Liu, C.; Jiang, G.; et al. Production potential and stability of hydrate-bearing sediments at the site GMGS3-W19 in the South China Sea: A preliminary feasibility study. *Mar. Pet. Geol.* **2017**, *86*, 447–473. [CrossRef]
91. Zhang, W.; Liang, J.; Wei, J.; Su, P.; Lin, L.; Huang, W. Origin of natural gases and associated gas hydrates in the Shenhu area, northern South China Sea: Results from the China gas hydrate drilling expeditions. *J. Asian Earth Sci.* **2019**, *183*, 103953. [CrossRef]
92. Qin, X.W.; Lu, J.A.; Lu, H.L.; Qiu, H.J.; Liang, J.Q.; Kang, D.J.; Zhan, L.S.; Lu, H.F.; Kuang, Z.G. Coexistence of natural gas hydrate, free gas and water in the gas hydrate system in the Shenhu Area, South China Sea. *China Geol.* **2020**, *3*, 210–220. [CrossRef]
93. Ye, J.L.; Qin, X.W.; Xie, W.W.; Lu, H.L.; Ma, B.J.; Qiu, H.J.; Liang, J.Q.; Lu, J.A.; Kuang, Z.G.; Lu, C. Main progress of the second gas hydrate trial production in the South China Sea. *Geol. China* **2020**, *47*, 557–568.
94. Yamamoto, K.; Boswell, R.; Collett, T. S.; Dallimore, S. R.; Lu, H. Review of Past Gas Production Attempts from Subsurface Gas Hydrate Deposits and Necessity of Long-Term Production Testing. *Energy Fuels* **2022**, *36*, 5047–5062.
95. Stern, L.A.; Kirby, S.H.; Durham, W.B. Polycrystalline methane hydrate: Synthesis from superheated ice, and low-temperature mechanical properties. *Energy Fuels* **1998**, *12*, 201–211. [CrossRef]
96. Wu, P.; Li, Y.; Sun, X.; Liu, W.; Song, Y. Mechanical Characteristics of Hydrate-Bearing Sediment: A Review. *Energy Fuels* **2020**, *35*, 1041–1057. [CrossRef]
97. Hyodo, M.; Yoneda, J.; Yoshimoto, N.; Nakata, Y. Mechanical and dissociation properties of methane hydrate-bearing sand in deep seabed. *Soils Found.* **2013**, *53*, 299–314. [CrossRef]
98. Kajiyama, S.; Wu, Y.; Hyodo, M.; Nakata, Y.; Nakashima, K.; Yoshimoto, N. Experimental investigation on the mechanical properties of methane hydrate-bearing sand formed with rounded particles. *J. Nat. Gas Sci. Eng.* **2017**, *45*, 96–107. [CrossRef]
99. Madhusudhan, B.N.; Clayton, C.R.I.; Priest, J.A. The Effects of Hydrate on the Strength and Stiffness of Some Sands. *J. Geophys. Res. Solid Earth* **2019**, *124*, 65–75. [CrossRef]
100. Hyodo, M.; Li, Y.; Yoneda, J.; Nakata, Y.; Yoshimoto, N.; Kajiyama, S.; Nishimura, A.; Song, Y. A comparative analysis of the mechanical behavior of carbon dioxide and methane hydrate-bearing sediments. *Am. Mineral.* **2014**, *99*, 178–183. [CrossRef]
101. Yun, T.S.; Santamarina, C.J.; Ruppel, C. Mechanical Properties of Sand, Silt, and Clay Containing Tetrahydrofuran Hydrate. *J. Geophys. Res. Solid Earth* **2007**, *112*, B04106.
102. Miyazaki, K.; Masui, A.; Sakamoto, Y.; Aoki, K.; Tenma, N.; Yamaguchi, T. Triaxial Compressive Properties of Artificial Methane Hydrate-Bearing Sediment. *J. Geophys. Res.* **2011**, *116*, B06102.
103. Masui, A.; Haneda, H.; Ogata, Y.; Aoki, K. Effects of Methane Hydrate Formation on Shear Strength of Synthetic Methane Hydrate Sediments. In Proceedings of the Fifteenth International Offshore and Polar Engineering Conference, Seoul, Republic of Korea, 19–24 June 2005; pp 364–369.
104. Miyazaki, K.; Oikawa, Y.; Haneda, H.; Yamaguchi, T. Triaxial Compressive Property of Artificial CO_2-Hydrate Sand. *Int. J. Offshore Polar Eng.* **2016**, *26*, 315–320.
105. Wang, L.; Li, Y.; Shen, S.; Liu, W.; Sun, X.; Liu, Y.; Zhao, J. Mechanical Behaviors of Gas Hydrate-Bearing Clayey Sediments of the South China Sea. *Environ. Geotech.* **2019**, *13*, 1.
106. Lee, J.Y. *Hydrate-Bearing Sediments: Formation and Geophysical Properties*; Georgia Institute of Technology: Atlanta, GA, USA, 2007.
107. Shankar, U.; Riedel, M. Gas hydrate saturation in the Krishna–Godavari basin from P-wave velocity and electrical resistivity logs. *Mar. Pet. Geol.* **2011**, *28*, 1768–1778. [CrossRef]
108. Weitemeyer, K.A.; Constable, S.C.; Key, K.W.; Behrens, J.P. First results from a marine controlled-source electromagnetic survey to detect gas hydrates offshore Oregon. *Geophys. Res. Lett.* **2006**, *33*, L03304. [CrossRef]

109. Schwalenberg, K.; Haeckel, M.; Poort, J.; Jegen, M. Evaluation of gas hydrate deposits in an active seep area using marine controlled source electromagnetics: Results from Opouawe Bank, Hikurangi Margin, New Zealand. *Mar. Geol.* **2010**, *272*, 79–88. [CrossRef]
110. Weitemeyer, K.A.; Constable, S.; Tréhu, A.M. A marine electromagnetic survey to detect gas hydrate at Hydrate Ridge, Oregon. *Geophys. J. Int.* **2011**, *187*, 45–62. [CrossRef]
111. Waite, W.F.; Santamarina, J.C.; Cortes, D.D.; Dugan, B.; Espinoza, D.N.; Germaine, J.; Jang, J.; Jung, J.W.; Kneafsey, T.J.; Shin, H.; et al. Physical properties of hydrate-bearing sediments. *Rev. Geophys.* **2009**, *47*, RG4003. [CrossRef]
112. Chen, G.Q.; Li, C.F.; Liu, C.L.; Xing, L.C. Effect of microscopic distribution of methane hydrate on resistivity in porous media. *Adv. New Renew. Energy* **2019**, *7*, 493–499.
113. Huang, D.; Fan, S. Measuring and modeling thermal conductivity of gas hydrate-bearing sand. *J. Geophys. Res. Solid Earth* **2005**, *110*, B01311. [CrossRef]
114. Chong, Z.R.; Yang, S.H.B.; Babu, P.; Linga, P.; Li, X.S. Review of natural gas hydrates as an energy resource: Prospects and challenges. *Appl. Energy* **2016**, *162*, 1633–1652. [CrossRef]
115. Chuvilin, E.; Bukhanov, B. Effect of Hydrate Formation Conditions on Thermal Conductivity of Gas-Saturated Sediments. *Energy Fuels* **2017**, *31*, 5246–5254. [CrossRef]
116. Cortes, D.D.; Martin, A.I.; Yun, T.S.; Francisca, F.M.; Santamarina, J.C.; Ruppel, C. Thermal conductivity of hydrate-bearing sediments. *J. Geophys. Res.-Solid Earth* **2009**, *114*, B11103. [CrossRef]
117. Yun, T.S.; Santamarina, J.C. Fundamental study of thermal conduction in dry soils. *Granul. Matter* **2008**, *10*, 197–207. [CrossRef]
118. Waite, W.F.; deMartin, B.J.; Kirby, S.H.; Pinkston, J.; Ruppel, C.D. Thermal conductivity measurements in porous mixtures of methane hydrate and quartz sand. *Geophys. Res. Lett.* **2002**, *29*, 82-1–82-4. [CrossRef]
119. Waite, W.F.; Gilbert, L.Y.; Winters, W.J.; Mason, D.H. Thermal property measurements in Tetrahydrofuran (THF) hydrate and hydrate-bearing sediment between −25 and +4 °C, and their application to methane hydrate. In Proceedings of the Fifth International Conference on Gas Hydrates, Trondheim, Norway, 12–16 June 2005.
120. Dai, S.; Cha, J.H.; Rosenbaum, E.J.; Zhang, W.; Seol, Y. Thermal conductivity measurements in unsaturated hydrate-bearing sediments. *Geophys. Res. Lett.* **2015**, *42*, 6295–6305. [CrossRef]
121. Li, B.; Li, X.-S.; Li, G.; Jia, J.-L.; Feng, J.-C. Measurements of Water Permeability in Unconsolidated Porous Media with Methane Hydrate Formation. *Energies* **2013**, *6*, 3622–3636. [CrossRef]
122. Konno, Y.; Yoneda, J.; Egawa, K.; Ito, T.; Jin, Y.; Kida, M.; Suzuki, K.; Fujii, T.; Nagao, J. Permeability of sediment cores from methane hydrate deposit in the Eastern Nankai Trough. *Mar. Pet. Geol.* **2015**, *66*, 487–495. [CrossRef]
123. Wang, J.; Zhao, J.; Zhang, Y.; Wang, D.; Li, Y.; Song, Y. Analysis of the effect of particle size on permeability in hydrate-bearing porous media using pore network models combined with CT. *Fuel* **2016**, *163*, 34–40. [CrossRef]
124. Vasheghani Farahani, M.; Foroughi, S.; Norouzi, S.; Jamshidi, S. Mechanistic Study of Fines Migration in Porous Media Using Lattice Boltzmann Method Coupled with Rigid Body Physics Engine. *J. Energy Resour. Technol.* **2019**, *141*, 123001. [CrossRef]
125. Jin, S.; Nagao, J.; Takeya, S.; Jin, Y.; Hayashi, J.; Kamata, Y.; Ebinuma, T.; Narita, H. Structural Investigation of Methane Hydrate Sediments by Microfocus X-ray Computed Tomography Technique under High-Pressure Conditions. *Jpn. J. Appl. Phys.* **2006**, *45*, L714. [CrossRef]
126. Jin, Y.; Hayashi, J.; Nagao, J.; Suzuki, K.; Minagawa, H.; Ebinuma, T.; Narita, H. New Method of Assessing Absolute Permeability of Natural Methane Hydrate Sediments by Microfocus X-ray Computed Tomography. *Jpn. J. Appl. Phys.* **2007**, *46*, 3159. [CrossRef]
127. Seol, Y.; Myshakin, E.; Kneafsey, T. Quantitative applications of X-ray CT observations for core-scale hydrate studies. In Proceedings of the 7th International Conference on Gas Hydrates, Edinburgh, UK, 17–21 July 2011.

energies

MDPI

Article

Evidence of Microbial Activity in Coal Seam Production Water and Hydrochemical Constraints

Yuan Bao [1,2,*], Xueru Chen [1], Zhidong Guo [3], Zhengyan Li [4], Yufei Zhuang [1] and Min Gao [1]

[1] College of Geology and Environment, Xi'an University of Science and Technology, Xi'an 710054, China; 22209071015@stu.xust.edu.cn (X.C.); 23209226137@stu.xust.edu.cn (Y.Z.); 20109071006@stu.xust.edu.cn (M.G.)
[2] Shaanxi Provincial Key Laboratory of Geological Support for Coal Green Exploitation, Xi'an 710054, China
[3] Institute of Engineering and Technology, PetroChina Coalbed Methane Company Limited, Xi'an 710082, China; guozd@petrochina.com.cn
[4] Baode Coal Mine, China Shenhua Shendong Coal Group, Xinzhou 036603, China; 15135302802@163.com
* Correspondence: y.bao@foxmail.com

Abstract: This study aims to explore microbial activity evidence, composition of archaeal communities, and environmental constraints in coalbed-produced waters from the Hancheng Block, a representative region for coalbed methane development on the eastern margin of Ordos Basin, China. The investigation involves analyzing microbial community composition using 16S rRNA sequencing analysis as well as examining hydrogeochemical parameters. The results indicate that *Euryarchaeota* and *Thaumarchaeota* are predominant phyla within archaeal communities present in coalbed-produced water from the Hancheng Block. Among these communities, *Methanobacterium* is identified as the most abundant genus, followed by *Methanothrix* and *Methanoregula*. Moreover, a positive correlation is observed between the abundance of *Methanobacterium* and the levels of total dissolved solids as well as Mn; conversely, there is a negative correlation with dissolved organic carbon, Zn concentrations, and pH. The abundance of Co and Ni primarily influence *Methanothrix* while pH and Zn play significant roles in controlling *Methanoregula*. Additionally, No. 5 coal seam waters exhibit greater species diversity in the archaeal community compared to No. 11 counterparts. The higher abundance of archaea in the No. 5 coal seam promotes biogas generation due to the correlation between bicarbonate and dissolved inorganic carbon isotope. These research findings hold scientific significance in guiding the exploration and development of biogas within coal seams.

Keywords: archaeal community; hydrochemistry composition; coalbed-produced water; dissolved inorganic carbon isotopes; trace elements

1. Introduction

Coal bed methane (CBM) refers to primarily methane adsorbed on the surface of the coal matrix, with a small portion existing as free gas in the pores and cracks of coal. CBM has demonstrated significant potential for efficient and clean energy production [1,2]. China possesses abundant CBM resources, with two commercially developed CBM bases established in the Qinshui Basin and the eastern margin of Ordos Basin [3,4]. The principle behind CBM extraction involves reducing pressure within the coal reservoir by pumping groundwater from both within and surrounding it [5], thereby releasing any trapped gas. This process allows for the desorption, diffusion, and migration of CBM into wellbores through pores and fissures for exploitation purposes [6]. Coal seam water serves as a habitat for underground microorganisms that have been exposed to coal seams over extended periods while residing within this water. Produced water derived from draining wells used during mining operations or other activities related to extracting CBM from such seams contains valuable geological information [7]. Paying attention to microbial diversity alongside hydrogeochemical characteristics present in produced water derived from coal seams can significantly impact our understanding of living environments and constraints

faced by microorganisms situated deep beneath the Earth's surface inside these same seams, ultimately guiding exploration efforts aimed at developing new sources of CBM.

With the rapid advancement of the CBM industry and increasingly stringent global environmental protection requirements, experts and scholars have been increasingly emphasizing studying water produced from coal seam mining processes [8–10]. Currently, research on the hydrogeochemical characteristics of coalbed-produced water primarily focuses on conventional ions [11,12], hydrogen, oxygen, and inorganic carbon isotopes [13,14], as well as trace elements [15,16]. Simultaneously, numerous studies have explored archaeal communities involved in coal metabolism within produced water from coal seams. These studies have found that *Methanosarcina* is the predominant methanogenic archaea species found in Powder River Basin's produced waters [17,18], while *Methanosaeta*/*Methanosarcina* are major methanogens present in San Juan Basin's CBM fields. Additionally identified were the main *Methanobacterium*, *Methanomicrobium*, *Methanolobus* [19,20], and *Methanospirillum* species present at Qinshui Basin's CBM field [21]. Therefore, studying both the hydrogeochemical characteristics of produced waters and the diversity among archaeal communities is crucial for indicating trends in CBM development.

The Hancheng Block, located in the eastern part of the Weibei Uplift within the southeastern Ordos Basin, stands as one of China's earliest regions where commercial success has been achieved in CBM development. This area contains abundant CBM resources primarily found within coal seams No. 5 and No. 11 of the Upper Carboniferous Taiyuan Formation [22]. To investigate the structure and composition characteristics of archaeal communities within situ coal seams, along with their controlling factors, this study collected a total of 12 samples from the Hancheng Block, comprising eight samples from No. 11 coal seams and four samples from No. 5 coal seams. The produced water was analyzed for conventional ions, hydrogen and oxygen isotopes, dissolved inorganic carbon isotopes, and trace elements, as well as a quantification of archaeal 16S rRNA. These research findings can provide theoretical guidance for predicting late-stage productivity in the Hancheng Block's CBM wells and conducting field tests on enhancing methane production through microorganism injection and nutrient solution supplementation.

2. Materials and Methods

2.1. Samples Collection

Based on CBM well locations and single-layer drainage analysis conducted in the Hancheng area, a comprehensive set of twelve representative produced water samples were systematically collected to ensure complete spatial coverage across all target areas. The precise sampling sites can be observed in Figure 1. Prior to collecting on-site samples, all polyethylene sample containers underwent thorough sterilization in the laboratory using ultraviolet light and were subsequently sealed for sterility purposes. Subsequently, polyethylene sampling bottles (one 2.5 L and two 500 mL) were flushed three times with output water from the targeted coal seam being mined to ensure the integrity of collected samples, while allowing the water valve to open and drain for a specific duration to avoid residual wellbore water in the pipeline. During the collection activities at drainage outlets of CBM wells, one 500 mL polyethylene sampling bottle underwent acidification using dilute hydrochloric acid until reaching pH < 3 conditions for testing cation concentration. Another 500 mL polyethylene bottle was filled and refrigerated at 0 °C. After completing the collection process, the air within these bottles was expelled by filling them completely before sealing them with bottle caps to check for any potential leakage issues. Finally, the time and place of each sampling event were recorded. The original water samples were collected using a larger capacity (2.5 L) polyethylene bottle while smaller volumes (500 mL) that had not undergone acidification were filtered under laboratory conditions utilizing filter membranes with pore sizes measuring either 0.22 μm or 5 μm as required. Following this process, the filter membranes were packed into a centrifuge tube and stored at −20 °C for subsequent high-throughput sequencing of archaeal community DNA analysis purposes. A 500 mL water sample was collected from a 2.5 L polyethylene sampling bottle for analyzing

pH levels, anions, total dissolved solids (TDS), trace elements, hydrogen and oxygen isotopes, as well as dissolved inorganic carbon isotopes. The hydrogeochemical test was submitted to the Guizhou Institute of Geochemistry, Chinese Academy of Sciences for analysis purposes, while the microbial 16S rRNA high-throughput sequencing was sent to Shanghai Piceno Biotechnology Co., Ltd. (Shanghai, China), for testing.

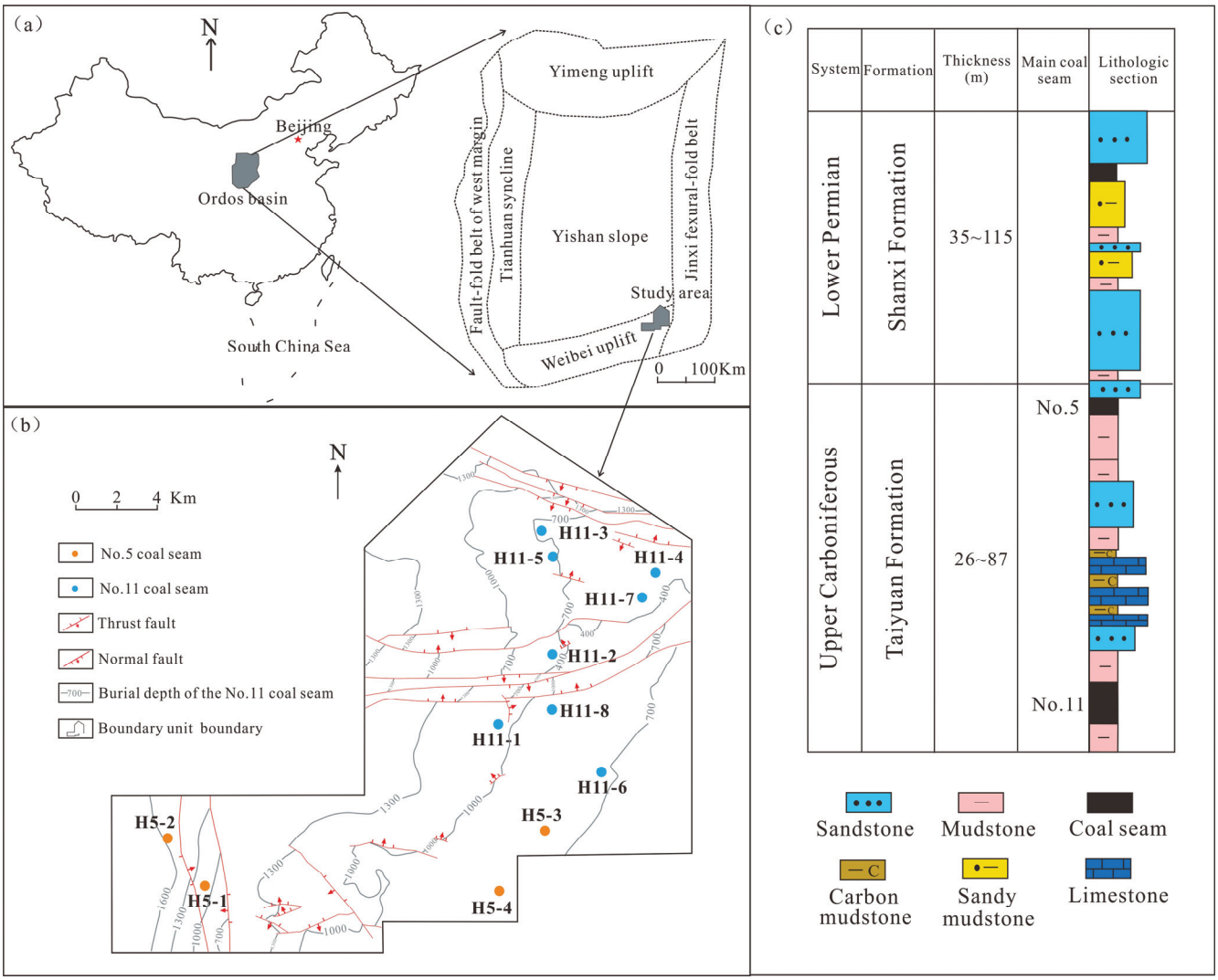

Figure 1. (**a**) The location and structural outline of Ordos basin; (**b**) the structure outline and sampling locations of the Hancheng Block; (**c**) column diagram depicting coal seam distribution.

2.2. Test Methods

The microbial samples were initially subjected to DNA extraction using the OMEGA Soil DNA Kit (M5635-02) from Omega Bio-Tek, Norcross, GA, USA. Subsequently, the quantity and quality of the extracted DNA were assessed using the NanoDrop NC2000 spectrophotometer from Thermo Fisher Scientific, Waltham, MA, USA. Additionally, agarose gel electrophoresis was performed for further verification. Following that step, Polymerase Chain Reaction (PCR) amplification utilizing archaea 16sv8v9-1106F (TTWAGTCAGGCAACGAGC) and 16sv8v9-1378R (TGTGCAAGGAGCAGGGAC) primers was conducted to target methanogen 16S rRNA genomes. Finally, the sequencing data analysis was conducted using the following method: equal amounts of PCR amplified sequences were pooled together and subjected to pair-end 2 × 250 bp sequencing on the Illumina NovaSeq platform with NovaSeq 6000 SP Reagent Kit (500 cycles) at Shanghai Personal Biotechnology Co., Ltd. (Shanghai, China). The sequence data analyses primarily utilized QIIME2 2019.4.

(https://docs.qiime2.org/2019.4/tutorials/, accessed on 31 October 2022) and R packages (v3.2.0).

The water sample test includes the analysis of cations, anions, hydrogen isotopes (δD), and oxygen isotopes (δ^{18}O) of water, dissolved inorganic carbon isotopes ($\delta^{13}C_{DIC}$), and trace elements. Cationic tests are performed using the Vista MPX inductively coupled plasma-emission spectrometer (Varian Company, Palo Alto, CA, USA), while anionic tests utilize ion chromatography (Thermer Fisher ICS-900). HCO_3^- and CO_3^{2-} ion detection relies on acid titration. The respective standards for cationic tests follow DIN EN ISO17294-1-2007 [23], and those for anionic tests adhere to EN ISO 10304-1-2009 [24]. For measuring δD and δ^{18}O, a liquid isotope analyzer 912-0026 (Los Gatos Research, San Jose, CA, USA) with a standard deviation of 0.6‰ for δD and 0.1‰ for δ^{18}O is employed. The gas isotope mass spectrometer MAT252 is employed for $\delta^{13}C_{DIC}$ testing with a measurement accuracy of less than 0.01‰. The testing methods for δD, δ^{18}O, and $\delta^{13}C_{DIC}$ have been outlined and documented in reference [14]. Trace element analysis uses the NexION300X ICP-MS instrument (PE Company, Cincinnati, OH, USA) following the test standard EPA Method 200.8 [25]. pH measurement was carried out using PP-50-p11 m, while TDS measurement utilized the DDSJ-308A conductivity meter (Shanghai Yilin Scientific Instrument Co., LTD, Shanghai, China). The corresponding analysis method and testing standards were referenced in the literature [26].

3. Results and Analysis

3.1. Archaeal Community Structure of Coalbed-Produced Water

To gain a deeper understanding of the species structure of archaeal communities in the produced water from different coal seams in the Hancheng Block, this study employed 16S rRNA gene amplification and sequencing of microbial samples from the produced water to determine the species composition of archaeal communities (Figure 2). *Euryarchaeota* and *Thaumarchaeota* were identified as the dominant phyla of archaea in the produced water from different coal seams. The proportion of *Euryarchaeota* was 33.38% for H11-4, 61.96% for H5-1, and over 80% for other CBM wells in the Hancheng Block. The relative abundance of *Thaumarchaeota* was relatively high at 4.51% for H11-4 and 6.37% for H11-6, respectively. At the genus level classification, *Methanobacterium* exhibited the highest content followed by *Methanothrix*, *Methanoregula*, *Methanococcus*, *Methanosarcina*, *Methanospirillum*, *Methanocella*, *Methanoculleus*, *Methanolobus*, and *Methanocalculus*. *Methanothrix* accounted for the highest proportion of 35.03% in H11-3 and 27.66% in H5-4. In addition, *Methanosarcina* constituted 10.61% in H11-6, while H5-3 and H5-4 contained respective proportions of 19.04% and 9.96% for *Methanoregula*.

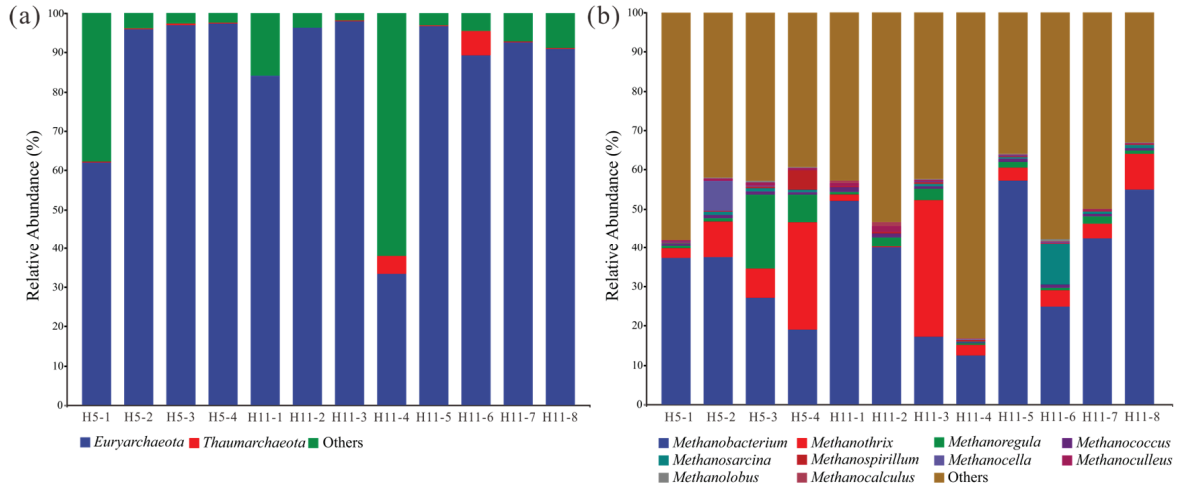

Figure 2. Taxonomic compositions of the top ten most abundant archaea in the Hancheng Block ((**a**). phylum level; (**b**). genus level. The remaining abundance is represented as the "others" group).

3.2. Conventional Ion of Coalbed-Produced Water

The conventional negative, cation, and geochemical parameters of produced water from different coal seams in the Hancheng Block are presented in Table 1. The pH value of the produced water from the No. 11 coal seam ranges from 7.61 to 8.21, with an average value of 7.82. Similarly, the pH value of the produced water from the No. 5 coal seam ranges from 7.66 to 8.32, with an average value of 7.92. The alkaline nature of formation waters in these coal seams creates a favorable environment for methanogen survival. Sodium (Na^+) is found predominantly as cations in both No. 11 and No. 5 coal seam-produced waters, with mass concentrations ranging from 330.29 to 1772.50 mg/L (average: 829.47 mg/L) and from 603.75 to 2003.00 mg/L (average: 1448.59 mg/L), respectively. Additionally, certain concentrations of calcium (Ca^{2+}), magnesium (Mg^{2+}), and potassium (K^+) are also present in water samples produced in this study area. Chloride ions (Cl^-) and bicarbonate ions (HCO_3^-) are identified as major anions within both coal seam-produced waters; higher levels of HCO_3^- suggest a relatively closed groundwater environment along with some sulfate (SO_4^{2-}) concentration observed. TDS concentration varies between 816.90 and 5038.39 mg/L (average: 2239.07 mg/L) in No. 11 coal seam samples, while ranging between 1276.44 and 4906.74 mg/L (average: 3160.50 mg/L) in No. 5 coal seam samples. Dissolved organic carbon (DOC) concentration ranges between 27.17 and 73.82 mg/L (average: 52.84 mg/L) in the No. 11 coal seam in the Hancheng area and between 44.88 and 49.08 mg/L (average: 47.03 mg/L) in No. 5 coal seam.

Table 1. Geochemical parameters of coalbed-produced water in the Hancheng Block.

Sample ID	Coal Seam	Concentration of Conventional Ion ($mg \cdot L^{-1}$)							pH	TDS ($mg \cdot L^{-1}$)	DOC ($mg \cdot L^{-1}$)
		Na^+	K^+	Ca^{2+}	Mg^{2+}	Cl^-	SO_4^{2-}	HCO_3^-			
H5-1	No. 5	2003.00	13.37	34.11	7.11	2416.89	0.56	863.39	7.66	4906.74	44.88
H5-2		1974.50	100.03	16.88	5.22	1811.99	11.86	1555.13	7.88	4698.05	49.08
H5-3		603.75	3.62	3.56	0.59	169.17	<0.10	991.49	8.32	1276.44	45.89
H5-4		808.51	9.69	4.69	0.64	500.38	0.05	873.64	7.96	1760.78	48.26
Average		1347.44	31.68	14.81	3.39	1224.61	4.16	1070.91	7.96	3160.50	47.03
H11-1	No. 11	1163.60	29.15	29.95	16.46	793.87	241.69	1211.83	7.64	2880.64	66.17
H11-2		330.29	3.60	12.54	2.26	109.68	0.06	716.93	7.69	816.90	57.53
H11-3		894.51	7.40	19.22	7.41	801.79	0.12	840.34	7.71	2150.62	27.17
H11-4		536.82	8.55	9.08	0.92	167.80	0.25	914.76	8.21	1180.80	73.82
H11-5		1772.50	30.46	135.72	64.77	1941.86	824.71	536.74	7.61	5038.39	41.40
H11-6		1132.10	46.12	163.11	48.25	602.70	987.22	538.75	7.97	3248.88	54.51
H11-7		366.55	13.51	8.57	2.90	86.71	0.13	815.14	8.16	885.94	58.08
H11-8		742.01	13.11	18.69	4.78	484.01	0.25	895.11	7.73	1710.41	44.04
Average		867.30	18.99	49.61	18.47	623.55	256.80	808.70	7.84	2239.07	52.84

The distinction between the two groups of coal seams can be clearly demonstrated by plotting a histogram of the conventional ion content data of produced water from different coal seams in the Hancheng Block (Figure 3). The concentration of HCO_3^- in the produced water from coal seams H11-1, H11-2, H11-3, H11-4, H11-7, and H11-8 is higher than that of Cl^-, while the concentration of Cl^- in the produced water from coal seams H11-5 and H11-6 is higher than that of HCO_3^-. Similarly, for the No. 5 coal seam, samples such as H5-3 and H5-4 exhibit a higher concentration of HCO_3^- compared to samples like H5-1 and H5-2, which have a higher concentration of Cl^-. Furthermore, elevated levels of SO_4^{2-} are observed in No. 11 coal seam samples, including those from wells H11-1, H11-5, and H11-6, while lower levels are found in the water produced the from No. 5 coal seam. The average cation concentrations in the produced water from the No. 11 coal seam follow this order: $Na^+ > Ca^{2+} > K^+ > Mg^{2+}$, whereas, for the No. 5 coal seam, they are $Na^+ > K^+ > Ca^{2+} > Mg^{2+}$.

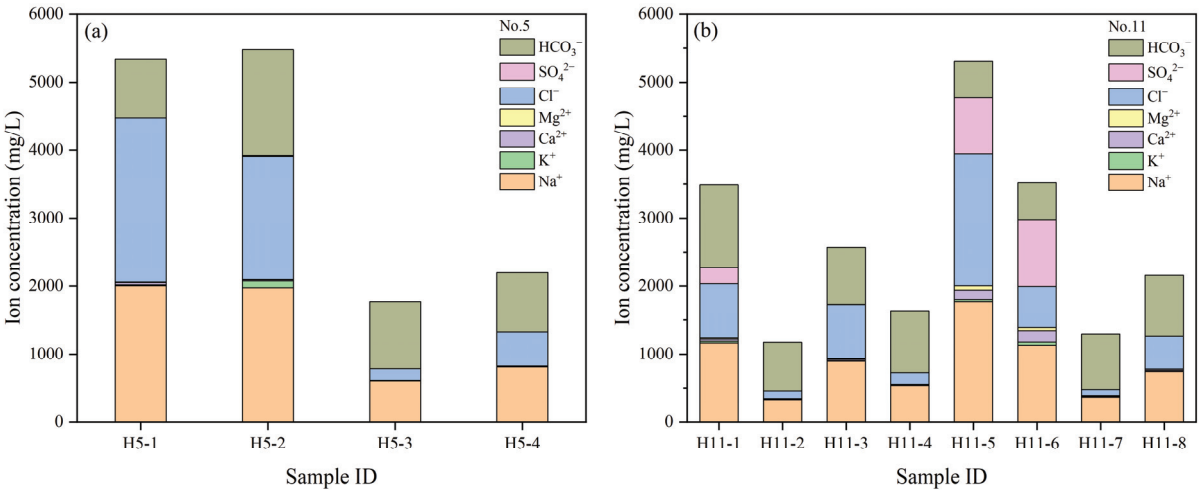

Figure 3. Conventional ion content of coalbed-produced water ((**a**). No. 5; (**b**). No. 11).

The Piper trigram of groundwater chemical composition can be utilized to analyze the types and characteristics of water chemistry, thereby revealing the hydrochemical environment of groundwater [27]. In the Piper ternary diagram (Figure 4), data from six groups of water samples in coal seam No. 11 and four groups of water samples in coal seam No. 5 within the Hancheng Block are plotted. Based on the diagram, H11-1, H11-2, H11-3, H11-4, H11-7, and H11-8 exhibit a hydrochemical type characterized by HCO_3-Na in the produced water from coal seam 11. Conversely, both H11-5 and H11-6 display a Cl-Na hydrochemical type due to their higher salinity levels and elevated chloride ion content as previously studied. Consequently, overall findings indicate that the produced water from the No. 11 coal seam is predominantly composed of HCO_3-Na and Cl-Na. In contrast to this pattern, both samples from H5-1 and H5-2 within the No. 5 coal seam demonstrate higher salinity levels with greater chloride ion content compared to bicarbonate ions; thus, exhibiting a Cl-Na type. Conversely, samples from both H5-3 and H5-4 belong to an HCO_3^- Na-type category within the produced water composition of the No. 5 coal seam.

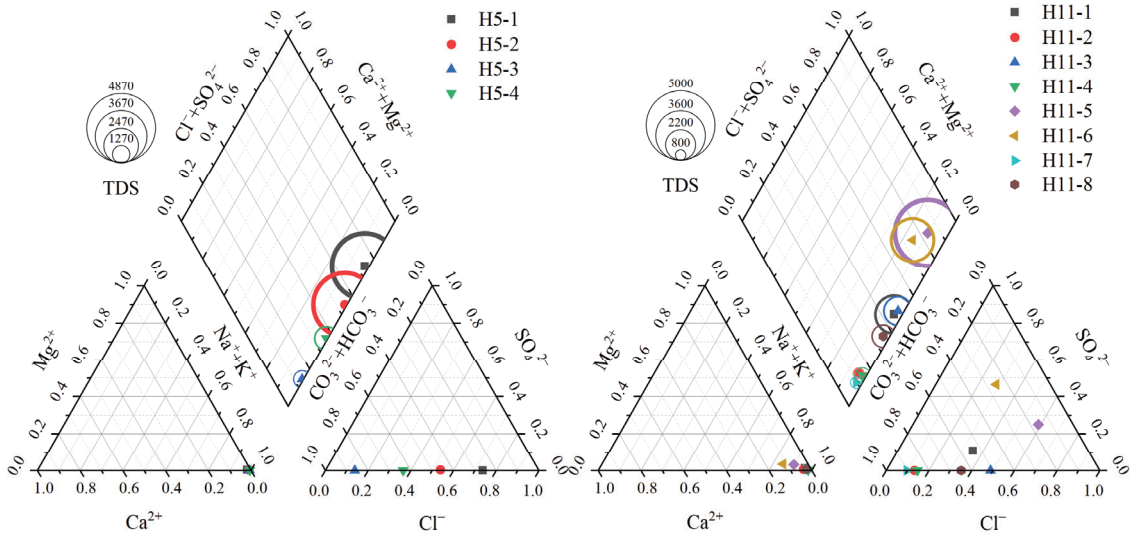

Figure 4. Piper diagram of coalbed-produced water in the Hancheng Block.

3.3. Hydrogen, Oxygen, and Carbon Isotopic Compositions of Coalbed-Produced Water

The test results of δD, δ^{18}O, and $\delta^{13}C_{DIC}$ in the produced water from the coal seam in the Hancheng Block are presented in Table 2. The δD values of coal seam No. 11's produced water range from −113.62‰ to −61.56‰, with an average value of −82.48‰. The δ^{18}O

values range from −15.36‰ to −9.22‰, with an average value of −11.53‰. For coal seam No. 5, the produced water exhibits a narrower range of δD values (−112.07‰ to −72.00‰) compared to coal seam No. 11, with an average value of −89.81‰. Similarly, its δ^{18}O values also show a smaller variation (−15.82‰ to −10.84‰), averaging at −12.78‰. Furthermore, it is worth noting that both the δD and δ^{18}O values for coal seam No. 5's produced water are more negative than those for coal seam No. 11, indicating potential differences in isotopic composition between these two sources. Regarding $\delta^{13}C_{DIC}$, the produced water from coal seam No. 11 displays a wider range (−27.77‰ to 4.02‰) compared to that from coal seam No. 5 (−5.27‰ to 20.54‰). However, their respective averages remain relatively close at 16.00‰ and 11.23‰, respectively. It is noteworthy that, except for well H5-2, the dissolved CO_2 in groundwater samples within this study area exhibit positive $\delta^{13}C_{DIC}$ values, indicating enrichment with ^{13}C [28].

Table 2. The isotopic compositions of hydrogen, oxygen, and dissolved inorganic carbon in coalbed-produced water of the Hancheng Block.

Sample ID	Coal Seam	δD_{H2O} (‰)	$\delta^{18}O_{H2O}$ (‰)	$\delta^{13}C_{DIC}$ (‰)
H5-1	No. 5	−72.00	−10.84	14.51
H5-2		−77.00	−10.99	−5.27
H5-3		−98.16	−13.46	20.54
H5-4		−112.07	−15.82	15.14
Average		−89.81	−12.78	11.23
H11-1	No. 11	−77.79	−11.04	10.18
H11-2		−84.12	−11.45	7.74
H11-3		−61.56	−9.22	19.19
H11-4		−81.47	−11.24	28.08
H11-5		−78.58	−11.27	9.85
H11-6		−113.62	−15.36	4.02
H11-7		−80.10	−11.00	27.77
H11-8		−82.60	−11.66	21.20
Average		−82.48	−11.53	16.00

The hydrogen and oxygen isotope composition of the coal seam-produced water can serve as an indicator of its origin [29]. According to Craig et al. [30], the equation for the Global Meteoric Water Line (GMWL) is $\delta D = 8\delta^{18}O + 10$. The China Meteoric Water Line (CMWL), initially proposed by Zheng et al. in 1983 [31], is represented by the equation: $\delta D = 7.9\delta^{18}O + 8.2$. By projecting the hydrogen and oxygen isotope data from Table 2 onto the δ^{18}O-δD relationship diagram (Figure 5), it becomes evident that the projections for produced water from different coal seams in the Hancheng Block are closely aligned with both GMWL and CMWL, indicating their origin from atmospheric precipitation and subsequent recharge through atmospheric precipitation. This provides a pathway for microbial transportation into coal seams, facilitating microbial degradation and favoring biogenic coalbed methane generation within these seams. However, it should be noted that some points on the graph deviate above or below this line; specifically, the No. 5 coal seam exhibits deviations above the line (left side, D-drift). The occurrence of drift in δ^{18}O may be attributed to water–coal interactions under conditions of evaporation and high temperature. On the other hand, D-drift is generally believed to result from the potential transformation of produced water within coal seams due to methanogenesis processes where methanogens preferentially utilize hydrogen derived from water sources while leaving behind residual groundwater enriched in deuterium. Alternatively, this could also arise due to water–coal interactions between groundwater and coal seams as shown in Equation (1). These observations indicate that generated and migrating produced water from coal seams exhibit dual drift characteristics in both δ^{18}O and δD isotopes, suggesting multiple geochemical processes such as water–coal interaction and methanogenesis during their formation.

$$H_2O + D_{coal} \leftarrow\rightarrow HDO + H_{coal} \quad (1)$$

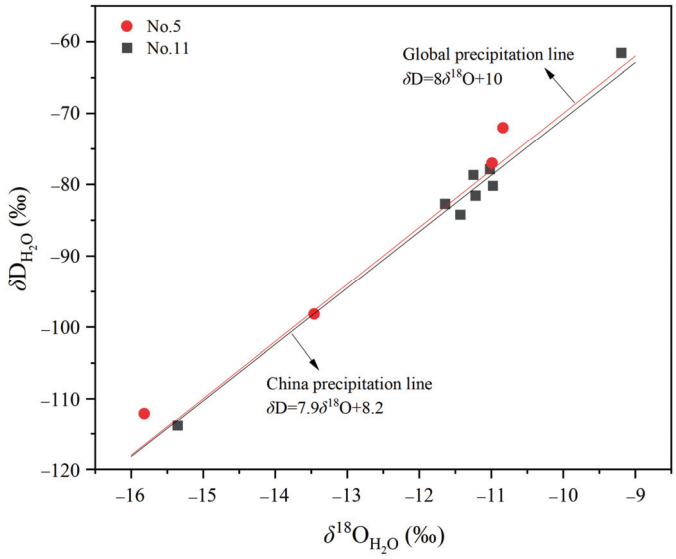

Figure 5. Relationship between δD and δ^{18}O of coalbed-produced water in the Hancheng Block.

3.4. Trace Elements Concentration of Coalbed-Produced Water

The concentration of trace elements in the water produced from the coal seam in the Hancheng Block is presented in Table 3. A total of 24 trace elements, including Al, As, Ba, Co, Cr, Cu, Hg, Li, Mn, Mo, Ni, Pb, Rb, Sb, Se, Sn, Sr, Ti, Tl, U, V, W, Zn, and Zr, were detected in this study. Among them, the contents of Ba, Li, Mn, and Sr were higher. The concentration ranges of Ba, Li, Mn, and Sr in No. 11 coal seam samples are 31.73–3587.82 ppb, 52.42–1185.12 ppb, 1.32–214.73 ppb, and 362.19–6547.09 ppb, respectively; while, in No. 5 coal seam samples, they range from 236.99 to 8455.96 ppb for Ba, from 59.41 to 276.20 ppb for Li, from 12.40 to 149.71 ppb for Mn, and from 552.85 to 8287.18 ppb for Sr. In addition, the presence of trace elements of Co and Ni associated with the archaeal community was also detected [32]. The subsequent Section 4.3 examines the correlation between Co and Ni in relation to the archaeal community.

Table 3. Trace element concentration of coalbed-produced water in the Hancheng Block (unit, ppb).

Sample ID	Coal Seam	Al	As	Ba	Co	Cr	Cu	Hg	Li	Mn	Mo	Ni	Pb	Rb	Sb	Se	Sn	Sr	Ti	Tl	U	V	W	Zn	Zr
H5-1	No. 5	104.24	1.70	7043.93	0.03	0.60	0.01	0.09	246.89	94.46	2.87	3.24	0.11	21.76	0.01	23.08	0.06	8287.18	0.44	0.02	0.02	10.96	0.40	2.55	0.10
H5-2		54.87	1.49	8455.96	0.15	0.71	0.03	0.12	276.20	149.71	12.23	12.26	0.09	32.24	0.12	24.27	0.10	6254.50	0.20	0.02	0.00	7.02	1.13	1.17	0.14
H5-3		74.42	1.21	236.99	0.07	0.39	0.87	0.09	91.04	12.40	7.80	0.14	1.34	5.09	0.04	21.08	0.06	552.85	0.21	0.05	0.01	5.69	1.12	0.00	0.16
H5-4		65.44	1.37	424.41	0.02	3.75	0.52	0.06	59.41	22.15	0.77	18.21	0.02	5.62	0.00	21.52	0.08	732.57	0.23	0.04	0.05	6.06	0.94	0.00	0.18
Average		74.75	1.44	4040.32	0.07	1.36	0.36	0.09	168.38	69.68	5.92	8.46	0.39	16.18	0.04	22.49	0.07	3956.77	0.27	0.03	0.02	7.43	0.90	0.93	0.14
H11-1	No. 11	86.21	1.15	40.76	0.04	0.56	1.05	0.04	327.01	120.97	1.43	1.43	0.08	18.87	0.02	24.32	0.05	2752.64	0.11	0.03	0.00	6.00	0.04	0.00	0.12
H11-2		76.03	0.72	591.53	0.13	1.49	0.00	0.09	52.42	114.82	0.82	0.43	3.57	5.16	0.01	21.05	0.03	495.75	0.27	0.05	0.00	4.35	1.01	0.00	0.07
H11-3		192.80	1.74	3587.82	2.30	1.17	0.09	0.31	177.44	89.39	1.23	4.09	0.09	5.29	0.06	22.19	0.13	2627.68	0.99	0.03	0.10	9.54	7.44	0.71	0.33
H11-4		65.72	1.01	221.40	0.15	0.31	0.27	0.11	169.20	34.22	3.59	0.42	0.07	7.75	0.08	23.54	0.05	282.13	0.03	0.04	0.01	3.59	1.40	60.25	0.08
H11-5		83.81	1.86	31.73	0.14	0.75	0.00	0.07	1185.12	214.73	1.18	3.85	0.21	25.04	0.03	24.15	0.09	6547.09	0.41	0.02	0.00	10.00	0.22	0.00	0.18
H11-6		51.41	2.24	37.30	0.05	0.41	0.00	0.04	480.59	1.32	0.21	1.88	0.00	43.89	0.01	22.81	0.10	5785.94	0.35	0.02	0.02	4.24	0.36	0.00	0.12
H11-7		68.98	0.74	241.55	1.11	0.44	0.25	0.07	106.96	108.68	14.30	2.06	0.03	15.33	0.04	20.92	0.06	362.19	0.22	0.04	0.00	3.46	0.00	0.00	0.06
H11-8		57.08	1.04	1617.65	0.04	0.44	0.00	0.09	113.82	122.18	16.32	0.19	0.03	6.68	0.02	22.64	0.05	1546.00	0.14	0.03	0.01	4.03	0.74	0.00	0.11
Average		85.25	1.31	796.22	0.50	0.70	0.21	0.10	326.57	100.79	4.89	1.75	0.51	16.00	0.03	22.70	0.07	2549.93	0.31	0.03	0.02	5.65	1.40	7.62	0.13

Note: The content is deemed indiscernible by the instrument when its value reaches 0.00.

4. Discussion

4.1. Microbial Diversity in Coalbed-Produced Water

ASV-level alpha diversity indices such as Chao1 richness estimator observed species count Shannon diversity index Simpson index and Good's coverage were calculated based on the ASV table in the QIIME2 software package (Version 2021.2). The alpha diversity index reflects the number, abundance, and evenness of species within a specific region or ecosystem sample, also known as within-habitat diversity [33,34]. To comprehensively evaluate the alpha diversity of archaeal communities in the produced water of coal seams in the Hancheng Block, we utilized the Chao1 and Observed species indices to characterize richness, Shannon and Simpson indices to measure diversity, and the Evenness index to assess evenness. The Coverage index was employed to determine coverage. Figure 6 presents the alpha diversity index of archaeal communities in the produced water from different coal seams in the Hancheng Block. The Coverage index for the archaeal community in coal seams No. 11 and No. 5 was found to be 99.18–99.50% and 98.98–99.40%, respectively, indicating that most archaea present in samples were successfully obtained and detected, ensuring reliable detection results. The Chao1 and Observed species indices for the archaeal community in production water from coal seam No. 11 are lower compared to those from coal seam No. 5, suggesting higher species richness for the archaeal community in production water from coal seam No. 5 than that from coal seam No. 11. The Shannon and Simpson indices along with Evenness indices showed minimal differences between both groups' archaeal communities, implying similar levels of diversity and evenness among them.

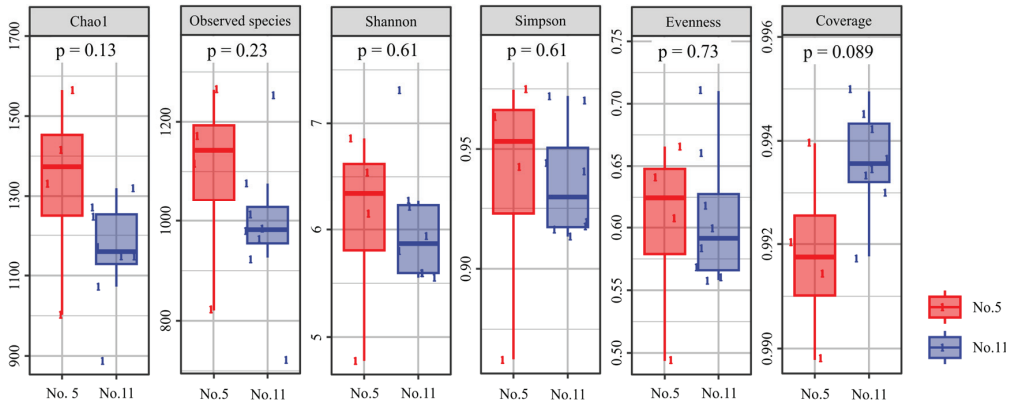

Figure 6. Alpha diversity analysis of archaeal communities.

4.2. Evidence of Microbial Activity in Coalbed-Produced Water

The $\delta^{13}C_{DIC}$ values of surface water and shallow groundwater typically range from −14‰ to −7‰ [35,36]. In contrast, the $\delta^{13}C_{DIC}$ value of produced water from deep underground coalbed methane wells is more enriched, usually ranging from −7‰ to 0‰. Previous studies have indicated that microbial activity can result in dissolved inorganic carbon isotopes in water ranging from 10‰ to 30‰ [36]. In the Hancheng Block, there were eight instances of coal seam producing water with $\delta^{13}C_{DIC}$ values exceeding 10‰ (Figure 7), with five occurring in the No. 11 coal seam and three occurring in the No. 5 coal seam. These findings suggest the occurrence of microbial action within the coal seams of the Hancheng Block.

The $\delta^{13}C_{DIC}$ values of H5-2 from the No. 5 coal seam in the Hancheng Block even demonstrate negative values (−5.27‰). Furthermore, well H11-2, H11-5, and H11-6 from the No. 11 coal seam exhibit relatively low values (<10‰). Other samples fall within the range of 10‰ to 30‰. Variations in burial depth among different well locations result in distinct $\delta^{13}C_{DIC}$ values, which can be attributed to metabolic pathway differences in key microorganisms within the coal seam. Furthermore, a negative correlation is observed between burial depth and $\delta^{13}C_{DIC}$ values in produced water from both the Nos. 5 and

11 coal seams in the Hancheng Block (Figure 8(a_1,b_1)), suggesting that carbon dioxide reduction pathways exist within microbial metabolism processes occurring within these coal seams (Formulas (2) and (3)). Additionally, well H5-2 is in the southwestern region of the study area, adjacent to the footwall of the Qiangao fracture zone. It should be noted that this coal seam exhibits a greater burial depth compared to both the No. 11 coal seam and other No. 5 coal seams, suggesting an evident influence of burial depth on microbial activity.

$$CH_3COOH \rightarrow CH_4 + CO_2 \quad (2)$$

$$CO_2 + 4H_2 \rightarrow CH_4 + 2H_2O \quad (3)$$

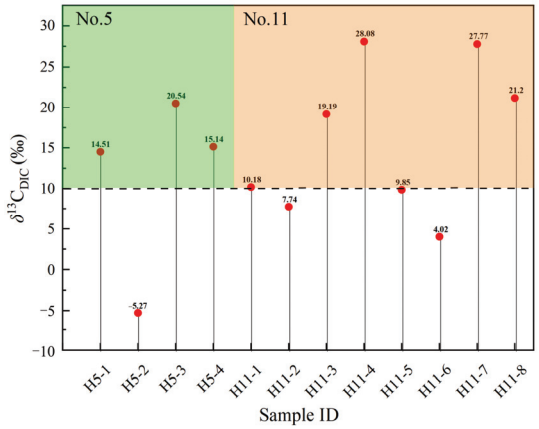

Figure 7. Distribution characteristics of $\delta^{13}C_{DIC}$ of coalbed-produced water in the Hancheng Block.

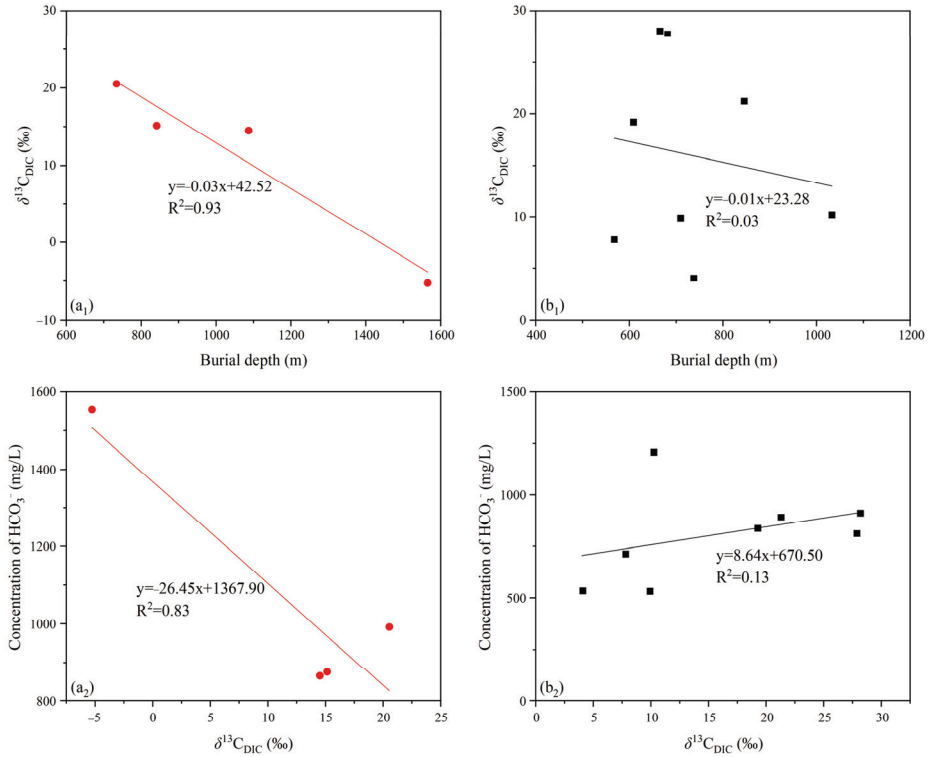

Figure 8. Relationship between $\delta^{13}C_{DIC}$ and buried depth, as well as the concentration of HCO_3^- in coalbed-produced water from the Hancheng Block ((**a_1**) Relationship between $\delta^{13}C_{DIC}$ and buried depth in No.5 coal seam (**b_1**) Relationship between $\delta^{13}C_{DIC}$ and buried depth in No.11 coal seam (**a_2**) Relationship between $\delta^{13}C_{DIC}$ and the concentration of HCO_3^- in No.5 coal seam (**b_2**) Relationship between $\delta^{13}C_{DIC}$ and the concentration of HCO_3^- in No.11 coal seam).

The sources of dissolved inorganic carbon in coal seam-produced water are generally attributed to the dissolution of carbonate minerals, the dissolution of CO_2 in coalbed methane, and microbial methanogenesis [37]. Figure 8(a_2,b_2) illustrate the relationship between HCO_3^- and $\delta^{13}C_{DIC}$ in the produced water from coal seam No. 5 in the Hancheng area. A clear negative correlation is observed between HCO_3^- and $\delta^{13}C_{DIC}$, indicating significant microbial activity within coal seam No. 5, where methanogens preferentially utilize $^{12}CH_4$. The remaining ^{13}C becomes enriched in CO_2 and DIC [38]. Conversely, a positive correlation is observed between HCO_3^- and $\delta^{13}C_{DIC}$ in the produced water from coal seam No. 11 due to its burial beneath coal seam No. 5, which prevents easy mixing with surface water and shallow groundwater. Additionally, coupled with carbonate mineral dissolution and microbial activity within more enriched coal measure strata, these factors contribute to their positive correlation.

4.3. Environmental Factors Influencing the Composition of Archaeal Communities

To investigate the environmental factors governing the archaeal community in the produced water of coal seams Nos. 11 and 5 in the Hancheng Block, we conducted a redundancy analysis (RDA) to investigate the relationship between the archaeal community and hydrogeochemical parameters (including trace elements Co, Ni, Zn, Mn, pH, TDS, DOC). The results of RDA revealed that at both the phylum level (Figure 9a) and genus level (Figure 9b), the cumulative variance of factors influencing the archaeal community accounted for 88.12% and 87.44%, respectively. This essentially reflects the characteristic associations among all variables investigated. At the phylum level, Wells H11-4, H11-6, and H5-1 exhibited significant dissimilarity from other CBM Wells in terms of microflora composition. This finding aligns with Figure 2a as well. Furthermore, as depicted in Figure 9a, *Euryarchaeota*—which is the dominant group of archaea found in coal seam-produced water from the Hancheng Block—was primarily influenced by TDS and trace elements Co, Ni, and Mn. These growth environment factors exhibited positive correlations with *Euryarchaeota* abundance. Additionally, the presence of DOC and Zn showed positive correlations with another dominant group, *Thaumarchaeota*. Zn, on the other hand, had negative correlations with both *Euryarchaeota* and *Thaumarchaeota*.

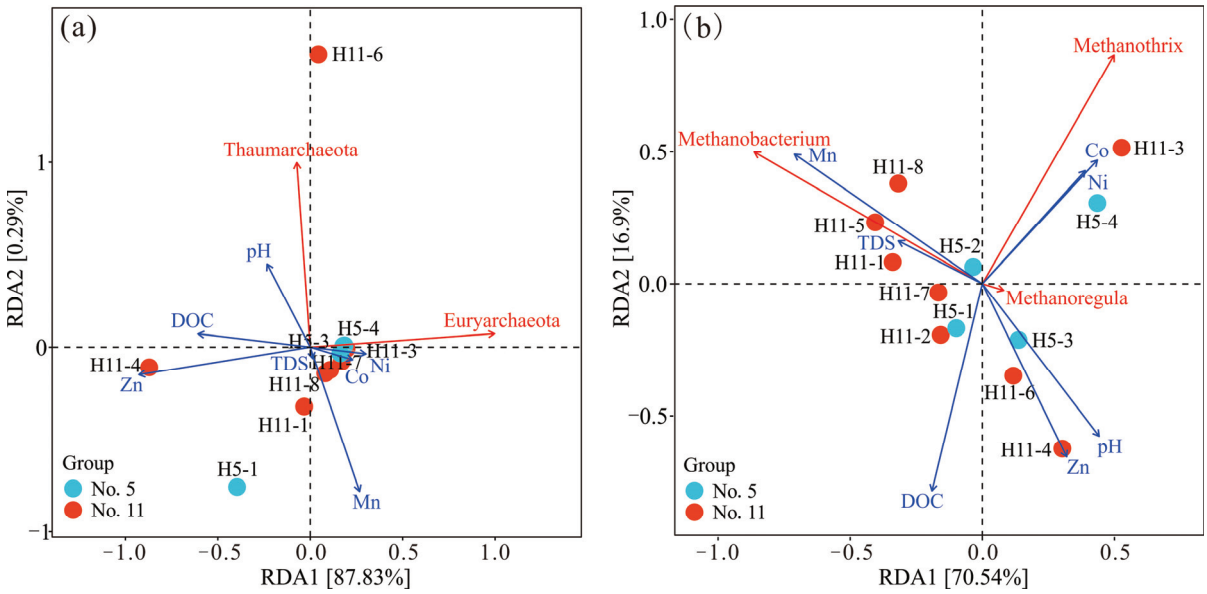

Figure 9. Redundancy analysis of archaea at both phylum (**a**) and genus (**b**) levels.

At the genus level, this study investigated the relationship between the archaeal community, specifically focusing on the first three dominant genera and their respective environmental factors in produced water from 12 CBM wells. *Methanobacterium* was identified

as the predominant genus within the archaeal community in the coal seam-produced water of the Hancheng Block. The data demonstrated a positive correlation between TDS and Mn while showing a negative correlation with DOC, Zn, and pH levels. Notably, relevant laboratory experiments have provided evidence that high TDS content enhances CBM production [39]. Furthermore, the abundance of *Methanothrix* was primarily influenced by Co and Ni. This can be attributed to Co's contribution to bioenzyme Co-dehydrogenase and Methyltransferase activity, while Ni plays a crucial role in Acetyl-CoA synthase and Hydrogenase anabolism processes [40,41]. *Methanoregula* exhibited a lower abundance compared to other dominant genera, primarily influenced by pH levels and Zn concentrations. Specifically, pH showed a negative correlation with *Methanobacterium* and *Methanothrix* but a positive correlation with *Methanoregula*, which may be related to metabolic differences among these different genera. Furthermore, previous studies have indicated that the diversity, abundance, and transcriptional activity of various archaea fluctuate under different pH conditions. This implies that distinct types of archaea can be selectively favored in environments characterized by varying pH levels [42,43]. Overall, there exists a strong association between these environmental factors and different dominant genera, indicating that they play significant roles in shaping the archaeal community present in coal seam-produced water from the Hancheng Block [44].

5. Conclusions

Biogenic coalbed methane is a relatively clean natural gas resource. The relatively light carbon isotope composition of methane indicates microbial degradation of the coal seam in the Hancheng Block during its geological history. The presence of methanogenic archaea in the coal seam water provides direct evidence for the occurrence of biogenic coalbed methane in this area. The presence of dual isotopic drift characteristics in both oxygen and deuterium isotopes within this set of produced water samples indicates various geochemical processes such as interactions between water and coal along with methanogenesis during its migration pathway.

The hydrochemical types of No. 5 and No. 11 coal seams are identified as HCO_3-Na and Cl-Na, respectively. The average pH value of produced water from the No. 11 coal seam measures 7.82, while the No. 5 coal seam records weak alkalinity with an average pH value of 7.92; this alkalinity supports methanogen survival within produced water. *Methanobacterium* is the most prevalent genus, followed by *Methanothrix* and *Methanoregula*. The richness of the archaeal community in coalbed-produced water from coal seam No. 5 surpasses that of coal seam No. 11, which favors biogas generation. The predominant archaeal bacterium, *Methanobacterium*, exhibits positive correlations with total dissolved solids and manganese while displaying negative correlations with dissolved organic carbon, Zn, and pH levels. Co primarily regulates *Methanothrix*, while Ni has a lesser influence on it. Conversely, pH levels and Zn mainly impact *Methanoregula*.

Author Contributions: Y.B.: Writing—review and editing, Conceptualization, Funding acquisition, Investigation, Supervision. X.C.: Formal analysis, Data curation, Methodology, Conceptualization. Z.G.: Writing—review and editing, Resources, Investigation. Z.L.: Writing—original draft, Methodology, Data curation, Y.Z.: Methodology, Investigation, Software, Conceptualization. M.G.: Conceptualization, Formal analysis, Investigation. All authors have read and agreed to the published version of the manuscript.

Funding: The research presented in this paper is financially supported by the National Natural Science Foundation of China (42172200; 41972183).

Data Availability Statement: The original contributions presented in the study are included in the article, further inquiries can be directed to the corresponding author.

Conflicts of Interest: Author Zhidong Guo was employed by the company Institute of Engineering and Technology, PetroChina Coalbed Methane Company Limited. Author Zhengyan Li was employed by the company Baode Coal Mine, China Shenhua Shendong Coal Group. The remain-

ing authors declare that the research was conducted in the absence of any commercial or financial relationships that could be construed as a potential conflict of interest.

References

1. Zhang, Z.; Qin, Y. A preliminary investigation on water quality of coalbed natural gas produced water for beneficial uses: A case study in the southern Qinshui Basin, North China. *Environ. Sci. Pollut. Res.* **2018**, *25*, 21589–21604. [CrossRef]
2. Bao, Y.; Ju, Y.; Yin, Z.; Xiong, J.; Wang, G.; Qi, Y. Influence of reservoir properties on the methane adsorption capacity and fractal features of coal and shale in the upper Permian coal measures of the south Sichuan coalfield, China. *Energy Explor. Exploit.* **2020**, *38*, 57–58. [CrossRef]
3. Huang, H.; Nie, Z.; Chao, H.; Chen, D.; Zhao, Z.; Liu, Y. Discussion of the selection for producing layers of deep CBM wells in Linfen block. *J. China Coal Soc.* **2018**, *43*, 1627–1633.
4. Bao, Y.; Li, Z.; Meng, J.; Chen, X.; Liu, X. Reformation of coal reservoirs by microorganisms and its significance in CBM exploitation. *Fuel* **2024**, *360*, 130642. [CrossRef]
5. Liu, H.; Sang, S.; Formolo, M.; Li, M.; Liu, S.; Xu, H.; An, S.; Li, J.; Wang, X. Production characteristics and drainage optimization of coalbed methane wells: A case study from low-permeability anthracite hosted reservoirs in southern Qinshui Basin, China. *Energy Sustain. Dev.* **2013**, *17*, 412–423. [CrossRef]
6. Tao, S.; Tang, D.Z.; Xu, H.; Lv, Y. Analysis on influence factors of coalbed methane wells productivity and development proposals in southern Qinshui Basin. *J. China Coal Soc.* **2011**, *36*, 194–198.
7. Bao, Y.; An, C.; Wang, C.; Guo, C.; Wang, W. Hydrogeochemical characteristics and water-rock interactions of coalbed-produced water derived from the Dafosi biogenic gas field in the southern margin of Ordos Basin, China. *Geofluids* **2021**, *2021*, 5972497. [CrossRef]
8. Guo, C.; Qin, Y.; Xia, Y.; Ma, D.; Han, D.; Chen, Y.; Chen, W.; Jian, K.; Lu, L. Geochemical characteristics of water produced from CBM wells and implications for commingling CBM production: A case study of the Bide-Santang Basin, western Guizhou, China. *J. Petrol. Sci. Eng.* **2017**, *159*, 666–678. [CrossRef]
9. Guo, C.; Qin, Y.; Wu, C.; Lu, L. Hydrogeological control and productivity modes of coalbed methane commingled production in multi-seam areas: A case study of the Bide–Santang Basin, western Guizhou, South China. *J. Petrol. Sci. Eng.* **2020**, *189*, 107039. [CrossRef]
10. Zhang, Z.; Qin, Y.; Bai, J.; Li, G.; Zhuang, X.; Wang, X. Hydrogeochemistry characteristics of produced waters from CBM wells in southern Qinshui basin and implications for CBM commingled development. *J. Nat. Gas Sci. Eng.* **2018**, *56*, 428–443. [CrossRef]
11. Huang, H.; Sang, S.; Miao, Y.; Dong, Z.; Zhang, H. Trends of ionic concentration variations in water coproduced with coalbed methane in the Tiefa Basin. *Int. J. Coal Geol.* **2017**, *182*, 32–41. [CrossRef]
12. Zhou, B.; Qin, Y.; Yang, Z. Ion composition of produced water from coalbed methane wells in western Guizhou, China, and associated productivity response. *Fuel* **2020**, *265*, 116939. [CrossRef]
13. Liu, H.; Fan, Y.; Ma, Y.; He, C.; Gong, F.; Zhu, Z.; Zhu, P. Hydro-chemical characteristics, genesis analysis and risk assessment of Fuyuan Laochang ore concentration area in Yunnan, China. *Pol. J. Environ. Stud.* **2024**, *33*, 727–739. [CrossRef]
14. Yang, Z.; Qin, Y.; Wu, C.; Qin, Z.; Li, G.; Li, C. Geochemical response of produced water in the CBM well group with multiple coal seams and its geological significance—A case study of the Songhe well group in Western Guizhou. *Int. J. Coal Geol.* **2019**, *7*, 39–51. [CrossRef]
15. Dai, S.; Ren, D.; Chou, C.; Finkelman, R.B.; Seredin, V.V.; Zhou, Y. Geochemistry of trace elements in Chinese coals: A review of abundances, genetic types, impacts on human health, and industrial utilization. *Int. J. Coal Geol.* **2012**, *94*, 3–21. [CrossRef]
16. Qin, Y.; Zhang, Z.; Bai, J.; Liu, D. Source apportionment of produced water and feasibility discrimination of commingling CBM production from wells in southern Qinshui Basin. *J. China Coal Soc.* **2014**, *39*, 1892–1898.
17. Rice, D.D. Composition and origins of coalbed gas. Hydrocarbons from coal: AAPG Studies in Geology. *US Geol. Surv.* **1993**, *38*, 159–184.
18. Fu, H.; Li, Y.; Su, X.; Yan, D.; Yang, S.; Wang, G.; Wang, X.; Zhao, W. Environmental conditions and mechanisms restricting microbial methanogenesis in the Miquan region of the southern Junggar Basin, NW China. *GSA Bull.* **2023**, *135*, 420–434. [CrossRef]
19. Flores, R.M.; Rice, C.A.; Stricker, G.D. Methanogenic pathways of coal-bed gas in the Powder River Basin, United States: The geologic factor. *Int. J. Coal Geol.* **2008**, *76*, 52–75. [CrossRef]
20. Wawrik, B.; Mendivelso, M.; Parisi, V.A.; Suflita, J.M.; Davidova, I.A.; Marks, C.R.; Nostrand, J.D.V.; Liang, Y.; Zhou, J.; Huizinga, B.J.; et al. Field and laboratory studies on the bioconversion of coal to methane in the San Juan Basin. *FEMS Microbiol. Ecol.* **2012**, *81*, 26–42. [CrossRef]
21. Yang, X.; Wu, R.; Han, Z.; Wang, B. Analysis of methanogenic community and pathway of coalbed methane fields in the Qinshui Basin based on mcrA gene. *Microbiol. China* **2017**, *44*, 795–806.
22. Bao, Y.; Lv, D.; Guo, Z.; Yun, Y.; Wang, Y.; Li, D. Contribution of sulfate-reducing bacteria in the formation of hydrogen sulfide in coal seams of Hancheng mining area, China. *Geomicrobiol. J.* **2024**, *41*, 35–47. [CrossRef]
23. *DIN EN ISO17294-1-2007*; Water Quality—Application of Inductively Coupled Plasma Mass Spectrometry (ICP-MS)—Part 1: General Guidelines. ISO: Geneva, Switzerland, 2007.

24. *EN ISO 10304-1:2007*; Water Quality—Determination of Dissolved Anions by Liquid Chromatography of Ions—Part 1: Determination of Bromide, Chloride, Fluoride, Nitrate, Nitrite, Phosphate and Sulfate. ISO: Geneva, Switzerland, 2009.
25. *EPA Method 200.8*; Determination of Trace Elements in Waters and Wastes by Inductively Coupled Plasma Mass Spectrometry (ICP-MS). EPA: Washington, DC, USA, 1994.
26. He, M.; Liu, G.; Li, Y.; Zhou, L.; Arif, M.; Liu, Y. Spatial-temporal distribution, source identification, risk assessment and water quality assessment of trace elements in the surface water of typical tributary in Yangtze River delta, China. *Mar. Pollut. Bull.* **2023**, *192*, 115035. [CrossRef]
27. Moreno Merino, L.; Aguilera, H.; González-Jiménez, M.; Díaz-Losada, E. D-Piper, a modified piper diagram to represent big sets of hydrochemical analyses. *Environ. Modell. Softw.* **2021**, *138*, 104979. [CrossRef]
28. Li, Y.; Chen, J.; Tang, S.; Zhang, S.; Xi, Z. Biogeochemical assessment of the coalbed methane source, migration, and fate: A case study of the Shizhuangnan block, southern Qinshui Basin. *ACS Omega* **2022**, *7*, 7715–7724. [CrossRef]
29. Qin, Y.; Wu, J.; Shen, J.; Yang, Z.; Shen, Y.; Zhang, B. Frontier research of geological technology for coal measure gas joint-mining. *J China Coal Soc.* **2018**, *43*, 1504–1516.
30. Craig, H. Isotopic Variations in Meteoric Waters. *Science* **1961**, *133*, 1702–1703. [CrossRef]
31. Zheng, S.; Hou, F.; Ni, B. Study on hydrogen and oxygen stable isotopes of meteoric water in China. *Chin. Sci. Bull.* **1983**, *13*, 801–806.
32. Jenny, G.; Sepehr, S.Y.; Carina, S.; Anna, K.; Jörgen, E.; Ulf, S.; Bo, H.S. Bioavailability of cobalt and nickel during anaerobic digestion of sulfur-rich stillage for biogas formation. *Appl. Energy* **2013**, *112*, 473–477.
33. Su, X.; Zhao, W.; Xia, D. The diversity of hydrogen-producing bacteria and methanogens within an in situ coal seam. *Biotechnol. Biofuels* **2018**, *11*, 245. [CrossRef]
34. Wang, X.; Hu, X.; Deng, K.; Cheng, X.; Wei, J.; Jiang, M.; Wang, X.; Chen, T. High-throughput sequencing of microbial diversity in implant-associated infection. *Infect. Genet. Evol.* **2016**, *43*, 307–311. [CrossRef]
35. Kinnon, E.C.P.; Golding, S.D.; Boreham, C.J.; Baublys, K.A.; Esterle, J.S. Stable isotope and water quality analysis of coal bed methane production waters and gases from the Bowen Basin, Australia. *Int. J. Coal Geol.* **2010**, *82*, 219–231. [CrossRef]
36. Golding, S.D.; Boreham, C.J.; Esterle, J.S. Stable isotope geochemistry of coal bed and shale gas and related production waters: A review. *Int. J. Coal Geol.* **2013**, *120*, 24–40. [CrossRef]
37. Yang, Z.; Qin, Y.; Qin, Z.; Yi, T.; Li, C.; Zhang, Z. Characteristics of dissolved inorganic carbon in produced water from coalbed methane wells and its geological significance. *Petrol. Explor. Dev.* **2020**, *47*, 1074–1083. [CrossRef]
38. Meng, Y.; Tang, D.; Xu, H.; Li, Y.; Gao, L. Coalbed methane produced water in China: Status and environmental issues. *Environ. Sci. Pollut. Res.* **2014**, *21*, 6964–6974. [CrossRef]
39. Li, Y.; Fu, H.; Yan, D.; Su, X.; Wang, X.; Zhao, W.; Wang, H.; Wang, G. Effects of simulated surface freshwater environment on in situ microorganisms and their methanogenesis after tectonic uplift of a deep coal seam. *Int. J. Coal Geol.* **2022**, *257*, 104014. [CrossRef]
40. Oleszkiewicz, J.A.; Sharma, V.K. Stimulation and inhibition of anaerobic processes by heavy metals—A review. *Biol. Wastes* **1990**, *31*, 45–67. [CrossRef]
41. Zandvoort, M.H.; Van Hullebusch, E.D.; Fermoso, F.G.; Lens, P.N.L. Trace metals in anaerobic granular sludge reactors: Bioavailability and dosing strategies. *Eng. Life Sci.* **2006**, *6*, 293–301. [CrossRef]
42. Mincer, T.J.; Church, M.J.; Taylor, L.T.; Preston, C.; Karl, D.M.; DeLong, E.F. Quantitative distribution of presumptive archaeal and bacterial nitrifiers in Monterey Bay and the North Pacific Subtropical Gyre. *Environ. Microbiol.* **2007**, *9*, 1162–1175. [CrossRef]
43. Nicol, G.W.; Leininger, S.; Schleper, C.; Prosser, J.I. The influence of soil pH on the diversity, abundance and transcriptional activity of ammonia oxidizing archaea and bacteria. *Environ. Microbiol.* **2008**, *10*, 2966–2978. [CrossRef]
44. Shan, T.; Bao, Y.; Liu, X.; Wang, X.; Li, D. Evolution characteristics and molecular constraints of microbial communities during coal biogasification. *Bioprocess Biosyst. Eng.* **2024**, *47*, 2075–2089. [CrossRef]

energies

MDPI

Article

The Prediction of Coalbed Methane Layer in Multiple Coal Seam Groups Based on an Optimized XGBoost Model

Weiguang Zhao [1,2], Shuxun Sang [1,3,4,*], Sijie Han [3,4,*], Deqiang Cheng [5], Xiaozhi Zhou [1,6], Zhijun Guo [7,8], Fuping Zhao [7,8], Jinchao Zhang [1] and Wei Gao [9]

1 School of Resources and Geosciences, China University of Mining and Technology, Xuzhou 221116, China
2 Artificial Intelligence Research Institute, China University of Mining and Technology, Xuzhou 221116, China
3 Jiangsu Key Laboratory of Coal-Based Greenhouse Gas Control and Utilization, China University of Mining and Technology, Xuzhou 221008, China
4 Carbon Neutrality Institute, China University of Mining and Technology, Xuzhou 221008, China
5 School of Information and Control Engineering, China University of Mining and Technology, Xuzhou 221116, China
6 Key Laboratory of Coalbed Methane Resources and Reservoir Formation Process, Ministry of Education, China University of Mining and Technology, Xuzhou 221116, China
7 Key Laboratory of Unconventional Natural Gas Evaluation and Development in Complex Tectonic Areas, Ministry of Natural Resources, Guiyang 550009, China
8 Guizhou Engineering Research Institute of Oil & Gas Exploration and Development, Guiyang 550009, China
9 Guizhou Provincial Engineering and Technology Research Center of Coalbed Methane and Shale Gas, Guiyang 550008, China
* Correspondence: shxsang@cumt.edu.cn (S.S.); hsj_cumt@126.com (S.H.)

Abstract: The prediction of the optimal coalbed methane (CBM) layer plays a significant role in the efficient development of CBM in multiple coal seam groups. In this article, the XGBoost model optimized by the tree-structured Parzen estimator (TPE) algorithm was established to automatically predict the optimal CBM layer in complex multi-coal seams of the Dahebian block in Guizhou Province, China. The research results indicate that the TPE XGBoost model has higher evaluation metrics than traditional machine learning models, with higher accuracy and generalization ability. The optimal coalbed methane layer predicted by the model for the Dacong 1–3 well is the 11th coal seam. In addition, the interpretation results of the model indicate that sonic (AC) and caliper logging (CAL) are relatively important in determining the optimal CBM layer. The favorable layers for coalbed methane development are distributed in coal seams with developed fractures and high gas content. The TPE-XGBoost model can help us objectively analyze the significance of different types of logging, quickly predict the optimal layer in complex multiple coal seam groups, and greatly reduce costs and subjective impact. It provides a new approach to predict the best CBM layer in multiple coal seam groups in the Guizhou Province in the southwest of China.

Keywords: tree-structured parzen estimator; XGBoost; multiple coal seam groups; coalbed methane layer prediction; geophysical logging

1. Introduction

Multiple coal seam groups have complex structures and diverse reservoir properties [1,2]. The determination of the optimal coalbed methane (CBM) layer for multiple coal seam groups involves the comparison and selection of multiple coal seam sections on the same stratigraphic column. By comparing different parameters and their combination characteristics, scientific evaluation methods are used to calculate the development potential of different layers to predict the coal seam with the most development potential. In recent years, scholars have used existing experience or functional relationships to predict coalbed methane reservoirs based on reservoir properties and geological conditions. For example, Wu et al. [3] established an optimization index system from the perspective of

geological conditions. Fu et al. [4] used the Analytic Hierarchy Process to identify favorable development areas for coalbed methane in the Yangjiapo Block, Eastern Ordos Basin, China. Based on multi-level fuzzy mathematical analysis, Wang et al. [5] evaluated the potential of the CBM system and predicted favorable areas in Gujiao blocks, Xishan coalfield, China. These classic research methods are established based on long-term experience accumulation. However, these methods rely on expert experience to determine specific indicator systems and artificially specify the weights of relevant indicators, thus possessing a certain degree of subjectivity. The Longtan Formation coal seam group in Guizhou Province has the characteristics of wide distribution, multiple layers, and significant differences in reservoir characteristics. The complex coal seam condition makes traditional research paradigms inadequate to solve the unknown and complex mapping relationship between input and output.

Machine learning has strong adaptive learning ability [6], which can greatly reduce human interference in the problem-solving process. Unlike traditional methods (Figure 1), this method is a new research paradigm based on data-driven methods to establish complex mapping relationships and predict CBM reservoirs, without any physical mechanism argumentation or subjective empirical analysis [7]. At the same time, the powerful data processing capabilities of machine learning enable precise analysis of massive amounts of data, enabling researchers to explore the potential laws of data from high-dimensional spaces in a non-linear manner [8]. Geophysical logging can obtain in situ stratigraphic physical information such as acoustic, electrical, nuclear/nuclear magnetic, etc. It can analyze the physical characteristics of reservoirs in detail and provide a large amount of data for machine learning [9–12]. In recent years, both geophysical logging and machine learning have been applied in research related to CBM [9,13–15]. The massive amount of logging data and the data analysis capabilities of machine learning make CBM research no longer limited by the amount of data, cost, and subjective expert experience.

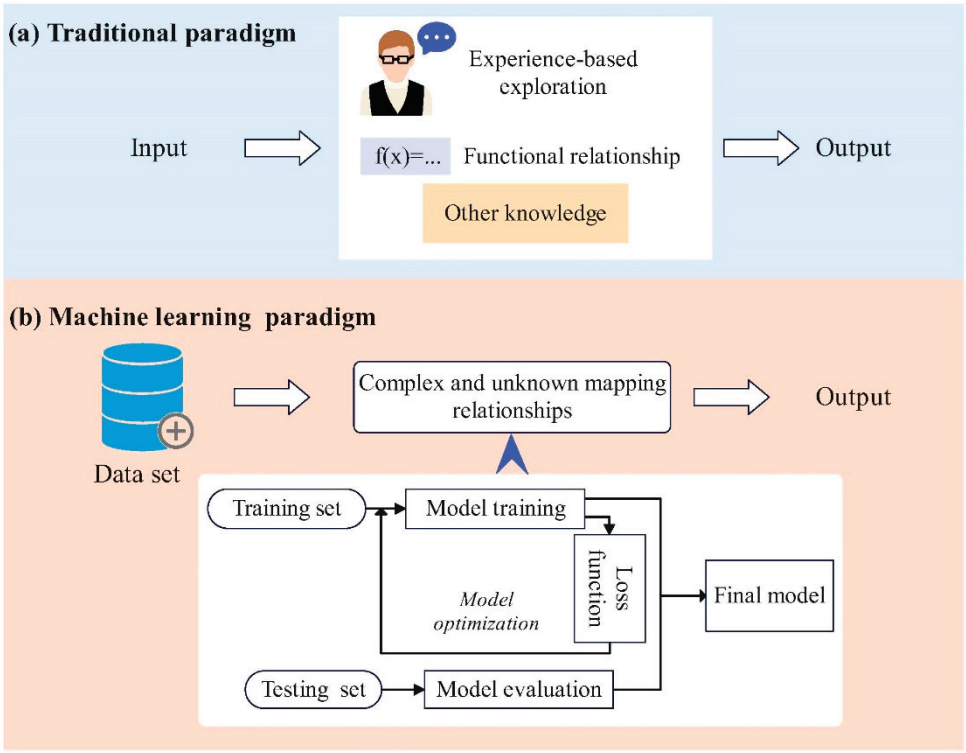

Figure 1. The process of traditional paradigm and machine learning paradigm.

With the deepening of research, classic machine learning showed some shortcomings such as insufficient operation speed, overfitting, and difficulty in dealing with data anomalies when processing logging data [16]. XGBoost (Extreme Gradient Boosting) [17] is an integrated learning algorithm, which can also better deal with missing data and outliers in the data set. It has the advantages of fast speed, high efficiency, and resistance to overfitting [18,19], which have attracted the attention of researchers in the oil and gas field. Liu et al. [20] confirmed that the interpretable PSO-XGBoost model has more advantages in permeability prediction. Liu et al. [21] used the XGBoost model to identify formation thickness and reservoirs, with better recognition performance than traditional machine learning models. Gu et al. [22] used the XGBoost model to predict tight sandstone reservoirs and achieved high accuracy. However, the XGBoost model has not been widely applied to predict the optimal CBM layer for multiple coal seams at present. The superior performance demonstrated by the XGBoot model in oil and gas fields confirms its ability to process complex data related to multiple coal seams and predict the selection of CBM layers.

In this paper, the method for predicting the optimal production layer of CBM is completely different from the traditional expert-experience-driven paradigm. Instead, it adopts the automatic intelligent determination of the XGBoost model driven by geophysical logging data, aiming to establish a more objective and rapid research method to overcome the drawbacks of traditional research methods. This study provides new solutions and guiding significance for similar problems in the field of CBM engineering.

2. Geological Setting

This study is based on nine CBM logging wells in the Dahebian block of the Liupanshui Basin (Group) in Guizhou Province. The Dahebian block is located in the northern part of Liupanshui City, Guizhou Province, with a direct distance of about 5 km. Its tectonic structure belongs to the Yangtze Plate (Class I), Qianbei Platform Uplift (Class II), Liupanshui Fault Depression (III), and the Weining NW trending tectonic deformation zone. It is part of the arc-shaped fold area in western Guizhou. The Longtan Formation (P_3l) is a coal bearing formation in this area, consisting of a set of coal bearing deposits between sea and land, with a thickness of 206–241 m. The lithology is mainly composed of sandstone, sandy mudstone, mudstone, argillaceous sandstone, and coal seams (Figure 2). The maximum coal content can reach 40 layers, and the total thickness of the coal seam is about 35 m. The coal seam is mainly black in color, with the coal body structure being mainly blocky and fragmented, with a small amount of powdery particles. Semi-bright coal cleats and fissures are relatively developed, and local calcite veins are filled. According to the analysis and testing of the gas content in the Longtan Formation coal seam of the DH Can1 well, methane is the main gas component of CBM. The methane concentration ranges from 95.22 to 98.12%. The gas content of the main coal seams ranges from 4.80 to 14.73 m^3/t. The trial production effect of CBM is good, with the highest daily gas production of a single well reaching over 1400 m^3, and it has the potential to continue increasing production.

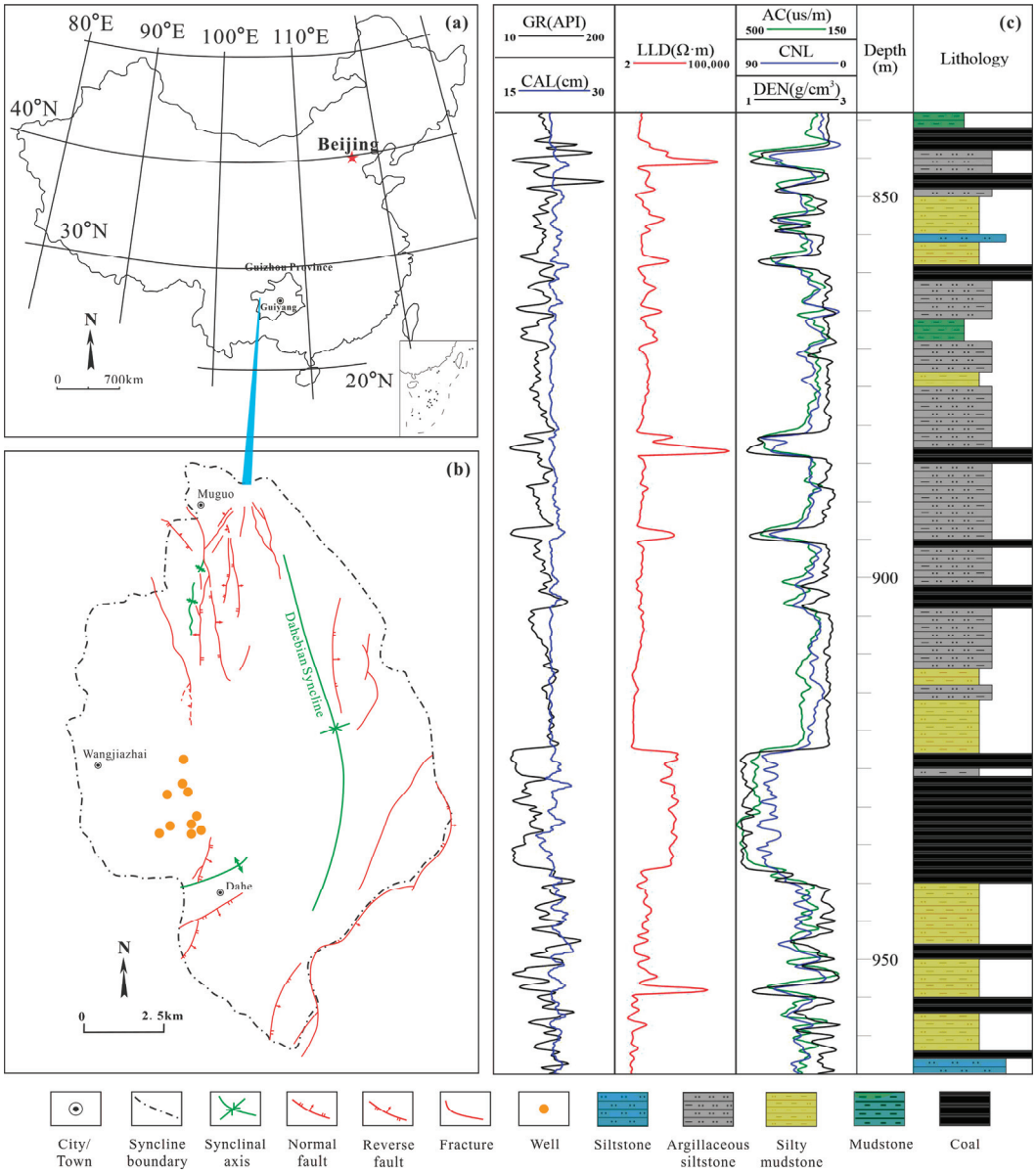

Figure 2. Location of study area and well: (**a**) Guizhou Province in China, (**b**) Dahebian syncline, (**c**) log data and lithology of Longtan formation.

3. Samples and Methods

3.1. Samples and Preprocessing

In this paper, data from 9 wells were collected. These wells include six types of logging data: natural gamma (GR), sonic (AC), compensated neutron (CNL), densities (DEN), deep lateral resistance (LLD), and caliper logging (CAL). The research object is coal seam, so it is necessary to extract the coal seam logging point data from all logging data, and discard other strata data. Then, the CBM production data of these 9 wells are collected, and the main CBM production seams of each well are obtained. According to the results, the logging data points of the CBM layers are marked as positive samples, and the logging data points of other coal seams are marked as negative samples to complete the construction of the data set.

In order to reduce the systematic error of various measuring tools and the dimensional impact between various logging curves, the GR, AC, CNL, DEN, LLD and CAL data of each well need to be standardized [23,24]. The standardization formula is as follows:

$$x_{id} = \frac{x_i - u}{x_{max} - x_{min}} \tag{1}$$

where x_{id} and x_i are the standardized logging value and actual value of each index, u is the mean value of each index, and x_{max} and x_{min} are the maximum and minimum value of each index. It can be seen from Figure 3 that the distribution of data before standardization is relatively discrete. After standardization, the difference in logging data is significantly reduced and the consistency is improved.

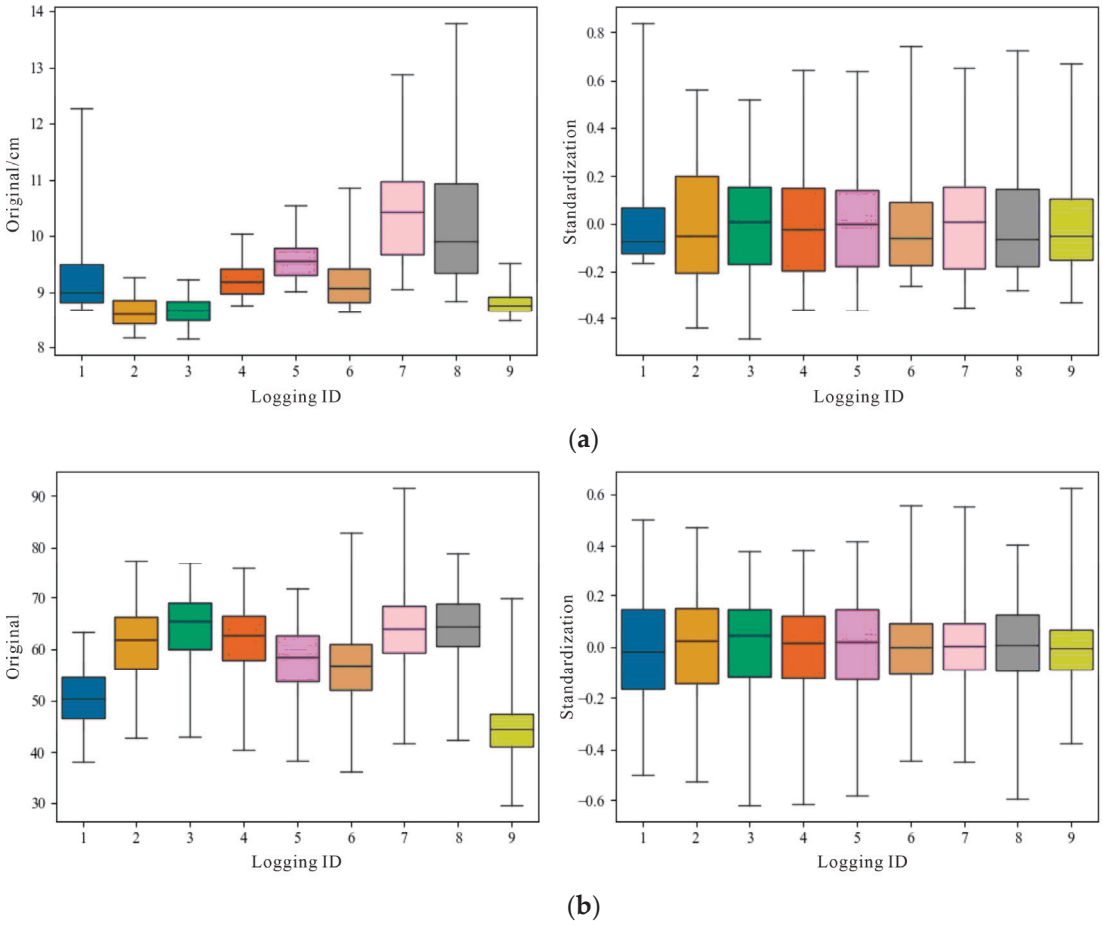

Figure 3. The distribution of the original and standardized logging data. (**a**) CAL; (**b**) CNL.

3.2. TPE-XGBoost Algorithm

XGBoost is a regularization extension based on the Gradient Boosting Decision Tree (GBDT) [17]. Compared with GBDT, XGBoost significantly improves the accuracy of the algorithm and is widely used in various industries [25–28]. The objective function of XGBoost consists of two parts (Equation (2)): the loss function used to measure the performance of the model on the training data, and the regularization term Ω used to control the complexity of the model. The regularization term in the objective function can avoid overfitting of the model.

$$\mathcal{L}^{(t)} = \sum_{i=1}^{n} \left[g_i f_t(x_i) + \frac{1}{2} h_i f_t^2(x_i) \right] + \Omega(f_t) \tag{2}$$

where $f_t(x_i)$ is the output of the i-th sample in the t-th iteration, g and h are the first-order and second-order gradient statistics of the loss function, and Ω is the regularization term. The regularization item can be expressed as follows [17]:

$$\Omega(f) = \gamma T + \frac{1}{2}\lambda \|w\|^2 \tag{3}$$

where T is the number of leaf nodes, w is the leaf weight, and γ and λ are regularization parameters. Regular terms can control the structural risk of the model, making the model simple and predictive.

The gain calculation method of each split candidate in XGBoost is as follows [17]:

$$\mathcal{L}_{split} = \frac{1}{2}\left[\frac{\left(\sum_{i\in I_L} g_i\right)^2}{\sum_{i\in I_L} h_i + \lambda} + \frac{\left(\sum_{i\in I_R} g_i\right)^2}{\sum_{i\in I_R} h_i + \lambda} - \frac{\left(\sum_{i\in I} g_i\right)^2}{\sum_{i\in I} h_i + \lambda}\right] - \gamma \tag{4}$$

TPE is a Bayesian optimization modeling strategy aimed at finding the optimal parameters from the configuration space to maximize the expected improvements (EI). EI can be expressed as follows [29]:

$$EI = \int_{-\infty}^{y^*} (y^* - y)\frac{p(x|y)p(y)}{p(x)}dy \tag{5}$$

where $y*$ divides the observation results into good results and bad results. In TPE, these two result sets are used to calculate $p(x|y)$ [29]:

$$p(x|y) = \begin{cases} l(x), & y < y^* \\ g(x), & y \geq y^* \end{cases} \tag{6}$$

where $l(x)$ and $g(x)$ are density estimation functions. The ratio between the two density functions can reflect the EI, and the ratio can be used to determine the evaluation of new parameter configuration.

XGBoost model has a large number of hyper-parameters, which have an important impact on the prediction ability of the model. The research shows that using TPE to optimize the parameters can better improve the performance of the XGBoost model [30–33].

3.3. Model Training

The workflow of model training is shown in Figure 4. The data set consisting of 9 wells was randomly divided into a training set (75%) and a testing set (25%). The training set was used for model training, and the testing data were used for subsequent model performance evaluation. The XGBoost contains some hyper-parameters that need to be carefully optimized. Table 1 provides the configuration space for these hyper-parameters. TPE was used to optimize the parameters of XGBoost model. In order to avoid overfitting, the average error loss of 10-fold cross-validation was used as the objective function of the hyper-parameter optimization. The error was calculated as follows:

$$Error = 1 - accuracy(\mathrm{y}, \hat{y}) \tag{7}$$

$$accuracy(\mathrm{y}, \hat{y}) = \frac{1}{n_{samples}} \sum_{i=0}^{n_{samples}-1} (\hat{y}_i = \mathrm{y}_i) \tag{8}$$

where y is the true value, and $\hat{y}$ is the predicted value.

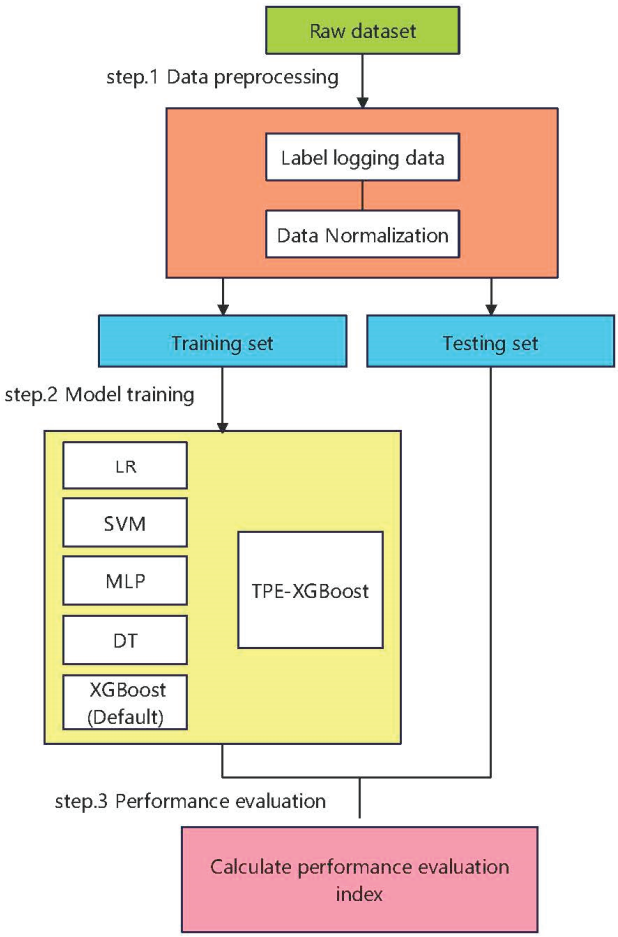

Figure 4. The workflow of model training and performance evaluation.

Table 1. Configuration space of the hyper-parameters.

Hyper-Parameters	Description	Range
n_estimators	Number of boosting rounds.	(100, 200)
max_depth	Maximum tree depth for base learners.	(1, 20)
learning_rate	Boosting learning rate.	(0, 1)
gamma	Minimum loss reduction required to make a further partition on a leaf node of the tree.	(0, 5)
alpha	L1 regularization term on weights.	(0, 5)
min_child_weight	Minimum sum of instance weight (hessian) needed in a child.	(0, 3)
subsample	Subsample ratio of the training instance	(0.6, 1)

In this paper, the number of iterations was 2000. During the iteration process, the hyper-parameter combination that minimizes the value of the objective function was constantly searched. At the same time, logistic regression (LR), support vector machine (SVM), multilayer perceptron (MLP), decision tree (DT), and XGBoost (default) were also trained as comparison models on the same data set.

3.4. Performance Evaluation Method

The testing set was used to evaluate the performance of the model. In this paper, the overall accuracy (OA), precision (precision), recall (recall), F1-score and area under the receiver operating characteristic curve (AUC) were used as the performance evaluation

metric of the models. AUC is the area under the receiver operating characteristic (ROC) curve, which is used to evaluate the generalization ability of the model. The ROC curve is a complete sensitivity or specificity index for model evaluation [34]. The calculation formulas of other metrics are as follows:

$$\text{Overall accuracy} = \frac{TP + TN}{TP + FP + TN + FN} \tag{9}$$

$$\text{Precision} = \frac{TP}{FP + TP} \tag{10}$$

$$\text{Recall} = \frac{TP}{FN + TP} \tag{11}$$

$$\text{F1} = \frac{2 \times Recall \times Precision}{Recall + Precision} \tag{12}$$

where *TP*, *TN*, *FN* and *FP* are the four elements in the confusion matrix: true positive, true negative, false negative, and false positive.

4. Results and Discussion

4.1. Hyper-Parameter Optimization and Performance Evaluation Result

After the optimization of the TPE algorithm, the optimal hyper-parameter combination of XGBoost model is as follows: n_estimators = 132, max_depth = 19, learning_rate = 0.02, gamma = 0.53, alpha = 0.37, min_child_weight = 0.30, subsample = 0.76. Table 2 shows the calculation results of each evaluation metric of LR, SVM, MLP, DT, XGBoost (default) and TPE-XGBoost models on the testing set.

Table 2. Performance measure of different models.

Model	Measurement Evaluation Metric				
	OA	**Precision**	**Recall**	**F1-Score**	**AUC**
LR	0.64	0.64	0.74	0.69	0.64
SVM	0.77	0.79	0.76	0.77	0.76
MLP	0.75	0.79	0.72	0.75	0.75
DT	0.79	0.83	0.76	0.79	0.79
XGBoost (default)	0.81	0.81	0.84	0.82	0.81
TPE-XGBoost	0.92	0.93	0.92	0.92	0.92

It can be seen from Table 2 that the performance evaluation metric of the XGBoost with default parameters is higher than most traditional machine learning models and only slightly lower in accuracy than the DT. The default XGBoost model needs to be optimized. The TPE-XGBoost with the optimal hyper-parameter configuration combination has a performance index greater than 0.9 in the testing set. In addition, it can be seen intuitively from Figure 5 that the ROC curve of LR model is at the bottom, the curves of SVM, MLP, DT and XGBoost (default) intersect each other, and the curves of TPE-XGBoost are above all the curves. It shows that the performance of the TPE-XGBoost model is optimum. After TPE algorithm optimization, the performance of the XGBoost model has been significantly improved, with high accuracy and generalization ability, and can be applied to the determination of the optimal CBM layer.

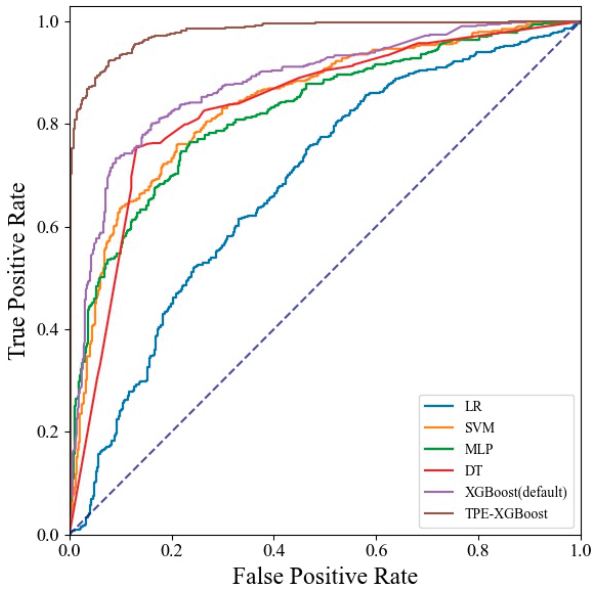

Figure 5. ROC curves of different models.

4.2. The Prediction of the Optimal CBM Layer

Part of the data (75%) were used for model training and hyperparametric optimization. The remaining data (25%) were used for the performance evaluation of the model and not used in the model training. Therefore, after determining the optimal hyper-parameter configuration, it was necessary to re-train the TPE-XGBoost model with all logging data sets. The model was used to predict the optimal CBM layer in the new well (Dacong1–3 well).

After standardizing the GR, AC, CNL, DEN, LLD and CAL data of the coal seams of the new well, they are input into the TPE-XGBoost model to predict the CBM exploit area of each coal seam. The prediction results are shown in Figure 6.

In Figure 6, the blue area represents the coal seam, and the red area represents the CBM exploit area predicted by the TPE-XGBoost model. The CBM exploit area is mainly distributed in No. 1, 7, 11, 13, 17 coal seams. In order to evaluate the exploitation value, the CBM exploit value (EV) of each coal seam is calculated. The value is used as the basis for determining the optimal CBM layer. The calculation method is as follows:

$$\mathrm{EV} = \mathrm{H} \times \frac{N_p}{N} \tag{13}$$

Here, H is the thickness of coal seam, N_p is the number of logging points predicted as CBM, and N is the total number of logging points in this coal seam.

The EV calculation results of each coal seam are shown in Figure 7. According to EV, the coal seams of Dacong1–3 well can be divided into three levels. The first level is the No. 11 coal seam, which has a relatively high CBM area proportion and thickness, and the EV is much higher than other coal seams. It is the optimal layer and the preferred scheme for CBM exploitation. The second level is the No. 17, 1, 13, and 7 coal seam. The coal seams at this level cannot meet the requirements for both the proportion and thickness of the CBM area, but still have certain mining value and can be used as alternative solutions. The remaining coal seams belong to the third level, with extremely low EV and no production value.

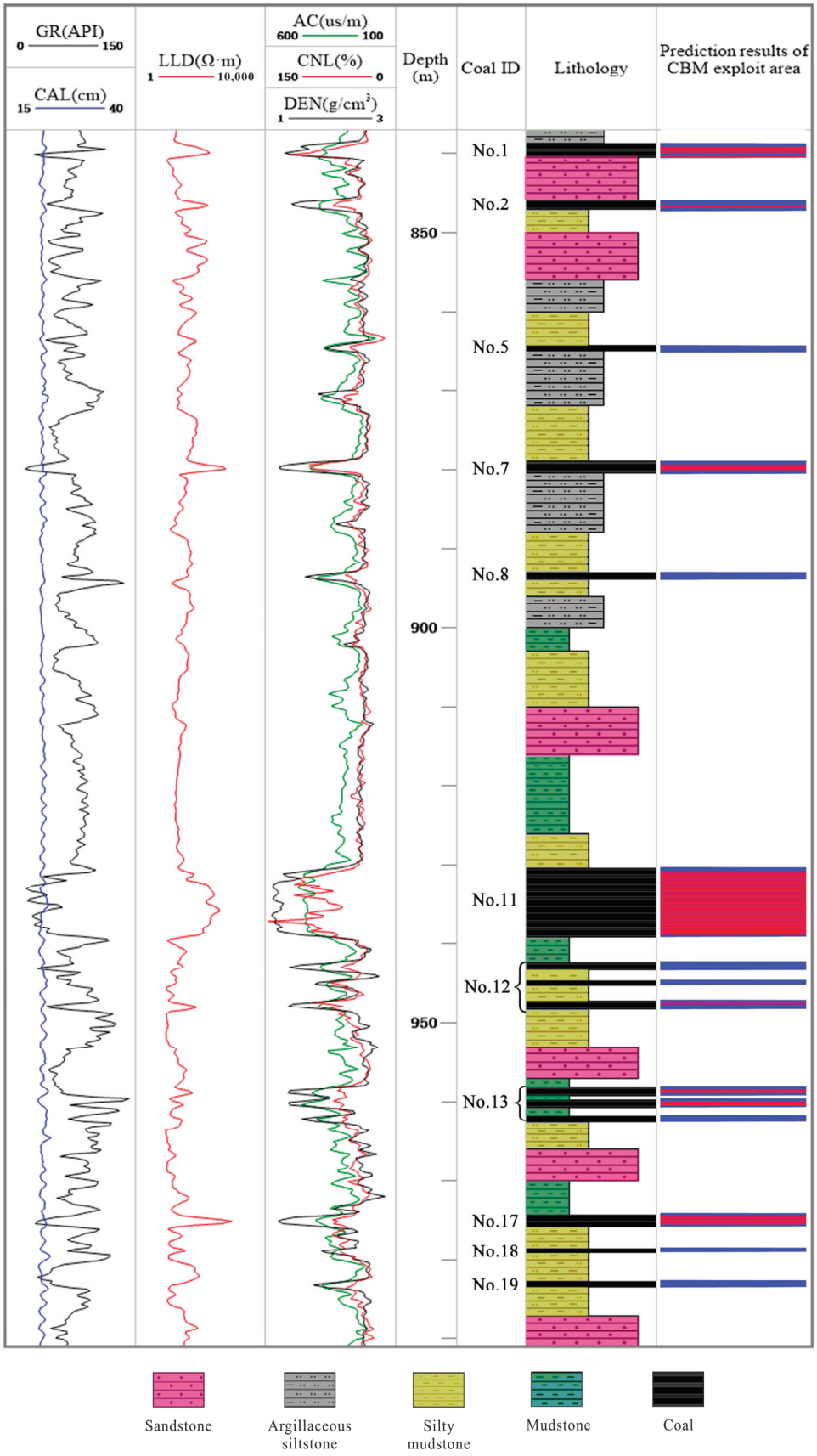

Figure 6. Prediction results of CBM exploit area.

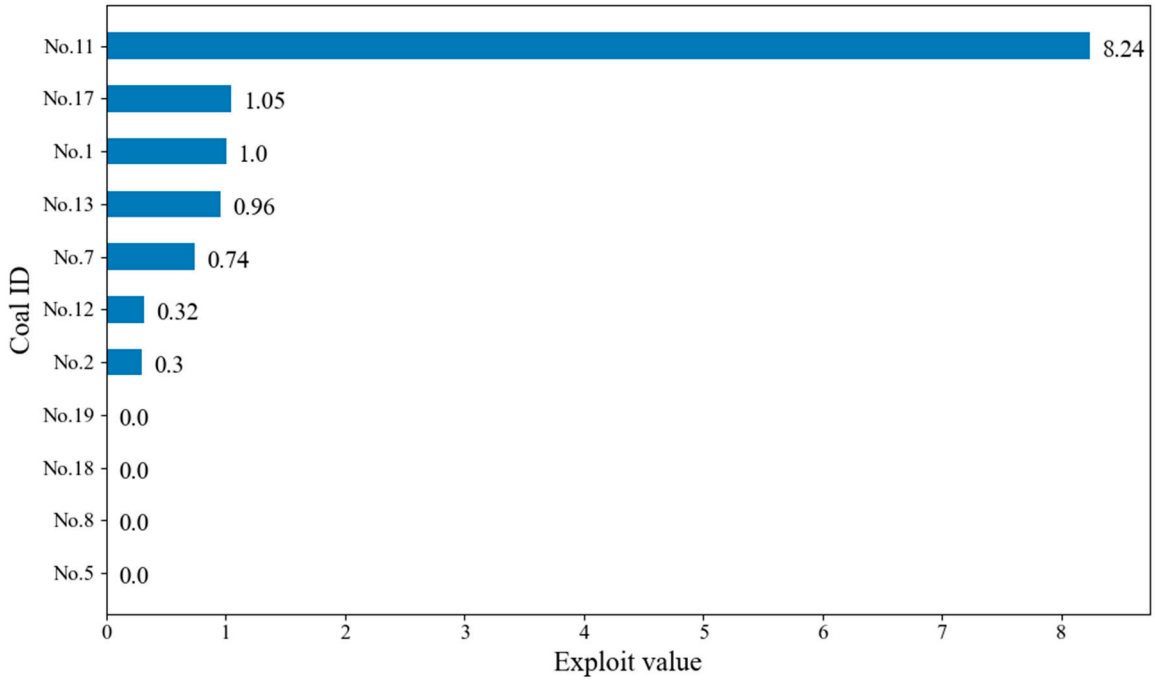

Figure 7. Exploit value graph.

4.3. Verification of Prediction Results

According to the TPE-XGBoost model, No. 11 coal is the optimal layer for Dacong1–3 well. The result needs to be validated for accuracy based on the actual gas production performance of CBM wells. Table 3 shows the statistics of some CBM wells that have already produced gas, whether they have extracted the No. 11 coal seam, and the corresponding gas production results.

Table 3. Gas production statistics of CBM wells.

Well ID	No. 11 Coal Seam	Maximum Daily Gas Production (m^3)
Z1-8-X8	Yes	1426
Z1-10-X8	Yes	1356
Z1-6-X6	Yes	1311.5
Z1-12-X1	Yes	1011.9
Z1-10-X2	No	397.30
Z1-12-X2	No	383
Z1-3-X1	No	279.5

From Table 3, it can be observed that the CBM wells that have extracted the No. 11 coal seam have significantly higher production. The No. 11 coal seam does indeed have good gas production performance. The accuracy of the TPE-XGBoost model has been verified by actual production results. Therefore, it can be confirmed that the TPE-XGBoost model can accurately predict the most favorable CBM layer in multiple coal seam groups.

4.4. Model Interpretability Analysis

In addition to the various performance evaluation indicators of the model, the interpretability of the model is also an important way to evaluate the model. The interpretation helps researchers understand the decision-making mechanisms and processes of the model from a human perspective. This study analyzes the interpretability of the model through feature importance. The characteristics refer to six types of logging. Based on the im-

portance of the features, it can obtain the potential relationship between input features and prediction results, explaining the geological significance of different features. The importance of each feature is evaluated by the gain score. The higher the gain score of a feature, the closer the relationship between the feature and the CBM layer. The gain score is defined as the average gain of all segments of the feature.

As shown in Figure 8, each logging feature is of certain importance for the selection of CBM layers. AC, CAL, and LLD have the highest importance, followed slightly by DEN and CNL. The impact of GR is relatively low.

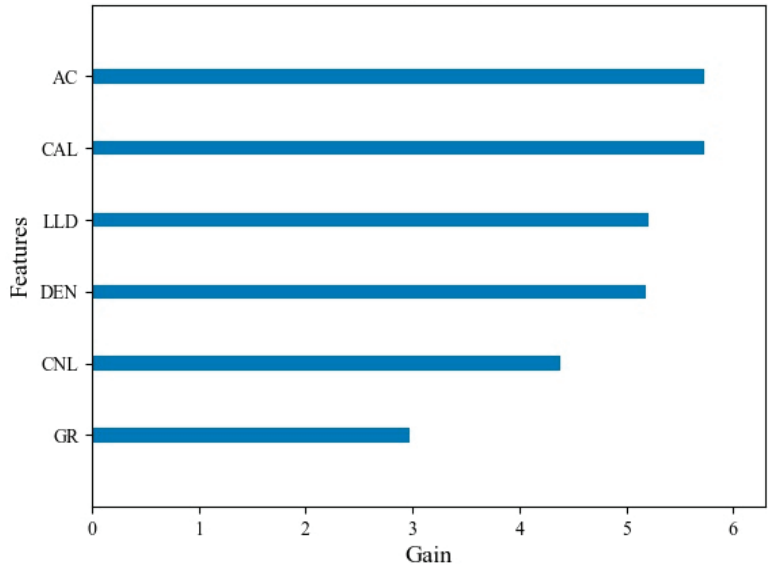

Figure 8. The result of feature importance (gain score).

By comparing the predicted results of CBM layer areas with logging data, it can be analyzed in detail how these logging data affect the distribution of CBM layers. Different types of coal have different geophysical logging characteristics. DEN and AC can reflect the degree of coal fragmentation, and coal with high fragmentation has the characteristics of high AC and low DEN [35,36]. LLD can reflect the gas content of coal, and coal with high gas content has a higher LLD value [24]. According to TPE-XGBoost's predictions, compared to non-minable areas, the DEN in coalbed methane areas (such as coal seams No. 11 and 17) is usually lower, while LLD and AC are slightly higher. The TPE-XGBoost model analysis shows that the favorable CBM layers in multiple coal seam groups in Guizhou Province have the characteristics of crack development and high gas content.

Table 4 shows some reservoir parameters and fracture development in the Dacong1–3 well. The No. 11 coal has high gas content, porosity, and permeability and good fracture development. The gas content of No. 7 and 17 coal in the alternative plan is slightly lower than that of coal No. 11, and the fractures are also relatively developed. The development of cracks in No. 19 coal seams is poor. The gas content, porosity, and permeability of No. 19 coal are the lowest. Through the above analysis, the correctness of the distribution rules of favorable CBM layers for multiple coal seam groups in Guizhou Province can be verified based on the TPE-XGBoost model analysis.

Table 4. Main coal seam characteristics.

Coal ID	Prediction Results	Gas Content (m^3/t)	Porosity (%)	Perme-Ability ($10^{-3} \cdot \mu m^2$)	Micro-Cracks *	
					Development Degree	Connectivity
No. 7		12.81	2.0	0.01	High	Medium
No. 11		16.07	6.5	0.06	High	Medium
No. 17		12.06	4.3	0.03	High	Medium
No. 19		12.19	3.4	0.02	Low	Poor

* Note: The micro-cracks originate from the testing of parameter wells located in the study area.

4.5. The Reliability and Application Significance of TPE-XGBoost Model in CBM Engineering

The reliability of the model is closely related to the comprehensiveness of the data set [37]. In this study, the data set used for training the model comes from geophysical logging data. Geophysical logging can obtain a large amount of continuous and reliable coal seam data, which can accurately reflect the characteristic information of multiple coal seams. Compared to traditional empirical methods, data-driven models have stronger analytical capabilities for well logging data. During the training process, the model can reliably learn the common features of high-yield gas coal seams (such as gas content, fractures, permeability, etc.) through the training of well logging data. When predicting unknown wells, the model will predict areas with high gas production characteristics as favorable production zones for CBM development based on the learned information. At the same time, this method no longer requires any expert experience to determine specific indicator systems or weights, greatly avoiding subjective interference in predicting the optimal CBM layer, and further improving the reliability of prediction results. Therefore, the model can provide accurate and reliable prediction results due to sufficient data, reasonable data labels, and the advantages of the TPE-XGBoost algorithm. These factors enable the model to accurately analyze all coal seam characteristics of multiple coal seam groups and, based on the learned information, predict favorable CBM layers for new wells.

The TPE-XGBoost model is based on data-driven algorithms. Compared to traditional expert experience methods, it can significantly reduce the time and cost of exploration and evaluation, provide objective and reliable prediction results, and make corresponding engineering decisions scientifically and quickly. When researchers predict the optimal layer of unknown wells, they only need to input the logging data of the coal seam into the TPE-XGBoost model to predict the distribution of the CBM area and the optimal layer. Time-consuming and expensive tasks are no longer needed to provide research evidence for traditional empirical methods, such as on-site sampling, indoor testing, and multiple trial productions. Researchers only need to input the logging data of all coal seams in the unknown area into the TPE-XGBoost model to obtain the best CBM layer prediction results.

In addition, the TPE-XGBoost model can explore the potential relationship between logging data and determined results, explain the geological significance of each logging in predicting CBM layers, and further derive the distribution rules of favorable layers, providing a more scientific basis for efficient development of CBM. This article uses TPE-XGBoost to predict the optimal CBM layer of multiple coal seam groups, which is a valuable and potential exploration in the field of CBM engineering in Guizhou Province, and also provides new solutions for other problems in CBM engineering.

5. Conclusions

In this study, an optimal CBM prediction model driven by well logging data was designed. The model aims to establish a more objective and rapid research method to solve the problems of traditional methods relying too much on subjective experience and complex logging data analysis. The main conclusions are as follows:

(1) The TPE-XGBoost model has great performance. The performance evaluation metrics of TPE-XGBoost are all above 0.9, indicating higher accuracy and generalization ability compared to LR, SVM, MLP, DT, and XGBoost (default).
(2) According to TPE-XGBoost prediction, the No. 11 coal seam is the optimal CBM layer for Dacong1–3 well, which is consistent with the actual results. No. 1, 17, 7, 3, and 4 coal seams can be used as alternative options. Other coal seams are unfavorable production layers.
(3) The characteristic gain score of TPE-XGBoost shows that each well logging has a certain impact on the determination of CBM layers. AC, CAL, and LLD are the most important. At the same time, it is further explained that the favorable CBM layers have the characteristics of higher LLD and AC. It is a coal seam with developed fractures and high gas content.
(4) TPE-XGBoost achieves accurate, objective, and fast prediction of the optimal CBM layer in complex multiple coal seam groups based on geophysical logging and overcomes the subjectivity and empiricism of traditional research paradigms.
(5) This study is a preliminary attempt to predict the optimal CBM layer based on well logging data, but it also has some limitations. For example, other factors that affect coalbed methane, such as water and reservoir dynamic characteristics, were not taken into consideration. The TPE-XGBoost model is based on manually extracted coal seam logging data to predict the optimal CBM layer. Future research may consider introducing more types of training data and designing more intelligent models to achieve automatic extraction of coal seam data and further improve the reliability and applicability of model predictions.

Author Contributions: Conceptualization, W.Z.; methodology, W.Z., S.S. and D.C.; software, W.Z.; investigation, W.Z.; resources, Z.G. and W.G.; data curation, S.S., D.C. and J.Z.; writing—original draft preparation, W.Z.; writing—review and editing, S.S., S.H. and D.C.; supervision, S.H. and X.Z.; funding acquisition, S.S., S.H., X.Z. and F.Z. All authors have read and agreed to the published version of the manuscript.

Funding: This work is financially supported by the "Belt and Road Initiative" Innovation cooperation project of Jiangsu Province (Grant No. BZ2022015), the National Natural Science Foundation of China (Grant No. 42030810), the Geological Exploration Foundation of Guizhou Province (Grant No. 208-9912-JBN-UTS0, 52000021MGQSE7S7K6PRP), and the Guizhou Provincial Science and Technology Plan Project (Grant No. CXTD [2022]016).

Data Availability Statement: Due to privacy concerns, the research data in this study are kept confidential and cannot be publicly shared.

Conflicts of Interest: The authors declare no conflicts of interest.

References

1. Gao, D.; Qin, Y.; Yi, T. Geological condition, exploration and exploitation strategy of coal-bed methane resources in Guizhou, China. *Coal Geol. China* **2009**, *21*, 20–23, (In Chinese with English Abstract)
2. Peng, C.; Zou, C.; Zhou, T.; Li, K.; Yang, Y.; Zhang, G.; Wang, W. Factors affecting coalbed methane (CBM) well productivity in the Shizhuangnan block of southern Qinshui basin, North China: Investigation by geophysical log, experiment and production data. *Fuel* **2017**, *191*, 427–441. [CrossRef]
3. Wu, C.; Liu, X.; Zhang, S. Construction of index system of "Hierarchical progressive" geological selection of coalbed methane in multiple seam area of eastern Yunnan and western Guizhou. *J. China Coal Soc.* **2018**, *43*, 1647–1653, (In Chinese with English Abstract)
4. Fu, X.; Meng, Y.; Li, Z.; Kong, P.; Chang, S.; Yan, T.; Liu, Y. Coalbed methane potential evaluation and development sweet spot prediction based on the analysis of development geological Conditions in Yangjiapo Block, Eastern Ordos Basin, China. *Geofluids* **2021**, *2021*, 1–12. [CrossRef]
5. Wang, G.; Qin, Y.; Xie, Y.; Shen, J.; Zhao, L.; Huang, B.; Zhao, W. Coalbed methane system potential evaluation and favourable area prediction of Gujiao blocks, Xishan coalfield, based on multi-level fuzzy mathematical analysis. *J. Pet. Sci. Eng.* **2018**, *160*, 136–151. [CrossRef]

6. Wang, Q.; Song, S.; Li, L.; Wen, D.; Shan, P.; Li, Z.; Fu, Y. An extreme learning machine optimized by differential evolution and artificial bee colony for predicting the concentration of whole blood with Fourier Transform Raman spectroscopy. *Spectrochim. Acta Part A Mol. Biomol. Spectrosc.* **2023**, *292*, 122423. [CrossRef]
7. Karianne, J.; Paul, A.; Maarten, V.; Gregory, C. Machine learning for data-driven discovery in solid earth geosciences. *Science* **2019**, *363*, eaau0323. [CrossRef]
8. Ohyama, J.; Nishimura, S.; Takahashi, K. Data driven determination of reaction conditions in oxidative coupling of methane via machine learning. *ChemCatChem* **2019**, *11*, 4307–4313. [CrossRef]
9. Teng, J.; Yao, Y.; Liu, D.; Cai, Y. Evaluation of coal texture distributions in the southern Qinshui basin, North China: Investigation by a multiple geophysical logging method. *Int. J. Coal Geol.* **2015**, *140*, 9–22. [CrossRef]
10. Hatherly, P. Overview on the application of geophysics in coal mining. *Int. J. Coal Geol.* **2013**, *114*, 74–84. [CrossRef]
11. Hou, H.; Shao, L.; Guo, S.; Li, Z.; Zhang, Z.; Yao, M.; Zhao, S.; Yan, C. Evaluation and genetic analysis of coal structures in deep Jiaozuo coal field, northern China: Investigation by geophysical logging data. *Fuel* **2017**, *209*, 552–566. [CrossRef]
12. Xu, H.; Tang, D.; Mathews, J.; Zhao, J.; Li, B.; Tao, S.; Li, S. Evaluation of coal macrolithotypes distribution by geophysical logging data in the Hancheng Block, Eastern Margin, Ordos Basin, China. *Int. J. Coal Geol.* **2016**, *165*, 265–277. [CrossRef]
13. Chai, Y.; Li, T.; Zhang, L. Production forecast of coalbed methane based on GA optimized BP neural network. In Proceedings of the 2019 IEEE 4th Advanced Information Technology, Electronic and Automation Control Conference (IAEAC), Chengdu, China, 20–22 December 2019. [CrossRef]
14. Xu, X.; Rui, X.; Fan, Y.; Yu, T.; Ju, Y. Forecasting of coalbed methane daily production based on T-LSTM neural networks. *Symmetry* **2020**, *12*, 861. [CrossRef]
15. Zhang, J.; Feng, Q.; Zhang, X.; Hu, Q.; Yang, J.; Wang, N. A novel data-driven method to estimate methane adsorption isotherm on coals using the gradient boosting decision tree: A Case Study in the Qinshui Basin, China. *Energies* **2020**, *13*, 5369. [CrossRef]
16. Zhong, R.; Raymond, J.J.; Chen, Z. Using machine learning methods to identify coal pay zones from drilling and logging-while-drilling (LWD) data. *SPE J.* **2020**, *25*, 1241–1258. [CrossRef]
17. Chen, T.; Guestrin, C. XGBoost: A scalable tree boosting system. In Proceedings of the 22nd ACM SIGKDD International Conference on Knowledge Discovery and Data Mining, New York, NY, USA, 13–17 August 2016. [CrossRef]
18. Liu, Y.; Yi, L.; Cheng, D. Application of XGBoost in identification of power quality disturbance source of steady-state disturbance events. In Proceedings of the 2019 IEEE 9th International Conference on Electronics Information and Emergency Communication (ICEIEC), Beijing, China, 12–14 July 2019. [CrossRef]
19. Seghier, M.E.B.; Hoche, D.; Zheludkevich, M. Prediction of the internal corrosion rate for oil and gas pipeline: Implementation of ensemble learning techniques. *J. Nat. Gas Sci. Eng.* **2022**, *99*, 104425. [CrossRef]
20. Liu, J.; Liu, J. Permeability predictions for tight sandstone reservoir using explainable machine learning and particle swarm optimization. *Geofluids* **2022**, 1–15. [CrossRef]
21. Liu, W.; Zhao, Y.; Yang, M.; Xu, Y.; Li, G.; Feng, Z. XGBoost formation thickness identification based on logging data. *Front. Earth Sci.* **2022**, *10*, 918384. [CrossRef]
22. Gu, Y.; Bao, Z.; Zhang, D. A smart predictor used for lithologies of tight sandstone reservoirs: A case study of member of Chang 4 + 5, Jiyuan Oilfield, Ordos Basin. *Pet. Sci. Technol.* **2021**, *39*, 175–195. [CrossRef]
23. Sabah, M.; Talebkeikhah, M.; Wood, D.A.; Khosravanian, R.; Anemangely, M.; Younesi, A. A machine learning approach to predict drilling rate using petrophysical and mud logging data. *Earth Sci. Inform.* **2019**, *12*, 319–339. [CrossRef]
24. Ren, P.; Xu, H.; Tang, D.; Li, Y.; Sun, C.; Tao, S.; Li, S.; Xin, F.; Cao, L. The identification of coal texture in different rank coal reservoirs by using geophysical logging data in northwest Guizhou, China: Investigation by principal component analysis. *Fuel* **2018**, *230*, 258–265. [CrossRef]
25. Zhang, D.; Qian, L.; Mao, B.; Huang, C.; Huang, B.; Si, Y. A Data-Driven Design for Fault Detection of Wind Turbines Using Random Forests and XGBoost. *IEEE Access* **2018**, *6*, 21020–21031. [CrossRef]
26. Nobre, J.; Neves, R.F. Combining principal component analysis, discrete wavelet transform and XGBoost to trade in the financial markets. *Expert Syst. Appl.* **2019**, *125*, 181–194. [CrossRef]
27. Jiang, Y.; Tong, G.; Yin, H.; Xiong, N. A pedestrian detection method based on genetic algorithm for optimize XGBoost training parameters. *IEEE Access* **2019**, *7*, 118310–118321. [CrossRef]
28. Wang, X.; Yan, X.; Ma, Y. Research on user consumption behavior prediction based on improved XGBoost algorithm. In Proceedings of the 2018 IEEE International Conference on Big Data, Seattle, WA, USA, 10–13 December 2018. [CrossRef]
29. Zhao, M.; Li, J. Tuning the Hyper-parameters of CMA-ES with Tree-structured Parzen Estimator. In Proceedings of the 2018 Tenth International Conference on Advanced Computational Intelligence (ICACI), Xiamen, China, 29–31 March 2018; pp. 613–618. [CrossRef]
30. Chen, B.; Zheng, H.; Luo, G.; Chen, C.; Bao, A.; Liu, T.; Chen, X. Adaptive estimation of multi-regional soil salinization using extreme gradient boosting with Bayesian TPE optimization. *Int. J. Remote Sens.* **2022**, *43*, 778–811. [CrossRef]
31. Kavzoglu, T.; Teke, A. Advanced hyperparameter optimization for improved spatial prediction of shallow landslides using extreme gradient boosting (XGBoost). *Bull. Eng. Geol. Environ.* **2022**, *81*, 1–22. [CrossRef]
32. Wang, Y.; Ni, X. A XGBoost risk model via feature selection and Bayesian hyper-parameter optimization. *Int. J. Database Manag. Syst.* **2019**, *11*, 1–17. [CrossRef]

33. Tim, H.; Elshafie, M.; Ying, J. Recreating passenger mode choice-sets for transport simulation. *Proc. Inst. Civ. Eng. Smart Infrastruct. Constr.* **2018**, *171*, 29–42. [CrossRef]
34. Xia, Y.; Liu, C.; Li, Y.; Liu, N. A boosted decision tree approach using Bayesian hyper-parameter optimization for credit scoring. *Expert Syst. Appl.* **2017**, *78*, 225–241. [CrossRef]
35. Shi, J.; Zeng, L.; Dong, S.; Wang, J.; Zhang, Y. Identification of coal structures using geophysical logging data in Qinshui Basin, China: Investigation by kernel Fisher discriminant analysist. *Int. J. Coal Geol.* **2020**, *217*, 103314. [CrossRef]
36. Kang, J.; Fu, X.; Shen, J.; Liang, S.; Chen, H.; Shang, F. Characterization of coal structure of high-thickness coal reservoir using geophysical logging: A case study in Southern Junggar Basin, Xinjiang, Northwest China. *Nat. Resour. Res.* **2022**, *31*, 929–951. [CrossRef]
37. Zhong, Z.; Carr, T.R. Application of mixed kernels function (MKF) based support vector regression model (SVR) for CO_2—Reservoir oil minimum miscibility pressure prediction. *Fuel* **2016**, *184*, 590–603. [CrossRef]

energies

MDPI

Article

NMR-Based Investigation of Pore–Fracture Structure Heterogeneity in Deep Coals of Different Macrolithotypes in the Daning-Jixian Block, Ordos Basin

Wei Zhang [1,2,3], Zheng Zhang [1,*], Liheng Bian [2,3], Rui Shi [1], Hewei Zhang [1] and Jian Shen [1]

[1] Key Laboratory of Coalbed Methane Resources and Reservoir Formation Process, Ministry of Education of China, China University of Mining and Technology, Xuzhou 221116, China
[2] China United Coalbed Methane National Engineering Research Center Co., Ltd., Beijing 100095, China
[3] PetroChina Coalbed Methane Company Limited, Beijing 100028, China
* Correspondence: zzcumt@cumt.edu.cn

Abstract: Deep coalbed methane (CBM) demonstrates significant production potential, and a fervent exploration and development boom is currently underway in China. The permeability of coal reservoirs is heavily influenced by pore–fracture structure heterogeneity. Some researches have been conducted on deep coals' pore–fracture structure; however, these studies mostly consider coal as a homogeneous material, neglecting the heterogeneity of the macrolithotypes within the coal. In this study, 33 deep coals with burial depths of more than 2000 m were obtained from the Daning-Jixian block of the Ordos Basin, covering all macrolithotypes: bright coal (BC), semi-bright coal (SBC), semi-dull coal (SDC), and dull coal (DC). These samples were subjected to three sets of NMR tests in dry, fully saturated, and irreducible water conditions, with the pore–fracture structure characteristics being analyzed. The results demonstrate that the sampled deep coals' pore–fracture structure is highly heterogeneous, with transitional pores being dominant, followed by mesopores, "macropores and fractures", and micropores. The NMR T_{2C} ranges from 0.61 to 2.44 ms, with an average of 1.19 ms; a higher T_{2C} value indicates more developed micropores. The ranges for producible water porosity (φ_{pr}) and producible water saturation (S_{pr}) are 0.31–7.24% (avg. 2.42%) and 6.97–71.47% (avg. 31.06%), respectively. Both of them exhibit a high positive correlation with the total volumes of "macropores and fractures" and mesopores. Compared to SDC and DC, the BC and SBC, especially the former, overall contain more "macropores and fractures" and mesopores, fewer transitional pores and micropores, and higher φ_{pr} and S_{pr}. These findings suggest that regions with abundant BC and SBC should be prioritized during deep CBM exploration and production due to the inherently superior permeability and gas extraction potential of BC and SBC, and these coals are likely to require less intensive stimulation to achieve higher recovery rates and could provide more sustainable gas production over time.

Keywords: deep coalbed methane; pore–fracture structure heterogeneity; macrolithotype; NMR; Ordos Basin

1. Introduction

Coalbed methane (CBM) is a key type of unconventional natural gas extracted from coal reservoirs [1,2]. Over the past decade, China's CBM production from surface wells has shown a steady increase, growing from 10×10^8 m^3 in 2009 [3] to 117.7×10^8 m^3 in 2023 [4]. However, these CBM productions are primarily extracted from coal reservoirs at depths shallower than 1500 m [5]. China possesses vast, deep CBM resources, with estimates indicating approximately 22.5×10^{12} m^3 at depths between 1000 and 2000 m [6], and up to 40.71×10^{12} m^3 at depths greater than 2000 m [7]. The immense potential of these deep CBM resources has attracted significant attention in China and it is anticipated to become a key assurance for boosting large-scale natural gas reserves and production [8,9].

From the 1980s to the early 21st century, researchers initiated deep CBM exploration in North America, with significant breakthroughs such as a high gas flow rate from a 1829 m deep CBM well in the Piceance Basin [10–13]. A subsequent trial project with 65 wells (1635–2591 m depth) demonstrated the promising potential for deep CBM development [14,15]. Meanwhile, China has begun to focus on the geological conditions and extraction technology applicability for deep CBM. In the basins like Ordos, Qinshui, and Junggar, pilot projects have been launched, achieving significant breakthroughs [7,9]. The deep CBM's successful development in certain regions of North America and China underscores the vast potential of this resource. However, the deep CBM's development is still in exploratory stage and is confronted with numerous scientific and technological challenges [7]. Among these, low permeability is a significant challenge that requires special attention for the development of deep CBM [8,15,16]. The permeability of the coal reservoir is heavily influenced by the pore–fracture structure heterogeneity [17–20]. Hence, a better understanding of a deep coal reservoir's pore–fracture structure heterogeneity characteristics is essential.

The coal reservoir consists of a dual-porosity structure, including pores and fractures [21–23]. The pores can be classified into four categories based on their diameters, d, macropores (d > 1000 nm), mesopores (d: 100 nm–1000 nm), transitional pores (d: 10 nm–100 nm) and micropores (d < 10 nm), as stated by Hodot [24]. Currently, a variety of experimental methods has been employed to study coal's pore–fracture structure characteristics. These methods could be broadly categorized into two types: fluid intrusion and photoelectric radiation techniques [25]. The fluid intrusion method includes low-pressure gas adsorption (N_2 and CO_2) [26], NMR (nuclear magnetic resonance) [27], as well as MIP (mercury intrusion porosimetry) [28]. The photoelectric radiation method mainly encompasses optical microscopy, SEM (scanning electron microscopy) [29], CT scanning [30], and SANS (small-angle neutron scattering) [31,32]. Among these techniques, the NMR has gained widespread use in recent years for three primary reasons [27,33]. First, NMR testing is non-destructive, meaning it does not damage the original pore–fracture structure of coal. Second, it can independently provide a full-scale size distribution of pore–fracture without requiring assistance from other methods. Third, it can effectively distinguish irreducible water porosity and producible water porosity, the latter of which is crucial for evaluating coal permeability.

Although there have been some researches on deep coals' pore–fracture structure [6,34–36], these investigations have primarily treated coal as a homogeneous material, overlooking the significant heterogeneity of their macrolithotypes (namely bright, semi-bright, semi-dull, and dull coals) within a single seam. This simplification neglects the potential impact of macrolithotype diversity on the coal's pore–fracture characteristics. In fact, the distinct macrolithotypes exhibit varying pore–fracture structures, which directly influence gas storage and permeability characteristics [37–39]. This heterogeneity plays a crucial role in determining the CBM recovery potential. Understanding these differences is essential for optimizing CBM extraction strategies in heterogeneous coal reservoirs [40]. However, relatively few studies have explored how the heterogeneity of macrolithotypes influences the overall pore–fracture structure of deep coals. This study aims to address this gap by providing a comprehensive analysis of the heterogeneous nature of deep coals, particularly focusing on the role of macrolithotype variations.

For this purpose, the relationships between macrolithotype characteristics and key pore structure parameters, including pore size distribution, total porosity, producible water porosity, irreducible water porosity, and producible water saturation were investigated through NMR testing. The findings obtained in this study not only contribute to a deeper understanding of coal heterogeneity but also provide practical insights that can be applied directly to the exploration and development of CBM resources in similar coal-bearing regions. By incorporating macrolithotype-based variability into CBM reservoir modeling, this research enhances the predictive accuracy of coal permeability and gas productivity, offering a more targeted approach for future CBM extraction.

2. Geological Settings

The Daning-Jixian block is situated on the eastern edge of Ordos Basin (Figure 1a). To be specific, it is at the southeastern edge of the Yishan slope and the southern end of the Jinxi flexural fold belt (Figure 1b), covering an area of 5648 km². The block's structural zones are clearly demarcated from the east to the west and consist of the western gentle slope zone, central steep slope zone, Taoyuan anticline zone, and eastern slope zone. (Figure 1c,d). Faults are commonly absent in the western central steep slope and gentle slope zones, whereas they are prominently developed in the Taoyuan anticline and eastern slope zones, striking in a NE or NNE direction (Figure 1c).

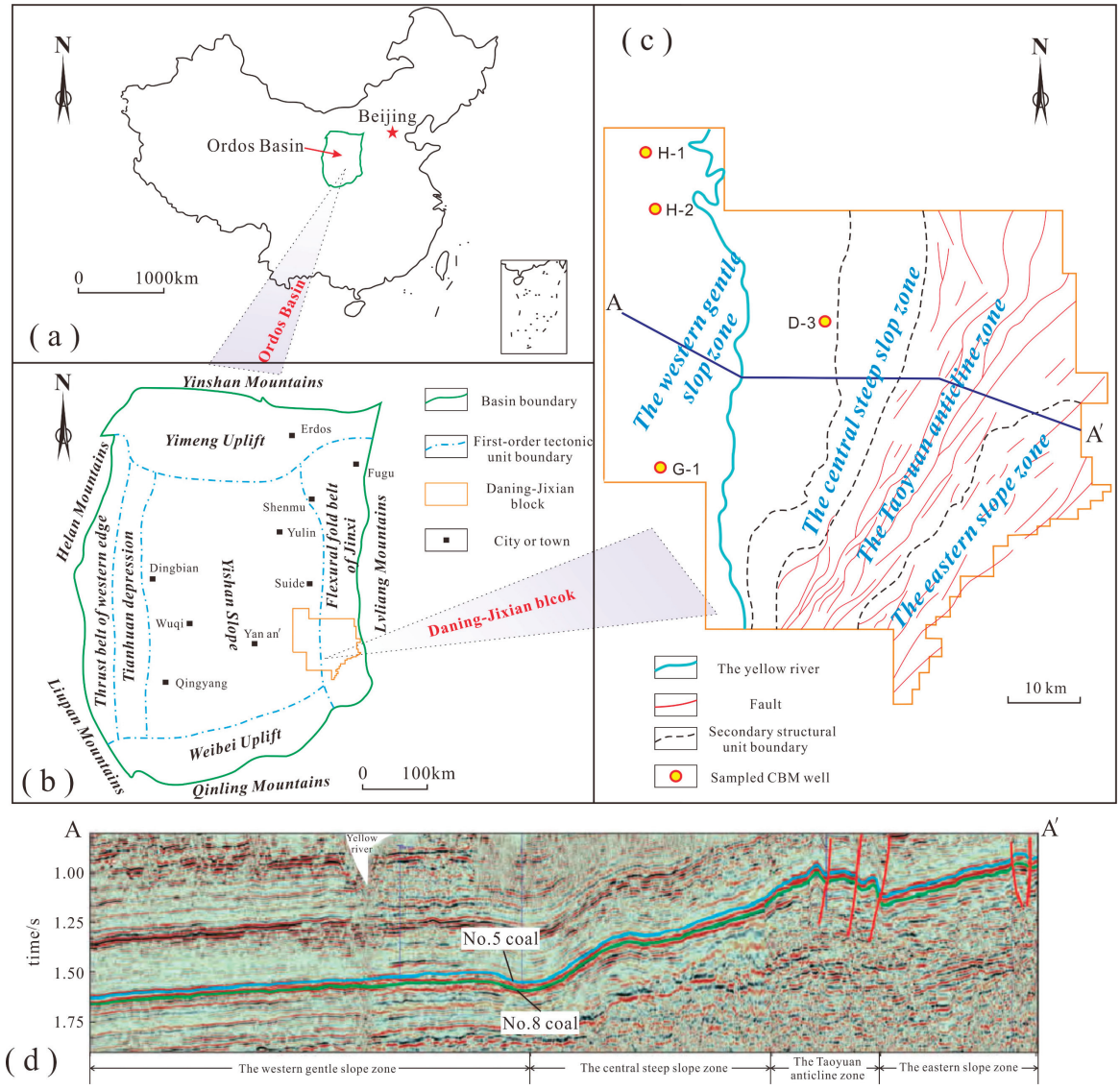

Figure 1. (**a**) The location of Ordos Basin in China; (**b**) a map illustrating the structural unit's division of the Ordos Basin and the location of the Daning-Jixian block within the basin; (**c**) the major structures of Daning-Jixian block and the locations of sampled CBM wells; (**d**) EW seismic profile (A-A′ in (**c**)) of the Daning-Jixian block. Parts (**c**,**d**) were modified from Zhang et al. [41].

The No. 8 coal seam, situated at the base of the Taiyuan Formation (Figure 2), is the primary target for the exploration and development of deep CBM in this region. The Taiyuan Formation mainly formed in carbonate platform and lagoon environments. Early during its deposition, a regional decline in sea level created a balance between accommodation space and sediment supply, which enabled the connection of lagoonal

and tidal peat flats. This process led to the formation of the extensive and continuous No. 8 coal seam. The seam varies in thickness from 3 to 12 m, averaging about 6 m, and is predominantly distributed in the northeastern region of the block, extending in a banded pattern. In the central portion, one to two layers of mudstone interbeds are present. The No. 8 coal seam largely consists of primary structure coal and exhibits a high coalification degree, being primarily classified as anthracite C in rank according to ISO 11706 [42].

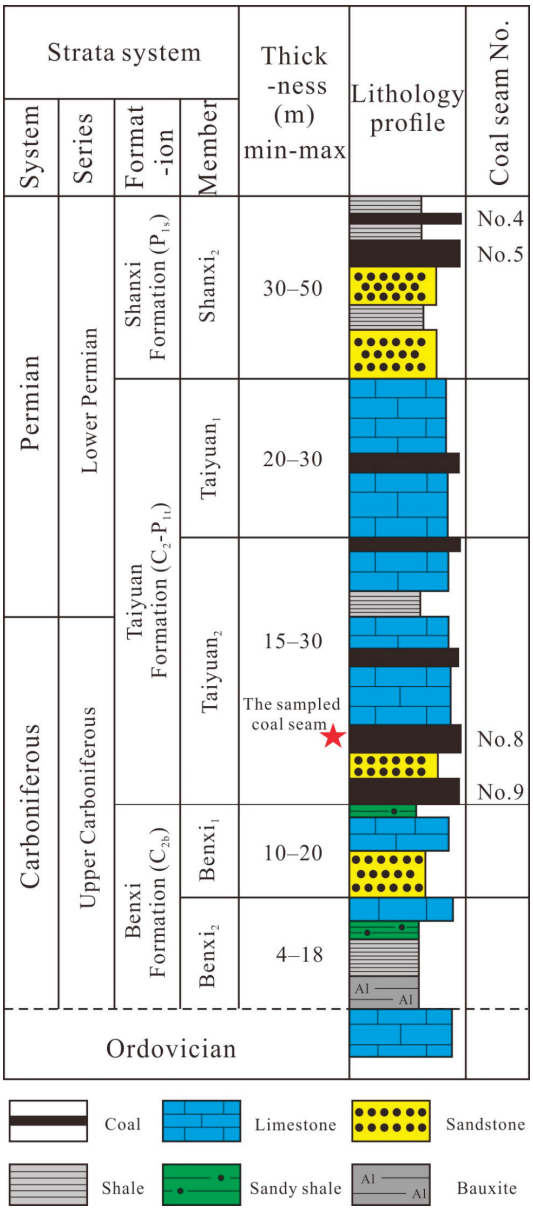

Figure 2. The integrated stratigraphic profile of coal-bearing strata in the study area. The red star in the figure represents the sampling position.

3. Samples and Experiments

3.1. Sample Collection and Preparation

In this study, a total of 33 core samples from the No. 8 coal seam (Figure 2) were collected from wells G-1, D-3, H-1, and H-2 in the Daning-Jixian block (Figure 1c), with sampling depths (bottom) ranging from 2067.62 to 2539.85 m (Table 1). These samples were selected according to the macrolithotypes of the coals. Macrolithotype classification was conducted in accordance with the Chinese Standard GB/T 18023-2000 [43], which categorizes coal into bright, semi-bright, semi-dull, and dull types (Figure 3) based on

luster intensity and the proportion of bright components (including vitrain and clarain). Bright coal is characterized by a very strong luster and over 80% bright components, while semi-bright coal exhibits a strong luster with 50% to 80% bright components. Semi-dull coal has a weak luster and contains 20% to 50% bright components, whereas dull coal displays very weak luster with less than 20% bright components. The samples collected comprised 6 bright coals (BC), 11 semi-bright coals (SBC), 10 semi-dull coals (SDC), and 6 dull coals (DC). Each sample was cut into dimensions of 1.6 cm × 1.6 cm × 3 cm using a wire saw and subsequently prepared for NMR experiments.

Table 1. Basic data about the Daning-Jixian block's deep coal samples and the interpretation results of NMR.

Well No.	Sample I.D.	Depth (m)		Macro Lithotype	Porosity, φ (%)			S_{pr} (%)	T_{2C} (ms)	Volume Percentage (%)			
		Bottom	Top		φ_t	φ_{pr}	φ_{ir}			Micropores	Transitional Pores	Mesopores	Macropores and Fractures
G-1	G-11-1	2067.62	2067.82	BC	4.48	1.70	2.78	37.95	0.81	2.81	67.49	8.71	20.98
	G-11-6	2071.39	2071.60	SBC	6.71	3.80	2.91	42.35	0.61	0.73	56.84	31.14	11.30
	G-11-7	2071.81	2072.02	DC	4.73	1.35	3.38	42.01	0.77	2.46	83.54	10.06	3.94
	G-11-8	2072.13	2072.38	SDC	4.45	0.31	4.14	39.98	1.66	20.64	69.47	1.51	8.37
D-3	D-7-1	2275.50	2275.73	SBC	4.55	0.78	3.77	45.56	1.20	9.42	79.55	3.83	7.21
	D-7-3	2277.37	2277.53	SBC	7.01	2.36	4.65	19.79	0.85	2.96	75.82	12.49	8.73
	D-7-4	2277.99	2278.11	SDC	7.66	3.32	4.34	56.63	0.75	1.63	69.63	21.30	7.45
	D-7-5	2278.54	2278.69	SBC	6.18	1.23	4.95	17.14	1.01	4.97	87.09	4.57	3.37
	D-7-7	2280.11	2280.25	BC	6.47	2.74	3.73	33.67	0.77	1.91	68.85	12.51	16.73
	D-7-9	2281.18	2281.43	SDC	6.20	1.88	4.32	19.90	0.88	3.13	80.52	9.82	6.53
	D-7-10	2281.60	2281.81	SDC	5.57	1.78	3.79	35.11	0.81	2.63	78.84	13.78	4.76
	D-7-11	2282.42	2282.57	SBC	6.75	2.37	4.38	34.65	0.81	2.22	75.81	16.42	5.55
	D-7-12	2283.2	2283.32	DC	5.88	1.71	4.17	20.93	0.91	3.72	80.52	8.68	7.09
	D-7-13	2283.72	2283.85	SBC	5.31	1.84	3.47	14.52	0.67	1.43	80.52	14.75	3.30
H-1	H-17-1	2427.25	2427.44	SBC	8.36	1.75	6.61	71.47	1.55	8.16	82.39	3.48	5.96
	H-17-2	2427.60	2427.76	SDC	7.93	1.96	5.97	18.72	1.36	6.99	79.63	7.10	6.28
	H-17-4	2429.04	2429.22	BC	10.26	4.31	5.95	28.16	1.01	1.95	75.15	21.47	1.43
	H-17-5	2430.58	2430.75	SBC	9.09	1.32	7.77	6.97	2.41	17.63	72.61	1.97	7.78
	H-17-6	2431.51	2431.67	SDC	8.99	1.18	7.81	43.34	2.44	12.81	80.35	0.58	6.26
	H-17-7	2432.62	2432.78	DC	8.01	2.84	5.17	30.32	1.01	3.37	75.89	14.89	5.85
	H-17-8	2432.98	2433.16	SDC	9.06	1.72	7.34	31.96	1.75	9.08	81.36	5.68	3.88
	H-17-9	2433.49	2433.69	DC	5.57	1.91	3.66	24.72	0.85	2.85	78.06	14.51	4.59
H-2	H-18-1	2534.87	2535.07	BC	8.48	3.39	5.09	13.13	1.07	2.64	70.72	18.39	8.25
	H-18-2	2535.27	2535.47	BC	9.79	4.46	5.33	18.98	0.99	2.01	66.96	22.47	8.55
	H-18-3	2535.9	2536.05	SBC	10.13	7.24	2.89	23.24	0.76	0.68	37.59	52.64	9.09
	H-18-4	2536.68	2536.88	SDC	11.62	2.70	8.92	30.85	1.78	9.34	76.95	4.58	9.14
	H-18-5	2536.88	2537.08	BC	9.45	1.87	7.58	30.64	1.76	9.21	79.60	3.51	7.68
	H-18-6	2537.27	2537.47	SBC	14.05	2.63	11.42	28.54	2.05	12.31	74.52	1.60	11.57
	H-18-7	2537.81	2538.01	SBC	10.51	2.96	7.55	29.08	1.30	5.33	79.40	11.18	4.08
	H-18-8	2538.01	2538.18	SDC	8.20	2.53	5.67	35.46	1.11	5.19	74.76	12.68	7.36
	H-18-9	2538.18	2538.37	DC	8.66	1.92	6.74	34.29	1.51	8.20	77.23	9.88	4.69
	H-18-10	2538.5	2538.72	DC	7.93	3.39	4.54	22.17	0.71	1.43	69.03	24.47	5.07
	H-18-11	2539.85	2539.99	SDC	8.03	2.46	5.57	42.75	1.32	3.94	77.15	16.46	2.45

Note: BC, bright coal; SBC, semi-bright coal; SDC, semi-dull coal; DC, dull coal; φ_t, total porosity, %; φ_{pr}, producible water porosity, %; φ_{ir}, irreducible water porosity, %; S_{pr}, producible water saturation, %.

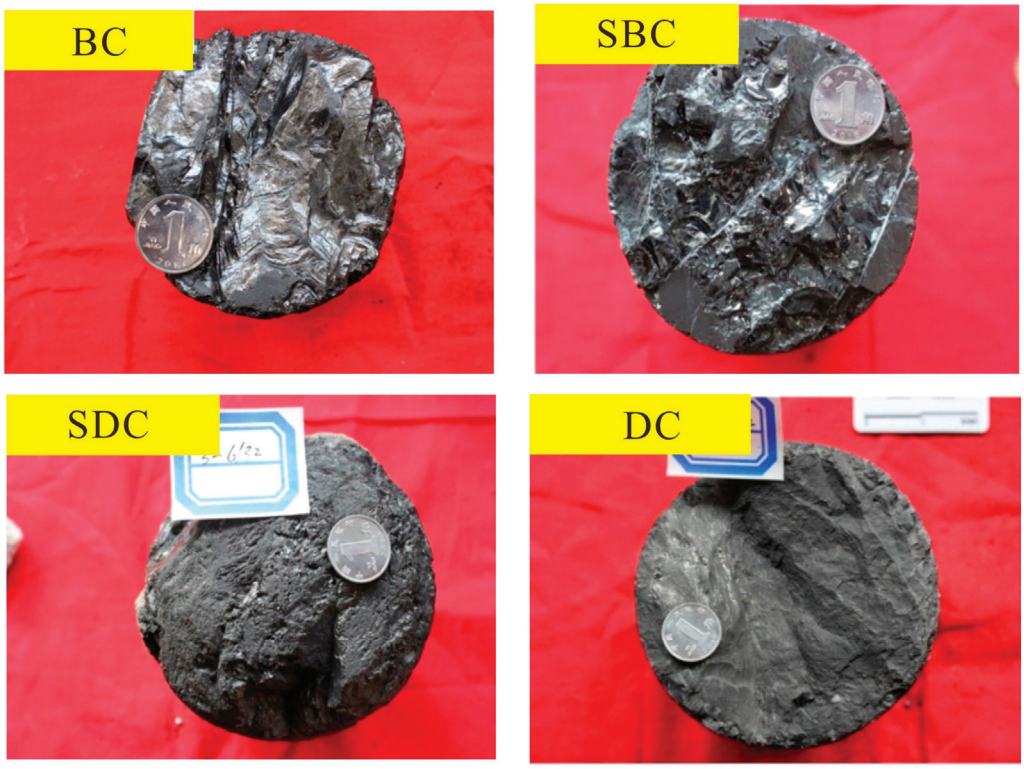

Figure 3. The collected coal samples representing four different macrolithotype coals (BC, SBC, SDC and DC) collected from the Daning-Jixian block. SB, SBC, SDC and DC represent bright, semi-bright, semi-dull, and dull coals, respectively.

3.2. NMR Experiments

NMR technology quantifies the number of hydrogen atoms (^{1}H) in rock samples, providing insights into the distribution and connectivity of pores and fractures through the transverse relaxation time (T_2) spectra. For an in-depth explanation of the theory behind NMR measurements, refer to Yao et al. [44]. Their work built a linear correlation between the NMR signal (T_2, which arises from surface interactions) and the pore size of coal sample. The relationship can be expressed by the following equation:

$$\frac{1}{T_2} = \rho_2 \left(\frac{S}{V} \right) \tag{1}$$

Here, T_2 denotes the transverse relaxation time, in ms; S represents the specific surface area of a pore, in m^2/g; V represents the specific volume of a pore, in cm^3/g. The constant ρ_2 reflects the strength of transverse relaxation. The equation clearly shows that the coal's pore and fracture sizes are linked to the T_2 time. A longer T_2 indicates larger pores and fractures.

A MesoMR23-060H-I NMR analysis and imaging system manufactured by Niumag Analytical Instrument Corporation in Suzhou of China was used for the NMR experiments in this study. To ensure methodological transparency in our NMR testing, the parameters that we set are as follows: resonance frequency at 11.854 MHz, temperature at 32.00 ± 0.02 °C, wait time of 3000 ms, echo time of 0.2 ms, an echo number of 3000, and a sampling repetition number of 32.

In this research, three sets of NMR experiments were carried out on coal samples under three conditions: dry, fully saturated (S_f), and irreducible water (S_{ir}). The procedure followed these steps: (1) The samples were dried at 110 °C for twenty-four hours and then subjected to vacuum treatment for 8 h. Subsequently, NMR testing was performed on the vacuum-dried samples, producing the baseline T_2 spectra (T_{2b}). (2) A vacuum

pressurization system, with a pressure as high as 10 MPa, was used to saturate the vacuum-dried samples with distilled water. The samples were weighed at 2h intervals, and once their weight stabilized, they were considered fully saturated (S_f). NMR testing on the fully saturated samples provided the T_2 spectra (T_{2f}'). (3) The T_{2b} was subtracted from the T_{2f}' to determine the fully saturated T_2 spectra (T_{2f}). (4) The S_f samples were centrifuged at 4.11 MPa for 1.5 h to obtain S_{ir} samples. (5) NMR testing was then performed on the S_{ir} samples to obtain the T_2 spectra (T_{2i}'). (6) Finally, the T_{2b} was subtracted from the T_{2i}' to yield the T_2 spectra (T_{2i}) in S_{ir} condition.

4. Results and Discussions

4.1. Pore–Fracture Size Distribution of Deep Coals

The NMR T_2 spectra (T_{2f} and T_{2i}) for all the deep coals in this study in fully saturated (S_f) and irreducible water (S_{ir}) conditions are presented in Figures 4 and 5, respectively. The T_2 values of T_{2f} spectral range from 0.01 to 10,000 ms, and the T_{2f} spectra exhibit either a bimodal or trimodal distribution (Figure 4). The spectral signal amplitude reflects the volume of pore/fracture at a corresponding pore/fracture size. Most T_{2i} spectra exhibit either a unimodal or bimodal distribution, with only a few, such as sample H-18-4, displaying a trimodal distribution (Figure 5). It is evident that the signal amplitude of the T_{2i} spectra for each sample is lower than that of the T_{2f} spectra (Figures 4 and 5) due to the discharge of producible water from the pore–fracture structure.

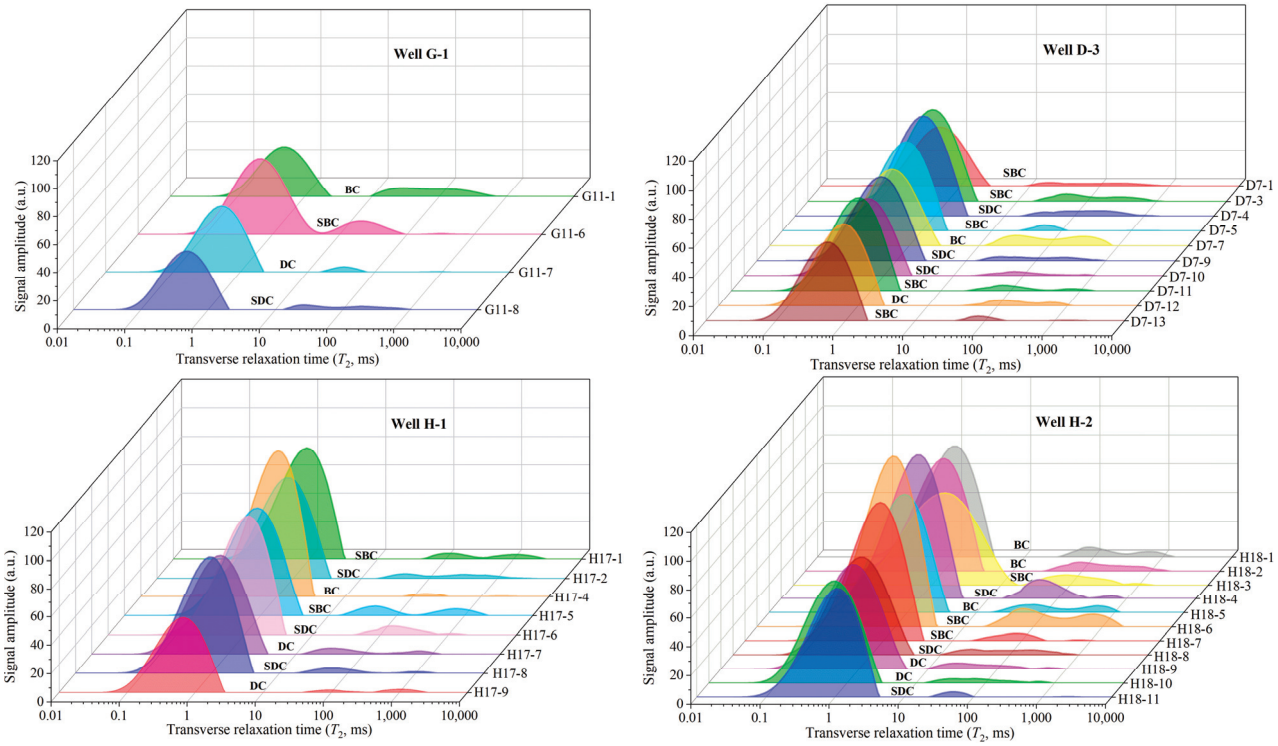

Figure 4. The sampled deep coals' NMR T_2 spectra (T_{2f}) in the S_f condition.

In the fully saturated spectra of coal, a critical T_2 value, referred to as T_{2C}, separates the spectra into two regions: producible and irreducible water [44]. Producible water, associated with T_2 values greater than T_{2C}, corresponds to seepage pores, where water can largely be drained, while irreducible water, linked to T_2 values below T_{2C}, indicates adsorption pores, where the drainage of water is hindered by capillary forces. Accurate determination of T_{2C} is crucial for assessing the proportions of producible and irreducible water volumes, as well as the distribution of pore–fracture sizes.

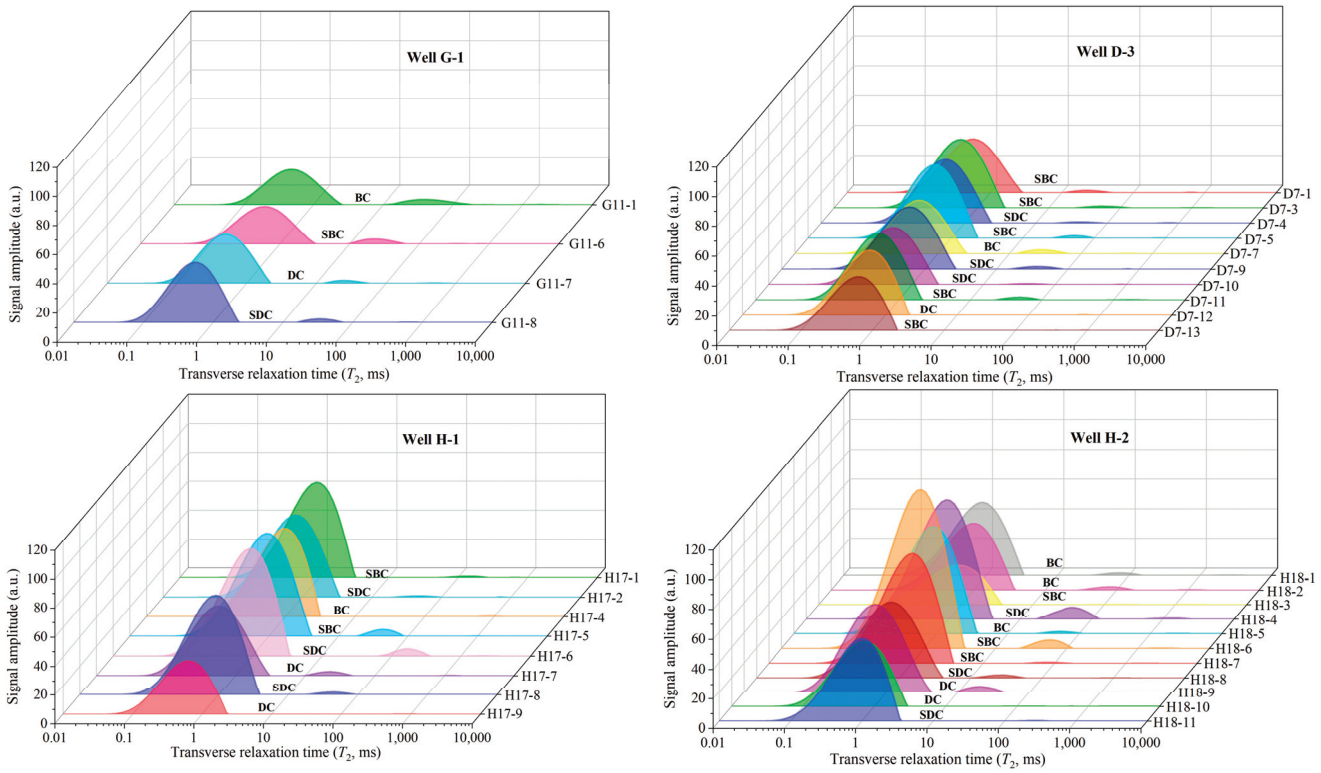

Figure 5. The sampled deep coals' NMR T_2 spectra (T_{2i}) in the S_{ir} condition.

The methodology for ascertaining the T_{2C} is illustrated in Figure 6, with the coal sample H-17-2 as a case. Initially, the cumulative signal amplitude curves of T_{2i} and T_{2f} spectra were plotted, respectively. Subsequently, a horizontal line was drawn from the peak of the cumulative signal amplitude of the T_{2i} spectra, intersecting the cumulative signal amplitude of the T_{2f} spectra. From the intersection point, a vertical line was extended down to the X-axis to determine corresponding X value, labeled as T_{2C}. (Figure 6). Utilizing this technique, the T_{2C} value for the coal sample H-17-2 was found to be 1.36 ms. Consequently, the T_{2C} values for other samples were determined and are presented in Table 1, revealing that T_{2C} values for the deep coals range from 0.61 to 2.44 ms, averaging 1.19 ms.

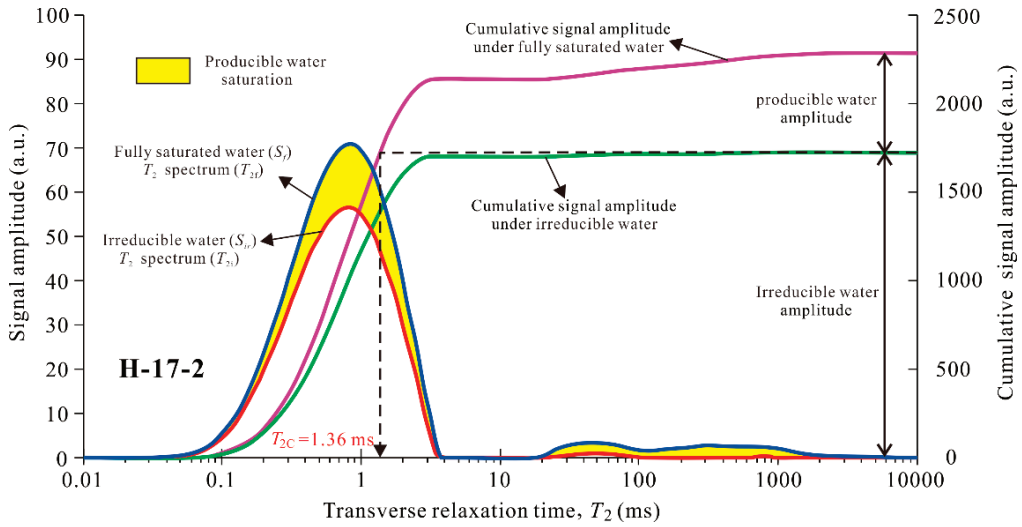

Figure 6. Methodology for determining the T_{2C} value in NMR experiments (using sample H-17-2 as an example).

Utilizing the T_{2C} method enables the determination of the distribution of pore-fracture size in coal. This approach is based on the principle that the pore diameter linked to T_{2C} is consistent across all coal samples [44]. If we define the T_{2C}-related pore diameter as a constant value d, the pore diameter d_{cj} associated with the i-th relaxation time T_{2j} could be represented as the following [44]:

$$\mathrm{d_{cj}} = dT_{2j}/T_{2C} \tag{2}$$

Here, T_{2j} represents an arbitrary transverse relaxation time in T_{2f} spectra, in ms; j denotes the index; d_{cj} is the pore diameter corresponding to the T_{2j}, in nm; T_{2C} corresponds to the transverse relaxation time that separates the spectra into producible and irreducible water, in ms; d is the pore diameter corresponding to the T_{2C}, in nm.

Additionally, Washburn's equation provides information about the minimum pore radius (r_c) associated with water expulsion driven by centrifugal force (P_c):

$$\mathrm{r}_c = -2\sigma\cos\theta/P_c \tag{3}$$

In this equation, r_c denotes the smallest pore radius at which water can be drained by applying the pressure P_c, in nm. P_c, centrifugal force, in MPa. The term σ stands for the surface tension at the coal–water interface, in N/m. θ denotes the contact angle between the coal's pore surface and water, in °. From prior research [45], the θ and σ are determined to be 60° and 0.076 N/m, respectively.

Consequently, Equation (3) can be streamlined to the following:

$$\mathrm{r}_c = 0.14/P_c \tag{4}$$

Equation (4) illustrates the direct correlation between r_c and the centrifugal pressure P_c. According to the NMR experiments stated in Section 3.2, the P_c applied in this study was 4.11 Mpa, which means that the pore radius matching this pressure is 34 nm as determined by Equation (4). This suggests that the pore diameter d associated with T_{2C} in Equation (2) is 68 nm. Furthermore, the T_{2C} values for each sample are presented in Table 1. Therefore, for a given coal sample, Equation (2) can be utilized to determine the d_{cj} values corresponding to different relaxation times T_{2j}. Hence, the T_{2f} spectra can be used to identify the pore–fracture size distribution within a given coal sample.

Figure 7 depicts the pore–fracture size distribution for all sampled deep coals. The distribution curves exhibit either a trimodal or bimodal pattern. The first and largest peak is observed between 10 and 100 nm, the second peak appears mainly between 1000 and 10,000 nm, and the third peak occurs at diameters greater than 10,000 nm. The larger the areas of the second and third peaks, the more developed the "macropores and fractures", suggesting higher permeability. Specifically, the volume percentages for "macropores and fractures" (>1000 nm, MAF), mesopores (100–1000 nm, ME), transitional pores (10–100 nm, TR), and micropores (<10 nm, MI) are displayed in Table 1. Taking all samples into account, the volume proportion of "macropores and fractures" accounts for 1.43% to 20.98% in the total pore–fracture volume, with an average of 7.13%; mesopores range from 0.58% to 52.54% (avg. 12.64%) and present a good negative correlation with T_{2C} value (Figure 8a). Transitional pores comprise 37.59% to 87.09%, with an average of 74.66%. Micropores range from 0.68% to 20.64% (avg. 5.57%) and exhibit a strong positive correlation with T_{2C} value (Figure 8b). It is evident that the pore–fracture structure of the sampled deep coals exhibits considerable heterogeneity. Overall, the pore–fracture structure is predominantly composed of transitional pores, followed by mesopores, "macropores and fractures", and micropores. A higher T_{2C} value indicates more developed micropores, which hinder gas flow in the coal and consequently affect coal permeability.

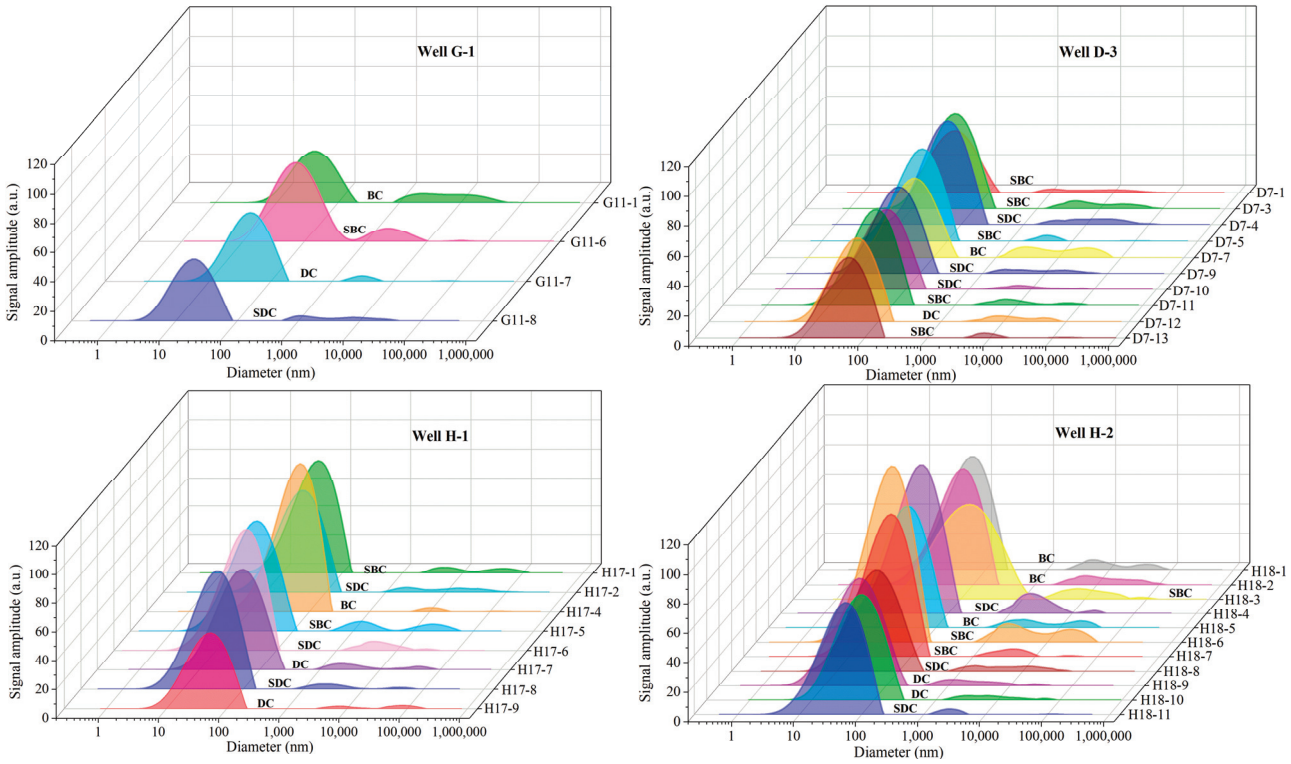

Figure 7. The pore–fracture size distributions of the sampled deep coals.

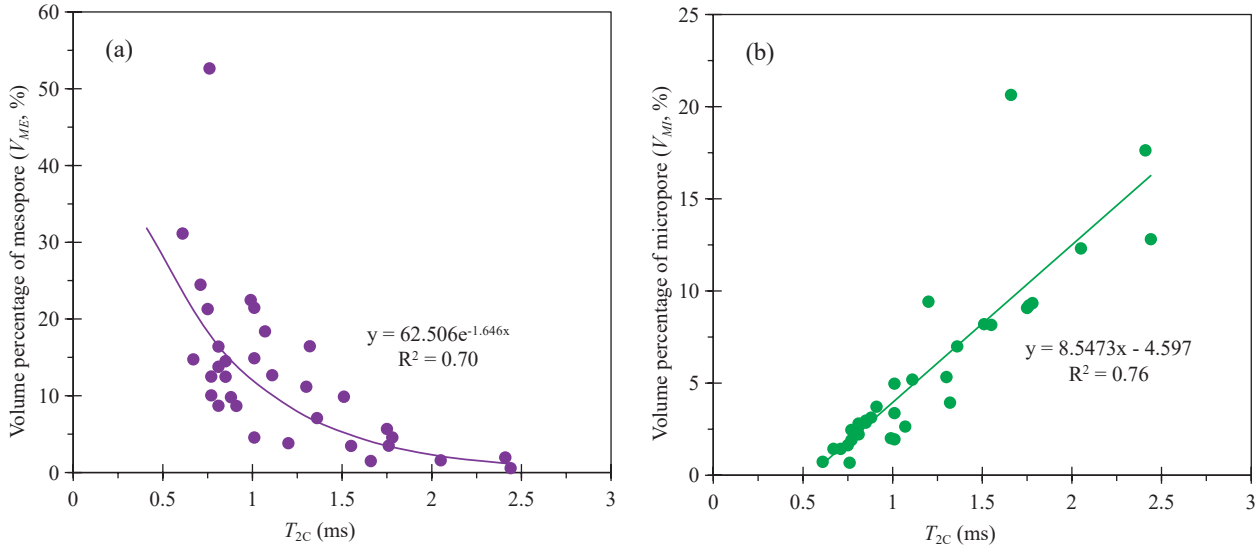

Figure 8. Plots showing T_{2C} versus the volume percentage for mesopores (**a**) and micropores (**b**).

4.2. Total Porosity and Producible Porosity of Deep Coals

Since NMR exclusively measures the quantity of ^{1}H atoms within a rock sample, the volume of water (V_w) present in the pore–fracture network of the sample is directly linked to the cumulative single amplitude of the T_2 spectra [46,47]. Actually, the V_w in the pore–fracture structure displays a linear positive correlation with the cumulative single amplitude. Thus, the total porosity (φ_t) of the sample can be obtained through the following equation:

$$\varphi_t = C_{Af}/k \times V_s \quad (5)$$

Here, φ_t represents the total porosity, in %; C_{Af} denotes the cumulative single amplitude of T_{2f} spectra, in a.u.; V_s is the volume of coal sample, in cm^3; k is the linear correlation

coefficient between the NMR cumulative signal amplitude of the standard sample and the V_w in the standard sample.

Thus, the irreducible water porosity (φ_{ir}), producible water porosity (φ_{pr}), and producible water saturation (S_{pr}) of the coals can be determined using the following equations:

$$\varphi_{ir} = C_{Ai}/C_{Af} \times \varphi_t \quad (6)$$

$$\varphi_{pr} = \varphi_t - \varphi_{ir} \quad (7)$$

$$S_{pr} = \varphi_t/\varphi_{pr} \quad (8)$$

Here, C_{Ai} represents the cumulative single amplitude of T_{2i} spectra, in a.u.; φ_{ir} and φ_{pr} denote the irreducible and producible water porosity, in %; S_{pr}, producible water saturation, in %.

Based on Equations (5)–(8), the φ_t, φ_{pr}, φ_{ir}, and S_{pr} of the sampled deep coals from the Daning-Jixian block were calculated and are shown in Table 1. Across all samples, the φ_t ranges from 4.45% to 14.05%, averaging 7.76%; the φ_{pr} varies from 0.31% to 7.24%, averaging 2.42%; the φ_{ir} is between 2.78% and 11.42%, averaging 5.34%; the S_{pr} spans from 6.97% to 71.47%, averaging 31.06%.

4.3. The Impact of Macrolithotypes on Pore–Fracture Structure Heterogeneity of Deep Coals

Although the pore–fracture structure of deep coals shows significant heterogeneity across different macrolithotypes and even within the same macrolithotype, the macrolithotype's influence on the pore–fracture structure still follows certain patterns (Figure 9). On average, compared to dull coal (DC) and semi-dull coal (SDC), the bright coal (BC) and semi-bright coal (SBC) overall have a higher abundance of "macropores and fractures" and mesopores, while containing fewer transitional pores and micropores (Figure 9). Notably, whether considering the median or the average, compared to other macrolithotype coals, the BC overall shows the most developed "macropores and fractures" (avg. 10.60%, med. 8.40%) and mesopores (avg. 14.51%, med. 15.45%), while transitional pores (avg. 71.46%, med. 69.78%) and micropores (avg. 3.42%, med. 2.33%) are the least developed (Figure 9).

Influenced by differences in pore structure, the porosity characteristics of the deep coals sampled also vary across different macrolithotypes. Firstly, while the overall distribution of total porosity across different macrolithotype coals shows relatively small differences, the average total porosity follows a clear decreasing trend, starting with BC, followed by SBC, SDC, and finally DC (Figure 10a). Additionally, compared to SD and SDC, the BC and SBC exhibit overall higher average producible water porosity (φ_{pr}) (Figure 10b) and producible water saturation (S_{pr}) (Figure 10c). This is because BC and SBC contain more "macropores and fractures" and mesopores, while both φ_{pr} and S_{pr} show a high positive correlation with the total volumes of "macropores and fractures" and mesopores (Figure 11a,b). As for irreducible water porosity, the distribution differences across different macrolithotype coals are relatively small (Figure 10d).

From the different macrolithotype coals' pore structure characteristics, it can be concluded that BC and SBC, especially the former, overall have more "macropores and fractures" and mesopores, and higher producible water porosity and saturation, implying that BC and SBC possess relatively higher permeability and better gas production capacity [44,48]. When studying the pore–fracture structure heterogeneity of coals with different macrolithotypes in the Jixi Basin, Wu et al. [39] also found that from BC, SBC, SDC to DC, the total pore volume and the proportion of macropores gradually decrease; furthermore, BC possesses a superior pore–fracture system.

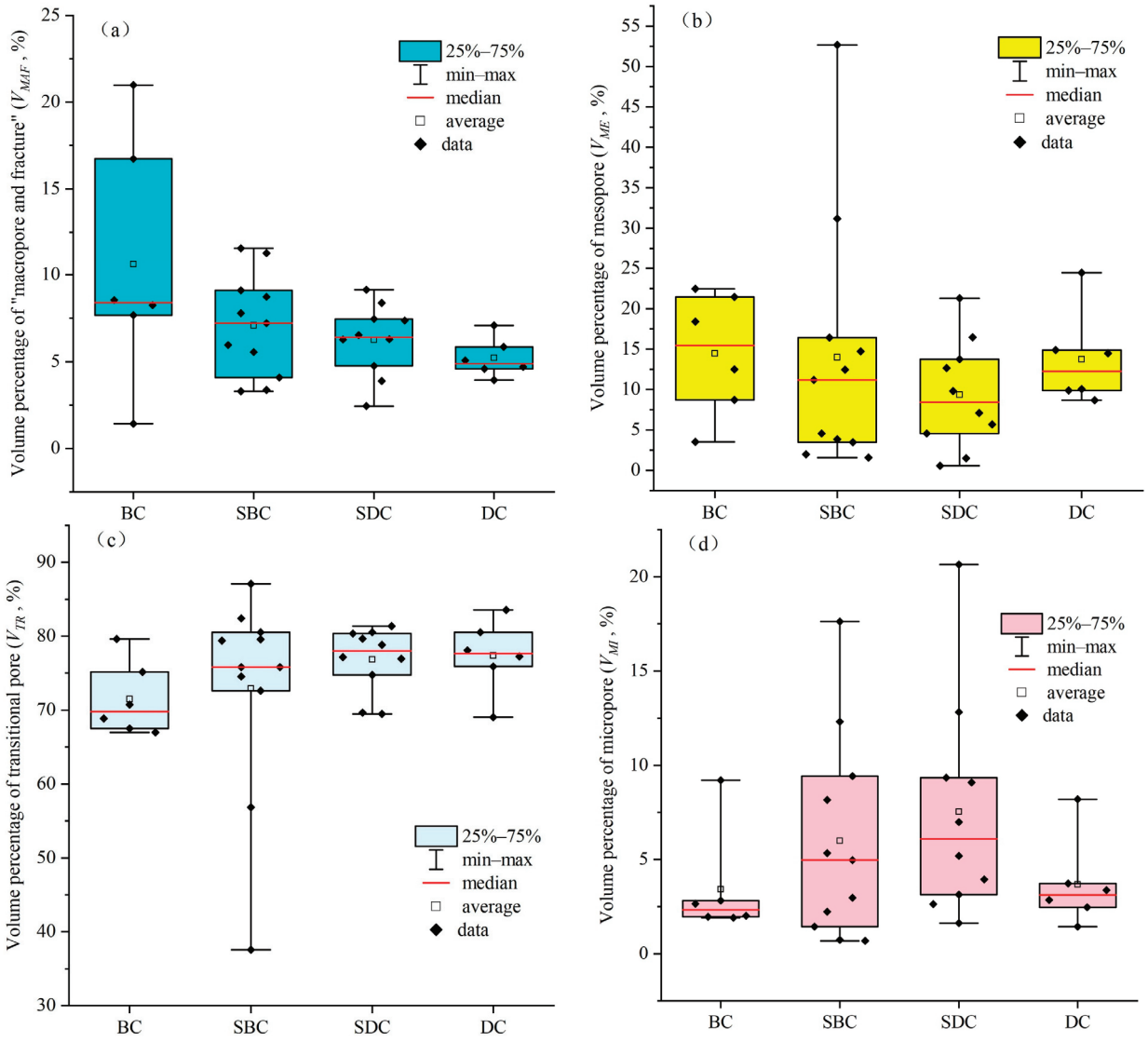

Figure 9. The volume percentages of "macropores and fractures" (**a**), mesopores (**b**), transitional pores (**c**), and micropores (**d**) in different macrolithotype coals.

Hence, during the exploration and development of deep CBM, regions with abundant BC and SBC should be prioritized due to their inherently superior permeability and gas extraction potential. These coals are likely to require less intensive stimulation to achieve higher recovery rates, reducing operational costs and risks; for example, the natural abundance of macropores and fractures in these coals suggests that lower fracturing pressures or simpler fracturing fluid systems might be sufficient to enhance permeability, avoiding over-fracturing that could damage the coal structure. Additionally, the naturally favorable pore–fracture structure of BC and SBC can lead to more sustainable gas production over time.

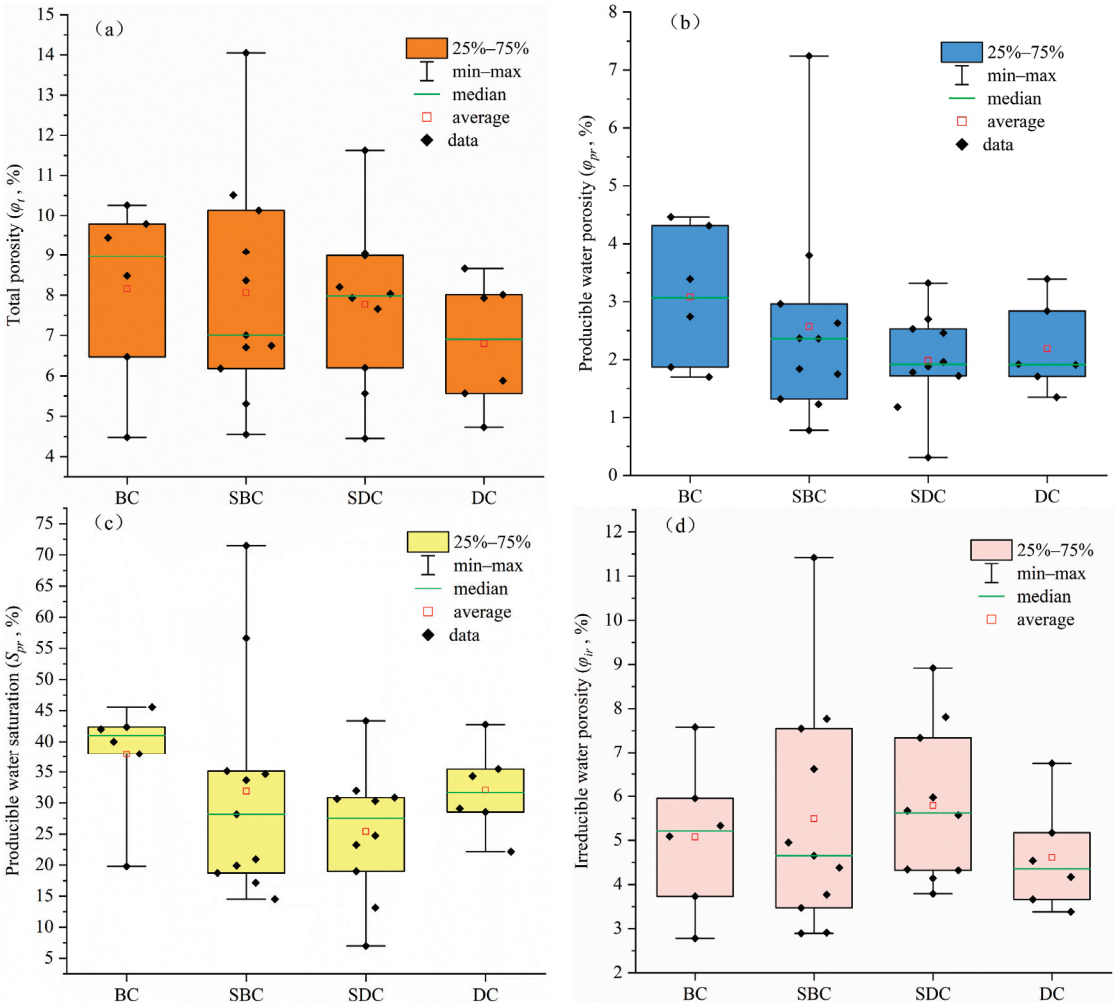

Figure 10. The total porosity (**a**), producible water porosity (**b**), producible water saturation (**c**), and irreducible water porosity (**d**) for different macrolithotype coals.

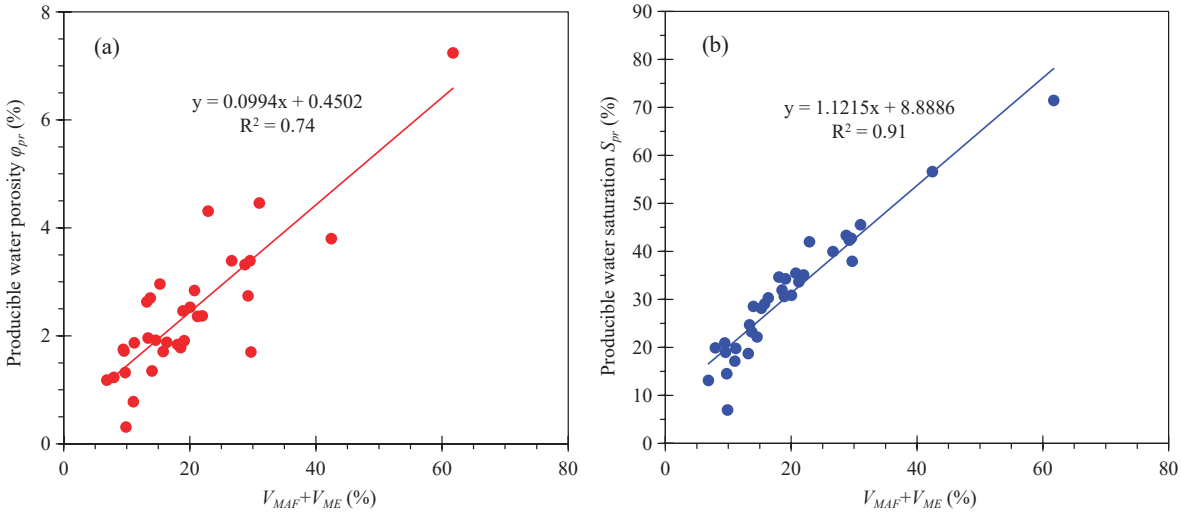

Figure 11. Plots of "V_{MAF} + V_{ME}" (total volumes of "macropores and fractures" and mesopores) versus φ_{pr} (**a**) and S_{pr} (**b**).

5. Conclusions

In this research, 33 deep coals covering four macrolithotypes were sampled from the Daning-Jixian block to explore the influence of macrolithotype on the heterogeneity of pore–fracture structure. Three sets of NMR experiments under dry, fully saturated, and irreducible water conditions were carried out on these samples and the pore–fracture structures were interpreted. The conclusions are as follows:

(1) The NMR T_{2C} for the deep coals is low, with values between 0.61 and 2.44 ms, averaging 1.19 ms. The pore–fracture structure of the samples shows considerable heterogeneity. On average, volumes of micropores (V_{MI}), transitional pores (V_{TR}), mesopores (V_{ME}), and "macropores and fractures" (V_{MAF}), respectively, account for 5.57%, 74.66%, 12.64%, and 7.13% in the total pore–fracture volume. The T_{2C} values exhibit a strong positive correlation with V_{MI} and a higher T_{2C} value indicates more developed micropores.

(2) The φ_{pr} and S_{pr} vary from 0.31 to 7.24% (avg. 2.42%) and 6.97 to 71.47%, respectively. Both φ_{pr} and S_{pr} show a high positive correlation with the total volumes of "macropores and fractures" and mesopores.

(3) Compared to SDC and DC, the BC and SBC (especially the former) overall have more "macropores and fractures" and mesopores, and higher φ_{pr} and S_{pr}, implying that BC and SBC possess relatively higher permeability and better gas production capacity. Hence, regions with abundant BC and SBC should be prioritized during CBM exploration and production. These coals are likely to require less intensive stimulation to achieve higher recovery rates and could provide more sustainable gas production over time.

Author Contributions: Conceptualization, W.Z. and Z.Z.; methodology, W.Z. and Z.Z.; software, R.S. and H.Z.; validation, L.B., Z.Z. and J.S.; formal analysis, W.Z.; investigation, W.Z., L.B., R.S. and H.Z.; resources, W.Z. and L.B.; data curation, W.Z. and L.B.; writing—original draft preparation, W.Z.; writing—review and editing, Z.Z. and J.S.; visualization, R.S. and H.Z.; supervision, L.B. and J.S.; project administration, L.B. and J.S.; funding acquisition, J.S., W.Z. and L.B. All authors have read and agreed to the published version of the manuscript.

Funding: This research was funded by the Natural Science Foundation of China (Grant No. 42272198) and Applied Science and Technology Projects of China National Petroleum Corporation (Grant No. 2023ZZ18-02).

Data Availability Statement: The original contributions presented in the study are included in the article, further inquiries can be directed to the corresponding author.

Acknowledgments: We sincerely thank the reviewers for their valuable comments and insightful suggestions, which significantly improved this work.

Conflicts of Interest: Authors Wei Zhang and Liheng Bian were employed by the company China United Coalbed Methane National Engineering Research Center Co., Ltd. and PetroChina Coalbed Methane Company Limited. The remaining authors declare that the research was conducted in the absence of any commercial or financial relationships that could be construed as a potential conflict of interest.

Nomenclature

CBM, coalbed methane; NMR, nuclear magnetic resonance; MIP, mercury intrusion porosimetry; SEM, scanning electron microscopy; CT, computerized tomography; SANS, small-angle neutron scattering; BC, bright coal; SBC, semi-bright coal; SDC, semi-dull coal; DC, dull coal; S_f, fully saturated condition; S_{ir}, irreducible water condition; MAF, macropores and fractures; ME, mesopores; TR, transitional pores; MI, micropores; V_{MI}, volumes of micropores; V_{TR}, volumes of transitional pores; V_{ME}, volumes of mesopores; V_{MAF}, volumes of macropores and fractures.

References

1. Moore, T.A. Coalbed methane: A review. *Int. J. Coal Geol.* **2012**, *101*, 36–81. [CrossRef]
2. Pan, Z.; Wood, D.A. Coalbed methane (CBM) exploration, reservoir characterisation, production, and modelling: A collection of published research (2009–2015). *J. Nat. Gas Sci. Eng.* **2015**, *26*, 1472–1484. [CrossRef]
3. Zhai, G.; He, W. Occurrence features and exploration orientation of coalbed methane gas in China. *Nat. Gas Ind.* **2010**, *30*, 1–3.
4. Li, G.; Zhang, S.; He, H.; He, X.; Zhao, Z.; Niu, X.; Xiong, X.; Zhao, Q.; Guo, X.; Hou, Y.; et al. Coal-rock gas: Concept, connotation, and classification criteria. *Pet. Explor. Dev.* **2024**, *51*, 783–795. [CrossRef]
5. Xu, F.; Hou, W.; Xiong, X.; Xu, B.; Wu, P.; Wang, H.; Feng, K.; Yun, J.; Li, S.; Zhang, L.; et al. The status and development strategy of coalbed methane industry in China. *Pet. Explor. Dev.* **2023**, *50*, 765–783. [CrossRef]
6. Tang, S.; Tang, D.; Yang, J.; Deng, Z.; Li, S.; Chen, S.; Feng, P.; Huang, C.; Li, Z. Pore structure characteristics and gas storage potential of deep coal reservoirs in Daning-Jixian Block of Ordos Basin. *Acta Pet. Sin.* **2023**, *44*, 1854–1866.
7. Qin, Y. Progress on geological research of deep coalbed methane in China. *Acta Pet. Sin.* **2023**, *44*, 1791–1811.
8. Li, S.; Qin, Y.; Tang, D.; Shen, J.; Wang, J.; Chen, S. A comprehensive review of deep coalbed methane and recent developments in China. *Int. J. Coal Geol.* **2023**, *279*, 104369. [CrossRef]
9. Zhang, X.; Lai, F.; Meng, Y.; Xu, X.; Li, H.; Liu, K. Dynamic production characteristics of deep coalbed methane: A case study of Daning-Jixian Block. *Energy Fuels* **2024**, *38*, 8700–8711. [CrossRef]
10. Kuuskraa, V.A.; Wyman, R.E. Deep Coal Seams: An Over-looked Source for Long-Term Natural Gas Supplies. In Proceedings of the SPE Gas Technology Symposium, Calgary, AB, Canada, 28–30 June 1993. SPE-26196.
11. Oison, T.; Hobbs, B.; Brooks, R.; Gale, B. Paying off for Tom Brown in White River Dome Field's tight sandstones, deep coals. *Am. Oil Gas Rep.* **2002**, *10*, 67–75.
12. Nelson, C.R. Deep Coalbed Gas Plays in the US Rocky Mountain Region. In Proceedings of the Annual Meeting Expanded Abstracts; American Association of Petroleum Geologists: Salt Lake City, UT, USA, 2003; pp. 5–8.
13. Wyman, R.E.; Kuuskraa, V.A. Deep coal seams: Potential for long-term natural gas supplies. *J. Pet. Technol.* **1995**, *47*, 774. [CrossRef]
14. Johnson, R.C.; Flores, R.M. Developmental geology of coalbed methane from shallow to deep in Rocky Mountain Basins and in Cook Inlet–Matanuska Basin, Alaska, USA and Canada. *Int. J. Coal Geol.* **1998**, *35*, 241–282. [CrossRef]
15. Tonnsen, R.R.; Miskimins, J. Simulation of deep-coalbed-methane permeability and production assuming variable pore-volume compressibility. *J. Can. Pet. Technol.* **2011**, *50*, 23–31. [CrossRef]
16. Ranathunga, A.S.; Perera, M.S.A.; Ranjith, P.G. Deep coal seams as a greener energy source: A review. *J. Geophys. Eng.* **2014**, *11*, 063001. [CrossRef]
17. Karacan, C.Ö.; Okandan, E. Fracture/cleat analysis of coals from Zonguldak Basin (northwestern Turkey) relative to the potential of coalbed methane production. *Int. J. Coal Geol.* **2000**, *44*, 109–125. [CrossRef]
18. Zhang, L.; Chen, S.; Zhang, C.; Fang, X.; Li, S. The characterization of bituminous coal microstructure and permeability by liquid nitrogen fracturing based on μCT technology. *Fuel* **2020**, *262*, 116635. [CrossRef]
19. Zhao, Y.; Wang, C.; Ning, L.; Zhao, H.; Bi, J. Pore and fracture development in coal under stress conditions based on nuclear magnetic resonance and fractal theory. *Fuel* **2022**, *309*, 122112. [CrossRef]
20. Hou, H.; Shao, L.; Tang, Y.; Li, Z.; Zhao, S.; Yao, M.; Zhang, J. Pore structure characterization of middle- and high-ranked coal reservoirs in Northern China. *AAPG Bull.* **2023**, *107*, 213–241. [CrossRef]
21. Mckee, C.; Bumb, A.C.; Koenig, R.A. Stress-dependent permeability and porosity of coal and other geologic formations. *SPE Form. Eval.* **1988**, *3*, 81–91. [CrossRef]
22. Clarkson, C.R. Production data analysis of unconventional gas wells: Review of theory and best practices. *Int. J. Coal Geol.* **2013**, *109*, 101–146. [CrossRef]
23. Ni, H.; Liu, J.; Chen, T.; Chen, S.; Meng, Q. Coal permeability prediction method based on the microscopic pore-fracture dual-porosity structure. *J. Pet. Sci. Eng.* **2022**, *211*, 110107. [CrossRef]
24. Hodot, B.B. *Outburst of Coal and Coalbed Gas (Chinese Translation)*; China Industry Press: Beijing, China, 1966.
25. Hu, B.; Cheng, Y.; Pan, Z.J. Classification methods of pore structures in coal: A review and new insight. *Gas Sci. Eng.* **2023**, *110*, 204876. [CrossRef]
26. Okolo, G.N.; Everson, R.C.; Neomagus, H.W.J.P.; Roberts, M.J.; Sakurovs, R. Comparing the porosity and surface areas of coal as measured by gas adsorption, mercury intrusion and SAXS techniques. *Fuel* **2015**, *141*, 293–304. [CrossRef]
27. Liu, Z.L.; Zhou, H.W.; Chen, B.C.; Song, L.; Sun, X.T. Integrated NMR analysis for evaluating pore-fracture structures and permeability in deep coals: A one-stop approach. *Energy Fuels* **2024**, *38*, 6854–6867. [CrossRef]
28. Raza, S.S.; Rudolph, V.; Rufford, T.; Chen, Z.W. A stochastic method to estimate the anisotropic stress-dependent coal permeability by pore-volume distribution and stress-strain measurements. *SPE J.* **2020**, *25*, 2582–2600. [CrossRef]
29. Li, Y.; Yang, J.H.; Pan, Z.J.; Tong, W.S. Nanoscale pore structure and mechanical property analysis of coal: An insight combining AFM and SEM images. *Fuel* **2020**, *260*, 116352. [CrossRef]
30. Roslin, A.; Pokrajac, D.; Zhou, Y.F. Cleat structure analysis and permeability simulation of coal samples based on micro-computed tomography (micro-CT) and scan electron microscopy (SEM) technology. *Fuel* **2019**, *254*, 115579. [CrossRef]
31. Prinz, D.; Pyckhout-Hintzen, W.; Littke, R. Development of the meso- and macroporous structure of coals with rank as analysed with small angle neutron scattering and adsorption experiments. *Fuel* **2004**, *83*, 547–556. [CrossRef]

32. Sakurovs, R.; Koval, L.; Grigore, M.; Sokolova, A.; Ruppert, L.F.; Melnichenko, Y.B. Nanometre-sized pores in coal: Variations between coal basins and coal origin. *Int. J. Coal Geol.* **2018**, *186*, 126–134. [CrossRef]
33. Zheng, S.; Yao, Y.; Liu, D.; Cai, Y.; Liu, Y. Characterizations of full-scale pore size distribution, porosity, and permeability of coals: A novel methodology by nuclear magnetic resonance and fractal analysis theory. *Int. J. Coal Geol.* **2018**, *196*, 148–158. [CrossRef]
34. Zhang, S.; Tang, S.; Qian, Z.; Pan, Z.; Guo, Q. Evaluation of geological features for deep coalbed methane reservoirs in the Dacheng Salient, Jizhong Depression, China. *Int. J. Coal Geol.* **2014**, *133*, 60–71. [CrossRef]
35. Wei, Q.; Li, X.; Zhang, J.; Hu, B.; Zhu, W.; Liang, W.; Sun, K. Full-size pore structure characterization of deep-buried coals and its impact on methane adsorption capacity: A case study of the Shihezi Formation coals from the Panji deep area in Huainan Coalfield, Southern North China. *J. Pet. Sci. Eng.* **2019**, *173*, 975–989. [CrossRef]
36. Wang, T.; Zhou, G.; Fan, L.; Zhang, D.; Shao, M.; Ding, R.; Deng, Z. Full-scale pore and microfracture characterization of deep coal reservoirs: A case study of the Benxi Formation coal in the Daning–Jixian Block, China. *Int. J. Energy Res.* **2024**, *2024*, 5772264. [CrossRef]
37. Karacan, C.Ö.; Okandan, E. Adsorption and gas transport in coal microstructure: Investigation and evaluation by quantitative X-ray CT imaging. *Fuel* **2001**, *80*, 509–520. [CrossRef]
38. Liu, Y.L.; Xu, H.; Tang, D.Z.; Xu, F.Y.; Mathews, J.P.; Hou, W.; Yan, X.; Ding, F.F. Coalbed methane production of a heterogeneous reservoir in the Ordos Basin, China. *J. Nat. Gas Sci. Eng.* **2020**, *82*, 103502. [CrossRef]
39. Wu, Y.N.; Tao, S.; Bi, C.Q.; Tang, S.L.; Men, X.Y. Pore-fracture and permeability heterogeneity of different marcolithotypes of medium-rank coals in Jixi Basin, China. *Geoenergy Sci. Eng.* **2023**, *231*, 212395. [CrossRef]
40. Zhao, J.; Xu, H.; Tang, D.; Mathews, J.P.; Li, S.; Tao, S. Coal seam porosity and fracture heterogeneity of macrolithotypes in the Hancheng Block, Eastern Margin, Ordos Basin, China. *Int. J. Coal Geol.* **2016**, *159*, 18–29. [CrossRef]
41. Zhang, L.; Bian, L.; Hou, W.; Li, Y.Z.; Li, Y.C.; Wu, P.; Li, W.; Li, X.; Li, C. Pore structure characteristics and exploration significance of deep coal reservoirs: A case study of the Daning-Jixian block in the eastern margin of the Ordos Basin. *Acta Pet. Sin.* **2023**, *44*, 1867–1878.
42. *ISO 11760-2005(E)*; Classification of Coals. International Organization for Standardization: Geneva, Switzerland, 2005.
43. *Chinese Standard GB/T 18023-2000*; Classification of Macrolithotype for Bituminous Coal; China National Standards: Beijing, China, 2000.
44. Yao, Y.; Liu, D.; Che, Y.; Tang, D.; Tang, S.; Huang, W. Petrophysical characterization of coals by low-field nuclear magnetic resonance (NMR). *Fuel* **2010**, *89*, 1371–1380. [CrossRef]
45. Fu, G.; Zhang, Y.; Zou, D. The measurement and analysis of the balanced contact angle between coal and pure water. *Coal Convers.* **1997**, *20*, 60–62.
46. Zhang, Z.; Qin, Y.; Zhuang, X.; Li, G.; Wang, X. Poroperm characteristics of high-rank coals from Southern Qinshui Basin by mercury intrusion, SEM-EDS, nuclear magnetic resonance and relative permeability analysis. *J. Nat. Gas Sci. Eng.* **2018**, *51*, 116–128. [CrossRef]
47. Cui, Z.; Zhang, Z.; Huang, W.; Liu, L.; Wang, J.; Wei, X.; Shen, J. Pore–fracture structure characteristics of low-medium rank coals from Eastern Surat Basin by FE-SEM and NMR experiments. *Nat. Resour. Res.* **2024**, *33*, 743–763. [CrossRef]
48. Li, S.; Tang, D.; Xu, H.; Yang, Z.; Guo, L. Porosity and permeability models for coals using low-field nuclear magnetic resonance. *Energy Fuels* **2012**, *26*, 5005–5014. [CrossRef]

energies

MDPI

Article

The Impacts of Reservoir Heterogeneities on the CO_2-Enhanced Oil Recovery Process—A Case Study of Daqingzijing Block in Jilin Oilfield, China

Zetang Li [1,2], Tianfu Xu [1,2,*], Hailong Tian [1,2,*] and Ruosheng Pan [3]

[1] Key Laboratory of Groundwater Resources and Environment, Ministry of Education, Jilin University, Changchun 130021, China; ztli23@mails.jlu.edu.cn
[2] Jilin Provincial Key Laboratory of Water Resources and Environment, Jilin University, Changchun 130021, China
[3] Oil and Gas Engineering Research Institute, CNPC Jilin Oilfield Company, Songyuan 138000, China; panruosheng@163.com
* Correspondence: tianfu_xu@jlu.edu.cn (T.X.); thl@jlu.edu.cn (H.T.)

Abstract: With the exploitation of oilfields, the oil production efficiency of traditional water flooding has been very low, and CO_2-enhanced oil recovery (EOR) has become an inevitable trend of development. CO_2-EOR is affected by many factors, among which the heterogeneity of reservoirs is one of the main influencing factors. In order to understand the impact of different reservoir conditions on the production of oil from CO_2 and the reasons behind it, and on the basis of researching the heterogeneity of reservoir porosity and permeability and its influence on the CO_2-enhanced oil recovery process, this study has altogether established three different reservoir characteristics for comparative analysis. Under the homogeneous and heterogeneous porosity and permeability conditions of a reservoir, the displacement characteristics during a CO_2–oil displacement process were analyzed. The layered heterogenous model had the best oil displacement effect, with its oil displacement amount reaching 8.46×10^4 kg, while the homogeneous model and the spatially heterogenous model had lower values; they were 1.51×10^4 and 1.42×10^4, respectively. The results indicate that the heterogeneous conditions overall improved the flooding effect of CO_2. Under the same injection volume and other reservoir conditions, the cumulative oil flooding effect of the layered heterogenous model was the best compared to the homogeneous and spatially heterogeneous models. Good permeability promotes the accumulation of oil, leading to a higher saturation of the oleic phase. This work provides an in-depth analysis of the effect of the non-uniform distribution of formation permeability on CO_2-enhanced oil recovery and can help to improve carbon sequestration efficiency and oil recovery in CO_2–oil recovery projects.

Keywords: CO_2-enhanced oil recovery; heterogeneity; Jilin Oilfield; numerical simulation

1. Introduction

The development of the economy and society urgently requires a large amount of fossil fuels such as oil and gas for support [1]. With the exploitation of oilfields, the oil output efficiency of traditional water flooding has been very low, and CO_2-enhanced oil production has become an inevitable trend of development. Under the existing energy structure conditions, CO_2 flooding technology not only increases the output of conventional energy but also stores CO_2. CO_2 flooding technology is relatively mature and has been widely used around the world, such as in the Permian Basin in Texas, USA [2], and the Weyburn oilfield in Saskatchewan, Canada [3]. As early as 1965, China began to explore CO_2 flooding technology in the Daqing oilfield. However, due to various problems, such as insufficient theoretical understanding, poor gas source conditions, and serious gas tampering, China's CO_2 flooding technology developed slowly until 2000 [4–6]. In 2005, Prof. Pingping Shen

first proposed the concept of combining CO_2 flooding with burial storage [4,5]. Since then, China's CO_2 flooding technology has begun to develop gradually. Since the 11th Five-Year Plan (2006–2010), China has set up several national projects including CO_2 storage and resource utilization and has made important progress [4,5]. In September 2020, the "double carbon" goal was proposed, and CCUS-EOR technology began to usher in a period of rapid development opportunities. The combination of CO_2 flooding and CCUS can not only realize the reuse of resources (economic benefits) but also reduce the emission of CO_2 (social benefits). At this stage, many countries are still in the developing phase in this context [4]. CCUS-EOR is not only the main way to reduce carbon emissions on a large scale but also an important way to improve the oil recovery of oilfields [7]. For the above reasons, CCUS-EOR has broad development and application prospects.

However, the process of CCUS-EOR technology is affected by many factors in oilfield blocks, which lead to a limited CO_2 displacement. The heterogeneity of a reservoir is one of the main influencing factors. An in-depth analysis of the mechanism of the non-uniform distribution of formation permeability acting on CO_2–oil production can help to improve the efficiency of carbon sequestration and oil recovery in CO_2–oil production engineering. Since the 1970s, foreign countries have gradually begun research on the influence of heterogeneity on oilfield development. At this stage, the understanding of reservoir heterogeneity is relatively shallow, and the theoretical research is not mature [8].

Around 1960, foreign scholars found the phenomenon of reservoir heterogeneity [9]. In 1990, the heterogeneity of reservoirs was categorized [10], and the principles of its description and analysis were discussed. It was discovered that heterogeneity influences reservoir development and concluded that heterogeneity is always unfavorable to oil recovery [11]. In recent years, the influence of heterogeneity on oilfield development has gradually been paid more attention, and scholars have begun to propose a variety of research methods, among which Yang [12] proposed the heterogeneity composite index method for the first time and established some computational models, which can be regarded as the predecessor of numerical simulation research methods. With the development of science and technology and oil reservoir production methods to increase the oil recovery of oil reservoirs, the research on the heterogeneity of oil reservoirs has become more and more in-depth and detailed. Since 2006, a variety of the effects of heterogeneity on oil recovery have been clarified. The relationship between heterogeneity and residual oil [13], the influence of different fracture directions and depositional rhythms on the oil recovery of CO_2 flooding [14], the influence of the heterogeneity of reservoirs on the mechanism and pattern of oil and gas transportation [15], the influence of vertical and interlayer heterogeneity on recovery [16], or the important influence of reservoir heterogeneity and the injection method on crude oil production [17] are some examples.

Most of the oilfields in China are dominated by terrestrial clastic reservoirs, with complex geological conditions, strong heterogeneity, and large differences in crude oil properties [18]. The research method for reservoirs in China is mainly based on numerical simulation and indoor physical experiments and started later than in other countries. Since 2010, scholars have begun to analyze the influence of different heterogeneity factors on CO_2 flooding by numerical simulation. Through the study of several factors, it has been shown that the stronger the heterogeneity is, the lower the oil recovery of CO_2 flooding is [19–23]. Therefore, some scholars have begun to study how to reduce the impact of reservoir heterogeneity. Liu [24] proposed adjusting well network, well spacing, and injection and production parameters. Kang et al. [25] proposed using polymer gel to improve reservoir heterogeneity. Subsequent studies have found that reservoir heterogeneity can easily lead to the existence of hypertonic channels in their formation, and these channels can lead to gas channels, which in turn can greatly reduce their recovery rate. Therefore, the focus of recent studies has been shifted to gas channels, such as the effect of different replacement pressures and permeability gradients [26,27] on gas channels, and the study of the permeability of tunnels [28].

In general, most of the studies on the effect of reservoir heterogeneity on the oil recovery effect have explored the heterogeneity of two-dimensional reservoirs. On the other hand, regarding three-dimensional reservoirs, heterogeneity caused by sedimentary rhythms has been mainly explored. In this study, we not only set up three different three-dimensional reservoirs for simulation but also set up a spatially heterogenous model to realize the random distribution of permeability and porosity in space. By setting the same injection conditions, the displacement characteristics in the process of CO_2 flooding are investigated. The oil displacement effect of the three models is compared, and the influence of different heterogeneities on the oil displacement effect and the reasons for this effect are analyzed. This study deeply analyzes the influence of different reservoirs on CO_2 flooding and provides technical support for further research on CO_2-EOR and CO_2 sealing stock.

2. Characteristics of the Study Area

In this paper, based on actual stratigraphic conditions and site-measured data, a variety of stratigraphic conditions were designed to investigate the influence of them on CO_2-enhanced oil recovery.

The study area selected for this simulation was the Daqingzi Wells of Jilin Oilfield, which is located in the southern part of the Songliao Basin (Figure 1a), and the main exploration area is shown in Figure 1b. The simulation area selected for this study was Block H59, and the site exploration well deployment map is presented in Figure 1c.

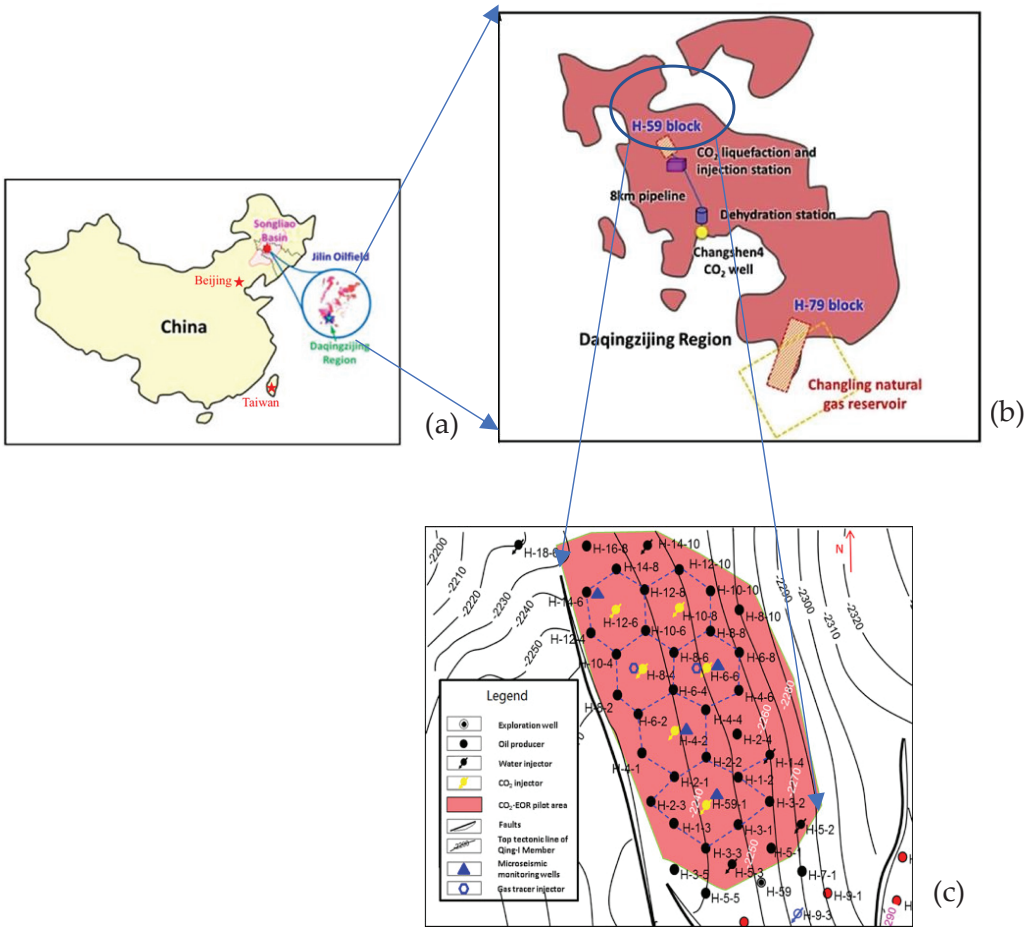

Figure 1. (**a**) Location of Jilin Oilfield (124.8° E, 45.1° N) [29]. (**b**) Main exploration areas [29]. (**c**) Site exploration well deployment map [30].

The regional exploration work of Daqingzijing block started in the early 1950s. At this stage, the basic geological structure of the area was mostly surveyed and understood

through the technical methods of physical exploration (the electric method, the magnetic method, gravity, etc.) [31].

In 2001, exploration work was completed in a total area of 600 km^2 in Daqingzijing block, and 3D seismic data within the area were collected and processed, and the block was officially entering the development stage. In several consecutive years, namely from 2000 to 2008, production was increased and the degree of reserve utilization in Daqingzijing block area exceeded 60%, with more than 1500 wells put into operation. The annual crude oil production was 100 × 10^4 t as a result of the decent development of the oilfield [32]. Figure 2 shows the composition of the crude oil production of Daqingzijing block over the mentioned years.

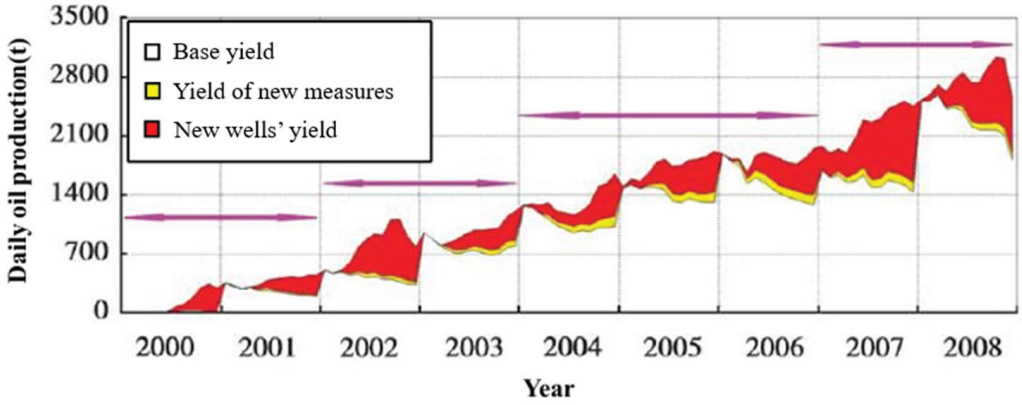

Figure 2. Historical crude oil production composition curve of Daqingzijing block [32].

At the end of 2010, Jilin Oilfield selected a total of 11 blocks such as Hei 79 and Hei 46 to promote the industrialization of CO2-EOR based on a series of achievements in theoretical research as well as indoor tests. A total of 171 gas injection wells and 697 oil production wells have been set up for oil recovery using the inverted five-point method.

Daqingzijing block is an early industrialized CO_2 flooding application oilfield in China, which has not only achieved an enhanced oil flooding operation but has also worked out a mature technology route and corresponding implementation measures through independent innovation. It provides a very valuable experience for the exploration of CO_2 flooding [33]. Therefore, Daqingzijing block seems to be very appropriate for the current study.

3. Theory and Equations

3.1. Three-Phase Relative Permeability

The existence of three-phase conditions in reservoirs requires the ability to approximate three-phase relative permeability. Various three-phase relative permeability models are implemented in TOGA (TOUGH Oil, Gas, Aqueous). Some are just simple extensions of two-phase (gas and water) relative permeability functions inherited from the TOUGH2 code (e.g., taking the "gas" relative permeability as a non-aqueous-phase relative permeability and then splitting it by the relative saturation of the gas phase in the non-aqueous phase).

The other functions are defined explicitly for three-phase conditions. In the following, we briefly describe the relative permeability models implemented in TOGA. The STONE II (IRP = 15) model assumes that the oil relative permeability can be estimated from the tabular data of the relative permeabilities of water–oil and oil–gas systems.

3.2. STONE II Model

When gas-, water-, and oil-phase conditions exist in a reservoir, the relative permeability is calculated by applying the modified STONE II model [34,35], which assumes that the relative permeability of the oil phase is a function of the relative permeability data of the

water–oil and oil–gas systems. The relative permeability data of these two systems need to be given by the user.

$$k_{ro}(S_l, S_g) = k_{rocl}\left[\left(\frac{k_{rol}}{k_{rocl}} + k_{rl}\right)\left(\frac{k_{rog}}{k_{rocl}} + k_{rg}\right) - \left(k_{rl} + k_{rg}\right)\right] \quad (1)$$

where k_{rocl} is the relative permeability of the oil phase at a residual water saturation (S_{lc}), k_{rol} is the relative permeability of the oil phase at $S_g = 0$, and k_{rl} is the relative permeability function of the water phase in the water–oil system at an S_l saturation. k_{rog} is the oil-phase relative permeability associated with S_g when $S_l = S_{lc}$, and k_{rg} is the gas-phase relative permeability function associated with S_g in the gas–oil system. All two-phase relative permeabilities can be obtained by interpolating the tabular data by the smooth monotonic interpolation method proposed by Steffen [36] based on user-given data.

In TOGA, the water saturation could become smaller than the connate water saturation because the water could vaporize or be dissolved into oil and be carried away by the flowing gas–oil phase that would cause the local dry-out of the formation. In this case (i.e., $S_l < S_{lc}$), if the specified oil relative permeability k_{rocl} is less than 1, the two-phase relative permeabilities will be adjusted before using Equation (1) to calculate the oil relative permeability as follows:

$$k_{rog}^{new} = k_{rog}^{old} + \left(1 - k_{rocl}^{old}\right)\left(1 - \frac{S_l}{S_{lc}}\right)$$

$$k_{rg}^{new} = k_{rg}^{old} + \left(1 - k_{rgcw}^{old}\right)\left(1 - \frac{S_l}{S_{lc}}\right)$$

$$k_{rol}^{new} = k_{rol}^{old} + \left(1 - k_{rocl}^{old}\right)\left(1 - \frac{S_l}{S_{lc}}\right)$$

$$k_{rocl}^{new} = k_{rocl}^{old} + \left(1 - k_{rocl}^{old}\right)\left(1 - \frac{S_l}{S_{lc}}\right)$$

where superscript "*old*" indicates the values originally obtained from the interpolation of the tabular data whereas "*new*" indicates the adjusted value.

4. Model Setting

4.1. Simulator Introduction

TOGA is a numerical reservoir simulator for modeling the non-isothermal flow and transport of water, CO_2, multicomponent oil, and related gas components for applications including CO_2-EOR and geologic carbon sequestration in depleted oil and gas reservoirs. TOGA uses an approach based on the Peng–Robinson equation of state (PR-EOS) to calculate the thermophysical properties of the gas and oil phases, including the gas–oil components dissolved in the aqueous phase, and uses a mixing model to estimate the thermophysical properties of the aqueous phase.

TOGA uses a multiphase version of Darcy's Law to model the flow and transport of mixtures through porous media with up to three phases over a range of pressures and temperatures appropriate for hydrocarbon recovery and geologic carbon sequestration systems. The transport of the gaseous and dissolved components is assumed to be taking place by advection and Fickian molecular diffusion. New methods for phase partitioning and thermophysical property modeling in TOGA have been validated against experimental data published in the literature for describing phase partitioning and phase behavior. Flow and transport had been verified by testing against related TOUGH2 EOS modules and CMG (Computer Modelling Group) simulators [37].

The TOGA simulator adopts the integral finite difference method for spatial discretization. For time discretization, it employs the fully implicit differences with unconditional convergence.

4.2. Geomodel and Boundary Conditions

The selected simulation area was the Jilin Oilfield Daqingzijing block. The actual reservoir conditions were used as the basis of the numerical simulation to construct the three-dimensional numerical model of the reservoir in the study area. A relatively complete five-point well network for the injection and production area was selected as the modeling domain. The boundary and the geological conditions of the reservoir were set as the confining boundary to simplify the simulation.

The reservoir in the area can be categorized as a stratified, low-permeability sandstone reservoir. To simplify the model, the reservoir was generalized as a low-permeability sandstone reservoir with horizontal stratification and a homogenous thickness, without considering its fracture development. The thickness of the reservoir was set to 10 m. The upper and lower caprocks of the reservoir were simplified as no-flow boundaries.

According to the actual situation of the oilfield, a 140 m × 140 m, five-point-method well network was used for injection and extraction. As shown in Figure 3, the pink square is the research area used to construct the conceptual model. One injection well (red circle in Figure 3) and one production well (blue circle) were considered at both ends of the square diagonal. CO_2 was injected through the injection well at a fixed rate. The fluid was extracted from the production well at a given pressure. Due to the symmetric properties of the five-point well network, the boundaries around the research area could be simplified as no-flow condition types.

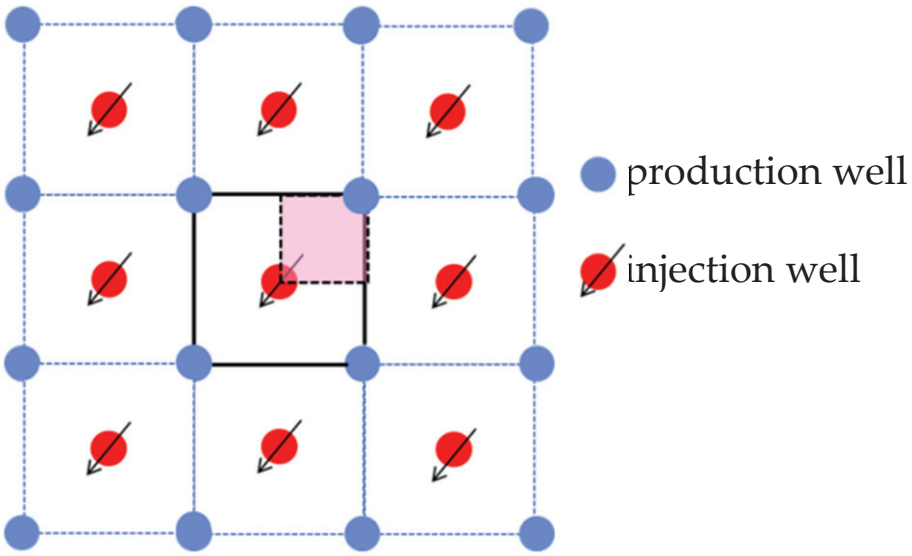

Figure 3. Schematic of the five-point well network and modeling area.

To simplify the modeling, the anisotropy in the reservoir properties was ignored and the model was assumed to be isotropic and homogeneous, with a small thickness. The three-dimensional simulation model was dissected in the horizontal plane into 14 × 14 segments with a total of 196 grids and was vertically divided into five layers with a total of 980 grids.

The entire model was a rectangular cube with a length of 140 m, a width of 140 m, and a height of 50 m. Each cell was also a cube of 10 m in length, 10 m in width, and 10 m in height. The grid dissection is shown in Figure 4. The bottom cell on the left side of the figure was selected as an injection well for constant-rate CO_2 injection, while the bottom cell on the right side was assumed to be a production well. Additionally, the yellow color in Figure 4 is the injection–production profile of the reservoir.

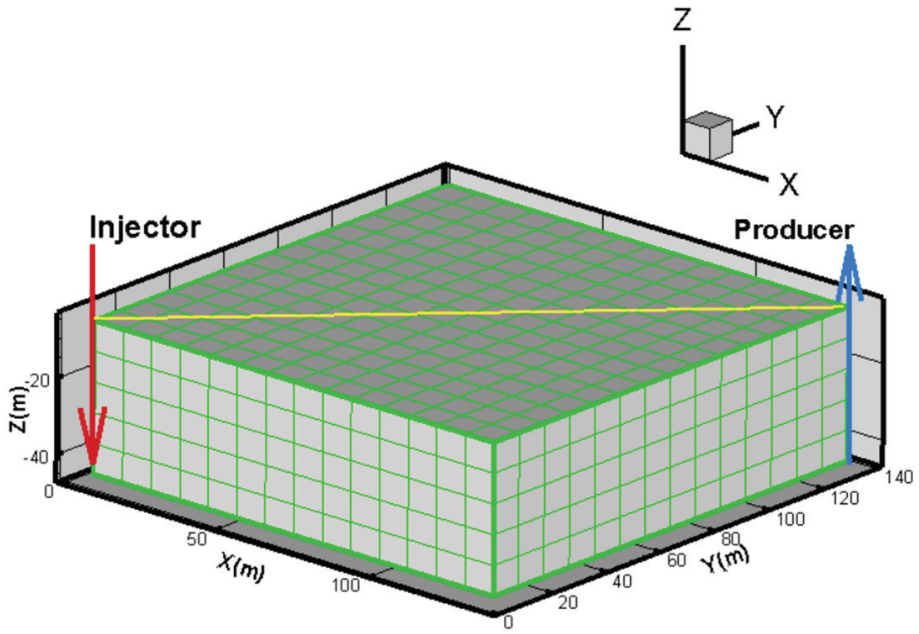

Figure 4. Reservoir sectional grid map.

4.3. Thermo-Hydrological Parameters and Initial Conditions

4.3.1. Thermo-Hydrological Parameters

Based on the data summarized from previous studies and the relevant information from Jilin Oilfield, the average values of the initial physical properties of the reservoir in the study area are presented in Table 1.

Table 1. Thermo-hydrological parameters [29,30,38].

Parameter	Value	Parameter	Value
temperature (°C)	98.9	MMP (MPa)	22.3
average porosity (%)	12.7	reservoir fracture pressure (MPa)	49
average permeability (mD)	3.0	oil viscosity (mPa.s)	2.02
initial well-head pressure (MPa)	24.15	oil density (g/m^3)	0.765
reservoir thickness (m)	11.2–18.2	oil saturation (before CO_2 injection)	0.35–0.38
salinity (ppm)	14,607		

4.3.2. Initial Conditions

Stratigraphic crude oil is a complex mixture of various hydrocarbon and non-hydrocarbon compounds. It is difficult to determine and quantify the physical and chemical properties of each component of crude oil, so it is necessary to construct the components of crude oil by using curve fitting and mathematical modeling based on the physical characteristics of crude oil presented elsewhere [39]. The initially proposed crude oil components of this study were obtained from previous studies, and their specific parameters are presented in Table 2.

Table 2. Properties of crude oil [30].

Components	CO_2	N_2 to Cl	C2 to C6	C7+
mole fraction (%)	0.407	15.574	24.384	59.635
critical pressure (atm)	72.8	44.2	41.24	15.35
critical temperature (°C)	30.42	18.35	38.71	73.54
critical volume (cm^3/mol)	94	97.89	21.45	87.69
molar mass (g/mol)	44.01	17.3	48.88	24.56
acentric factor	0.225	0.013638	0.16345	0.34353

The relative permeabilities of gasses, oil, and aqueous phases are important during CO_2 flooding within a reservoir. The STONE II model is commonly employed to calculate these relative permeabilities [40]. To obtain the proper parameters of the STONE II model, the regression technique was used based on the relative permeability curves (Figure 5) from Zhang et al. [29]. The relevant parameter settings in the STONE II model are summarized in Table 3.

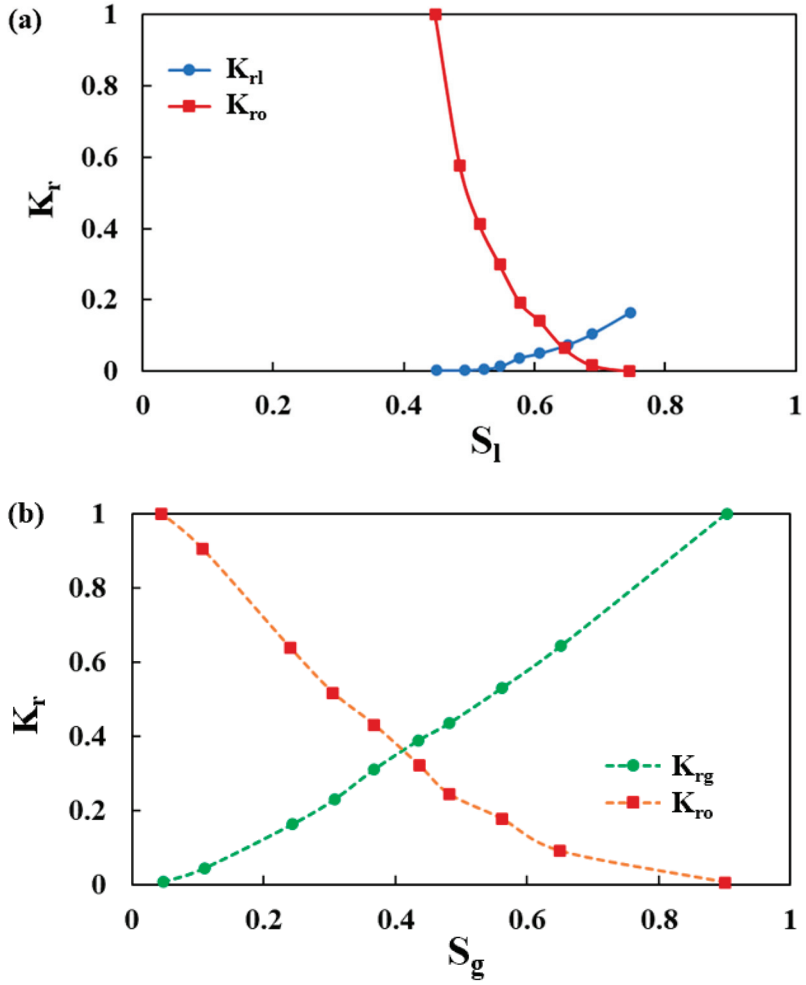

Figure 5. (**a**) Water–oil relative permeability curve; (**b**) gas–oil relative permeability curve [29].

Table 3. Parameter settings for STONE II model.

Parameter	Value
S_{lc}: Residual water saturation	0.45
S_{gc}: Residual gas saturation	0.05
k_{rol}: When $S_g = S_{lg}$, relativeoil − phase permeability with respect to S_l.	Figure 5a
k_{rl}: When $S_g = S_{lg}$, relativeliquid − phase permeability with respect to S_l.	
k_{rocl}: When $S_l = S_{lc}$, relative oil-phase permeability.	1.0
k_{rog}: When $S_l = S_{lc}$, relative oil − phase permeability related to S_g.	Figure 5b
k_{rg}: When $S_l = S_{lc}$, relative gas − phase permeability related to S_g.	

4.4. Case Design

To achieve these objectives, we generated random heterogeneous fields of hydrological parameters [41] (permeability and porosity). In this study, three kinds of reservoir characteristics were set up: homogeneous formation, layered heterogeneous formation, and

spatially heterogeneous formation. By specifying the same initial conditions, gas injection volume, and oil flooding time, comparative analysis was carried out to obtain the influence of the heterogeneities of the hydrological parameters on the oil recovery of CO_2 flooding.

4.4.1. Homogeneous Formation

Based on the thermo-hydrological parameters in Section 4.3.1, some parameters were optimized to model the reservoir. The permeability and porosity of the reservoir were unchanged, the simulation time was set to 20 years, and carbon dioxide was injected at a constant rate of 1.5625×10^{-3} kg/s. The pressure of the production well was considered 18 MPa.

4.4.2. Layered Heterogenous Strata

The oil reservoirs in Jilin Oilfield are distributed in different strata, and the bottom strata consist of alternating layers of mudstone and sandstone with different permeabilities and porosities.

As a result, the layered heterogenous strata model set up mudstone and sandstone with different permeabilities to be interbedded in the vertical direction (five layers in total) and in the horizontal direction. The permeability of the reservoir was considered constant. The rest of the parameters were assumed to be the same as the homogeneous model.

Due to the lack of actual data from Jilin Oilfield, the average value of the porosity of the reservoir in the study area was moved up and down by 40%, and the order of magnitude of the permeability was adjusted up and down by two orders of magnitude to form the high-permeability and low-permeability layers. The specific data are shown in Table 4, and the reservoir was set up as an interbedded layer of siltstone–mudstone–siltstone–siltstone–mudstone–siltstone. Figure 6 shows the final effect of the layered heterogenous reservoir model setup.

Table 4. Layered heterogenous model reservoir parameters.

Permeability	Rock Type	Permeability m^2	Porosity %
High	Siltstone	2.961×10^{-13}	17.78
Low	Mudstone	2.961×10^{-17}	7.62

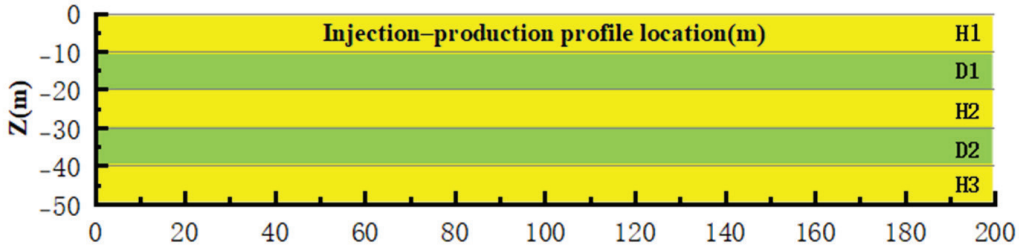

Figure 6. Layered heterogenous reservoir model (H: high permeability; D: low permeability).

4.4.3. Spatially Heterogenous Strata

The construction of the spatially heterogenous model used the random field theory detailed by Vanmarcke and Grigoriu [42]. According to the data from Jilin Oilfield, to obtain the spatial distribution of the reservoir permeability and porosity, the permeability was taken as an average value according to the overall normal distribution and was also randomly distributed in different grids (porosity was positively correlated with permeability). Figure 7 displays the spatial distribution of the reservoir porosity.

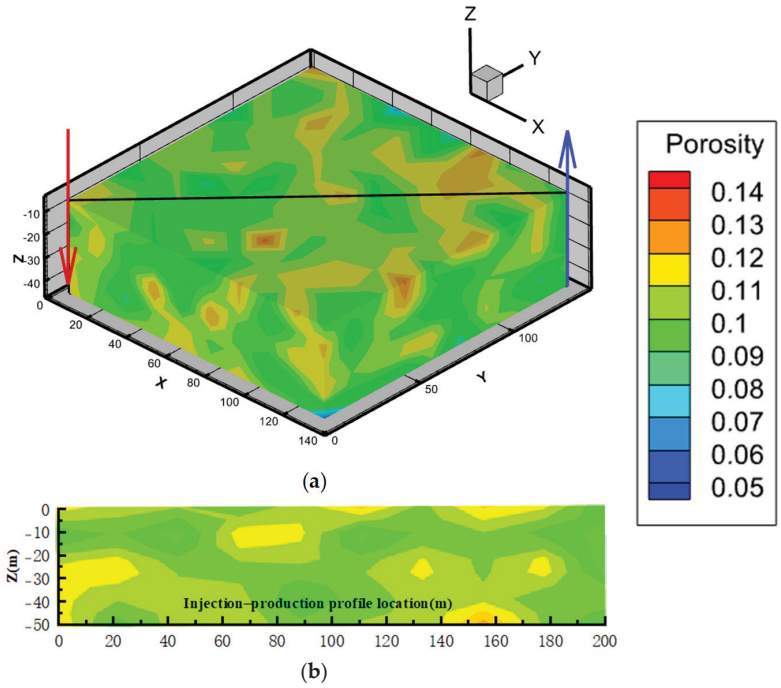

Figure 7. Spatial heterogeneity: (**a**) spatial distribution of reservoir porosity; (**b**) porosity distribution of reservoir injection–production profile.

5. Results and Discussion

5.1. Influence of Heterogeneity on Distribution of Residual Oil Phase in Reservoirs

The initial oil saturation of the three models is shown in Figure 8, which is the same as 0.37. The red color in Figure 8 is the injection well and the blue color is the production well. The yellow color is the location of the dissection of the injection–production profile. The effect of heterogeneity on the distribution of the residual oil phase in the reservoir is observed through the variation in oil saturation.

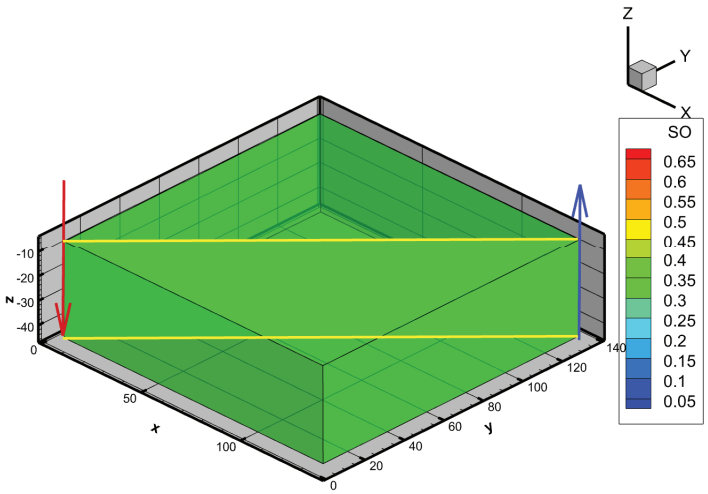

Figure 8. Spatial distribution of initial oil saturation of homogeneous model.

To facilitate the observation, the oil saturation variations in the injection–production profiles are analyzed. The distribution of the oil saturation (in the injection–production profiles) through different years of production in the homogeneous model is presented in Figure 9.

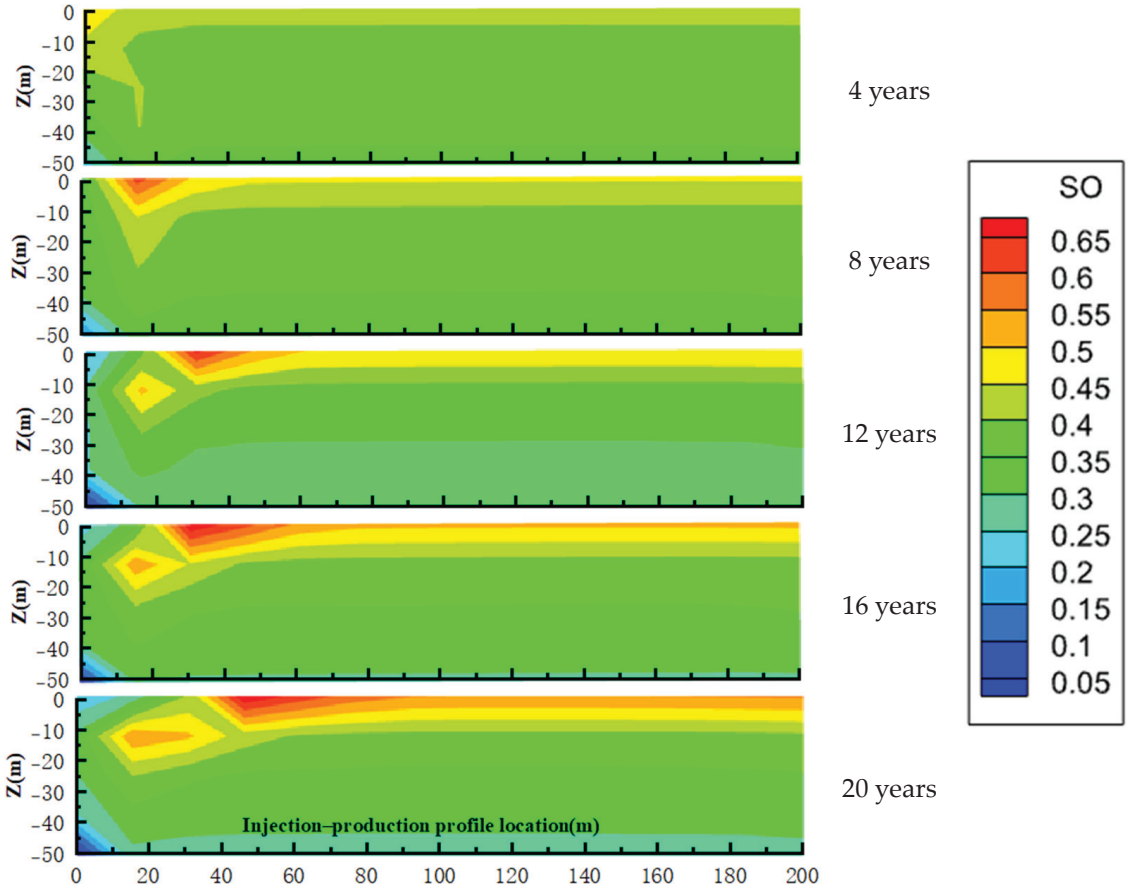

Figure 9. Oil saturation in the injection–production profile of the homogeneous model.

As can be observed from the figure, in general, the oil saturation changes in the homogeneous model mainly occurred at the top of the reservoir and near the injection wells. With the injection of CO_2, the oil phase in the reservoir gradually accumulated and formed areas with high oil saturation (oil saturation greater than 0.55), and these highly saturated areas of the oil phase gradually moved toward the production well. Consequently, there was a trend of oil-phase replacement in the reservoir from the injection wells towards the production wells. Spatially, the highest oil saturation of the reservoir was 0.65. At the injection well, the oil saturation of the reservoir decreased significantly. Moreover, the oil phase of the reservoir gathered in the upper reservoir near the injection well. There were two obvious centers of high oil saturation (oil saturation greater than 0.55), which signified the phenomenon of the uplift of the oil phase in the homogeneous model. This oil-phase uplift led to the phenomenon of the layering of the oil saturation, in which the oil saturation in the upper reservoir was higher than that in the bottom. Therefore, the oil flooding effect was more obvious in the upper part of the reservoir.

In general, the starting point of CO_2 flooding was from the bottom. This allowed the oil phase to gather at the top of the reservoir under the action of buoyancy and CO_2 flooding. The displacement speed was faster in the vertical direction and slower in the lateral direction. Therefore, the oil accumulated at the top of the reservoir and moved with the CO_2 flooding, forming two oil-phase accumulation zones. Because of the different times of formation, the two oil accumulation areas were not continuous. In the process of oil recovery in the actual site, there would also be a slight oil-phase floating phenomenon because the thickness of the reservoir is thick, so the oil-phase uplift phenomenon would be more obvious.

Figure 10 displays the distribution of oil saturation in the injection–production profiles for different years of production for the layered heterogenous model.

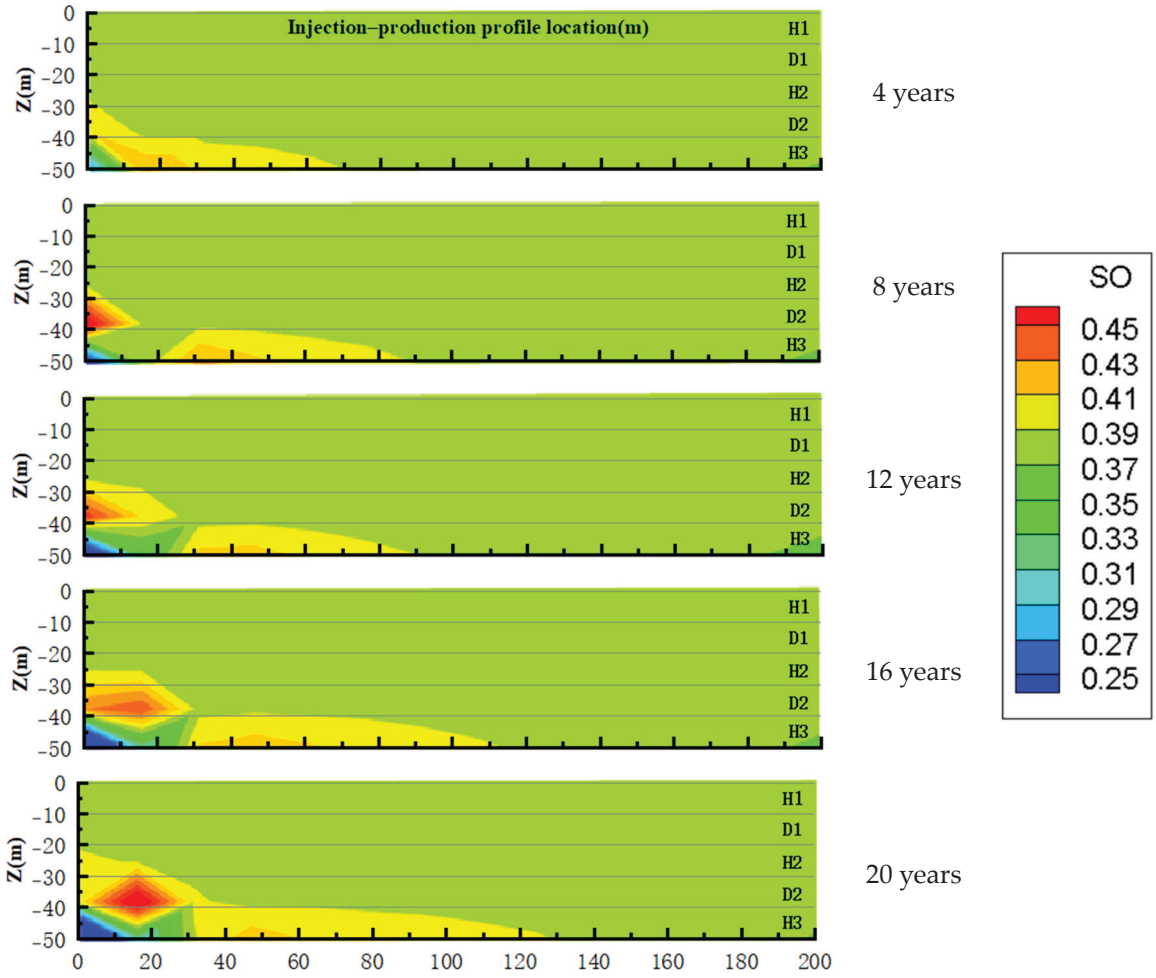

Figure 10. Oil saturation in the injection–production profile of the layered heterogenous model.

Laterally, due to CO_2 injection, the oil phase in the reservoir was gradually transported towards the production well. It could be found that the oil phase in the H3 (specified in Figure 6) reservoir had a very good flooding effect, and in the part near the injection well, the oil saturation was reduced, and the area with high oil saturation had been transported to two-thirds of the injection–production profile. Vertically, due to the existence of the low-permeability reservoir, D2, the CO_2 could not be smoothly transported from the bottom of the reservoir to the top. This caused the CO_2 to recover the oil, which was present in only two layers in the model (layers D2 and H3). The oil-repelling effect of the D2 layer was poor, and a large amount of oil was accumulated in the left side of the D2 layer, and the transportation speed to the production wells was very slow. The difference in the repelling effect caused the difference in the spatial distribution of the oil saturation, and, hence, there was a situation of intermittent, discontinuous oil saturation.

Generally speaking, the oil flooding effect of the layered heterogenous model was more obvious in the lower layer of the reservoir, in which the oil phase was mainly concentrated in the bottom of the reservoir, and only the oil saturation of the D2 and H3 layers changed significantly. The transport of the oil saturation of the layered heterogenous model had the characteristics of oil production by layer, distinguishing the transport of different reservoirs. Comparing the D2 and H3 layers, there was a center of higher oil saturation in both reservoirs, which showed the displacement of the two reservoirs, respectively.

Comparing the reservoir settings of the layered heterogenous model in Section 4.4.3, it can be concluded that the lowest reservoir (H3) was a highly permeable reservoir, while D2 was a low-permeability reservoir, which indicates that the injected CO_2 preferentially flooded off the oil in the reservoir with better permeability.

In addition, there was no oil-phase stratification in the reservoirs of the layered heterogenous model, which may have been due to the low-permeability strata in the layered inhomogeneous strata hindering the vertical transportation of the oil phase.

Figure 11 displays the spatial distribution of oil saturation for the spatially heterogenous model. Temporally, the oil saturation in the part of the reservoir close to the injection wells decreased continuously with the CO_2 injection. The oil saturation in the injection wells was about 0.25 after 4 years of simulation, and most of the areas with a saturation of 0.15 or less were already present after 12 years. The oil saturation in the areas with good reservoir permeability gradually increased with the CO_2 injection. After 4 years, the oil saturation in the areas with good permeability was about 0.5, whereas after 20 years, the oil saturation in these areas had already reached 0.75, with an increase in the number and extent of these areas.

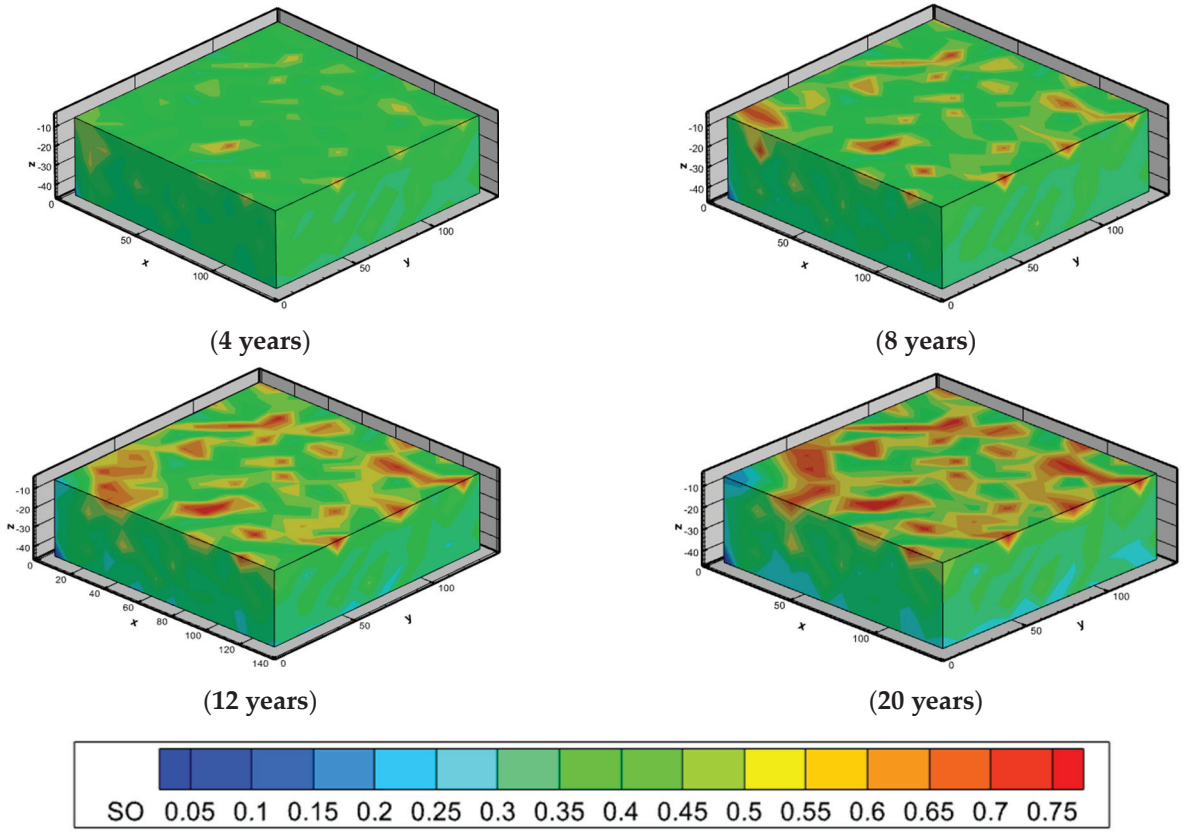

Figure 11. Oil saturation for spatially heterogenous modeling of spatial distribution.

Spatially, the areas with higher oil saturation tended to be transported to the production wells, and the reservoir also showed the phenomenon of oil-phase uplift.

To further understand the effect of the spatial non-uniform distribution of permeability and porosity on the distribution of the remaining oil phase, the spatially heterogenous model's oil saturation injection–production profile distribution is plotted in Figure 12.

Comparing Figures 6 and 7, it can be found that the high-oil-saturation area of the reservoir corresponded to the area with high permeability and high porosity, which indicates that the spatially heterogenous model of the displacement contained the two characteristics of the homogeneous model and the heterogenous model of the displacement. Unlike the stratified heterogenous model, due to the uneven distribution of permeability and porosity in the reservoir, the oil phase in the reservoir could only be connected to the adjacent high-permeability reservoir to realize the transportation, and because of the uplift of the oil phase similar to that of the homogeneous model, these uplifted oil phases, flooded by CO_2, would gather at the top of the reservoir to choose the area with better permeability and move to the production wells.

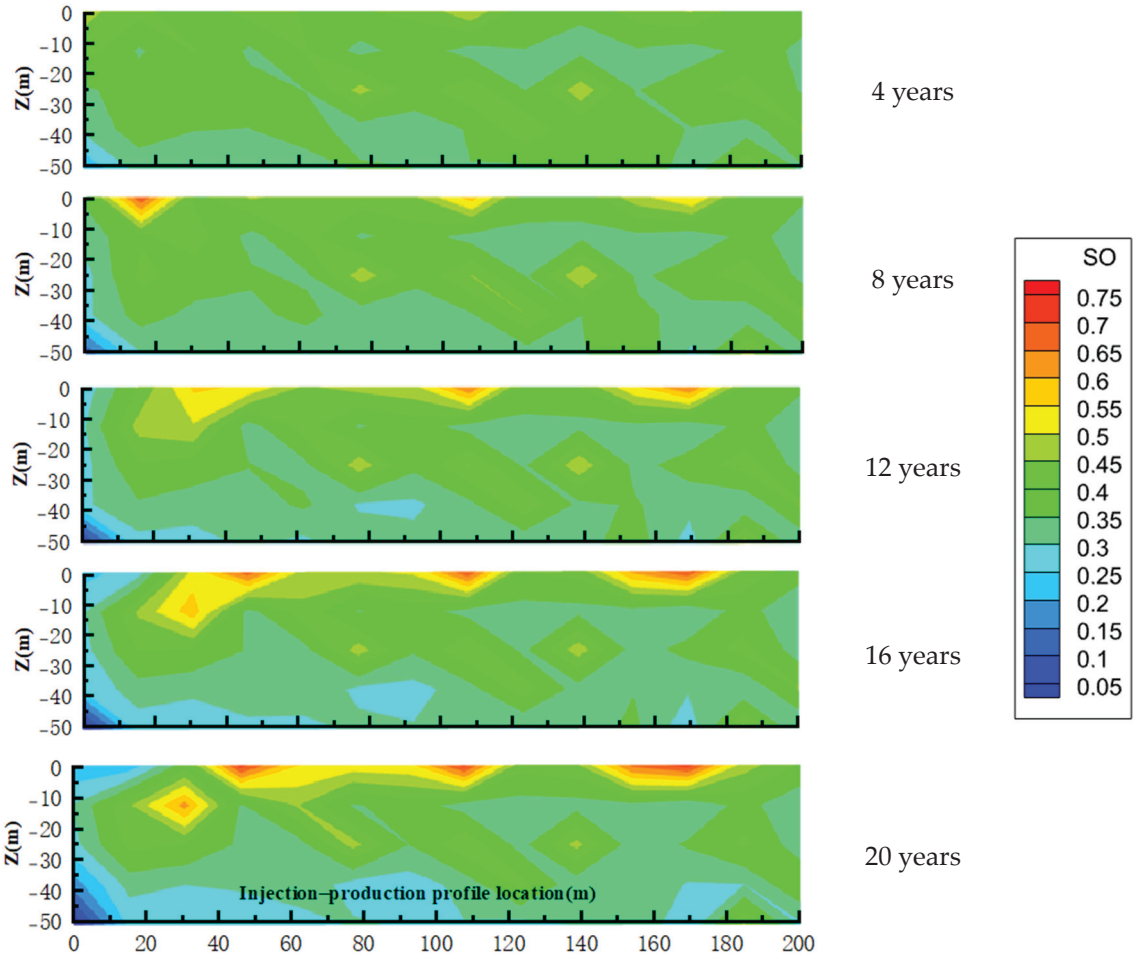

Figure 12. Oil saturation in the injection–production profile of the spatially heterogenous model.

5.2. Influence of Heterogeneity on CO_2 Distribution in Reservoirs

The oil production of the reservoir can be better analyzed by examining the transport of CO_2 in the reservoir. In this section, the CO_2 gas saturation distribution maps of the reservoir are explored for comparative analysis. The gas saturation injection and production profile distribution maps of the three different reservoirs (homogeneous, layered heterogenous, and spatially heterogenous) in different years are plotted in Figure 13. As observed in Figure 13, the injected CO_2 is all concentrated in one-third of the reservoir's injection-well side.

Based on Figure 13 a, the CO_2 was injected from the bottom of the reservoir, was gradually transported upward, and finally (after 20 years) began to diffuse at the top of the reservoir.

Observing the gas saturation distribution of the injection–production profile of the layered heterogenous model (Figure 13 b), after CO_2 injection, the CO_2 did not move to the upper part of the reservoir as it did in the homogeneous model but moved along the bottom of the reservoir towards the production wells. This was due to the fact that the bottom part of the reservoir was highly permeable with high porosity, while the lower permeability of the reservoir in the middle part restricted the upward CO_2 movement. This, in turn, made the majority of CO_2 enter the high-permeability part of the reservoir at the bottom, and, thus, the oil-phase replacement of the reservoir mainly occurred in the lower part of the reservoir.

Figure 13c displays the gas saturation along the injection–production profile for the spatially heterogenous model, which indicates that the gas saturation distribution of the spatially heterogenous model was similar to that of the homogeneous model. The CO_2 was

injected from the bottom of the reservoir and gradually transported upward and finally started to diffuse at the top of the reservoir. This could be attributed to the fact that the spatially heterogenous model, because of the random porosity–permeability condition, did not form a relatively closed low-permeability capping layer like that of the layered heterogenous model. This, in turn, allowed the upward transport of the injected CO_2 in the reservoir.

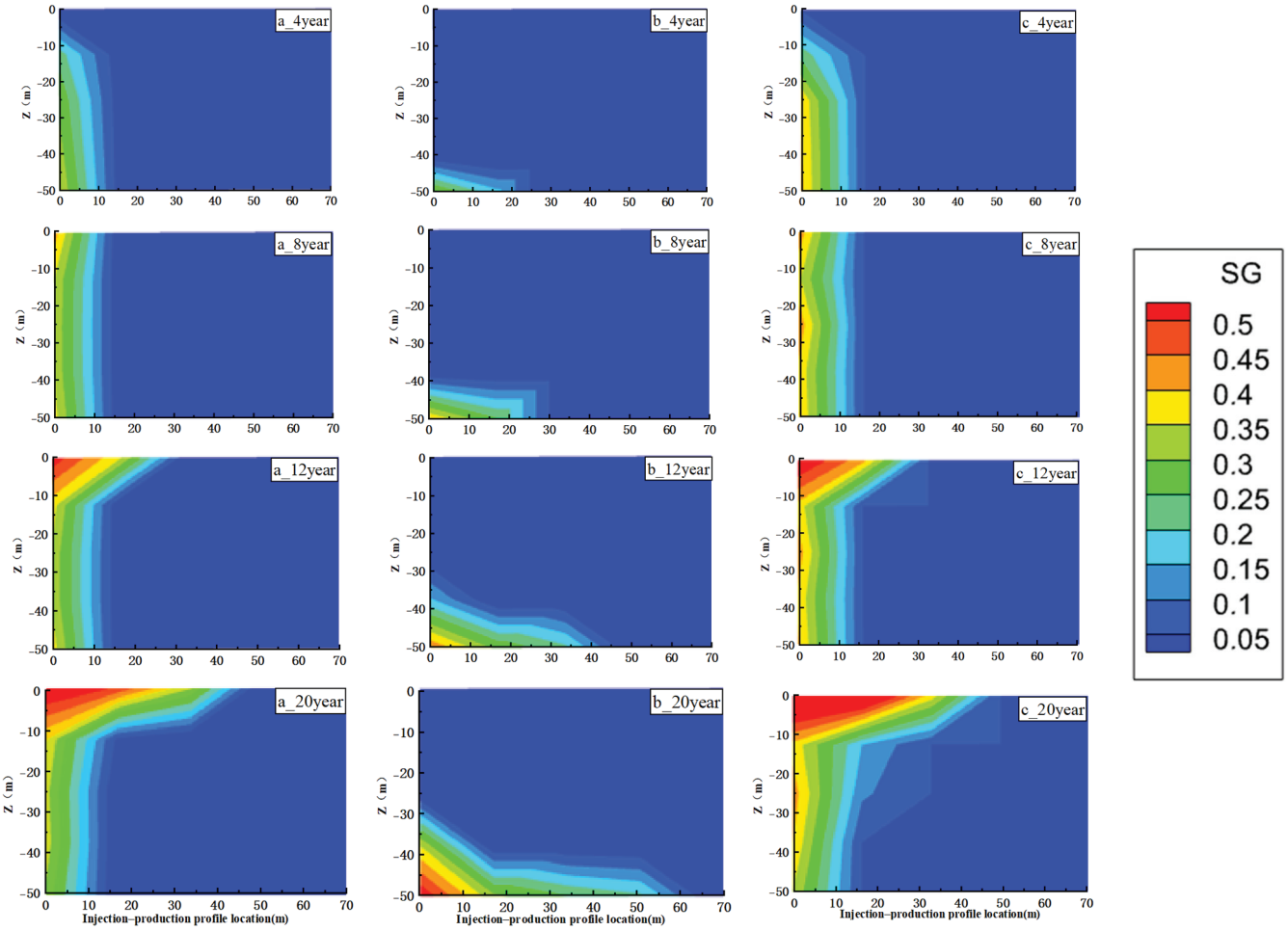

Figure 13. Distribution of gas saturation along injection–production profiles (on injection-well side): (**a**) homogeneous model; (**b**) layered heterogenous model; (**c**) spatially heterogenous model.

The difference between the gas saturation distribution maps of the spatially heterogenous model and the homogeneous model is that the CO_2 in the homogeneous model was uniformly diffused upward while the upward diffusion of the CO_2 in the spatially heterogenous model was uneven, as can be observed from Figure 13. The areas with high gas saturation close to the side of the injected wells were not contiguous but rather were in the form of a jagged distribution. Moreover, the injected CO_2 in the spatially heterogenous model was transported laterally in addition to the upward transport (Figure 13 c_20 years). According to Figure 7, these regions had higher permeability, which indicates that the injected CO_2 would preferentially diffuse into regions with higher permeability in the process of CO_2-EOR.

5.3. Influence of Heterogeneity on Cumulative Oil Production

Figure 14 presents the cumulative water, CO_2, and oil production from different years of the simulation. The cumulative production of the CO_2 from the production well after 20 years of simulation in the homogeneous model was 8.11×10^2 kg, while the cumulative water production was 2.46×10^6 kg, and the cumulative output of the oil phase

was 1.51 × 10^4 kg. After continuous injection, the quantity of the water phase from the production well was much higher than that of the CO_2 and oil phases, which was probably due to the fact that the initial water content was high, and during the CO_2 injection, these water phases were flooded out of the reservoir along with the oil phase. The CO_2 had the lowest production amount, which may have been due to the fact that the injected CO_2 had not yet been transported to the production well and all the CO_2 output at this stage was the CO_2 initially contained within the reservoir.

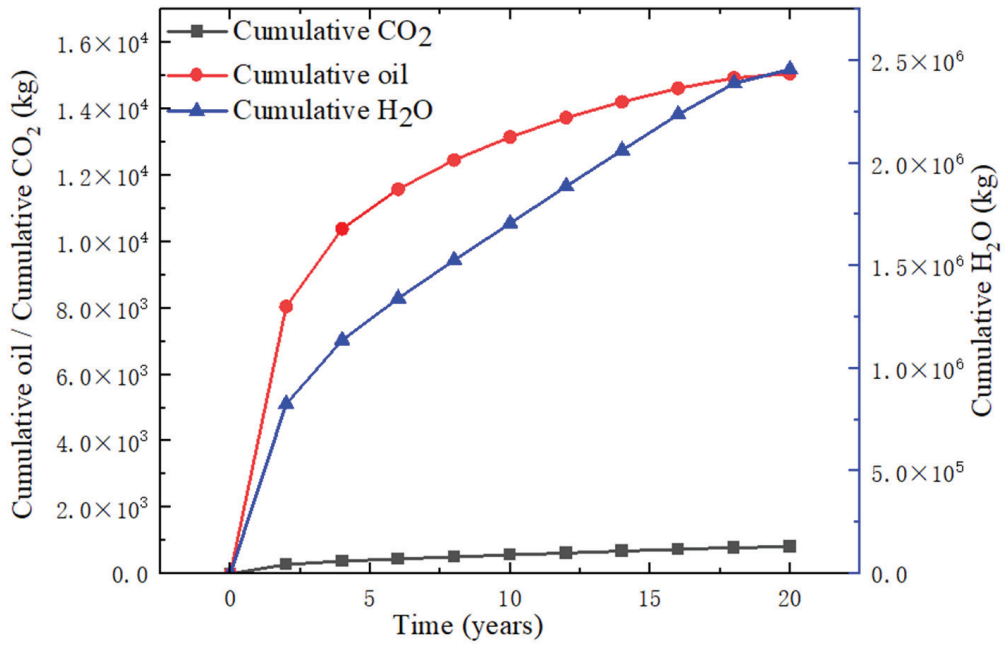

Figure 14. The cumulative amount of each phase in the production well for the homogeneous model.

In addition, with the injection of CO_2, the rate of oil production gradually decreased and the amount of oil production gradually tended to stabilize.

The cumulative production of the CO_2 phase after 20 years from the production well in the layered heterogenous model was 9.57 × 10^2 kg, the cumulative output of the water was 2.66 × 10^6 kg, and the cumulative output of the oil was 8.46 × 10^4 kg. The cumulative productions at different years of the simulation are plotted in Figure 15.

With the injection of CO_2, the output efficiency of the water and oil phases of the reservoir was high in the beginning (after 2 years of production). However, the subsequent output efficiency decreased and remained low. The CO_2 output efficiency of the reservoir did not change significantly with time, which indicates that the injected CO_2 had not yet reached the output well, and gas flushing did not occur.

Compared to the homogeneous model, the layered heterogenous model was more effective in flooding oil as more oil was produced after 20 years of production.

The cumulative output of the CO_2 from the production well for the spatially heterogenous model after 20 years was 8.11 × 10^2 kg, the cumulative output of the water phase was 2.45 × 10^6 kg, and the cumulative output of the oil phase was 1.42 × 10^4 kg. The cumulative production of these phases at different years are plotted in Figure 16.

The production volumes of each phase of the spatially heterogenous model were basically very close to those of the homogeneous model. However, the output volume of the oil phase was slightly smaller than that of the homogeneous model. This was due to the existence of some randomly distributed low-permeability areas in the reservoir, which could affect the oil flooding effect of the CO_2 if they were distributed along the injection–production profile.

The cumulative production data from the three cases are summarized in Table 5.

Table 5. Comparison of cumulative production from different cases.

Case / Output (kg)	Injection	Production		
	All Three Models Are The Same	Homogeneous	Layered Heterogeneity	Spatial Heterogeneity
CO_2	9.856×10^5	8.11×10^2	9.57×10^2	8.11×10^2
Water	0	2.46×10^6	2.66×10^6	2.45×10^6
Oil	0	1.51×10^4	8.46×10^4	1.42×10^4

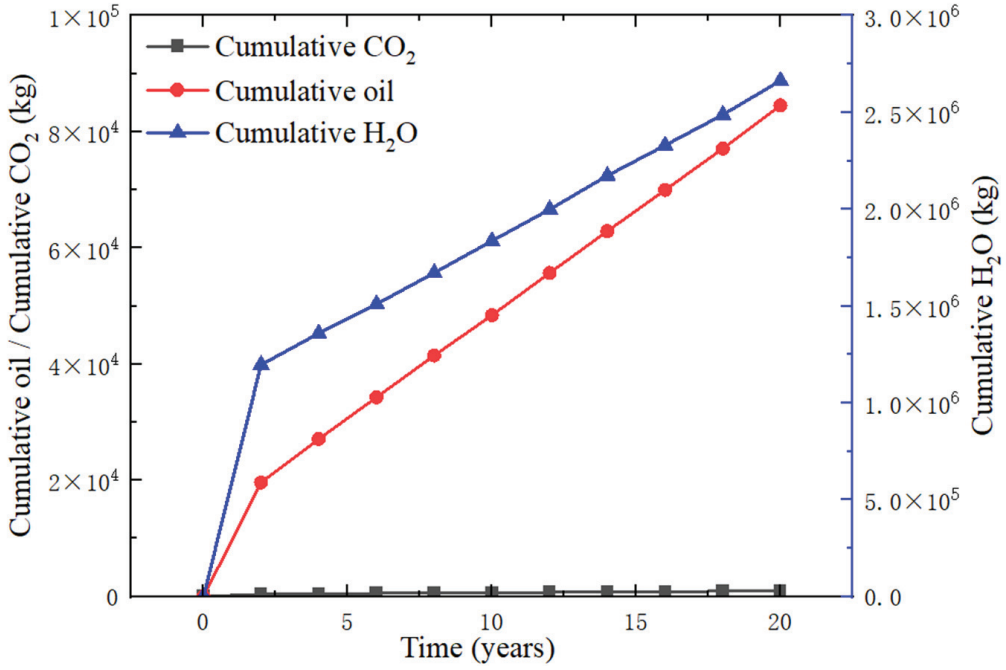

Figure 15. The cumulative amount of each phase in the production well for the layered heterogenous model.

Based on Table 5, it can be concluded that with the same amount of injected CO_2, the layered heterogenous model had the best oil displacement effect, with its oil displacement amount reaching 8.46×10^4 kg, while the homogeneous model and the spatially heterogenous model had lower values.

The year-by-year change in the oil recovery volume of different cases is plotted in Figure 17, which shows that with the injection of the gas phase, the cumulative oil phase output from each case continued to accumulate, among which the cumulative oil recovery volume of the layered heterogenous model was the largest, the cumulative oil recovery volume of the homogeneous model was the second largest, and the cumulative oil recovery volume of the spatially heterogenous model was the smallest.

The largest cumulative oil removal in the layered heterogenous model may have been due to the existence of a continuous hypertonic reservoir connecting the injection wells and the output wells in this model, where CO_2 could replace the oil phase more easily. Meanwhile, the homogeneous model and the spatially heterogenous model did not have such a connecting reservoir. The spatially heterogenous model may have had a low-permeability region in the reservoir, which may have made it difficult to transport CO_2 in the reservoir, thus affecting the oil removal efficiency of the reservoir, resulting in less oil removal in the spatially heterogenous model than in the homogeneous model.

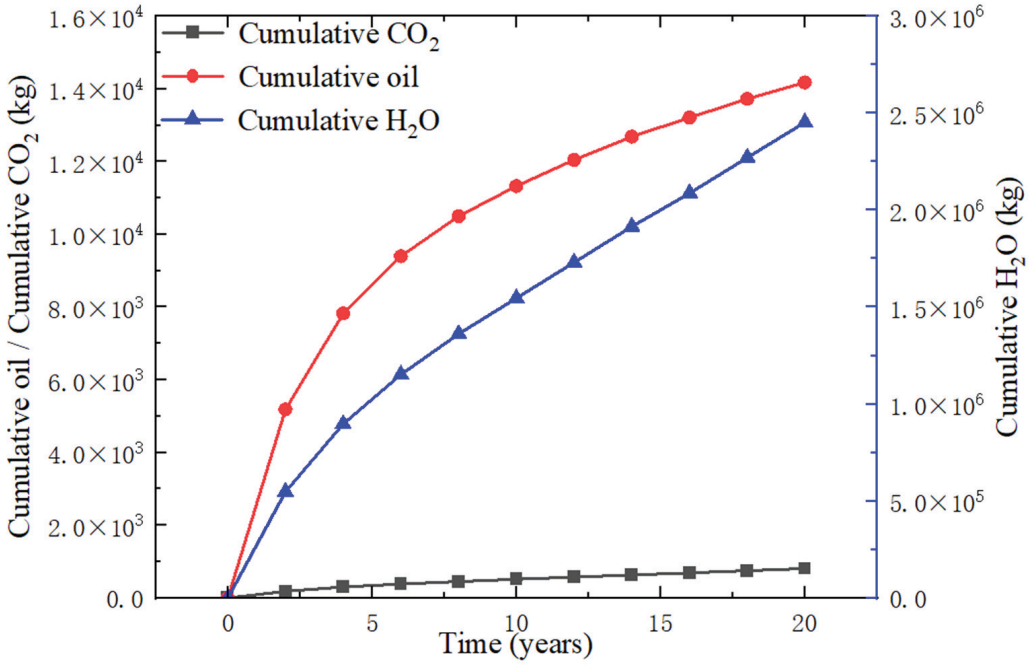

Figure 16. The cumulative amount of each phase in the production well for the spatially heterogenous model.

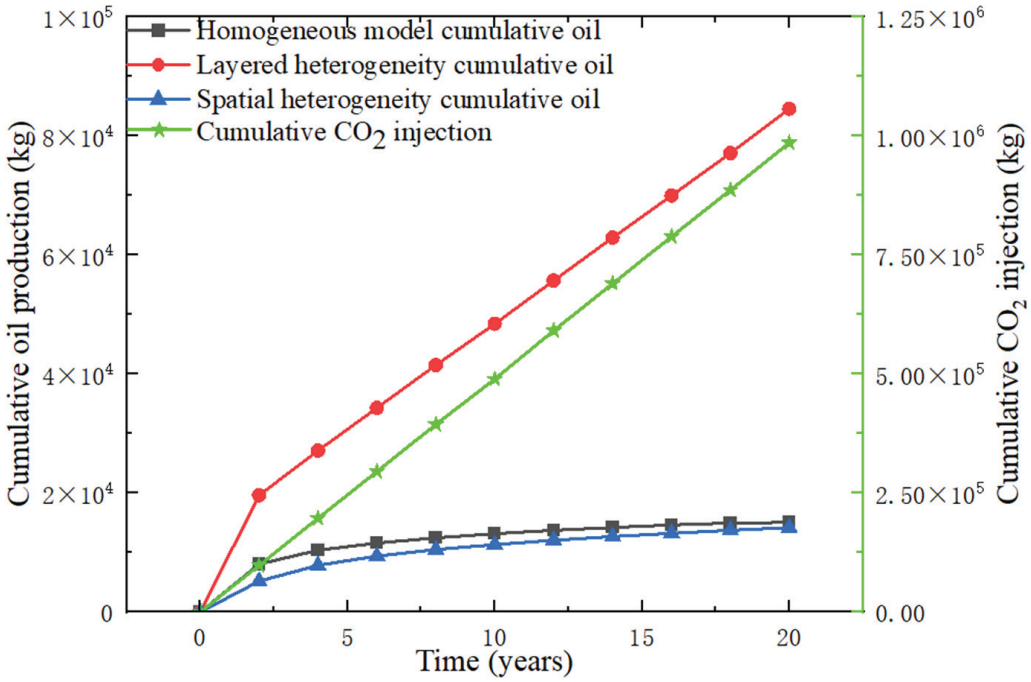

Figure 17. CO_2 injection volume and oil repelling volume of different cases.

6. Conclusions

In this work, three CO_2-EOR cases of oil reservoirs' conditions of permeability were set up. After the end of the flooding off, the distribution of the remaining oil phases as well as the distribution of the CO_2 in the reservoirs were analyzed to understand the characteristics of CO_2 flooding in different reservoir conditions. By changing only one property in each simulation case, and comparing the amount of oil production, the case with the best oil production effect was determined. The following conclusions can be made from this study:

(1) It can be concluded that, under the same injection volume condition, the cumulative oil flooding effect of the layered heterogenous model was the best, the cumulative oil flooding amount of the homogeneous model was the second best, and the spatially heterogenous model had the worst oil flooding effect.
(2) In different cases, high oil saturation centers would appear in the process of CO_2 flooding. They were generally formed near the injection wells and in the areas with good permeability. The centers of high oil saturation were formed for different reasons. With the injection of CO_2, these centers would gradually move to the production wells, and the location and movement of the high oil saturation corresponded to the modeled oil flooding effect.
(3) In the process of CO_2 flooding, if the porosity–permeability conditions of the reservoir were consistent, the oil phase had a tendency to float upward, which would cause the oil phase in the reservoir to float on the top of the reservoir, and then the oil at the top of the reservoir would be flooded off preferentially.
(4) In the process of CO_2 flooding, when the porosity and permeability of the reservoirs varied spatially, the flooding effect of the CO_2 in the highly permeable reservoirs was better than that in the low-permeability reservoirs. The transport of oil in the layered heterogenous model appeared to have different behaviors between layers. In the spatial heterogenous model, the oil phase flooded by the CO_2 gathered at the top of the reservoir and moved to the production wells through the zones with higher permeabilities.

Author Contributions: Conceptualization—Formal analysis and Software, Z.L. and H.T.; Data curation—Investigation and Methodology, Z.L. and R.P.; Funding acquisition—Project administration and Resources, T.X.; Validation—Visualization and Writing—Original draft, Z.L.; Supervision, T.X.; Writing—Review and editing, H.T. and T.X. All authors have read and agreed to the published version of the manuscript.

Funding: This work was performed in support of the National Natural Science Foundation of China (Grant No. 42141013) and Jilin Province Science and Technology Department Development Plan Project (Grant No. YDZJ202401330ZYTS).

Data Availability Statement: The data that support the findings of this study are available on request from the corresponding author.

Acknowledgments: The authors would like to thank the Key Laboratory of Groundwater Re-sources and Environment, Ministry of Education, Jilin University, for financial support and facilities, the National Natural Science Foundation of China for financial support, and the Oil and Gas Engineering Research Institute, CNPC Jilin Oilfield Company, for supplying field data.

Conflicts of Interest: Author Ruosheng Pan was employed by the CNPC Jilin Oilfield Company. The remaining authors declare that the research was conducted in the absence of any commercial or financial relationships that could be construed as a potential conflict of interest.

References

1. Li, Q.; Li, Q.; Li, Q.; Li, Q.; Wang, Y. The Carrying Behavior of Water-Based Fracturing Fluid in Shale Reservoir Fractures and Molecular Dynamics of Sand-Carrying Mechanism. *Processes* **2024**, *12*, 2051. [CrossRef]
2. Yu, H.; Fu, W.; Zhang, Y.; Lu, X.; Cheng, S.; Xie, Q.; Qu, X.; Yang, W.; Lu, J. Experimental study on EOR performance of CO_2-based flooding methods on tight oil. *Fuel* **2021**, *290*, 119988. [CrossRef]
3. Rajkumar, P.; Pranesh, V.; Kesavakumar, R. Influence of CO_2 retention mechanism storage in Alberta tight oil and gas reservoirs at Western Canadian Sedimentary Basin, Canada: Hysteresis modeling and appraisal. *J. Pet. Explor. Prod. Technol.* **2021**, *11*, 327–345. [CrossRef]
4. Song, X.; Wang, F.; Ma, D.; Gao, M. Progress and outlook of CO_2 capture, oil drive and burial technology for petroleum in China. *Pet. Ex-Ploration Dev.* **2023**, *50*, 206–218.
5. Hu, Y.; Hao, M.; Chen, G.; Sun, R. Technology and practice of CO_2 oil drive and burial in China. *Pet. Explor. Dev.* **2019**, *46*, 716–727.
6. Ji, B.; Wang, Y.; Nie, J.; Zhang, L. Research progress and application of enhanced recovery technology in Sinopec. *Oil Gas. Geol.* **2016**, *37*, 572–576.

7. Yuan, S.; Wang, Q.; Li, J.; Han, H. Technology progress and prospects of enhanced oil recovery by gas injection. *Acta Pet. Sin.* **2020**, *41*, 1623–1632.
8. Jia, J. *Numerical Simulation of CO_2 Miscible Flooding in Heterogeneous and Anisotropic Porous Media*; Dalian University of Technology: Dalian, China, 2022. [CrossRef]
9. Hopkinson, J.L.; Natanson, S.G.; Temple, A.P. Effects of Reservoir Heterogeneity on Performance. In Proceedings of the Society of Petroleum Engineers—Fall Meeting of the Society of Petroleum Engineers of AIME, Denver, CO, USA, 2–5 October 1960.
10. Weber, K.J. How heterogeneity affects oil recovery. *Reserv. Charact.* **1986**, 487–544.
11. Khataniar, S.; Peters, E.J. The effect of reservoir heterogeneity on the performance of unstable displacements. *J. Pet. Sci. Eng.* **1992**, *7*, 263–281. [CrossRef]
12. Yang, S.C. A new method for quantitatively studying reservoir heterogeneity. *J. Univ. Pet. China* **2000**, *24*, 53–56.
13. Wang, G.; Yang, S.C.; Liao, F. Reservoir Heterogeneity and Remaining Oil Distribution of Debouch Bar Reservoir. *Fault -Block Oil Gas. Field* **2006**, *13*, 18–19.
14. Shedid, S. Influences of different modes of reservoir heterogeneity on performance and oil recovery of carbon dioxide miscible flooding. *J. Can. Pet. Technol.* **2009**, *48*, 29–36. [CrossRef]
15. Guo, K.; Zeng, J.; Lu, X.; Cui, Z.; Shi, Y. An Experimental Study of Oil Migration Controlled by Vertical Conduction of Faults and Reservoir Heterogeneity. *Geoscience* **2010**, *24*, 1164–1170.
16. Wang, J.; Xie, J.; Lu, H. CO_2 miscible flooding influence degree analysis of reservoir heterogeneity in low permeability reservoir. *Int. J. Oil Gas Coal Technol.* **2016**, *13*, 142–158. [CrossRef]
17. Hadipoor, M.; Taghavi, H.; Taghavi, H. Experimental investigation of CO_2 injection performance in heterogeneous reservoirs: Parametric analysis. *Pet. Sci. Technol.* **2020**, *38*, 837–848. [CrossRef]
18. Wang, C. Investigation on the Influence of Reservoir Heterogeneity on CO_2 Flooding. Master's Thesis, China University of Petroleum, Beijing, China, 2019.
19. Dong, Y.; Li, J.; Wu, X.; Mei, Y. Study on Effect of Reservoir Heterogeneity on CO_2 Flooding. *Contemp. Chem. Ind.* **2016**, *45*, 2370–2373.
20. Liao, H.; Lv, C.; Zhao, S.; Chen, Y.; He, Y.; Zhou, Y.; Wang, Q. Numerical simulation to study the influence factors of CO_2 drive in low-permeability reservoirs. *Xinjiang Pe-Troleum Geol.* **2011**, *32*, 520–522.
21. Zhang, L.; Kuang, X.; Li, J. Numerical simulation of CO_2 gas drive in inhomogeneous reservoir. *China New Technol. Prod.* **2010**, 6.
22. Zhang, M. Numerical simulation of CO_2 drive influencing factors in low-permeability oilfield of Fang 48 block. *J. Daqing Pet. Inst.* **2011**, *35*, 64–67+118.
23. Zhao, M.; Chen, X.; Jia, H.; Yang, H. Study on the effect of carbon dioxide oil repulsion in Fang 48 inhomogeneous fault block reservoir. *Spec. Oil Gas. Reserv.* **2014**, *21*, 119–122+157.
24. Liu, J. A quantitative study to investigate the effect of reservoir inhomogeneity on CO_2 oil-driving efficiency in medium- and high-permeability extra-high water-bearing reservoirs. *China Chem. Trade* **2017**, *9*, 203.
25. Kang, W.-L.; Zhou, B.-B.; Issakhov, M.; Gabdullin, M. Advances in enhanced oil recovery technologies for low permeability reservoirs. *Pet. Sci.* **2022**, *19*, 1622–1640. [CrossRef]
26. Jia, K.; Cui, C.; Wu, Z.; Yan, D. Influences of Reservoir Heterogeneity on Gas Channeling During CO_2 Flooding in Low Permeability Reservoirs. *Xinjiang Pet. Geol.* **2019**, *40*, 208–212.
27. Zhang, S.; Shi, L.; Kang, K.; Wang, W.; Wang, X. Influence law of heterogeneity on CO_2 driven gas flushing in low/extra-low permeability reservoirs and ex-perimental study of plugging. *Deilling Prod. Technol.* **2018**, *41*, 69–72.
28. Liu, B.; Liu, Y. Evaluation of carbon dioxide flooding effect based on reservoir heterogeneity. *Chem. Eng.* **2017**, *31*, 40–42+33.
29. Zhang, L.; Li, X.; Ren, B.; Cui, G.; Zhang, Y.; Ren, S.; Chen, G.; Zhang, H. CO_2 storage potential and trapping mechanisms in the H-59 block of Jilin oilfield China. *Int. J. Greenh. Gas. Control* **2016**, *49*, 267–280. [CrossRef]
30. Ren, B.; Ren, S.; Zhang, L.; Chen, G.; Zhang, H. Monitoring on CO_2 migration in a tight oil reservoir during CCS-EOR in Jilin Oilfield China. *Energy* **2016**, *98*, 108–121. [CrossRef]
31. Liu, Q. Research on Optimization Technology of Lithological Reservoir Enrichment in Daqingzijing Oilfield. Master's Thesis, Northeast Petroleum University, Daqing, China, 2015.
32. Li, Y. Philosophy of Daqingzijing Oilfield Development in Jilin. *Unconventonal Oil Gas.* **2016**, *3*, 88–92.
33. Sun, R.; Ma, X.; Wang, S. Process technology of CO_2 drive surface engineering in Jilin oilfield. *Pet. Plan. Des.* **2013**, *24*, 1–6+31+48.
34. Abou-Kassem, J.H.; Farouq-Ali, S.M.; Islam, M.R. *Petroleum Reservoir Simulations*; Elsevier: Amsterdam, The Netherlands, 2013.
35. Li, Y.; Xu, T.; Xin, X.; Yang, B.; Xia, Y.; Zang, Y.; Yuan, Y.; Zhu, H. Pore-scale study of the dynamic evolution of multi-phase seepage parameters during hydrate dissociation in clayey silt hydrate-bearing sediments. *J. Hydrol.* **2024**, *635*, 131178. [CrossRef]
36. Steffen, M. A simple method for monotonic interpolation in one dimension. *Astron. Astrophys.* **1990**, *239*, 443.
37. Pan, L.; Oldenburg, C.M. *TOGA: A Tough Code for Modeling Three-Phase, Multi-Component, and Non-Isothermal Processes Involved in CO_2-Based Enhanced Oil Recovery*; Lawrence Berkeley National Lab: Berkeley, CA, USA, 2016.
38. Lei, H. Deposition Mechanisms and Reservoir Protection Countermeasures of a Low-Permeability Formation in CO_2 Flooding Process. Ph.D. Thesis, China University of Petroleum, Beijing, China, 2017.
39. Shi, H.; Bai, Y.; Dong, W. Feedstock Components into a Virtual Method. *Guangzhou Chem. Ind.* **2009**, *37*, 114–117.
40. Hu, T. *Study on the Process Model of CO_2 Migration and Phase Transformation in Enhanced Oil Recovery System*; Jilin University: Jilin, China, 2022. [CrossRef]

41. Tian, H.; Pan, F.; Xu, T.; McPherson, B.J.; Yue, G.; Mandalaparty, P. Impacts of hydrological heterogeneities on caprock mineral alteration and containment of CO_2 in geological storage sites. *Int. J. Greenh. Gas. Control* **2014**, *24*, 30–42. [CrossRef]
42. Vanmarcke, E.; Grigoriu, M. Stochastic finite element analysis of simple beams. *J. Eng. Mech.* **1983**, *109*, 1203–1214. [CrossRef]

energies

MDPI

Article

Numerical Simulation on Pore Size Multiphase Flow Law Based on Phase Field Method

Tianjiang Wu [1,2], Changhao Yan [1,2], Ruiqi Gong [2,3], Yanhong Zhao [2,3], Xiaoyu Jiang [4] and Liu Yang [4,*]

[1] Oil and Gas Technology Research Institute of Changqing Oilfield, China National Petroleum Corporation, Xi'an 710018, China
[2] National Engineering Laboratory for Exploration and Development of Low-Permeable Oil and Gas Fields, Xi'an 710018, China
[3] Xi'an Changqing Chemical Group Industry Co., Ltd. of Changqing Oilfield, China National Petroleum Corporation, Xi'an 710018, China
[4] School of Chemical and Environmental Engineering, China University of Mining and Technology-Beijing, Beijing 100083, China
* Correspondence: shidayangliu@cumtb.edu.cn

Abstract: The characteristics of CO_2 seepage in reservoirs have important research significance in the field of CCS technology application. However, the characteristics of macro-scale seepage are affected by the geometrical characteristics of micro-scale media, such as pore size and particle shape. Therefore, in this work, a series of numerical simulations were carried out using the phase field method to study the effect of pore structure simplification on micro-scale displacement process. The influences of capillary number, wettability, viscosity ratio, interfacial tension, and fracture development are discussed. The results show that the overall displacement patterns of the real pore model and the simplified particle model are almost similar, but the oil trapping mechanisms were totally different. There are differences in flow pattern, number of dominant flow channels, sensitivity to influencing factors and final recovery efficiency. The real pore model shows higher displacement efficiency. The decrease in oil wet strength of rock will change the CO_2 displacement mode from pointing to piston displacement. At the same time, the frequency of breakage will be reduced, thus improving the continuity of CO_2. When both pores and fractures are developed in the porous media, CO_2 preferentially diffuses along the fractures and has an obvious front and finger phenomenon. When CO_2 diffuses, it converges from the pore medium to the fracture and diverges from the fracture to the pore medium. The shape of fracture development in the dual medium will largely determine the CO_2 diffusion pattern.

Keywords: phase field method; simplification of pore structure; CO_2 displacement; wettability; fractures

1. Introduction

The technology of CO_2 displacement to enhance oil recovery can effectively achieve oil increase and emission reduction, which is the focus of attention in reservoir development all over the world [1–3]. Transport properties in porous media play an important role in the field of CO_2 geological storage and enhanced oil recovery (EOR) [4–6]. The macroscopic transport characteristics, such as permeability and diffusivity, are greatly affected by the geometrical characteristics (such as pore size and particle shape) of the microcosmic medium [7–9]. The role of geometric features-controlled displacement mechanisms in enhanced recovery has been widely recognized in the oil industry. Therefore, it is imperative

to strengthen the study of the effect of pore geometry and particle size on the CO_2–oil two-phase flow.

There has been a lot of research on the effect of pore geometry on the properties of single- and multiphase transport [10–13]. Ahfir et al. studied the displacement effect of suspensions in porous media at different flow rates and analyzed the influence of different size and distribution of model particles. An increase in the average particle size leads to the accumulation of particles in suspension, thereby lowering recovery [14]. Rad et al. used X-ray tomography to evaluate the effect of particle and pore throat size on the microscopic mechanism of salt precipitation dynamics [15]. Using pore network modeling, Xu et al. analyzed the impact of pore geometry and the distribution of simplified particles on N2 adsorption and desorption isotherms [16]. Lacey et al. conducted polymer displacement experiments using the microfluidic platform to analyze the effects of pore shape and particle size in simplified models on recovery efficiency [17]. Guo et al. evaluated the impact of shape differences in a simplified geometric model of real sandstone on displacement efficiency and the morphology of remaining oil clusters [18]. Man et al. studied the pore geometry influence on capillary pressure. The structural heterogeneity of porous media also has a great influence on the filtration of solid particles [19].

The study of CO_2 displacement in porous media with different structures through physical experiments is often faced with difficult, costly, and time-consuming problems [20–23]. At present, the simulation of pore scale two-phase flow has become more and more diversified. The commonly used simulation methods mainly include VOF, LBM, PF, and MD [24–26]. The phase-field method simulates discontinuous phenomena through continuous variables, which provides strong support for the research and application of materials science. It can efficiently manage complex topological changes through approximate models, while accurately capturing fluid interfaces during microscopic two-phase transitions. Raeini et al. validated the generalized network model on a hole-by-hole basis using microscopic CT images from two-phase flow experiments. This model can simulate two-phase flow in porous media from the pore scale to the core scale [27]. Liu et al. developed a numerical model of complex mixed wettability to simulate oil–water flow, emphasizing that complex wettability behavior arises from the intricate wettability of the pore walls [28]. Guo et al. used the Markov chain Monte Carlo method to reconstruct 3D digital cores. The reconstructed 3D digital core structures are similar to the real structures, although their apertures are smaller than those of the actual pores [29]. Zhu et al. established a two-phase flow model using BFPM and tracked the oil–water interface with the phase-field method. The influence of size parameters was analyzed, and it was concluded that improving wettability significantly enhances oil recovery [30].

In summary, numerous scholars have conducted extensive and effective research on the transport mechanisms in porous media, analyzing the influence of pore geometry and particle size on two-phase flow behavior. However, the impact of crack development within the medium has received less attention. Therefore, the mechanism of CO_2 displacement under the real pore model and the simplified particle model is studied by using the phase field method. The effects of capillary number, wettability, viscosity ratio, surface tension, and fracture development on displacement recovery were analyzed. The research findings are highly significant for guiding the integration of CO_2 displacement and storage in engineering applications.

2. Numerical Modeling

2.1. Phase Field Method

At the core of phase field theory is the idea of using a continuous scalar field, known as the phase field variable, to describe the state of the system. The evolution of the phase field is governed by a set of coupled partial differential equations (PDEs), typically derived

from thermodynamic principles. The CO_2–oil two-phase moving interface was tracked by the coupling of the Navier–Stokes and Cahn–Hilliard equations. Its continuity equation and equation of motion are as follows: Equation (1) is the Navier–Stokes equation, i.e., the momentum conservation equation, which describes the momentum conservation during the flow of viscous incompressible fluid.

① Equation of Motion

$$\rho\frac{\partial \boldsymbol{u}}{\partial t} + \rho(\boldsymbol{u}\cdot\nabla)\boldsymbol{u} = \nabla\cdot[-p\boldsymbol{I}+\kappa] + \boldsymbol{F} \tag{1}$$

$$\boldsymbol{F} = \left(\frac{\lambda}{\varepsilon_{pf}^2}\psi - \frac{\partial f}{\partial \phi}\right)\nabla\phi \tag{2}$$

where ρ represents the fluid density, P represents pressure, $\boldsymbol{F}$ represents the volumetric force on the fluid, ψ is an auxiliary variable of the phase field, and $\boldsymbol{I}$ represents the unit tensor. Equation (1), i.e., the Navier–Stokes equation (momentum conservation equation), describes the momentum conservation during the flow of a viscous incompressible fluid.

② Continuity equation

$$\nabla\cdot\boldsymbol{u} = \boldsymbol{0} \tag{3}$$

where $\boldsymbol{u}$ denotes the fluid velocity field. The practical significance of the continuity equation is that the velocity dispersion is **0**, which controls the conservation of mass during fluid flow while the volume remains constant.

③ Two-phase flow interface control equation

$$\lambda = \frac{3\varepsilon_{pf}\sigma}{\sqrt{8}},\ \gamma = \chi\varepsilon_{pf}^2,\ \psi = psi \tag{4}$$

$$\frac{\partial\phi}{\partial t} + \boldsymbol{u}\cdot\nabla\phi = \nabla\cdot\frac{\gamma\lambda}{\varepsilon_{\mathrm{pf}}^2}\nabla\psi,\ \phi = phipf \tag{5}$$

$$\psi = -\nabla\cdot\varepsilon_{\mathrm{pf}}^2\nabla\phi + \left(\phi^2-1\right)\phi + \frac{\varepsilon_{\mathrm{pf}}^2}{\lambda}\partial f/\partial\phi \tag{6}$$

Equations (4)–(6) are the phase field interface control equations, where γ represents surface energy density, λ represents mixing energy density, σ represents two-phase interfacial tension and the two-phase fluid interfacial tension is equal to the integral of the free energy density at the interface, i.e., $\sigma = 2\sqrt{2}\lambda$, and χ is the phase field mobility tuning parameter.

$$V_{f1} = \frac{1-\phi}{2} \tag{7}$$

$$V_{f2} = \frac{1+\phi}{2} \tag{8}$$

$$V_{f1} + V_{f2} = 1 \tag{9}$$

$$\rho = \rho_1 V_{f1} + \rho_2 V_{f2} \tag{10}$$

$$\mu = \mu_1 V_{f1} + \mu_2 V_{f2} \tag{11}$$

where V_{f1} and V_{f2} represent the two-phase fluid volume fractions, ρ_1 and ρ_2 represent the two-phase fluid density magnitudes, and μ_1 and μ_2 are the two-phase fluid viscosity magnitudes, respectively.

④ Boundary condition control equations

$$\mathbf{n}\cdot\frac{\gamma\lambda}{\varepsilon_{pf}^2}\nabla\psi = 0 \tag{12}$$

$$\mathbf{n} \cdot \varepsilon_{pf}^2 \nabla\phi = \varepsilon_{pf}^2 cos(\theta_w)|\nabla\phi| \tag{13}$$

where **n** represents the normal unit vector, θ_w represents the contact angle, ε_{pf} represents the thickness of the control interface for the phase field parameter, and φ is the capillary width corresponding to the thickness of the dispersive interface between the two phases.

2.2. Geometry and Mesh

The geometric size of the model is 20 mm × 15 mm. In order to evaluate the influence of grain size and shape on the displacement process, two basic geometric models were mainly constructed, as shown in Figure 1. Figure 1a shows the real pore model, and Figure 1b shows the simplified particle model (replacing the solid matrix with round particles at the same location in the real pore region). At the same time, the simplified model is modified based on Matlab, and the simplified model of circular particles with 6 kinds of radius sizes is generated [31]. The number of particles and throat was consistent in both models. The porosity, permeability, and mean geometric properties of the two models are very close, ensuring that the models match in terms of pore number and connectivity. The mesh constructed by the real pore model and the simplified model contains 131,254 and 156,359 triangle elements, 7216 and 8952 boundary elements and 624 and 697 vertex elements, respectively. The locally enlarged mesh is shown in Figure 1. The minimum cell size is 0.00236 mm and 0.00159 mm, respectively, and the average mesh quality is 0.8623 and 0.9312, respectively.

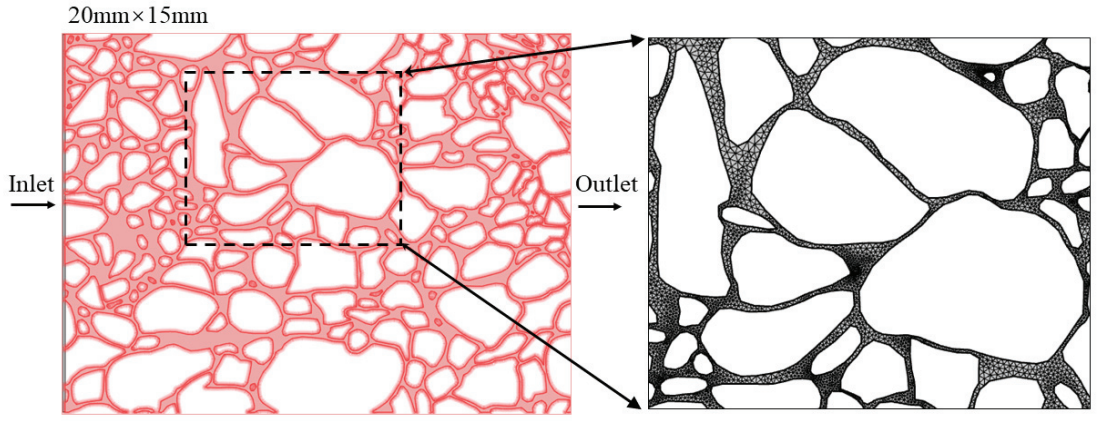

(**a**) real pore model

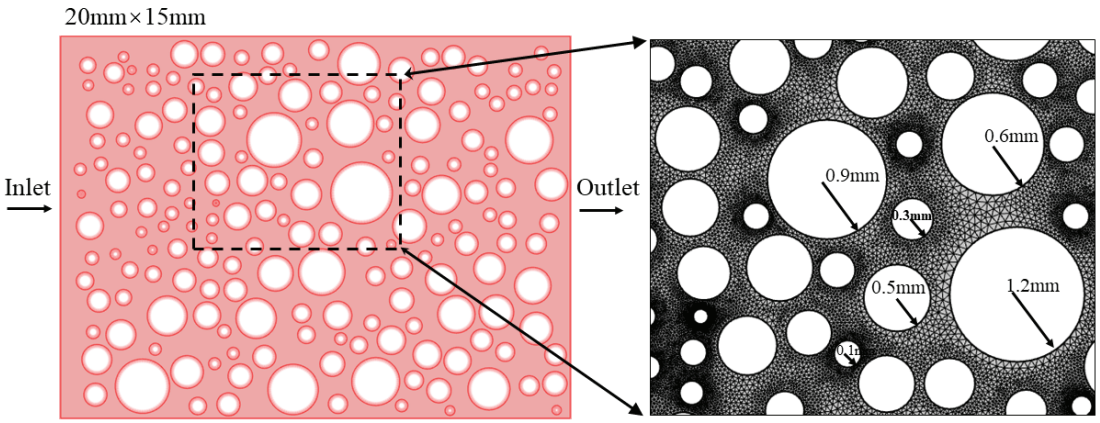

(**b**) simplified particle model

Figure 1. Geometric modeling and meshing.

The SnappyHexMesh tool in OpenFOAM was used to construct a computational mesh with a realistic pore model and a simplified particle model. Ten kinds of grid were constructed, and the dependence of the simulation results on the number of grids was analyzed. An error analysis of CO_2 flooding oil saturation is presented in Figure 2. The selected grid configuration ensures that the simulation errors in saturation and concentration are less than 2% and 3%, respectively.

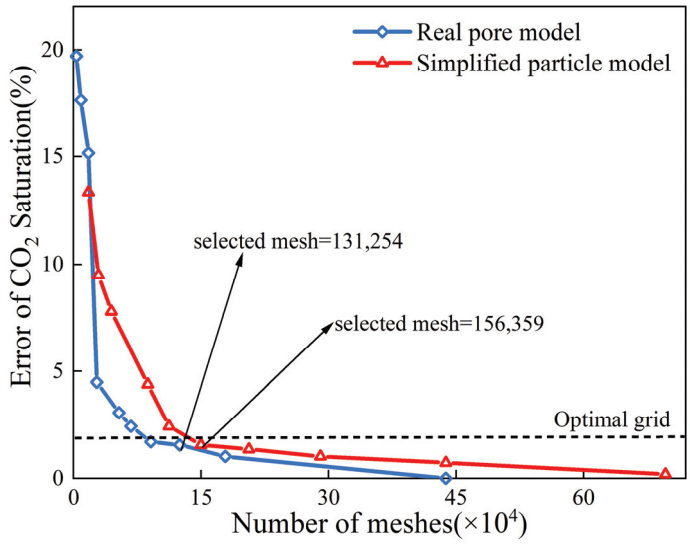

Figure 2. Grid independence verification.

2.3. Boundary Conditions and Simulation Parameters

The time steps sizes were controlled by the numerical solver during the computations, using backward differentiation formulas (BDF). The initial time step sizes (1×10^{-9} s) were small enough to avoid singularity. The interface thickness is set to 1×10^{-14} m and the mobility is set to 2 m·s/kg to ensure stable convective motion. For all simulations, constant velocity inlet boundary conditions are used, which control the continuous injection of CO_2 from the inlet at a constant injection efficiency. The outlet uses a constant pressure boundary condition, set to 0 (i.e., one standard atmosphere), while suppressing reflux. The constant pressure at the outlet boundary is used as a pressure reference and calculate the dynamic pressure change from the pressure difference between the inlet and the outlet. The top and bottom boundaries are set to symmetrical boundary conditions. The pore walls were set to fixed wetting, and different contact angles were set to cover a wide range of wetting conditions. The density of CO_2 and oil was set to 1.816 kg/m^3 and 840 kg/m^3, and the viscosity was 0.5×10^{-4} mPa·s and 7.6×10^{-3} mPa·s, respectively. The interfacial tension (σ) is set to 27 mN/m.

3. Results and Discussions

3.1. The Effect of Different Capillary Number

Figure 3 shows the two-phase distribution of CO_2 clusters and oil when displacement reaches steady state in both the real pore model and the simplified particle model. The capillary number is one of the important factors affecting reservoir development. In order to study the effect of different capillary numbers on the distribution of CO_2 clusters and oil recovery in porous media, the capillary number was increased from 7×10^{-5} to 2.81×10^{-4} by changing the injection velocity of displacement fluid (0.05 m/s, 0.1 m/s, 0.15 m/s, 0.2 m/s). The displacement effects of the two models were compared by analyzing the simulation results under different capillary numbers.

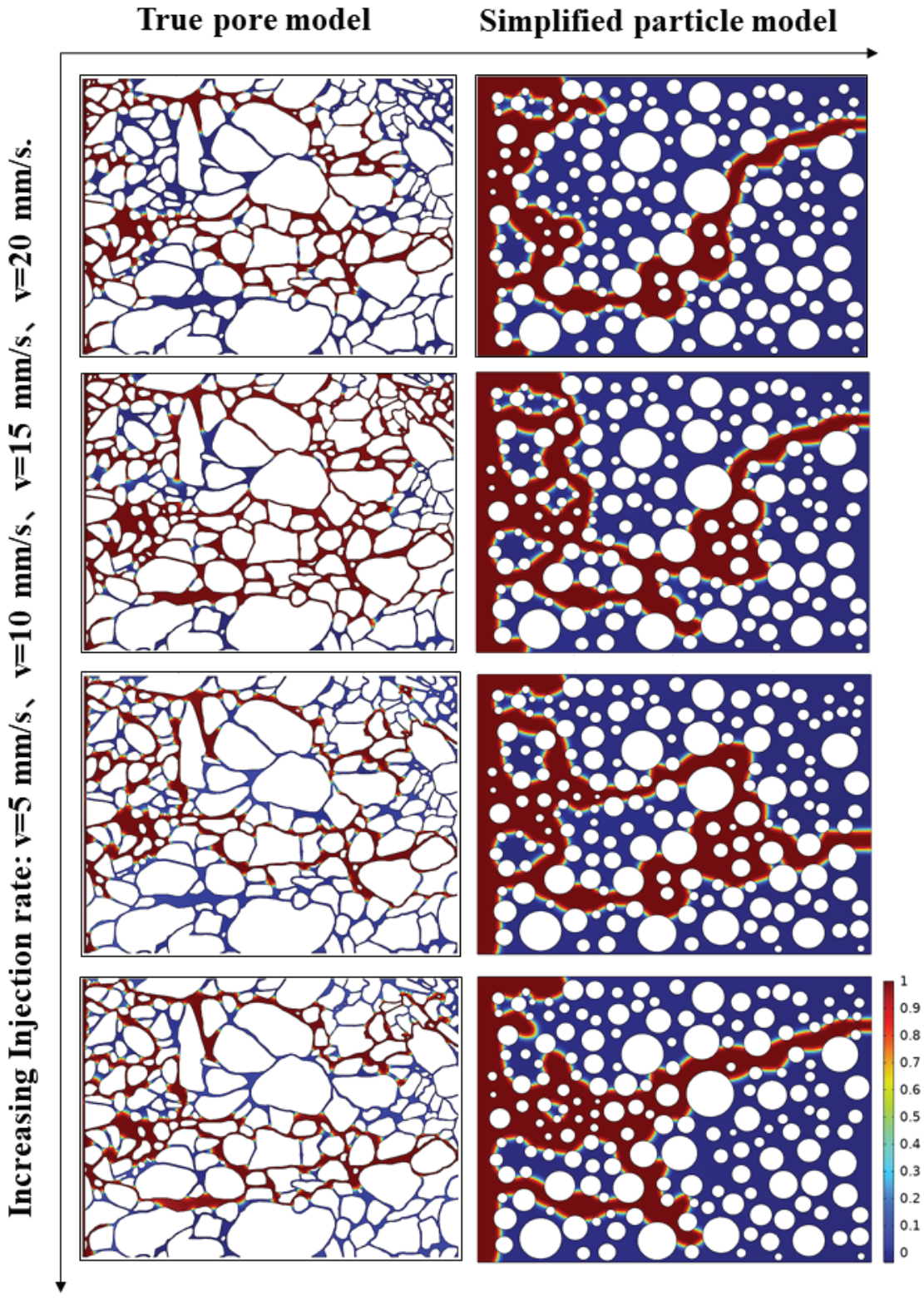

Figure 3. CO_2–oil two-phase distribution at different capillary numbers.

The two-phase fluid distribution was observed when displacement reached steady state. It can be concluded that with the increase in capillary number, the seepage capacity of CO_2 clusters is enhanced, and the degree of oil recovery in pores is increased. In the process of displacement, CO_2 shows obvious capillary fingering, which can enter more narrow pores and throats, thereby enhancing the efficiency of oil utilization within the pores. When the capillary number is smaller, the capillary fingering breakthrough of

CO_2 clusters is more significant. However, it is difficult to sweep some small pores and residual oil in the throat, so the diffusion range is small. It can be seen from the simulation results of the two models that there are the same dominant flow channels, but there are two dominant flow channels in the real pore model, while only one dominant flow channel breaks through in the simplified particle model. This is because the heterogeneity of the simplified model is relatively reduced, and the pore throat size is increased, which ultimately leads to a decrease in the number of dominant flow channels. In general, the CO_2 displacement efficiency in the real pore model is higher. In the simplified particle model, the circular dominant flow channel with matrix wall breaks through faster, the synergistic effect between the flow channels is poor, and the driving force of the lower flow channel is weakened and finally blocked. The overall displacement effect is poor. The larger capillary number increases the sweep range of CO_2 to oil in porous media. This can not only improve oil recovery in pores, but also serve as a way to increase CO_2 storage.

Capillary number is one of the important parameters affecting fluid flow. The influence of capillary number on CO_2 flooding oil recovery was further quantified, as shown in Figure 4. The overall recovery efficiency of the real pore model is higher than that of the simplified particle model, and the average recovery efficiency is 59.3% and 37.89%, respectively. With the increase in capillary number, the overall recovery efficiency showed an increasing trend. In the real pore model, with the increase in capillary number from 7×10^{-5} to 2.81×10^{-4}, the recovery efficiency gradually increases from 48.75% to 82.15%. However, when the capillary number is 1.41×10^{-4}, the recovery efficiency is the highest, up to 82.35%. The value of Ca = 1.41×10^{-4} is likely indicative of the point where the capillary forces are just low enough to prevent significant fluid trapping, while the viscous forces are strong enough to push fluid through the pore network without causing flow instabilities or bypassing. This value represents an optimal regime for efficient recovery, where the displacement front moves uniformly through the pore network. After the two models reached the steady state, the lowest recovery rate was 42.35% and 32.01%, the highest recovery efficiency was 82.15% and 48.75%, and the growth rate was 93.97% and 52.30%, respectively. The recovery efficiency of the two models increased to a certain extent, but the real pore model was more affected by the capillary number and the flow channel distribution was complex, and the growth rate was as high as 93.97%. The average breakthrough time of the real pore model is 0.5 s, and the breakthrough time is faster. The breakthrough time of simplified particle model is greatly affected by capillary number. The breakout time is between 0.21 s and 0.75 s, and the volatility is strong.

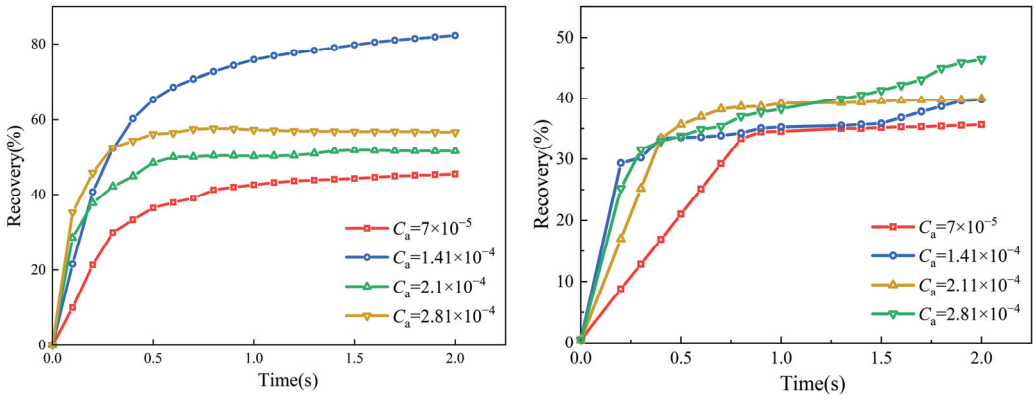

(**a**)True pore model (**b**) Simplified particle model

Figure 4. Recovery curve under different capillary numbers.

3.2. The Effect of Different Wettability

The wettability of porous media affects the distribution of two-phase fluids in the pore structure and determines the connectivity and flow ability of the fluid. In the pore scale two-phase flow simulation, the wettability of porous media is characterized by changing the contact angle between solid wall and displacement fluid. The natural reservoir rocks have uneven contact angles at the pore scale. Therefore, four groups of simulation models of real pores and simplified particles at different contact angles were set up, which were 30°, 60°, 90° and 120°, respectively. To cover a range of reservoir wetting conditions. Angles of 30° and 60° represent weak CO_2 wetting, 90° indicates moderate CO_2 wetting, and 120° corresponds to strong CO_2 wetting. The seepage law of CO_2 flooding under different wettability conditions is revealed.

The two-phase distribution under different wettability conditions was compared (Figure 5). It was observed that wettability strongly affected the size and spread range of CO_2 clusters, and thus affected the displacement efficiency. With the increase in the wetting degree of CO_2, the affinity between CO_2 and rock surface increases, and the affinity between oil phase and rock surface decreases. The capillary force gradually became the driving force of CO_2 diffusion, and the seepage capacity of CO_2 was enhanced. The CO_2 clusters have a larger size during displacement, allowing more CO_2 to enter the pore space to displace the oil. Compared with the simplified particle model, the change in wettability in the real pore model has a more significant effect on the CO_2 flow capacity. With the increase in wettability, the spread range of CO_2 expands significantly in the real pore model. CO_2 tends to form a thin film on the surface of porous media, occupying most of the small pores and corners. Compared with the real pore model, the simplified particle model cannot accurately predict the details of displacement, including the fingering patterns formed and the amount of oil trapped in the medium. In the simplified particle model, the displacement process gradually favors the stable displacement (similar to piston) mode. The capillary finger phenomenon weakens and displaces in the form of forward and lateral moving fronts of the thick front. When $\theta = 120°$, the spread range of CO_2 in the two models is the widest.

The changes of CO_2 displacement recovery under different wettability conditions are shown in Figure 6. By comparing the recovery curve under different wetting angles, it can be seen that the ultimate recovery rate increases to some extent with the increase in wetting angle. The slope of the curve increases with the increase in wettability. In other words, in the stable displacement stage after CO_2 breakthrough, the higher the wettability, the faster the recovery efficiency will increase. This is because the enhanced wettability will make CO_2 better contact with the rock surface, stripping the non-wetting phase of the oil from the rock matrix surface. The inflection point of the curve corresponds to the breaking point of the CO_2 cluster. When the wetting angle is changed, the breakthrough time and the final recovery efficiency are similar under the conditions of weak wet ($\theta = 60°$) and medium wet ($\theta = 90°$). The average recovery efficiency of the two models was 61.37% and 43.56%, respectively. The recovery efficiency of the two models is 87.93% and 52.36%, respectively, under the strong wet condition ($\theta = 120°$). Moreover, with the increase in wettability, the recovery efficiency increased from 41.09% to 87.93% after the real pore model changed the wettability.

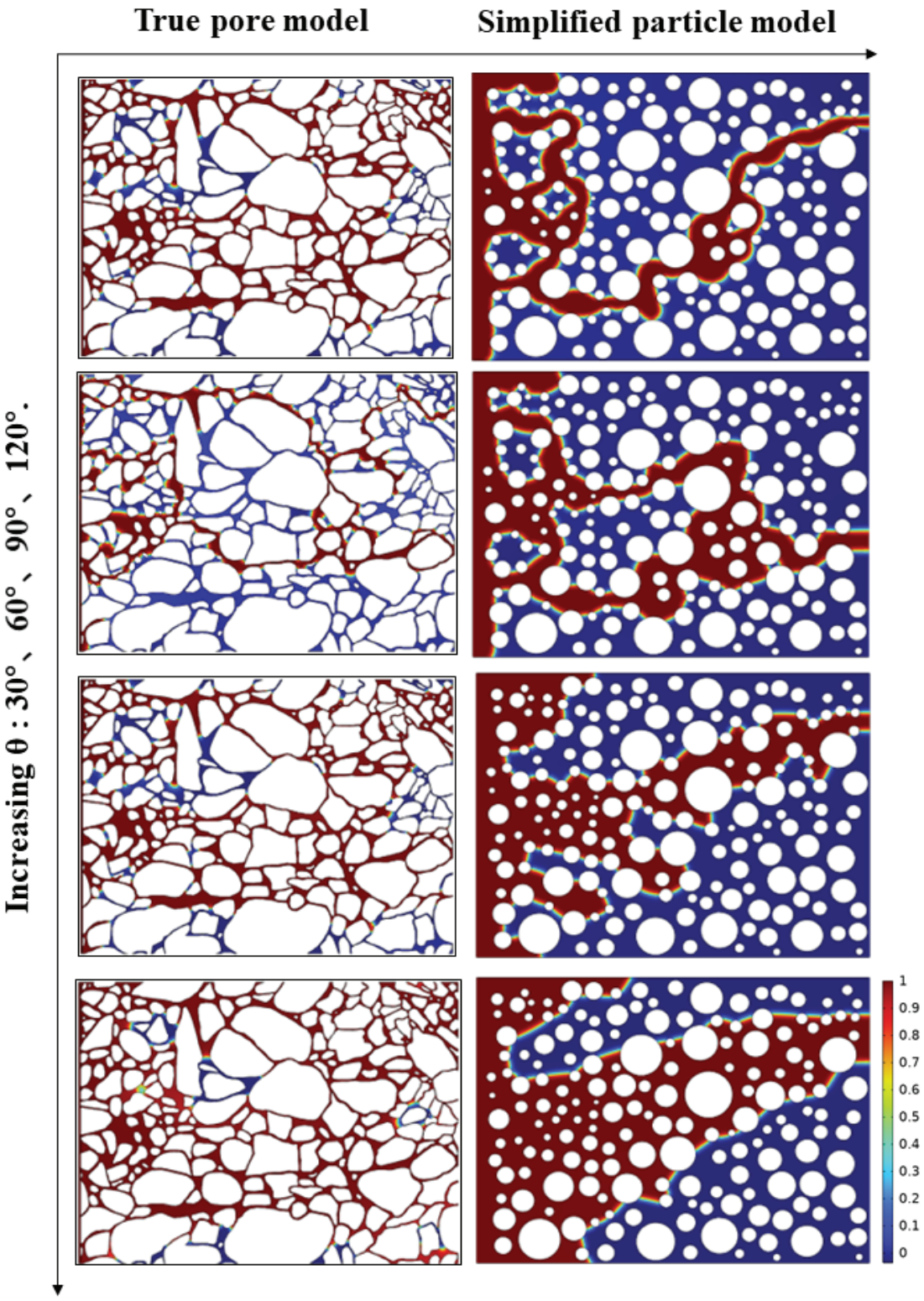

Figure 5. Oil recovery curves of the two models at different wettability.

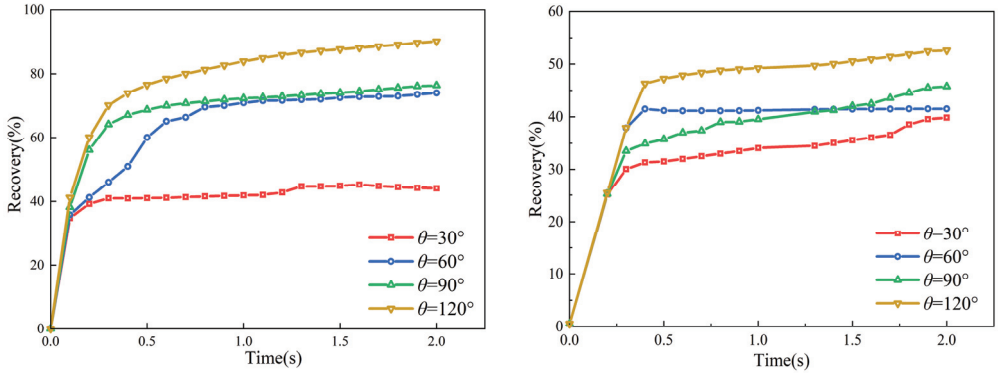

(**a**)True pore model (**b**) Simplified particle model

Figure 6. Recovery curve under different wettability.

3.3. Effect of Different Viscosity Ratios

The CO_2 viscosity is significantly affected by temperature and pressure and decreases with the increase in temperature and increases with the increase in pressure. The CO_2 viscosity is different under different reservoir conditions. To study the effect of viscosity ratio (*M*, that is, the viscosity ratio of CO_2 to oil) on the distribution of CO_2 clusters and the displacement process in porous media under different reservoir conditions. Based on the two-phase flow model established above, simulation cases with different viscosity ratios (logM = −3.2, −3.5, −3.8, −4.1, respectively) are constructed. Ensure that other parameters affecting fluid flow are the same. The CO_2–oil two-phase distribution when CO_2 displacement reaches steady state is shown in Figure 7.

With the increase in viscosity ratio, the sweep range of CO_2 clusters increases and the oil recovery rate increases. The viscosity ratio of the two-phase fluid has a direct influence on the viscous force. Therefore, when the viscosity of CO_2 is increased, the viscous force formed by the friction between CO_2 and the oil phase decreases, and the viscous dissipation rate between the fluid phase interface decreases. It also helps the relative motion between the two phases of the fluid. From the simulation results of the two models, it can be found that they have the same dominant flow channels, but there are many dominant flow channels in the real pore model. In the simplified particle model, when the viscosity ratio is large enough, multiple breakthrough channels are formed and break through from the lower boundary. When the viscosity ratio is increased and the CO_2 viscosity is gradually close to the oil viscosity, the CO_2 phase is easier to flow, so as to achieve better oil displacement and storage effect.

The changes in CO_2 displacement recovery under different viscosity ratios are shown in Figure 8. With the increase in viscosity ratio, the flow of CO_2 along the dominant channel is more obvious. The front end of the finger is thin and long, resulting in a shorter breakthrough time and higher recovery efficiency. When the two-phase viscosity is closer, the breakthrough process of CO_2 along the dominant flow channel has a reduced impact on its flow capacity in other channels, thereby minimizing its effect on the overall displacement efficiency. In the real pore model, changes in the viscosity ratio have a minimal impact on pre-breakthrough recovery. After breakthrough, although the CO_2 flow in the remaining channels is slow, the viscous force is sufficient to overcome the capillary force, allowing diffusion to continue. As a result, the spread range expands, and the recovery efficiency progressively increases. In the simplified particle model, the breakthrough recovery efficiency increases significantly with the increase in viscosity ratio. The breakthrough recovery efficiency increased from 32.35% to 44.97%, with a higher growth rate of 39.01%. When the viscosity ratio increases from LogM = −3.2 to

LogM = −4.1, the ultimate recovery efficiency of the real pore model increases from 62.35% to 80.15%, with a growth rate of 25.55%.

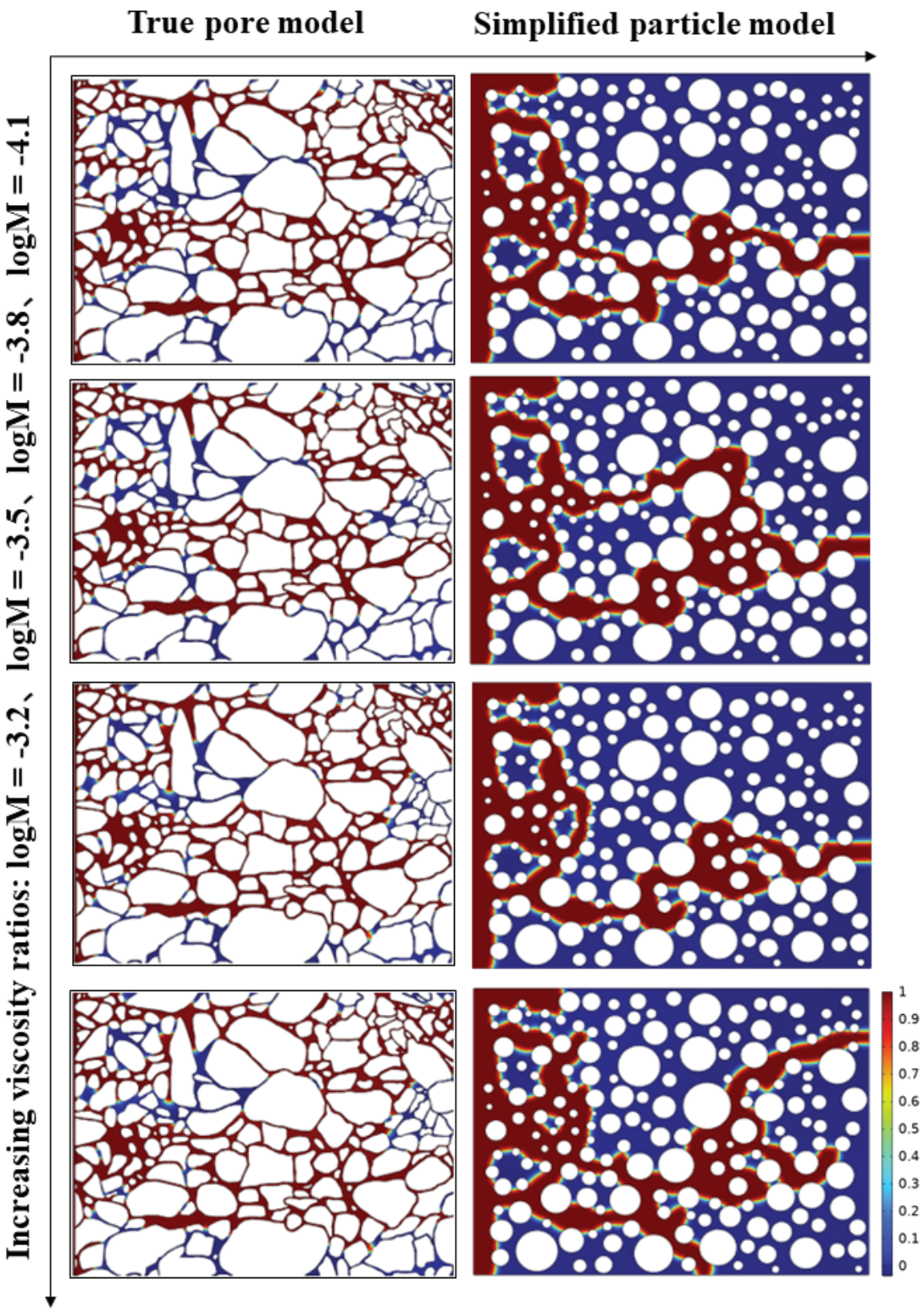

Figure 7. Oil recovery curves of the two models at different viscosity ratios.

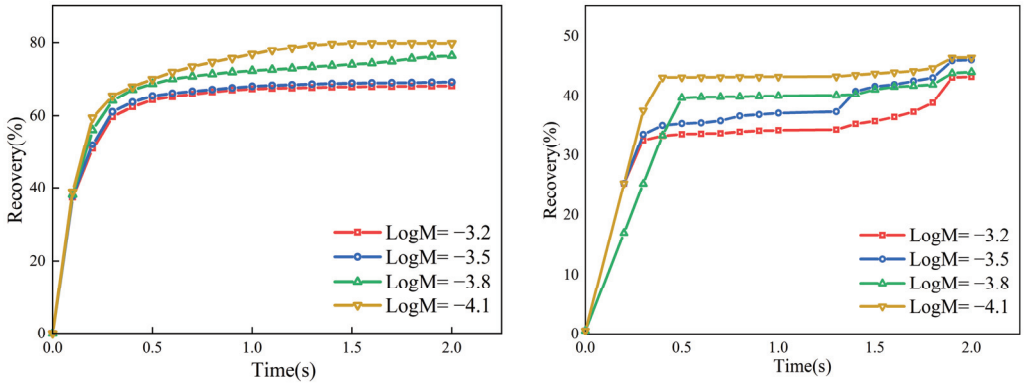

(**a**)True pore model (**b**) Simplified particle model

Figure 8. Recovery curve under different viscosity ratios.

3.4. Effect of Different Interfacial Tension

Figure 9 shows the two-phase distribution of CO_2–oil in porous media under different interfacial tension. Under the same temperature and pressure conditions, the interfacial tension of porous media can be changed by the concentration and salinity of CO_2. In the process of porous media displacement, lower interfacial tension makes it easier for CO_2 to expel oil from porous media. As interfacial tension increases, the diffusion area of CO_2 gradually decreases, resulting in a higher amount of residual oil remaining in the pores. In the real pore model, the resistance to CO_2 diffusion increases with the increase in interfacial tension. The content of various residual oils increased greatly when the displacement was stable. In the simplified particle model, an increase in interfacial tension amplifies the fingering phenomenon during CO_2 breakthrough. After CO_2 breakthrough, the oil utilization efficiency of other flow channels is weakened, and the displacement efficiency is significantly reduced.

Figure 10 shows the recovery curve under different interfacial tension, which shows a trend of obvious decrease with the increase in interfacial tension. When the interfacial tension is 13 mN/m, the recovery efficiency of the two models is 91.32% and 49.73%, respectively. In the real pore model, the interfacial tension has a great influence on the diffusion process of CO_2 and the ultimate recovery efficiency. The lowest and highest recovery efficiency are 50.31% and 91.32%, respectively, and the growth rate is as high as 81.51%. This is because the pore throats in the real pore model are relatively small, making the displacement process highly sensitive to interfacial tension. When interfacial tension is high, CO_2 clusters face greater difficulty in breaking through due to the frictional resistance from the pore walls. In the simplified spherical model, the pore throat is wider, the contact area between CO_2 and oil is larger, and the interfacial tension has less influence on the ultimate recovery efficiency. The lowest and highest recovery rates are 39.32% and 46.35%, respectively, with a growth rate of only 17.87%.

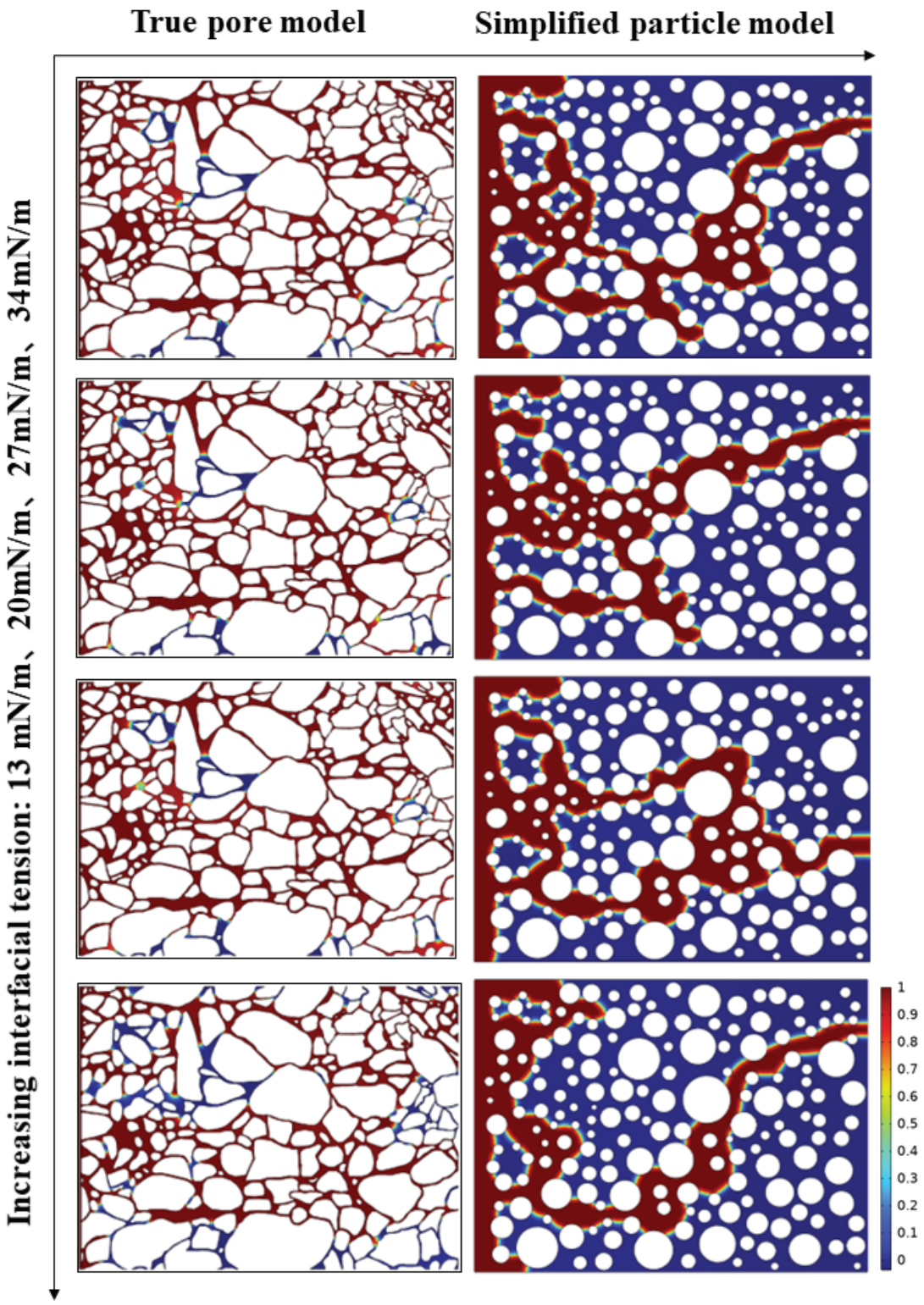

Figure 9. Oil recovery curves of the two models at different interfacial tension.

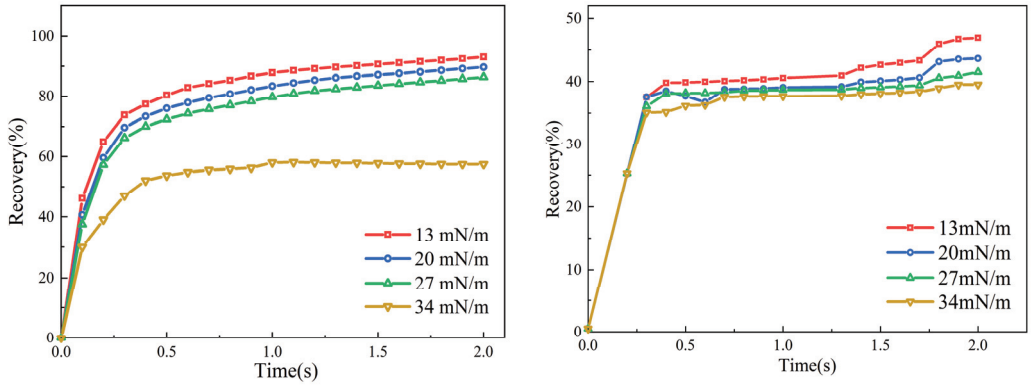

(**a**)True pore model (**b**) Simplified particle model

Figure 10. Recovery curve under different interfacial tension.

3.5. The Impact of Cracks

Figure 11 shows the two-phase distribution of CO_2 displacement process in a dual medium with Y-shaped fractures. The blue and red regions represent the oil phase and CO_2 phase, respectively. Multi-scale pores and fractures are developed in the dual medium, and the interior is filled with fluids such as oil. CO_2 begins to displace oil in pores and fractures after flowing into the medium from the left inlet.

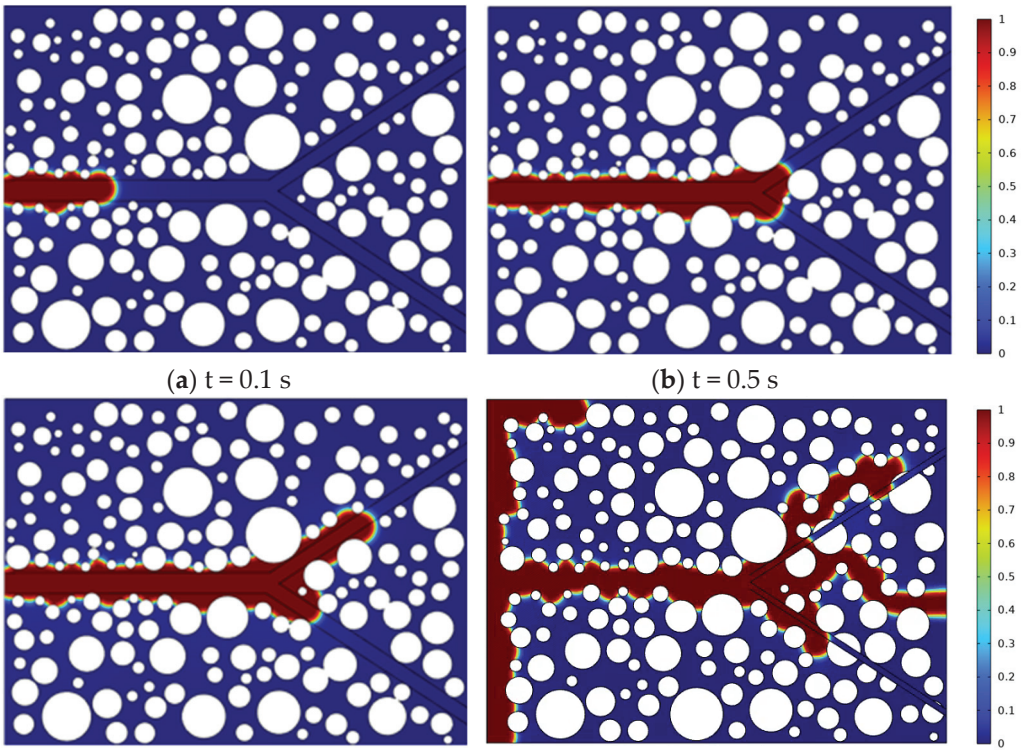

(**a**) t = 0.1 s (**b**) t = 0.5 s

(**c**) t = 1 s (**d**) t = 2 s

Figure 11. CO_2 displacement process in dual media.

There is an obvious difference between the permeability of pores and fractures in dual media. The throat development degree is higher in the fracture with larger opening, and the flow resistance of CO_2 is smaller. When CO_2 flows into the medium and diffuses along the crack, the crack fingering phenomenon is obvious, and the fingering phenomenon becomes more and more obvious with the passage of time. However, the narrow throat in other parts limited the migration and diffusion of CO_2 in the porous medium, and the flow rate was slow. CO_2 diffusion shows the phenomenon of convergence from the pore medium to

the fracture, and at the same time dispersion and infiltration from the fracture to the pore medium. Under continuous injection, CO_2 diffuses along the joint surface fractures and some pores to discharge the oil in the medium. Due to the strong heterogeneity of the dual medium, there are still dominant flow channels in the pores when CO_2 is displaced in the fractures. At the same time, after CO_2 breaks through along the dominant flow channel, the flow in the fracture is basically stable, and the CO_2 front does not advance along the fracture. The displacement reaches a stable state.

To simulate the displacement process in dual media with varying fracture configurations at the core scale, four numerical models of fracture-controlled matrix units were established using a method that randomly fills non-overlapping irregular polygons to represent the matrix system [32]. These models include: single fracture (Figure 12a), Y-shaped fracture (Figure 12b), L-shaped fracture (Figure 12c), and multi-scale fractures (Figure 12d). The simulation results of CO_2 displacement in four dual media with fractures of different shapes are shown in Figure 11. Pure porous media exhibit high structural integrity but low seepage capacity. The absence of fracture development, combined with narrow pore throats, makes CO_2 diffusion challenging. In contrast, the dual-medium system features well-developed fractures, improved seepage capacity, and a distinct fingering phenomenon during CO_2 diffusion. Therefore, regions with a high degree of fracture development in the joint plane play a dominant role in the diffusion and migration of CO_2. As the potential energy of the CO_2-oil contact layer increases, CO_2 diffusion along the fractures becomes more prioritized over other regions. The fracture shape basically determines the diffusion form of CO_2 in the dual medium.

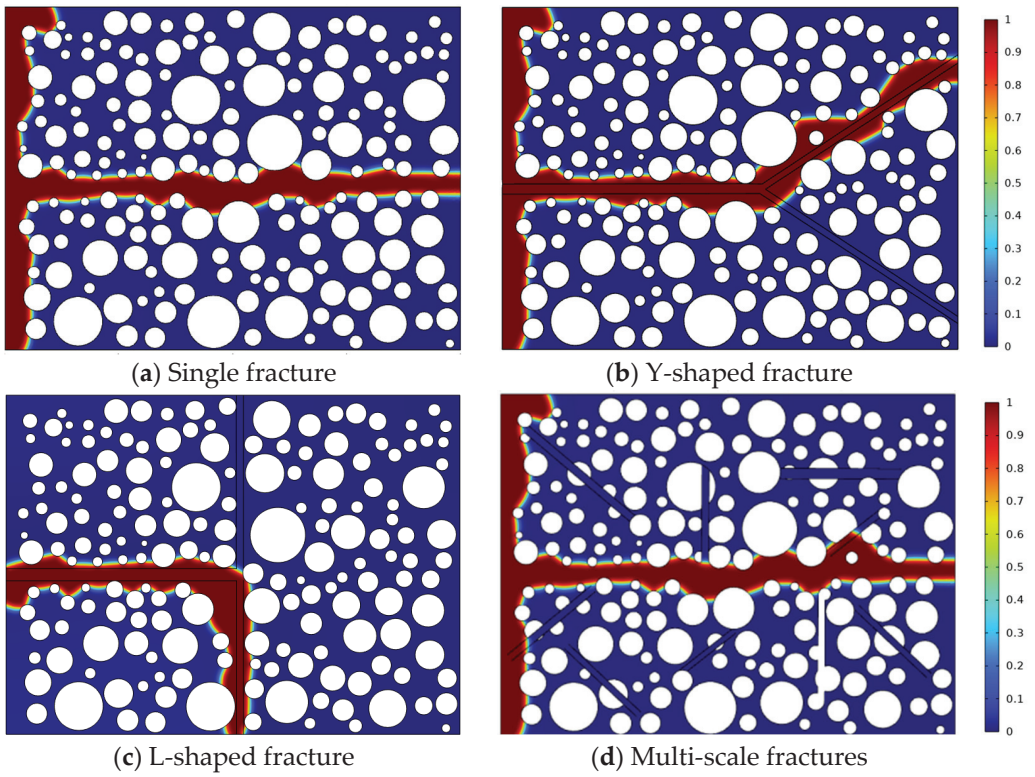

(**a**) Single fracture (**b**) Y-shaped fracture

(**c**) L-shaped fracture (**d**) Multi-scale fractures

Figure 12. Simulation results of CO_2 displacement with different fracture morphology.

The development of fractures significantly influences the CO_2 flow path and diffusion range within porous media, leading to variations in recovery efficiency. To quantify the impact of fracture development on CO_2 flooding oil recovery, we present the results in Figure 13. As fractures form in the porous media, fluid preferentially flows along these cracks, which slows diffusion within the pores. When CO_2 breaks through the fractures,

the sweep efficiency within the pores is limited. As a result, in all four models, the recovery rate decreases significantly after fracture breakthrough, with the highest recovery rate reaching only 20.34%. As fracture complexity increases, the ultimate recovery rate gradually improves, rising from 15.63% to 20.34%. Notably, when L-shaped fractures develop in the dual medium, the recovery rate is the lowest. This is because the flow path of CO_2 is short, and the breakthrough time is too fast. This affects the effective diffusion of CO_2 through the pores after the L-shaped fracture breakthrough.

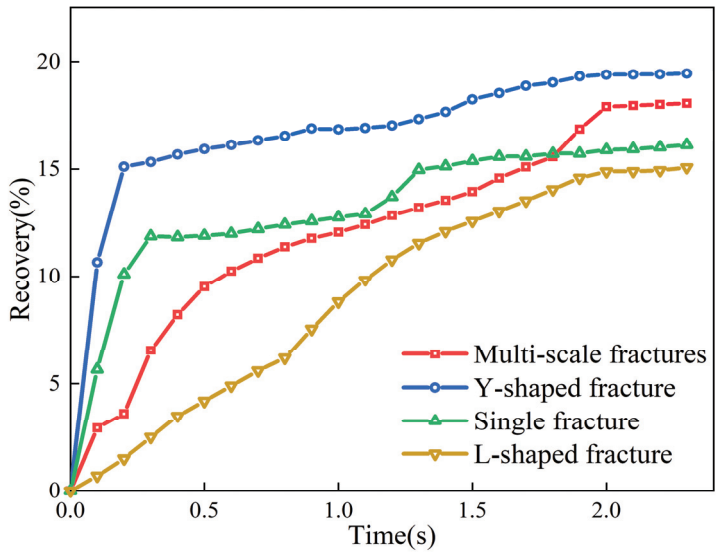

Figure 13. Recovery of CO_2 displacement with different fracture morphology.

The application of CCS technology involves complex physical and chemical reactions. Evaluating the complexity of the CO_2 displacement process requires a comprehensive approach that integrates chemical, stress, and seepage field analyses. The current study does not account for the effects of stress, dissolution or the three-phase interactions among oil, gas, and water. In addition, under real reservoir conditions, the density difference between CO_2 and crude oil is not an order of magnitude. In this work, we simulate the immiscible flooding process with an interfacial tension of 13–34 mN/m under extremely low-pressure conditions, which differ significantly from real reservoir environments. In future research, we plan to address these challenges and further explore the associated issues. Our goal is to evaluate the advantages and limitations of pore structure simplification on the microscale CO_2 displacement process more effectively.

4. Conclusions

We construct the real pore model and the corresponding simplified particle model. Based on the numerical simulation method of N-S equation coupled phase field method, the oil–water two-phase flow model is established. The effects of capillary number, wettability, viscosity ratio, interfacial tension and fracture development on CO_2 displacement were studied. The main conclusions are as follows:

1. In the simulation results of the real pore model and simplified particle model, the diffusion details of CO_2 displacement process have changed significantly. There are differences in the shape of pointing, the number of dominant flow channels, the sensitivity to influencing factors, and the ultimate recovery efficiency. In the simulation results of the simplified particle model, the number of dominant CO_2 flow channels decreased, and the overall recovery efficiency decreased. It is less sensitive to capillary number, rock wettability, and other factors.

2. With the decrease in oil-wet strength of rock, the displacement mode changes from finger-like displacement to piston displacement, and the CO_2 sweep range becomes wider. At the same time, the breaking frequency of CO_2 clusters is reduced, and their continuity is improved. It will promote the gradual convergence of isolated flow channels into sheets, leading to more efficient and complete displacement.
3. The displacement pattern changes from capillary finger-pointing to stable displacement by increasing the number of capillaries. When the viscosity of the injected CO_2 is closer to that of the oil, the flow resistance between the two phases decreases, enhancing the flow capacity of the CO_2 phase and resulting in a higher final recovery efficiency.
4. When CO_2 is displaced in the dual media with pores and fractures, CO_2 will preferentially diffuse along the fractures. There is a pointing phenomenon with an obvious front, and the pointing phenomenon becomes more and more obvious with the passage of time. The morphology of CO_2 diffusion is different in the dual media with different fractures. The shape of the fracture basically determines the diffusion form of CO_2 in the dual medium.

Author Contributions: Conceptualization, T.W. and L.Y.; Methodology, C.Y. and L.Y.; Writing—original draft, T.W., C.Y., R.G., Y.Z., X.J. and L.Y. All authors have read and agreed to the published version of the manuscript.

Funding: This work is supported by the National Natural Science Foundation of China (52374014), and the Fundamental Research Funds for the Central Universities (2024ZKPYSB03).

Data Availability Statement: The original contributions presented in this study are included in the article. Further inquiries can be directed to the corresponding author.

Conflicts of Interest: T.W., C.Y., R.G. and Y.Z. were employed by Oil and Gas Technology Research Institute of Changqing Oilfield, China National Petroleum Corporation. R.G. and Y.Z. were employed by Xi'an Changqing Chemical Group Industry Co., Ltd. of Changqing Oilfield, China National Petroleum Corporation. The remaining authors declare that the research was conducted in the absence of any commercial or financial relationships that could be construed as a potential conflict of interest.

References

1. Brown, K.; Whittaker, S.; Wilson, M.; Srisang, W.; Smithson, H.; Tontiwachwuthikul, P. The history and development of the IEA GHG Weyburn-Midale CO_2 Monitoring and Storage Project in Saskatchewan, Canada (the world largest CO_2 for EOR and CCS program). *Petroleum* **2017**, *3*, 3–9. [CrossRef]
2. An, S.; Sahimi, M.; Niasar, V. Upscaling hydrodynamic dispersion in non-Newtonian fluid flow through porous media. *Water Resour. Res.* **2022**, *58*, e2022WR032238. [CrossRef]
3. Hu, R.; Wan, J.-Y.; Kim, y.; Tokunaga, T.K. Wettability effects on supercritical CO_2–brine immiscible displacement during drainage: Pore-scale observation and 3D simulation. *Int. J. Greenh. Gas Control* **2017**, *60*, 129–139. [CrossRef]
4. Soleymanzadeh, A.; Gahrooei, H.R.E.; Joekar-Niasar, V. A new empirical model for bulk foam rheology. *J. Energy Resour. Technol.* **2018**, *140*, 032911. [CrossRef]
5. Celia, M.A.; Bachu, S.; Nordbotten, J.M.; Bandilla, K.W. Status of CO_2 storage in deep saline aquifers with emphasis on modeling approaches and practical simulations. *Water Resour. Res.* **2015**, *51*, 6846–6892. [CrossRef]
6. Zhao, X.-L.; Wang, Z.-L.; Zhao, Y.-Z.; Zuo, J.-Q.; Li, P.; Liang, W.; Wang, B.; Chen, X.; Lei, H.-W.; Jin, G.-G. Coupled thermal-hydrodynamic-mechanical numerical simulation of natural gas hydrate horizontal well depressurization production: Method and application in South China Sea. *Nat. Gas Ind.* **2022**, *42*, 138–149. [CrossRef]
7. Ali, M.; Arif, M.; Sahito, M.F.; Al-Anssari, S.; Keshavarz, A.; Barifcani, A.; Stalker, L.; Sarmadivaleh, M.; Iglauer, S. CO_2-wettability of sandstones exposed to traces of organic acids: Implications for CO_2 geo-storage. *Int. J. Greenh. Gas Control.* **2019**, *83*, 61–68. [CrossRef]
8. Tahmasebi, P.; Sahimi, M.; Andrade, J.E. Image-based modeling of granular porous media. *Geophys. Res. Lett.* **2017**, *44*, 4738–4746. [CrossRef]

9. Li, Y.-W.; Yang, Y.-F.; Dong, M.-Z.; Liu, C.-F.; Iglauer, S.; Kang, L.-X.; Yao, J.; Zhang, K.; Sun, H.; Zhang, L. Effect of pore structure and capillary number on gas-water flow patterns in carbonate rocks. *SPE J.* **2022**, *27*, 1895–1904. [CrossRef]
10. Yang, L.; Ge, H.-K.; Shi, X.; Cheng, Y.-F.; Zhang, K.-H.; Chen, H.; Shen, Y.-H.; Zhang, J.-J.; Qu, X.-M. The effect of microstructure and rock mineralogy on water imbibition characteristics in tight reservoirs. *J. Nat. Gas Sci. Eng.* **2016**, *34*, 1461–1471. [CrossRef]
11. Rokhforouz, M.; Akhlaghi Amiri, H.A. Phase-field simulation of counter-current spontaneous imbibition in a fractured heterogeneous porous medium. *Phys. Fluids* **2017**, *29*, 062104. [CrossRef]
12. Tsuji, T.; Jiang, F.; Christensen, K.T. Characterization of immiscible fluid displacement processes with various capillary numbers and viscosity ratios in 3D natural sandstone. *Adv. Water Resour.* **2016**, *95*, 3–15. [CrossRef]
13. Hassanpouryouzband, A.; Yang, J.-H.; Tohidi, B.; Chuvilin, E.; Istomin, V.; Bukhanov, B.; Cheremisin, A. Insights into CO_2 Capture by Flue Gas Hydrate Formation: Gas Composition Evolution in Systems Containing Gas Hydrates and Gas Mixtures at Stable Pressures. *ACS Sustain. Chem. Eng.* **2018**, *6*, 5732–5736. [CrossRef]
14. Ahfir, N.D.; Hammadi, A.; Alem, A.; Wang, H.-Q.; Le Bras, G.; Ouahbi, T. Porous media grain size distribution and hydrodynamic forces effects on transport and deposition of suspended particles. *J. Environ. Sci.* **2017**, *53*, 161–172. [CrossRef] [PubMed]
15. Rad, M.N.; Shokri, N.; Keshmiri, A.; Withers, P.J. Effects of grain and pore size on salt precipitation during evaporation from porous media. *Transp. Porous Media* **2015**, *110*, 281–294. [CrossRef]
16. Xu, R.; Prodanović, M. Effect of pore geometry on nitrogen sorption isotherms interpretation: A pore network modeling study. *Fuel* **2018**, *225*, 243–255. [CrossRef]
17. Lacey, M.R.; Hollis, C.; Oostrom, M.; Shokri, N. Effects of pore and grain size on water and polymer flooding in micromodels. *Energy Fuels* **2017**, *31*, 9026–9034. [CrossRef]
18. Guo, C.-H.; Wang, X.; Wang, H.; He, S.; Liu, H.; Zhu, P. Effect of pore structure on displacement efficiency and oil-cluster morphology by using micro computed tomography (μCT) technique. *Fuel* **2018**, *230*, 430–439. [CrossRef]
19. Man, H.N.; Jing, X.-D. Network modelling of wettability and pore geometry effects on electrical resistivity and capillary pressure. *J. Pet. Sci. Eng.* **1999**, *24*, 255–267. [CrossRef]
20. Huang, R.-T.; Herring, A.L.; Sheppard, A. Investigation of supercritical CO_2 mass transfer in porous media using X-ray micro-computed tomography. *Adv. Water Resour.* **2023**, *171*, 104338. [CrossRef]
21. Prasittisopin, L.; Termkhajornkit, P.; Kim, Y.H. Review of concrete with expanded polystyrene (EPS): Performance and environmental aspects. *J. Clean. Prod.* **2022**, *366*, 132919. [CrossRef]
22. Zhang, Y. Physicalsimulation of staged-fracturing horizontal wells using CO2 huff and puff in tight oil reservoirs. *Aeta Pelrolei Sinica.* **2015**, *36*, 724–729. Available online: https://iopscience.iop.org/article/10.1088/1755-1315/371/5/052022/pdf (accessed on 3 November 2024).
23. Liu, H.; Tao, J.-P.; Meng, S.-W.; Li, D.-X.; Gao, g.; Gao, Y. Application and prospects of CO2 enhanced oil recovery technology in shale oil reservoir. *China Pet. Explor.* **2022**, *27*, 127–134. [CrossRef]
24. Liu, J.; Zhang, T.; Sun, S.-Y. Mechanism analysis of shale gas adsorption under carbon dioxide–moisture conditions: A molecular dynamic study. *Energy Fuels* **2022**, *36*, 14865–14873. [CrossRef]
25. Zhang, T.; Tang, M.; Ma, Y.-K.; Zhu, G.-P.; Zhang, Q.-H.; Wu, J.; Xie, Z.-Z. Experimental study on CO_2/Water flooding mechanism and oil recovery in ultralow-Permeability sandstone with online LF-NMR. *Energy* **2022**, *252*, 123948. [CrossRef]
26. Haeri, F.; Tapriyal, D.; Matranga, C.; Crandall, D.; Goodman, A. Variation of CO_2-brine contact angles on natural rocks of different compositions. *J. Energy Power Technol.* **2021**, *3*, 1–14. [CrossRef]
27. Raeini, A.Q.; Yang, J.-H.; Bondino, I.; Bultreys, T.; Blunt, M.J.; Bijeljic, B. Validating the generalized pore network model using micro-CT images of two-phase flow. *Transp. Porous Media* **2019**, *130*, 405–424. [CrossRef]
28. Liu, Q.; Li, J.-L.; Liang, B.; Liu, J.-J.; Sun, W.-J. Complex wettability behavior triggering mechanism on imbibition: A model construction and comparative study based on analysis at multiple scales. *Energy* **2023**, *275*, 127434. [CrossRef]
29. Yang, Y.-F.; Cai, S.-B.; Yao, J.; Zhong, J.-J.; Zhang, K.; Song, W.-H. Pore-scale simulation of remaining oil distribution in 3D porous media affected by wettability and capillarity based on volume of fluid method. *Int. J. Multiph. Flow* **2021**, *143*, 103746. [CrossRef]
30. Zhu, Z.-W.; Liu, J.-J.; Liu, H.-J.; Wu, M.-Y.; Song, Z.-L. Numerical investigation of single- and two-phase flow in porous media with a bifurcated fracture. *Phys. Fluids* **2021**, *33*, 052117. [CrossRef]
31. Rokhforouz, M.R.; Akhlaghi Amiri, H.A. Effects of grain size and shape distribution on pore-scale numerical simulation of two-phase flow in a heterogeneous porous medium. *Adv. Water Resour.* **2019**, *124*, 84–95. [CrossRef]
32. Liu, Q.; Liu, J.-J.; Liang, B.; Sun, W.-J.; He, J.; Lei, Y. The influence of pore structure of the core-scale fracture-controlled matrix unit on imbibition: Model construction and definition of the fractal coefficient. *Lithosphere* **2022**, *2022*, 6245345. [CrossRef]

energies

MDPI

Article

Gas Content and Gas Occurrence Mechanism of Deep Coal Seams in the Shenfu-Linxing Block

Litao Ma [1,2], Fan Yang [3,*], Jianghao Yang [1,2], Yi Cui [4], Wei Wang [1,2], Cheng Liu [1,2], Bo Zhang [1,2], Jiang Yang [1,2] and Shu Tao [5,*]

[1] CNOOC EnerTech-Drilling & Production Co., Tianjin 300452, China; malt@cnooc.com.cn (L.M.); yangjh38@cnooc.com.cn (J.Y.); wangwei193@cnooc.com.cn (W.W.); liucheng14@cnooc.com.cn (C.L.); zhangbo53@cnooc.com.cn (B.Z.); jiangyang4@cnooc.com.cn (J.Y.)
[2] CNOOC Energy Technology & Services Limited Key Laboratory for Exploration & Development of Unconventional Resources, Tianjin 300452, China
[3] PetroChina Research Institute of Petroleum Exploration and Development, Beijing 100083, China
[4] Zhalainuoer Coal Industry Co., Ltd., Hulunbuir 021410, China; cuiyicugb@126.com
[5] School of Energy Resources, China University of Geosciences (Beijing), Beijing 100083, China
* Correspondence: yangfan84@foxmail.com (F.Y.); taoshu@cugb.edu.cn (S.T.)

Abstract: The Shenfu-Linxing block in the Ordos Basin holds abundant deep coalbed methane (CBM) resources, which can alleviate gas shortages and aid dual carbon target achievement. Considering isothermal adsorption traits and parameters like vitrinite reflectance, temperature, pressure, and water saturation, a prediction model for adsorbed and free gas content was formulated. This model helps to reveal the deep CBM occurrence mechanism in the Shenfu-Linxing block. Results show that deep CBM exists in both adsorbed and free states, with adsorbed gas initially increasing then decreasing, and free gas rising then stabilizing as burial depth increases. A critical transition depth for total CBM content exists, shallowing with higher water saturation. As depth increases, temperature and pressure evolution results in a "rapid growth—slow growth—stability—slow decrease" pattern in total gas content. Adsorbed gas resides in micropores, while free gas occupies larger pores.

Keywords: prediction model; gas content; coalbed methane; occurrence characteristics

1. Introduction

The composition of gas in deep coal reservoirs primarily consists of adsorbed and free gas [1–7]. The measured gas content in coal seams is mainly composed of desorption gas, residual gas, and escaping gas. At present, the test samples used are mainly obtained through rope coring. Alternatively, during the process from drilling to loading into the desorption tank, a significant decrease in pressure will result in significant gas loss, especially for deep coal reservoirs rich in free gas. Therefore, the estimated gas loss is usually much lower than the actual gas loss, resulting in low total gas content test results [8–11]. In recent years, pressure maintaining coring technology has significantly improved the accuracy of gas content testing. However, it remains challenging to quantitatively measure the free gas content [12,13]. Many scholars have developed prediction models for deep CBM content using methods such as principal component analysis, isothermal adsorption techniques, and adsorption potential theory [12,14–19]. Nevertheless, the research focus is mainly on relatively shallow coal reservoirs, lacking quantitative characterization of gas content in deep coal seams.

In contrast to traditional shallow coal reservoirs, the geological characteristics of deep coal reservoirs, including high stress, high temperature, and high pressure, result in considerable alterations in the pore structure of coal, ultimately causing substantial variations in the occurrence state of CBM [2,20,21]. As burial depth increases, the quantity of adsorbed gas increases and subsequently decreases, whereas the quantity of free gas progressively rises. The content of free gas is also affected by the level of water saturation [1,15,22]. In deep coal reservoirs, both adsorbed gas and free gas coexist, with a distinct "critical depth" serving as a separator between them. Above this critical depth, a notable positive pressure effect is observed, leading to an augmentation in the adsorbed gas content as the burial depth increases [22–24]. Beyond the depth, the negative effect of temperature becomes significant. Thus, as the burial depth increases, the negative effect of temperature intensifies, while the positive effect of pressure gradually weakens. As a result, the amount of adsorbed gas decreases progressively, while the amount of free gas rises. While free gas and adsorbed gas both exist in deep coal reservoirs, adsorbed gas continues to dominate in terms of overall proportion [25–28]. Conversely, when water saturation diminishes and burial depth intensifies, the content of free gas has the potential to exceed that of adsorbed gas. Generally, low-rank deep coal reservoirs contain a relatively free gas content, while medium- and high-rank deep coal reservoirs still have a high proportion of adsorbed gas [29–33].

To quantify the CBM content of different phases in deep coal seams and improve prediction accuracy, this study established prediction models for adsorbed gas and free gas content based on high-temperature and high-pressure isothermal adsorption experiments. By combining the Langmuir model, the evolution characteristics and occurrence mechanism of methane in different phases of deep coal reservoirs were revealed.

2. Geological Setting

The Ordos Basin, a significant intra-cratonic basin situated in North China, holds the second-largest coal resource reserves in the country [34] (Figure 1a). The basin is segmented into seven structural subdivisions [35,36] (Figure 1b). The Shenfu-Linxing area is situated at the central-eastern fringe of the Ordos Basin, bordered by the Baode region to the north and the Sanjiaobei area to the south (Figure 1c). It spans the northern slope of Shaanxi and the western Shanxi fold belt in structure. The internal structure is relatively complex, with locally developed small faults and folds, and multiple secondary structural units. The Shenfu-Linxing block mainly develops strata such as Ordovician Majiagou Formation (O_1m), Carboniferous Benxi Formation (C_2b), Taiyuan Formation (C_3t), Shanxi Formation (P_1s), Permian Lower Shihezi Formation (P_2x), Upper Shihezi Formation (P_2s), Shiqianfeng Formation (P_3sh), Triassic Liujiagou Formation (T_1l), Heshanggou Formation (T_1h), Zhifang Formation (T_2z), Yanchang Formation (T_3y), and Quaternary System (Q). Among them, Taiyuan Formation and Shanxi Formation contain a significant number of coal seams. At present, the No. 8+9 coal seam of Taiyuan Formation is the key layer for deep CBM exploration and development in the entire region (Figure 2).

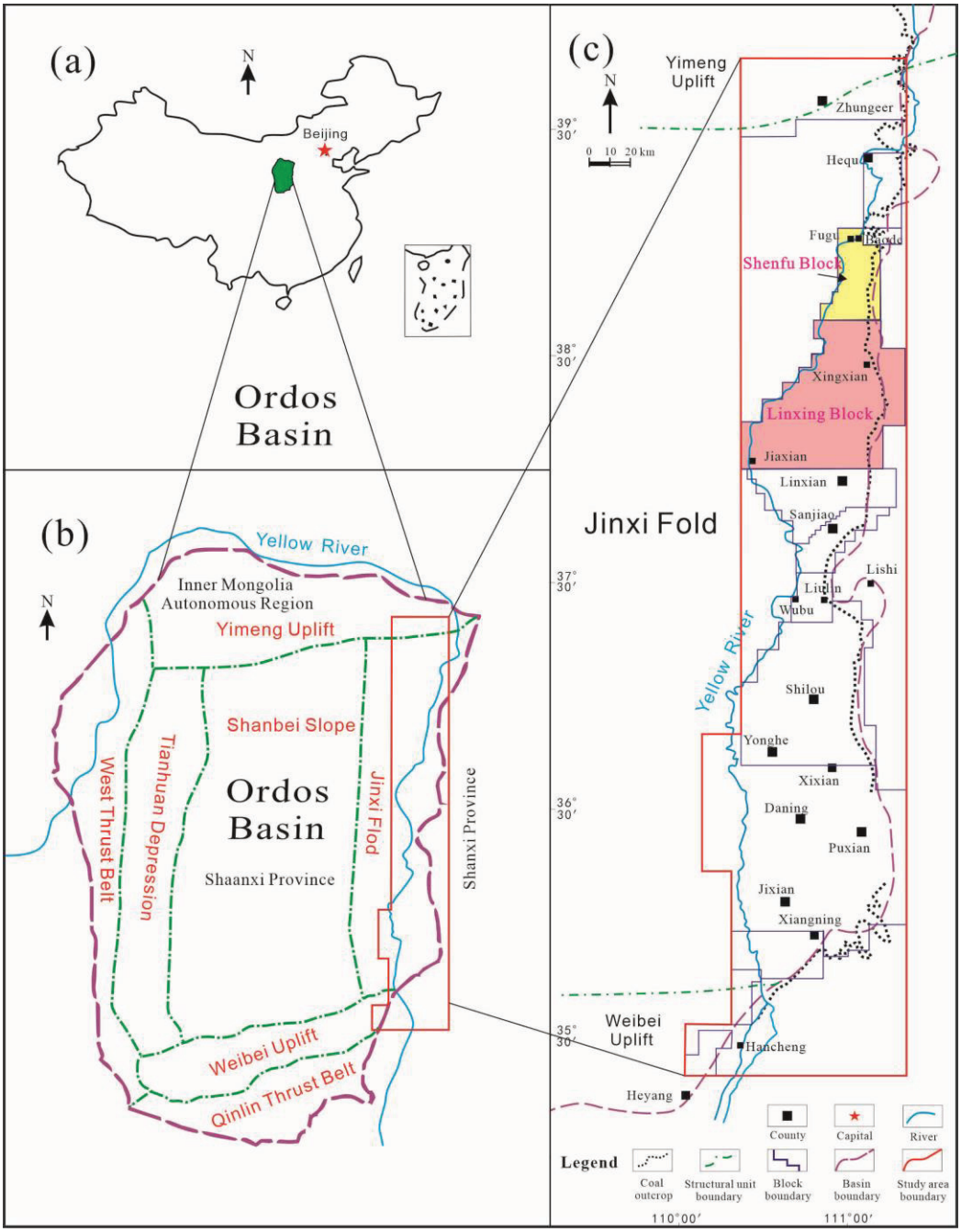

Figure 1. (**a**) Location of the Ordos Basin; (**b**) Tectonic units of the Ordos Basin; (**c**) Division of eastern margin of Ordos Basin and the location of Shenfu-Linxing block (modified from [37]).

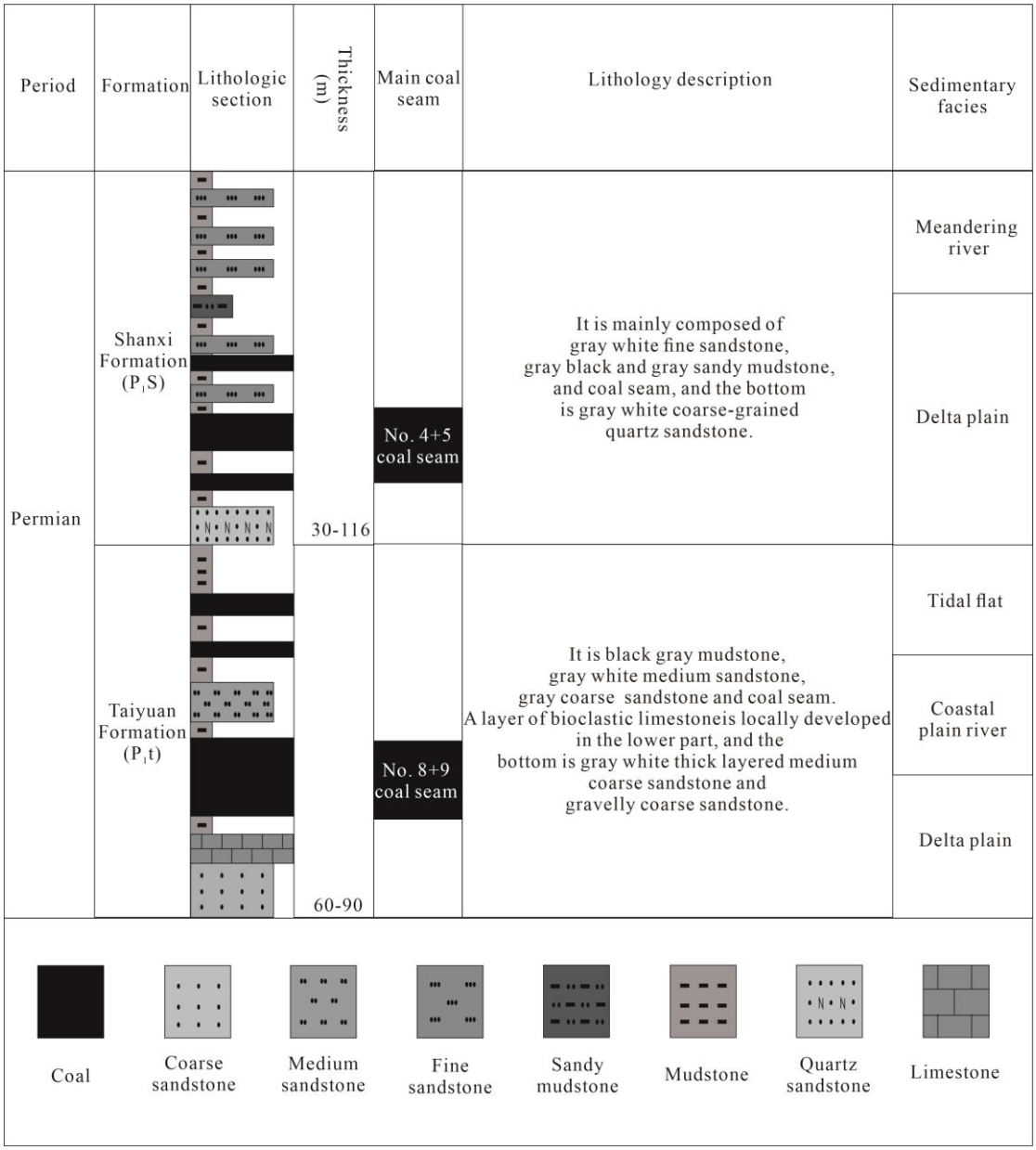

Figure 2. Lower Permian stratigraphic column in the Shenfu-Linxing block (modified from [37]).

3. Experiments and Methods

3.1. Material Composition

Six coal samples were taken from the No. 8+9 coal seam in the Shenfu-Linxing block, with a sampling depth of 1968–2344 m. All of the samples were used to conduct proximate analysis tests and microscopic component tests following the Chinese national standard GB/T 30732-2014 [38] and GB/T 8899-2013 [39], respectively. Meanwhile, the vitrinite reflectance (Ro) of the coal samples was tested according to GB/T 6948-2008 [40].

3.2. Isothermal Adsorption Test

According to the national standard GB/T 19560-2008 [41], adsorption tests were performed under varying temperature and pressure conditions to analyze isothermal behavior. To further understand the mechanism by which temperature affects methane adsorption capacity, the temperature points were set as 30 °C, 50 °C, and 70 °C, with a maximum pressure of 30 MPa.

3.3. Gas Content Prediction Methods

The Langmuir adsorption equation (Equation (1)) is a single-molecule layer adsorption theoretical model, which is an isothermal equation obtained from the adsorption system in dynamic equilibrium. It is widely used to calculate the amount of adsorbed gas in coal [42,43].

$$V = \frac{P \cdot V_L}{P + P_L} \tag{1}$$

where, V is the methane adsorption capacity of the coal, cm^3/g; P_L is the Langmuir pressure, MPa; V_L is the Langmuir volume, cm^3/g; P is the reservoir pressure, MPa.

When the reservoir temperature is above 20 °C and the gas pressure is less than 20 MPa, it can be considered as an ideal gas state. Therefore, the calculation of free gas content can be based on the ideal gas state equation (Equations (2) and (3)).

$$\frac{P_0 V_0}{T_0} = \frac{P V_1}{T} \tag{2}$$

$$P = \frac{\rho R T}{M} \tag{3}$$

where, P_0 represents the standard gas pressure, which is 0.101 MPa; V_0 is the gas volume under standard conditions, m^3; T_0 is the absolute temperature, 273.15 K; P is the reservoir pressure, MPa; V_1 is the volume of free gas, m^3; T is the actual reservoir temperature, K; ρ is the gas density, kg/m^3; R is the Avogadro constant; M is the molar mass of the gas.

By combining the general gas state equation [44] and the Boyle Malotte law [45], the final equation for calculating free gas is obtained (Equation (4)).

$$V_1 = \frac{K(\Phi - \Phi_W)}{\rho_1} \tag{4}$$

where, V is the volume of free gas, m^3; K is the porosity stress attenuation coefficient; Φ is the porosity of the coal reservoir, %; Φw is the porosity occupied by water, %; ρ_1 is the measured apparent density of coal, t/m^3.

4. Results and Discussion

4.1. Basic Information of Coals

The primary macrolithotype of coal in the Shenfu-Linxing block is semi-bright coal, with a relatively complete coal structure. The basic information of coal samples is shown in Table 1. The Ro of coal samples varies from 0.95% to 1.33%, belonging to medium-rank coal. According to proximate analysis results, the moisture content, ash yield, and volatile matter account for 0.8–2.44%, 8.71–29.74%, and 13.21–30.41%, respectively. The vitrinite group has the highest content in the macerals (63.7–91.3%), followed by the inertinite group (8.6–36.2%), while the exinite group is basically undeveloped.

Table 1. Results of the proximate and maceral analyses.

Sample No.	Coal Seam No.	Depth (m)	Ro (%)	Maceral Composition (%)			Proximate Analysis (%)			
				Vitrinite	Inertinite	Exinite	M_{ad}	A_{ad}	V_{ad}	FC_{ad}
lx1	8+9	1968.4–1969.3	1.25	90.6	9.3	0.1	0.84	29.74	15.41	54.01
lx2	8+9	1980.8–1981.1	1.2	72.5	27.5	/	2.44	27.91	13.21	56.44
lx3	8+9	2004.3–2004.9	1.33	63.7	36.3	/	1.33	10.41	18.14	70.12
sm1	8+9	2135.1–2135.4	1.25	91.2	8.8	/	0.80	8.71	25.61	64.88
sm2	8+9	2235.2–2235.5	1.19	81.3	18.6	0.1	1.06	11.33	20.14	67.47
sm3	8+9	2343.9–2344.1	0.95	84.3	15.4	0.3	1.35	9.68	30.41	58.56

Notes: M_{ad} is moisture content; A_{ad} is ash yield; V_{ad} is volatile yield; FCad is fixed carbon content; ad is air-dried basis.

4.2. Isothermal Adsorption Characteristics

As depicted in Figure 3, there is a notable positive relationship observed between pressure and Langmuir volume. As the burial depth increases, the pressure of the coal reservoir rises, leading to an increase in Langmuir volume and enhanced coal adsorption capacity.

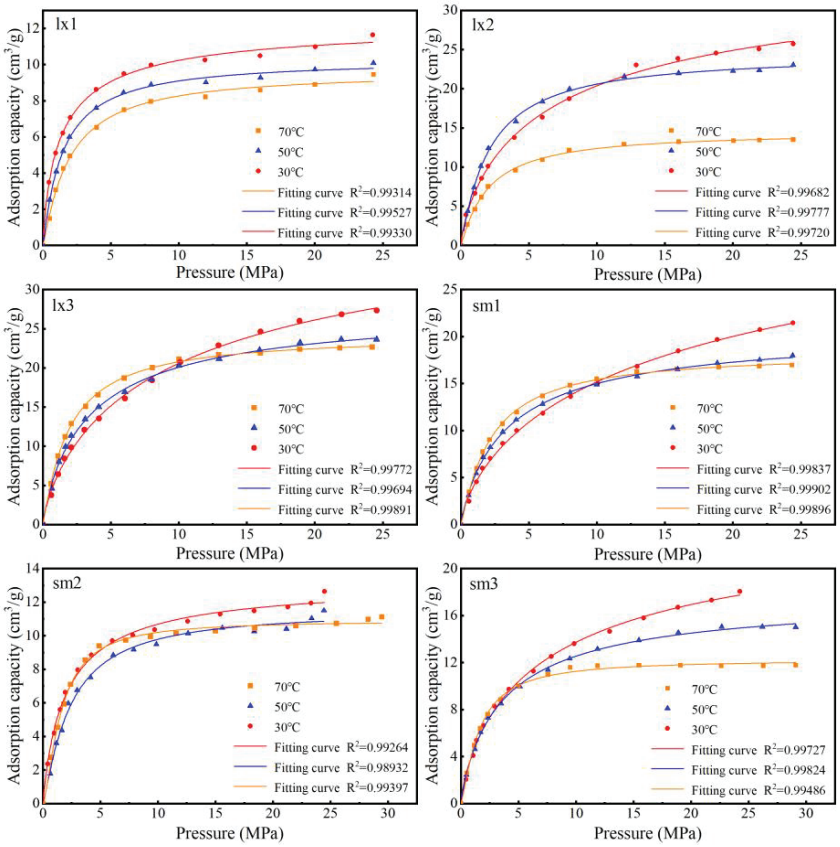

Figure 3. Characteristic diagram of isothermal adsorption curves under different temperatures (30 °C, 50 °C, 70 °C) and pressure conditions in the Shenfu-Linxing block.

In the range of low pressure (0–5 MPa), an abrupt and substantial increase in the coal's adsorption capacity is observed as pressure rises, suggesting a strong influence of pressure on the coal's adsorption capacity during this phase. Nevertheless, in the medium-pressure range, the rate of increase in adsorption capacity significantly diminishes (5–10 MPa). In the high-pressure section (>10 MPa), the adsorption capacity of the coal gradually reaches a plateau, indicating that in deep coal seams under high pressure, the influence of pressure on the coal's adsorption capacity becomes less significant [46,47].

The V_L of coal is 11.97–32.30 m^3/t, and the P_L is 1.49–4.79 MPa. As the temperature increases, the V_L decreases (Table 2), and the adsorption capacity of the coal decreases at the same pressure (Figure 3). However, in the low-pressure range, the adsorption capacity does not vary significantly with temperature, as evidenced by the overlapping isotherm adsorption lines. Hence, at shallower burial depths, the effect of temperature on adsorption capacity is comparatively minor. As the burial depth increases, in the medium- to high-pressure section, the adsorption capacity is significantly affected by temperature.

Therefore, the adsorption capacity of the in situ coal seam is jointly controlled by the temperature and pressure of the formation. Pressure has a positive impact on the adsorption capacity of coal, while temperature has a negative impact on it [48]. Under the combined influence of temperature and pressure, the adsorption capacity is predominantly controlled by the pressure in the low-pressure region. As the burial depth increases, the

negative effect of temperature begins to emerge, and the coal samples quickly reach their maximum adsorption capacity under high-temperature conditions, resulting in a reduction of P_L (Table 2).

Table 2. V_L and P_L values of coal samples under different temperature and pressure conditions.

Sample No.	30 °C		50 °C		70 °C	
	V_L	P_L	V_L	P_L	V_L	P_L
lx1	11.97	1.49	10.61	1.60	10.20	2.12
lx2	29.57	4.18	25.00	2.19	14.73	2.11
lx3	32.30	5.58	26.35	2.99	24.63	2.01
sm1	26.45	6.75	19.83	3.12	18.91	2.34
sm2	12.84	1.95	12.02	2.56	11.68	1.70
sm3	20.50	4.55	16.82	3.26	12.93	1.66

4.3. Gas Content Characteristics

4.3.1. Adsorbed Gas Content

Based on the Langmuir model, an improved prediction equation for the adsorption gas volume in the Linxing-Shenfu block was built. Conversely, the Ro of the collected coal samples varies slightly, ranging from 0.95% to 1.33%, and the data are limited (Table 1). To enhance the precision of the model's data fitting, isothermal adsorption experimental data from other blocks in Eastern Ordos Basin, such as Baode, Liulin, and Hancheng, were collected and used.

As illustrated in Figure 4, the relationship between P_L and temperature adheres to an exponential function. Meanwhile, the relationship between P_L and the maximum Ro displays a "U"-shaped trend, initially decreasing and then increasing as the maximum Ro rises. Furthermore, V_L exhibits a linear positive relationship with the maximum Ro and a negative relationship with temperature.

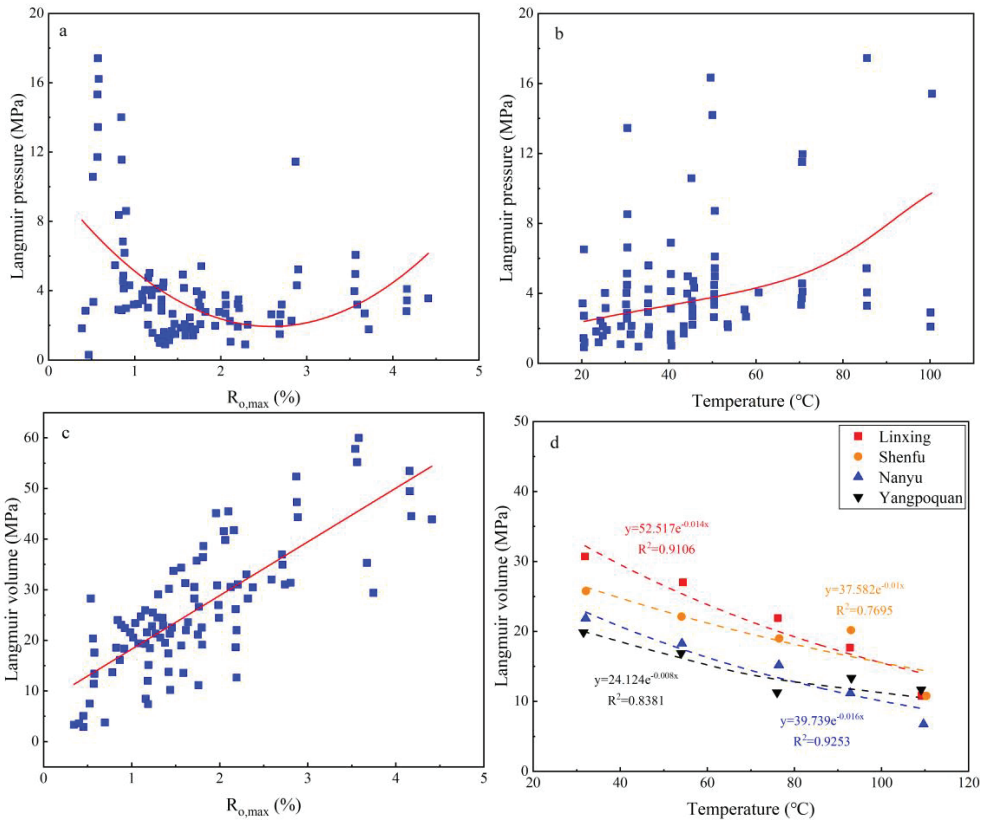

Figure 4. (**a**) Relationship between Langmuir pressure and $R_{o,max}$; (**b**) Relationship between Langmuir pressure and temperature; (**c**) Relationship between Langmuir volume and $R_{o,max}$; (**d**) Relationship between Langmuir volume and temperature.

According to the isothermal adsorption experimental data, combined with the analysis of the interactions and correlations between the single factors mentioned above, a nonlinear analysis method is used to improve the Langmuir equation and establish a prediction equation for the Langmuir constant (Equations (5) and (6)).

$$V_L = (13.89R_{o,max} + 11.97)e^{-0.0071T}\ R^2 = 0.83 \quad (5)$$

$$P_L = (0.71R_{o,max} - 3.58R_{o,max} + 5.52)e^{0.014T}\ R^2 = 0.67 \quad (6)$$

The above equation is brought into the Langmuir equation to obtain the prediction model of adsorbed gas volume suitable for the Shenfu-Linxing block (Equation (7)).

$$V = \frac{P(13.89R_{o,max} + 11.97)e^{-0.0071T}}{P + (0.71R_{o,max} - 3.58R_{o,max} + 5.52)e^{0.014T}} \quad (7)$$

Provided that the geothermal and pressure gradients within the Shenfu-Linxing block remain consistent, with a pressure gradient of 0.9 MPa/hm, a geothermal gradient of 2.4 °C/hm, and a surface temperature of 20 °C, it is possible to determine the adsorbed gas volume for different Ro values and burial depths. Eight samples with measured gas content from the Shenfu-Linxing block were selected to validate the prediction model for adsorption gas content, and the results are summarized in Table 3. The predicted adsorbed gas content is 2.86–15.28 m^3/t. The error rates ranged from −4.81% to −25%, with an average error rate of −17.19%. The main reason for this error is the presence of free gas in deep coal reservoirs, which results in predicted adsorbed gas content being lower than the measured total gas content. The difference between the two basically represents the content of free gas (0.72–5.09 m^3/t). The observed free gas content is notably minimal, aligning with the expected low levels of free gas typically found in environments with restricted porosity under in situ conditions [11].

Table 3. Validation of prediction model for adsorbed gas content.

Sample No.	Depth (m)	R_o (%)	Measured Total Gas Content (m^3/t)	Predicted Adsorbed Gas Content (m^3/t)	Error Rate (%)
L1	2086.65	1.32	15.04	14.32	−4.81
L2	1786	1.33	16.39	14.98	−8.58
L3	1855.7	1.22	17.24	13.81	−19.92
L4	1800.9	1.11	15.78	12.86	−18.52
S1	1923.7	1.32	18.09	14.63	−19.11
S2	2157.9	1.44	20.37	15.28	−25.00
S3	2027.2	1.38	19.29	15.00	−22.26
S4	2029.3	1.41	18.94	15.27	−19.35
Average					−17.19

4.3.2. Free Gas Content

The average porosity of coal in the Shenfu-Linxing block is 4%, with an average apparent density of 1.46 t/m^3, and a stress decline coefficient of 1. Figure 5 illustrates the variation of free gas content with burial depth and water saturation. With greater burial depth, the free gas content shows a progressive rise, though the rate of increase diminishes over time. This pattern suggests that while deeper layers contain more free gas, the growth rate is tempered by factors like reduced coal porosity at greater depths. On the other hand, higher water saturation levels lead to a decline in free gas content. At 100% water saturation, the free gas content reaches 0 m^3/t, indicating that all pores are filled with water and no free gas remains.

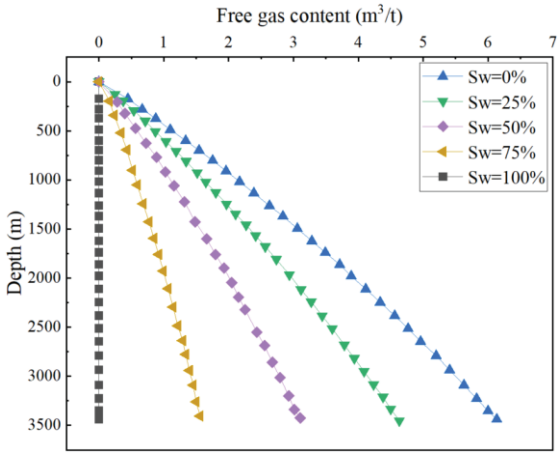

Figure 5. Variation of free gas content with depth.

4.3.3. Dynamic Coupling of Methane Content in Different Phase States

Based on the predictive models for adsorbed and free gas, a clear relationship exists between the total gas content in the coal reservoir of the Shenfu-Linxing block and its depth. As depicted in Figure 6, the saturated adsorption capacity rises initially with greater burial depth before eventually declining. The depth at which the gas content of coal reaches its peak before gradually declining with further burial is referred to as the critical transition depth, which is influenced by factors such as the geothermal gradient, porosity, water saturation, and in situ stress. The overall gas content and the critical transition depth are determined by the interplay between adsorbed and free gas at specific burial depths. Adsorbed gas exhibits a distinct critical transition depth, whereas free gas content shows a linear rise as burial depth increases [49]. Additionally, with rising water saturation in deep coal seams, the adsorbed gas content steadily declines while the free gas content rises, leading to a shallower critical transition depth (Figure 6).

4.4. CBM Occurrence Mechanism

4.4.1. Occurrence Mechanism of Adsorbed Gas

Adsorbed gas can occur in pores through two modes: single-layer adsorption and micropore filling. The theoretical single-layer adsorption capacity is derived from the specific surface area and volume of the pores. By comparing this theoretical adsorption capacity (TAC) with the actual single-layer adsorption capacity obtained from isothermal adsorption experiments, it can be determined whether the adsorbed gas occurs primarily through single-layer adsorption or micropore filling.

Hypothesis I. *The gas is completely adsorbed by a single layer in the pores. Based on the single-layer adsorption theory, the TAC can be calculated by the following equation (Equation (8)).*

$$V_{tm} = \frac{SSA}{A_m \cdot N_a} \times 22.4 \times 1000 \tag{8}$$

Hypothesis II. *The gas is completely contained in the pores in the form of micropore filling. According to the microporous filling theory, the TAC can be determined using the following formula (Equation (9)).*

$$V_{tp} = \frac{PV}{V_{mo} \cdot N_a} \times 22.4 \times 1000 \tag{9}$$

where, V_{tm} is the theoretical adsorption gas volume of single layer, m^3/t; V_{tp} is the theoretical adsorption gas volume of micropore filling, m^3/t; SSA is the specific surface area of pores, m^2/g; PV is the pore volume, m^3/g; A_m is the area occupied by a single methane molecule, 1.134×10^{-19} m^2; V_{mo} is the volume occupied by a single methane molecule, 2.873×10^{-29} m^3; N_a is the Avogadro constant, 6.02×10^{23}.

For Hypothesis I, Figure 7 shows that the micropore adsorption capacity closely matches the TAC. This suggests that the micropores in the deep coal reservoirs of the Shenfu-Linxing block provide the main adsorption sites for methane. For Hypothesis 2, the micropore adsorption capacity is basically slightly higher than the theoretical adsorption capacity, and the mesopore adsorption capacity is low, far lower than the theoretical adsorption capacity.

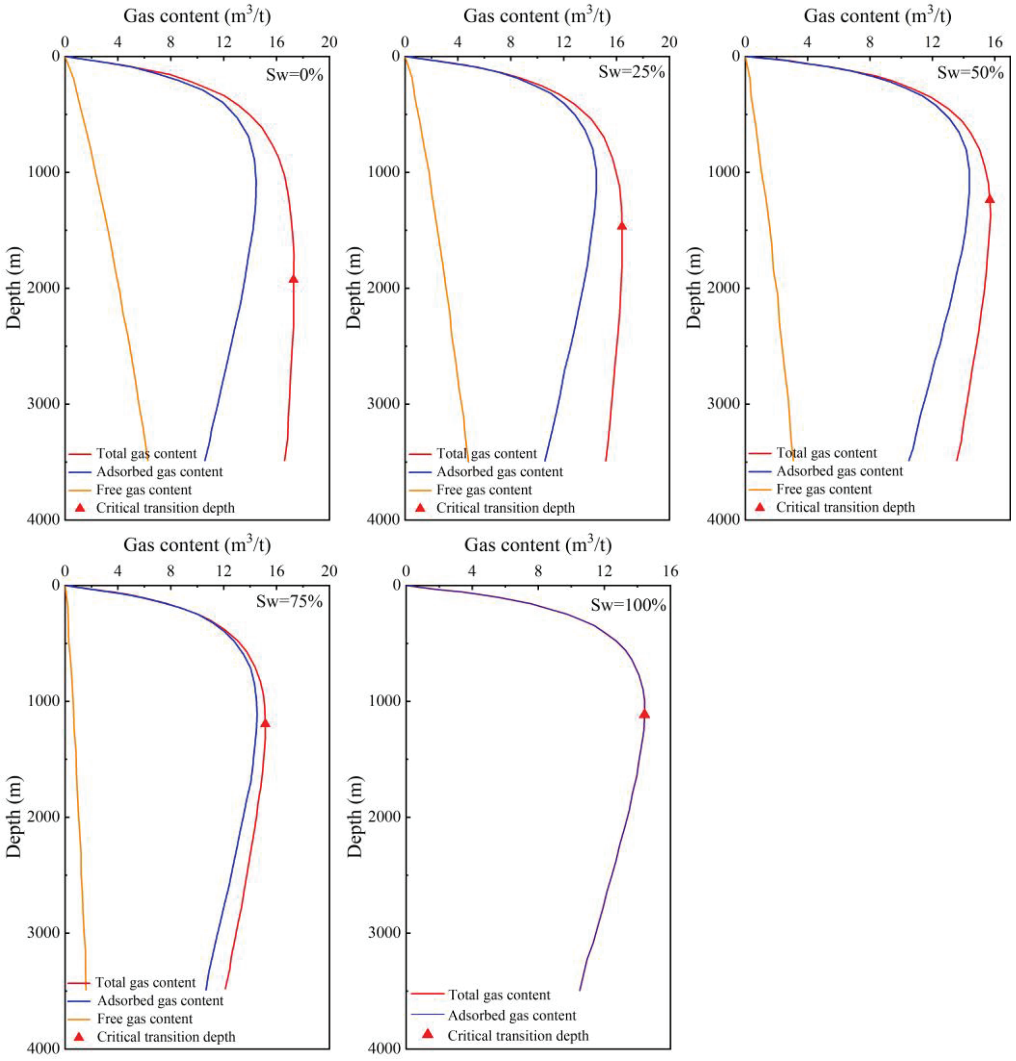

Figure 6. Variation of gas content and critical transition depth with burial depth of coal seam under different water saturation conditions.

Integrating the adsorption potential theory, the adsorption potential on solid surfaces is primarily influenced by curvature. The micropore curvature is the largest in micropores, mesopores, and macropores, and the adsorption potential energy is the highest. The microporous surface exhibits a strong adsorption potential, favoring the adsorption of methane molecules [18]. Thus, when sufficient adsorption space is available, methane molecules are primarily stored in micropores through a filling mechanism. According to

the calculation model, adsorbed gas is characterized by methane molecules exclusively occupying micropores in a filled state, with no such filling observed in mesopores [50,51].

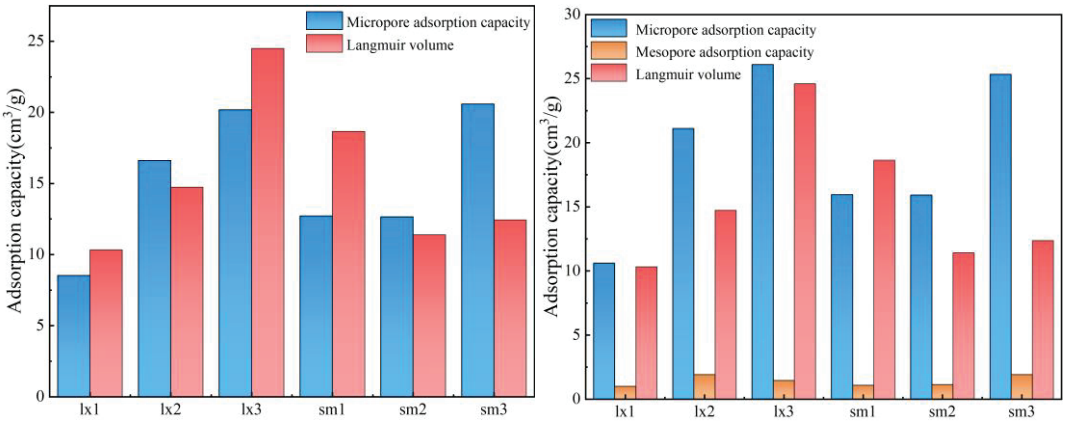

Figure 7. Comparison of adsorption capacity of micropores and mesopores with Langmuir volume (left: Hypothesis I, right: Hypothesis II).

The occurrence characteristics of adsorbed gas are related to the development of pore structure, and the different pore structure results in different occurrence mechanisms. A large number of micropores are developed in the deep coal of the Shenfu-Linxing block. Although the pore volume of micropores is much smaller than that of mesopores, the total pore volume of micropores is relatively high due to the high proportion of micropores and the low content of mesopores, providing sufficient space for the filling of methane molecules [52]. For the shallow and middle reservoirs with relatively low micropore content, there are certain differences in the occurrence mechanism of adsorbed gas. When the volume of micropores is insufficient to accommodate all methane molecules, a portion of them may be stored in mesopores through monomolecular adsorption.

4.4.2. Occurrence Mechanism of Free Gas

Generally, large porosity allows for greater amounts of free gas in the pores. Based on the calculation model for gas content, and considering the actual formation conditions and water saturation characteristics of the Shenfu-Linxing block, the free gas content ranges from 2.03 to 3.26 m^3/t, while the adsorbed gas content ranges from 9.58 to 19.16 m^3/t. The adsorbed gas content is significantly higher than the free gas content. This is mainly because the deep coal reservoirs in the Shenfu-Linxing block predominantly develop micropores, with a low content of mesopores and macropores, resulting in low free gas content and low gas saturation in coal seams [43,52].

4.5. Phase Evolution of Deep CBM

Through the calculation of gas content in the deep coal, along with the analysis of their occurrence characteristics, it is showed that the adsorbed gas content exhibits a pattern of "rapid growth—slow growth—slow reduction" with increasing burial depth. Conversely, the free gas content follows a pattern of "stable growth—slow growth—gradual stabilization". The total gas content can be divided into four stages: "rapid growth—slow growth—stable—slow reduction". Besides the effects of burial depth, temperature, and pressure, the gas content is also influenced by the coal metamorphism degree and water saturation. As the coal metamorphism degree increases, both adsorbed and free gas contents increase [15]. As water saturation rises, the contents of both adsorbed and free gas decline, resulting in a decrease in the overall gas content (Figure 8).

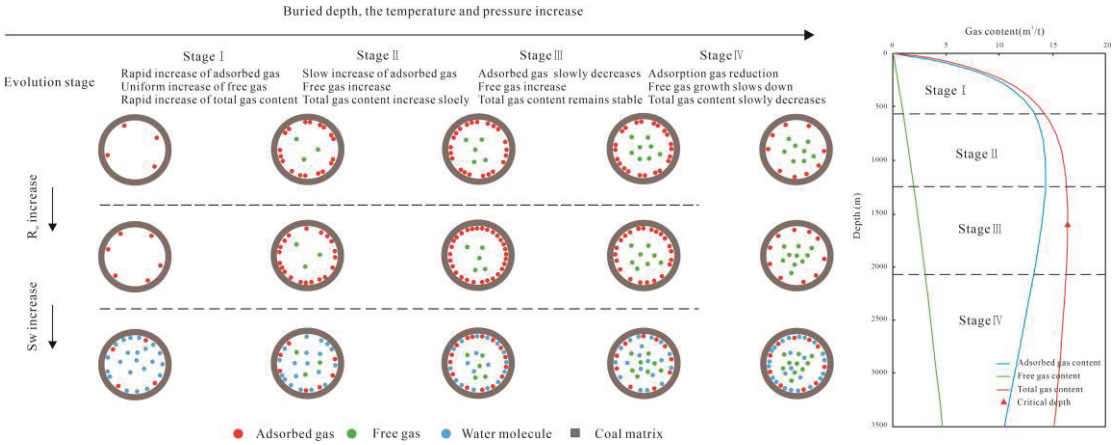

Figure 8. Phase evolution model of deep CBM (modified from [15]).

When the coal burial depth is below 600 m, the total gas content shows a significant upward trend. At this stage, the beneficial effect of pressure on adsorbed gas content surpasses the adverse effect of temperature, leading to a rapid rise in adsorbed gas content as depth increases. Meanwhile, the free gas content, although relatively small, shows a steady increase. Overall, the total gas content displays rapid growth characteristics.

In the depth range of 600 to 1300 m, the total gas content experiences a gradual increase. During this phase, while the positive influence of pressure remains notable, the negative effect of temperature on adsorbed gas content becomes more pronounced. Consequently, the rate of adsorbed gas content growth diminishes. On the other hand, free gas content maintains a consistent upward trend. Overall, the total gas content exhibits characteristics of slow growth during this period.

When the buried depth ranges from 1300 to 2100 m, the total gas content remains stable. At this stage, the adverse effect of temperature on adsorbed gas content surpasses the beneficial influence of pressure, causing a gradual decline in adsorbed gas. Meanwhile, free gas content continues to rise. This equilibrium between declining adsorbed gas and increasing free gas results in the total gas content stabilizing. Typically, this stage marks the appearance of a critical depth.

At depths exceeding 2100 m, the total gas content shows a gradual decline. During this phase, the negative influence of temperature on adsorbed gas content remains dominant, causing a steady reduction in adsorbed gas as depth increases. Concurrently, the proportion of micropores rises, while mesopores and macropores become scarcer, reducing the storage capacity for free gas within the coal seam. As burial depth increases further, the growth rate of free gas content gradually slows down until it stabilizes. Consequently, the total gas content exhibits characteristics of slow reduction during this stage.

5. Conclusions

This study is based on the isothermal adsorption characteristics of deep coal seams, combined with vitrinite reflectance, temperature, pressure, and water saturation parameters, to establish prediction models for coalbed methane content in different phases, revealing the occurrence mechanism of deep coalbed methane, and the following conclusions are drawn.

The adsorption capacity is obviously controlled by the positive effect of pressure in the shallow buried area and is less affected by the temperature. The overall performance is that the buried depth increases and the adsorption capacity increases. In the deep buried area, the adsorption capacity is obviously controlled by the negative effect of temperature.

Based on isothermal adsorption experiments under varying temperature and pressure, and incorporating parameters such as R_o, temperature, pressure, and water saturation, a prediction model for adsorbed and free gas content was constructed with an average error rate of less than 20%. The adsorbed gas content first rises and then declines as burial depth increases, whereas the free gas content grows before eventually leveling off. With higher water saturation, the share of adsorbed gas steadily diminishes, while the proportion of free gas rises.

Adsorbed gas is predominantly stored in coal micropores through a filling mechanism, whereas free gas is largely contained in mesopores and macropores in an unbound state. With increasing burial depth, the total gas content follows a trend of "rapid growth—slow growth—stability—slow reduction".

Author Contributions: Conceptualization, L.M. and F.Y.; methodology, L.M.; software, L.M.; validation, J.Y. (Jianghao Yang) and S.T.; formal analysis, J.Y. (Jiang Yang) and Y.C.; investigation, L.M.; resources, W.W.; data curation, C.L.; writing—original draft preparation, L.M.; writing—review and editing, F.Y. and S.T.; visualization, B.Z.; supervision, S.T.; project administration, S.T.; funding acquisition, S.T. All authors have read and agreed to the published version of the manuscript.

Funding: This work was financially supported by the National Natural Science Foundation of China (42272200); The Technology Project of Huaneng Group Headquarters (Medium-Deep Low-Rank Coalbed Methane Resource Potential Evaluation and Key Development Technologies of Zhalainuoer Coalfield, HNKJ23-H51); The Science and Technology Major Project of China National Petroleum Corporation (2023ZZ18-03); The Science and Technology Major Project of Changqing Oilfield (2023DZZ01). The authors also thank the reviewers and editors for their constructive comments and suggestions on improving this manuscript.

Data Availability Statement: The data presented in this study are available upon request from the corresponding author due to privacy restrictions.

Acknowledgments: The authors are grateful to the editor and anonymous reviewers for their careful reviews and detailed comments, which helped to substantially improve the manuscript.

Conflicts of Interest: Author Litao Ma, Jianghao Yang, Wei Wang, Cheng Liu, Bo Zhang and Jiang Yang were employed by the company Zhalainuoer Coal Industry Co., Ltd. Author Yi Cui was employed by the company Zhalainuoer Coal Industry Co., Ltd. The remaining authors declare that the research was conducted in the absence of any commercial or financial relationships that could be construed as a potential conflict of interest.

References

1. Tao, S.; Chen, S.D.; Tang, D.Z.; Zhao, X.; Xu, H.; Li, S. Material composition, pore structure and adsorption capacity of low-rank coals around the first coalification jump: A case of eastern Junggar Basin, China. *Fuel* **2018**, *211*, 804–815. [CrossRef]
2. Xu, H.; Tang, D.; Tao, S.; Li, S.; Tang, S.; Chen, S.; Zong, P.; Dong, Y. Differences in geological conditions of deep and shallow coalbed methane and their formation mechanisms. *Coal Geol. Explor.* **2024**, *52*, 33–39.
3. Chalmers, G.R.L.; Marc Bustin, R. On the effects of petrographic composition on coalbed methane sorption. *Int. J. Coal Geol.* **2007**, *69*, 288–304. [CrossRef]
4. Tao, S.; Pan, Z.J.; Tang, S.L.; Chen, S.D. Current status and geological conditions for the applicability of CBM drilling technologies in China: A review. *Int. J. Coal Geol.* **2019**, *202*, 95–108. [CrossRef]
5. Ye, J.C.; Tao, S.; Zhao, S.P.; Li, S.; Chen, S.D.; Cui, Y. Characteristics of methane adsorption/desorption heat and energy with respect to coal rank. *J. Nat. Gas. Sci. Eng.* **2022**, *99*, 104445. [CrossRef]
6. Qin, Y.; Moore, T.A.; Shen, J.; Yang, Z.B.; Shen, Y.L.; Wang, G. Resources and geology of coalbed methane in China: A review. *Int. Geol. Rev.* **2018**, *60*, 777–812. [CrossRef]
7. Tao, S.; Tang, D.; Xu, H.; Li, S.; Geng, Y.; Zhao, J.; Wu, S.; Meng, Q.; Kou, X.; Yang, S.; et al. Fluid velocity sensitivity of coal reservoir and its effect on coalbed methane well productivity: A case of Baode Block, northeastern Ordos Basin, China. *J. Pet. Sci. Eng.* **2017**, *152*, 229–237. [CrossRef]

8. Men, X.Y.; Tao, S.; Liu, Z.X.; Tian, W.G.; Chen, S.D. Experimental study on gas mass transfer process in a heterogeneous coal reservoir. *Fuel Process Technol.* **2021**, *216*, 106779. [CrossRef]
9. Hou, H.; Shao, L.; Guo, S.; Li, Z.; Zhang, Z.; Yao, M.; Zhao, S.; Yan, C. Evaluation and genetic analysis of coal structures in deep Jiaozuo Coalfield, northern China: Investigation by geophysical logging data. *Fuel* **2017**, *209*, 552–566. [CrossRef]
10. Li, J.; Wu, Q.; Jin, W.; Lu, J.; Nan, Z. Logging evaluation of free-gas saturation and volume content in Wufeng-Longmaxi organic-rich shales in the Upper Yangtze Platform, China. *Mar. Pet. Geol.* **2019**, *100*, 530–539. [CrossRef]
11. Tao, S.; Zhao, X.; Tang, D.; Deng, C.; Meng, Q.; Cui, Y. A model for characterizing the continuous distribution of gas storing space in low-rank coals. *Fuel* **2018**, *233*, 552–557. [CrossRef]
12. Li, Y.; Gao, S.; Wu, P.; Xu, L.; Ma, L.; Hu, W.; Yang, J. Evaluation and correction of the prediction model for free gas content in deep coalbed methane: A Case study of deep coalbed methane in the eastern margin of Ordos Basin. *Acta Pet. Sin.* **2023**, *44*, 1892–1902.
13. Tao, S.; Chen, S.; Pan, Z. Current status, challenges, and policy suggestions for coalbed methane industry development in China: A review. *Energy Sci. Eng.* **2019**, *7*, 1059–1074. [CrossRef]
14. Xu, H.; Pan, Z.; Hu, B.; Liu, H.; Sun, G. A new approach to estimating coal gas content for deep core sample. *Fuel* **2020**, *277*, 118246. [CrossRef]
15. Yang, J.; Feng, P.; Tang, S.; Tang, D.; Wang, M.; Li, S.; Zhao, Y.; Li, Z. Phase control factors and content prediction model of deep coalbed methane in Daning-Jixian Block. *Acta Pet. Sin.* **2023**, *44*, 1879–1891.
16. Jing, G.; Chen, Z.; Hui, G. A novel model to determine gas content in naturally fractured shale. *Fuel* **2021**, *306*, 121714. [CrossRef]
17. Shi, J.; Chang, Y.; Wu, S.; Xiong, X.; Liu, C.; Feng, K. Development of material balance equations for coalbed methane reservoirs considering dewatering process, gas solubility, pore compressibility and matrix shrinkage. *Int. J. Coal Geol.* **2018**, *195*, 200–216. [CrossRef]
18. Feng, R. A Method to Evaluated Gas Content with Coalbed Methane Reservoir Based on Adsorption Theory and Production Analysis. *Geofluids* **2022**, *1*, 7341886. [CrossRef]
19. Liu, D.; Yao, Y.; Chang, Y. Measurement of adsorption phase densities with respect to different pressure: Potential application for determination of free and adsorbed methane in coalbed methane reservoir. *Chem. Eng. J.* **2022**, *446*, 137103. [CrossRef]
20. Wang, Y.; Kang, J.; Zhou, F.; Yuan, L.; Pan, Z. Evaluation of lost gas in the borehole drilling stage: Implication for the direct method of coalbed methane content determination. *J. Nat. Gas. Sci. Eng.* **2022**, *105*, 104711. [CrossRef]
21. Ji, Y.S.; Ma, D.M.; Chen, Y.; Li, W.B.; Li, G.F.; Zheng, C.; Ma, Z.Y.; Wang, L.Y.; Wang, X. Study on gas content variation and main controlling of low-rank coal in Huanglong Jurassic coalfield. *Energ. Explor. Exploit.* **2023**, *41*, 561–584. [CrossRef]
22. Xiong, X.; Yan, X.; Xu, F.; Li, S.; Nie, Z.; Feng, Y.; Liu, Y.; Chen, M.; Sun, J.; Zhou, K.; et al. Analysis of multi-factor coupling control mechanism, desorption law and development effect of deep coalbed methane. *Acta Pet. Sin.* **2023**, *44*, 1812–1826+1853.
23. Li, S.; Qin, Y.; Tang, D.; Shen, J.; Wang, J.; Chen, S. A comprehensive review of deep coalbed methane and recent developments in China. *Int. J. Coal Geol.* **2023**, *279*, 104369. [CrossRef]
24. Xie, Y.G.; Qin, Y.; Meng, S.Z.; Pan, X.Z.; Gao, L.J.; Duan, C.J. Study on occurrence characteristics and controlling factors of Permian Deep Coalbed Methane in Linxing Block. *Fresen Environ. Bull.* **2022**, *31*, 3408–3414.
25. Zhang, Z.; Qin, Y.; Yang, Z.; Li, G.; You, Z. Primary Controlling Factors of Coalbed Methane Well Productivity and High Productive Well Patterns in Eastern Yunnan and Western Guizhou, China. *Nat. Resour. Res.* **2023**, *32*, 2711–2726. [CrossRef]
26. Cui, S.; Wu, P.; Zhao, F.; Niu, Y.; Cai, W.; Wang, B. Shale Gas Accumulation Factors and Enrichment Area Prediction in Linxing block, Eastern Margin of the Ordos Basin. *Geoscience* **2022**, *36*, 1271–1280.
27. Wang, D.; Cheng, Y.; Yuan, L.; Wang, C.; Wang, L. Implications of Geological Conditions on Gas Contents: A Case Study in the Pingdingshan Coalfield. *Energ. Fuel* **2023**, *37*, 6465–6478. [CrossRef]
28. Guo, J.; Zhang, Z.; Xiao, H.; Zhang, C.; Zhu, L.; Wang, C. Quantitative interpretation of coal industrial components using a gray system and geophysical logging data: A case study from the Qinshui Basin, China. *Front. Earth Sci.* **2023**, *10*, 1031218. [CrossRef]
29. Li, Y.; Wang, Z.; Tang, S.; Elsworth, D. Re-evaluating adsorbed and free methane content in coal and its ad- and desorption processes analysis. *Chem. Eng. J.* **2022**, *428*, 131946. [CrossRef]
30. Pan, Z. Modeling of coal swelling induced by water vapor adsorption. *Front. Chem. Sci. Eng.* **2012**, *6*, 94–103. [CrossRef]
31. Liu, J.; Chang, S.; Zhang, S.; Li, Y.; Hao, Y.; He, G.; He, Y.; Liu, B. Prediction of coalbed methane content based on seismic identification of key geological parameters: A case in a study area, Southern Qinshui Basin. *Acta Geophys.* **2023**, *71*, 2645–2662. [CrossRef]
32. Qin, Y.; Song, Q.; Fu, X. Feasibility Study on Co extraction of Coalbed Methane and Conventional Oil and Gas—Adsorption Effect under Equilibrium Water Conditions in Deep Coal Reservoirs. *Nat. Gas. Geosci.* **2005**, *04*, 492–498.
33. Ma, Z.Y.; Tao, S.; Gao, L.C.; Cui, Y.; Jing, Q.H.; Chen, S.D.; He, W.; Guo, J.; Hai, L.F. Detailed Characterization of Microscopic Pore Structure in Low-Rank Coal: A Case Study of Zhalainuoer Coalfield. *Nat. Resour. Res.* **2024**, *33*, 2261–2277. [CrossRef]
34. Xu, H.; Tang, D.Z.; Liu, D.M.; Tang, S.H.; Yang, F.; Chen, X.Z.; He, W.; Deng, C.M. Study on coalbed methane accumulation characteristics and favorable areas in the Binchang area, southwestern Ordos Basin, China. *Int. J. Coal Geol.* **2012**, *95*, 1–11. [CrossRef]

35. Tang, X.; Zhang, J.; Shan, Y.; Xiong, J. Upper Paleozoic coal measures and unconventional natural gas systems of the Ordos Basin, China. *Geosci. Front.* **2012**, *3*, 863–873. [CrossRef]
36. Xue, G.; Liu, H.; Li, W. Deformed coal types and pore characteristics in Hancheng coalmines in Eastern Weibei coalfields. *Int. J. Min. Sci. Technol.* **2012**, *22*, 681–686. [CrossRef]
37. Chen, H.; Tian, W.; Chen, Z.; Zhang, Q.; Tao, S. Genesis of Coalbed Methane and Its Storage and Seepage Space in Baode Block, Eastern Ordos Basin. *Energies* **2022**, *15*, 81. [CrossRef]
38. *GB/T 30732-2014*; Proximate Analysis of Coal. Instrumental Method. Standardization Administration of China: Beijing, China, 2014. (In Chinese)
39. *GB/T 8899-2013*; Determination of Maceral Group Composition and Minerals in Coal. Standardization Administration of China: Beijing, China, 2013. (In Chinese)
40. *GB/T 6948-2008*; Method of Determining Microscopically the Reflectance of Vitrinite in Coal. Standardization Administration of China: Beijing, China, 2008. (In Chinese)
41. *GB/T 19560-2008*; Experimental Method of High-Pressure Isothermal Adsorption to Coal. Standardization Administration of China: Beijing, China, 2008. (In Chinese)
42. Song, D.; Ji, X.; Li, Y.; Zhao, H.; Song, B.; He, K. Heterogeneous development of micropores in medium-high rank coal and its relationship with adsorption capacity. *Int. J. Coal Geol.* **2020**, *226*, 103497. [CrossRef]
43. Li, H.; Zhou, G.; Chen, S.; Li, S.; Tang, D. In Situ Gas Content and Extraction Potential of Ultra-Deep Coalbed Methane in the Sichuan Basin, China. *Nat. Resour. Res.* **2025**, *34*, 563–579. [CrossRef]
44. Feng, P.; Li, S.; Tang, S.; Tang, D.; Zhang, C.; Yang, J.; Liu, N.; Zhong, G. Estimation of Adsorption Isotherm for Deep Coalbed Methane: A Monolayer-Filling Model Based on Pore Fractal Dimension. *Energ. Fuel* **2024**, *38*, 1987–2000. [CrossRef]
45. Feng, P.; Li, S.; Tang, S.; Tang, D.; Zhang, C.; Zhong, G.; Fan, L.; Zhang, Z. Unraveling the Nanopores Evolution: Chemical Structure Control in Coal during Coalification. *Energ. Fuel* **2024**, *38*, 8688–8699. [CrossRef]
46. Zhang, D.; Cui, Y.; Liu, B.; Li, S.; Song, W.; Lin, W. Supercritical Pure Methane and CO_2 Adsorption on Various Rank Coals of China: Experiments and Modeling. *Energ. Fuel* **2011**, *25*, 1891–1899. [CrossRef]
47. Krooss, B.M.; van Bergen, F.; Gensterblum, Y.; Siemons, N.; Pagnier, H.J.M.; David, P. High-pressure methane and carbon dioxide adsorption on dry and moisture-equilibrated Pennsylvanian coals. *Int. J. Coal Geol.* **2002**, *51*, 69–92. [CrossRef]
48. Wang, Q.; Shen, J.; Glover, P.; Lorinczi, P.; Duncan, I. Improving the Prediction of Production Loss in Heterogeneous Tight Gas Reservoirs Using Dynamic Threshold Pressure. *Energ. Fuel* **2022**, *36*, 11991–12003. [CrossRef]
49. Ma, X.; Song, Y.; Liu, S.; Jiang, L.; Hong, F. Quantitative research on adsorption capacity evolution of medium-high rank coal reservoirs in geological history: A case study from Hancheng area in the Ordos Basin. *Acta Pet. Sin.* **2014**, *35*, 1080–1086.
50. Wu, J.; Tang, D.; Li, S.; Ren, P. Characteristics and influence factors of pore structure of coal reservoirs in the eastern margin of Ordos basin. *Coal Geol. Explor.* **2017**, *45*, 58–65.
51. Fu, X.; Qin, Y.; Wang, G.G.X.; Rudolph, V. Evaluation of gas content of coalbed methane reservoirs with the aid of geophysical logging technology. *Fuel* **2009**, *88*, 2269–2277. [CrossRef]
52. Ge, X.; Liu, D.; Cai, Y.; Wang, Y. Gas Content Evaluation of Coalbed Methane Reservoir in the Fukang Area of Southern Junggar Basin, Northwest China by Multiple Geophysical Logging Methods. *Energies* **2018**, *11*, 1867. [CrossRef]

energies

MDPI

Article

Geochemical Characteristics of Crude Oil and Oil–Source Correlations in the Yongfeng Sub-Sag of the Bogda Mountain Front Belt

Xiangcan Sun [1,2,3], Jianwei Wu [1,2,3], Xingui Zhou [1,2,3], Yongjin Gao [1,2,3], Youxing Yang [1,2,3], Zhongkai Bai [1,2,3], Kun Yuan [1,2,3], Lei Wen [1,2,3,*] and Yi Chen [1,2,3,*]

[1] Oil & Gas Survey, China Geological Survey, Beijing 100083, China; sunxiangcan@mail.cgs.gov.cn (X.S.); wujianwei@mail.cgs.gov.cn (J.W.); zhouxingui@mail.cgs.gov.cn (X.Z.); gaoyongjin@mail.cgs.gov.cn (Y.G.); yangyouxing@mail.cgs.gov.cn (Y.Y.); baizhongkai@mail.cgs.gov.cn (Z.B.); yuankun@mail.cgs.gov.cn (K.Y.)
[2] State Key Laboratory of Continental Shale Oil, Beijing 100029, China
[3] Key Laboratory of Unconventional Oil & Gas, China Geological Survey, Beijing 100029, China
* Correspondence: wenlei@mail.cgs.gov.cn (L.W.); chenyi@mail.cgs.gov.cn (Y.C.)

Abstract: The exploration level of the Bogda Mountain front belt is relatively low, and the research on hydrocarbon accumulation is limited, resulting in unclear sources of discovered oil. To further investigate the geochemical characteristics and sources of crude oil in the Bogda Mountain front belt, this study conducted geochemical experimental analysis and oil–source correlations on crude oil and hydrocarbon source rock samples from the Permian Lucaogou Formation in the Yongfeng sub-sag and surrounding areas of the Bogda Mountain front belt. By using gas chromatography–mass spectrometry technology, the geochemical characteristics of saturated hydrocarbons and aromatic compounds were analyzed. Combined with stable carbon isotopes of saturated hydrocarbons and aromatic hydrocarbons, the organic matter source, maturity, and sedimentary environment were determined. The research results indicate that the crude oil from Well Xyd 1 exhibits mature characteristics, and the source material was deposited in a reducing to weakly oxidizing, weakly reducing environment. The source rocks of the Lucaogou Formation in Well Xyd 1 were formed in a reducing, semi-saline–saline sedimentary environment, while those from the Gjg and Dhs outcrops developed in a weakly oxidizing–weakly reducing, non-high-salinity, weakly stratified sedimentary environment. Carbon isotope, terpane, and isoalkane characteristics confirm a significant genetic relationship between the crude oil from Well Xyd 1 and the local Luzhaogou Formation source rocks. The source rocks of the Luzhaogou Formation in the Yongfeng sub-sag exhibit strong heterogeneity, with significant differences in sedimentary environments and parent materials in their spatial distribution. Maturity analysis indicates that the Luzhaogou Formation source rocks in Well Xyd 1 have reached a mature stage, whereas those from the Gjg and Dhs outcrops are at a relatively low maturity level.

Keywords: geochemical characteristics; oil–source correlations; Lucaogou Formation; Yongfeng sub-sag; Bogda Mountain front belt

1. Introduction

The Bogda Mountain front belt is located in the eastern part of the thrust belt in the southern margin of the Junggar Basin, with a low degree of oil and gas exploration. In the early stage, oil companies conducted extensive oil and gas exploration and research work in the western section of the thrust belt in the southern margin of the Junggar Basin, and

successively discovered Dushanzi, Qigu, Hutubi, and other oil and gas fields [1,2], showing good oil and gas exploration prospects in the southern margin of the Junggar Basin. In recent years, significant progress has been made in the exploration of the eastern part of the thrust belt in the southern margin of the Junggar Basin. The exploration is mainly concentrated in the sag area in the northern margin of Bogda Mountain, and a billion-ton oil field has been discovered in Jimsar Sag [3]. The Permian Lucaogou Formation is the main source rock series and exploration target layer. The main types of oil and gas reservoirs are shale oil and gas reservoirs with source reservoir integration or tight oil and gas reservoirs adjacent to source rocks. However, due to the complex structural deformation, faults, difficult stratigraphic correlation, unclear understanding of sedimentary facies, and unclear distribution range of source rocks in the Bogda Mountain front belt, the understanding of oil and gas reservoir characteristics, distribution patterns, and resource potential in the Bogda Mountain front belt is unclear, resulting in significant delays in exploration progress. In order to solve the key geological problems of oil and gas accumulation, expand the new field of oil and gas survey, and promote the exploration process in the Bogda Mountain front belt, the China Geological Survey has conducted a series of basic research and oil and gas surveys in the Bogda Mountain front belt since 2013, deployed and implemented Well Xjc 1 in the northern edge of the Bogda Mountain front belt, and obtained industrial gas flow in the Permian Lucaogou Formation and the shallow Triassic Karamay Formation, achieving a major breakthrough in new-layer and new-type oil and gas exploration in the new area, confirming that the Bogda Mountain front belt was the sedimentary center during the sedimentary period of the Permian Lucaogou Formation [4], and developing high-quality hydrocarbon source rocks of the Permian Lucaogou Formation. In order to further expand the scope of the Permian Lucaogou Formation oil and gas system on the plane, the overall deployment strategy has been shifted towards the western edge of the Bogda Mountain front belt. In the Yongfeng sub-sag, Well Xyd 1 has been deployed and drilled [5,6], which is the first exploration well deployed in the Yongfeng sub-sag in nearly 30 years. The low yield oil and gas flow obtained from oil testing in the Lucaogou Formation confirms that the area has the basic elements for oil and gas accumulation and shows that the Bogda Mountain front belt has good exploration prospects. As mentioned above, early exploration mainly focused on the sag area in the northern margin of Bogda Mountain, represented by the Jimsar sag. A lot of research has been conducted on the characteristics of the Lucaogou Formation source rocks and the evaluation of unconventional shale oil and gas reservoirs in the Jimsar sag, and a series of geological understandings have been obtained, promoting the construction of a national shale oil demonstration zone [7–13]. Unlike the sag area, the exploration level of the Bogda Mountain front belt is low, and early exploration has not yet discovered oil and gas, resulting in unclear understanding of the basic oil and gas accumulation elements, accumulation processes, and resource potential of the area. The recent exploration discoveries of Wells Xjc 1 and Xyd 1 provide a good data basis for studying the oil and gas accumulation conditions in the Bogda Mountain front belt. Therefore, in order to further implement the oil and gas exploration prospects in the Bogda Mountain front belt, especially in the Yongfeng sub-sag, this study focuses on the geochemical characteristics analysis of source rocks and crude oil in the research area and surrounding areas. Combining the various biomarker parameter characteristics of source rocks and crude oil, fine oil source correlation is carried out to clarify the contribution of oil sources, in order to provide a basis for the study of oil and gas accumulation in the study area and provide direction for the next step of oil and gas exploration.

2. Regional Geological Condition

The Yongfeng sub-sag is located in the western section of the Chaiwopu sag on the southern edge of Bogda Mountain (Figure 1), with an area of about 1500 km^2. The sedimentary strata in the study area are mainly Permian to Jurassic, and the Middle Permian Lucaogou Formation has developed high-quality lacustrine source rocks with a large sedimentary thickness, providing an important material basis for oil and gas accumulation in the study area [14]. The study area relies on the source rocks of the Lucaogou Formation for hydrocarbon supply, which can form multiple sets of reservoir combinations vertically and develop various types of oil and gas reservoirs, coexisting with conventional and unconventional oil and gas reservoirs. Among them, the Permian Lucaogou Formation has a well-developed source and reservoir relationship, forming interbedded shale oil and gas reservoirs as well as adjacent tight sandstone oil and gas reservoirs (Figure 2). Moreover, it is distributed continuously on the plane, not controlled by structures, with a large area and overall resource scale, making it the most important exploration target layer in the study area.

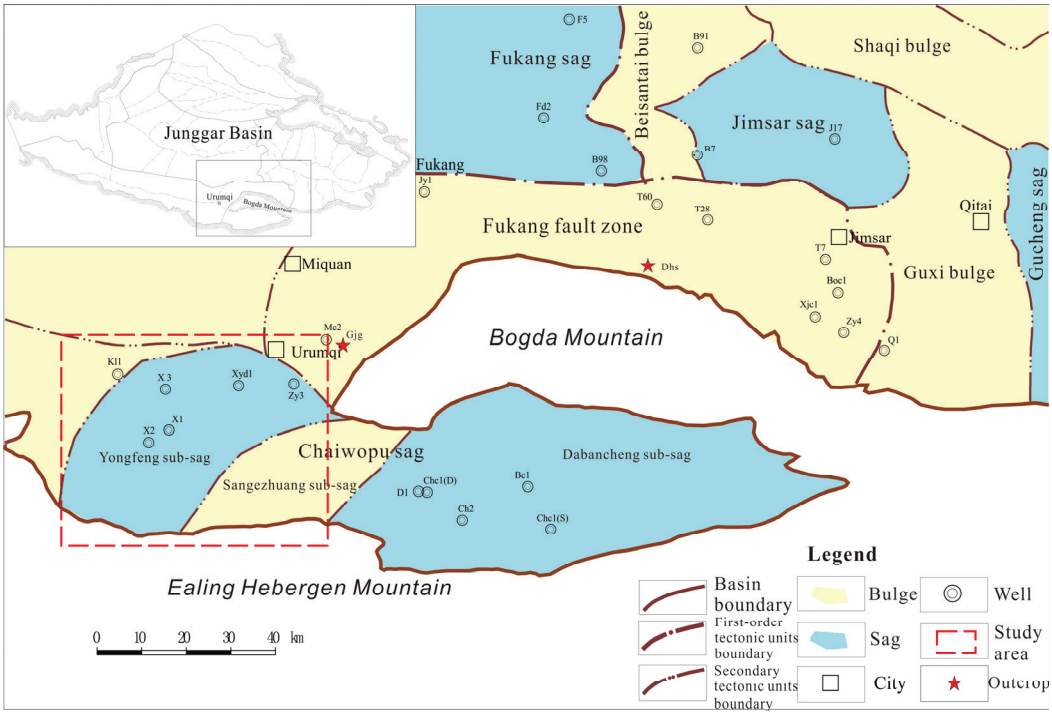

Figure 1. Location map of the study area [6].

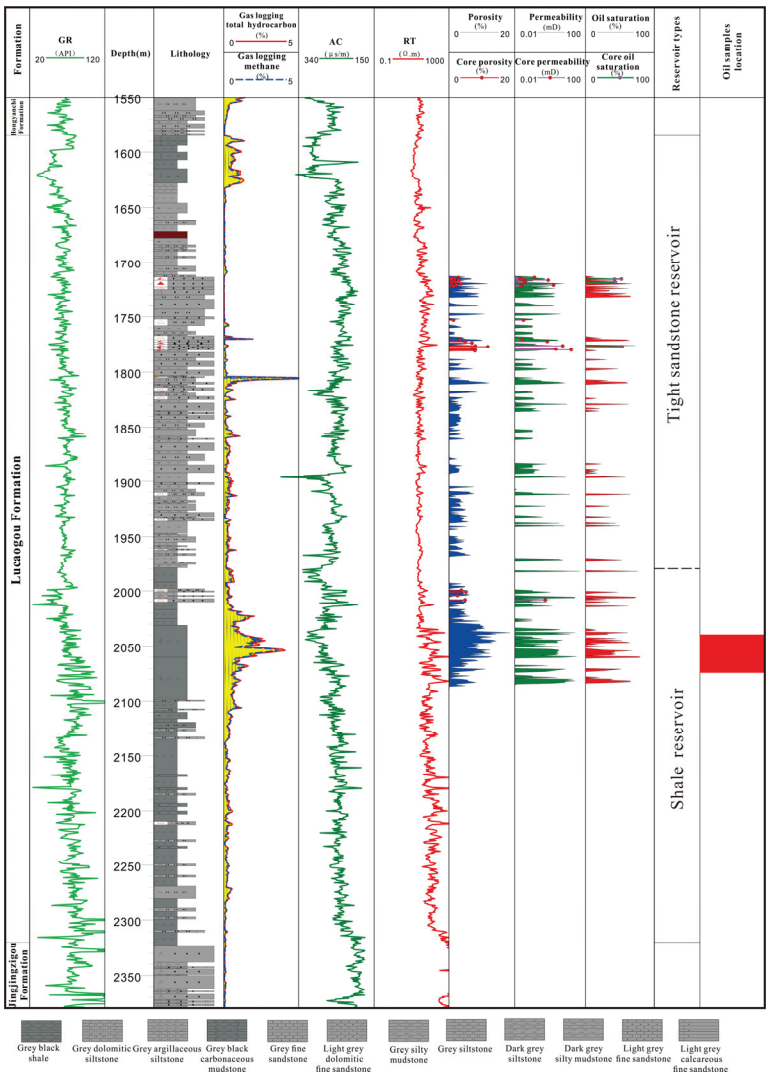

Figure 2. Column of Well Xyd 1.

3. Sample Collection and Analysis

3.1. Sample Collection

In this study, two crude oil samples were collected from Well Xyd 1, with a depth of 2045 m to 2072 m (Figure 2); 62 samples of source rocks were collected, including 18 samples of source rocks cuttings of the Lucaogou Formation from Well Xyd 1, 24 samples of source rocks of the Lucaogou Formation from the Gjg outcrop, and 20 samples of source rocks of the Lucaogou Formation from the Dhs outcrop. The source rock samples were mainly collected from the black mudstone section of the Lucaogou Formation. Chromatographic analysis of total hydrocarbons, light hydrocarbons, and saturated hydrocarbons, biomarker compound analysis, and carbon isotope analysis were conducted for the crude oil samples. Total organic carbon content (TOC) analysis, chloroform bitumen "A" analysis, rock pyrolysis, kerogen vitrinite reflectance (R_o), group component analysis, biomarker compound analysis, and carbon isotope analysis were conducted for the source rock samples.

3.2. Sample Analysis Method

The analysis of organic carbon, chloroform bitumen "A", rock-eval pyrolysis, and determination of kerogen vitrinite reflectance for source rocks were carried out using the same methods as in reference [6], and the analysis method will not be described in detail here.

Organic carbon isotope analysis was carried out using an American-made Delta V Advantage isotope mass spectrometer. The analysis of total hydrocarbon gas chromatography of crude oil was carried out using an American-made Agilent 7890B chromatograph, with an HP-PONA elastic quartz capillary column (50 m × 0.20 mm × 0.5 m), nitrogen gas as the carrier gas (constant flow rate 1.0 mL/min), and injection using a split-flow mode (split ratio 10:1). Set the initial temperature of the chromatography to 40 °C (hold for 10 min), raise it to 310 °C at a rate of 3 °C/min, and hold for 30 min.

The experimental process for analyzing biomarker compounds was as follows: first, Soxhlet extraction was performed on the source rock and crude oil to separate the components and obtain soluble organic matter. After the solvent evaporated, n-hexane was added, and the mixture was refrigerated overnight to precipitate asphaltene. After removing asphaltene, a chromatography column filled with alumina stationary phase was used to separate the group components. Add n-hexane, benzene, and mixed solvent of dichloromethane and methanol (9:1, v/v) in sequence to wash out saturate, aromatic, and resin. The processing method for crude oil samples was the same as that for soluble organic matter in source rocks. Chromatographic analysis and chromatography–mass spectrometry analysis were performed on the separated saturated hydrocarbon components using an American-made Agilent 7890B gas chromatograph and an American-made Agilent 7890B/5977A gas chromatography–mass spectrometer, respectively. Isotopes of saturate, aromatic, resin, asphaltene, and chloroform bitumen "A" in the extracted and separated source rocks were determined using a German-made Elementar isotope precision stable isotope ratio mass spectrometer.

Agilent 7890B/5977A gas chromatography–mass spectrometry was used for analysis. The saturated hydrocarbon chromatography column is an HP-5MS elastic quartz capillary column (60 m × 0.25 mm × 0.25 m), with constant flow mode injection and helium gas as the carrier gas (constant flow rate 1.0 mL/min). Heating program: Initial temperature of 50 °C, hold for 1 min, heat up at a rate of 15 °C/min to 100 °C, heat up at a rate of 2 °C/min to 200 °C, and then heat up at a rate of 1 °C/min to 315 °C, and hold for 20 min.

4. Physical Characteristics and Group Components of Crude Oil

4.1. Physical Characteristics of Crude Oil

The crude oil density of Well Xyd 1 in the Yongfeng sub-sag ranges from 0.8930 g/cm^3 to 0.9034 g/cm^3, with an average density of 0.8982 g/cm^3; at 50 °C, the viscosity of crude oil ranges from 230.06 mpa.s to 618.52 mpa.s, with an average of 424.29 mpa.s; the wax content of crude oil ranges from 6.36% to 9.56%, with an average of 7.96%; the freezing point of crude oil ranges from 8.0 °C to 22.0 °C. Overall, the crude oil from Well Xyd 1 has relatively high density and viscosity, and belongs to heavy oil.

4.2. Group Components SARA (Saturate, Aromatic, Resin, and Asphaltene) of Crude Oil

The content of saturates and aromatics in the crude oil of Well Xyd 1 in the Yongfeng sub-sag is from 54.25% to 59.96% and from 15.33% to 17.68%, respectively, the ratio of saturates to aromatics (saturates/aromatics) is from 3.39 to 3.54, and the content of resins and asphaltene is from 13.82% to 15.80%. The content of saturates and aromatics of the black mudstone in the Lucaogou Formation of Well Xyd 1 is from 19.43% to 52.33% and from 8.57% to 20.71%, respectively, the saturates/aromatics value is from 1.31 to 4.49, and the content of resins and asphaltene is from 31.32% to 67.43%. The content of saturates and aromatics of the black mudstone in the Lucaogou Formation of the Gjg outcrop is from 19.88% to 28.07% and from 10.22% to 23.14%, respectively, the saturates/aromatics value is from 1.11 to 2.32, and the content of resins and asphaltene is from 48.34% to 60.76%. The content of saturates and aromatics of the black shale in the Lucaogou Formation of

the Dhs outcrop is from 18.93% to 23.25% and from 8.50% to 15.38%, respectively, the saturates/aromatics value is from 1.50 to 2.24, and the content of resins and asphaltene is from 57.69% to 62.73% (Table 1). The content of SARA in the soluble organic matter of source rocks is influenced by various factors, including parent material type, maturity, and secondary transformation [15]. The crude oil from Well Xyd 1 has a low content of polar compounds and a high saturates/aromatics value, exhibiting the characteristics of mature crude oil as a whole. The source rocks of the Lucaogou Formation in Well Xyd 1 have strong heterogeneity, with relatively high saturate content and a high saturates/aromatics value greater than 3 in some sample extracts; the other part of the sample extracts is mainly composed of resins and asphaltene, with a lower content of saturates. This heterogeneity may be related to the widespread development of fractures in the area, and the strong biodegradation or water washing of the Lucaogou Formation source rocks, resulting in a significant decrease in the content of relatively light components such as saturates in the group components. In contrast, resin components dominate the source rock extracts of the Lucaogou Formation in the Gjg and Dhs outcrops, with a low saturates/aromatics value less than 2, and the content of resins and asphaltene is relatively high. This indicates that compared with the source rocks of the Lucaogou Formation in Well Xyd 1, the maturity of the source rocks in these two outcrops is lower, and the degree of organic matter transformation and evolution has not yet reached the level of the source rocks in Well Xyd 1.

Table 1. Group component characteristics of crude oil and source rocks around the Bogda Mountain front belt.

Sample Source	Sample No.	Type	Saturate /%	Aromatic /%	Resin /%	Asphaltene /%	Resin and Asphaltene /%	Collection Rate /%	Saturates/Aromatics
Well Xyd 1	70	Rock cutting	52.33	11.66	18.65	15.54	34.19	98.19	4.49
	91		19.43	8.57	32.00	35.43	67.43	95.43	2.27
	97		27.22	20.71	33.14	15.98	49.12	97.04	1.31
	102		32.43	9.26	35.97	16.89	52.86	94.55	3.50
	112		40.60	12.26	26.98	14.99	41.97	94.82	3.31
	117		40.40	19.19	22.90	8.42	31.32	90.91	2.11
	121		29.90	19.28	29.74	16.99	46.73	95.92	1.55
	127		35.03	18.84	29.94	10.52	40.46	94.34	1.86
	Oil-1	Crude oil	59.96	17.68	10.57	3.25	13.82	91.46	3.39
	Oil-2		54.25	15.33	10.85	4.95	15.80	85.38	3.54
Gjg outcrop	35	Rock	25.62	23.14	28.51	19.83	48.34	97.11	1.11
	37		23.21	20.98	34.37	18.75	53.12	97.32	1.11
	39		28.07	17.84	33.63	14.91	48.54	94.44	1.57
	41		23.62	15.35	38.19	14.57	52.76	91.73	1.54
	43		27.40	15.75	33.33	18.95	52.28	95.43	1.74
	45		23.66	10.22	39.25	21.51	60.76	94.62	2.32
	47		19.88	16.67	30.92	26.91	57.83	94.38	1.19
Dhs outcrop	12	Rock	23.08	15.38	50.00	7.69	57.69	96.15	1.50
	15		18.93	10.44	65.78	4.37	70.15	99.51	1.81
	18		19.00	8.50	57.25	5.00	62.25	89.75	2.24
	21		23.25	11.81	56.83	5.90	62.73	97.79	1.97

5. Geochemical Characteristics of Crude Oil

The distribution characteristics and composition of biomarkers can reflect information such as the sedimentary environment, parent material source, and maturity of source rocks [16]. Based on the characteristics of biomarkers such as alkanes, terpenes, and hopane in crude oil and source rock samples, this paper systematically analyzed the sedimentary environment, water salinity, and parent material sources of crude oil in the Yongfeng sub-sag and source rocks around the Bogda Mountain front belt.

5.1. Composition and Distribution Characteristics of Alkane Series

The gas chromatography–mass spectrometry analysis results show that the carbon number distribution range of n-alkanes in the saturated hydrocarbon fractions of two crude oil samples from the Xinyingdi 1 well is nC_9–nC_{32}, and the main peak carbon number is concentrated in nC_{14}–nC_{15}. The oil sample Oil-1 suffered from a certain degree of mud contamination, and the baseline of the Oil-2 sample's alkane chromatography also showed obvious "UCM" (Unsolved Complex Mixture) bulges, which is sufficient to prove its potential for biodegradation. The distribution of CPI ranges from 1.09 to 1.18, and the distribution of OEP ranges from 1.06 to 1.13. Normal alkanes have a slight odd–even advantage, indicating that the maturity of crude oil is in the early to mid-maturity stage and has not yet fully reached the peak of mature oil generation (Figure 3).

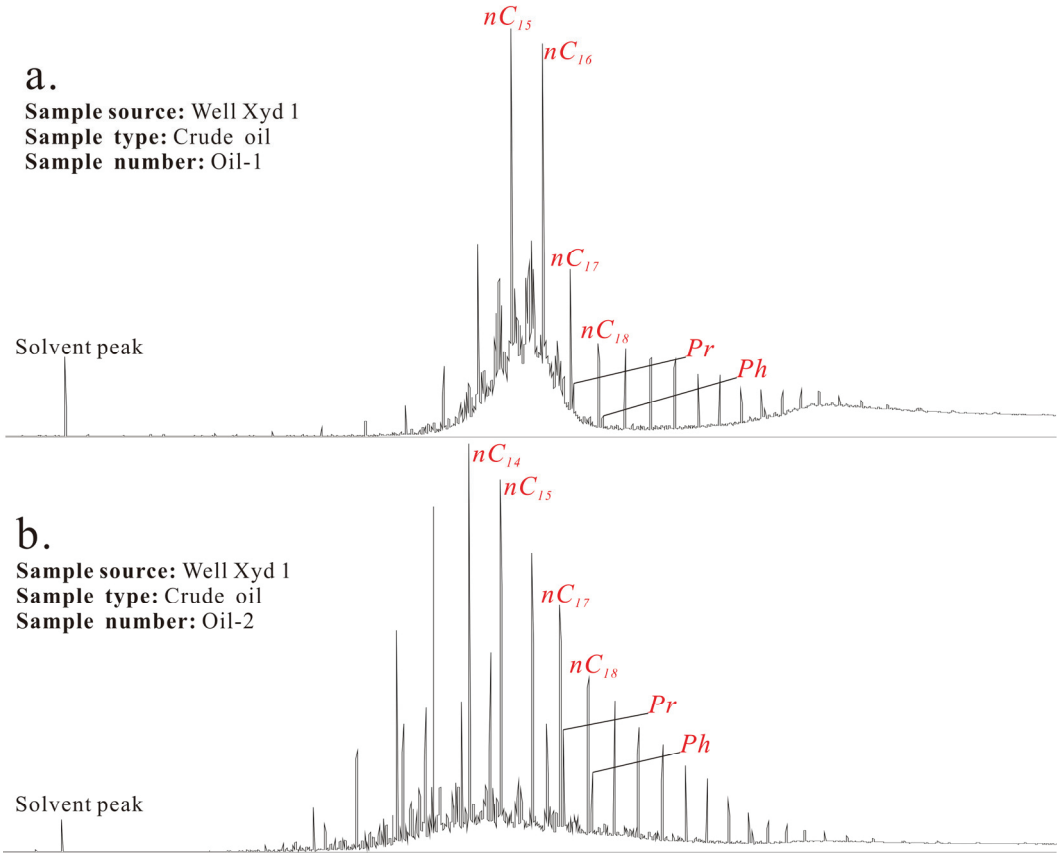

Figure 3. Distribution characteristics (**a**,**b**) of alkane series in crude oil from Well Xyd 1.

In oil and gas geochemical analysis, the ratio of pristane to phytane (Pr/Ph) is considered an important indicator reflecting the sedimentary environment [17]. Generally, higher Pr/Ph values are often associated with oxidative sedimentary environments, while hypoxic or high salt conditions are often accompanied by lower Pr/Ph values [18]. Specifically, test data indicate that a Pr/Ph value less than 1 indicates a hypoxic environment; when the Pr/Ph value is greater than 1, it represents a weakly oxidizing environment; and a Pr/Ph

value greater than 3 usually means that terrestrial organic matter is deposited in oxidized water environments [19].

Taking Well Xyd 1 as an example, the crude oil contains generally high levels of pristane and phytane, with the advantage of pristane being particularly evident. The Pr/Ph values of the crude oil in this well are generally high, ranging from 1.06 to 1.66. These data reflect that the sedimentary environment of the crude oil source material is a reducing to weakly oxidizing and weakly reducing environment. In the extracts of the source rocks of the Lucaogou Formation in Well Xyd 1, the Pr/Ph values are generally low, ranging from 0.53 to 0.73, with an average value of 0.62. This indicates that the original sedimentary environment of the source rocks has strong reducibility. In contrast, the Pr/Ph values in the source rock extracts of the Gjg and Dhs outcrops are higher than that of Well Xyd 1, ranging from 0.15 to 0.94, with an average value of 0.77, which reflects that these source rocks were formed in the sedimentary environment of weak oxidation and reduction (Table 2).

Table 2. Biomarker compound parameters of crude oil and source rocks around the Bogda Mountain front belt.

Sample Source	Sample No.	Type	Pr /Ph	Pr/nC_{17}	Ph/nC_{18}	Ga/ C_{30}H	Ts/Tm	C_{24}TET/C_{26}TT	MPI-1	Rc /%	4-/1-MDBT	C_{29}-ααβ/(ααββ + ααα)	C_{29}-ααα20S/(20S + 20R)
Well Xyd 1	70	Rock cutting	0.71	0.42	0.58	0.22	4.43	0.90	0.51	0.72	5.26	0.44	0.40
	91		0.58	0.48	0.89	0.31	2.28	0.64	0.51	0.72	9.68	0.51	0.40
	97		0.57	0.49	0.95	0.27	2.48	0.70	0.54	0.74	11.83	0.49	0.39
	102		0.58	0.54	1.03	0.32	2.77	0.50	0.52	0.73	8.64	0.51	0.38
	112		0.60	0.55	1.07	0.35	2.09	0.61	0.55	0.74	10.25	0.43	0.39
	117		0.53	0.53	1.05	0.38	1.91	0.61	0.66	0.80	11.36	0.42	0.40
	121		0.65	0.54	0.90	0.35	2.39	0.56	0.67	0.81	10.44	0.51	0.41
	127		0.73	0.64	1.12	0.45	2.31	0.60	0.69	0.82	11.69	0.40	0.41
	Oil-1	Crude oil	1.66	0.31	0.24	0.24	1.49	0.54	0.54	0.74	3.27	0.53	0.41
	Oil-2		1.06	0.54	0.60	0.24	1.04	0.51	1.08	1.04	2.57	0.51	0.40
Gjg outcrop	35	Rock	0.79	0.25	0.26	0.18	0.55	0.65	0.32	0.62	4.67	0.33	0.46
	37		0.54	0.48	0.92	0.10	0.19	1.55	0.55	0.74	2.98	0.37	0.44
	39		0.83	0.36	0.40	0.10	0.98	1.03	0.20	0.55	3.45	0.39	0.46
	41		0.85	0.40	0.43	0.14	0.70	0.63	0.31	0.61	4.22	0.38	0.46
	43		0.83	0.48	0.52	0.16	0.72	0.92	0.26	0.58	3.27	0.36	0.46
	45		0.80	0.24	0.27	0.16	0.68	0.92	0.29	0.60	2.27	0.34	0.47
	47		0.85	0.24	0.27	0.19	0.64	0.98	0.26	0.58	2.82	0.32	0.45
Dhs outcrop	12	Rock	0.15	0.47	0.74	0.15	0.59	0.77	/	/	/	0.37	0.30
	15		0.93	0.49	0.52	0.20	0.14	1.48	0.39	0.65	0.98	0.36	0.33
	18		0.94	0.43	0.43	0.07	0.19	2.61	0.37	0.65	4.57	0.25	0.27
	21		0.83	0.63	0.82	0.09	0.27	1.36	0.36	0.64	1.99	0.24	0.23

5.2. Composition and Distribution Characteristics of Terpenoid Hopane Series

Among the numerous biomarker parameters in the terpene series, tricyclic and tetracyclic terpenes play extremely important roles and can provide a lot of information about the source material of oil. Tricyclic terpenes are widely distributed in petroleum and sedimentary organic matter, possibly originating from the cell membranes of protozoa, with tricyclohexaisoprenol as its precursor [20], and algae as another source [21]. C_{24} tetracyclic terpenes are widely distributed in crude oil and rock extracts. Many scholars believe that the abundant C_{24} tetracyclic terpenes are often associated with terrestrial parent materials [22,23]. Therefore, the relative content of C_{24} tetracyclic terpenes and tricyclic terpenes can reflect the organic matter source of crude oil. Generally speaking, in source rocks from lower organic matter and related crude oils, C_{23} tricyclic terpenes dominate, while C_{24} tetracyclic terpenes have relatively low content; however, C_{19} and C_{20} tricyclic terpenes

are more abundant in source rocks and related crude oils derived from terrestrial organic matter, and the content of C_{24} tetracyclic terpenes is relatively high. Abundant terpenoids are detected in the crude oil and source rock extracts of Well Xyd 1, including pentacyclic triterpenes, tricyclic terpenes, tetracyclic terpenes, and gammacerane (Figure 4). Among them, the main peaks of tricyclic terpenes are C_{21} and C_{23}, indicating that the contribution of lower aquatic organisms dominates in their organic matter sources.

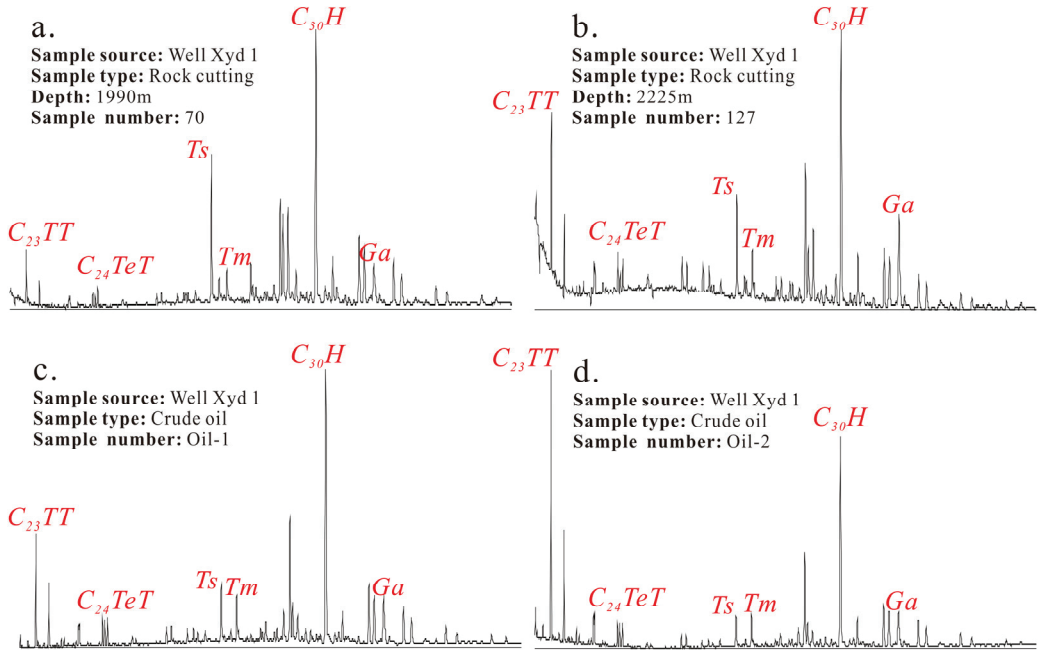

Figure 4. (**a**–**d**) Mass chromatogram (m/z 191) of source rocks and crude oil from Well Xyd 1.

Tetracyclic terpenes are generally believed to be formed by the cleavage of the five-membered ring, i.e., the E ring, in hopane or its precursor, hopene, due to thermal or biodegradation effects. This compound has stronger thermal stability than hopane and is sometimes associated with high-salt sedimentary environments [24]. In the crude oil and source rock extracts from Well Xyd 1, the ratio of C_{24} tetracyclic terpenes to C_{26} tricyclic terpenes (C_{24}TeT/C_{26}TT) ranges from 0.51 to 0.90, with an average value of 0.62; the ratio of hydrocarbon source rock extracts in the Gjg outcrop ranges from 0.63 to 1.55, with an average value of 0.96; the ratio of hydrocarbon source rock extracts in the Dhs outcrop ranges from 0.77 to 2.61, with an average value of 1.56. These data show that the contribution of low-grade bio organic matter in the source rocks of the Lucaogou Formation in the area where Well Xyd 1 is located is significantly higher than that in the Gjg and Dhs outcrops.

Among pentacyclic terpenes, C_{30} hopane has a high abundance, while the abundance of other hopanes is relatively low. It is particularly obvious that the ratio of Ts/Tm in the crude oil of Well Xyd 1 is greater than 1, and the ratio of Ts/Tm in source rock extracts of Well Xyd1 is generally greater than 2, with an average of 2.58, which is significantly higher than that in the source rock extracts of the Gjg and Dhs outcrops. This phenomenon not only confirms the existence of sedimentary environment differences in the source rocks of the Lucaogou Formation around the Bogda Mountain front belt, but also reflects the differences in their maturity on the plane.

Abundant gammaceranes were detected in crude oil and source rock extracts, and their relative abundance has a good correlation with the salinity of sedimentary water bodies. Therefore, they are often used to indicate the ancient salinity of water bodies during source rock deposition. The gammacerane index (Ga/C_{30}H, the ratio of gammaceranes to C_{30}

hopane) can reflect the relative content of gammacerane in samples. Due to its sensitivity to hyper-saline environments, it is currently the most commonly used molecular geochemical parameter to reflect paleosalinity in sedimentary environments. The gammacerane index in the crude oil and source rock extracts of Well Xyd 1 ranges from 0.22 to 0.45, indicating certain characteristics of brackish water to saline sedimentary environments [25]; the gammacerane index in source rock extracts of the Lucaogou Formation from the Gjg and Dhs outcrops range from 0.07 to 0.20, reflecting the original sedimentary environment of non-high salinity and relatively weak stratification.

5.3. Composition and Distribution Characteristics of Sterane Series

The distribution characteristics of C_{27}-C_{28}-C_{29} regular steranes are commonly used to indicate the species contributing to sedimentary organic matter. Generally, the dominance of C_{27} regular steranes indicates the contribution of algae and aquatic organisms, while the dominance of C_{29} regular steranes reflects the contribution of terrestrial higher plants [26]. The C_{27}-C_{28}-C_{29} regular sterane source identification chart (Figure 5a) shows that the hydrocarbon generating parent materials of the crude oil from Well Xyd 1 all have contributions from phytoplankton and terrestrial plants; the distribution of regular steranes shows a "V" shape distribution of C_{27} to C_{29} (Figure 5b–d), indicating that their organic matter is mainly contributed by algae, aquatic organisms, and terrestrial higher plants.

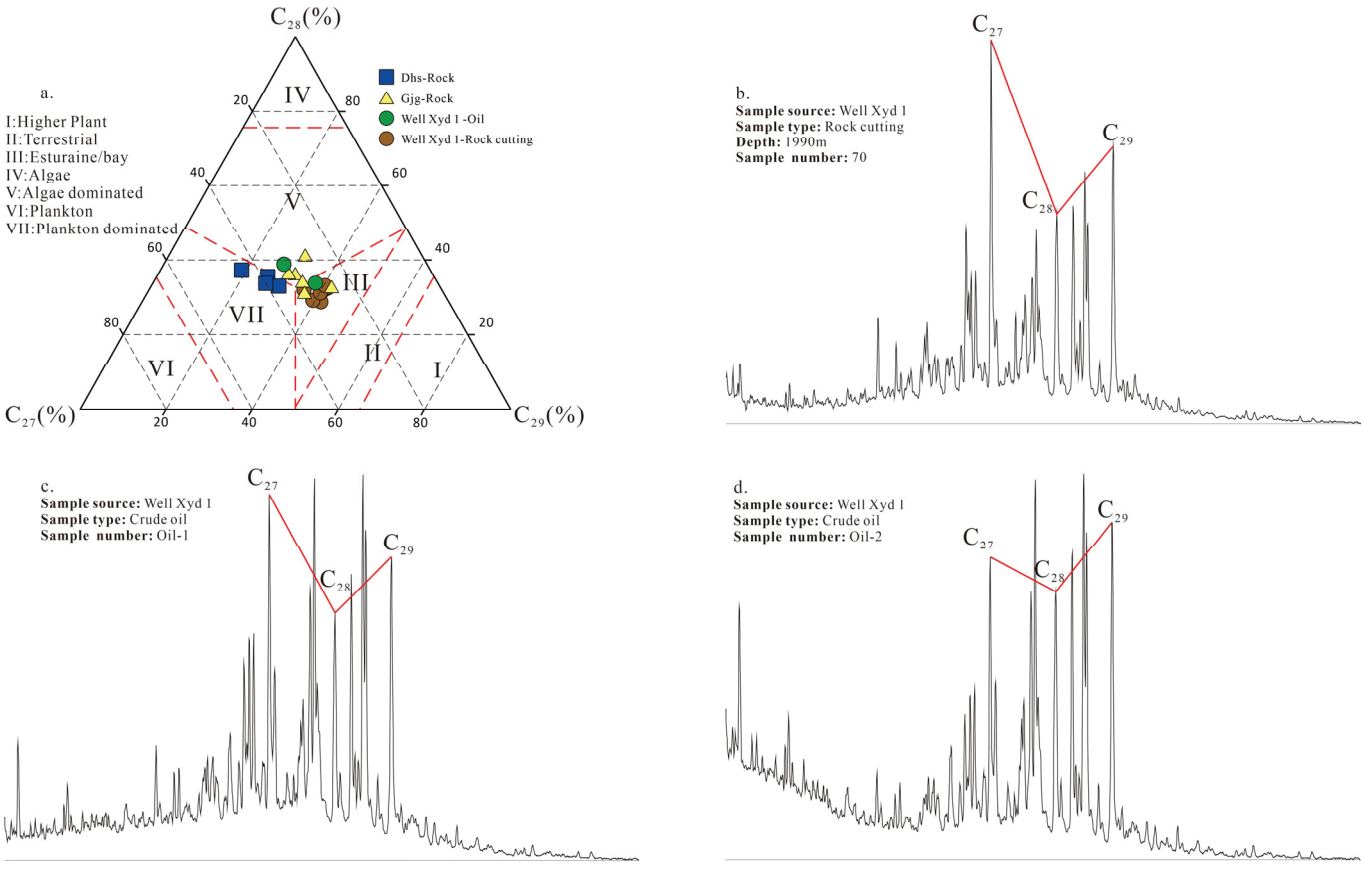

Figure 5. Identification of organic matter input types based on sterane series (**a**) and distribution of sterane compounds (**b**–**d**) in crude oil and source rocks from Well Xyd 1.

6. Oil Maturity

Biomarkers are the most common and reliable method for determining the maturity of crude oil at present, but not every parameter among the numerous biomarker maturity parameters can reflect the original maturity well. In the context of a saline lake sedimentary

environment, higher salinity is not conducive to the conversion of Tm to Ts, resulting in a lower ratio of Ts to Tm (Ts/Tm) of crude oil compared to the source rock extract from Well Xyd 1.

As the degree of thermal evolution increases, the R configuration of regular steranes will transition to the S configuration, and similarly, the less thermally stable α configuration of regular steranes will transition to the β configuration [27,28]. The crude oil sample from Well Xyd 1 has weak odd–even dominance. In addition, the regular sterane isomerization parameters show that the crude oil in this area has basically not exceeded the equilibrium endpoint and is in the mature interval, so it is judged that the crude oil is from the mature source rock. The regular sterane isomerization parameters of the source rock extracts from the Gjg and Dhs outcrops show that their maturity is in the low-maturity to mature stage (Figure 6a).

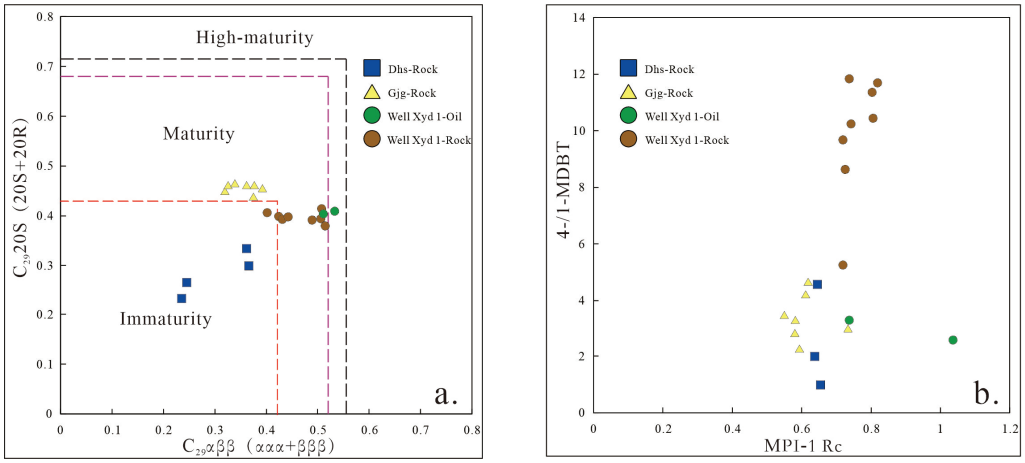

Figure 6. Maturity characteristics of C_{29} regular sterane isomerization parameters (**a**) and aromatics maturity characteristics (**b**) in crude oil and source rocks around the Bogda Mountain front belt.

As an important component of aromatics, the maturity parameters of phenanthrene series compounds are widely used in the evaluation of source rocks. The maturity parameters of the methyl phenanthrene series have a good indicative effect in the low-maturity to maturity stage, and have been compared with vitrinite reflectance in some studies [29]. A method for measuring organic matter maturity using the relative abundance of phenanthrene and four isomers of methyl phenanthrene, namely the methyl phenanthrene index MPI-1, has been proposed. Some scholars have corrected the relationship between the methyl phenanthrene index and vitrinite reflectance and established a conversion relationship between them [30]. The crude oil and source rocks in the Yongfeng sub-sag have not reached the high maturity evolution stage (R_o < 1.3%), so Formula (1) can be used to convert the equivalent maturity of crude oil and source rock extracts.

$$Rc = 0.6MPI\text{-}1 + 0.4 \quad (1)$$

In the formula, Rc is the kerogen vitrinite reflectance value converted from MPI-1, measured in %; the results (Table 2) show that the maturity of crude oil in Well Xyd 1 ranges from 0.74 to 1.04, and the maturity of source rock extracts in Well Xyd 1 ranges from 0.72 to 0.82, with an average value of 0.76; the maturity of hydrocarbon source rock extracts in the Gjg outcrop ranges from 0.55 to 0.74, with an average of 0.61; the maturity of hydrocarbon source rock extracts in the Dhs outcrop ranges from 0.63 to 0.65, with an average of 0.64 (Figure 6b). This is consistent with the maturity characteristics of C_{29} regular sterane isomerization parameters.

Dibenzothiophene has a unique thiophene molecular structure, which is widely used in oil and gas tracing. The relative abundance ratio between different isomers also has a certain linear relationship with the degree of thermal evolution. As the degree of thermal evolution increases, unstable compounds will gradually transform into stable compounds, and the parameter values will also increase accordingly, making it a good maturity parameter [31]. It should be noted that the maturity parameter of dibenzothiophene is mainly applicable to the mature to high-maturity stage of the source rock. The relative contents of 1-MDBT and 4-MDBT in the source rock extracts of Well Xyd 1 change significantly, indicating that their maturity is much higher than that of the source rock of the Lucaogou Formation in the Gjg and Dhs outcrops, while the response of the crude oil of Well Xyd 1 to this parameter is not obvious.

7. Oil–Source Correlations

7.1. Geochemical Characteristics of Source Rocks

High-quality hydrocarbon source rocks from the Permian Lucaogou Formation, deposited in deep to semi-deep lacustrine environments, with high organic matter abundance, good types, and varying degrees of maturity, are widely developed in the surrounding area of Bogda Mountain. The Pr/Ph values of hydrocarbon source rock extracts of the Permian Lucaogou Formation from Well Xyd 1, as well as the Gjg and Dhs outcrops, are all less than 1, reflecting that the sedimentary environment is a weak reduction environment (Figure 7a), and the gammacerane index indicates that the paleosalinity of the water body during the deposition of the hydrocarbon source rock from the Lucaogou Formation in Well Xyd 1 is higher than that in the Gjg and Dhs outcrops (Figure 7b).

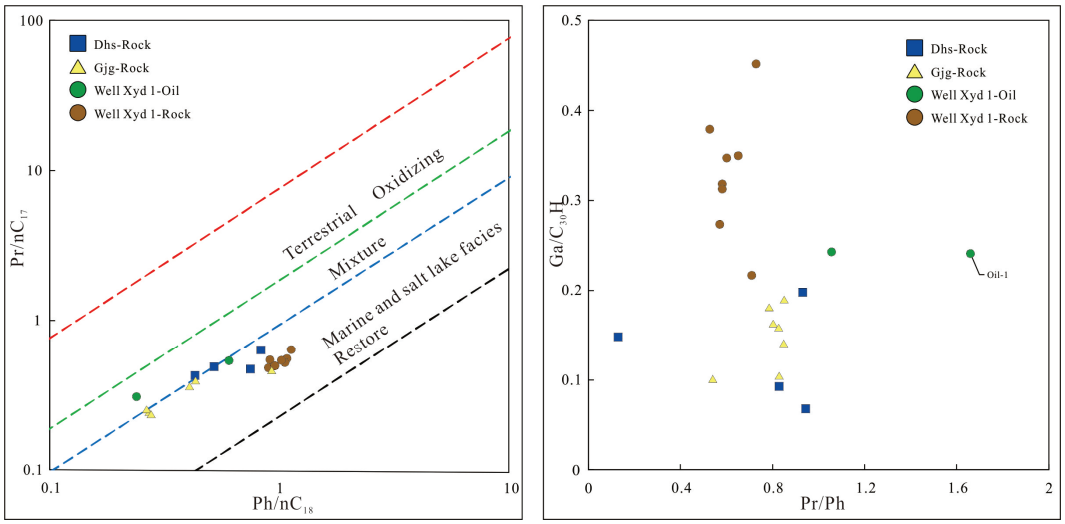

Figure 7. Integrated identification of sedimentary environment (**a**) and paleosalinity of water body (**b**) based on Ph/nC_{18} and Pr/nC_{17} ratios in crude oil and source rocks around the Bogda Mountain front belt.

Steroids in rocks are important organic compounds that can provide rich information. Steroids include various types, among which 4-methyl steroids and dinoflagellates have important indicative significance in environmental discrimination. Abundant 4-methylsterane was detected in the hydrocarbon source rock extracts of the Lucaogou Formation in the Gjg outcrop (Figure 8). 4-methylsterane mainly comes from marine organisms such as dinoflagellates, but can also exist in lacustrine environments. The content of 4-methylsterane in the crude oil and source rock extracts of Well Xyd 1 is relatively low. The C_{27} regular sterane

abundance in the Lucaogou Formation source rock of Well Xyd 1 is high (Figure 5), while the C_{28} regular sterane content in the Lucaogou Formation source rock of the Gjg outcrop is relatively high. Similar findings have been made by predecessors. Chen Jianping et al. believe that a high abundance of C_{28} regular steranes is a typical distribution form of hydrocarbon source rocks of the Permian Lucaogou Formation in the Junggar Basin [32]. Wang Jian et al. believe that the high abundance of C_{28} steranes is derived from hydrocarbon generating parent materials, mainly algae and supermicroorganisms, and may be related to various phytoplankton groups such as diatoms, coccoliths, and dinoflagellates that are increasing in the geological history of the Lucaogou Formation [33,34]. This phenomenon can reflect the differences in the sedimentary environment and source material on the plane of the hydrocarbon source rocks in the Lucaogou Formation around the Yongfeng sub-sag, and can also serve as evidence for distinguishing different types of hydrocarbon source rocks in the region.

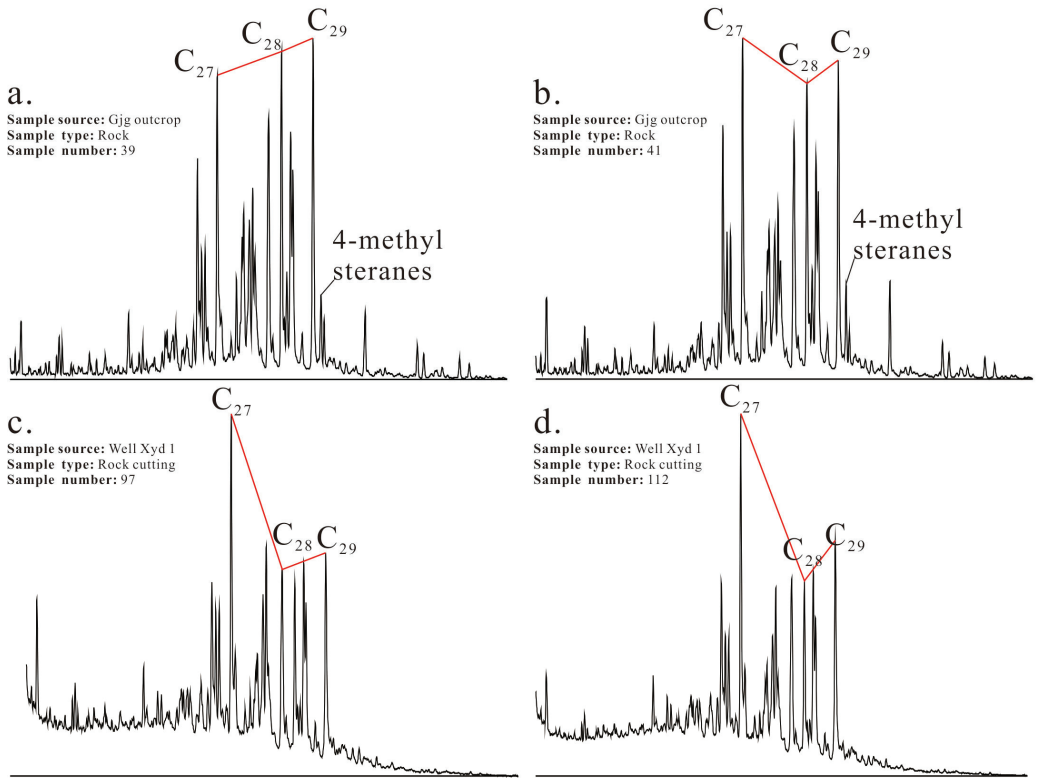

Figure 8. (**a**–**d**) Distribution of sterane series compounds in crude oil and source rock extracts in the Yongfeng sub-sag.

7.2. Multi Factor Oil–Source Correlations

7.2.1. Correlations of Carbon Isotope Composition Characteristics

Figure 9a shows the correlation between stable carbon isotopes ($\delta^{13}C$) of saturates and aromatics of the crude oil and source rocks in the Yongfeng sub-sag. The stable carbon isotope of saturates in the crude oil and source rock extracts of Well Xyd 1 ranges from −30.6‰ to −28.2‰, that in the Gjg outcrop is from −33.7‰ to −31.7‰, and that in the Dhs outcrop is from −40.5‰ to −32.2 ‰. By comparison, it can be found that the crude oil and source rock extracts from Well Xyd 1 have relatively heavy carbon isotope values, and the sample data distribution shows high consistency. However, due to the lack of clear regularity in the stable carbon isotopes of aromatics in crude oil and source rocks in the Yongfeng sub-sag, further tracing of the origin of crude oil in Well Xyd 1 requires the use of more biomarker parameters for judgment.

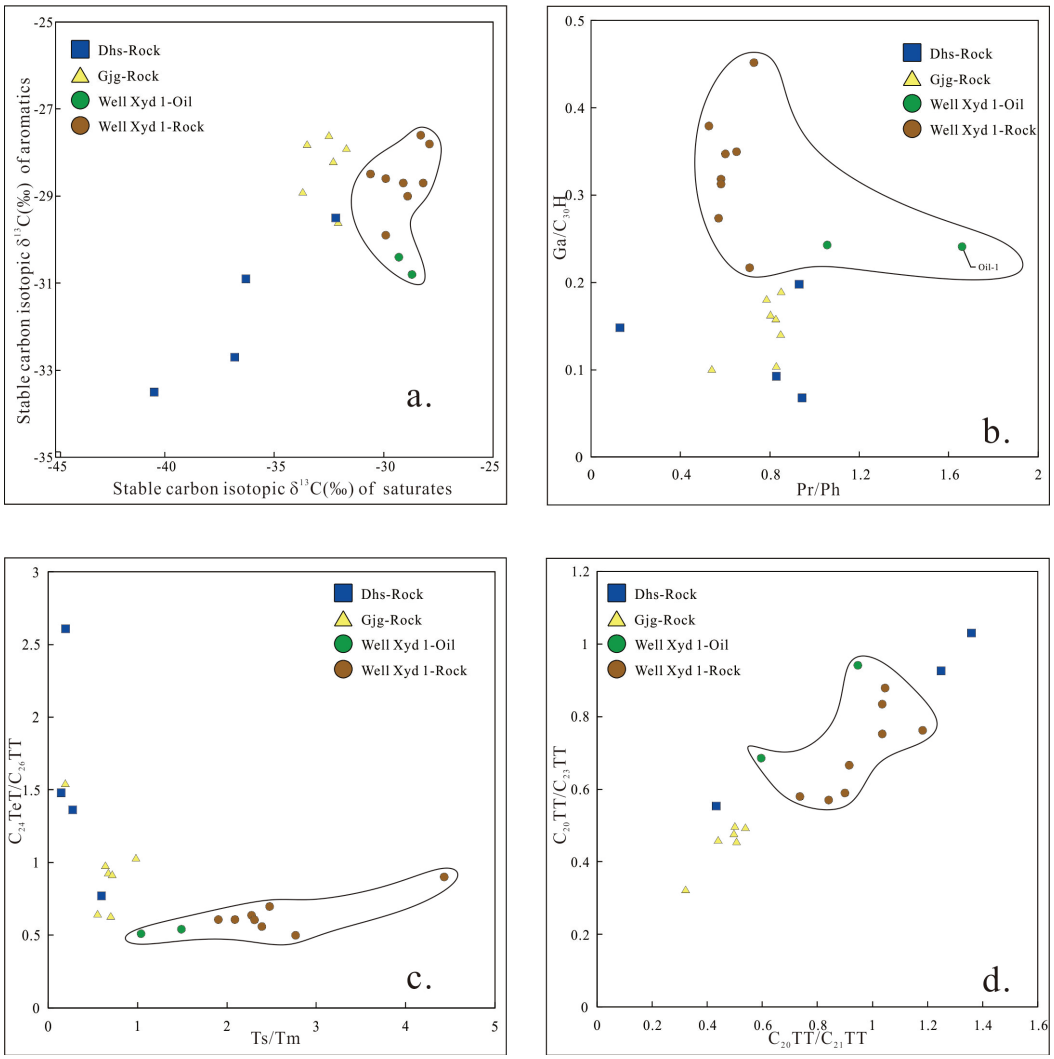

Figure 9. Geochemical analysis for oil–source correlation. (**a**) Correlation between stable carbon isotopes ($\delta^{13}C$) of saturates and aromatics; (**b**) correlation between Pr/Ph and the gammacerane index (Ga/C30H); (**c**) correlation between the Ts/Tm and C_{24}TeT/C_{26}TT; (**d**) correlation between C_{20}TT/C_{21}TT and C_{20}TT/C_{23}TT.

7.2.2. Correlations of Distribution Characteristics of Isoprene Alkanes

Figure 9b shows the correlation between the Pr/Ph and gammacerane index in the crude oil and source rocks in the Yongfeng sub-sag. Both of these parameters can effectively reflect the sedimentary environment during the deposition of the source rock. The gammacerane index of source rock extracts from the Gjg and Dhs outcrops is less than 0.2. The gammacerane index of crude oil and source rock extracts from Well Xyd 1 is more than 0.2. This difference provides a strong basis for us to distinguish source rocks in different sedimentary environments. It is worth noting that the Pr/Ph value of the crude oil sample Oil-1 from Well Xyd 1 is relatively high, which may be related to mud contamination. However, overall, the sedimentary environment of the crude oil and source rocks in Well Xyd 1 is similar.

7.2.3. Correlations of Distribution Characteristics of Terpenoid Compounds

Figure 9c shows the correlation between the Ts/Tm value and C_{24}TeT/C_{26}TT value in the crude oil and source rocks in the Yongfeng sub-sag. By comparison, it can be found that the salinity of the paleowater body during the deposition of the source rocks in Well Xyd 1 is higher, and the input of algae is also more abundant; in the Gjg and Dhs outcrops, the input

of terrigenous organic matter is dominant. In addition, the Ts/Tm value and C_{24}TeT/C_{26}TT value of the crude oil from Well Xyd 1 are more similar to their corresponding ratios in the source rocks from Well Xyd 1, further confirming their genetic relationship.

Figure 9d shows the correlation between the ratio of C_{20} tricyclic terpenes to C_{21} tricyclic terpenes (C_{20}TT/C_{21}TT) and the ratio of C_{20} tricyclic terpenes to C_{23} tricyclic terpenes (C_{20}TT/C_{23}TT) in the crude oil and source rocks in the Yongfeng sub-sag. Generally speaking, C_{19} to C_{23} tricyclic terpenes in freshwater lacustrine source rocks and crude oil samples mostly have a C_{21}TT advantage, while in saline lacustrine source rocks and crude oil samples, C_{19} to C_{23} tricyclic terpenes mostly have a C_{23}TT relative advantage. Through comparison, it can be found that the salinity of the paleowater body during the deposition of the source rocks of Well Xyd 1 is significantly different from that of the source rocks of the Gjg and Dhs outcrops, which is consistent with the analysis of the sedimentary environment. At the same time, the content characteristics of C_{19} to C_{23} tricyclic terpenes in crude oil and source rock extracts from Well Xyd 1 also show high similarity.

In summary, we can draw the following conclusion: the crude oil from Well Xyd 1 mainly comes from the local Permian Lucaogou Formation source rocks. At the same time, the source rocks of the Lucaogou Formation in the Yongfeng sub-sag and around the Bogda Mountain front belt have strong heterogeneity, and there are significant differences in their sedimentary environment and hydrocarbon parent materials on the plane.

8. Conclusions

(1) The source rocks of the Lucaogou Formation from the Yongfeng sub-sag exhibit significant heterogeneity on the plane. Based on the analysis of alkanes, terpenes, and hopanes in the extracts of source rock samples, the source rocks of Lucaogou Formation from Well Xyd 1 were formed in a reducing, semi-saline–saline sedimentary environment, while those from the Gjg and Dhs outcrops developed in a weakly oxidizing–weakly reducing, non-high-salinity, weakly stratified sedimentary environment.

(2) The source rocks of the Lucaogou Formation from Well Xyd 1 have strong heterogeneity, with some sample extracts showing relatively high saturated hydrocarbon content and a saturates/aromatics value greater than 3, and the other part of the samples is mainly composed of resins and asphaltene, with low saturate content. The group components extracted from the source rocks of the Lucaogou Formation from the Gjg and Dhs outcrops are mainly composed of resins, with a saturates/aromatics value less than 2, a high resins/asphaltene value, and low maturity. The crude oil from Well Xyd 1 has mature crude oil characteristics, with a high saturates/aromatics value (3.39–3.54) and low polarity components.

(3) The crude oil and source rock extracts from Well Xyd 1 have heavy carbon isotope values and exhibit high consistency in sample data distribution, with the gammacerane index greater than 0.2. The distribution characteristics of terpenes show that the Ts/Tm value and C_{24}TeT/C_{26}TT value of the crude oil from Well Xyd 1 are more similar to their corresponding values in the source rock. The content characteristics of C_{19} to C_{23} tricyclic terpenes in crude oil and source rock extracts from Well Xyd 1 also show high similarity. Multiple parameters confirm that the crude oil from Well Xyd 1 mainly comes from the local Middle Permian Lucaogou Formation source rock.

Author Contributions: Conceptualization and methodology, X.S.; validation, formal analysis, investigation, and resources, L.W. and Y.C.; data curation, J.W., X.Z., Y.G., Y.Y., Z.B. and K.Y.; writing—original draft preparation, L.W., Y.C., and X.S.; writing—review and editing, visualization, supervision, and project administration, X.S. All authors have read and agreed to the published version of the manuscript.

Funding: This research was funded by the Geological Survey Project of China Geological Survey (DD20190090, DD20230042, DD20240044, and DD20242210).

Data Availability Statement: We state that the data are unavailable due to privacy or ethical restrictions of the company and university.

Conflicts of Interest: The authors declare no conflicts of interest.

References

1. Chen, J.; Wang, X.; Ni, Y.; Xiang, B.; Liao, F.; Liao, J. The accumulation of natural gas and potential exploration regions in the southern margin of the Junggar basin. *Acta Geol. Sin.* **2019**, *93*, 1002–1019.
2. Du, J.; Zhi, D.; Li, J.; Yang, D.; Tang, Y.; Qi, X.; Xiao, L.; Wei, L. Major breakthrough of Well Gaotan l and exploration prospects of lower assemblage in southern margin of Junggar basin, NW China. *Pet. Explor. Dev.* **2019**, *46*, 205–215. [CrossRef]
3. Zhi, D.; Song, Y.; He, W.; Jia, X.; Zou, Y.; Huang, L. Geological characteristics, resource potential and exploration direction of shale oil in Middle-Lower Permian, Junggar Basin. *Xinjiang Pet. Geol.* **2019**, *40*, 389–401.
4. Yang, Y.; Zhang, J.; Zhang, J.; Gao, Y.; Zhou, X.; Sun, X.; Wen, L.; Miao, M. Sedimentary characteristics and main controlling factors of the Middle-Upper Permian and Middle-Upper Triassic around Bogda Mountain of Xinjiang, NW China. *Pet. Explor. Dev.* **2022**, *49*, 770–784. [CrossRef]
5. Wu, P.; Zhao, P.; Chen, Y.; Yang, H.; Yang, Y.; Dong, Q.; Chang, Y.; Wen, L.; Yuan, K.; Du, Y.; et al. Tight Reservoir Characteristics and Controlling Factors of Permian Lucaogou Formation in Yongfeng Sub-Sag, Chaiwopu Sag. *Processes* **2023**, *11*, 3068. [CrossRef]
6. Sun, X.; Chen, Y.; Zhou, X.; Bai, Z.; Du, Y.; Wen, L.; Yuan, K. Characteristics and Origin of Natural Gas in Yongfeng Sub-Sag of Bogda Mountain Front Belt. *Appl. Sci.* **2024**, *14*, 9085. [CrossRef]
7. Jin, Z.; Zhu, R.; Liang, X.; Shen, Y. Several issues worthy of attention in current lacustrine shale oil exploration and development. *Pet. Explor. Dev.* **2021**, *48*, 1276–1287. [CrossRef]
8. Qiu, Z.; Shi, Z.; Dong, D.; Lu, B.; Zhang, C.; Zhou, J.; Wang, H.; Xiong, B.; Pang, Z.; Guo, H. Geological characteristics of source rock and reservoir of tight oil and its accumulation mechanism: A case study of Permian Lucaogou Formation in Jimusar sag, Junggar Basin. *Pet. Explor. Dev.* **2016**, *43*, 928–939. [CrossRef]
9. Song, Y.; Luo, Q.; Jiang, Z.; Yang, W.; Liu, D. Enrichment of tight oil and its controlling factors in central and western China. *Pet. Explor. Dev.* **2021**, *48*, 492–506. [CrossRef]
10. Zhi, D.; Xie, A.; Yang, F.; Ma, Q.; He, C.; Gou, H. Exploration prospects of the whole oil and gas system in the Permian hydrocarbon depressions in the Eastern Junggar Basin. *J. Geomech.* **2024**, *30*, 781–794.
11. Yang, Y.; Zheng, X.; Xiao, Y.; Lei, Z.; Xing, H.; Xiong, T.; Liu, M.; Liu, S.; Hou, M.; Zhang, Y. Progress in exploration and development of high-mature shale oil of PetroChina. *China Pet. Explor.* **2023**, *28*, 23–33.
12. Wang, J.; Liu, J.; Pan, X.; Zhang, B.; Li, E.; Zhou, X. Precursor and Mechanism of Hydrocarbon Generation for Shale Oil in Lucaogou Formation, Jimsar Sag. *Xinjiang Pet. Geol.* **2024**, *45*, 253–261.
13. Jia, C.; Wang, Z.; Jiang, L.; Zhao, W. Progress and key scientific and technological problems of shale oil exploration and development in China. *World Pet. Ind.* **2024**, *31*, 1–11.
14. Cao, Z.; Zhou, C.; Gong, D.; Wang, R.; Ding, L.; Yang, C.; Zhang, Z. Tectono-lithofacies paleogeographic characteristics and source rock distribution of the Middle-Lower Permian in Junggar Basin. *Acta Pet. Sin.* **2024**, *45*, 1349–1371.
15. Price, L.C. Thermal stability of hydrocarbons in nature: Limits, evidence, characteristics, and possible controls. *Geochim. Cosmochim. Acta* **1993**, *57*, 3261–3280. [CrossRef]
16. Kruge, M.A.; Hubert, J.F.; Akes, R.J.; Meriney, P.E. Biological markers in Lower Jurassic synrift lacustrine black shales, Hartford basin, Connecticut, U.S.A. *Org. Geochem.* **1990**, *15*, 281–289. [CrossRef]
17. Chandra, K.; Mishra, C.S.; Samanta, U.; Gupta, A.; Mehrotra, K.L. Correlation of different maturity parameters in the Ahmedabad-Mehsana block of the Cambay basin. *Org. Geochem.* **1994**, *21*, 313–321. [CrossRef]
18. Bao, J.; Zhu, C.; Wang, L. Geochemical characteristic comparison of crude oil samples from the western Qaidam Basin. *Oil Gas Geol.* **2010**, *31*, 353–359.
19. Zhang, M.; Liu, C.; Tian, J.; Pang, H.; Zeng, X.; Kong, H.; Yang, S. Characteristics of crude oil geochemical characteristics and oil source comparison in the western part of Qaidam Basin. *Nat. Gas Geosci.* **2020**, *31*, 61–72.
20. Ourisson, G.; Albrecht, P.; Rohmer, M. Predictive microbial biochemistry—From molecular fossils to procaryotic membranes. *Trends Biochem. Sci.* **1982**, *7*, 236–239. [CrossRef]
21. Revill, A.T.; Volkman, J.K.; O'Leary, T.; Summons, R.E.; Boreham, C.J.; Banks, M.R.; Denwer, K. Hydrocarbon biomarkers, thermal maturity, and depositional setting of tasmanite oil shales from Tasmania, Australia. *Geochim. Cosmochim. Acta* **1994**, *58*, 3803–3822. [CrossRef]
22. Philp, R.P.; Gilbert, T.D. Biomarker distributions in Australian oils predominantly derived from terrigenous source material. *Org. Geochem.* **1986**, *10*, 73–84. [CrossRef]

23. Boreham, C.J.; Blevin, J.E.; Radlinski, A.P.; Trigg, K.R. Coal as a source of oil and gas: A case study from the Bass basin, Australia. *Appea J.* **2003**, *43*, 117–148. [CrossRef]
24. Moldowan, J.M.; Seifert, W.K.; Gallegos, E.J. Identification of an extended series of tricyclic terpanes in petroleum. *Geochim. Et Cosmochim. Acta* **1983**, *47*, 1531–1534. [CrossRef]
25. Damsté, J.S.S.; Kenig, F.; Koopmans, M.P.; Koster, J.; Schouten, S.; Hayes, J.M.; De Leeuw, J.W. Evidence for gammacerane as an indicator of water column stratification. *Geochim. Cosmochim. Acta* **1995**, *59*, 1895–1900. [CrossRef] [PubMed]
26. Huang, W.Y.; Meinschein, W.G. Sterols as ecological indicators. *Geochim. Cosmochim. Acta* **1979**, *43*, 739–745. [CrossRef]
27. Walters, C.C. *The Biomarker Guide*; Cambridge University Press: Cambridge, UK, 2005; pp. 322–352.
28. Moldowan, J.M.; Seifert, W.K.; Gallegos, E.J. Relationship between petroleum composition and depositional environment of petroleum source rocks. *Am. Assoc. Pet. Geol. Bull.* **1985**, *69*, 1255–1268.
29. Radke, M.; Vriend, S.P.; Ramanampisoa, L.R. Alkyldibenzofurans in terrestrial rocks: Influence of organic facies and maturation. *Geochim. Cosmochim. Acta* **2000**, *64*, 275–286. [CrossRef]
30. Boreham, C.J.; Crick, I.H.; Powell, T.G. Alternative calibration of the Methylphenanthrene Index against vitrinite reflectance: Application to maturity measurements on oils and sediments. *Org. Geochem.* **1988**, *12*, 289–294. [CrossRef]
31. Li, M.; Shi, S.; Wang, T.; Fang, R.; Zhu, L. The identification of C3- and C4- alkylated dibenzothiophenes in petroleum and sedimentary organic matter. *Geochimica* **2014**, *43*, 157–165.
32. Chen, J.; Liang, D.; Wang, X.; Deng, C.; Xue, X.; Jin, T.; Song, F.; Zhong, N. Oil-source identification for the mixed oils derived from multiple source rocks in the Cainan Oilfield, Junggar Basin, Northwest China. Part I: Fundamental geochemical features of source rocks. *Pet. Explor. Dev.* **2003**, *30*, 20–24.
33. Wang, J.; Li, E.; Chen, J.; Mi, J.; Ma, C.; Lei, H.; Xie, L. Characteristics and hydrocarbon generation mechanism of high- quality source rocks in Permian Lucaogou Formation, Jimsar Sag, Junggar Basin. *Geol. Rev.* **2020**, *66*, 755–764.
34. Volkman, J.K. A review of sterol markers for marine and terrigenous organic matter. *Org. Geochem.* **1986**, *9*, 83–99. [CrossRef]

energies

MDPI

Article

Occurrence Mechanism of Crude Oil Components in Tight Reservoirs: A Case Study of the Chang 7 Tight Oil in the Jiyuan Area, Ordos Basin, China

Mengya Jiang [1,2,3], Dongxia Chen [1,2,3,*], Qiaochu Wang [1,2,3], Fuwei Wang [1,2,3], Xiujuan Wang [1,4], Kuiyou Ma [1,2,3], Yuchao Wang [1,2,3], Wenzhi Lei [1,2,3], Yuqi Wang [1,2,3], Zaiquan Yang [1,2,3], Renzeng Wanma [1,2,3] and Lanxi Rong [1,2,3]

[1] State Key Laboratory of Petroleum Resources and Engineering, China University of Petroleum (Beijing), Beijing 102249, China; jiangmycup@163.com (M.J.); currywang2@163.com (Q.W.); wangfw_cup@163.com (F.W.); 17801170985@163.com (X.W.); mky7201128@126.com (K.M.); wyc1996cupb@163.com (Y.W.); 18382244604@163.com (W.L.); wyq17801231929@163.com (Y.W.); yzqtx2010@163.com (Z.Y.); 2022215011@student.cup.edu.cn (R.W.); ronglanxi3019@163.com (L.R.)
[2] College of Geoscience, China University of Petroleum (Beijing), Beijing 102249, China
[3] Hainan Institute of China University of Petroleum (Beijing), Sanya 572024, China
[4] PetroChina Changqing Oilfield Co., Xi'an 710018, China
* Correspondence: lindachen@cup.edu.cn

Abstract: Tight oil is an important unconventional hydrocarbon resource. The differences in occurrence characteristics between light components (LCs) and heavy components (HCs) of tight oil profoundly affect its mobility and recovery. Current research has focused mainly on the rapid evaluation of the relative contents of LCs, whereas few studies have systematically analyzed the occurrence characteristics of LCs and HCs and their controlling factors. In this study, the differential occurrence characteristics between LCs and HCs are clarified on the basis of data from thin-section petrography, X-ray diffraction, nuclear magnetic resonance, confocal laser scanning microscopy, and reservoir pyrolysis analysis. An innovative quantitative characterization methodology for the relative occurrence volumes of LCs and HCs is proposed. On the basis of this method, the controlling factors that cause the different occurrence characteristics of LCs and HCs are elucidated. Furthermore, the occurrence characteristics of LCs and HCs in various source–reservoir combinations, physical properties, and development intensities of argillaceous laminae are summarized. Finally, an occurrence model of the crude oil components in the Chang 7 tight reservoir is established. The results show that LCs and HCs in the Chang 7 tight reservoir exhibit differences in occurrence volume, state, morphology, and pore size. These differences are primarily controlled by the hydrocarbon generation intensity of the source rock, the source-to-reservoir distance (SRD), and the content of oil-wet minerals in the reservoir. The source sandwich combination exhibits high physical properties, low hydrocarbon generation intensity, high SRD, and low oil-wet mineral content, resulting in relatively high LCs. The source–reservoir interbed and reservoir sandwich combinations feature a high content of argillaceous laminae, high hydrocarbon generation intensity, low SRD, and high oil-wet mineral content, resulting in relatively low LCs. There are three occurrence models of crude oil components in the Chang 7 tight reservoir: the charging force controlling model, the adsorption effect controlling model, and the argillaceous laminae controlling model. The results of this study provide significant guidance for predicting the fluidity of tight oil, accurately assessing the amount of recoverable tight oil resources, and achieving efficient extraction of tight oil.

Keywords: occurrence mechanism; oil components; tight sandstone; Jiyuan area

1. Introduction

Tight oil, also known as tight reservoir oil, refers to petroleum resources stored in tight reservoirs, such as tight sandstone or tight carbonate rocks, with an in-situ matrix permeability of $\leq$0.1 mD [1]. Compared to conventional oil, tight oil is near mature, high-quality source rocks, lacks distinct trapping boundaries, and exhibits no natural productivity [2]. As an important component of unconventional oil and gas resources, tight oil is widely distributed and holds great resource potential for exploration and development [3,4]. At present, 66 identified basins contain tight oil resources, with a total globally recoverable reserve estimated at 639.3 billion tons [5]. The United States, recognized as the leading region for tight oil resource development, produced 378 million tons in 2022, representing 64% of its total crude oil output [6]. China also possesses abundant continental tight oil resources, totaling approximately 106.7 billion tons [7], which are located primarily in the Ordos, Songliao, Sichuan, and Junggar Basins [8]. Among them, the Ordos Basin has the highest quantity of tight oil resources, approximately 3.42 billion tons, making it an important potential replacement area for future oil and gas development in China [9,10].

The productivity and recovery efficiency of tight oil are influenced by various factors, including the physical properties of tight reservoirs [11], mineral wettability [12], oil saturation [13,14], crude oil mobility [15], and the stimulability of tight reservoirs [16]. Among these factors, crude oil mobility is one of the most important indicators from a geological perspective for evaluating the economic recoverability of a tight oil reservoir [3,17,18]. Moreover, under similar reservoir conditions, the fluid properties of crude oil are among the primary factors controlling the mobility of tight oil [15,19]. Compared with the heavy components (HCs) of crude oil, the light components (LCs) exhibit greater mobility in the same tight reservoir [15], which results in tight oil accumulation with a high LCs-to-HCs ratio (LHR), which is often an important target for economic recoverability [20]. In unconventional oil and gas reservoirs, which accumulate oil and gas driven by nonbuoyancy forces, including tight and shale reservoirs, the micromigration or short-distance migration of hydrocarbons results in the differential occurrence of LCs and HCs [21]. This causes an uneven distribution of the LHR within the reservoir, even under the condition of a uniform oil and gas source with the same fluid properties [22]. On the basis of crude oil injection experiments and confocal laser scanning microscopy (CLSM), Gao et al. [23] observed and quantitatively characterized the differential occurrence of HCs and LCs during the oil and gas injection process into shale reservoirs. The results revealed that HCs tend to occur more often on the surfaces of oil-wet minerals as adsorbed fluids than LCs do and are more enriched in the inner dark laminae, which contain high concentrations of clay minerals, inorganic carbon, or organic matter. Wang et al. [24] used molecular dynamics simulations to investigate the occurrence characteristics of crude oil with different component compositions in shale reservoirs. The results indicated that, compared with crude oil with a lower proportion of HCs, crude oil with a higher proportion of HCs has more adsorption layers and a greater adsorption density. On the basis of the results of pore network structure characterization of shale reservoirs and multistage pyrolysis experiments, Ma et al. [25] analyzed the effects of pore network structure, organic matter abundance, and maturity on the occurrence characteristics of crude oil. The results indicated that shale pore characteristics have a minor influence on the amounts of LCs and HCs, and that reservoirs with high organic matter abundance and maturity tend to have a relatively high LHR and free hydrocarbon content, making them favorable areas for exploration. In a study on the micromigration mechanisms of shale oil and gas, Hu et al. [21] reported that LCs, as the primary migrating fluid from hydrocarbon-rich layers to hydrocarbon-poor layers, are predominantly enriched in pores ranging from 100–5000 nm in size. In contrast,

HCs, as the main residual fluid in hydrocarbon-rich layers, are enriched primarily in pores ranging from 1 to 2 nm. This suggests that, in shale reservoirs where significant migration phenomena occur, the pore distribution characteristics play a distinct role in controlling the differential distributions of LCs and HCs. In summary, in shale reservoirs, mineral wettability [23], pore structure characteristics [21,25], the presence of laminae rich in clay or inorganic carbon [23], organic matter content [26], and organic matter maturity [25] collectively control the differential distribution characteristics of LCs and HCs.

Tight oil and shale oil share many similarities, including their hydrocarbon charging force, which is overpressure within the source rock; their reservoir pore networks, which are composed of nanopores and micropores; their lithology, which contains a high content of clay minerals; and their reservoirs, which contain substantial amounts of carbonaceous and argillaceous laminae [20]. Moreover, the short-distance migration of oil during the charging process in tight reservoirs is significantly greater than the micromigration between different laminae within shale reservoirs [20,27]. Therefore, tight reservoirs also commonly exhibit different distributions of LCs and HCs [28]. However, research on the occurrence characteristics of crude oil and the differential distributions of LCs and HCs in tight reservoirs is very limited, resulting in an unclear understanding of the mechanisms and controlling factors for the differential occurrence of LCs and HCs in tight reservoirs. To address this scientific question, this study innovatively proposes a method that combines Rock-Eval reservoir pyrolysis with confocal laser scanning microscopy (CLSM) observations to characterize the differential distributions of LCs and HCs in tight reservoirs quantitatively. With this approach, the Chang 7 tight oil reservoir in the Jiyuan area of the Ordos Basin is taken as an example. Core data, field emission scanning electron microscopy (FE-SEM) observations, nuclear magnetic resonance (NMR) experiments, and whole-rock X-ray diffraction (XRD) analysis are used to clarify the controlling effects of the pore structure, source-to-reservoir distance (SRD), mineral wettability, and argillaceous laminae on the differential occurrence of LCs and HCs. Furthermore, the differential occurrence characteristics and controlling factors of crude oil in three different source–reservoir combinations within the Chang 7 tight reservoir are summarized and compared. Finally, a model for the occurrence of crude oil in the Chang 7 tight reservoir in the Jiyuan area is established. The findings of this study provide a method for rapidly predicting the spatial distribution of tight oil with high LCs contents and offer significant guidance for predicting the mobility and large-scale economic extraction of crude oil in tight reservoirs.

2. Geological Setting

The Ordos Basin is the second largest oil- and gas-bearing basin in China, with an area of approximately 37×10^4 km^2 [29]. The Ordos Basin can be further divided into six structural units, from south to north, namely, the Yimeng uplift, the Weibei uplift, the western margin thrust belt, the Tianhuan depression, the Yishan slope, and the Jinxi folding belt [30] (Figure 1a). The Jiyuan area is one of the most important tight oil exploration blocks in the Ordos Basin [31]. It is located in the central–western part of the Ordos Basin and is distributed mainly in the Tianhuan depression, with a small part in the Yishan slope (Figure 1a). In the Jiyuan area, the Upper Triassic Yanchang Formation is the main oil-bearing stratum. It can be subdivided into ten members, from bottom to top, ranging from the Chang 10 member to the Chang 1 member (Figure 1b), which records the entire development process of the Ordos Basin [32]. Among them, the Chang 7 member is an important source rock and tight reservoir (Figure 1c). The Chang 7 member was deposited in an environment where the delta interacted with the lake. It is mainly composed of fine-grained sandstone interbedded with dark shale. The fine-grained sandstones, including fine sandstone, siltstone, and argillaceous siltstone, developed primarily in

the subaqueous distributary channel environment of the delta front and the gravity flow environment of the prodelta (Figures 1b and 2), providing important reservoir spaces for the development of tight oil [33,34]. The sandstone in the study area contains a high abundance of argillaceous laminae, which appear dark brown or gray-black under the microscope, with well-defined boundaries and a thickness of 0.1–3 mm per layer. These laminae have a high clay mineral content and contain a small amount of well-sorted quartz and other clastic minerals [35]. The dark shale mainly occurs in the Chang 7_3 submember, which developed in a semideep lake environment (Figure 1b) and is a thick source rock with good organic matter type, moderate maturity, and enormous resource potential, providing favorable oil-source conditions for the formation of tight oil (Figure 1c) [36,37].

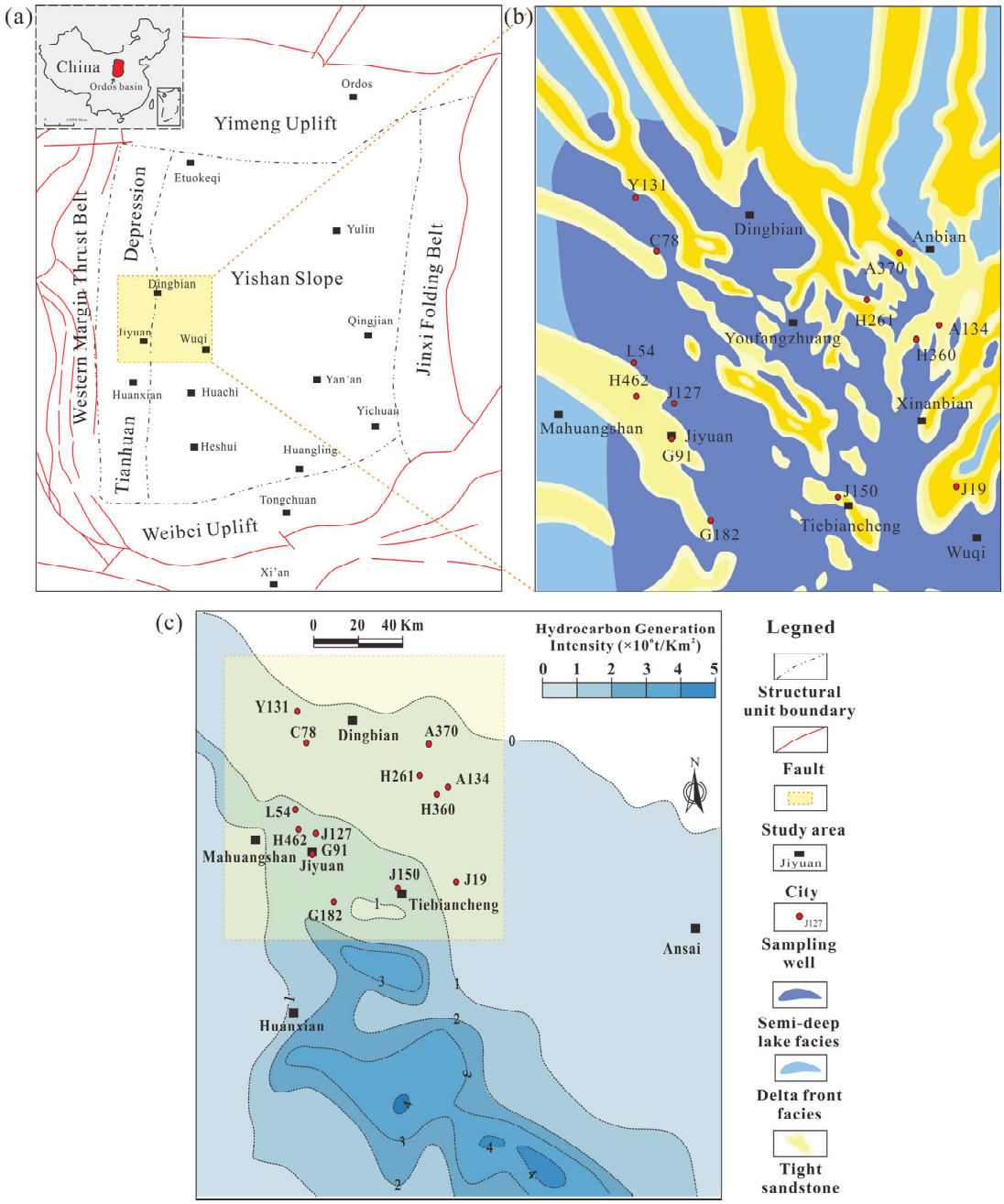

Figure 1. (**a**) Structural unit division diagram of the Ordos Basin (modified from [32]); (**b**) Distribution characterization diagram of the sedimentary facies and thickness of the sandstone in the Chang 7 member; (**c**) Characterization diagram of the hydrocarbon generation intensity of the Chang 7_3 source rock in the Jiyuan area (according to [36]).

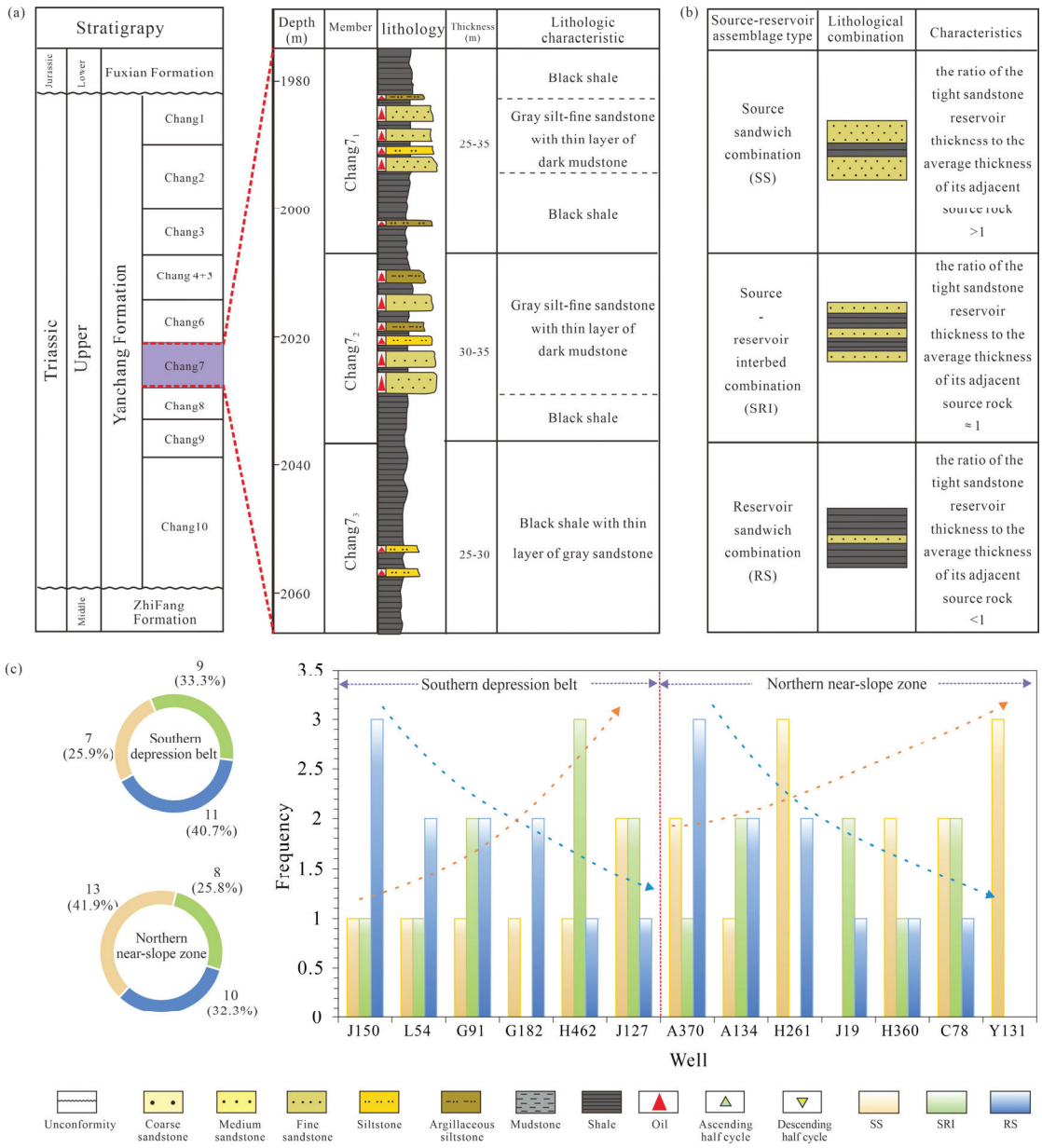

Figure 2. (**a**) Stratigraphic columns of the Triassic Chang 7 Member in the Jiyuan area, Ordos Basin. (**b**) Definition and geological model of the source–reservoir combination types. (**c**) Distribution characteristics of distinct source–reservoir combination types.

The hydrocarbon generation intensity of the Chang 7_3 source rock ranges from 0 to 5 × 10^6 t/km^2 (Figure 1c). In the Jiyuan area, the hydrocarbon generation intensity of the Chang 7_3 source rock is relatively weak, at less than 2 × 10^6 t/km^2. The hydrocarbon generation intensity in the southern part of the Jiyuan area is greater than 1 × 10^6 t/km^2, whereas in the northern part of the Jiyuan area, it ranges from 0 to 1 × 10^6 t/km^2 (Figure 1c) [36]. The source–reservoir combination type is an important element affecting the hydrocarbon supply conditions, hydrocarbon charging conditions, and occurrence characteristics of crude oil in tight reservoirs [32]. In the Jiyuan area, there are three types of source–reservoir combinations: the source sandwich combination (SS), source–reservoir interbed combination (SRI), and reservoir sandwich combination (RS) (Figure 2). In this study, the source–reservoir combination types are defined on the basis of the ratio of the tight sandstone reservoir thickness to the average thickness of its adjacent source rock. A ratio greater than 1, approximately equal to 1, and less than 1 corresponds

to SS, SRI, and RS, respectively. Moreover, as this ratio increases, the probability of the development of argillaceous laminae in tight reservoirs also increases (Figure 2). In the Jiyuan area, the SS is mainly developed in the low hydrocarbon generation intensity area in the northern near-slope zone, whereas the SRI and RS are primarily developed in the area with high hydrocarbon generation intensity in the southern depression belt (Figure 2).

The study area is characterized by the development of nearly SN-trending and NW-trending faults, followed by NE-trending faults [32]. Faults and associated fractures play a crucial role in modifying tight sandstones, serving as key controlling factors for tight gas production and significantly influencing the occurrence space and occurrence state of tight oil and gas [38]. However, the faults in the study area are relatively large in scale, and the overlying strata of the target formation mainly consist of sandstone reservoirs. This results in a lack of effective sealing conditions, leading to the faults acting as conduits and destructive forces on the tight oil reservoirs rather than significantly affecting the occurrence differentiation of LCs and HCs in tight oil.

3. Materials and Methodology

3.1. Samples

This study extensively collected optical thin section data from 165 wells in the Jiyuan area, specifically focusing on the Chang 7 member of tight sandstone reservoirs, to determine the main lithology characteristics, pore types, and pore sizes of the reservoir. Additionally, 13 representative wells were selected for intensive sampling of the tight reservoir cores, and a further series of experiments was conducted (Figure 1b,c). In the Jiyuan area, these wells are evenly distributed across the northern slope area, where the delta front and semideep lake sedimentary system are mainly developed, to the central depression, where the semideep lake and gravity flow sedimentary system are primarily developed (Figure 1b). A total of 40 representative samples of tight sandstone were selected from representative wells to further conduct Rock-Eval reservoir pyrolysis experiments, XRD analysis, and FE-SEM observations. Additionally, 12 samples with different source–reservoir combination types were selected from 40 samples for further analysis using nuclear magnetic resonance (NMR) experiments. Moreover, among these 40 samples, three tight reservoir samples with high crude oil saturation with different source–reservoir combination types were selected for CLSM observation to clarify the occurrence characteristics of crude oil in the tight reservoirs, including the sample from 2557.5 m in J127 (denoted as Sample I), the sample from 2407.8 m in L54 (denoted as Sample II), and the sample from 2710.1 m in G91 (denoted as Sample III). The lithology of Sample I is gray–brown fine sandstone, and its source–reservoir combination type is SS, while that of Sample II is gray fine sandstone with dark-colored argillaceous laminae, and its source–reservoir combination type is SRI. In contrast, Sample III is gray–brown siltstone, and its source–reservoir combination type is RS.

3.2. Experiments

3.2.1. XRD, FE-SEM, and NMR Analysis

In this study, the X-ray diffraction (XRD) experiment was performed using a Bruker D2 Phaser instrument (Bruker AXS GmbH, Karlsruhe, Germany) at the State Key Laboratory of Petroleum Resources and Engineering, China University of Petroleum (Beijing), following the specific operating procedures described by Wang et al. [32]. The purpose of the XRD experiment was to determine the mineral composition and relative abundance of each tight sandstone reservoir sample. The field emission scanning electron microscopy (FE-SEM) observations were conducted using a Hitachi SU8010 instrument (Hitachi High-Tech Corporation, Tokyo, Japan) at the Energy Materials Microstructure Laboratory, China

University of Petroleum (Beijing), and the specific operating procedures were described by Zang et al. [39]. The FE-SEM observations aimed to identify the mineral distribution characteristics and the geometric morphology, size, and connectivity of the pore structures in each tight reservoir sample. The nuclear magnetic resonance (NMR) experiment was conducted using a SPEC-RC035 low-field NMR spectrometer (Suzhou Niumag Analytical Instrument Corporation, Suzhou, China) at the State Key Laboratory of Petroleum Resources and Engineering, China University of Petroleum (Beijing). Additionally, the methods for sample pretreatment and obtaining T_2 relaxation time spectra followed those described by Qiao et al. [40]. After the sample was centrifuged for 1 h under a pressure of 300 psi, NMR was performed on the sample again to obtain the T_2 spectrum of the centrifuged sample. The T_2 relaxation time, spectra obtained before and after centrifugation were used to characterize the physical properties of each sample.

3.2.2. Reservoir Rock Pyrolysis Analysis

Reservoir rock pyrolysis experiments are methods that simulate the petroleum distillation process [41]. These methods are based on the differences in the boiling points of various components in crude oil, which are separated within specific temperature ranges as the temperature gradually increases. In this study, reservoir pyrolysis experiments on tight reservoir samples were conducted using a Rock-Eval II instrument (Vinci Technologies, Nanterre, France) at the State Key Laboratory of Petroleum Resources and Engineering, China University of Petroleum (Beijing). First, a sample weighing 99.5–100.5 mg was crushed to a particle size of 60–80 mesh. The crushed samples were subsequently placed in the crucible of the Rock-Eval II pyrolyzer to conduct the pyrolysis experiments. To prevent significant evaporation of light hydrocarbons, the crushing and testing of the samples were completed within 2 h. The pyrolysis crucible was initially heated at a constant temperature of 90 °C for 2 min to obtain the S_0 signal. The sample was subsequently heated at a constant temperature of 200 °C for 1 min to obtain the S_1 signal. Next, the temperature was increased at a rate of 50 °C/min to 350 °C and maintained at that temperature for 1 min to obtain the S_{21} signal. Afterward, the temperature was increased at 50 °C/min to 450 °C and maintained for 1 min to obtain the S_{22} signal. The temperature was increased at 50 °C/min to 600 °C and maintained for 1 min to obtain the S_{23} signal. Finally, the S_4 signal was obtained at 600 °C for 7 min at a constant temperature. On the basis of this pyrolysis heating rate, the S_0, S_1, S_{21}, S_{22}, $S_{23,}$ and S_4 signals represent the natural gas components, gasoline components, kerosene and diesel components, wax and heavy oil components, resin and asphaltene components, and residual carbon components in the crude oil, respectively (Figure 3a) [41]. The various components of crude oil are composed of hydrocarbons and nonhydrocarbons with different carbon chain lengths. The hydrocarbon and nonhydrocarbon components of natural gas, gasoline, kerosene, diesel, wax, heavy oil, resin, and asphaltene have carbon chain lengths ranging from 1–4, 5–12, 10–16, 12–20, 20–40, 20–60, 50–200, and 50–200, respectively. Additionally, on the basis of the carbon chain length of hydrocarbons, crude oil components can be classified into LCs and HCs. Crude oil components with a carbon chain length less than or equal to 20 have lower density and belong to the LCs of the crude oil, whereas other components of crude oil have higher density and belong to the HCs of the crude oil [42]. After pyrolysis, some residual oil remains. The residual oil content is determined by measuring the residual organic carbon through heat oxidation, and the residual organic carbon is divided by 0.9 to convert it into residual oil. Residual oil refers to the heavy oil components remaining in the rock after pyrolysis of the source rock, which mainly consists of the residues of resins and asphaltenes after pyrolysis [41]. For the reservoir rock pyrolysis experiments in this study,

the mass of the LCs of crude oil is the sum of the S_0, S_1, and S_{21} signals, whereas the HCs are the sum of the S_{22}, S_{23}, and $S_4/0.9$ signals.

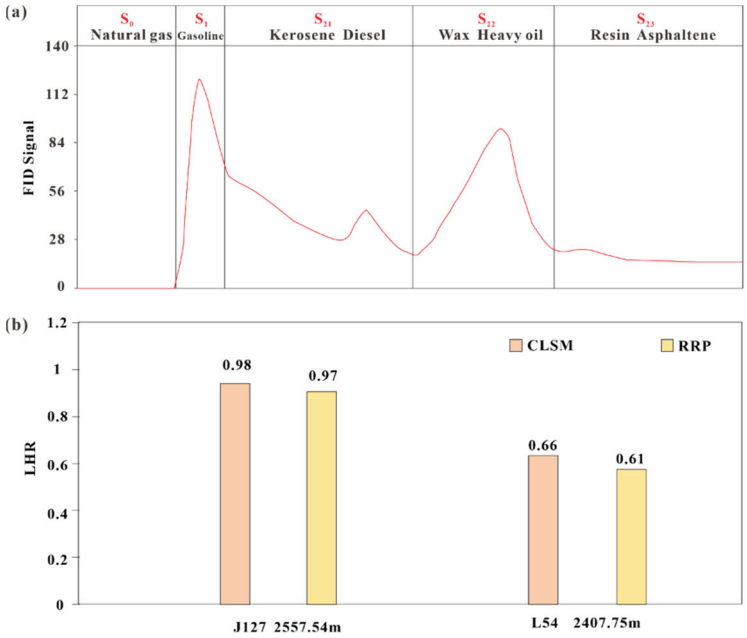

Figure 3. (**a**) Representative quantitative analysis spectrum of oil and gas components obtained from the reservoir rock pyrolysis experiment on Sample I. (**b**) Histogram showing the comparison of experimental results between the CLSM and reservoir rock pyrolysis experiment.

3.2.3. Laser Scanning Confocal Microscopy

The laser scanning confocal microscopy (CLSM) experiment was conducted using a Leica TCS SP8 (Leica Microsystems, Wetzlar, Germany) at the State Key Laboratory of Petroleum Resources and Engineering, China University of Petroleum (Beijing). First, objective areas in the sample were selected for observation. The selected areas were then finely ground into slices with a thickness of 0.04–0.05 mm, and these slices were placed on a stage maintained at a temperature of 25 °C and a relative humidity of 30–46% for observation. The maximum imaging resolution of this equipment is approximately 200 nm, and a fixed wavelength 488 nm laser was used to excite the sample. On the basis of the wavelength of the fluorescence signals obtained from the excited sample, CLSM can independently observe and quantitatively characterize the occurrence volumes of the LCs and HCs in the tight reservoir. The fluorescence capture range for the LCs of crude oil is 490–600 nm, whereas the fluorescence capture range for the HCs is 600–800 nm [23]. CLSM distinguishes between LCs (including low-carbon saturated hydrocarbons and short-chain aromatic hydrocarbons) and HCs (including high-carbon saturated hydrocarbons, long-chain aromatic hydrocarbons, nonhydrocarbons, and asphaltenes) in crude oil on the basis of the different wavelength ranges of the fluorescence signals generated by excitation.

3.3. Characterization Method for LHR_v

Although the CLSM and reservoir rock pyrolysis experiments have different principles for distinguishing LCs and HCs [43,44], both classify the crude oil components with lower density, i.e., those with shorter carbon chains, as LCs, and the crude oil components with higher density, i.e., those with longer carbon chains, as HCs. The differences in the principles of the two experiments lead to only slight differences in defining the critical conditions for distinguishing the LCs and HCs. This also indicates a high likelihood of a good correlation between the results of the two experiments. CLSM is an important experimental technique for observing the microscale characteristics of the LCs and HCs

of crude oil, but it is difficult to characterize their macroscopic occurrence patterns [45]. On the other hand, the reservoir rock pyrolysis experiment is suitable for analyzing the macroscopic occurrence patterns of the LCs and HCs of crude oil, but their microscopic occurrence characteristics cannot be observed [46]. Therefore, if the linkage between the two experiments for the quantitative characterization of crude oil LCs and HCs is established, the results of the two experiments can complement each other to analyze the occurrence characteristics of the LCs and HCs on both the microscopic and macroscopic scales jointly. However, the results of reservoir pyrolysis experiments reveal the masses of different components [15], whereas CLSM provides the volume fractions of LCs and HCs [47]. In addition to the dimensional difference, the results obtained from CLSM are not absolute contents of the LCs and HCs but rather relative proportions [23]. To establish a connection between the results of the two experiments, the volume ratio of LCs and HCs (LHR_v) was used to characterize the relative proportions of LCs and HCs (Formula (1)). The LHR_v can be directly calculated according to the results of CLSM experiments. For the reservoir rock pyrolysis experiment, LHR_v can be calculated via Formula (2). The LHR_v values calculated on the basis of both experiments on Sample I and Sample II show small differences and are strongly relevant, demonstrating the feasibility of this approach (Figure 3b).

$$LHR_v = \frac{LCs_v}{HCs_v} \tag{1}$$

$$LHR_v = \left(\frac{S_0}{\rho_0} + \frac{S_1}{\rho_1} + \frac{S_{21}}{\rho_{21}}\right) / \left(\frac{S_{22}}{\rho_{22}} + \frac{S_{23}}{\rho_{23}} + \frac{S_4}{0.9 * \rho_4}\right) \tag{2}$$

where LHR_v represents the volume ratio of LCs and HCs, dimensionless; LCs_v and HCs_v denote the volume fraction of the LCs and HCs obtained from the CLSM experiment, nm^3; S_{11}, S_{21}, S_{22}, $S_{23,}$ and S_4 denote the masses of gasoline, kerosene and diesel, wax and heavy oil, colloid and asphaltene, and residual oil obtained from the reservoir rock pyrolysis experiment, mg/g, respectively; and $\rho_{0,}$ ρ_1, ρ_{21}, ρ_{22}, ρ_{23}, and ρ_4 represent the densities of the natural gas, gasoline, kerosene, and diesel, wax and heavy oil, colloidal and asphaltene, and residual oil components of the crude oil, g/cm^3, with values of 0.0007, 0.7, 0.8, 1.0, 1.25, and 1.4, respectively [48].

Notably, in this study, the core samples were not saturated with oil during the experimental process. Additionally, during the processing of the raw experimental data, no light hydrocarbon recovery was performed on the results of the reservoir pyrolysis experiment. This approach was taken because it is challenging to replicate the actual geological conditions of the oil charging process under laboratory conditions [49]. This could impact the occurrence state of LCs and HCs and result in significant differences between the occurrence characteristics of LCs and HCs in processed core samples and their actual occurrence under geological conditions. In addition, there are numerous methods for light hydrocarbon recovery, and the factors influencing light hydrocarbon dissipation are diverse and complex [44]. Using a unified recovery method alone may increase the differences in the relative contents of LCs and HCs under actual geological conditions. Furthermore, this study focused primarily on the relative changes in LCs and HCs in tight oil. The trend of changes in the relative proportions of LCs and HCs in all samples caused by the dissipation of light hydrocarbons is the same. Therefore, not performing light hydrocarbon recovery on the results of the reservoir pyrolysis experiment allows for the maximum preservation of information on the relative contents of LCs and HCs in tight oil reservoirs.

4. Results

4.1. Tight Reservoir Characteristics

The lithology of the Chang 7 tight sandstone reservoir in the Jiyuan area is mainly composed of arkose and lithic arkose (Figure 4a). The clastic components are primarily clay minerals, quartz, and feldspar (including plagioclase and potassium feldspar), followed by calcite and dolomite (Figure 4b). The sandstone in the Chang 7 member is dominated by fine sandstone, moderately sorted, subangularly rounded, and presents point–line contacts between particles (Figure 4c_1,c_2). On the basis of microscopic observations, the pore types in the sandstone samples from the Jiyuan area can be classified into five categories: residual intergranular pores, intergranular dissolution pores, intragranular dissolution pores, and intercrystalline pores (Figure 4d,e). Residual intergranular pores dominate the pore system and are characterized by regular shapes between the clastic particles. Intergranular dissolution pores are formed by dissolving mineral particles (such as feldspar) or cementing materials (such as carbonate). Intragranular dissolution pores are distributed mainly within feldspar grains and often follow cleavage. In addition, intragranular dissolution pores can also occur within lithic fragments. The tight sandstone in the study area contains a significant number of intercrystalline pores. These pores often appear in the inner walls of dissolution pores and residual intergranular pores or on the surface of grains. Since faults and fractures primarily act as conduits and destructive factors in the tight oil reservoirs of the study area, with minimal impact on the occurrence differentiation of LCs and HCs in tight oil, this study focuses on the characteristics of pore storage space and does not provide a detailed discussion of fracture characteristics.

The reservoir water saturation NMR data in the study area can be classified into three types: unimodal, symmetric bimodal, and right-skewed bimodal (Figure 5a). By using the water saturation and centrifuged NMR results, the micropores, small pores, and large pores in tight sandstone reservoirs can be identified [50]. The boundary between micropores and small pores is defined by the T_2 value corresponding to the point where differences start to appear in the T_2 spectrum before and after centrifugation. Moreover, the boundary between small pores and large pores is defined by the T_2 value corresponding to the point where a significant difference begins to appear in the T_2 spectrum before and after centrifugation (Figure 5b). In addition, the T_2 value of NMR is proportional to the pore size [5]. Previous studies have commonly used 1 ms and 10 ms as the boundary values between micropores and small pores, and between small pores and large pores, respectively [51,52]. Based on the distribution range of boundary values determined before and after centrifugation of the study area samples, this study adjusted the boundary values, defining 0.5 ms as the threshold between micropores and small pores and 10 ms as the threshold between small pores and large pores, to better reflect the actual conditions of the study area. The T_2 value distribution of small pores in the study area generally ranges from 0.3 to 3 ms, whereas the T_2 values of large pores are primarily distributed in the >3 ms range. The proportion of large pores in the SS is relatively high, with an average value of 95.88%. In contrast, the proportion of small pores corresponding to the SRI and RS is greater, with a distribution range of 30.03% to 82.91% (Figure 5c).

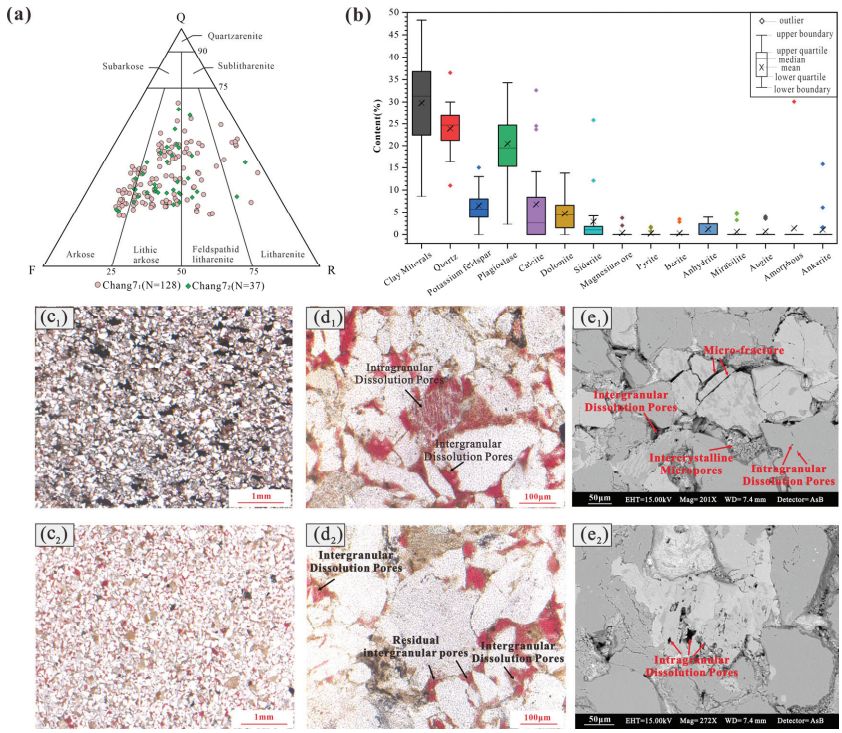

Figure 4. (**a**) Ternary plot illustrating the type of sandstones, with Q, F, and R representing quartz, feldspar, and rock fragments, respectively; (**b**) Box plot of the relative contents of different minerals in the Chang 7 tight reservoir; (**c**) Optical microscopy images under plane-polarized light with a 2.5× field of view, showing the grain size, sorting, roundness, and grain contact relationships of the Chang 7 tight reservoir. (**c$_1$**) Fine sand predominates, followed by very fine sand. The development of rock pores is poor, with low connectivity (Well G91, 2677.6 m). (**c$_2$**) Fine sand is in absolute dominance, with very little medium sand and very fine sand. The rock pores are moderately developed, and the connectivity is average (Well J127, 2557.5 m, 2.5x); (**d**) Optical microscopy images under plane-polarized light with a 20× field of view, showing the characteristics of distinct types of pores. The red areas are cast epoxy resin. (**d$_1$**) The intergranular dissolution pores developed between clastic particles; the intragranular dissolution pores developed in feldspar grains (Well J127, 2557.5 m). (**d$_2$**) Residual intergranular pores and intergranular dissolution pores developed between clastic particles (Well J127, 2557.5 m).; (**e**) FE-SEM images showing the characteristics of distinct types of pores. C represents calcite. (**e$_1$**) Intergranular dissolution pores, intercrystalline micropores, and intragranular dissolution pores in feldspar grains (Well J127, 2557.5 m, 331x). (**e$_2$**) Intragranular dissolution pores developed within calcite (Well J127, 2557.5 m, 272x).

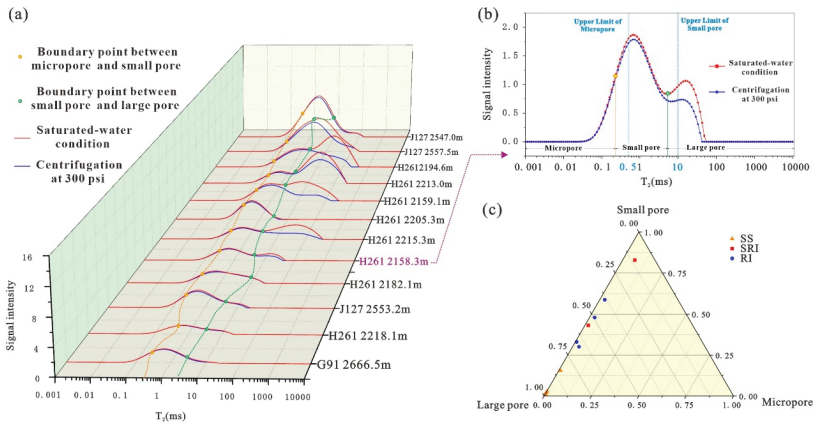

Figure 5. (**a**) Characteristics of T_2 relaxation time spectra before and after centrifugation of the Chang 7 tight reservoir; (**b**) Typical sample T_2 relaxation time spectra before and after centrifugation and pore distribution; (**c**) Pore distribution characteristics of different source–reservoir combinations.

4.2. Occurrence Characteristics of LCs and HCs

4.2.1. Occurrence Volume Characteristics

The volumetric transition results of the reservoir rock pyrolysis experiments reveal that there is a significant variation in the occurrence volume of crude oil in different tight reservoir samples, ranging from 0.20–18.16 mm^3/g, with an average value of 4.39 mm^3/g. However, the standard deviation can reach 3.69 mm^3/g (Figure 6a). The LHR_v in each sample also greatly differed, ranging from 0.22–4.23, with an average of 1.49 and a standard deviation of 0.97 (Figure 6a). Notably, even samples from adjacent depths within the same well show significant differences in the occurrence volumes of crude oil and LHR_v (Figure 6a). For example, in the case of the four tight reservoir samples from well G182, the maximum depth difference between the samples is only 23.3 m, but the range of occurrence volumes of crude oil and LHR_v can reach 7.48 mm^3/g and 2.14, respectively (Figure 6a). Additionally, even within different CLSM fields of the same sample, there are still small variations in LHR_v (Figure 6b). The range of LHR_v in Sample I is 0.89–1.06, with a mean of 0.98 and a standard deviation of 0.06 (Figure 6b). The range of LHR_v in Sample II is 0.55–1.01, with a mean of 0.66 and a standard deviation of 0.14 (Figure 6b). Among them, the anomalously high value of LHR_v appears in fields of view II–4, which may be due to the large difference between the local reservoir characteristics corresponding to fields of view II–4 and the overall reservoir characteristics of Sample II. The range of LHR_v in Sample III is 0.66–0.75, with a mean of 0.71 and a relatively low standard deviation of only 0.03 (Figure 6b).

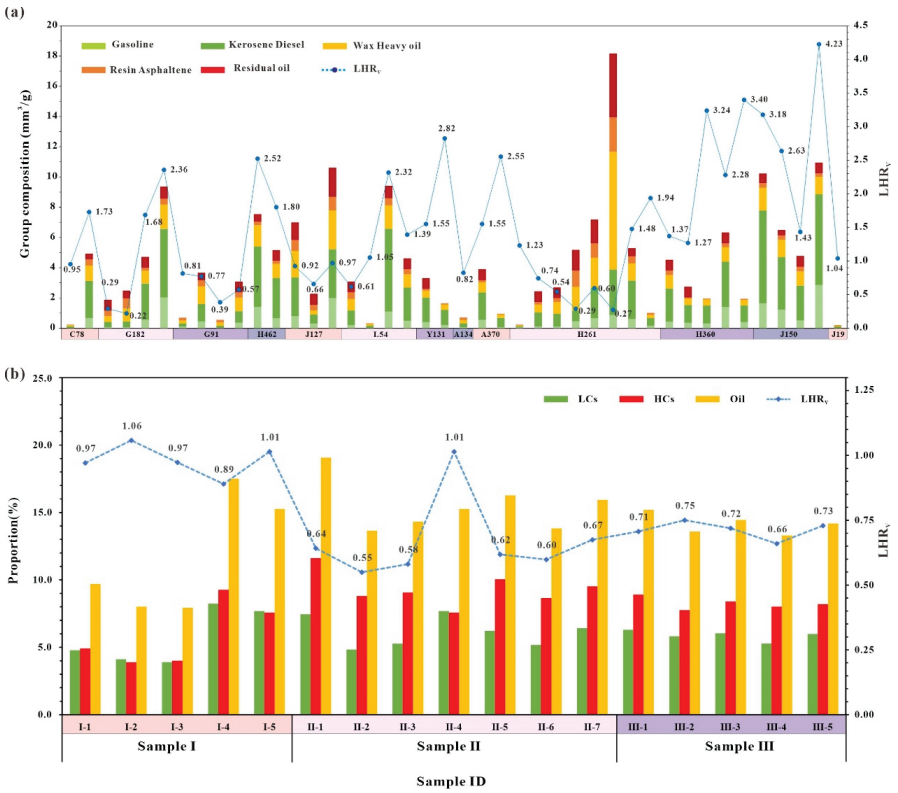

Figure 6. (**a**) Volumetric transition results of the reservoir rock pyrolysis experiment with different components and the distribution characteristics of LHR_v in the Chang 7 tight reservoir. (**b**) CLSM results for LCs and HCs and the distribution characteristics of LHR_v in the Chang 7 tight reservoir.

The composition of the expelled crude oil from source rocks during each hydrocarbon expulsion stage is approximately the same, which means that the LHR_v values of the expelled crude oil in each stage should also be approximately consistent and have a smaller

standard deviation. The significant fluctuations in the LHR_v among the different samples of the Chang 7 tight oil formation indicate that there was significant differentiation in the occurrence of LCs and HCs during the formation process, which primarily arises from the differences in fluid properties between the LCs and HCs of the crude oil and their interactions with the reservoir.

4.2.2. Occurrence State and Morphology Characteristics

In the original CLSM observation field, minerals can be identified as transparent or opaque on the basis of their light-transmitting properties [23]. Transparent minerals, such as quartz, calcite, potassium feldspar, and sodium feldspar, appear in light gray tones in the field of view, whereas opaque minerals, such as plagioclase feldspar, biotite, and pyroxene, appear darker (Figure 7). In the Chang 7 tight reservoir, the oil occurrence volume around translucent minerals is relatively large, whereas the oil occurrence volume around opaque minerals is relatively small. (Figure 7a_1,b_1,c_1,d_1). Moreover, the occurrence state of crude oil can be inferred from its occurrence morphology in tight or shale reservoirs [23]. For the Chang 7 tight reservoir, free oil is predominantly present in the form of spots, short columns, and clusters, which are mainly found in intergranular pores, intragranular pores, and throats. In contrast, bound oil occurs as films, strips, and clumps, which are primarily distributed in intergranular pores and intragranular pores (Figure 7a_1,b_1,c_1,d_1). The LCs and HCs of crude oil in tight reservoirs mainly exist as mixtures, but their occurrence states and morphologies slightly differ (Figure 7). In some small-sized intragranular pores and throats, only LCs are present in free states (Figure 7a,c). In contrast, in some large intragranular pores and intergranular pores, the area occupied by HCs is greater than that occupied by LCs (Figure 7). In addition, the LCs are distributed mainly in the middle of these pores, whereas the pore surfaces are exclusively occupied by HCs. This observation indicates that the adsorption capacity of HCs on pore surfaces is greater than that of LCs (Figure 7).

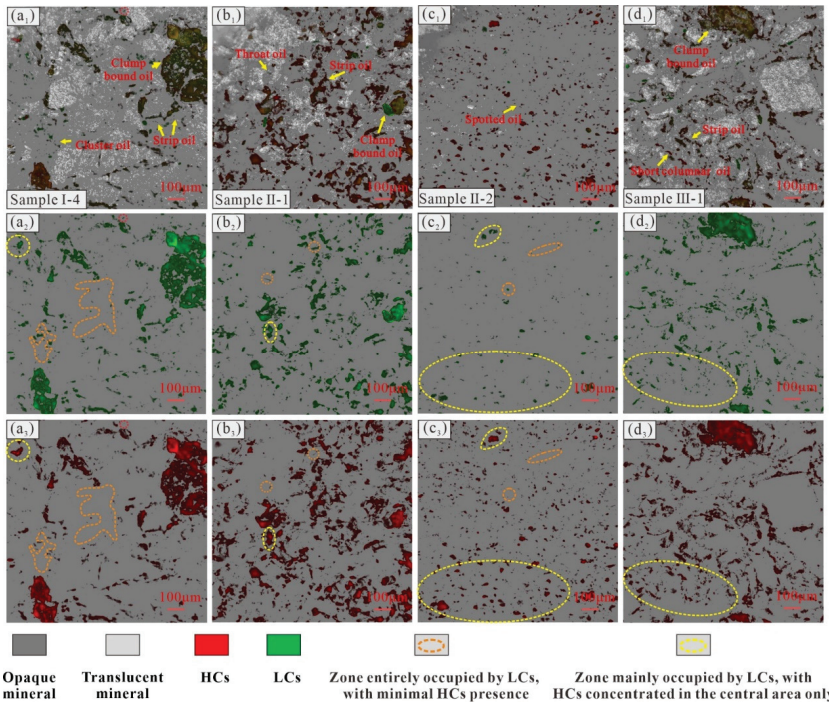

Figure 7. CLSM images illustrating the occurrence states and morphological characteristics of crude oil in the Chang 7 tight reservoir. From top to bottom: original CLSM images, LCs images, and HCs images for (**$a_{1–3}$**) Sample I (Well J127, 2557.5 m), (**$b_{1–3}$**,**$c_{1–3}$**) two fields of view of Sample II (Well L54, 2407.75 m), and (**$d_{1–3}$**) Sample III (Well G91, 2677.6 m).

4.2.3. Occurrence Pore Size Distribution Characteristics

On the basis of the CLSM observations, Image-Pro Plus software (version 6.0) was used to characterize the occurrence volume of LCs and HCs of crude oil in pores of different sizes in each field of view of each sample. The overall occurrence volume of the LCs and HCs in the Chang 7 tight reservoir initially tended to increase but then decreased with increasing pore size (Figure 8b–d). The crude oil is primarily distributed in pores with radii ranging from 1–8 μm, with less than 10% distributed in pores with radii smaller than 1 μm or larger than 8 μm (Figure 8a). In pores with radii of 1–2 μm, the content of the LCs was significantly greater than that of the HCs, with the former occurrence volume ranging from 5–15%, whereas the latter occurrence volume ranged from 0–5% (Figure 8a). This is consistent with the phenomenon described in Section 4.2.2, where the LCs almost entirely occupied the point-like small pores and short columnar throats (Figure 7a,c). In pores with radii of 2–4 μm, the overall content of the LCs remained higher than that of the HCs, but the difference between the two was relatively small (Figure 8a). In pores with radii of 4–6 μm, the content of HCs begins to slightly exceed that of LCs (Figure 8a). In pores with radii of 6–8 μm, the content of HCs was significantly greater than that of LCs, with the former occurrence volume mainly ranging from 15–20% and the latter ranging from 5–15% (Figure 8a). This may be attributed to the stronger adsorption and occupation capacities on the pore surfaces of HCs than on those of LCs in larger pores (Figures 7 and 8).

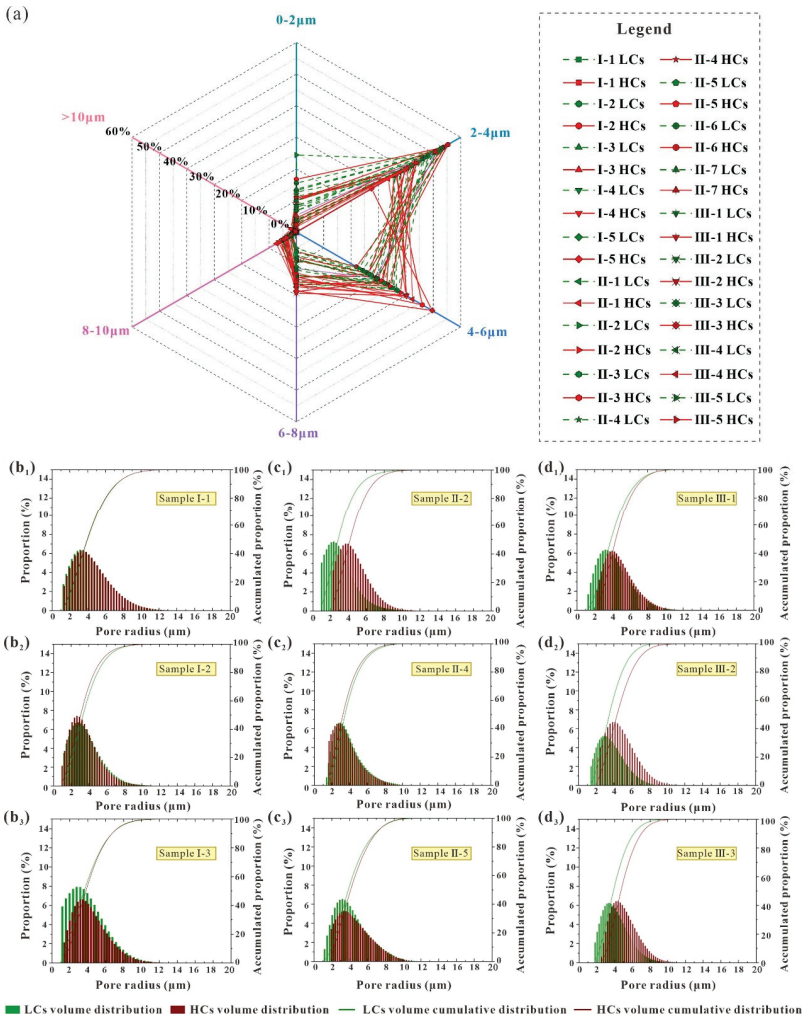

Figure 8. (**a**) Distribution characteristics of LCs and HCs with different pore sizes; (**b**–**d**) Distribution histograms of LCs and HCs contents under different pore sizes for (**b$_{1–3}$**) Sample I (Well J127, 2557.5 m), (**c$_{1–3}$**) Sample II (Well L54, 2407.75 m), and (**d$_{1–3}$**) Sample III (Well G91, 2677.6 m).

According to the differential characteristics of the occurrence of LCs and HCs in different-sized pores, the differences in the pore sizes of LCs and HCs can be divided into two categories: complete differentiation and partial differentiation. Complete differentiation refers to the phenomenon where only the LCs or HCs of the crude oil occur in specific-sized pores. If only LCs occur, it is referred to as LCs-dominated complete differentiation, and vice versa (Figures 7a,c and 8c_1,d). Partial differentiation refers to the phenomenon where the LCs and HCs of crude oil occur simultaneously in specific-sized pores, but their occurrence volumes significantly differ (Figures 7 and 8b_3,c_3). If the occurrence volume of the LCs is greater than that of the HCs, it is referred to as LCs-dominated partial differentiation, and vice versa. In summary, in pores with radii of 1–2 μm, there is mainly LCs-dominated complete differentiation, with a small amount of LCs-dominated partial differentiation (Figures 7 and 8). In pores with radii of 2–8 μm, partial differentiation primarily occurs. Among them, LCs-dominated partial differentiation occurs mainly in pores of 2–4 μm (Figures 7 and 8), whereas HCs-dominated partial differentiation occurs mainly in pores with radii of 4–8 μm (Figures 7 and 8).

4.3. Controlling Factors for the Occurrence Characteristics

The occurrence characteristics of LCs and HCs in tight reservoirs are influenced primarily by three critical mechanisms: the coupled control effects of the crude oil charging force and resistance [53], the adsorption effects of reservoir minerals [23], and the chromatographic effects of crude oil migration [54]. On the basis of these mechanisms, this study analyzes the impacts of hydrocarbon generation intensity, SRD, and mineral wettability on the occurrence of LCs and HCs in various source–reservoir combinations within the Chang 7 tight reservoir. Among these factors, the control effect of hydrocarbon generation intensity and SRD on occurrence can be summarized as the control effect of the crude oil charging force on occurrence, which helps to systematically elucidate the coupled effects of the charging force and resistance on the differential occurrence of LCs and HCs.

4.3.1. Charging Force

The physical properties of different crude oil components vary significantly, resulting in distinct capillary resistance between LCs and HCs under the same reservoir conditions [55]. During each individual hydrocarbon generation and expulsion period, the differences in the physical properties of crude oil are relatively minor [54]. Under such conditions, the differences in occurrence characteristics resulting from variations in the physical properties of different crude oil components are nearly unchanged. However, owing to the heterogeneous distribution of hydrocarbon generation pressure in source rocks [36] and the gradual attenuation of the crude oil charging force in the direction away from the source rock–reservoir contact surface [56], significant differences in the charging force of crude oil are distributed across various spatial locations. This can lead to very large differences in pore size and volume between LCs and HCs within tight reservoirs. To further explore the control mechanisms of the charging force on the occurrence characteristics of different crude oil components, two types of crude oils, LCs-rich and HCs-rich crude oils, are selected for use as approximate examples of LCs and HCs, respectively. Numerical simulation methods are employed to discuss the differential occurrence characteristics of LCs and HCs under different charging forces. The density and oil–water interfacial tension data for the two types of crude oils, as well as the wettability angle data for the HCs-rich crude oil referenced from numerical simulation parameters, are derived from relevant studies on the Chang 7 tight oil [57]. The wettability angle data for the LCs-rich crude oil in the oil–water–tight sandstone system are based on test results for similar-density oils in quartz-rich tight sandstone reservoirs [55]. The average pore–throat size ratio and the

maximum hydrocarbon generation pressure of the Chang 7 tight reservoir are sourced from the studies of [58] and [59], respectively (Table 1).

Table 1. Physical and geological parameters of LCs-rich and HCs-rich crude oils in the Chang 7 tight reservoir [55,57–59].

Type of Crude Oil	Density	Interfacial Tension	Contact Angle	Mean Size Ratio of Pore and Throat	Maximum Hydrocarbon Generation Pressure
LCs-rich	772 kg/m^3	19.3 mN/m	142°	400	21 Mpa
HCs-rich	842 kg/m^3	30 mN/m	180°		

On the basis of the Young–Laplace equation (Formula (3)), the capillary resistance of the two types of crude oil under different throat radius conditions was obtained through numerical simulation.

$$P_c = \frac{2\sigma \cos\theta}{r} \quad (3)$$

where P_c is the capillary force exerted on the crude oil, σ is the interfacial tension between the crude oil and the formation water interface, θ is the wetting angle at the interface between the crude oil-tight reservoir mineral-formation water, and r is the throat radius of the tight reservoir.

LCs-rich crude oil is characterized by a lower density, smaller interfacial tension, and lower contact angle, which results in consistently lower capillary resistance than HCs-rich crude oil under the same throat radius conditions (Figure 9a,b). The relationship between the charging force of crude oil and the capillary force resistance it encounters determines whether it can overcome resistance and subsequently enter the pores of tight sandstone [53]. The throat radius at which the capillary force equals the charging force is defined as the critical throat radius (r_c). During the initial charging process of crude oil into tight reservoirs, the crude oil can only overcome throats with radii larger than r_c and subsequently enter the pores connected to these throats. The hydrocarbon generation pressure is a critical charging force for the Chang 7 tight reservoir. During geological history, the maximum hydrocarbon generation pressure of the Chang 7_3 source rock reached 21 MPa [59]. When the charging force is set to its maximum value (21 MPa), the r_c for the LCs-rich crude oil is approximately 15 nm, whereas that for the HCs-rich crude oil is slightly larger, at approximately 30 nm (Figure 9a). On the basis of the mean throat-to-pore ratio of the Chang 7 tight sandstones [58], the critical charging pore radii for the LCs-rich and HCs-rich crude oils are approximately 0.6 μm and 1.2 μm, respectively (Figure 9a). The pore size of the Chang 7 tight reservoir is distributed primarily within the range of 1.2 μm to 12 μm (Figure 8). Therefore, under conditions of strong charging force, there is no significant difference in the occurrence pore size between LCs-rich crude oil and HCs-rich crude oil. The CLSM observations of Sample I in the second field of view are highly consistent with the aforementioned mechanism (Figure 9a). However, when the charging force is set to a low value of 10 MPa, the r_c values for the LCs-rich and HCs-rich crude oils are approximately 30 nm and 60 nm, respectively. The corresponding critical charging pore radii are approximately 1.2 μm and 2.4 μm (Figure 9b). Under these conditions, only LCs-rich crude oil can occupy pores smaller than 2.4 μm, resulting in the complete differentiation of LCs-rich crude oil (Figure 9b). Furthermore, there is no strictly functional relationship between pore size and throat size, as a throat of a certain size often corresponds to a range of pores of similar sizes. This leads to the partial differentiation of LCs-rich crude oil within the pore size range adjacent to the complete differentiation range of LCs-rich crude oil (Figure 9b). The CLSM observations of Sample III in the third field of view validate the occurrence mechanism discussed above under weak charging

force conditions. The complete differentiation of LCs is observed within the pore radius range of 1.6 μm to 2.4 μm, whereas partial differentiation of LCs occurs within the range of 2.4 μm to 3.2 μm (Figure 9b). In summary, under conditions of weak charging force, the complete and partial differentiation of LCs may occur within a range of pore radii, from the smallest pores to a certain pore radius in tight sandstone reservoirs, which will cause the occurrence volume of LCs to be significantly larger than that of HCs within these pores. The aforementioned mechanisms effectively explain the phenomenon observed in the Chang 7 tight reservoirs, where the volume of LCs exceeds that of HCs (Figure 8a), and complete and partial differentiation of LCs occurs in pores with sizes ranging from 0 μm to 4 μm (Figure 8b–d).

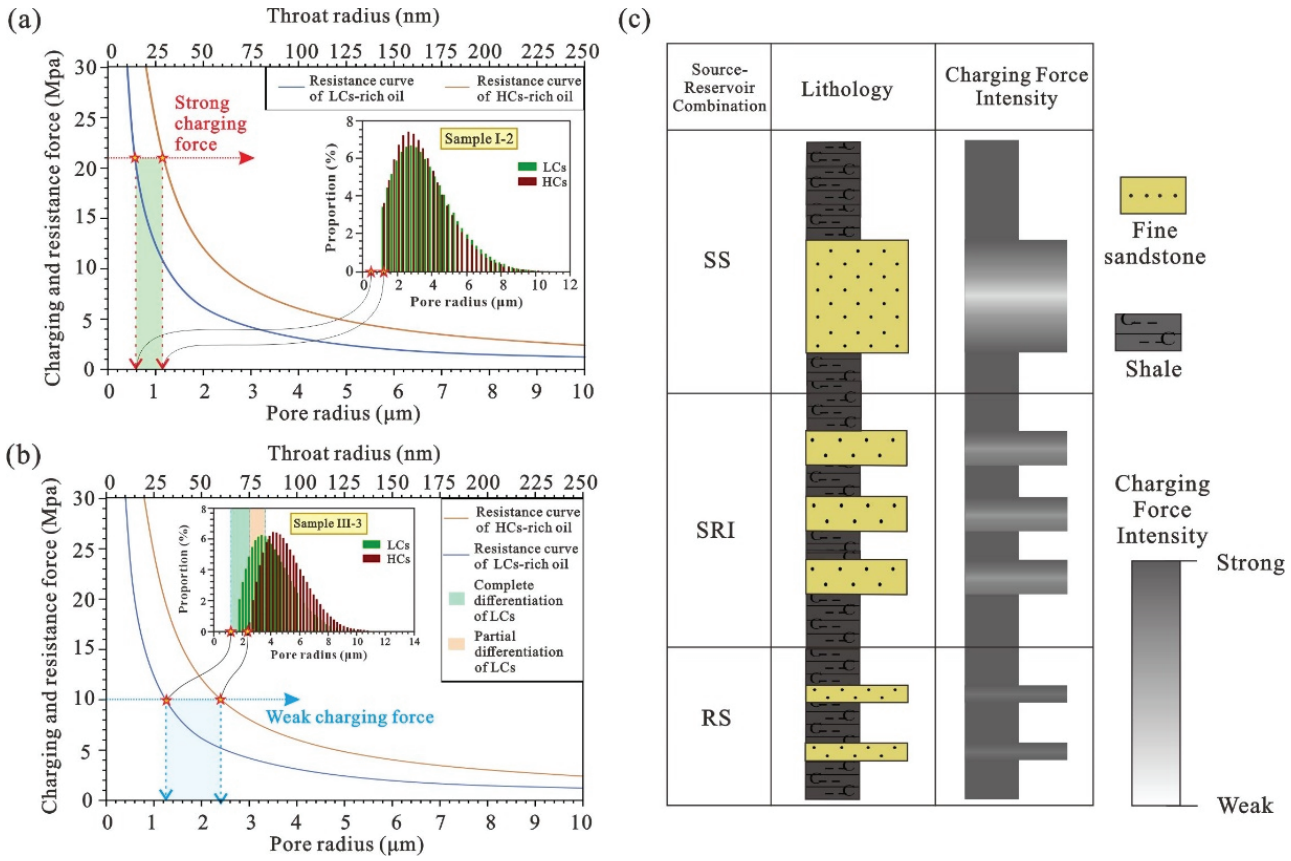

Figure 9. (**a**,**b**) Schematic diagram showing the differentiation mechanism of occurrence pore radius between LCs and HCs under (**a**) strong charging force conditions and (**b**) weak charging force conditions; (**c**) Charging force attenuation patterns within different source–reservoir combinations.

The variation trend of LHR_v in the Chang 7 tight reservoir can also effectively validate the controlling mechanism of the charging force on pore size differentiation between LCs and HCs proposed in this study. Under geological conditions, weak charging forces of crude oil are primarily distributed in areas with low hydrocarbon generation intensities or in the middle of thick tight reservoirs [58]. As the distance from the contact face between the source rock and the tight reservoir, referred to as the source–reservoir distance, increases, the pressure gradually decreases, resulting in less remaining pressure in the middle of the thick tight reservoir. Therefore, under the same intensity of hydrocarbon generation, a weak charging force is more likely to occur in the SS than in the RS or SRI (Figure 9c). In the Chang 7 tight reservoir, the LHR_v tends to decrease gradually with increasing hydrocarbon generation intensity (Figure 10a), especially when the hydrocarbon generation intensity is less than 0.6 t/km^2. These findings indicate that under conditions of weak

hydrocarbon generation intensity, the complete and partial differentiation of LCs within 0–4 μm pores is an important factor controlling the LHR_v in tight reservoirs. Additionally, the control effect of the source–reservoir distance (SRD) on LHR_v is more pronounced. CLSM observations reveal that, as the SRD increases, the minimum pore radius at which LCs occur remains relatively stable and is mainly distributed at approximately 2 μm (Figure 10b). However, from Sample I, with a low SRD, to Sample III, with a high SRD, the minimum pore radius for HCs shifted from approximately 2 μm to approximately 3 μm (Figure 10b). Moreover, the difference in the lower limit for the concentrated distribution between LCs and HCs, indicated by the boxed area in the box plot, also shows an increasing trend with increasing SRD (Figure 10b). Macroscopically, there is a strong and clear positive correlation between SRD and LHR_v (Figure 10c). Nevertheless, charging forces can only cause relative enrichment of LCs within the 0–4 μm range in the Chang 7 tight reservoir and do not necessarily lead to an increase in the overall relative content of LCs. Therefore, the chromatographic effect is considered another important factor influencing the strong positive correlation between SRD and LHR_v. During oil migration, the chromatographic effect causes HCs in crude oil to be lost along the migration pathway due to differences in the physicochemical properties of different components, leading to relatively high levels of LCs [54]. According to the above analyses, oil charging forces are important factors that cause the complete and partial differentiation of LCs within pores smaller than 4 μm; under conditions of weak hydrocarbon generation intensity, the hydrocarbon generation intensity has a significant effect on the LHR_v, and SRD has a distinct control on the LHR_v under the combined effects of the charging force and the chromatographic effect.

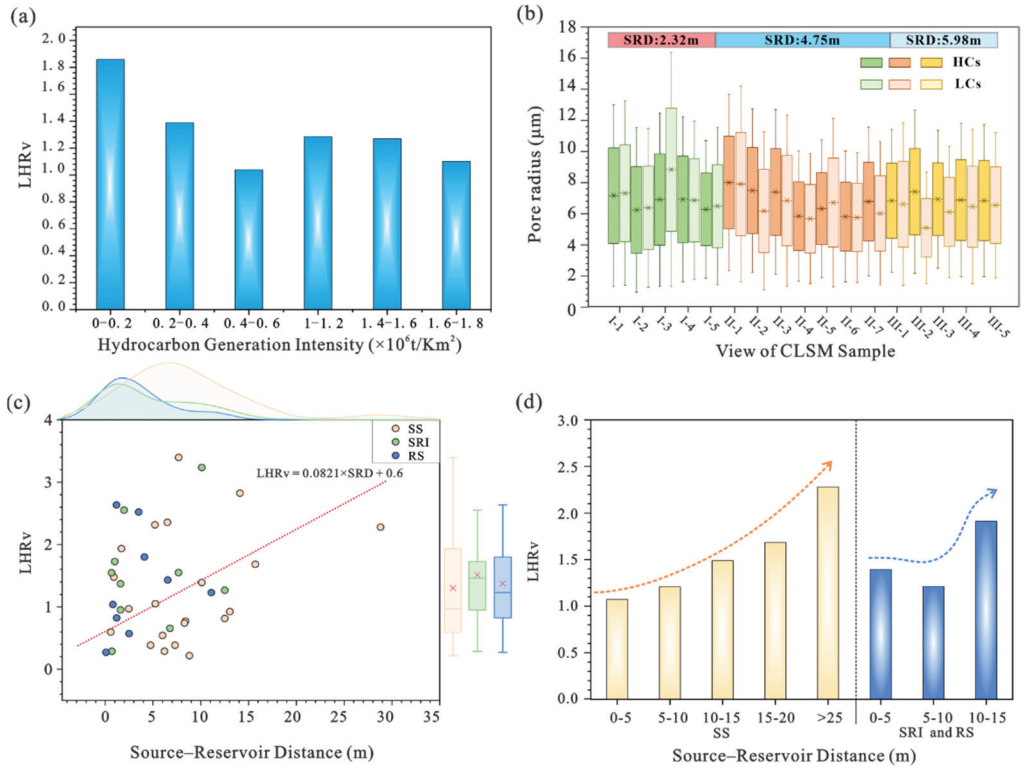

Figure 10. (**a**) Control effect of hydrocarbon generation intensity on LHR_v; (**b**) Pore radius distributions of LCs and HCs under different SRD conditions; (**c**) Distribution characteristics of SRD and LHR_v and their cross-plots; (**d**) Correlation analysis of SRD and LHR_v for different source–reservoir combinations.

Owing to differences in geological conditions and tight reservoir thickness, the control of SRD on LHR_v also varies among different source–reservoir combinations. The SS, characterized by thick tight sandstone, exhibits relatively weak hydrocarbon generation

intensity and large SRD (Figure 10c). In this combination, LHR_v shows a distinct increasing trend with increasing SRD (Figure 10d). In contrast, the SRI and RS are characterized by strong hydrocarbon generation intensity and short SRD, which results in an insignificant relationship between SRD and LHR_v, especially under small SRD conditions (Figure 10d).

4.3.2. Mineral Wettability

The sandstone reservoir surface experiences varying degrees of adsorption forces on different components of the boundary fluid. This adsorption force originates primarily from the interaction between minerals and their adjacent fluids within the reservoir [60]. In the oil–water–tight reservoir system, the adsorption of crude oil by different minerals varies. Additionally, minerals have different wetting characteristics due to their specific chemical compositions and crystal structures and can be classified into three types: water-wet minerals, intermediate-wet minerals, and oil-wet minerals [61]. Water-wet minerals and intermediate-wet minerals have almost no adsorption force on crude oil, and include mainly quartz, illite, sodium feldspar, and potassium feldspar. Oil-wet minerals, including mixed-layer illite/smectite, chlorite, kaolinite, and carbonate minerals, such as calcite and dolomite, have strong absorption effects on crude oil [62]. Moreover, owing to their higher polarity and molecular weight, HCs adsorb more strongly on the surface of oil-wet minerals than LCs do [63]. Thus, oil-wet minerals play a significant controlling role in the occurrence volume of HCs in tight reservoirs.

In the Chang 7 tight reservoir, the content of oil-wet minerals exerts a distinct controlling effect on the LHR_v. As the content of oil-wet minerals in tight reservoirs increases, the volume of HCs relative to LCs significantly increases, thereby leading to a decrease in LHR_v (Figure 11a). Additionally, owing to the adsorption effect, pore surfaces composed of oil-wet minerals are almost exclusively occupied by HCs (Figure 7b–d), and HCs partial differentiation is always observed at pore radii greater than 4 μm (Figure 8). The control effect of the content of oil-wet minerals on the LHR_v in a reservoir varies among different source–reservoir combinations due to differences in mineral components and the degree of complete and partial differentiation of LCs. In the SRI and RS, the content of oil-wet minerals strongly controls the LHR_v (Figure 11b). However, in the SS, this control is not evident (Figure 11b), which may be attributed to the relative enrichment of LCs in pores smaller than 4 μm resulting from complete and partial differentiation (Figure 10d).

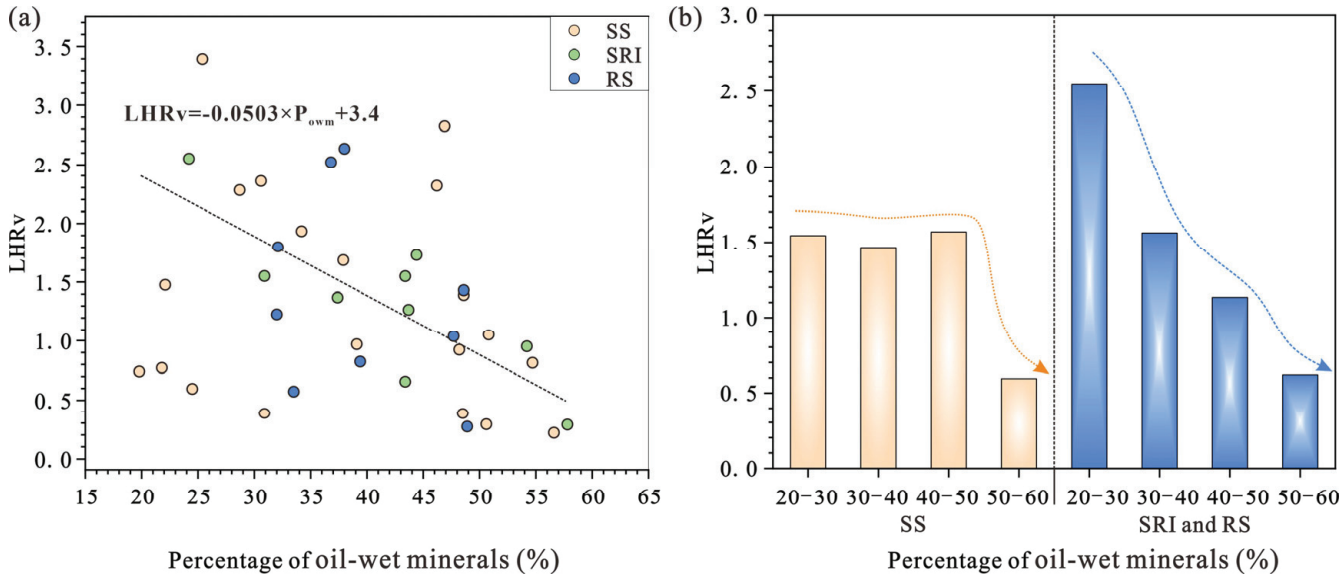

Figure 11. Correlation analysis between the percentage of oil-wet minerals and LHR_v.

5. Discussion

5.1. Rock Physical Properties

The physical properties of rock are important factors affecting the degree of crude oil occurrence space in tight reservoirs [64]. In the Chang 7 tight reservoir, the content of micropores is relatively low, accounting for less than 10%, and the crude oil occurrence space is mainly distributed in small and large pores (Figure 5). For different source–reservoir combinations, the differences in the physical properties of tight reservoirs are significant. The NMR results reveal that the pore type for the SS is mainly large pores, with a low proportion of small pores, whereas the pore types for the SRI and RS are primarily small pores, with a relatively high proportion of small pores (Figure 12a). Owing to the differences in the main factors controlling the occurrence characteristics of LCs and HCs in tight reservoirs with different source–reservoir combinations, the influence of rock physical properties on the occurrence characteristics of LCs and HCs also varies across different source–reservoir combinations. For the SS, the difference in LCs and HCs occurrence characteristics arises mainly from the partial and complete differentiation of LCs in pores with a radius of 4 μm or less under weak charging force conditions. This leads to a greater proportion of small pores in the tight reservoir of the SS, which increases the space where partial and complete differentiation of LCs may occur, further resulting in greater relative enrichment of LCs in the reservoir (Figure 12a). For the SRI and RS, the main reason for the difference in LCs and HCs occurrence characteristics is the adsorption of HCs by oil-wet minerals in pores where LCs differentiation does not occur. This also indicates that, for the SRI and RS, the main reason for the difference in LCs and HCs occurrence characteristics is not the size of the crude oil occurrence space but the content of oil-wet minerals within the reservoir. Clay minerals, as important oil-wet minerals, also control the physical properties of reservoirs [62]. That is, the higher the clay mineral content is, the poorer the physical properties of the reservoir, but the greater the content of oil-wet minerals. In the Chang 7 tight reservoir, for the SRI and RS, the content of oil-wet minerals shows a significant positive correlation with the proportion of small pores in the reservoir (Figure 12b). This suggests that in the SRI and RS, the poorer the reservoir physical properties are, the more oil-wet minerals are enriched, which results in a significant negative correlation between the reservoir physical properties and LHR_v (Figure 12a).

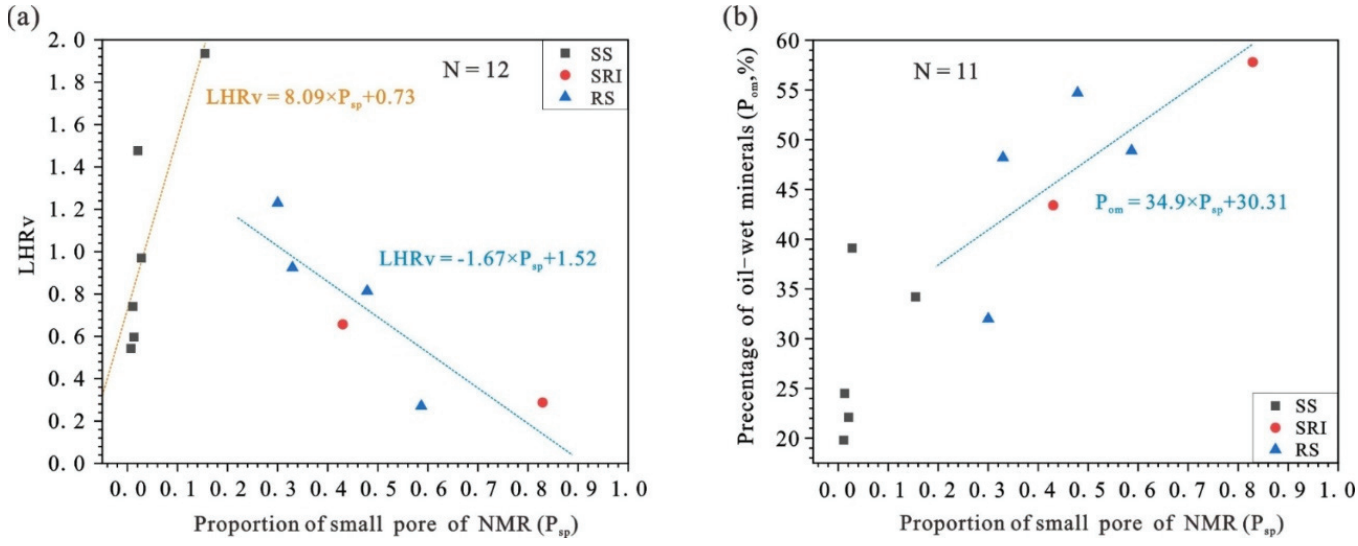

Figure 12. Correlation analysis between LHR_v (**a**), the percentage of oil-wet minerals (**b**), and reservoir physical properties.

5.2. Argillaceous Laminae

Argillaceous laminae are commonly developed in tight sandstone reservoirs. Owing to the significant mineralogical differences between argillaceous laminae and pure sandstone, argillaceous laminae play an important role in controlling the distributions of LCs and HCs in tight sandstone reservoirs. The reservoir in the study area has many argillaceous laminae, which contain many clay minerals. Clay minerals, as important oil-wet minerals, have a strong adsorption effect on HCs [62]. Therefore, the difference in the adsorption effects of oil-wet minerals on LCs and HCs can be clearly observed in the argillaceous laminae. On the basis of the development position of the argillaceous laminae, the CLSM observation field of Sample II can be divided into three regions: the bright zone, dark zone, and transition zone (Figure 13b). The bright zone is mainly composed of relatively large quartz particles with a minimum pore radius of approximately 1.5 μm (Figure 13b,f). The dark zone is located in the development area of the argillaceous laminae and is mainly composed of clay minerals. The minimum pore radius is smaller than that in the bright zone, approximately 1 μm (Figure 13b,h). The transition zone is located at the boundary between the bright zone and the dark laminae. There is a noticeable change in particle size, with the particle diameter gradually decreasing from the bright zone to the dark zone. The minimum pore radius is approximately 1.2 μm (Figure 13b,g). The content of oil-wet minerals gradually increases, and the minimum pore radius of the reservoir progressively decreases from the bright zone to the dark zone. In addition, there are obvious differences in the distribution characteristics of LCs and HCs in different regions. In the bright zone, crude oil mostly exists in clusters and is present in a free state within the pores. Additionally, there are no significant differences in the occurrence state or volume of LCs and HCs in the reservoir (Figure 13c). A slight complete and partial differentiation of LCs occurs in pores smaller than 4 μm in radius, whereas in pores larger than 4 μm in radius, there is almost no differentiation in the occurrence volumes of LCs and HCs (Figure 13f). In the transition zone, crude oil mainly exists in the form of clusters and spots within the pores. LCs are primarily distributed in the middle of the pores, while the surfaces of the pores are mainly occupied by HCs (Figure 13d). In pores smaller than 4 μm in radius, the complete and partial differentiation of LCs is more pronounced, and in pores larger than 4 μm in radius, HCs also begin to show slight partial differentiation (Figure 13g). In the dark zone, crude oil mainly exists in the form of spots within the pores, and almost all the pore surfaces are occupied only by HCs. The occurrence volume of HCs is significantly larger than that of LCs (Figure 13e). In pores smaller than 4 μm in radius, the complete and partial differentiation of LCs is very pronounced, whereas in pores larger than 4 μm in radius, the partial differentiation of HCs is also quite evident (Figure 13h). The average LHR_v in the bright zone, transition zone, and dark zone gradually decreases, with values of 0.83, 0.65, and 0.55, respectively (Figure 13a).

In tight sandstone reservoirs with larger pores and fewer oil-wet minerals, there is almost no differentiation in the occurrence of LCs and HCs. However, in the argillaceous laminae, owing to the small pore size and high content of oil-wet minerals in the reservoir, the differentiation of LCs in smaller pores and the differentiation of HCs in larger pores are very pronounced. However, because the adsorption effect of oil-wet minerals on HCs influences a broader pore size range, the overall LHR_v in the argillaceous laminae continues to decrease.

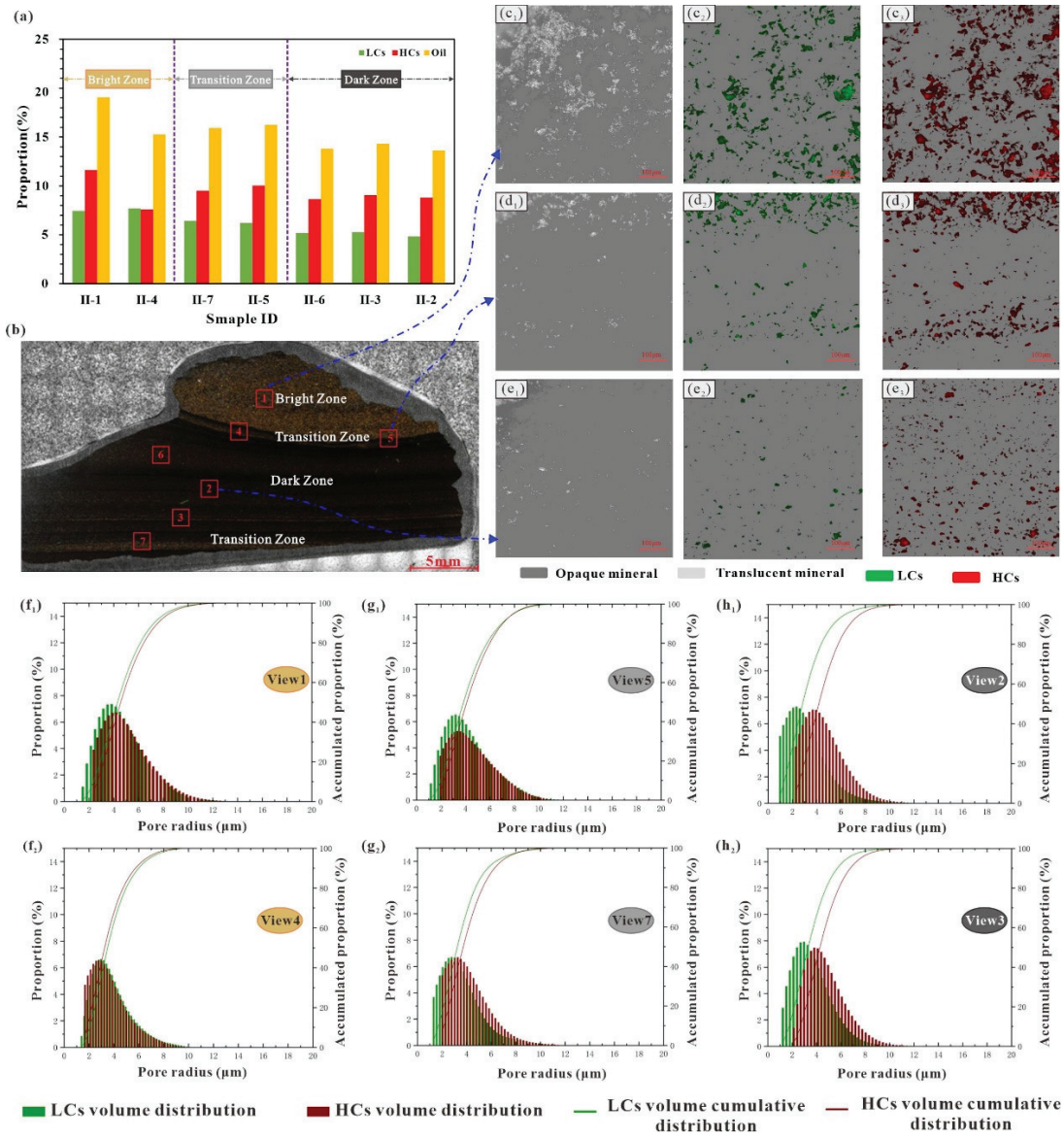

Figure 13. (**a**) Occurrence volume of LCs and HCs in different regions of Sample II (L54, 2407.75 m); (**b**) Positional distribution in different regions of Sample II(L54, 2407.75 m); (**c**–**e**) Occurrence state characteristics of LCs and HCs in the bright, transitional, and dark zones, respectively. (**c**$_{1–3}$) represent the mineral images, LCs images, and HCs images in Field of view 1, respectively; (**d**$_{1–3}$) and (**e**$_{1–3}$) represent those in Fields of view 5 and 2, respectively.; (**f**–**h**) Pore size distributions of LCs and HCs of Sample II, in the bright, transitional, and dark zones, respectively. (**f**$_{1,2}$) represent view 1 and view 4 in the bright zone, respectively. (**g**$_{1,2}$) represent view 5 and view 7 in the transitional zone, respectively. (**h**$_{1,2}$) represent view 2 and view 3 in the dark zone, respectively.

5.3. Geological Occurrence Mode of Crude Oil

On the basis of this comprehensive analysis, three occurrence differentiation models of LCs and HCs have been identified in the tight sandstone reservoirs of the Chang 7 member in the study area. These models correspond to different source–reservoir combinations. Model A is developed in source sandwich combination (SS), is primarily controlled by the charging force, and is mainly distributed in near-slope areas (Figure 14a). In contrast, Model B and Model C, which are developed in source–reservoir interbed combination (SRI), and reservoir sandwich combination (RS), are primarily distributed in the sag and are dominated by mineral adsorption and argillaceous laminae, respectively (Figure 14b,c).

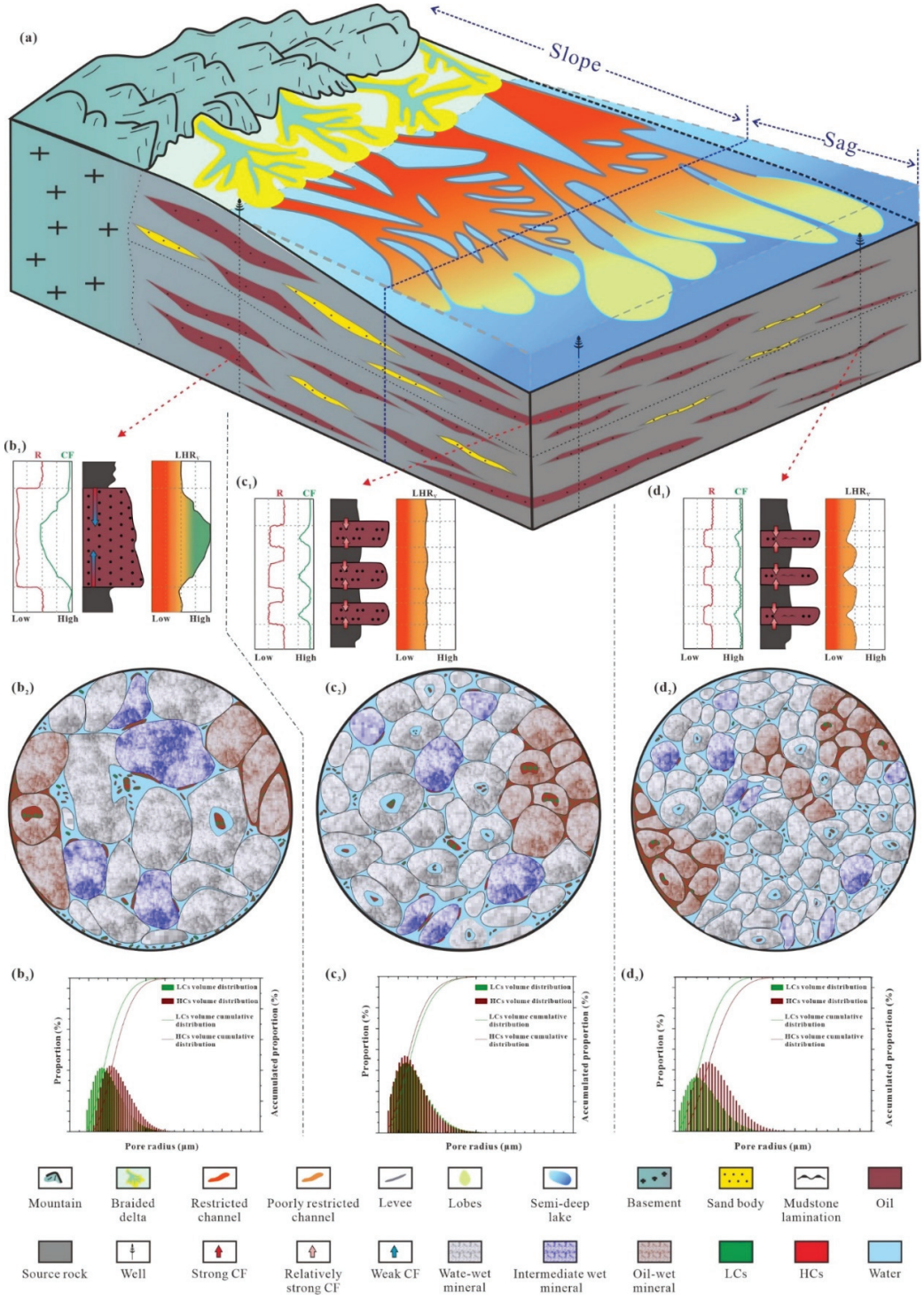

Figure 14. Geological mode of crude oil occurrence in the Chang 7 tight reservoir in the research area. CF represents the charging force. (**a**) Sedimentary facies and lithology distribution model of the chang 7_{1+2} submember in the jiyuan area; ($\mathbf{b_1}$), ($\mathbf{c_1}$), and ($\mathbf{d_1}$) represent the vertical evolution characteristics of crude oil charging force and capillary resistance in Models A, B, and C, respectively; ($\mathbf{b_2}$), ($\mathbf{c_2}$), and ($\mathbf{d_2}$) represent the occurrence state and morphological model of crude oil in Models A, B, and C, respectively; ($\mathbf{b_3}$), ($\mathbf{c_3}$), and ($\mathbf{d_3}$) represent the typical pore size distribution characteristics of light and heavy components of crude oil in Models A, B, and C, respectively.

Model A is developed in SS and is primarily distributed in the northern part of the study area, on slopes with low hydrocarbon intensities. This region is characterized by delta-front depositional environments and relatively thick reservoirs with lower contents

of oil-wet minerals and larger pore sizes. The occurrence differentiation of LCs and HCs mainly occurs in pores smaller than 4 μm in radius, where LCs are significantly more abundant than HCs. In pores exceeding 4 μm, little differentiation is observed, resulting in a relatively high LHR_v. Model B and Model C are developed in SRI and RS and are primarily distributed in the southern part of the study area, which is in a sag with relatively high hydrocarbon intensity. These models are characterized mainly by semideep lacustrine and gravity flow depositional environments, as well as relatively thin reservoirs with higher contents of oil-wet minerals and smaller pore sizes. Model B, with stronger charging forces, exhibits weak differentiation of LCs in pores smaller than 4 μm. However, in pores larger than 4 μm, HCs tend to fully occupy oil-wet mineral surfaces due to adsorption effects, leading to a higher volume of HCs than LCs and a lower overall LHR_v. While Model C also has a high charging force, the presence of argillaceous laminae further reduces the reservoir properties and increases the content of oil-wet minerals. In pores smaller than 4 μm, a clear differentiation of both complete and partial LCs is observed. Similarly, in pores larger than 4 μm, partial differentiation of HCs is also notable. However, the overall LHR_v is further reduced compared with that in Model B reservoirs.

It is worth noting that the three occurrence differentiation models of LCs and HCs constructed in this study are based on research findings from continental tight reservoirs. These reservoirs are characterized by a highly complex geological background and sedimentary environment, well-developed laminar structures, and strong heterogeneity in pore-throat structure, mineral composition, and physical properties [65,66]. As a result, even within the same basin, the same block, or even the same structural belt and stratigraphic horizon, multiple occurrence differentiation models with different controlling factors often coexist. In contrast, marine tight reservoirs, such as Bakken, Eagle Ford, and Wolfcamp in North America, exhibit stronger homogeneity and are typically dominated by a single occurrence differentiation models of LCs and HCs. Therefore, the findings of this study provide valuable insights and have a certain degree of applicability across different geological settings.

6. Conclusions

(1) In the Chang 7 tight reservoir, LCs and HCs exhibit differences in occurrence volume, state, morphology, and pore size. The LHR_v of crude oil varies significantly, ranging from 0.22 to 4.23, with an average value of 1.49. LCs predominantly occur in the form of spots, short columns, and clusters, and exist in a free state within intergranular pores, intragranular pores, and throats. The HCs mostly occur in the form of films, strips, and clumps in an adsorbed state and are present in intergranular pores and intragranular pores. In addition, the HCs mainly exhibit partial differentiation in pores with a pore radius greater than 4 μm, whereas the LCs primarily show complete or partial differentiation in pores with a pore radius smaller than 4 μm.

(2) The differences in occurrence between the LCs and HCs of crude oil are primarily controlled by the coupled effects of the crude oil charging force and resistance, the adsorption effects of reservoir minerals, and the chromatographic effects of crude oil migration. The weaker the hydrocarbon generation intensity of the source rock is, the more likely the LCs are to undergo complete or partial differentiation in pores with radii smaller than 4 μm, increasing the LHR_v. The larger the source-to-reservoir distance is, the more severe the attenuation of the charging force from the source rock, and the more significant the chromatographic effects during crude oil migration. This also led to a relative enrichment of the crude oil LCs and an increase in LHR_v. Moreover, the adsorption effects of oil-wet minerals in tight reservoirs are important controlling factors for the relative enrichment of HCs in the pores of crude oil.

(3) The extensive development of argillaceous laminae in tight reservoirs reduces the minimum pore size of the reservoir and increases the content of oil-wet minerals in the reservoir. This leads to the complete and partial differentiation of LCs in pores with radii smaller than 4 μm under strong charging forces, whereas strong partial differentiation of HCs develops in pores larger than 4 μm, which further reduces the overall LHR_v of the reservoir.

(4) In the Jiyuan area, there are three types of source–reservoir combinations: the source sandwich combination (SS), source–reservoir interbed combination (SRI), and reservoir sandwich combination (RS). The SS is characterized by high physical properties, low hydrocarbon generation intensity, high source-to-reservoir distance, and low oil-wet mineral content. It has a relatively high LHR_v and is mainly developed in the northern part of the study area, near the slope area. In contrast, the RS and SRI are characterized by a high frequency of argillaceous laminae development, high hydrocarbon generation intensity, low source-to-reservoir distance, and high oil-wet mineral content, leading to a relatively low LHR_v. They are mainly developed in the southern part of the study area in the sag. Three oil component differentiation models have been developed for the Chang 7 tight sandstone reservoir in the study area. First, Model A, developed in the SS, represents the charging force-dominated occurrence mode of crude oil in the near slope zone. Model B is developed in the SRI and RS, representing the mineral adsorption-dominated oil occurrence mode of crude oil. Model C is developed in both the SRI and RS, representing the argillaceous laminae-dominated oil occurrence mode of crude oil, both in the sag.

(5) This study proposes three occurrence models of LCs and HCs based on the study area's source–reservoir combination types, reservoir characteristics, and argillaceous laminae characteristics. For regions with geological settings similar to the study area, this research approach can be used as a reference to quantitatively characterize the occurrence characteristics of LCs and HCs and further explore their controlling factors. Moreover, this model can be further integrated with seismic data and well log information to effectively predict regions with relatively high LCs content, thereby achieving efficient extraction.

Author Contributions: Conceptualization, M.J., D.C., Q.W. and F.W.; Methodology, M.J.; Software, X.W. and K.M.; Validation, Q.W. and F.W.; Formal analysis, Y.W. (Yuchao Wang), W.L. and Y.W. (Yuqi Wang); Investigation, X.W., K.M., Y.W. (Yuchao Wang), W.L., Y.W. (Yuqi Wang), Z.Y., R.W. and L.R.; Data curation, M.J.; Writing—original draft, M.J.; Writing—review & editing, D.C.; Supervision, D.C. All authors have read and agreed to the published version of the manuscript.

Funding: This work was funded by the National Natural Science Foundation of China (Grant Nos. 42302141, 42402152) and the Science Foundation of China University of Petroleum, Beijing (No. 2462023XKBH011).

Data Availability Statement: The original contributions presented in the study are included in the article, further inquiries can be directed to the corresponding author.

Acknowledgments: We appreciate the support from the PetroChina Changqing Oilfield Company for providing the data and tight sandstone samples used in this study and the permission to publish the results. Additionally, we would like to thank everyone who provided valuable comments and suggestions during the interpretation and revision process of this paper.

Conflicts of Interest: Author Xiujuan Wang was employed by the company PetroChina Changqing Oilfield Co. The remaining authors declare that the research was conducted in the absence of any commercial or financial relationships that could be construed as a potential conflict of interest.

References

1. Ledingham, G.W. Santiago pool, kern county, california: Geological notes. *AAPG Bull.* **1947**, *31*, 2063–2067.
2. Law, B.E.; Curtis, J.B. Introduction to unconventional petroleum systems. *AAPG Bull.* **2002**, *86*, 1851–1852.
3. Jiang, M.; Fang, H.; Liu, Y.; Zhang, Y.; Wang, C. On movable fluid saturation of tight sandstone and main controlling factors —Case study on the Fuyu oil layer in the Da'an oilfield in the Songliao basin. *Energy* **2023**, *267*, 126476. [CrossRef]
4. Li, J.; Zhou, X.; Gayubov, A.; Shamil, S. Study on production performance characteristics of horizontal wells in low permeability and tight oil reservoirs. *Energy* **2023**, *284*, 129286. [CrossRef]
5. Wang, Y.; Chen, D.; Rong, L.; Chen, J.; Wang, F.; He, S.; Wang, Y.; Yang, Z.; Lei, W. Evaluation of fluid mobility and factors influencing the deep tight sandstone of the third member of the Shahejie formation in the Jiyang depression, Bohai Bay Basin. *Mar. Pet. Geol.* **2024**, *170*, 107090. [CrossRef]
6. Kazemzadeh, E.; Ahmadi Shadmehri, M.T.; Ebrahimi Salari, T.; Salehnia, N.; Pooya, A. Modeling and forecasting United States oil production along with the social cost of carbon: Conventional and unconventional oil. *Int. J. Energy Sect. Manag.* **2023**, *17*, 288–309. [CrossRef]
7. Jia, C.; Zheng, M.; Zhang, Y. Unconventional hydrocarbon resources in China and the prospect of exploration and development. *Pet. Explor. Dev.* **2012**, *39*, 139–146. [CrossRef]
8. Yao, W.; Chen, Z.; Hu, T.; Liang, Z.; Jia, C.; Wu, K.; Pan, T.; Yu, H.; Dang, Y. Storage space, pore structure, and primary control of igneous rock reservoirs in Chepaizi Bulge, Junggar Basin, western China: Significance for oil accumulation. *J. Pet. Sci. Eng.* **2020**, *195*, 107836. [CrossRef]
9. Luo, Q.; Gong, L.; Qu, Y.; Zhang, K.; Zhang, G.; Wang, S. The tight oil potential of the Lucaogou Formation from the southern Junggar Basin, China. *Fuel* **2018**, *234*, 858–871. [CrossRef]
10. Zhang, G.; Wang, Z.; Guo, X.; Sun, Y.; Sun, L.; Pan, L. Characteristics of lacustrine dolomitic rock reservoir and accumulation of tight oil in the Permian Fengcheng Formation, the western slope of the Mahu Sag, Junggar Basin, NW China. *J. Asian Earth Sci.* **2019**, *178*, 64–80. [CrossRef]
11. Nelson, P.H. Pore-throat sizes in sandstones, tight sandstones, and shales. *AAPG Bull.* **2009**, *93*, 329–340. [CrossRef]
12. Mirzaei-Paiaman, A. New methods for qualitative and quantitative determination of wettability from relative permeability curves: Revisiting Craig's rules of thumb and introducing Lak wettability index. *Fuel* **2021**, *288*, 119623. [CrossRef]
13. Wang, X.; Bai, X.; Li, J.; Jin, Z.; Wang, G.; Chen, F.; Zheng, Q.; Hou, Y.; Yang, Q.; Li, J.; et al. Enrichment model and major controlling factors of below-source tight oil in Lower Cretaceous Fuyu reservoirs in northern Songliao Basin, NE China. *Pet. Explor. Dev.* **2024**, *51*, 279–291. [CrossRef]
14. Hu, T.; Pang, X.; Jiang, S.; Wang, Q.; Zheng, X.; Ding, X.; Zhao, Y.; Zhu, C.; Li, H. Oil content evaluation of lacustrine organic-rich shale with strong heterogeneity: A case study of the Middle Permian Lucaogou Formation in Jimusaer Sag, Junggar Basin, NW China. *Fuel* **2018**, *221*, 196–205. [CrossRef]
15. Hu, T.; Pang, X.; Jiang, F.; Wang, Q.; Liu, X.; Wang, Z.; Jiang, S.; Wu, G.; Li, C.; Xu, T.; et al. Movable oil content evaluation of lacustrine organic-rich shales: Methods and a novel quantitative evaluation model. *Earth Sci. Rev.* **2021**, *214*, 103545. [CrossRef]
16. Shi, X.; Wang, J.; Ge, X.; Han, Z.; Qu, G.; Jiang, S. A new method for rock brittleness evaluation in tight oil formation from conventional logs and petrophysical data. *J. Pet. Sci. Eng.* **2017**, *151*, 169–182. [CrossRef]
17. Xiao, F.; Yang, J.; Li, S.; Yao, Y.; Huang, Y.; Gao, X. Enrichment and movability of lacustrine tight shale oil for the first member of the Upper Cretaceous Qingshankou Formation in the Sanzhao Sag, Songliao Basin, NE China: Insights from saturated hydrocarbon molecules. *Fuel* **2024**, *368*, 131615. [CrossRef]
18. Qu, Y.; Sun, W.; Wu, H.; Huang, S.; Li, T.; Ren, D.; Chen, B. Impacts of pore-throat spaces on movable fluid: Implications for understanding the tight oil exploitation process. *Mar. Pet. Geol.* **2022**, *137*, 105509. [CrossRef]
19. Sanei, H.; Wood, J.M.; Ardakani, O.H.; Clarkson, C.R.; Jiang, C. Characterization of organic matter fractions in an unconventional tight gas siltstone reservoir. *Int. J. Coal Geol.* **2015**, *150–151*, 296–305. [CrossRef]
20. Zhao, W.; Hu, S.; Hou, L.; Yang, T.; Li, X.; Guo, B.; Yang, Z. Types and resource potential of continental shale oil in China and its boundary with tight oil. *Pet. Explor. Dev.* **2020**, *47*, 1–11. [CrossRef]
21. Hu, T.; Liu, Y.; Jiang, F.; Pang, X.; Wang, Q.; Zhou, K.; Wu, G.; Jiang, Z.; Huang, L.; Jiang, S.; et al. A novel method for quantifying hydrocarbon micromigration in heterogeneous shale and the controlling mechanism. *Energy* **2024**, *288*, 129712. [CrossRef]
22. Guo, Q.; Yao, Y.; Hou, L.; Tang, S.; Pan, S.; Yang, F. Oil migration, retention, and differential accumulation in "sandwiched" lacustrine shale oil systems from the Chang 7 member of the Upper Triassic Yanchang Formation, Ordos Basin, China. *Int. J. Coal Geol.* **2022**, *261*, 104077. [CrossRef]
23. Gao, Z.; Duan, L.; Jiang, Z.; Huang, L.; Chang, J.; Zheng, G.; Wang, Z.; An, F.; Wei, W. Using laser scanning confocal microscopy combined with saturated oil experiment to investigate the pseudo in-situ occurrence mechanism of light and heavy components of shale oil in sub-micron scale. *J. Pet. Sci. Eng.* **2023**, *220*, 111234. [CrossRef]
24. Wang, S.; Feng, Q.; Javadpour, F.; Xia, T.; Li, Z. Oil adsorption in shale nanopores and its effect on recoverable oil-in-place. *Int. J. Coal Geol.* **2015**, *147–148*, 9–24. [CrossRef]

25. Ma, B.; Hu, Q.-H.; Pu, X.; Yang, S.; Wang, X.; Han, W.; Wen, J. Occurrence Mechanism and Controlling Factors of Shale Oil from the Paleogene Kongdian Formation in Cangdong Sag, Bohai Bay Basin, East China. *J. Mar. Sci. Eng.* **2024**, *12*, 1557. [CrossRef]
26. Lu, M.; Duan, G.; Zhang, T.; Liu, N.; Song, Y.; Zhang, Z.; Qiao, J.; Wang, Z.; Fang, Z.; Luo, Q. Influences of paleoclimatic changes on organic matter enrichment mechanisms in freshwater and saline lacustrine oil shales in China: A machine learning approach. *Earth Sci. Rev.* **2025**, *262*, 105061. [CrossRef]
27. Zhu, R.; Zou, C.; Mao, Z.; Yang, H.; Hui, X.; Wu, S.; Cui, J.; Su, L.; Li, S.; Yang, Z. Characteristics and distribution of continental tight oil in China. *J. Asian Earth Sci.* **2019**, *178*, 37–51. [CrossRef]
28. Zhang, D.; Han, M.; Zhou, Q.; Ye, T.; Zhou, Y.; Chang, J.; Lin, X. The Micro-Occurrence Mechanisms of Tight Oil: Fluid–Rock Interactions at Microscale Pores, Nanoscale Pores, and Mineral Surfaces. *Energies* **2023**, *16*, 3917. [CrossRef]
29. Wang, J.; Wu, S.; Li, Q.; Zhang, J.; Guo, Q. Characterization of the pore-throat size of tight oil reservoirs and its control on reservoir physical properties: A case study of the Triassic tight sandstone of the sediment gravity flow in the Ordos Basin, China. *J. Pet. Sci. Eng.* **2020**, *186*, 106701. [CrossRef]
30. Yang, Y.; Li, W.; Ma, L. Tectonic and stratigraphic controls of hydrocarbon systems in the Ordos basin: A multicycle cratonic basin in central China. *AAPG Bull.* **2005**, *89*, 255–269. [CrossRef]
31. Gu, Y.; Zhang, D.; Bao, Z. A new data-driven predictor, PSO-XGBoost, used for permeability of tight sandstone reservoirs: A case study of member of chang 4+5, western Jiyuan Oilfield, Ordos Basin. *J. Pet. Sci. Eng.* **2021**, *199*, 108350. [CrossRef]
32. Wang, F.; Chen, D.; Yao, D.; Cheng, M.; Wang, Q.; Tian, Z.; Du, W.; Wang, C.; Chang, S.; Jiang, M. Disparities in tight sandstone reservoirs in different source-reservoir assemblages and their effect on tight oil accumulation: Triassic Chang 7 member in the Qingcheng area, Ordos Basin. *J. Pet. Sci. Eng.* **2022**, *217*, 110914. [CrossRef]
33. Haughton, P.; Davis, C.; McCaffrey, W.; Barker, S. Hybrid sediment gravity flow deposits—Classification, origin and significance. *Mar. Pet. Geol.* **2009**, *26*, 1900–1918. [CrossRef]
34. Talling, P.J. Hybrid submarine flows comprising turbidity current and cohesive debris flow: Deposits, theoretical and experimental analyses, and generalized models. *Geosphere* **2013**, *9*, 460–488. [CrossRef]
35. Xi, K.; Li, K.; Cao, Y.; Lin, M.; Niu, X.; Zhu, R.; Wei, X.; You, Y.; Liang, X.; Feng, S. Laminae combination and shale oil enrichment patterns of Chang 73 sub-member organic-rich shales in the Triassic Yanchang Formation, Ordos Basin, NW China. *Pet. Explor. Dev.* **2020**, *47*, 1342–1353. [CrossRef]
36. Cui, J.; Zhang, Z.; Liu, J.; Liu, G.; Huang, X.; Qi, Y.; Mao, Z.; Li, Y. Hydrocarbon generation and expulsion quantification and contribution of multiple source rocks to hydrocarbon accumulation in Yanchang Formation, Ordos Basin, China. *J. Nat. Gas Geosci.* **2021**, *6*, 375–391. [CrossRef]
37. Zhang, W.; Yang, W.; Xie, L. Controls on organic matter accumulation in the Triassic Chang 7 lacustrine shale of the Ordos Basin, central China. *Int. J. Coal Geol.* **2017**, *183*, 38–51. [CrossRef]
38. Li, H.; Tang, H.; Qin, Q.; Zhou, J.; Qin, Z.; Fan, C.; Su, P.; Wang, Q.; Zhong, C. Characteristics, formation periods and genetic mechanisms of tectonic fractures in the tight gas sandstones reservoir: A case study of Xujiahe Formation in YB area, Sichuan Basin, China. *J. Pet. Sci. Eng.* **2019**, *178*, 723–735. [CrossRef]
39. Zang, Q.; Liu, C.; Awan, R.S.; Yang, X.; Li, G.; Wu, Y.; Lu, Z.; Feng, D. Occurrence characteristics of the movable fluid in heterogeneous sandstone reservoir based on fractal analysis of NMR data: A case study of the Chang 7 Member of Ansai Block, Ordos Basin, China. *J. Pet. Sci. Eng.* **2022**, *214*, 110499. [CrossRef]
40. Qiao, J.; Zeng, J.; Chen, D.; Cai, J.; Jiang, S.; Xiao, E.; Zhang, Y.; Feng, X.; Feng, S. Permeability estimation of tight sandstone from pore structure characterization. *Mar. Pet. Geol.* **2022**, *135*, 105382. [CrossRef]
41. Wu, L.; Zhang, Z.; Ma, W. Method for quantitative analysis of oil and gas components in reservoir rock. *Mud Logging Eng.* **2000**, *3*, 50–58, (In Chinese with English abstract).
42. Speight, J. *An Introduction to Petroleum Technology, Economics, and Politics*; John Wiley & Sons: Hoboken, NJ, USA, 2011; pp. 1–320.
43. Seifried, C.M.; Crawshaw, J.; Boek, E.S. Kinetics of Asphaltene Aggregation in Crude Oil Studied by Confocal Laser-Scanning Microscopy. *Energy Fuels* **2013**, *27*, 1865–1872. [CrossRef]
44. Jiang, C.; Chen, Z.; Mort, A.; Milovic, M.; Robinson, R.; Stewart, R.; Lavoie, D. Hydrocarbon evaporative loss from shale core samples as revealed by Rock-Eval and thermal desorption-gas chromatography analysis: Its geochemical and geological implications. *Mar. Pet. Geol.* **2016**, *70*, 294–303. [CrossRef]
45. Li, Y.; Yang, Y.; Sun, X.; Yang, D.; Zhang, N.; Yang, H.; Guo, H.; Zheng, J. The application of laser confocal method in microscopic oil analysis. *J. Pet. Sci. Eng.* **2014**, *120*, 52–60. [CrossRef]
46. Pang, X.; Li, M.; Li, B.; Wang, T.; Hui, S.; Liu, Y.; Liu, G.; Hu, T.; Xu, T.; Jiang, F.; et al. Main controlling factors and movability evaluation of continental shale oil. *Earth Sci. Rev.* **2023**, *243*, 104472. [CrossRef]
47. Pironon, J.; Canals, M.; Dubessy, J.; Walgenwitz, F.; Laplace-Builhe, C. Volumetric reconstruction of individual oil inclusions by confocal scanning laser microscopy. *Eur. J. Mineral.* **1998**, *10*, 1143–1150. [CrossRef]

48. Liang, C.; Wu, J.; Cao, Y.; Liu, K.; Khan, D. Storage space development and hydrocarbon occurrence model controlled by lithofacies in the Eocene Jiyang Sub-basin, East China: Significance for shale oil reservoir formation. *J. Pet. Sci. Eng.* **2022**, *215*, 110631. [CrossRef]
49. Zhao, W.; Wu, K.; Jiang, L.; He, M.; Li, X.; Jia, C. Charging and microscopic gas-water occurrence characteristics of tight sandstone gas based on pore network model. *Nat. Gas Ind.* **2022**, *42*, 69–79.
50. Yao, Y.; Liu, D.; Cai, Y.; Li, J. Advanced characterization of pores and fractures in coals by nuclear magnetic resonance and X-ray computed tomography. *Sci. Sin.* **2010**, *40*, 1598–1607, (In Chinese with English abstract). [CrossRef]
51. Yang, L.; Wang, S.; Tao, Z.; Leng, R.; Yang, J. The Characteristics of Oil Migration due to Water Imbibition in Tight Oil Reservoirs. *Energies* **2019**, *12*, 4199. [CrossRef]
52. Xu, T.; Wang, J.; Lu, Y.; Wang, D.; Yu, L.; Tian, Y. Exploring pore-scale production characteristics of oil shale after CO_2 huff 'n' puff in fractured shale with varied permeability. *Int. J. Coal Sci. Technol.* **2024**, *11*, 12. [CrossRef]
53. Li, C.; Liu, G.; Cao, Z.; Sun, M.; Liu, N. Oil charging pore throat threshold and accumulation effectiveness of tight sandstone reservoir using the physical simulation experiments combined with NMR. *J. Pet. Sci. Eng.* **2021**, *208*, 109338. [CrossRef]
54. Chen, J.; Ma, K.; Pang, X.; Yang, H. Secondary migration of hydrocarbons in Ordovician carbonate reservoirs in the Lunnan area, Tarim Basin. *J. Pet. Sci. Eng.* **2020**, *188*, 106962. [CrossRef]
55. Xu, Y.; Yan, G.; Hou, B.; Su, K.; Zhang, F.; Liu, B.; Li, S.; Zhao, S.; Liu, Y. Different effects of resins and asphaltenes concentration of crude oil on sandstone wettability. *Fuel* **2024**, *370*, 131825. [CrossRef]
56. Pang, Z.; Tao, S.; Zhang, Q.; Yang, J.; Zhang, B.; Wu, S.; Chen, R.; Huang, D.; Wei, T. Simulation experiments of tight oil secondary migration driving force and resistance: A case study of Jurassic oilfield in middle Sichuan basin. *J. China Univ. Min. Technol.* **2016**, *45*, 754–764, (in Chinese with English abstract).
57. Zhang, H.; Zhang, S.; Liu, S.; Hao, J.; Zhao, M.; Tian, H.; Jiang, L. A theoretical discussion and case study on the oil-charging throat threshold for tight reservoirs. *Pet. Explor. Dev.* **2014**, *41*, 408–416. [CrossRef]
58. Zhang, P.; Zhang, J.; Zhao, Q.; Chang, B.; Zhang, L.; Gao, F.; Cao, C.; Li, K. The application of constant-rate mercury penetration technology of Chang 7 tight sandstone reservoir pore-throat space representation in Dingbian Oildom. *J. Northwest Univ.* **2018**, *48*, 423–430, (in Chinese with English abstract).
59. Wang, S. Overpressure Evolution Caused by Hydrocarbon Generation of Chang 7 Section in Yanchang Oilfield and Its Control Effect on Accumulation. Master's Thesis, China University of Petroleum, Beijing, China, 2018. (In Chinese with English Abstract).
60. Liu, G.; Wang, H.; Tang, J.; Liu, Z.; Yang, D. Effect of wettability on oil and water distribution and production performance in a tight sandstone reservoir. *Fuel* **2023**, *341*, 127680. [CrossRef]
61. Wang, Z.; Luo, X.; Liu, K.; Fan, Y.; Wang, X. Impact of chlorites on the wettability of tight oil sandstone reservoirs in the Upper Triassic Yanchang Formation, Ordos Basin, China. *Sci. China Earth Sci.* **2021**, *64*, 951–961. [CrossRef]
62. Zhong, J.; Wang, P.; Zhang, Y.; Yan, Y.; Hu, S.; Zhang, J. Adsorption mechanism of oil components on water-wet mineral surface: A molecular dynamics simulation study. *Energy* **2013**, *59*, 295–300. [CrossRef]
63. Ritter, U.; Grøver, A. Adsorption of petroleum compounds in vitrinite: Implications for petroleum expulsion from coal. *Int. J. Coal Geol.* **2005**, *62*, 183–191. [CrossRef]
64. Liu, G.; Ding, Y.; Wang, J.; Ge, L.; Chen, X.; Yang, D. Effect of pore-throat structure on air-foam flooding performance in a low-permeability reservoir. *Fuel A J. Fuel Sci.* **2023**, *349*, 128620. [CrossRef]
65. Sun, L.; Zou, C.; Jia, A.; Wei, Y.; Zhu, R.; Wu, S.; Guo, Z. Development characteristics and orientation of tight oil and gas in China. *Pet. Explor. Dev.* **2019**, *46*, 12. [CrossRef]
66. Luo, Q.; Goodarzi, F.; Zhong, N.; Qiu, N.; Wang, X.; Such, V.; Khan, I.; Zheng, X.; Liu, B.; Ardakani, O.H. Dispersed organic matter from pre-Devonian marine shales: A review on its composition, origin, evolution, and potential for hydrocarbon prospecting. *Earth Sci. Rev.* **2025**, *261*, 105027. [CrossRef]

energies

MDPI

Review

Overview of Modern Methods and Technologies for the Well Production of High- and Extra-High-Viscous Oil

Inzir Raupov, Mikhail Rogachev and Julia Sytnik *

Department of Oil and Gas Fields Development and Operation, Empress Catherine II Saint Petersburg Mining University, 2, 21st Line, 199106 St. Petersburg, Russia; inzirrr@yandex.ru (I.R.); rogatchev@mail.ru (M.R.)
* Correspondence: julia.andreevna.97@mail.ru

Abstract: This paper presents a review of modern methods and technologies for extracting high- (HVO) and extra-high-viscous oil (EHVO). Special attention is given to thermal, physico-chemical, and combined enhanced oil recovery (EOR) methods based on the synergistic effect of these approaches. Theoretical aspects of these technologies, their applicability limits, and their practical implementation are considered. The article describes the main complicating factors in the extraction of HVO and EHVO using the reviewed methods, one of which is the high water cut in well production. We analyse the mechanisms of water production in HVO and EHVO fields. The paper highlights the experience of developing HVO and EHVO fields, primarily in Russia, and examines laboratory and field studies, ongoing projects, and future prospects. The authors of this paper have analysed the available literature and have provided further recommendations for studying these technologies. We hope that this work will be useful to all those interested in the challenges of oil production.

Keywords: high- (HVO) and extra-high-viscous oil (EHVO); heavy and super-heavy oil; physico-chemical enhanced oil recovery (EOR); thermal EOR; combined EOR; oil recovery factor

1. Introduction

Regarding the extraction of HVO and EHVO, methods are categorised into well based and non-well based. Well-based methods can be divided into primary, secondary, and tertiary techniques. Primary, or cold production techniques, are applicable when the oil has relatively low viscosity, allowing it to flow towards the wellbore due to the natural forces within the reservoir. The average oil recovery factors (ORF) at this stage for HVO and EHVO are 5–10%. Fields in the Orinoco Belt in Venezuela, the Brazilian shelf, and pilot projects in Russian fields such as the Usinskoye and Mishkinskoe are developed using primary techniques. Notably, the "Cold Heavy Oil Production with Sand" (CHOPS) is applied at the Lloydminster field in Canada, where a mixture of sand and oil is extracted in weakly cemented rocks through gas-driven screw pumps [1]. Despite high annual production rates, developing HVO and EHVO in this way alters the reservoir properties and can lead to its damage. One of the primary methods for accessing and producing HVO and EHVO from low-permeability reservoirs could be the hydraulic fracturing [2,3].

Secondary recovery methods, like flooding, are also used for HVO and EHVO fields, as they are for traditional oil reservoirs. The average oil recovery factors at this stage range from 20 to 40%, but they significantly decrease as the viscosity of the oil increases. In the case of EHVO fields with no underlying water, the technology is almost ineffective.

Experience with developing HVO and EHVO fields shows that the injection of large-volume polymer solution slugs, instead of traditional water flooding, is a viable secondary recovery method.

Tertiary recovery methods typically involve the introduction of additional energy into the reservoir, increasing the displacement or sweep efficiency. In the case of HVO and EHVO extraction, thermal, physico-chemical methods, and their combinations are most commonly used. The development of HVO and EHVO extraction technologies in Russia is associated with scientific work led by researchers such as Altunina, L. [4], Antoniadi, D. [5], Gazizov, A. [6], Ibatullin, R. [7], Ruzin, L. [8,9], Morozyuk, O. [10], and others. In the international scientific community, studies by Farouq Ali, S. [11], Butler, R. [12], Bai, B. [13], Shah, A. [1], Hascakir, B. [14], Edmunds, N., Lake, L., Seright, R. [15,16], Delamaide, E. [17], Zhahg, H., Thomas, A. et al. [18] have been recognised. The injection of thermal agents is used in certain fields as a primary or secondary method of extracting HVO and EHVO. This paper focuses particularly on these extraction methods. For easier navigation, the following flowchart is provided (Figure 1).

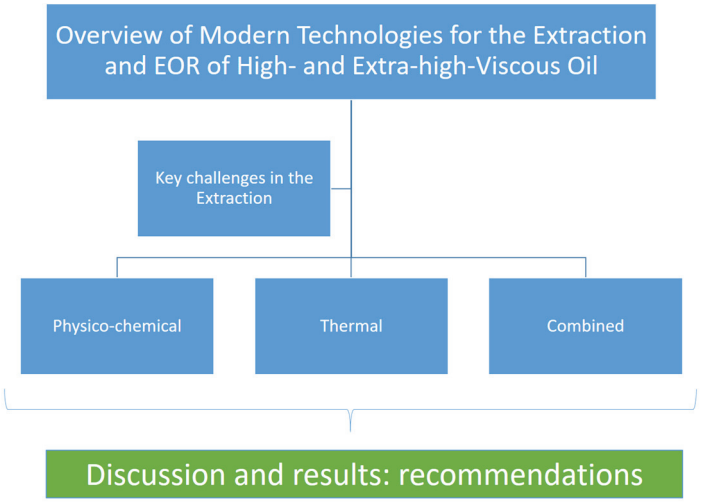

Figure 1. Navigation flowchart.

2. Key Challenges in the Extraction of Heavy and Super-Heavy Oil

According to the current classification of oil reserves and resources in Russia, natural bitumens (NB) are not distinguished as a separate category of reserves, as is the case in the American Petroleum Institute (API) classification. There is a classification of oils based on density, where heavy oils have a density of 0.871–0.895 g/cm^3, oils with a density greater than 0.895 g/cm^3 are classified as bituminous, and there is also a classification of oils based on viscosity: 30.1–200 mPa·s—HVO, >200 mPa·s—EHVO. The viscosity of NB can typically reach >10,000 mPa·s, and in this regard, they are classified as EHVO according to the current Russian classification. Thus, the terms "heavy oil" and "super-heavy oil" in this article are based on the Russian classification and only partially correspond to the term "heavy oil" in the API.

The extraction mechanism for HVO and EHVO through the introduction of additional energy into the reservoir via steam flooding or in situ combustion is primarily aimed at reducing the viscosity of the extracted fluid. At the same time, the increase in the displacement efficiency occurs due to the improvement of the mobility ratio between the oil and the displacing fluid (water, polymer solution, etc.). The enhancement of the recovery factor for HVO and EHVO is also related to the synergy of these mechanisms, for example, through the injection of hot water or hot polymer into the reservoir or by expanding the coverage of the reservoir impact via fluid flow redirection with plugging systems (e.g.,

injection of small volumes of chemical solutions into already thief zones of the reservoir). More details on each of these technologies will be presented in the relevant section of this paper.

Globally, capital- and energy-intensive thermal methods dominate the number of EOR projects for HVO and EHVO extraction. A complicating factor for the extraction of HVO and EHVO, from the perspective of project profitability, is the production of associated water [19]. Previous works did not sufficiently address the mechanisms of water production in fields with HVO and EHVO being developed by thermal methods. In general, the extracted water can be divided into two types. The first is water coming from active aquifers or injection wells, which aids in the displacement of oil towards the production wells, with minimal volume not exceeding the economic limit defined by the water–oil ratio (WOR). The second type is excessive, disproportionate water volumes entering the well. It is known that the WOR in conventional reservoirs is around 3, but in HVO and EHVO reservoirs, the WOR increases and is approximately 10 [20].

Based on accumulated global experience in developing HVO and EHVO fields, water production mechanisms can be generalised relative to the depth of productive layers (Figures 2 and 3). It should be noted that the depth of the productive layer is one of the determining factors when choosing the working agent: steam or water.

In general, there are both geological and technological causes for the water breakthrough in production wells. Geological factors are associated with the geological and physical characteristics of the reservoir, including the presence of bottom water, zones of vertical cracks, highly permeable channels and fractures, water lenses, and other features.

The technological factor relates to the operational regime of wells. In the Russian Federation, the development of carbonate formations of the Lower and Middle Carboniferous in the Usinskoe (Moscovian, Kasimovian, and Asselian stages), Gremihinskoe (Bashkirian stage), and Mishkinskoe (Tournai stage, Cherepetsky horizon) fields is predominantly carried out using thermal methods (hot water or steam flooding) combined with a reservoir pressure maintenance (RPM) system. The injection well stock primarily consists of vertical or deviated wells drilled into the reservoir with top depths of 800 m or more. The development experience of these fields demonstrates water breakthroughs from the RPM system (both cold and hot water) into overlying formations via vertical cracks. Reservoirs developed using steam injection show its breakthrough and subsequent condensation in non-target reservoir zones and vertical fracturing areas. Field geophysical surveys (FGS) have identified low steam quality (dryness < 75%) at the outlet of perforation zones in injectors, which, in some cases, has become the primary mechanism for water breakthrough to production wells.

In the context of hydrocarbon production from terrigenous formations (Cenomanian stage, Uvat horizon, and Pokur suite) at the Severo-Komsomol'skoe, Russkoe, and Vostochno-Messoyahskoe fields, a technogenic mechanism has been identified for the development of preferential flow zones originating from the RPM system (both cold and hot water). This has resulted in the upward movement of bottom water toward the perforation zones of production wells. These fields are developed using a row-based well system with horizontal completions extending up to 1 km in length.

The hydrocarbon fields in the Republic of Tatarstan (Ufimian stage, Sheshminsky horizon) are developed using steam flooding, predominantly employing row-based production well systems with horizontal completions. These systems include horizontal production wells or production wells using the steam-assisted gravity drainage (SAGD). Figure 3 outlines several operational challenges in production and injection wells identified through FGS.

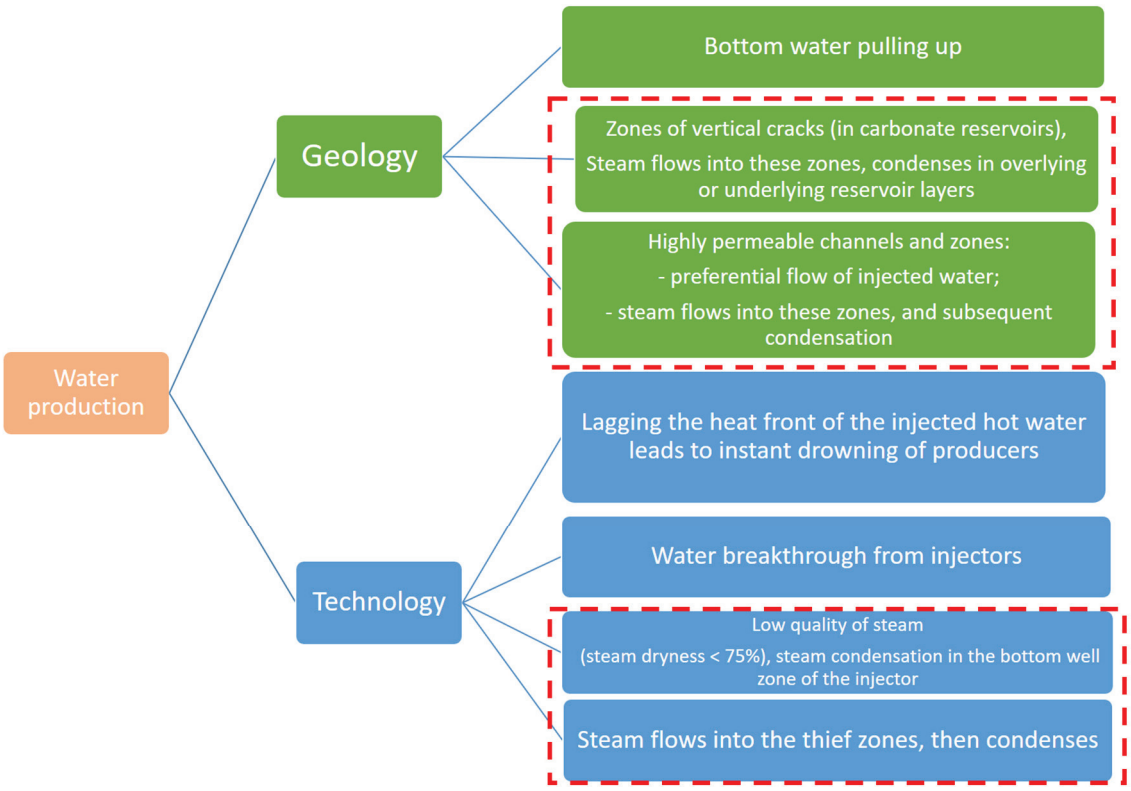

Figure 2. Mechanisms of water production in producers draining productive layers at depths > 800 m (mechanisms of ineffective steam use are marked with a red dashed line) [Compiled by the authors].

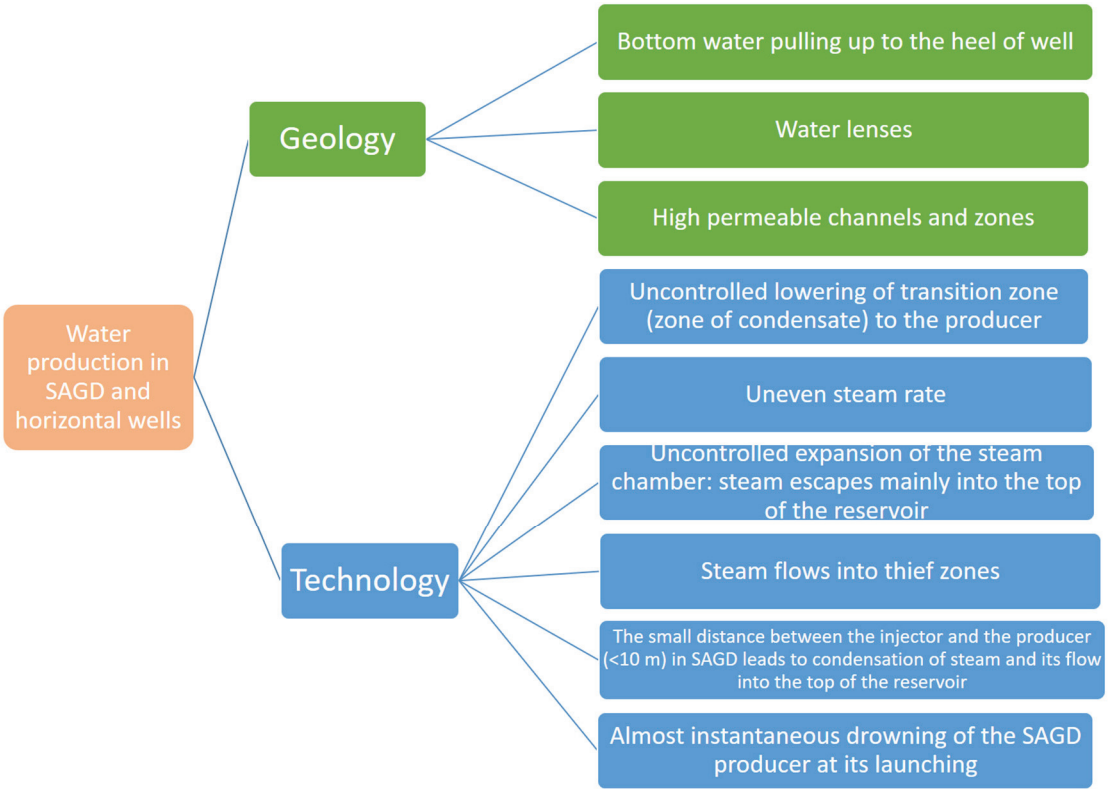

Figure 3. Mechanisms of water production in producers draining productive layers at depths < 800 m (mechanisms of ineffective steam use are marked with a red dashed line) [Compiled by the authors].

3. Thermal Methods

The heat introduced into the reservoir affects the oil's component composition, changing its physicochemical and flow properties: reducing its viscosity, increasing its mobility in the reservoir, distilling it, weakening structural–mechanical properties, decreasing the thickness of boundary layers, improving conditions for capillary impregnation, and enhancing the wettability of the displacing agent. The drawbacks of all thermal methods include heat losses along the wellbore, as well as at the top and bottom of the reservoir, a delayed effect due to the gradual advance of the thermal front, and the high cost of heat agents.

Thermal methods are generally classified by the type of working agent: hot water, steam, alternating injection of thermal agents and cold water, and injection of gas mixtures to ensure combustion in the reservoir (Figure 4). They are further categorised by scale: point and area treatments. The application of the reviewed technologies in the fields and the obtained results are summarised in Table 1.

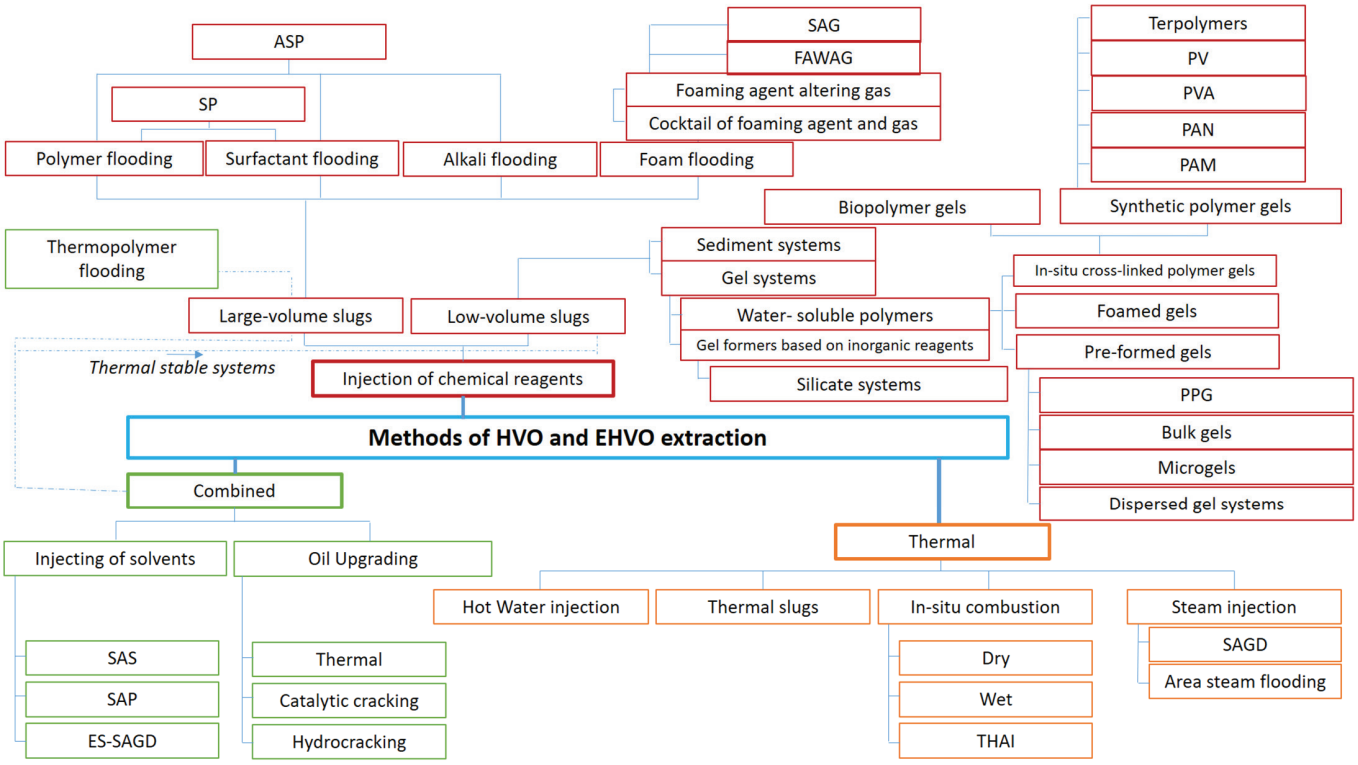

Figure 4. Methods of HVO and EHVO extraction [Compiled by the authors].

Table 1. Performance of considered thermal technologies.

№	Field, Country	Technology	Reservoir Type	Temperature of the Reservoir, °C	Temperature of the Thermal Agent, °C	Oil Viscosity, mPa·s	Salinity of Reservoir Water,g/L	Permeability, mD and Porosity	Results
1	Gremikhinskoe (Russia) [5]	Hot water injection	Carbonate fractured-cavernous-pore formation	28	60–100	90–300	Not Given	105	Specific heat carrier consumption 7 t/t
2	Usinskoe (Russia) [21]	Area Steam Flooding	Carbonate, fractured-cavernous-pore formation	21	200	710	Not Given	567 0.189%	Increase in the ORF to 22%; SOR = 11.5 t/t; Low steam quality at the level of the upper perforations

Table 1. *Cont.*

№	Field, Country	Technology	Reservoir Type	Temperature of the Reservoir, °C	Temperature of the Thermal Agent, °C	Oil Viscosity, mPa·s	Salinity of Reservoir Water,g/L	Permeability, mD and Porosity	Results
3	Ashalchinskoe (Russia) [22]	SAGD	Sandstone	8–10	<300	>1000–10,000	<5	1300–2100 29–32%	SOR > 10; By 2016, the development target had reached almost 60% of the recoverable reserves, with an ORF of 0.408
4	Russkoe (Russia) [23,24]	Hot water injection	Sandstone	18	60–80	206.8–500	<15	520 32%	Regarding cold water injection, the slow rate of water-cut increase in the production wells necessitates the implementation of water treatments for conformance improvement.

3.1. Hot Water Injection

Injection of hot water (60–100 °C) into the reservoir is most relevant for fields with a top located at depths of 800 m or more, where the heat agent must be injected under high pressure, as well as in clayey reservoirs. There is also a need for thermal water flooding in fields with low-viscosity oil (Uzen, Kazakhstan) or oil with increased viscosity (Mangala, India), where the saturation temperature of the oil with paraffin is nearly equal to the initial formation temperature, which significantly worsens the oil-to-water mobility ratio in the reservoir. During well operation, asphalt–resin–paraffin (ARP) deposits can form in the production zone and inside the wellbore, requiring additional operational costs to remove or prevent their formation [25,26].

The development of the Gremikhin field has been ongoing since the 1980s. For oil with a viscosity of 90–300 mPa·s, methods such as area hot water flooding, injection of thermal slugs, thermal pulse treatments, and their modifications have been applied. Experience from the field has shown a lag in the thermal front of the injected water, resulting in a delayed effect from the heat agent injection, accompanied by a sharp increase in water cut, high thermal energy losses to the top and bottom of the reservoir, and a low sweep efficiency due to the presence of highly permeable zones [5]. Alternating cycles of steam and cold water flooding in the Bashkirian strata demonstrated high production costs, but it is worth noting the advantage of this method in terms of energy savings, achieved by limiting the amount of heat agent injected based on the required reservoir temperature [27].

It should be noted that low formation pressures complicate the application of physicochemical EOR in the Bashkirian strata of the Gremikhin field. Currently used hydrodynamic EOR has short-term effects. In this regard, the development of new technologies to enhance oil recovery through the synergy of thermal and physicochemical effects is relevant.

3.2. Steam Injection (Saturated or Dry Steam)

The effectiveness of heating the oil-saturated reservoir with steam is higher than with hot water due to the higher heat content. The drier the steam, the greater its enthalpy, which means higher heating efficiency. In practice, steam with subcritical parameters is generated, with a dryness degree of less than 80%. The efficiency of steam injection and the heating of the target formation is determined by the steam–oil ratio (SOR), with the SOR < 3 being considered successful [7]. When designing and implementing heat carrier injection technology, it is necessary to evaluate the temperature range at which oil viscosity

reduction occurs and then select the thermobaric properties of the steam, such as the operational pressure and temperature for its generation.

3.2.1. Area Steam Flooding

Area steam flooding involves the frontal displacement of oil from the reservoir. The key factors that increase oil recovery include viscosity reduction, thermo-elastic expansion of formation fluids, and intensified capillary impregnation. However, area steam injection has several drawbacks: low oil production rates, high SOR (>5), breakthrough of the heat carrier into preferential flow zones, and low technological efficiency in formations less than 10 m thick with low permeability zones ($<10 \times 10^{-3}$ μm^2) [5].

Area steam injection has been applied in the development of the PTW-3, A-15, A-19, PTW-Southwest, and central parts of the Usinsk field. The effect of its application on the central part of the field showed a 22% increase in oil recovery from 1992 to 2016. The well stock in 2016 consisted of 50 producers and 199 injectors across three operating units. The well placement system was an inverted nine-point pattern. The compensation since the beginning of the development was 47%. The SOR since the start of development initially demonstrated stable growth, then plateaued over three years at 11.5 units. At this site, most production wells drain two operating units.

Thus, the area steam flooding at the Usinsk field demonstrated low energy efficiency. Additionally, the void replacement ratio (VRR) suggests potential leakage of condensate and water into non-target zones of the reservoir through highly permeable channels and thief zones. Well logging methods revealed steam breakthrough into overlying units from lower zones due to vertical fractures [21]. Research results on steam injection wells showed low steam dryness at the upper perforation intervals, with only 28.2% of the produced steam performing useful work.

3.2.2. Steam-Assisted Gravity Drainage (SAGD)

Originally implemented at the Yaregskoe Field in the USSR, SAGD technology subsequently evolved in Canada during the development of bituminous sands at such fields as Cold Lake and Primrose, among others [28,29]. In its conventional form, this technology involves drilling a pair of wells—an injector and a producer—with horizontal section lengths of 300–1000 m, positioned one above the other at a vertical distance of about 10 m. Steam is injected through the injector to heat the oil-saturated reservoir, thereby reducing oil viscosity and facilitating oil flow into the producer well under the influence of gravity. As the reservoir becomes progressively heated, a steam chamber forms and gradually expands. An adaptation of this technology exists for thin oil zones, where steam injection and oil production are performed sequentially in the same well. Key advantages of SAGD include a high oil recovery factor (up to 70%) and the capability to develop reservoirs containing oil with viscosities exceeding 50,000 mPa·s.

Since 2007, tests have been conducted to extract EHVO using a dual-wellhead SAGD at a pilot section of the Ashalchinskoe Field, drained by three pairs of wells. By 2010, total oil production had reached 100 tonnes/day (see Figure 5), a rate that was subsequently maintained for six years, with a SOR of 3 t/t. The producer well took approximately three months to be brought fully onstream. Compared to a single-wellhead SAGD, the average initial flow rates were roughly twice as high. Overall, the production profile exhibited fluctuations, reflecting the cyclical nature of injection and the soak period required for capillary imbibition. Starting in the 18th month of testing and continuing for nearly nine months thereafter, the well pair 241–240 was shut off—possibly due to sand production or a rapid rise in the water cut, since a sharp and prolonged decline in daily oil production was observed from the 15th month onwards. In such systems, abrupt spikes in water cut

typically stem from the influx of bottom water, insufficient control of the steam injection, steam cycling within already heated zones (often near the "heel" of the well), and its subsequent condensation. Thus, the transition zone (steam–water mixture) lowers and causes the instant drowning of the producing well. By 2016, approximately 60% of the initial recoverable reserves at the Ashalchinskoe Field had been produced, and the oil recovery factor stood at 0.408. Overall, the technology has proven promising under similar reservoir properties and has gained worldwide recognition in both scholarly and industry circles.

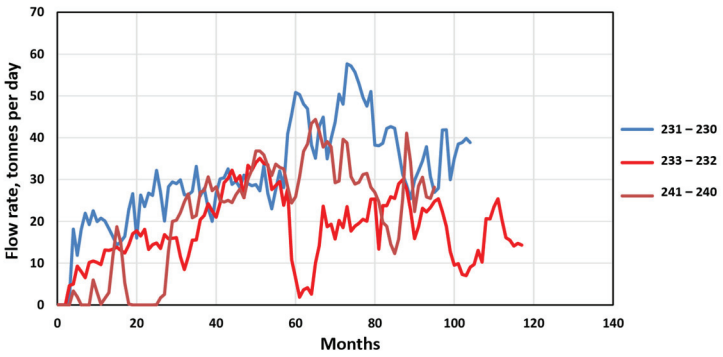

Figure 5. Daily EHVO Production Using a Dual-Injection SAGD System [22].

A complicating factor for heavy and extra-heavy oil production at the Ashalchinskoe Field is the steam breakthrough from the injector well toward the reservoir cap and the heel zone of the conventional SAGD configuration, which consequently leads to steam breakthrough to the producer well. The mechanism of water production into the producer well after steam condensation mirrors that observed during the operation of dual-wellhead SAGD wells. Since 2020, the operator has applied emulsion-based formulations containing polyacrylamide (PAM), guar, biocides, and gelation inducers to steam plugging in heated zones. According to PJSC Tatneft, the cumulative technological effect across 10 wells amounted to an additional 10.3 million tonnes of oil per well treatment. The stability of the gel's physicochemical properties lasts for under one year.

The primary drawback of SAGD lies in the high cost of steam generation, including water treatment and fuel conditioning operations. Notably, producing 1 m^3 of oil can require around 4 m^3 of boiler feed water [30]. The experience at Ashalchinskoe Field reveals a rapid rise in water cut in producers—up to 70.8–99.7%—during the early production stage and correspondingly low oil rates (0.1–4 t/day). As field operations continue, water cut declines while oil production ramps up, eventually reaching a stable plateau. This phenomenon is associated with the expansion of the steam chamber and the upward shift in the transition zone saturated by the steam–water mixture. Over time, the steam chamber reaches the reservoir cap, facilitating the maximum feasible oil inflow. In addition, project design must account for the costs of establishing hydrodynamic connectivity between the injector and producer when justifying economic parameters.

Based on the Cuban experience in developing heavy and extra-heavy oil fields, further SAGD drawbacks include the need for continuous monitoring of injection and production to avert steam breakthrough into the producer well, as well as upward into the overlying formations or even to the surface. Since downhole pumping equipment operates under harsh thermal conditions, risks include gas breakthrough into the pump intake and salt deposition within the equipment, collectively constraining allowable steam injection pressure [7].

The geological and physical constraints of the technology include elevated water saturation in the top area of the reservoir, stratigraphic heterogeneity due to clay and

water lenses, limited pay-zone thickness (less than 10 m), high vertical and horizontal permeability contrasts, and the presence of gas caps or bottom water zones.

3.3. In Situ Combustion (ISC)

ISC involves injecting an oxidant—typically air or a steam–gas mixture (dry in situ combustion)—into the injection well. ISC technology performs best in high-permeability, homogeneous sandstones. To establish initial hydrodynamic connectivity between the injector and producer, steam is pre-injected. After achieving adequate connectivity between the injection and production zones, the oxidation process is initiated. The combustion mechanism entails the migration of lighter hydrocarbon fractions into more permeable zones, while heavier fractions burn, generating heat and sustaining the combustion front deeper into the reservoir.

One documented case of ISC implementation in a Louisiana field is thoroughly described in [31]. To date, the in situ combustion process has yielded over 0.95 million m^3 of oil from an initial recoverable volume of 1.56 million m^3, leading to an ultimate recovery factor of roughly 60%.

A variant of ISC is the "Toe-to-Heel Air Injection" (THAI) approach, mainly used for bitumen production. Air is injected into a vertical injector well, while fluid is produced in a horizontal well [32,33]. At the Whitesand Field in Canada, pilot tests of THAI demonstrated notable outcomes. During combustion, the process enhances product quality by burning off and upgrading bitumen (with an original viscosity of 1850 mPa·s) left behind after lighter fractions move ahead of the combustion front, driving oil recovery factors up to 70%. During the pilot project, the cost-effective depth (<800 m) and thickness of the reservoir (<45 m) for the successful implementation of this technology were justified for these geological and physical conditions.

The main disadvantages of ISC include the complexity of controlling the combustion front, limited applicability in low-permeability formations or those with clay layers or water lenses, and significant vertical and horizontal permeability heterogeneity that can result in uneven heat distribution within the reservoir. The process also demands a continuous supply of oxidant, adding to both capital and operating expenditures.

4. The Low-Volume and Large-Volume Slug Injection of Chemical Reagents

Almost all physicochemical methods of oil extraction can be divided into low-volume and large-volume slug injections. The application of the reviewed technologies in the fields and the obtained results are summarised in Table 2.

4.1. Low-Volume Slug Injections

These injections are used to plug high-permeability intervals and zones in the reservoir and, consequently, to connect previously unswept zones to development through water-plugging treatments. The primary goal of implementing these treatments is to extract residual oil reserves. This is accomplished by redistributing the flows of the injected fluid (water or polymer solution). Highly permeable zones are plugged through placing into them insoluble precipitations or gels, which are the products of the chemical reaction of the injected solution. Water management treatments are classified into conformance-improving, profile modification, and water shut-off. Conformance treatments and profile modification are mostly applied at the injection well, whereas water shut-off treatments are applied at the production side.

Table 2. Performance of the considered chemical formulation and their field implementation.

№	Field, Country	Technology	Chemical Formulation	Reservoir Type	Temperature of Reservoir, °C	Oil Viscosity, mPa·s	Salinity of Reservoir Water,g/L	Permeability, mD Porosity	Results
1	Usinskoe (Russia) [4,34]	Inorganic gels + Steam flooding	GALKA-Thermogel-S: aluminium salt-urea-water	Carbonate	21	710	Not Given	105	The injection volume of the composition ranged from 80 to 160 m^3. A total of more than 150 well treatments were performed. An increase in oil production rates from 2.5 to 24 tons/day was observed. The water-cut decreased to 33–35%, the success rate of the operations was about 90%, the average incremental oil production was 981 tons per well treatment, the average increase in oil production rate was 13 tonnes/day, and the water-cut reduction was 21.1%.
2	Usinskoe (Russia) [4,34]	Inorganic gels + Steam flooding	ROMKA						
3	Usinskoe (Russia) [4,34]	Inorganic gels + Steam flooding	METKA	Carbonate	21	710	Not Given	105	The specific effect amounted to 2100 tonnes per well for the treatment of 5 wells.
4	Emlichheim, (Germany) [4,34]	Inorganic gels + Steam flooding	GALKA						The effect was observed in 3 out of 5 responding wells, with two demonstrating a decrease in daily oil production rates and an increase in water-cut.
5	Vostochno-Messoyahskoe, Russkoe, Severo-Komsomol'skoe (Russia) [23,24]	Water soluble polymers + P flooding	HPAM + chromium acetate	Sandstone, Cenomanian stage, Uvat horizon, and Pokur suite	18–30	500 is average value	<15	<5000	At these fields, 4–5 injections of gel-forming solutions based on 0.15–0.5 mass% polyacrylamide (PAM) with chromium acetate as the crosslinker in a 7:1 ratio were used to plug high-permeability zones in the reservoir. The life span of gel plugs in the reservoir averaged less than 2 months

Table 2. *Cont.*

№	Field, Country	Technology	Chemical Formulation	Reservoir Type	Temperature of Reservoir, °C	Oil Viscosity, mPa·s	Salinity of Reservoir Water,g/L	Permeability, mD Porosity	Results
6	Pelican Lake (Canada) [17,35]	P flooding	HPAM Flopaam 3630S	Sandstone	12–17	1650–15,000	Not Given	300–5000 28–32%	Incremental ORF 25%
7	Daqing (China) [18,36]	P flooding	HPAM	Sandstone	45	9	3–7	1100 25%	Incremental RF 15–18%
8	Vostochno-Messoyahskoe (Russia) [23,24]	P flooding	HPAM 3630S	Sandstone	16	111	12	50–5000 28–30%	Additional oil production 13,176 tonnes
9	Moskudinskoe (Russia)	P flooding	HPAM 5205 VHM	Sandstone	28	69	220	158–220 20%	Additional oil production 11%
10	Daqing (Chaina) [36]	SP flooding	0.2 wt.% amphoteric (HLW) surfactant + 0.25 wt.% HPAM	Sandstone	52	12	6	1400 26%	Increase in oil production from 0.2 mt/y to 4.06 mt/y
11	Mooney (Canada) [18,37]	ASP flooding	0.75 wt.% sodium hydroxide, 0.15 wt.% ORS-97HF, 0.12 wt.% of the polymer Flopaam 3630	Sandstone	29	300–600	24.5	1500 26%	Increase in oil production from 100 to 200 bpd to 2000 bpd. Decrease in water-cut from 75% to 55%

Gel-forming agents are reagents that promote the formation of three-dimensional gel-like systems with an inorganic or organic solid phase of high dispersion in either an aqueous or non-aqueous medium. The gelation mechanism involves the coagulation of sols followed by the development of a spatial structure due to the molecular interconnection of dispersed phase particles. Gel formation can occur in cases of coagulation of both lyophobic and lyophilic sols. Particle aggregates form precipitations by lyophobic sols; gelatinous precipitates are created by lyophilic soles. Therefore, one of the key properties of gels is their solid-like nature, including plasticity, thixotropy, elasticity, coagulative structure, and others.

Chemical reagents are differentiated by the type of formulation they create. For convenience, the flowchart of modern methods for influencing high-permeability and low-permeability reservoirs is presented in Figure 4.

4.1.1. Silicate Systems

They interact with polyvalent metal ions or other agents, forming precipitations such as $CaSiO_3$, $MgSiO_3$, $Mg(OH)_2$, $Ca(OH)_2$, or gel-like systems. One of the widely used reagents for water-plugging operations is liquid glass (LG) [38]. In an acidic environment, LG forms colloidal solutions of silicic acid, and over time, the sols transition into gels. Gels formed in acidic conditions are stronger than those structured in alkaline environments. In neutral conditions, in the presence of polyvalent metals, LG forms insoluble sediments [39,40]. Liquid glass solutions have low viscosity and flow capacity at reduced permeability (0.01–0.03 μm^2), forming stable and quite durable gels that are stable up to 200 °C or more under laboratory conditions. Thus, these systems can be used for conformance improvement and profile modification in both traditional and polymer flooding, as well as in conjunction with thermal methods.

The limitations of applying this technology include the high shale-to-sand ratio (SSR) of the reservoir and the lack of control and management of the gelation process. This technology is predominantly used in the Republic of Tatarstan. Over 100 wells have been treated at pilot sites of Public Joint Stock Company (PJSC) Tatneft, with additional oil production totalling over 250,000 tonnes, with an average of 2300 tonnes of extra oil per treatment.

4.1.2. Gels Based on Inorganic Reagents

These groups include GALKA-Thermogel-S, which forms during the hydrolysis of aluminium salts, urea, and water. Formulations such as “ROMKA” and “METKA” are derived from aqueous solutions of methylcellulose, ammonium thiocyanate, and urea. In contrast to METKA, the ROMKA is irreversible upon heating [4,34]. A key mechanism for gel management is temperature, ranging from 20 to 350 °C for METKA and 30 to 200 °C for ROMKA. These formulations have the following advantages: they reduce clay swelling, remain stable under reservoir water salinity up to 4000 mg/L, and can reduce permeability by up to 35 times. The penetrating ability of these systems is limited to permeability between 0.01 μm^2 and 10 μm^2. One drawback is their short-term stability in reservoir conditions (up to 1 year). In 2011, when GALKA was injected into high-permeability zones of the Emlichheim oil field (Germany), developed using thermal methods, the effect was observed in three out of five responding wells, with two demonstrating a decrease in daily oil production rates and an increase in water cut.

Technologies using the METKA formulation are industrially implemented in oil fields in Russia and Oman. In Oman, during 2005–2006, successful operations were conducted to limit water inflow during cyclic steam stimulation (CSS) at the HVO and EHVO Gaoshen field, and in 2007, at nine wells in the Lekhwair, Jibal, and Daleel fields. In the Russian

Federation, during 2014–2015, operations to limit water inflow were successfully carried out at the steam-assisted thermal recovery site of the Permo-Carboniferous reservoir of the Usinsk oil field, known for its high-viscosity oil. The additional oil production (AOP) from five wells totalled 11,000 tonnes over 1.5 years, averaging 2100 tonnes of oil per well intervention.

Inorganic formulations "GALKA-ThermoGel-S" are applied during the development of the HVO reservoir of the Usinsk oil field, which is developed using steam-assisted thermal recovery methods. Due to the uniform properties and low viscosity of the injected aqueous solutions, these formulations are suitable for use in low-permeability reservoirs. Between 2007 and 2010, a total of 87 well interventions were conducted to enhance the efficiency of CSS and to limit water inflow using GALKA-S formulations. The injection volume ranged from 80 to 160 m^3. Following the injection of the GALKA-S formulation, oil production rates increased by 2.5 to 24 tonnes per day, which is 20–30% higher than the average CSS results, while water cut decreased to 30–35%. The average AOP per treatment was 981 tonnes, with an average increase in oil production rates of 6 tonnes per day.

4.1.3. Water-Soluble Polymers

Polymer gel-forming systems typically consist of water-soluble polymers or monomers with crosslinkers and some additions. Polymer formulations based on water-soluble polymers must be thermally stable in water-plugging treatments in HVO and EHVO fields. Maximum temperatures are observed near the injection wells, and as the fluid moves further away, the thermal stability requirements for the polymer solutions decrease proportionally with the drop in temperature.

The first group includes polymer systems that form crosslinked gels in situ [41]. These systems are based on synthetic polymers (such as polyacrylamide, polyacrylonitrile, polyvinyl alcohol, terpolymers, etc.), biopolymers (such as xanthan, methylcellulose, etc.), and their derivatives (such as hydroxyethylcellulose) that are crosslinked in the reservoir by trivalent metal salts.

In Western Siberia, the main region for Russian oil extraction, the development of heavy oil is conducted at the Russkoye (207–500 mPa·s), Vostochno-Messoyahskoe (111–121 mPa·s), and Severo-Komsomol'skoe (34–111 mPa·s) fields. Extraction is complicated by factors such as extensive gas caps, bottom water, high SSR (8–55), sand production, and the presence of high-permeability zones (>10 μm^2), which promote premature breakthrough of injected water to production wells and flow into deeper water-saturated zones. To save energy resources, including the associated natural gas, underground gas storages are widely implemented at these sites for use by the enterprises or for further supply through pipeline systems [42].

At these fields, 4–5 injections of gel-forming solutions based on 0.15–0.5 mass% polyacrylamide (PAM) with chromium acetate as the crosslinker in a 7:1 ratio were used to plug high-permeability zones in the reservoir. The life span of gel plugs in the reservoir averaged less than 2 months. Control of conformance treatment was ensured through field geophysical methods and tracer studies, which confirmed the reformation of flows. The short-term effect from treatment is due to the washing out of gel by the displacing agent. Therefore, it can be concluded that for plugging high-permeability zones in the reservoir, rigid, more durable, and thermally stable polymer systems are required.

The second group of technologies includes preformed gels crosslinked on the surface before injection. These are divided into four types: bulk gels, gels with preformed particle gels [43,44], microgels [18], and gels with dispersed particles. These technologies have been successfully applied for over 20 years at oil fields in China and the USA [45]. At the fields of

Western Siberia, under high reservoir temperatures, technologies using preformed particle polymer systems such as "RITIN-10", "Tempocrine" [46], and others have been applied.

Gels with pre-formed particles, as described in [47], can swell more than 30 times their original volume in mineralised water with various ionic bonds. The thermostability of HT-PPG was evaluated for over 370 days in solutions with varying mineralisation and swelling coefficients. Robust, high-temperature-resistant hydrogel was synthesised from dimethylacetamide (DMA) monomers and sodium 4-styrenesulfonate (NaSS) with divinylbenzene (DVB) as the crosslinker. The use of this thermally stable crosslinker helped create stable covalent bonds within the hydrogel, making it more durable. Laboratory analysis confirmed that the gel is thermally stable at temperatures >150 °C for over 18 months and can be used in conjunction with thermal methods. One disadvantage of this system is the high cost of the monomers, which can negatively impact the economy of projects.

The "Bright Water" consists of polymeric submicron particles (0.1–1 μm) that can greatly increase their diameter by 5–10 times under reservoir conditions. As a result, it forms a microgel with a dispersed phase size of approximately 10 μm [18]. Also, there are nanogels. Their primary distinction from microgels is that the particle size of the dispersed phase in the aqueous solution typically reaches the nanometre scale. Nanogels are usually polymerised using monomers and crosslinkers that transform the polymers from linear structures into three-dimensional structures. The physicochemical properties of nanogels, including their swelling coefficient and strength, can be modified by the concentration of the crosslinker [48]. Microgels and nanogels are most often reverse emulsions. The boundary conditions for the application of such technologies are a formation water mineralisation of less than 250 mg/L and a rock permeability greater than 0.1 μm^2.

Water-swellable gels with pre-crosslinked particles and microgels containing water-absorbing carboxyl ($-COOH$) and amide ($-CONH_2$) groups exhibit elasticity and strength sufficient to effectively obstruct water flows in oil reservoirs, thereby curbing water production. Gels with pre-crosslinked particles are extensively used in oil fields for conformance control during water flooding due to their ease of preparation and injection, as well as the superior quality control they offer compared to in situ crosslinked polymer gels. However, drawbacks include the high cost of reagents.

Dispersed gel systems are classified under a subgroup of technologies due to the presence of plugging fillers (such as clay powder, wood flour, etc.). In reservoir conditions, clay and wood flour are not subject to decomposition, leading to the plugging of high-permeability zones. The main drawback of these systems is their narrow applicability temperature range (<60 °C), associated with the thermal degradation of PAM. The application of these systems is limited to low-permeability reservoirs. When designing an injection, it is essential to consider the pore size of the reservoir rock and the size of the solid phase filler to ensure the solution's flow through the rock. The thermal stability of the system can be improved up to 120 °C by using PAM with additives in the form of thermally stabilising monomers, such as n-vinyl-pyrrolidone (NVP).

One of the widely used compositions in Russia today is "AC-CSE-1313 Grade A" [49], which contains PAM, a crosslinker (chromium acetate III), and a filler—fine-dispersed reagent AC-CSE-1313 Grade B. Laboratory tests have shown that the gelation rate is directly proportional to the temperature. This composition has the following advantages: high penetration capacity into the porous media, low corrosive activity of downhole equipment, low initial viscosity (2.5 mPa·s), controllable gel formation, stability, and durability of the formulation over time within a temperature range of 20–90 °C. The disadvantage of this formulation is the narrow temperature range of application.

The third group involves foam–gel systems. These systems are mainly used in flooding processes. However, there is experience with using foams in the conformance improvement

and water shut-off [50,51]. The effectiveness of foamed gels for water management is linked to the specific formation of the gel's spatial structure within the porous medium: the system possesses the properties of foams (deep penetration into the porous media, improving the conformance coefficient) and impermeable gel systems (redirecting water flows in the rock, improving the conformance coefficient). To maintain the foam's spatial structure, acrylic acid polymers and crosslinkers are added to the solution. The foam system in the porous media is created by saturating the foaming agent with gas [52], making it possible to utilise carbon dioxide and associated gas, as well as exhaust gases from industrial enterprises. Typically, more than one foaming agent is required, as the half-life of most foaming agents is less than 10 min [53].

It should be noted that "foamed gels" are currently poorly studied systems, although they are quite promising. It can be assumed that to improve their stability in high-temperature-resistant conditions, more expensive reagents will need to be used. The stability of foam systems for profile modification and subsequent polymer flooding remains an unexplored issue.

4.2. Large-Volume Slugs Injection

These injections have the following primary mechanisms for recovery HVO and EHVO. The first mechanism involves thickening the oil-displacing water to reduce its mobility relative to oil. The second mechanism aims to reduce the interfacial tension at the water–oil interface, forming a microemulsion. The third focuses on further oil recovery from the rock surface. The specificity of large-volume injections lies in the continuous injection of the chemical solution, followed by the creation of a uniform oil displacement front in the productive formation.

Currently, there are three most widely used technologies: polymer (P flooding), surfactant-polymer (SP flooding), and alkali-surfactant-polymer flooding (ASP).

4.2.1. Polymer Flooding (P Flooding)

P flooding involves adding thickening agents to water—powdered or emulsified polymers—to increase the viscosity of the water relative to the extracted oil. Acrylic-based polymers with a hydrolysis degree of up to 30% are typically used for polymer flooding. The average concentration of PAM is 0.05–1 wt.%.

Over 700 successful polymer flooding projects have been implemented abroad, including projects in Canada (Pelican Lake) [35], Oman (Marmul) [54], China (Daqing) [36], and others. However, in Russia, polymer flooding and its modifications have only been conducted in the three pilot projects in the fields: Vostochno-Messoyahskoe [23,24] (2) and Moskudinskoe (1).

One of the key criteria for selecting a polymer is the mineralisation of reservoir water and thermobaric conditions [55]. The most commonly used polymers are PAM and xanthan. Polymer solutions undergo thermal degradation at temperatures of 60 °C and 80 °C, respectively, for the mentioned polymers. In contrast to PAM, xanthan is more resistant to hardness salts. It has been established that interaction with oxygen leads to oxidative degradation of the polymer bounds, so it is necessary to ensure airtight conditions during preparation. Therefore, the absence of oxygen and divalent cations (in the case of PAM) can ensure the stability of the solution at temperatures up to 120 °C.

When injecting polymers at temperature conditions < 95 °C, global experience shows that the inclusion of the monomer acrylamide tert-butylsulfonic acid (ATBS) in the polymer chain can improve the stability of PAM, even in highly mineralised waters. By increasing the temperature limit to 140 °C, NVP is added to maintain the stability of the PAM solution.

However, the disadvantages of this additive include the relatively high concentrations of the polymer, which increase the costs of implementing the technology.

In the analysis of P flooding for HVO and EHVO, the following advantages have been highlighted [18,56,57]: applicability with fluid viscosity < 8000 mPa·s (Pelican Lake, Canada), uniform reservoir depletion without viscous fingering by implementing it in the early stage of field development, and the environmental safety of the technology. The drawbacks include possible viscous fingers of water when alternating polymer and water injection [17,58]; the lack of domestic industrial capacity for their production, leading to high costs due to imports; high retention of polymers in clayey rocks, requiring the addition of modified copolymers (ATBS, NVP); loss of injectivity due to insufficiently prepared water or incorrect polymer concentration; minimal effect at high permeability heterogeneity (>10 units); polymer degradation due to thermo-oxidative processes, as well as high mineralisation of reservoir and injected water: and the necessity for specialised equipment and facilities for injecting polymer solution.

4.2.2. Surfactant Flooding (S Flooding)

There are two main mechanisms involved in surfactant flooding. The first involves reducing the surface tension at the oil-rock interface, which leads to further oil displacement, its capture, and extraction into the main water flow. The second mechanism concerns the reduction in interfacial tension between the aqueous solution and oil phases, forming microemulsions. The oil recovery factor during surfactant flooding can reach up to 0.5 units [59].

The main drawbacks of S flooding are the high cost of reagents and the sensitivity of surfactant solutions to increased mineralisation and high temperatures. Due to the high adsorption of surfactants on the rock and their taking out into the general fluid flow, alkali solutions are introduced. So, it preserves the properties of surfactants and reduces their losses and, consequently, lowers operational costs. This technology is known as alkali-surfactant flooding. The greatest efficiency in HVO and EHVO production can be achieved by incorporating a cycle of polymer slug injection into S flooding or by employing sequential injection cycles of alkali, surfactant, and polymer solutions, or by injecting an alkali-surfactant-polymer (ASP) solution.

SP flooding involves injecting solutions of surfactants (along with co-solvents, stabilisers, etc.) and polymers to achieve a synergistic effect on oil recovery. In SP flooding, the surfactant content is typically up to 2 wt%. However, modern surfactants are emerging in the market that exhibit their properties at significantly lower concentrations (<0.5 wt%). The increase in oil recovery factor can reach up to 18% [16].

This technology has been most widely applied in China, where over 10 pilot projects have been implemented since 2003, including those targeting heavy oil production. For example, SP flooding has been successfully employed at the Daqing and Shengli fields [36], where the crude oil viscosity under reservoir conditions was 33.7 and 66.9 mPa·s, respectively. At the pilot sites of these fields, the additional oil recovery achieved was 12% and 10%, respectively, compared to water flooding.

ASP involves injecting solutions of alkali, surfactants, and polymers, which can enhance oil recovery by up to 30%. A notable case of successful ASP was observed at the Mooney field in Canada, where oil with a density of 959 kg/m^3 and a viscosity ranging from 150 to 1500 mPa·s is produced from a low-temperature reservoir at a depth of 900 m (Watson et al., 2014 [37]). By 2014, the oil production rate reached 400 m^3/day, with an average injection capacity of 1600 m^3/day. The alkali slug consisted of an aqueous solution of Na_2CO_3 (1.25 wt%), the surfactant slug was of the anionic group (0.15 wt%), and the polymer solution contained partially hydrolysed polyacrylamide (2200 mg/L).

However, ASP has certain limitations, including high reagent consumption and significant capital expenditures due to the complexity of the required technological installations. For instance, at the Mooney field, approximately 55 tonnes of soda ash, 11 tonnes of dry polymer, and 7 m^3 of surfactants are required daily [37]. Compared to SP, the cost of ASP flooding equipment is 2–3 times higher, primarily due to the need for water softening.

In formations composed of sands and sandstones, anionic surfactants are widely used. For clay-bearing reservoirs, cationic surfactants are preferred due to their low adsorption on the rock surface. Nonionic surfactants (NISs) are capable of dissolving well in formation waters without precipitating. Common NISs include ethoxylated alkylphenols (Hostapal CV, Nonal, Syptopan), sulfonols, sulfoethoxylates, alkyl sulfonates, and reagents of the OP series (OP-4, OP-10). It has been demonstrated that the combined use of nonionic and ionic surfactants results in a more stable water-oil emulsion.

Surfactant flooding, whether as an independent technology or as part of ASP or SP, can be implemented with both low and high surfactant concentrations, resulting in micelle formation at the critical micelle concentration.

4.2.3. Foam Flooding

There are two primary mechanisms for foam formation in porous media. The first involves the simultaneous injection of gas and a foaming agent into the reservoir, while the second employs alternating injection of gas and a foaming agent, referred to as "Surfactant Alternating Gas" (SAG) and "Foam-Assisted Water Alternating Gas" (FAWAG), respectively. FAWAG is a variation of the "Water Alternating Gas" (WAG) technique, primarily aimed at developing viscous oil rims with underlying water and gas caps [60].

Foam can be characterised as a dispersed system with a cellular, film-based, honeycomb-like (aerated) structure. The ability of foam to maintain its distinctive structure (longevity) is one of the critical criteria for assessing the stability of a dispersed system. Foam stability is influenced by several factors, including the nature and concentration of the foaming agents used, their dispersibility, the salinity and pH of the foaming agent solutions, compatibility with reservoir fluids, thermodynamic conditions, and others. Foam stability increases with the elongation of the hydrocarbon chain in oil, making it more stable when in contact with more viscous oils. Stabilisers commonly employed in foams include nanoparticles, enzymes, and polymers such as xanthan, scleroglucan, polyacrylamide, and others.

The mechanisms of foam generation and collapse are largely dependent on the pore-to-fracture size ratio and the physicochemical properties of the oil. In porous media, foam represents a dispersed gas phase within a continuous aqueous phase, primarily composed of thin films known as lamellae. Foam in porous media is generated by injecting carbon dioxide, nitrogen, steam, or other gases into a continuous aqueous phase containing surfactants. In the past decade, there has been growing interest in the technology of injecting carbon dioxide into surfactant solutions as a component of foam generation [61].

The historical application of foam flooding in the USSR, the United States, and Norway has demonstrated that oil recovery factors can be increased by up to 20%. Foaming agents can be broadly categorised into three groups of reagents:

- Lower and medium homologs, including alcohols and fatty acids;
- Water-soluble substances that form colloidal and semi-colloidal solutions;
- Water-insoluble substances that form monomolecular films on the water's surface when a droplet of solution in a volatile nonpolar hydrocarbon solvent evaporates.

Currently, several key research areas in foam flooding remain unresolved. These include the impact of polymer molecular weight on foam stability, the selection of the chemical charge of polymers and their effects on foam physicochemical properties, and

the creation of dynamic foam systems during injection into rock samples. Additionally, unresolved challenges include evaluating foam stability under specified thermodynamic conditions, controlling and regulating foam cell size, and addressing a range of other technical issues in laboratory investigations and field applications.

5. Combined Methods

The application of the reviewed technologies in the fields and the obtained results are summarised in Table 3.

Table 3. Combined technologies and their field implementation.

№	Field, Country	Technology	Chemical Formulation	Reservoir Type	Temperature of Reservoir, °C	Oil Viscosity, mPa·s	Salinity, g/L	Permeability, mD and Porosity	Results
1	Mangala (India) [62]	TP flooding	Heated solution of HPAM, 2500–3000 ppm	Sandstone	62	9–22	Not Given	20–20,000 21–28%	The trend of decreasing water-cut. Incremental RF 25%
2	Mishkinskoye (Russia) [63,64]	TP flooding	Heated solution of HPAM PDA-1012, 0.05 wt.%	Carbonate	<90	50–500	260	231 16.4%	Incremental RF 15–20%.
3	Christina lake (Canada) [65]	SAP	Butane	Sandstone	Not Given	Not Given	Not Given	5000	In a period spanning over half a year of pilot operation, the production rate showed an increase from 100 t/dt 250 t/d. SOR in the same period came down from 5 to 1.6. Oil quality has also started showing signs of improvement.
4	Strelovskoe (Russia) [66–68]	Catalytic aquathermolysi	Thallate of iron	Carbonate reservoir, fractured-cavernous-pore formation	28–31	53	Not Given	3458 mD, 0.27	The highest efficiency at temperature 3000 °C and 96 h of exposure. Dynamic viscosity at 100 °C decreased by 4 times compared to the original sample
5	Vishnevo-Polyanskoe (Russia) [66–68]	Catalytic aquathermolysi	Solution of nickel and iron thallates in petroleum solvent	Sandstone	23–25	355.7	Not Given	310–956 mD 0.21	An increase of 61.3% in oil displacement was obtained relative to the variant with conventional steam injection

5.1. Low-Volume Injections

Typically involve the use of thermally stable formulations to plug highly permeable intervals of the reservoir, enabling subsequent activation of untapped zones through thermal exposure. The injected chemical formulations must meet several requirements dictated by the geological and physical conditions of the reservoir, including thermal stability at temperatures exceeding 100 °C, adjustable gelation kinetics, resistance to shear forces, the ability to withstand high-pressure gradients, and high penetration capacity, among others.

For the development of high-temperature-resistant (>130 °C) formulations, biopolymers capable of maintaining their stated properties in aqueous solutions have shown promise, with polysaccharides being particularly noteworthy [69–71]. However, a significant drawback of these biopolymers is their high molecular weight (MW, >20 million Da) and susceptibility to oxidative degradation. Consequently, when implementing polymer systems based on these biopolymers, it is essential to ensure an oxygen-free environment

during the preparation of the aqueous solution and to carefully optimise the composition's formulation to ensure injectivity into the porous media.

When designing geological and technical measures, the high cost of biopolymers must be considered. However, the benefits of their application, compared to polyacrylamide- or xanthan-based formulations, may outweigh their costs due to the long-term stability of the rheological and physicochemical properties of the gel, resulting in improved conformance and recovery factors. Table 4 presents the characteristics of aqueous solutions based on biopolymers and PAM formulations.

Table 4. Characteristics of Biopolymer and Polyacrylamide-Based Aqueous Solutions.

№	Polymer	The Main Characteristics of Water Solutions	Field Application	Disadvantages
1	HPAM (+crosslinker) *	Anion/cation water-soluble polymer; Thermal degradation during >60 °C A good penetration into the porous media.	P flooding, conformance and shut-off treatments, profile modification *	Sensitivity to the content of hardness salt, large shear stress, and high temperatures
2	Xanthan (+crosslinker) *	Thermal degradation during >80 °C; Stability in wide range of pH; Stability to shear stress.	P flooding, conformance and shut-off treatments, profile modification *	Biodestruction and oxidative degradation
3	Welan gum	Anion water-soluble polymer; Thermal degradation during >130 °C; Pseudo-plastic behaviour with good viscoelastic ability, on which sodium ions and potassium cannot influence; Stability to shear stress.	Not given	Sensitivity to the content of hardness salt
4	Diutan gum	Anion water-soluble polymer; Thermal degradation during >150 °C; Can recovery its rheological characteristics after cooling of the environment from 150 to 24 °C.	Not given	Potential infectivity issues since high MW
5	Hydroxyethyl cellulose	Non-ionic water-soluble polymer; It is well soluble in high mineralization solutions; Has bad solubility in water within zinc.	Conformance and shut-off treatments, profile modification	Oxidative destruction, biodestruction, enzymic destruction
6	Scleroglucan	Non-ionic water-soluble polymer; Denaturation of triple chains under >130 °C, in the process of renaturation it can recover and improve its rheological characteristics; Stable under Ph < 13, when pH increases a conformation transition happens; Long-term stability under influence high temperatures.	P flooding, conformance and shut-off treatments, profile modification	Biodestruction, oxidative destruction, Potential infectivity issues since high MW
7	Schizophyllan	Nonionic water-soluble polymer; Denaturation of triple chains under >130 °C; Stable under pH < 13, when pH increases a conformation transition happens; Low adsorption ability; Long-term stability under high temperatures.	P flooding	Biodestruction, oxidative destruction, Potential infectivity issues since high MW

The (*) means using the crosslinked polymer systems in conformance, shut-off treatments, and profile modification.

The implementation of steam and water management treatments in reservoirs developed using thermal methods significantly increases operational costs due to the procurement, transportation, and storage of known commercial reagents. In this regard, industrial

waste containing the necessary components should be considered as primary reagents. Promising waste materials include lignin sludge from pulp and paper mills [72]. Lignin sludge, with a high biopolymer lignin content (40–60%), can serve as the polymeric base for gel-forming formulations.

For crosslinkers in polymer systems, industrial waste containing multivalent metal cations can be utilised, such as red mud from the metallurgical industry. Red mud is a byproduct of bauxite leaching with NaOH and contains up to 12.36% Na_2O. According to [73], the composition of red mud from various facilities includes the following components, %: Fe_2O_3 (6.8–65.7), Al_2O_3 (2.12–33), SiO_2 (0.6–23.8), CaO (0.19–46), TiO_2 (2.5–22.6), Na_2O (0–12.36), and moisture, volatiles, and rare earth elements (1–30). Nowadays, approximately 4 billion tonnes of red mud have been accumulated, with most of it unprocessed and stored in specialised tailing ponds, resulting in significant environmental contamination [74]. Therefore, the productive utilisation of industrial waste is a promising approach for steam and water management treatments in hydrocarbon reservoirs. The authors intend to demonstrate an example of industrial waste utilisation in future studies.

5.2. Large-Volume Injections

Thermal polymer flooding (TP flooding) provides for the injection of a slug of hot polymer solution, which has been heated on the surface or injected cold after preheated reservoir by heat-transfer fluid. In the world at this moment, the two biggest projects of TP flooding are known: on the Mangala field (India) and on the Mishkinskoe field (Russia).

The pilot project of TP flooding is planned on the Tagul'skoe field (Russia). The object is described by difficult lenticular rock construction of continental genesis, high SSR (8.6), and the existence of shale barriers with different water-oil and gas-oil contact marks. The field is multilayer; the layer shows up in section, the resources of which fall under the category of EHVO (oil viscosity is 558 mPa·s). In the paper [75], based on available experience with large slugs injections of chemical solutions, the formed criteria for preparing hot water, heated, and cold polymer solutions are presented. Therewith, in the work presented, variants of capital and operating cost improvement for the chemical and water treatment works. In the paper [10], the results of research on the sand-packed tubes with the same geological-physical characteristics of the Tagul'skoe field are given. The results of 18 core-flooding experiments, in which 6 technologies of HVO and EHVO recovery are tested, demonstrate the same displacement factor of using hot water at 90 °C (60%), at 120 °C (66.2%), and hot water with PAM slugs injection (63.5%) against cold water flooding (44.5%). Under displacement by polymer-alkaline (44.5%) and surfactant-polymer solution (49.9%), high gradients of pressure connected with low oil mobility are observed.

The production target at the Mangala FM1-2 reservoir is characterised by the complex structure of fluvial deposits and high heterogeneity, in contrast to the more homogeneous structure of the $FM_{3–5}$ reservoir. The permeability of the Fatehgarh group formations ranges from 20 to 20,000 mD, with porosity values between 21 and 28%. The oil at the Mangala field exhibits elevated viscosity (9–22 mPa·s), is paraffinic in nature, and has a paraffin precipitation point close to reservoir temperature (62 °C). Since 2009, the field has been developed using a nine-spot inverted pattern of TP flooding. However, the results of TP flooding demonstrated low reservoir sweep efficiency and a high mobility ratio between the injected and displaced fluids. Consequently, the development strategy transitioned to full-scale TP flooding using a five-spot pattern [62]. The shift to injecting heated polymer solutions improved reservoir oil recovery, reduced water-cut in production from responding wells by 9–15%, and enhanced the overall development efficiency. The referenced study also provides recommendations on preparation for injection and monitoring the properties of the displacement fluid under the specified geological and physical conditions.

At the Mishkinskoe field, four development targets are identified: Vereiskan, Bashkirian, Yasnopolyanian, and Tournai. Most of the heavy and super-heavy oil reserves are contained in carbonate-fractured-porous reservoirs of the Tournais stage, characterised by high cavernosity and extensive cracks. The oil viscosity under reservoir conditions averages 78 mPa·s. The development experience at the Mishkinskoe field has led to the establishment of criteria for the applicability of TP flooding, including oil viscosity (50–500 mPa·s), reservoir permeability (231 mD), and the depth of productive reservoirs, which is limited by reservoir temperature (<90 °C) [63]. Furthermore, TP flooding is recommended for implementation during the early stages of field development in the absence of underlying aquifers to prevent conical breakthroughs of formation water from the pressure maintenance system or the upward migration of bottom water into wellbores.

Studies [63,64] have compared the effects of TP with P flooding, displacement by water, and natural drive development across four sites with comparable geological and technical characteristics (Figure 6). For TP and P flooding, the same brand of acrylic polymer (PDA-1012) was used at a concentration of 0.05 wt%. The results of the pilot project demonstrated a significant advantage of TP flooding: the current ORF at the time of the study was 40.9%, compared to 21.9% at the site with displacement by water. Compared to P, TP flooding demonstrated superior oil displacement from the rock matrix, as evidenced by quantitative development performance metrics: since the introduction of polymer injection, 289,500 m^3 of cold polymer solution (approximately 16% of pore volumes) were injected, compared to 336,400 m^3 of heated solution (20% of pore volumes). Traditional flooding showed a significant increase in the water cut during the study period (approximately 81%), while TP flooding reached a water cut of 86%. Cumulative oil production under natural drive conditions was more than two times lower than under water flooding. At the Mishkinskoe field, cyclic thermal polymer flooding was employed, involving alternating slugs of heat carrier and cold polymer slug. Compared to TP flooding, this technology increases reservoir sweep efficiency and is less energy intensive.

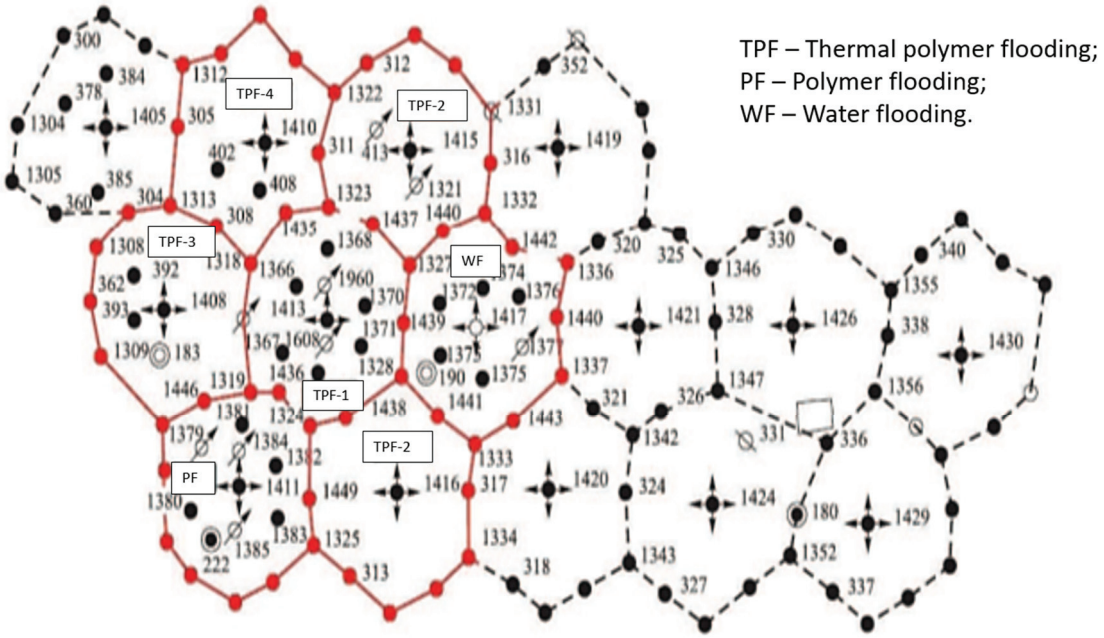

Figure 6. Layout of Study Sites at the Mishkinskoe Field [64] (red lines indicate pilot project areas; black dashed lines indicate areas for further research).

5.3. Solvent and Steam Injection

Solvent injection technologies have primarily employed chemical reagents, high-pressure water, nitrogen, or carbon dioxide. These methods began to gain widespread adoption in international projects over a decade ago. The first field tests were conducted in Canada at the Christina Lake field. As a result of pilot tests, steam conformance reached 73% after 25 days of exposure, with a total solvent volume of 400 m^3. Compared to 13 other well pairs operating without solvents under the SAGD, the use of solvents reduced steam circulation time by 46% and achieved steam savings of approximately 50% under otherwise identical conditions.

This technology significantly reduces steam generation costs compared to traditional SAGD while maintaining well production rates and lowering the SOR. Research [28] demonstrated the effectiveness of solvents in enhancing the development of heavy oil reservoirs. At low injection rates (IR), oil displacement occurs predominantly via diffusion, while at higher solvent IR, convection becomes the dominant displacement mechanism. Increasing solvent rates improves the oil displacement factor due to deeper penetration driven by convective forces. The final oil displacement efficiency was observed to be 8%, 11.5%, 14%, and 16% under reservoir conditions of 28 °C, 50 °C, 75 °C, and 100 °C, respectively.

Currently, three solvent injection methods are recognised:

- Steam Alternating Solvent (SAS): A modified SAGD technology where steam and solvent are injected alternately. SAS is carried out in several stages. Initially, hydrodynamic communication between wells is established using steam to create an optimal steam chamber. This is followed by solvent injection and subsequent steam flooding;
- Solvent Aided Process (SAP): Similarly to SAS, SAP is a modification of SAGD; however, solvent is co-injected with steam rather than alternated;
- Expanding Solvent SAGD (ES-SAGD): Like SAP, ES-SAGD involves the co-injection of hydrocarbon mixtures with steam at low concentrations. The most effective solvents are those with condensation and vaporisation temperatures close to that of water [76]. Research [77] highlights the potential of ES-SAGD using cracking naphtha and gas condensate. This technology significantly reduces SOR and increases oil production rates. Maximum differences in asphaltene content in oil recovered using ES-SAGD with cracking naphtha and gas condensate compared to the original oil were 3.5% and 3.6%, respectively. The use of multicomponent solvents in ES-SAGD improves the energy efficiency of SAGD due to the presence of light hydrocarbon fractions, which typically lower the effective temperature of the steam chamber. Additionally, gas condensates can be effectively utilised in HVO and EHVO fields.

5.4. In Situ Oil Cracking

Research into in-reservoir cracking focuses on the "in situ upgrading" of crude oil to reduce asphaltene and resin content, increase saturated and aromatic hydrocarbon fractions, decrease molecular weight, lower sulphur content, and increase the hydrogen-to-carbon (H/C) ratio [78–80]. In-reservoir cracking can be classified into thermal, hydrocracking, and catalytic processes. The underlying concept is to break atomic bonds in heavy oil molecules and convert macromolecules into micromolecules.

One of the most promising methods for in-reservoir oil upgrading is catalytic aquathermolysis. This reaction occurs at temperatures of 200–320 °C and targets the breakdown of asphaltene molecules in heavy and super-heavy oil via the synergy of steam and chemical reagents. When designing EOR treatments, both oil properties and the mineralogical composition of the reservoir rock must be considered. Global experience has revealed cases where aquathermolysis reactions unexpectedly increased oil viscosity due to the formation of new free radicals, initiating polymerisation reactions and forming larger molecules.

The technology has been successfully piloted in fields operated by PJSC Tatneft and PJSC Lukoil in collaboration with RITEK LLC and JSC Zarubezhneft, with the results documented in a book [66]. Laboratory studies [67,68] have demonstrated the effects of sodium and iron nanoparticles on the compositional and physical properties of heavy oil from the Vishnevo-Polyanskoe and Strelovskoe fields. These catalysts have been shown to reduce sulphur content, lower the concentration of sulphur-containing aromatic compounds, and improve oil properties by reducing viscosity and density.

Developing a methodology for selecting chemical reagents and testing them under laboratory conditions is essential before conducting pilot tests. Screening reagents for their preliminary effects (e.g., improving reservoir sweep efficiency) can be supported by mathematical and hydrodynamic modelling of in-reservoir upgrading processes. It should be noted that predicting the effects of geological and technical measures through the creation of hydrodynamic models and the development of digital twins (DTs) is a promising direction in the development of the global oil and gas industry. According to research conducted by Gartner, the use of DTs has increased annually [81,82]. However, there are several challenges in obtaining reliable data, among which the manifestation of the nonlinear properties of HVO and EHVO can be highlighted. These properties depend on the component composition of the oil, the formulation of chemical reagents, as well as geological, physical, and thermobaric conditions. Modelling aquathermolysis requires accounting for phase transitions, changes in the geomechanical properties of the rock [83], heat exchange processes, and changes in the physicochemical properties of the oil.

For example, a numerical model of three cycles of catalytic cracking using hydrogen donors and a base solvent was developed in [76]. The study utilised molybdenum oleate and formic acid injected alongside cyclic steam stimulation. A drawback of this technology was the formation of heavy hydrocarbon components such as carbynes, carboids, and coke, which plugged the near-wellbore zones of vertical wells. However, the addition of hydrogen donors in aquathermolysis reactions increased reservoir sweep efficiency by breaking C-S and C-O bonds, reducing high-molecular-weight components in oil by 1.5 times.

This technology is relatively new in the petroleum industry, and many questions remain unresolved, including the reaction kinetics of aquathermolysis and methods for monitoring the reaction in real time. Further research is needed to establish a comprehensive understanding of this process.

6. Results and Discussion

Analysing the aforementioned technologies from the perspective of their technical and economic feasibility, the following conclusions can be drawn:

1. Thermal methods remain the predominant methods for heavy oil when its viscosity exceeds 8000 mPa·s. In addition to the low mobility of the fluid, several complicating factors hinder its production, such as premature water breakthrough in producing wells. To reduce operating costs associated with steam generation and hot water preparation, as well as to decrease water cut, the potential of implementing physicochemical EOR, such as the injection of flow-control solutions, should be considered.

- Durability-Oriented: Using more thermally resistant systems to reduce re-treatments.
- Cost-Orientated: Maintaining the existing treatments trend (taking into account the lifetime of plugging systems up to 1 year) by using cheaper reagents, such as industrial waste.

Many Russian oil production companies operate within isolated energy systems [84]. Utilising industrial waste would allow companies to implement active energy-saving and energy-efficiency policies, even in remote regions [85].

2. Polymer flooding shows promising results in reservoirs with oil viscosities below 10,000 mPa·s. However, there are some permeability requirements (minimum 500 mD) to ensure that the polymer penetrates the pore media without plugging the near-wellbore zone or reducing infectivity.

For lower-viscosity fluids, the selection of extraction technology lies between physico-chemical methods (e.g., displacement by water combined with conformance improvement and profile modification or chemical flooding) and thermal methods. Key selection criteria include reservoir depth, vertical and lateral permeability heterogeneity, reservoir type, the presence of aquifers or water lenses, clay interlayers, the distance of the production facility from heat sources, and other factors.

The author of research [58] comparing SAGD and chemical flooding indicates the superiority of the last one over thermal methods (steam injection) in reservoirs with high vertical and lateral permeability heterogeneity. Development experience from Russian fields (e.g., Russkoye, Vostochno-Messoyahskoe, and Severo-Komsomol'skoe) generally supports this thesis. However, in certain areas, a combined approach—hot water flooding with conformance improvement or profile modification—remains the most viable.

As mentioned above, systems for plugging high-permeability channels and zones require improved stability under specific thermobaric conditions. Additionally, low reservoir pressure is a critical factor in designing chemical solutions injection. Safe reservoir repressuring maps are essential to ensure the effective placement of plugging fluids without triggering uncontrolled hydraulic fracturing.

Permafrost conditions in Arctic regions must also be taken into the account in selecting extraction technology. At the Vostochno-Messoyahskoe field, which has geological and physical characteristics similar to the Russkoye field, pilot tests of hot water flooding and steam injection did not yield the expected technical and economic benefits (incremental ORF of 5–10%) due to significant heat losses to the top and bottom of the reservoir and also for warming the target volume of rock. Steam injection in reservoirs with clay layers caused a deterioration in reservoir properties, steam breakthrough into overlying zones (including the gas cap zone), and condensation. Therefore, chemical flooding technologies are more suitable for such geological and physical conditions.

An unresolved issue remains: sand production during chemical flooding of weakly or unconsolidated sands contains HVO and EHVO. It is well known that in HVO and EHVO fields, the flow of oil is the major sand production force. Addressing mobility contrasts between displacing and displaced fluids is essential, requiring further research to develop guidelines for the safe operation of wells under polymer flooding.

3. For Russian HVO and EHVO fields, thermal methods are most favourable due to the availability of centralised heat production and supply systems or modular heating units in Arctic conditions. Chemical and TP flooding require more complex modular facilities, which increase in number relative to the range of injected fluids (e.g., surfactant, alkaline solution). In addition to solution preparation and injection units, a water treatment system for softening and deoxygenating water is needed. Numerous studies highlight the adverse effects of oxygen and hardness ions on polymer solution properties. From a technical perspective, water management treatments, which can combine effectively with thermal methods, are simpler due to the wide availability of facilities (wellhead reagent batching unit, cementing truck).

4. The implementation of novel technologies, such as foam flooding, presents certain risks due to their limited research. However, these methods have significant potential at the intersection of oil production and the energy sector, improving oil displacement processes while enabling the beneficial utilisation of associated gas or industrial waste

gases. Promising areas of research include the study of foam-assisted displacement of oil and monitoring the compositional changes in produced hydrocarbon.

7. Conclusions

This study has reviewed the main methods and technologies for HVO and EHVO production. One of the main challenges is managing associated water production, which often exceeds economically viable levels under current conditions.

Based on the review, the following conclusions can be drawn:

1. Thermal will remain the predominant method of extraction for most HVO and EHVO fields.
2. For fluids with viscosities below 10,000 mPa·s, chemical flooding is a viable option.
3. Reservoir depth is a critical factor influencing the economic viability of thermal or physicochemical methods.
4. Synergy between thermal and physicochemical methods holds significant potential for conformance improvement and profile modification and requires further research and optimisation in development processes.
5. When combining thermal methods with technology of conformance improvement or profile modification, two strategies for reducing re-treatments are recommended:
    - Using more thermally stable resistant systems (typically more expensive);
    - Substituting reagents partially with industrial waste to adhere to the policy of energy-saving and energy efficiency increase.
6. Thermal polymer flooding may be particularly effective for low-viscosity oils with low paraffin saturation temperatures. In carbonate reservoirs with high-permeability interlayers, this technology has proven advantageous compared to hot- or cold-water flooding and P flooding. Laboratory studies also indicate its potential application in terrigenous reservoirs.
7. In Arctic conditions, factors such as permafrost rocks and energy-logistics infrastructure of the region must be carefully considered when selecting technologies.
8. Unlike chemical flooding, which requires substantial capital investment and complex water and polymer preparation facilities, conformance improvement and profile modification are simpler, more cost-effective, and widely available.

Author Contributions: I.R.: Conceptualization, Methodology, Investigation, Writing—Original Draft, Visualization, Project administration; M.R.: Validation, Writing—Review and Editing, Supervision; J.S.: Formal Analysis, Resources, Data Curation, Writing—Original Draft. All authors have read and agreed to the published version of the manuscript.

Funding: This research received no external funding.

Data Availability Statement: Not applicable.

Conflicts of Interest: Authors declare no conflict of interests.

References

1. Shah, A.; Fishwick, R.; Wood, J.; Leeke, G.; Rigby, S.; Greaves, M. A review of novel techniques for heavy oil and bitumen extraction and upgrading. *Energy Environ. Sci.* **2010**, *3*, 700–714. [CrossRef]
2. Li, Q.; Li, Q.; Wu, J.; Li, X.; Li, H.; Cheng, Y. Wellhead Stability During Development Process of Hydrate Reservoir in the Northern South China Sea: Evolution and Mechanism. *Processes* **2024**, *13*, 40. [CrossRef]
3. Li, Q.; Li, Q.; Cao, H.; Wu, J.; Wang, F.; Wang, Y. The Crack Propagation Behaviour of CO_2 Fracturing Fluid in Unconventional Low Permeability Reservoirs: Factor Analysis and Mechanism Revelation. *Processes* **2025**, *13*, 159. [CrossRef]

4. Altunina, L.K.; Kuvshinov, V.A.; Kuvshinov, I.V.; Stasyeva, L.A.; Chertenkov, M.V.; Shkrabyuk, L.S.; Andreev, D.V. Physical-chemical and complex EOR/IOR technologies for the Permian-Carboniferous deposit of heavy oil of the Usinskoye oil field. *Neft. Khozyaystvo-Oil Ind.* **2017**, *2017*, 26–29. [CrossRef]
5. Antoniadi, D.G.; Garushev, A.R.; Ishkhanov, V.G. *Thermal Recovery Methods Handbook*; Sovetskaya Kuban: Krasnodar, Russia, 2000. (In Russian)
6. Khisamov, R.S.; Gazizov, A.A.; Gazizov, A.S. *Enhanced Oil Recovery Technologies*; OJSC 'VNIIOENG': Moscow, Russia, 2005. (In Russian)
7. Ibatullin, R.R. *Technological Processes of Oil Field Development*; JSC VNIIOENG: Moscow, Russia, 2011.
8. Durkin, S.M.; Menshikova, I.N.; Terentev, A.A.; Ruzin, L.M.; Morozyuk, O.A.; Kalinin, S.A. Substantiation of the differentiated SAGD technology by the numerical simulation for conditions of the Yaregskoye field. *Neft. Khozyaystvo Oil Ind.* **2017**, *2017*, 101–103. [CrossRef]
9. Ruzin, L.M.; Morozyuk, O.A.; Kalinin, S.A.; Scvortsov, A.S.; Durkin, S.M. The study of the filtration mechanism in reservoirs of the Timan-Pechora oil and gas province, based on physical modeling. *Neft. Khozyaystvo-Oil Ind.* **2017**, *2017*, 88–91. [CrossRef]
10. Morozyuk, O.A.; Kochetov, A.V.; Zagorovsky, A.A.; Cherepanova, N.A.; Blinova, T.S.; Isaeva, M.I.; Novosadova, I.V.; Shulga, R.S.; Serkin, M.F. Experimental confirmation of the performance of high-viscosity oil extraction method. *Neft. Khozyaystvo Oil Ind.* **2023**, *2023*, 66–70. [CrossRef]
11. Ali, S.M.F.; Abad, B. Bitumen Recovery From Oil Sands, Using Solvents In Conjunction With Steam. *J. Can. Pet. Technol.* **1976**, *15*, 80–90. [CrossRef]
12. Butler, R.M. *Thermal Recovery of Oil and Bitumen*; GravDrain: Calgary, AB, Canada, 1997.
13. Zhu, D.; Bai, B.; Hou, J. Polymer Gel Systems for Water Management in High-Temperature Petroleum Reservoirs: A Chemical Review. *Energy Fuels* **2017**, *31*, 13063–13087. [CrossRef]
14. Mathews, T.A.; Cortes, J.; Hascakir, B. Evaluation of Environmentally Friendly Green Solvents for the Recovery of Heavy Oils. In Proceedings of the SPE Improved Oil Recovery Conference, Virtual, 25–29 April 2022. [CrossRef]
15. Moe Soe Let, K.P.; Manichand, R.N.; Seright, R.S. Polymer Flooding a ~500-cp Oil. In Proceedings of the SPE Improved Oil Recovery Symposium, Tulsa, OK, USA, 14–18 April 2012. [CrossRef]
16. Seright, R.S.; Chang, H.L.; Zhang, Z.Q.; Wang, Q.M.; Xu, Z.S.; Guo, Z.D.; Sun, H.Q.; Cao, X.L.; Qi, Q. Discussion and Reply to 'Advances in Polymer Flooding and Alkaline/Surfactant/Polymer Processes as Developed and Applied in the People's Republic of China'. *J. Pet. Technol.* **2006**, *58*, 80–81. [CrossRef]
17. Delamaide, E. *Pelican Lake: Learning from the Largest Polymer Flood Expansion in a Heavy Oil Field*; European Association of Geoscientists & Engineers: Utrecht, The Netherlands, 2021. [CrossRef]
18. Thomas, A. Essentials of Polymer Flooding. In *Essentials of Polymer Flooding Technique*; Wiley: Hoboken, NJ, USA, 2019; p. 300.
19. Muskat, M. *Physical Principles of Oil Production*; McGraw-Hill Book Company: New York, NY, USA, 1949.
20. Seright, R.S.; Zhang, G. A Comparison of Polymer Flooding With In-Depth Profile Modification University of North Dakota. In Proceedings of the Canadian Unconventional Resources Conference, Calgary, AB, Canada, 15–17 November 2011. [CrossRef]
21. Petukhov, A.V.; Kuklin, A.I.; Petukhov, A.A.; Vasquez Cardenas, L.C.; Roschin, P.V. Origins and Integrated Exploration of Sweet Spots in Carbonate and Shale Oil-Gas Bearing Reservoirs of the Timan-Pechora Basin. In Proceedings of the Day 2 Wed, Vienna, Austria, 25–27 February 2014. [CrossRef]
22. Zaripov, A.T.; Shaikhutdinov, D.K.; Khafizov, R.I.; Zakharov, Y.V. Analysis of efficiency of heavy oil production technologies in PJSC Tatneft fields. *Neft. Territ.* **2016**, *7*, 42–50. (In Russian)
23. Ilyasov, I.; Gudz, A.; Podkorytov, A.; Komarov, V.; Glushchenko, N. Results of the First Polymer Flooding Pilot at East-Messoyakhskoe Oil Field. In Proceedings of the SPE Russian Petroleum Technology Conference, 26–29 October 2020. [CrossRef]
24. Ilyasov, I.; Glushchenko, N. *Results of the Second Polymer Flooding Pilot at East-Messoyakhskoe Oil Field and Future Plans*; European Association of Geoscientists & Engineers: Utrecht, The Netherlands, 2021; pp. 1–10. [CrossRef]
25. Korobov, G.Y.; Parfenov, D.V.; Nguyen, V.T. Long-term Inhibition of Paraffin Deposits Using Porous Ceramic Proppant Containing Solid Ethylene-vinyl Acetate. *Int. J. Eng.* **2025**, *38*, 1887–1897. [CrossRef]
26. Korobov, G.Y.; Vorontsov, A.A.; Buslaev, G.V.; Nguyen, V.T. Analysis of Nucleation Time of Gas Hydrates in Presence of Paraffin During Mechanized Oil Production. *Int. J. Eng.* **2024**, *37*, 1343–1356. [CrossRef]
27. Bogomolsky, E.I. *Intensification of Production of Highly Viscous Paraffinic Oils from Carbonate Reservoirs of Udmurtia Deposits*; Institute of Computer Research: Moscow, Russia, 2003. (In Russian)
28. Sun, X.; Xu, B.; Qian, G.; Li, B. The application of geomechanical SAGD dilation startup in a Xinjiang oil field heavy-oil reservoir. *J. Pet. Sci. Eng.* **2021**, *196*, 107670. [CrossRef]
29. Duerksen, J.H.; Cruikshank, G.W.; Wasserman, M.L. Performance and Simulation of a Cold Lake Tar Sand Steam-Injection Pilot. *J. Pet. Technol.* **1984**, *36*, 1781–1790. [CrossRef]
30. Guo, K.; Li, H.; Yu, Z. In-situ heavy and extra-heavy oil recovery: A review. *Fuel* **2022**, *185*, 886–902. [CrossRef]

31. Sharma, J.; Dean, J.; Aljaberi, F.; Altememee, N. In-situ combustion in Bellevue field in Louisiana – History, current state and future strategies. *Fuel* **2021**, *284*, 118992. [CrossRef]
32. Ado, M.R. Improving oil recovery rates in THAI in situ combustion process using pure oxygen. *Upstream Oil Gas Technol.* **2021**, *6*, 100032. [CrossRef]
33. Ado, M.R. Comparisons of predictive ability of THAI in situ combustion process models with pre-defined fuel against that having fuel deposited based on Arrhenius kinetics parameters. *J. Pet. Sci. Eng.* **2021**, *208*, 109716. [CrossRef]
34. Altunina, L.K.; Kuvshinov, V.A. Physicochemical methods for enhancing oil recovery from oil fields. *Russ. Chem. Rev.* **2007**, *76*, 971–987. [CrossRef]
35. Delamaide, E.; Zaitoun, A.; Renard, G.; Tabary, R. Pelican Lake Field: First Successful Application of Polymer Flooding in a Heavy Oil Reservoir. In Proceedings of the All Days, Kuala Lumpur, Malaysia, 2–4 July 2013. [CrossRef]
36. Sun, C.; Guo, H.; Li, Y.; Song, K. Recent Advances of Surfactant-Polymer (SP) Flooding Enhanced Oil Recovery Field Tests in China. *Geofluids* **2020**, *2020*, 8286706. [CrossRef]
37. Watson, A.; Trahan, G.A.; Sorensen, W. An Interim Case Study of an Alkaline-Surfactant-Polymer Flood in the Mooney Field, Alberta, Canada. In Proceedings of the SPE Improved Oil Recovery Symposium, Tulsa, OK, USA, 12–16 April 2014. [CrossRef]
38. Hashemi, S.J.; Hormozi, F.; Mokhtari, R. Controlling the gelation time of sodium silicate gelants for fluid management in hydrocarbon reservoirs. *Fuel* **2023**, *341*, 127645. [CrossRef]
39. Islamov, S.R.; Bondarenko, A.V.; Gabibov, A.F.; Mardashov, D.V. Polymer compositions for well killing operation in fractured reservoirs. In *Advances in Raw Material Industries for Sustainable Development Goals*; CRC Press: London, UK, 2020; pp. 343–351. [CrossRef]
40. Dvoynikov, M.; Sidorov, D.; Kambulov, E.; Rose, F.; Ahiyarov, R. Salt Deposits and Brine Blowout: Development of a Cross-Linking Composition for Blocking Formations and Methodology for Its Testing. *Energies* **2022**, *15*, 7415. [CrossRef]
41. Wang, B.; Lin, M.; Guo, J.; Wang, D.; Xu, F.; Li, M. Plugging properties and profile control effects of crosslinked polyacrylamide microspheres. *J. Appl. Polym. Sci.* **2016**, *133*, 43666. [CrossRef]
42. Smirnova, E.A.; Saychenko, L.A. Hydrodynamic Modeling and Evaluation of Partial Substitution of Cushion Gas During Creation of Temporary Underground Gas Storage in an Aquifer. *Int. J. Eng.* **2024**, *37*, 1221–1230. [CrossRef]
43. Blinov, P.A.; Salakhov, K.N.; Nikishin, V.V.; Kuchin, V.N. Development of Cement Slurry Composition with Self-healing Properties. *Int. J. Eng.* **2025**, *38*, 236–246. [CrossRef]
44. Ketova, Y.; Bai, B.; Khizhnyak, G.; Gladkikh, Y.; Galkin, S. Testing of preformed particles polymer gel technology on core filtration models to limit water inflows. *J. Min. Inst.* **2020**, *241*, 91–96. [CrossRef]
45. Bai, B.; Zhou, J.; Yin, M. A comprehensive review of polyacrylamide polymer gels for conformance control. *Pet. Explor. Dev.* **2015**, *42*, 525–532. [CrossRef]
46. Barabanov, V.L.; Dem'yanovsky, V.B.; Kaushansky, D.A.A. The study of rheological heterogeneity of the liquid systems in the instance of the water-swollen dispersed gels of polyacrylamide. *Actual Probl. Oil Gas* **2016**, *1*, 13. [CrossRef]
47. Salunkhe, B.; Schuman, T.; Al Brahim, A.; Bai, B. Ultra-high temperature resistant preformed particle gels for enhanced oil recovery. *Chem. Eng. J.* **2021**, *426*, 130712. [CrossRef]
48. Skauge, T.; Hetland, S.; Spildo, K.; Skauge, A. Nano-Sized Particles for EOR. In Proceedings of the All Days, Tulsa, OK, USA, 24–28 April 2010. [CrossRef]
49. Fakhretdinov, R.N.; Yakimenko, G.K.; Selimov, D.F. Polymer Composition for Controlling Development of Oil and Gas Fields. RU 2639339 C, 21 December 2017.
50. Jin, J.; Wang, Y.; Wei, M.; Ma, H.; Wang, K. Coreflooding and Pore-Scale Visualization of Foamed Gel Flowed in Porous Network Media. *J. Dispers. Sci. Technol.* **2016**, *37*, 1436–1443. [CrossRef]
51. Lai, N.; Yuan, L.; Li, W.; Xiong, W.; Yu, G.; Du, Z.; Song, Z.; Wen, Y. Research on the Properties of Natural Gas Foamed Gel as a Profile Control and an Oil Displacement Agent in Strong Heterogeneous Reservoirs. *Energy Fuels* **2021**, *35*, 7738–7755. [CrossRef]
52. Savenok, O.V.; Chuikova, E.P.; Agaguena, A. Justification of Waterless Hydraulic Fracturing Methods. *Int. J. Eng.* **2025**, *38*, 1462–1475. [CrossRef]
53. Mardashov, D.V.; Limanov, M.N.; Onegov, N.A.; Shamsutdinova, G.T.; Fiterman, S.I. Influence of Clay Content in Reservoir Rocks on Efficiency of Killing Production Wells. *Int. J. Eng.* **2025**, *38*, 78–85. [CrossRef]
54. Koning, E.J.L.; Mentzer, E.; Heemskerk, J. Evaluation of a Pilot Polymer Flood in the Marmul Field, Oman. In Proceedings of the SPE Annual Technical Conference and Exhibition, Houston, TX, USA, 2–5 October 1988. [CrossRef]
55. Podoprigora, D.G.; Byazrov, R.R.; Lagutina, M.A.; Arabov, D.V.; Galimov, V.V.; Ermolin, D.S. A novel integrated methodology for screening, assessment and ranking of promising oilfields for polymer floods. *Adv. Geo-Energy Res.* **2024**, *12*, 8–21. [CrossRef]
56. Ameli, F.; Moghadam, S.; Shahmarvand, S. Polymer flooding. In *Chemical Methods*; Elsevier: Amsterdam, The Netherlands, 2022; pp. 33–94. [CrossRef]
57. Saleh, L.D.; Wei, M.; Bai, B. Data Analysis and Updated Screening Criteria for Polymer Flooding Based on Oilfield Data. *SPE Reserv. Eval. Eng.* **2014**, *17*, 15–25. [CrossRef]

58. Delamaide, E. Investigation on the Impact of Voidage Replacement Ratio and Other Parameters on the Performances of Polymer Flood in Heavy Oil Based on Field Data. In Proceedings of the SPE Latin America and Caribbean Petroleum Engineering Conference, Buenos Aires, Argentina, 17–19 May 2017. [CrossRef]
59. Guo, H.; Zitha, P.L.J.; Faber, R.; Buijse, M. A Novel Alkaline/Surfactant/Foam Enhanced Oil Recovery Process. *SPE J.* **2012**, *17*, 1186–1195. [CrossRef]
60. Skauge, A.; Stensen, J.A. A Review of wag field experience. In Proceedings of the 1st International Conference and Exhibition Modern Challenges in Oil Recovery, Gubkin University, Moscow, Russia, 19–23 May 2003; p. 11.
61. Farajzadeh, R.; Andrianov, A.; Krastev, R.; Hirasaki, G.J.; Rossen, W.R. Foam–oil interaction in porous media: Implications for foam assisted enhanced oil recovery. *Adv. Colloid Interface Sci.* **2012**, *183–184*, 1–13. [CrossRef] [PubMed]
62. Kumar, P.; Raj, R.; Koduru, N.; Kumar, S.; Pandey, A. Field Implementation of Mangala Polymer Flood: Initial Challenges, Mitigation and Management. In Proceedings of the SPE EOR Conference at Oil and Gas West Asia, Muscat, Oman, 21–23 March 2016. [CrossRef]
63. Shakhmelikyan, M.G.; Matveeva, I.S. The analysis of efficiency of technology of thermo-polymer impact on the layer in fields with high-typed oils on the example of the Mishkinskoye oil field. *Bull. Stud. Sci. Dep. Inf. Syst. Program.* **2018**, *1*, 25. Available online: https://s.esrae.ru/vsn/pdf/2018/01/19.pdf (accessed on 12 March 2025). (In Russian)
64. Borhovich, S.; Kolmogorova, D.; Vasiljeva, A.; Yatskovskaya, A. Termopolymeric techniques of development of complex structure fields with viscous and high-viscosity oil in carbon-bearing reservoirs. *Perm J. Pet. Min. Eng.* **2012**, *11*, 95–104. (In Russian)
65. Gupta, S.C.; Gittins, S.D. Christina Lake Solvent Aided Process Pilot. *J. Can. Pet. Technol.* **2006**, *45*, 15–25. [CrossRef]
66. Yuan, C.; Varfolomeev, M.A.; Kok, M.V.; Nurgaliev, D.K.; Gabbasov, A.H. Applications of Enhanced Oil Recovery Techniques of Heavy Crudes. In *Catalytic In-Situ Upgrading of Heavy and Extra-Heavy Crude Oils*; Wiley: Hoboken, NJ, USA, 2023; pp. 153–167. [CrossRef]
67. Mukhamatdinov, I.I.; Ali, M.O.N.; Mukhamatdinova, R.E.; Affane, B.; Vakhin, A.V.; Tsvetkov, S.V.; Malaniy, S.Y.; Protsenko, A.N. Optimization of thermal steam treatment technology applied to Strelovskoye field using aquathermolysis catalysts. *Fuel* **2024**, *359*, 130389. [CrossRef]
68. Usmanov, S.A.; Usmanov, S.A.; Minkhanov, I.F.; Simakov, Y.O.; Vakhin, A.V.; Sudakov, V.A.; Varfolomeev, M.A.; Nurgaliev, D.K. Efficiency estimation of super-viscous oil recovery by in-situ catalytic upgrading in cyclic steam stimulation: From laboratory screening to numerical simulation. *Georesursy* **2023**, *25*, 106–114. [CrossRef]
69. Pu, W.; Shen, C.; Wei, B.; Yang, Y.; Li, Y. A comprehensive review of polysaccharide biopolymers for enhanced oil recovery (EOR) from flask to field. *J. Ind. Eng. Chem.* **2018**, *61*, 1–11. [CrossRef]
70. Sorbie, K.S. *Polymer-Improved Oil Recovery*; Springer Netherlands: Dordrecht, The Netherlands, 1991; ISBN 978-94-010-5354-9. [CrossRef]
71. Navarrete, R.C.; Seheult, J.M.; Coffey, M.D. New Bio-Polymers for Drilling, Drill-in, Completions, Spacer Fluids and Coiled Tubing Applications. In Proceedings of the IADC/SPE Asia Pacific Drilling Technology, Kuala Lumpur, Malaysia, 11–13 September 2000. [CrossRef]
72. Pashkevich, M.A.; Petrova, T.A.; Rudzisha, E. Lignin Sludge Application for Forest Land Reclamation: Feasibility Assessment. *J. Min. Inst.* **2019**, *235*, 106–112. [CrossRef]
73. Gräfe, M.; Power, G.; Klauber, C. Bauxite residue issues: III. Alkalinity and associated chemistry. *Hydrometallurgy* **2011**, *108*, 60–79. [CrossRef]
74. Zinoveev, D.V.; Grudinskii, P.I.; Dyubanov, V.G.; Kovalenko, L.V.; Leont'ev, L.I. Global recycling experience of red mud—A review. Part i: Pyrometallurgical methods. *Izv. Ferr. Metall.* **2018**, *61*, 843–858. [CrossRef]
75. Gornov, D.; Osokin, A.; Pchela, K.V.; Gilaev, G.G. On the Possibility to Reduce the Need in Reagents When Injecting Heated Water and Thickened Polyacrylamide Aqueous Solutions in High-Viscous Oil Fields. *Neft. Gas. Novacii* **2024**, *6*, 34–42. Available online: https://neft-gaz-novacii.ru/ru/archive/82-2017/2344 (accessed on 12 March 2025).
76. Bondarenko, A.A.; Rogachev, M.K.; Sharifov, A.R.; Mardashov, D.V. Increasing Efficiency of Solvent Assisted Cyclic Steam Stimulation of the Bottomhole Formation Zone of a Carbonate Reservoir using Aquathermolysis Catalysts. *Int. J. Eng.* **2025**, *38*, 758–766. [CrossRef]
77. Al-Muayri, M.T. Experimental Investigation of Expanding Solvent Steam Assisted Gravity Drainage Using Multicomponent Solvents. Ph.D. Thesis, University of Calgary, Calgary, AB, Canada, 2012.
78. Brown, A.R.; Hart, A.; Coker, V.S.; Lloyd, J.R.; Wood, J. Upgrading of heavy oil by dispersed biogenic magnetite catalysts. *Fuel* **2016**, *185*, 442–448. [CrossRef]
79. Angeles, M.J.; Leyva, C.; Ancheyta, J.; Ramírez, S. A review of experimental procedures for heavy oil hydrocracking with dispersed catalyst. *Catal. Today* **2014**, *220–222*, 274–294. [CrossRef]
80. Ajumobi, O.O.; Muraza, O.; Kondoh, H.; Hasegawa, N.; Nakasaka, Y.; Yoshikawa, T.; Al Amer, A.M.; Masuda, T. Upgrading oil sand bitumen under superheated steam over ceria-based nanocomposite catalysts. *Appl. Energy* **2018**, *218*, 1–9. [CrossRef]

81. Ilyushin, Y.V.; Nosova, V.A. Development of Mathematical Model for Forecasting the Production Rate. *Int. J. Eng.* **2025**, *38*, 1749–1757. [CrossRef]
82. Ilyushin, Y.; Nosova, V.; Krauze, A. Application of Systems Analysis Methods to Construct a Virtual Model of the Field. *Energies* **2025**, *18*, 1012. [CrossRef]
83. Kostina, A.; Zhelnin, M.; Plekhov, O. Numerical analysis of a caprock integrity during oil production by steam-assisted gravity drainage method. *Frat. Ed Integrità Strutt.* **2019**, *13*, 302–313. [CrossRef]
84. Lebedev, V.; Deev, A.; Deev, K. Method for Calculating Heat Transfer in a Heat Accumulator Using a Phase Change Material with Intensification Due to Longitudinal Fins. *Energies* **2024**, *17*, 5281. [CrossRef]
85. Litvinenko, V.; Petrov, E.; Vasilevskaya, D.; Yakovenko, A.; Naumov, I.; Ratnikov, M. Assessment of the role of the state in the management of mineral resources. *J. Min. Inst.* **2022**, *259*, 95–111. [CrossRef]

energies

MDPI

Review

Recent Developments in the CO_2-Cyclic Solvent Injection Process to Improve Oil Recovery from Poorly Cemented Heavy Oil Reservoirs: The Case of Canadian Reservoirs

Daniel Cartagena-Pérez, Alireza Rangriz Shokri * and Rick Chalaturnyk

Department of Civil and Environmental Engineering, University of Alberta, Edmonton, AB T6G 1H9, Canada; dfcartagenap@ualberta.ca (D.C.-P.); rjchalaturnyk@ualberta.ca (R.C.)
* Correspondence: alireza.rangrizshokri@ualberta.ca

Abstract: One of the limitations of Cold Heavy Oil Production with Sand (CHOPS) is the low recovery factor (5–15%). To target the remaining 85–95% heavy oil resources, several enhanced oil recovery (EOR) techniques, such as cyclic solvent injection (CSI), have been proposed. Due to its potential success in Canada and elsewhere, this paper reviews the technical and efficiency requirements of CSI EOR in post-CHOPS heavy oil reservoirs. We explain the dominant driving mechanisms of CSI with a focus on the application of CO_2 as a solvent. Limitations of current thermal and non-thermal EOR methods were compared to the CSI in thin oil reservoirs. To complete the assessment, several case studies and lessons learned were included based on the latest laboratory experiments, numerical studies, and CSI pilot/field tests. Specific to thin and shallow heavy oil reservoirs with sand production (e.g., CHOPS), the key to recover incremental oil was found to re-energize depleted reservoirs in a cyclic manner with unexpensive solvents (e.g., CO_2). Regarding the solvent use, laboratory experiences have not been conclusive about what solvent stream could improve oil recovery. To this end, successful field scale CO_2 EOR applications have been reported in several post-CHOPS reservoirs indicating that highly productive wells during primary production might also outperform during a follow up CSI process. Numerical modeling still faces challenges to properly model the main CSI driving mechanisms, including fluid–solvent interaction and the deformation of subsurface reservoirs.

Keywords: cyclic solvent injection; cold production; heavy oil reservoirs; CO_2 injection; unconsolidated sandstones; CHOPS

1. Introduction

Heavy oil resources continue to show a significant demand in the global energy market. Despite a decline in energy consumption due to the COVID-19 pandemic, fossil fuels (i.e., oil and gas) remain dominant players, accounting for 55.9% of the global primary energy market [1]. Heavy oil production is still essential for some countries, such as Canada. The Canada Energy Regulator [2] reported that heavy oil exports have played a major role in Canada's export participation. In 2020, the total volume of heavy oil export was estimated at 2.81 million barrels per day, with 90% of Canada's heavy oil originating from Alberta's heavy oil reservoirs, which amounted to 2.53 million barrels per day.

The Lloydminster area, which straddles Alberta and Saskatchewan, represents a key area in the energy framework of Canada [3]. The western region of Canada is estimated to contain a total of 5201 million m^3 of heavy oil resources. Given the abundance of

such resources and the unceasing energy demand, it is imperative to employ innovative techniques to recover these resources from the subsurface. Notably, approximately 80% of heavy oil reservoirs in Western Canada are less than 5 m thick [4]. For instance, in the Lloydminster area, around 95% of the oil reserves are found within sands with a maximum thickness of 10 m, highlighting the significant proportion of oil located in thin and medium-thick reservoirs (Figure 1).

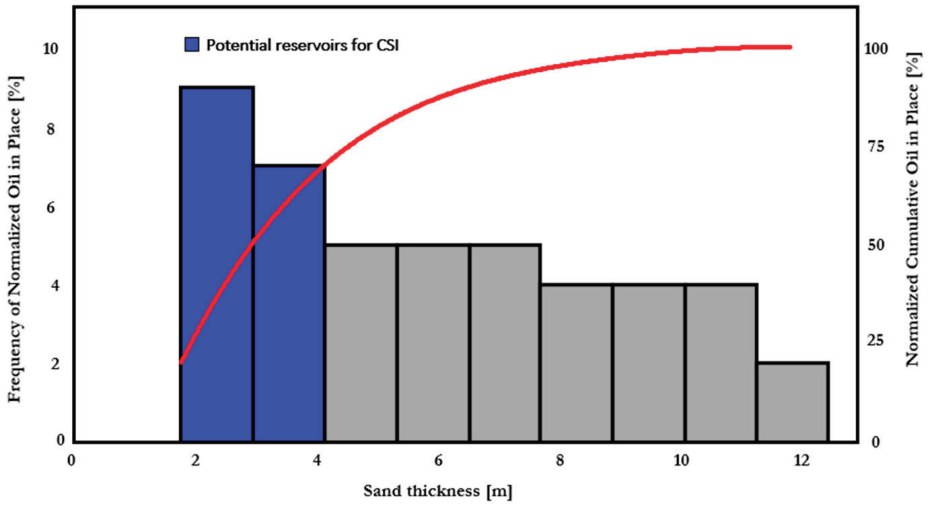

Figure 1. Estimated distribution of oil in place vs. sand thickness in the Lloydminster area. The bars represent the frequency of normalized oil in place: blue bars indicate potential reservoirs suitable for CSI application, while grey bars represent reservoirs that are not suitable for CSI. The red line depicts the normalized cumulative oil in place; data from [5].

According to Dusseault [6], a typical Canadian heavy oil reservoir is composed of quarzose sand zones with porosities ranging from 28% to 32%, an average connate water saturation of 25%, and permeabilities between 1 to 4 Darcies. The viscosities of heavy oil in such reservoirs vary from 500 to 50,000 cp, while the oil API gravity ranges from 10° to 16° [3]. Despite the high permeability of these unconsolidated reservoirs, the oil properties pose significant challenges for fluid production. A summary of the typical properties of Canadian CHOPS reservoirs is provided by [7,8] in Table 1.

Table 1. Typical properties of Canadian CHOPS reservoirs; modified after [7,8].

Property	**Value**
Depth (m)	480
Net pay (m)	5
Porosity (%)	33
Permeability (Darcies)	2 to 4
Oil saturation (%)	80
Initial reservoir pressure (kPa)	2750
Reservoir temperature (°C)	20
Dead-oil viscosity (cp)	25,000
Formation compressibility (kPa^{-1})	5×10^{-6}
Wormhole radius (m)	0.05

The significance of this work lies in providing a review of the key mechanisms underlying the CSI technique for post-CHOPS heavy oil reservoirs in Canada, along with field cases that offer a comprehensive understanding of the challenges involved in implementing CSI as an enhanced recovery method.

2. Recovery Techniques in Thin Unconsolidated Heavy Oil Reservoirs

Due to its high viscosity, production from heavy oil reservoirs requires additional driving mechanisms than only fluid expansion with pressure drawdown. The theoretical relationship between viscosity and flow velocity is established by the Darcy law:

$$v = -\frac{k(\varphi)}{\mu(T, m_s)}\frac{dP}{dx} \quad (1)$$

where v is the Darcy velocity, $k(\varphi)$ is the permeability of the porous media as a function of the porosity, $\mu(T, m_s)$ is the fluid viscosity as a function of temperature and solvent mass, and dP/dx is the pressure gradient. From (1), $v \propto \mu^{-1}$, which means that higher viscosity is detrimental to fluid flow. Here, fluid viscosity is basically defined as the fluid resistance to flow. A decrease in oil viscosity, an enhancement in formation permeability, or an increase in viscous forces and pressure gradient can be achieved through fluid and sand production, fluid injection, such as waterflooding, steam assisted gravity drainage, polymer flooding, in situ combustion, and solvent-based recovery techniques (e.g., VAPEX—vapor extraction), among others.

2.1. Cold Production with Sand

CHOPS (Cold Heavy Oil Production with Sand) is a primary heavy oil recovery technique that involves deliberate initiation and continuous sand production to significantly increase the permeability of the target formation. In this technique, the low rock consolidation (very common in heavy oil reservoirs with unconsolidated/poorly cemented sandstones and friction angle of 15°) is used to detach the grain from the formation matrix by the action of viscous forces and effective stresses to increase oil production [6]. Some authors have noted that the sole action of viscous forces is not sufficiently large to detach the sand grains [9].

Compared to other recovery techniques, CHOPS is a relatively low-cost technology because it does not require any fluid injection (increase in heat, pressure, or add diluents). Most authors agree that CHOPS can achieve a recovery factor of 5% to 15% by the end of its primary production lifetime [10–12]. Field experience in the Lloydminster area also suggests an average recovery of 8% of the original oil in place for CHOPS reservoirs [3]. This provides potential to recover the remaining 90% of oil in place through follow up enhanced oil recovery techniques, such as CO_2 injection. However, the design of a successful CO_2 injection process to re-energize CHOPS reservoirs requires an understating of fluid flow and geomechanical issues that govern the behavior of deformable heavy oil reservoirs.

Table 2 summarizes the main recovery mechanisms in thin unconsolidated heavy oil formations; some of the major recovery mechanisms will be further described in the next section.

Foamy Oil Behavior. Due to high oil viscosity (order of 10,000–25,000 cp), the formation of dispersed gas bubbles is one of the main flow characteristics and drive forces in CHOPS [6,8]. Foamy oil drive mechanism has been extensively studied in the literature [13–17]. Figure 2 illustrates a sequence of images from a fluid depletion experiment in which a 2D view of the heavy oil sample, saturated with gas, was subject to fluid depletion at a rate of 300 kPa/min from 1200 kPa to 100 kPa. Figure 2 visualizes the non-equilibrium nature of the foamy oil drive; the released gas bubbles initially do

not form a single gas phase and remain dispersed in the oil which causes significant fluid expansion; comparison of the total fluid column with respect to the initial oil level, depicted by the dashed lines.

Table 2. Production mechanisms of CHOPS adapted from [6].

Primary Driver Category	Consequence
Gravity	Causes vertical stress from overlying rocks and impacts rock yielding and dilation
Pressure drop	Viscous force drives fluids to production well
Foamy oil	Enhances production via gas nucleation and fluid expansion dynamics
Sand production	Increases reservoir permeability and boosts extraction efficiency
Wellbore damage	Maintains flow by clearing obstructive deposits (e.g., asphaltenes, fine-grained particles, or mineral deposits).

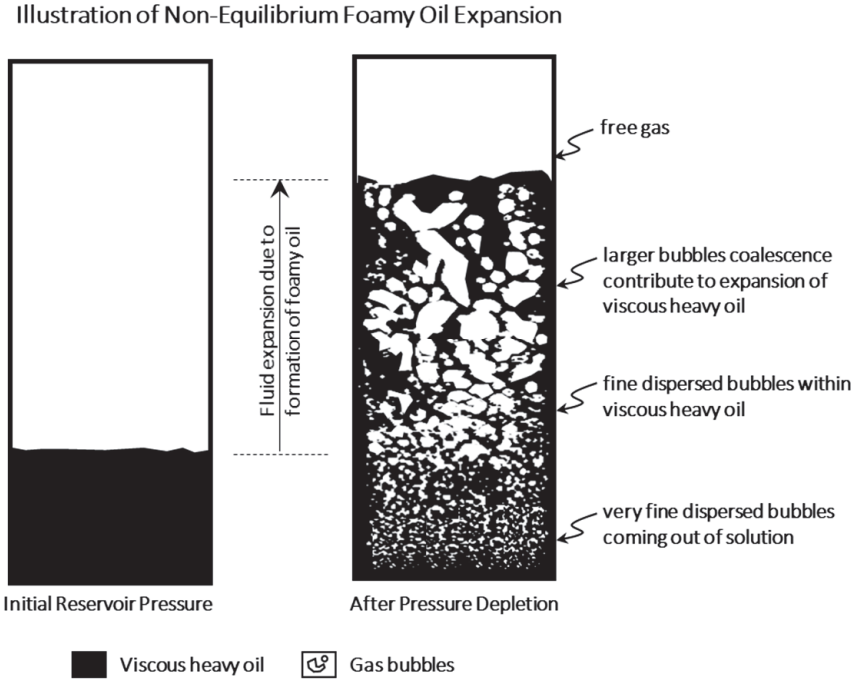

Figure 2. Illustration of non-equilibrium foamy oil expansion, adapted from [18].

Wang et al. [18] described the evolution of the foamy oil in three main stages: (i) expansion, (ii) peaking, and (iii) decay. Basically, the bubbles within the foamy oil expand during depletion and push the oil out of the reservoir. Some authors noted the dependency of foamy oil to the magnitude of the pressure depletion rate (e.g., [19]). The strength of foamy oil behavior and depletion rate in heavy oil has a direct impact on the established pore pressure during the fluid production phase. It is also worth mentioning that a lower pressure drop could lead to a more lasting foamy oil peak and declining phases.

Figure 3 shows a visual microscale confirmation of fluid flow through porous media due to the foamy oil driving mechanism [20].

Formation of High Permeability Channels. Wormhole, in the context of heavy oil and sand production, refers to a zone in which there is no grain-to-grain contact [6]; that lack of contact between grains translates into high porosity and permeability channels [21]. The formation of high permeability channels (i.e., wormhole network) has a few advantages [22].

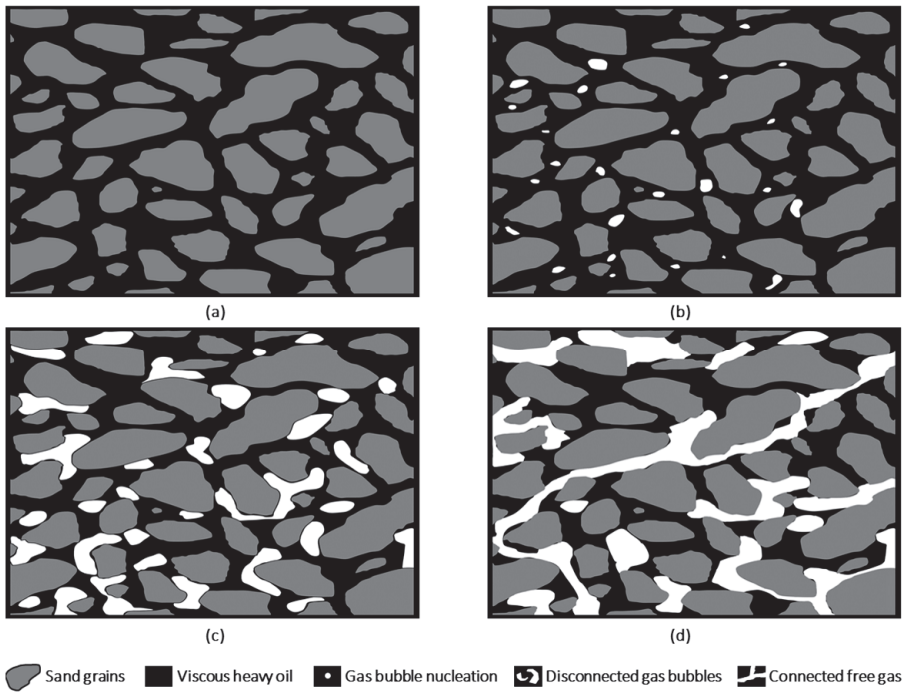

Figure 3. Illustration of foamy oil expansion within porous medium due to pressure drop, (**a**) single oil phase flow at initial reservoir pressure, (**b**) nucleation of gas bubbles, (**c**) formation of disconnected gas bubbles, and (**d**) free gas phase flow due to pressure drops. Adapted from [15,20].

First, since wormholes have a higher permeability, it is a preferential route for the fluid flow from the inner reservoir to reach the wellbore. If this feature is described in terms of pressure, the wormhole network can be understood as isobaric lines within the reservoir [8]. This means that the high permeability of the wormhole network creates the condition in which fluid can flow at low pressures. Figure 4 shows the inclusion of wormholes using different modeling techniques, including dual porosity models and multi-lateral wells. Pressure distribution during the depletion of a reservoir, affected by the presence of wormholes (represented through numerical multi-lateral wells) could be observed by well testing [23–25].

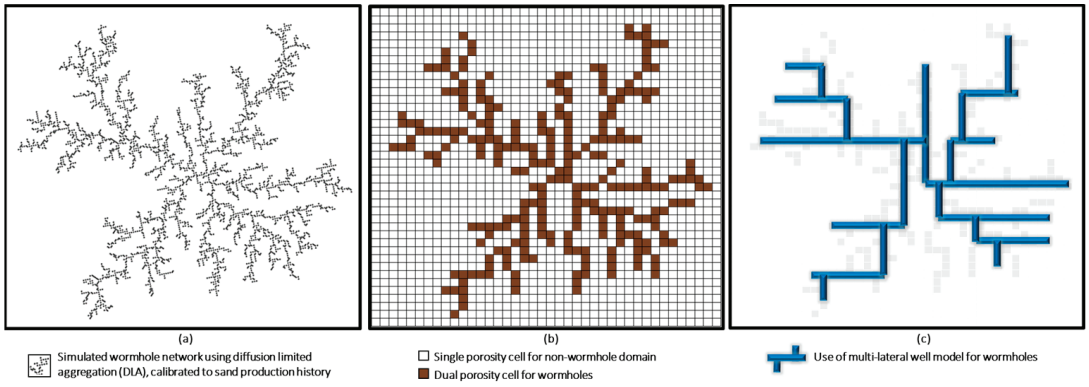

Figure 4. (**a**) Simulated wormhole network developed using diffusion limited aggregation, calibrated to sand production history, and the inclusion of the wormholes (**b**) using the partial dual porosity model, similar to [26], and (**c**), using a multi-lateral well model, similar to [8].

Second, the wormhole network enhances the productivity and injectivity qualities of the reservoir; in the context of fluid injection processes, such as CSI, the injection performance is strongly improved. Additionally, the creation of high-permeability channels

increases the fluid access and contact area of the injected fluid within the reservoir compared to the case when a fluid is injected into an intact reservoir.

In the context of petroleum geomechanics, the growth of the wormhole network is governed by the yielding of the sandstone [6,27]. Due to the loss of confining stress as a result of the non-grain contact state in the cavity zone, the radial stress σ_r decreases while the tangential stress σ_θ increases. The research in [6,22] showed a stress state diagram as a function of the radial distance into a reservoir with a cavity. The shear stress increases because the difference between the radial and tangential stresses is higher until the yielding is reached. Experimental studies have shown that under an anisotropic stress state, the wormholes tend to grow in the direction of the lower horizontal stress [28].

Those geomechanical phenomena result in an increase in porosity due to the removal of mass (i.e., sand grains) in a constant bulk volume. Table 3 shows the porosity estimations based on data and reported measurements in the literature.

Table 3. Experimental observation of an increase in porosity due to sand production.

No.	Reference	Initial Porosity [%]	Final Porosity [%]
1	[29]—Sandstone low density	36.31	85.61
2	[29]—Max. density of 1860 kg/m^3	36.31	79.86
3	[29]—Experiment 2, Low density sandstone density	31.03	71.85
4	[29]—Experiment 2, max density of 1860 kg/m^3	31.03	70.65
5	[29]—Experiment 3, max density of 1860 kg/m^3	31.03	85.47
6	[29]—Experiment 3, max density of 1860 kg/m^3	31.03	83.86
7	[30]—Silica well sorted	41.08	57.30
8	[30]—Silica poorly sorted	32.2	41.65
9	[30]—Silica well sorted 2	40.82	53.87
10	[30]—Silica no fine fraction	38.4	48.6
11	[30]—Husky field	38.2	62
12	[31] *	20.56	60
13	[32]	21.80	52.99
14	[33]	37	46
15	[34] *	32	60
15	[34] *	32	60
16	[21] $^{\xi,}$	32	52
	Mean	33.18	63.23
	Standard Deviation	5.69	14.01

* Used for numerical modeling; $^{\xi,}$ results obtained from history matching.

A look at the CHOPS literature suggests an average initial porosity of 38.13% (standard deviation of 3.5%) for different sandstones. The final porosity has an average of 51.67% (a standard deviation of 9.2%). Similarly, some authors have noted an increase in the formation permeability due to sand production from 3 to 67 Darcies [30,35].

2.2. Waterflooding in Heavy Oil Reservoirs

Although the most common practice for heavy oil and bitumen recovery are the thermal techniques [4], the costs associated with steam generation, greenhouse gas emission, and upgrading facilities may affect the viability of thermal EOR projects. This makes viscosified waterflooding an alternative for some heavy oil reservoirs [36]. In the waterflooding process, the viscosity difference between the injected water and in situ oil often creates adverse mobility ratios with a negative impact on the oil recovery factor and sweep efficiency [36]. The mobility ratio can be described as follows:

$$M = \frac{\lambda_{displacing\ phase}}{\lambda_{displaced\ phase}} = \frac{k_{rw}}{k_{ro}} \frac{\mu_o}{\mu_w} \quad (2)$$

where M is the mobility ratio, λ is the mobility of the phase, $k_{rw,o}$ are the relative permeabilities of water or oil, and $\mu_{w,o}$ is the viscosity of water or oil. From Equation (2), it is apparent that if $\mu_o \gg \mu_w$ then $M \gg 1$, a condition that leads to fingering where fully water-saturated channels connect the injection and production wells [37], bypassing oil in the pore space, and ultimately leading to poor oil recovery; a further phenomenal explanation can be found in the work of [38]. Ref. [36] developed an experiment to show that an early breakthrough due to fingering can be experienced in heavy oil reservoirs.

2.3. Thermal EOR in Heavy Oil Reservoirs

The most applicable thermal EOR technique for heavy oil in Canada is steam-assisted gravity drainage (SAGD). SAGD involves the use of a pair of parallel horizontal wells for the injection of steam into the reservoir. This is intended to reduce the heavy oil viscosity by heating the oil using the latent heat of steam in the reservoir. A reduction in oil viscosity is the main reason behind all variations in thermal EOR methods, such as steam flooding, and cyclic steam stimulation (CSS). Figure 5 is a based on [4], who conducted numerical simulations to compare the efficiency of various thermal EOR techniques; they compared the thermal EOR results with cold production without sand in thin reservoirs (<10 m).

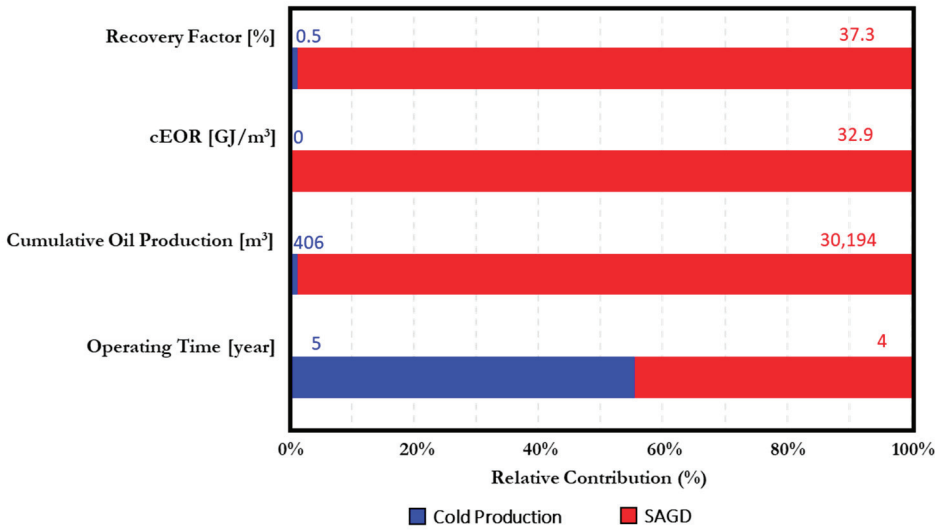

Figure 5. Performance of SAGD vs. cold production recovery techniques in thin reservoirs; data from [4].

The simulation results revealed an adverse cumulative energy–oil ratio (cEOR), which is a measure of energy input required to produce a unit volume of oil. An economically reasonable cEOR is typically around 10 GJ/m^3, corresponding to a cumulative steam–oil ratio (cSOR) of 4 m^3/m^3 [4]. The simulations showed that a high cEOR (three times larger than typical values) can be attributed to high heat loss to underburden and overburden formations in thin formations (less than 10 m thick). In a 10 m thick reservoir, heat loss was calculated to be 10%, while in a thinner reservoir of 4 m, the heat loss increased by 40%.

Considering the limitations of waterflooding and thermal techniques in thin unconsolidated heavy oil formations, the implementation of follow up recovery methods, such as Cyclic Solvent Injection (CSI), has been proposed to improve the recovery from heavy oil reservoirs. It is worth mentioning that some authors have studied the in situ upgrading of heavy crude oil using catalysts as a potential technology [39].

3. Cyclic Solvent Injection Process

The cyclic solvent injection process is intended to target the large amounts of oil remaining in the reservoir through solvent diffusion. The CSI technique is applied when

either the reservoir is too thin (<10 m) for thermal EOR methods, or heavy oil is too viscous to cause an adverse mobility ratio during the flooding process. Specific to CHOPS reservoirs, solvent access to the reservoir can be through high permeability channels and taking advantage of its high contact area with the reservoir [40]. The CSI technique can also be thought of as an in situ upgrading technology because it changes the composition and properties of the heavy oil at reservoir conditions [41]. The CSI involves alternating between solvent injection, soaking, and oil production phases, using a variety of solvents, such as CH_4, CO_2, alkali metal silicide, among others [42].

During the injection phase, the wellbore is used to inject the solvent or a mixture of solvents into the heavy oil reservoir. This phase results in an increase in the pore pressure around the wellbore and a reduction in the effective stress as an immediate consequence. In field practice, the injection is applied until the initial pressure of the reservoir is reached; but in some instances, the injection can go beyond the initial reservoir pressure [5].

The injection phase is followed up by a soaking period in which the wellbore is shut in. The soaking phase is a critical step to dissipate the pore pressure and to allow the slow process of solvent diffusion to occur within the heavy oil reservoir. Solvent diffusion can permanently reduce the oil viscosity. In Table 4, viscosity on Lloydminster's oil varies from 7600 mPa at 20 °C to 2000 mPa due to the application of propane as a diluent (i.e., a viscosity reduction of 74%). A similar response is observed on Athabasca where bitumen's viscosity changes from 700,000 mPa·s at 20 °C to 80–100,000 mPa·s after the application of toluene.

Table 4. Oil properties and their change after solvent treatment. Modified after [41].

Oil/Reservoir	Viscosity [mPa·s] (Temperature)	Solvent	Viscosity After Dissolution [mPa·s]
Lloydminster	7600 (20°)	Propane	2000
Athabasca	148 (104°)	Propane	8.6
Cold lake	70,000 (20°)	Ethane	80
Athabasca bitumen	700,000(20)	Toluene	2000
Frog lake	18,600 (21.6 °C)	Butane	8
Du84, Liaohe	400,000 (60 °C)	Toluene	291.8
Gao3624, Liaohe	600 (50°)	CO_2	150
Fengcheng, Xinjiang	21,584 (25.6°)	Propane	4362

Once the soaking period has allowed the interaction between the injected solvent and heavy oil to occur for a sufficient time, the wellbore is opened to production. A mixture of in situ fluids (both water and oil with solvent) is produced. The production stage lasts until the oil rate becomes uneconomical, or the costs of water management become unacceptable [5].

A comparison of CSI with a continuous solvent injection is conducted in Table 5.

Table 5. Differences between continuous and cyclic solvent injection; modified after [43].

	Continuous Solvent Injection	Cyclic Solvent Injection
Operation Strategy	Two types: Vapex and Lateral SVX	Huff—n-puff
Driving Mechanisms	▪ Gravity (Traditional Vapex) ▪ Constant pressure may apply for lateral SVX	▪ Gravitational forces ▪ Pressure gradient ▪ Foamy oil flow ▪ Sand influx ▪ Reduction in skin

Table 5. *Cont.*

	Continuous Solvent Injection	Cyclic Solvent Injection
EOR Mechanisms	▪ Viscosity reduction ▪ Asphaltene precipitation ▪ Diffusion and dispersion-based mass transfer ▪ Capillarity mixing	▪ Viscosity reduction ▪ Asphaltene precipitation ▪ Diffusion and dispersion-based mass transfer ▪ Capillary mixing ▪ Foamy oil
Rules of Wormholes	Establish communication between the injector and the producer. They may cause solvent quick breakthrough.	Increase contact area for solvent and crude oil. Help the diluted oil flow to the producer.
Main Challenges	▪ Low mass transfer rate ▪ Small gravity head (for thin-net pay reservoirs)	▪ Pressure depletion ▪ Viscosity regain
Geomechanics Implications	▪ Continuous decrease in the effective stress and tensional failure ▪ Stability of the wormholes	▪ Cyclic loading and fatigue of the rock ▪ Stability of the wormholes

To analyze further details about CSI and CO_2 as a solvent, the following part of this review will be split into three sections: experimental approach; field pilot projects and experiences; and modeling and numerical descriptions. It is worth noting that there have been recent developments to reduce the price of CO_2 capture and allow its use, e.g., [44,45].

3.1. Recent CSI Experimental Studies

Coskuner et al. explored how different solvents (e.g., heptane, distillate) may help to achieve a higher recovery factor [3]. The general laboratory procedure was to place saturated rock samples with oil inside a glass container, and add hot water and solvent. This experimental process was performed in multiple time steps to emulate the cyclic nature of solvent injection. Experimental data suggested recovery factors ranging from 42% to 88%; it is very likely that these high recovery factors will not be achieved in the field application of solvent injection. In these experiments, the solvent was in contact with all faces of the submerged rock sample, and the complexity of fluid flow regimes, dispersion, reservoir heterogeneity, and limited access to a large volume of solvents at reservoir conditions was not considered.

The impact of some of the characteristics of a physical model (reservoir volumes, wormholes and high-permeability channels, and their spatial location within the reservoir) was addressed by [43] using an experimental design. To capture the possible effects, ref. [43] varied the diameter of the test sample, the position of the wormholes, and the vertical and horizontal orientations of the sample. Their experimental results showed the impact of reservoir–wormhole geometry, the length and relative positions of the wormholes with respect to the reservoir limits on the final oil recovery factor. They concluded that the presence of longer, high-permeability channels and wormholes is effective in delivering solvent to access the lower-permeability portion of the reservoir; this provides increased access for the solvent to dilute heavy oil in the reservoir matrix and ultimately increases the oil recovery factor in shorter time. This means that in such geological settings, higher permeability zones and wormholes not only improve the total recovery but also increase the oil rate in the production phase [43]. This was also confirmed through a visual inspection of the sample during experiments where lower oil saturation near a high-permeability zone suggested more oil production.

Although Du et al. [43] used a broad range for their experimental study, further analysis is required to understand the impact of observed cavities in unconsolidated sandstone reservoirs, changes in in situ stresses, and heterogeneities during cyclic loading/unloading of solvent injection process. These geometries have been experimentally shown to induce different flow regimes that may impact the final recovery [29].

In addition to the impact of the reservoir discontinuities, other empirical works are available in the literature that focus on the driving mechanisms during cyclic solvent injection. In [12], the impact of parameters, such as gravity, pressure depletion rate, solvent composition, and initial oil saturation, are studied. The tests were conducted on the oil from Cold Lake formation and CH_4 was injected into the samples subject to primary production. The follow up CSI process was performed in the sand pack at low pressure (2.76 MPa); the sand pack was scanned before the primary production and after the end of each cycle of solvent injection to obtain fluid saturation profiles. The experiments showed the bubble nucleation and foamy oil behavior as the key driving mechanisms. From a linear decrease in pressure and low gas–oil ratio at the beginning of the test, the expansion of the fluid in response to the drawdown was found to mainly contribute to oil production. Once the sample reached the bubble point, the recovery factor was improved with the foamy oil flow in which the dispersed gas bubbles helped to maintain the sample pressure for an extended time. It seems that the first cycle of each test was the one with the highest impact on recovery factor because the main driving forces (especially foamy oil behavior) were strongly active during the first cycle, when no continuous gas phase was present. Similar observations have also been observed at field scale.

The composition and type of solvent stream for CSI are other highly debated topics in the literature. For EOR applications in heavy oil reservoirs, solvent type is sometimes selected based on the intended recovery mechanisms. For instance, a reservoir may benefit from activating foamy oil drive while a reduction in oil viscosity is a priority for another EOR project. As a result, a wide diversity exists on the type of solvent to meet specific EOR requirements in different regions. The cost of solvent is another issue to be considered for the success of the CSI process. In the current literature, popular gaseous solvents are methane, propane, carbon dioxide, or a combination of them.

Huerta et al. [46] proposed to take advantage of some produced gases like CO_2 and H_2S; in some fields, a stream of CO_2 and H_2S (known as acid gas) is a usual production sub-product, but they pose operational challenge in terms of management and safety, so the disposal of CO_2 and H_2S in geological formations is a more common practice than their use for EOR purposes. The researchers in [46] studied the impact of the cyclic injection of acid gas on oil recovery factor through a set of experiments where multiple tests were carried out with two cycles. They used pure CO_2 solvent (as reference), CO_2 72%-CH_4 28%, CH_4 70%-C_3H_8 30%, and CO_2 90%-H_2S 10%. The experimental results showed that a combination of CO_2 and H_2S offers a better performance than pure CO_2 or any methane/propane mixture. Mixtures of CO_2 and propane showed the best results in terms of oil recovery. An interesting observation was that regardless of the solvent composition, all the experiments confirmed that most of the oil recovery is achieved through the first cycle. This observation has been reported in other different experimental studies and field tests.

In a more detailed experimental design, ref. [40] used a 1.5 m long sand pack sample to study solvent injection and key parameters related to fluid expansion, gas dissolution, and foamy oil behavior using a combination of gaseous solvents, including methane, propane, and carbon dioxide. Soh et al. [40] observed that some gases can function as "mainly diluents" to reduce oil viscosity while other gases can act as "foamy helpers" to provide the right conditions to establish foamy oil flow. Previously, ref. [46] suggested that the mixture of methane/propane could be a good performer to increase oil recovery. However,

the results from [40], specifically for the heavy oil reservoir, implied that solvents with noticeable mixing properties (e.g., propane) are not recommended to be used with the solvents that aid the formation of foamy oil (e.g., CH_4 or CO_2). This might suggest that the type and concentration of solvent is case specific to the heavy oil reservoir and that laboratory experiments are required to understand the interaction of solvent–heavy oil at reservoir pressure and temperature before conducting any CSI field test.

The physical modeling of the post-CHOPS CSI has recently found a new dimension with the use of a geotechnical centrifuge to model the drainage area of heavy oil reservoirs. Cartagena-Perez et al. [47] developed a geotechnical centrifuge cell that allows the integration of triaxial stresses with 3D printed samples that contained wormholes. The results of this work highlight the pivotal role that geomechanics has during the post-CHOPS phase of the reservoir when CSI is applied.

3.2. Recent Development in Numerical Modeling of CSI

Most of the literature on modeling the CSI process in unconsolidated heavy oil reservoirs has focused its effort on two main topics, namely, (i) the numerical modeling of solvent–heavy oil interactions that include foamy oil behavior and non-equilibrium dissolution/exsolution processes, and (ii) the numerical modeling of wormholes and high-permeability channels within the reservoir after cold production with sand.

The proper representation of the dissolution/exsolution process seems to directly impact the numerical evaluation of CSI performance in heavy oil reservoirs [48]. In general, the non-equilibrium behavior for gas dissolution into heavy oil can be described as follows:

$$SG \rightarrow SG + SL \tag{3}$$

where SG is the solvent in gaseous phase; SL is the solvent in liquid phase. Similarly, the dissolution at non-equilibrium behavior is represented as follows:

$$SG + SL \rightarrow 2SL \tag{4}$$

Non-equilibrium can be thought of as a delay in the gas dissolution/exsolution process, compared to equilibrium phase behavior, in which dissolved gas could release into free phase, for instance, due to pressure depletion at an instant [15,49]. The modeling can be achieved through multiple Arrhenius kinetic reaction types of modeling for the release of dissolved gas, to dispersed gas, to free gas. Ref. [48] compared the impact of non-equilibrium and instant equilibrium phase behavior on the solubility for CSI processes for a solvent mixture of CO_2 and propane (Figure 6). They reported significant differences in oil recovery, solvent recovery, and solvent-to-oil ratio. Non-equilibrium phase behavior resulted in larger bottomhole pressures and higher cumulative oil production. The observed differences were explained through the advection, diffusion, dispersion, and dissolution of the non-equilibrium mixing process.

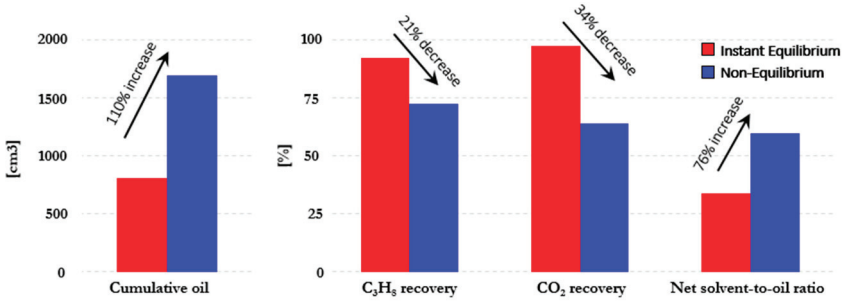

Figure 6. Comparative impact of non-equilibrium and instant equilibrium simulation of solubility. Data from [48]. Simulations are run for a CSI process with solvent of 72% CO_2 and 28% propane.

In addition to the modeling of solvent–heavy oil interactions, it is important that the modeling tools are capable of including and history matching the presence of wormholes and high-permeability zones with field data during the cold heavy oil production phase; this step is required prior to numerically simulating the CSI process [48,50]. Different modeling approaches are presented in the literature. Rivero et al. [51] suggested the use of an effective permeability model that represents the wormholes and high-permeable zones. Rangriz Shokri et al. [52] used partial dual-permeability models, in which the matrix represents the intact reservoir, and the fractures represent the wormhole domain. Haddad et al. [53] employed dilated-zone model with wormholes and cavities represented as dilated zones around the wellbore. In a numerical study, Chang et al. [48] illustrated that the selected method to represent the reservoir and high-permeability zones affects the cumulative oil production and recovery factor, predicted for primary production and follow-up EOR scenarios.

In summary, the large-scale simulation of CSI scenarios in heavy oil reservoirs could face many other numerical challenges, including longer simulation run times, difficulty to model sand production and wormhole growth, and upscaling issues of the laboratory results when foamy oil behavior from the bulk fluid phase (e.g., PVT cell) is used to represent foamy oil flow in the porous media (e.g., [32,50,52,54]). Given the range of these modeling uncertainties, numerical simulations are still required to assess and optimize the performance of the CSI process in unconsolidated heavy oil reservoirs [26,35,55–57]. Optimization parameters for the CSI process include the type and concentration of solvents, injection rate and pressure, duration of injection, soaking, production phases, number of cycles, and incremental oil production per cycle. The available literature on the numerical simulation of CSI also suggests the highest oil recovery in the early cycles and a general declining trend in cumulative oil production in the subsequent cycles (Figure 7); this is consistent with previous laboratory experiments and field tests (e.g., [58]). If we assume that each cycle takes one year, after five years, the recovery would be approximately 38%, which is comparable to the performance shown for the SAGD technique in 4 years (Figure 5). It is important to note that this recovery is obtained in a reservoir where SAGD is not suitable.

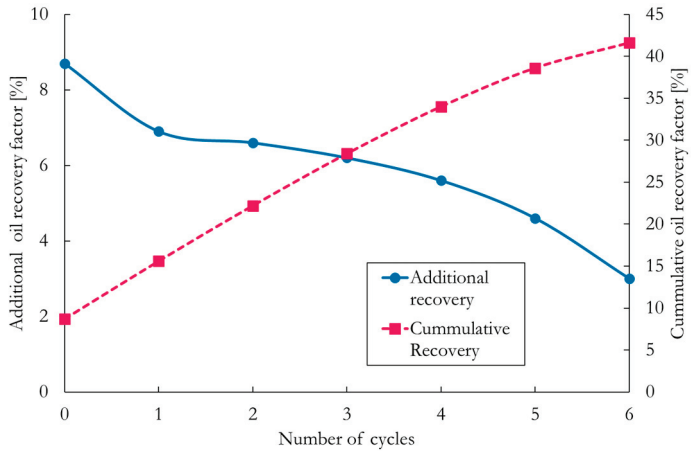

Figure 7. A declining trend in incremental oil recovery factor with the number of CSI cycles, modified after [57].

A fully coupled numerical model between geomechanics and fluid flow is still a task to accomplish. From the geomechanics perspective, extra work is needed to understand the constitutive model that may be applied to a granular material as its fabric changes with the sand production. Also, yielding criteria, such as Mohr–Coulomb, that were developed for continuous mechanics, may be limited.

3.3. Recent CSI Pilot Projects and Case Studies

In this section, field cases from the Lloydminster area, Canada, will be described with emphasis on some CHOPS wells from the following reservoirs: Nexen Plover Lake, Husky Mervin, Devon Manatokan East, and Husky Lashburn. Our focus is on the application of gaseous hydrocarbon solvents and CO_2. However, CSI projects that employed other gases, such as nitrogen, are also available in the literature [59].

Overall, the performance of CSI in an unconsolidated heavy oil reservoir is closely related to its primary production history of that reservoir; this due to the fact that large volumes of sand might have been produced with oil during primary production and that affects the creation of high permeability regions and wormholes within the reservoir. Figure 8 illustrates the typical behavior of a CHOPS well in the Lloydminster area. Initial production begins with an increase in oil and sand production rates; the reason to allow some sand production along with heavy oil is to increase the oil rate and accelerate production. With more production, sand production significantly declines; the oil is produced until the water production makes oil recovery from that particular well uneconomical [5]. During the primary production, the compaction of unconsolidated formation and other geomechanical issues are responsible for 30% of the production drive energy.

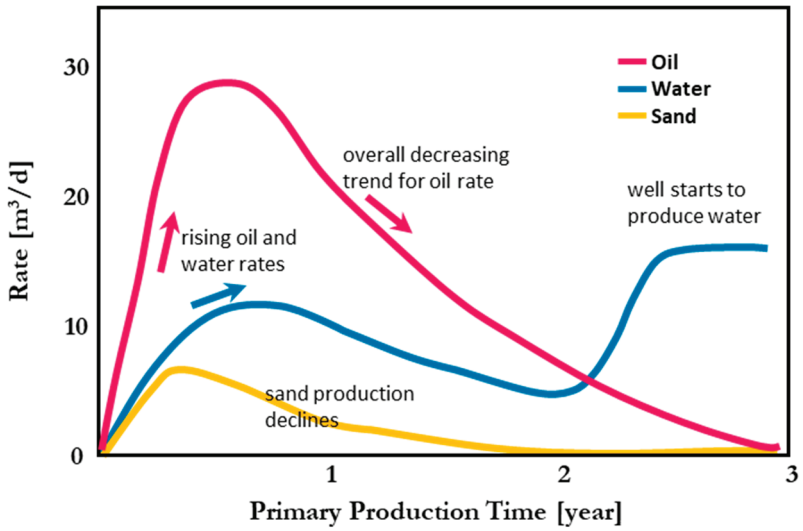

Figure 8. Production behavior from a typical CHOPS well at the Lloydminster area, adapted from [5].

Case Study of the Nexen Plover Lake. In this field project, a propane-based CSI was applied. The wellbore experienced a high water rate and low oil production prior to the first cycle; this has made the production from this well uneconomical. The injection of propane during CSI was sufficient to increase the oil rate by six times the pre-CSI rate. It was reported that most of the injected propane was recovered from the produced reservoir fluids [5]. This retrieval of solvent added to the economic viability of the project. It is worth mentioning that one of the key challenges that determines the economic success of CSI field implementation is the high cost of solvents and the existence of the possibility to retrieve the injected solvents. During the CSI process, a reduction in oil viscosity was observed due to the use of injected propane in the reservoir [5]. A direct consequence of this oil viscosity reduction was a decrease in the water cut that resulted from an improved mobility ratio.

A description of the production record is shown in Figure 9.

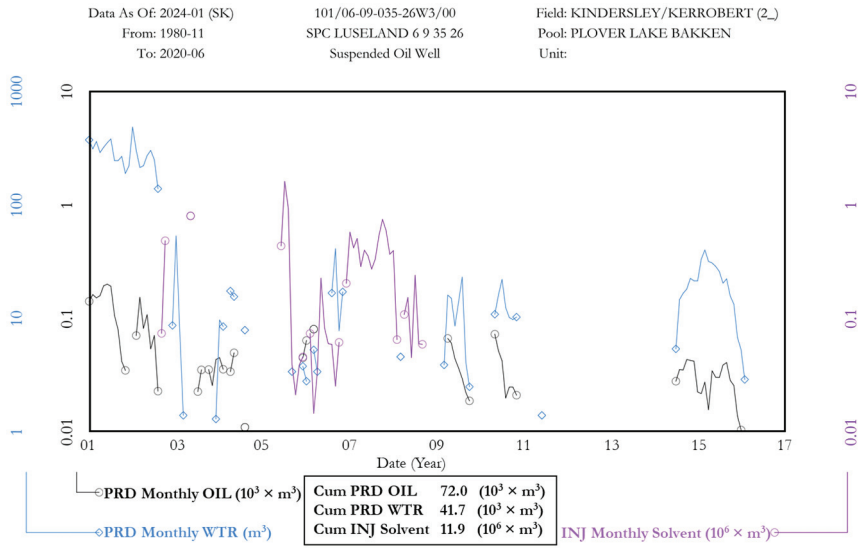

Figure 9. Production record of Nexen Plover Lake 3–9.

Case Study of the Husky Edam. This project employed a combination of methane-propane injection. The oil recovery during the primary production is 11,000 m^3, and after the first five cycles of CSI, an additional 5500 m^3 oil could be produced; this translates to 50% of the initial oil recovery [5]. Each CSI cycle has resulted in a high oil rate that declined with time during the production phase [5]. The field observation suggested that the water cut decreased not only within each cycle but also showed a decreasing general trend over a total of five cycles (Figure 10). This was believed to be due to the continuous change in heavy oil properties (e.g., viscosity) caused by the solvents that positively affected the mobility ratio. Further research is required to address wettability alteration in the reservoir because of solvent use during the CSI process. Recently, there is evidence of multiple cycles of CO_2 injection (Since 2019) with a total injection of almost 5.3 × 10^6 m^3 of CO_2, showing the transition in the solvents.

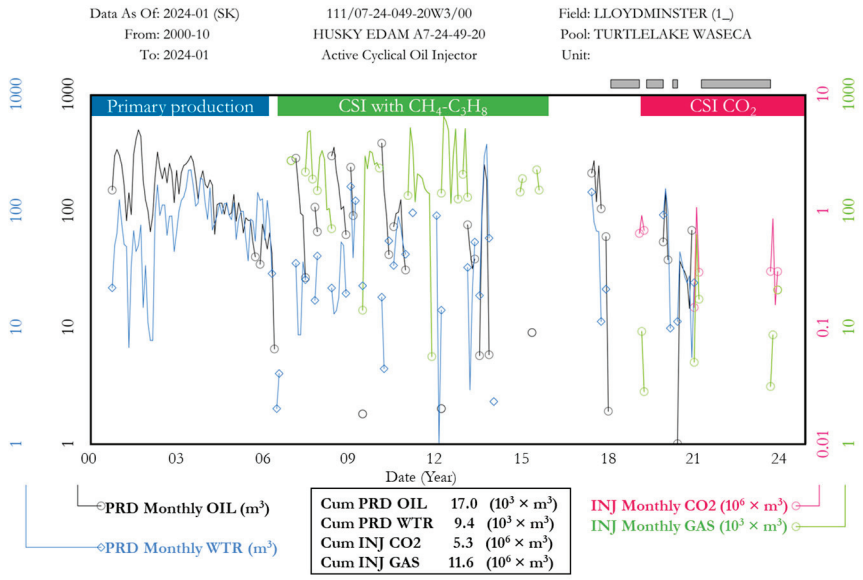

Figure 10. Production record for Waseca 7A-24 on the Husky Edam.

Case Study of the Husky Mervin. This pilot project is of special interest, because of the CO_2 use. The first well (Mervin 05-36) injected pure CO_2 in the first two cycles (Figure 11). The primary recovery of this well was 11,700 m^3; the recovery improvement during the first and the second cycles of a follow up CSI operation was over 14% and 10%

of the primary recovery, respectively. From the same reservoir, another well (Mervin 15-01 Colony—Figure 12) presented a different response to the application of CSI. This well had a higher primary oil production of about 51,000 m^3 (4.4 times higher than the Mervin 05-36); this probably indicates a more developed network of wormhole and high permeability channels due to sand production. The CSI process added incremental oil production, about 60% of the primary recovery in the first cycle, and 73% in the second cycle. The high recovery factor observed during the CSI cycles suggests that a productive CHOPS well may potentially perform better during CSI operation [5]. This could be associated with a larger reservoir contact area to solvents (e.g., extended wormhole network and high permeability channels due to sand influx) that had been created during primary production. A third case (Mervin 12-31) offered insights on the impact of CSI on water cut (Figure 13). The well was productive with a primary recovery of 59,000 m^3, but with a high water cut of 80% [5]. The high water cut was observed in all the CSI cycles, which might be interpreted as a limited action of the injected CO_2 in gas phase on the mobility ratio.

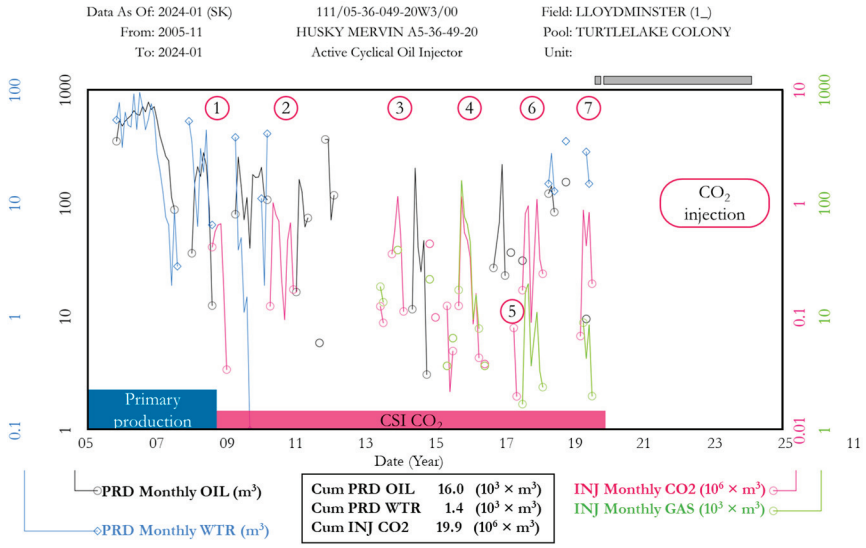

Figure 11. Mervin 05-36 production record. CO_2 injection cycles are numbered from 1 to 7.

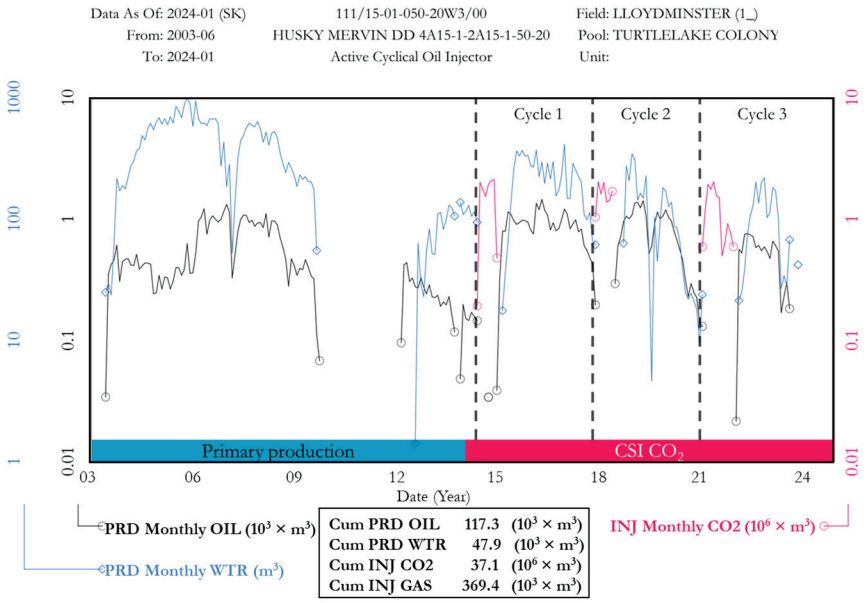

Figure 12. Production record of Mervin 15-01. CO_2 injection cycles are numbered from 1 to 3.

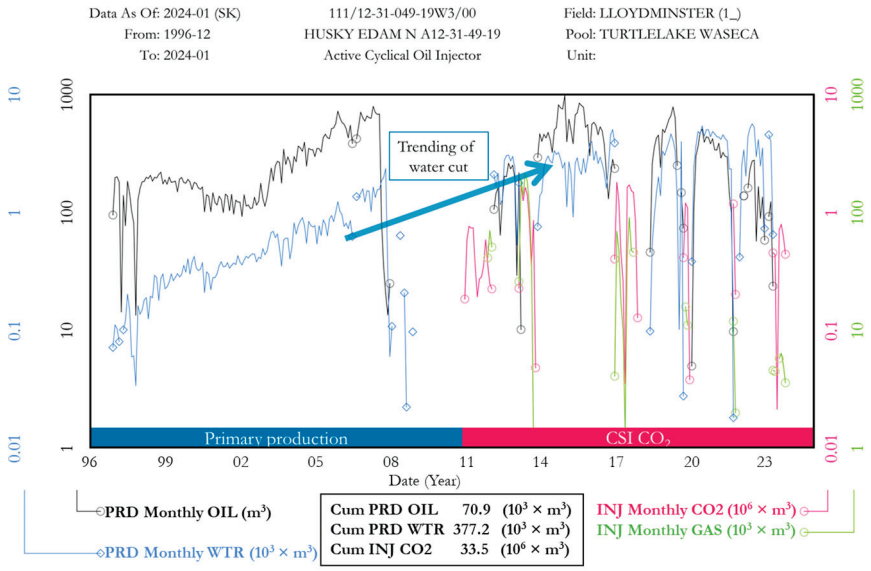

Figure 13. Production record for Mervin 12-31.

Case Study of the Husky Lashburn. This project also involved the cyclic injection of CO_2 (Figure 14). In this reservoir, the behavior of each cycle seems to decline with a high initial oil rate and low water cut. The water cut during CSI cycles was high, which again suggests that CO_2 injection in gas phase may not help improve the mobility ratio. Field operational data indicated that 40% of the injected CO_2 remained in the reservoir [5]; the increasing trend of stored CO_2 eventually helped to transition from CO_2 EOR to permanent CO_2 storage.

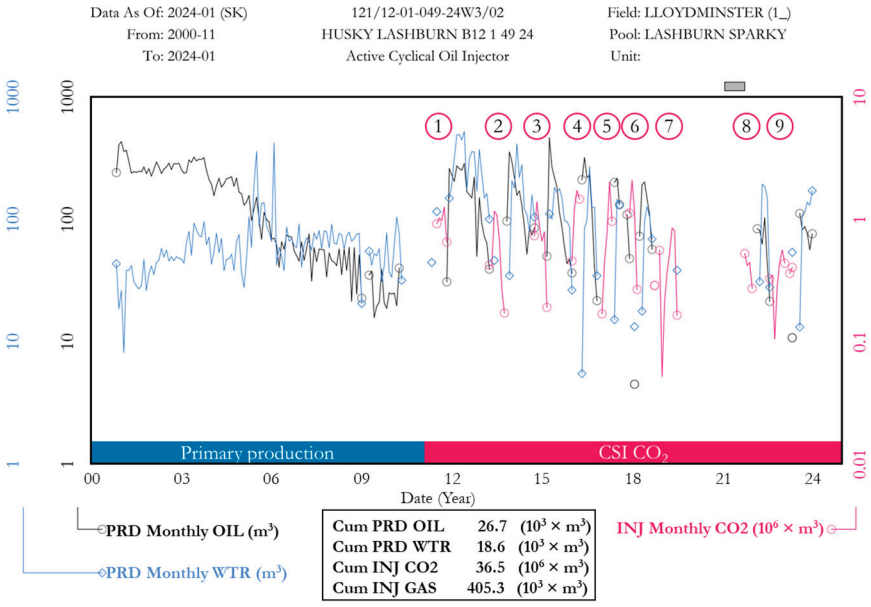

Figure 14. Production record for Sparky 12-01. CO_2 injection cycles are numbered from 1 to 9.

Case Study of the Dee Valley. This project has at least six wellbores (05-10-049-22W3, 06-10-049-22W3, 10-09-049-22W3, 14-09-049-22W3, 15-09-049-22W3, 16-09-049-22W3) where CO_2-CSI has been applied, taking advantage of the proximity of the wellbores (Figure 15). All the wells were subject to the cyclic injection of CO_2 at the beginning of 2015 with approximately three or four cycles until the end of 2018 or beginning of 2019.

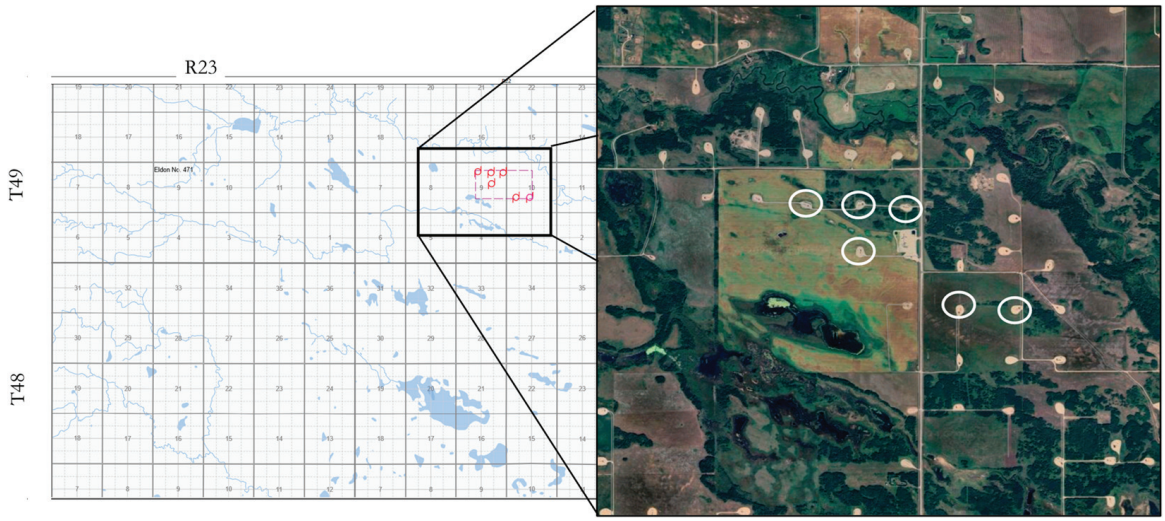

Figure 15. Layout and location of the CSI wellbores.

The wells display a characteristic pattern observed in CHOPS reservoirs during primary production, marked by a decline in oil rate and an increase in water cut, necessitating the implementation of a CSI program. CO_2 injection in one of these wells commenced in 2015, resulting in an equal water cut compared to the end of primary production but also an increased oil rate (Figure 16). Over the next 3 years, three cycles of CO_2 injection were carried out until 2024, leading to peaks in oil production equivalent to some of the highest levels during primary production, and progressively increasing the water cut with subsequent cycles, which again challenge the possibility of a favorable mobility ratio for the oil with the injection of CO_2.

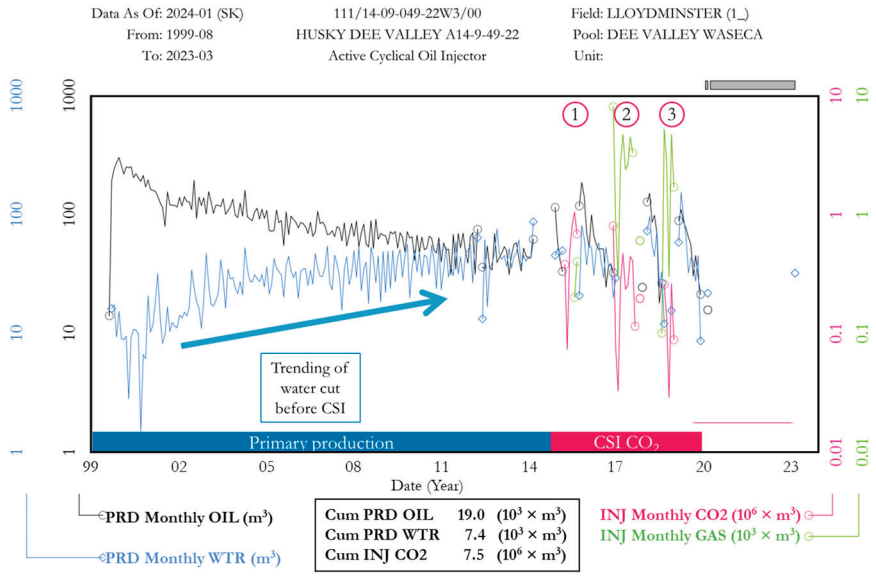

Figure 16. Record production for wellbore 121/12-01-049-24W3 at Dee Valley. CO_2 injection cycles are numbered from 1 to 3.

Those field observations, next to the numerical and experimental ones, may result in some driving mechanisms of the production in post-CHOPS CO_2-CSI reservoirs that are summarized in Table 6.

Table 6. Driving mechanism during the CSI in post-CHOPS reservoirs.

Mechanism	Explanation	References
Larger wormhole network or cavities	The wellbores with well-developed wormholes or cavity areas have a larger contact area for the solvent to act. It has been observed in the field experience that wells with good performance during CHOPS have higher production during the CSI.	[5]
Re-energization	Due to the injection of solvent, the increase in the pore pressure derived in a re-energization of the reservoir. This means a higher reservoir pressure around the wellbore to facilitate the production.	[35]
Foamy oil	Experimental approaches have shown that the foamy oil promoted by the CO_2 as a discontinuous phase may play a key role in the recovery due to the expansion of it during the drawdown.	[60]
Increase in the compaction	Physical modeling of post-CHOPS reservoirs concludes that geomechanical driving mechanics are key by influencing the flow behavior and pressure distribution in CO_2-CSI processes.	[29,47,61]
Capillarity mixing	During the production stage, the zone around the wormholes reduces its saturation of oil. During the injection and soaking periods, and due to the capillary forces and wettability of the formation, there is a redistribution of saturations, allowing the oil to migrate from the far to the near zone surrounding the wormholes or cavities.	[43]
Reduction in oil viscosity	Field experiences have shown that this mechanism is limited (Case Dee Valley or Husky Mervin), and the impact of the CO_2 in the mobility ratio is not always dominant.	[5]

4. Conclusions and Remarks

Looking at the recent development of the CSI process in thin unconsolidated heavy oil reservoirs, it appears that the popularity of cyclic solvent injection (as opposed to VAPEX and continuous solvent injection) has increased as a follow up EOR technique after cold production. Other IOR/EOR methods, including waterflooding, gas flooding, and thermals (e.g., SAGD, CSS) can face efficiency issues with fingering, sweep efficiency, and significant heat loss; this again makes CSI a feasible EOR alternative to consider for thin heavy oil reservoirs. Regarding the solvent type and concentration, laboratory experiments are not conclusive to achieve high recovery factors; however, most of the solvents either act to reduce heavy oil viscosity or to increase the strength of the foamy oil behavior (non-equilibrium nucleation and stability of the dispersed bubbles). Of interest, the injection of CO_2 in gas phase has been employed at field scale in different reservoirs with some success to improve recovery factor. Numerical simulations still need to overcome modeling challenges to properly address the complex interplay of solvent–heavy oil reactions, foamy oil flow, sand production, and stress-deformations during loading/unloading cycles of CSI. Progress has been made to integrate kinetic reactions to model non-equilibrium phase behavior. The lessons learned from the field implementation of CSI indicated that highly productive wells during primary cold production are probably good performers during follow-up CSI operations, which confirms the important role of creating high-permeability channels and a wormhole network so solvents can access more intact portions of reservoirs. A common observation from numerical simulations, laboratory experiments, and field tests is that the first CSI cycles are more effective to improve oil recovery; the additional recovery after each cycle decreases, meaning that field development strategies should

be focused on the first cycles of CSI. This paradigm has been challenged by some field experiences, demanding further research about the hierarchy in the driving mechanisms of the production with CSI in post-CHOPS reservoirs.

Author Contributions: D.C.-P. conducted the primary literature review and made the conceptual plan, performed data analysis, and wrote the first manuscript. A.R.S. reviewed and commented on the manuscript. A.R.S. and R.C. supervised the whole process and the final manuscript. All authors have read and agreed to the published version of the manuscript.

Funding: This research was supported by Mitacs through the Mitacs Accelerate program (Grant No. IT22832).

Data Availability Statement: No data were used for the research described in the article.

Acknowledgments: We sincerely appreciate the invaluable support, resources, and contributions provided by the Heavy Oil Research Network program, managed by the Petroleum Technology Research Centre, Regina, as well as the NSERC/Energi Simulation Industrial Research Chair in Reservoir Geomechanics in Unconventional Resources.

Conflicts of Interest: The authors declare no competing interests.

References

1. BP. *Statistical Review of World Energy*; BP Plc: London, UK, 2020.
2. Canada Energy Regulator. Crude Oil Annual Export Summary—2025. 2025. Available online: https://www.cer-rec.gc.ca/en/data-analysis/energy-commodities/crude-oil-petroleum-products/statistics/crude-oil-export-summary/index.html (accessed on 8 May 2025).
3. Coskuner, G.; Naderi, K.; Babadagli, T. An enhanced oil recovery technology as a follow up to cold heavy oil production with sand. *J. Pet. Sci. Eng.* **2015**, *133*, 475–482. [CrossRef]
4. Zhao, D.W.; Wang, J.; Gates, I.D. Thermal recovery strategies for thin heavy oil reservoirs. *Fuel* **2014**, *117*, 431–441. [CrossRef]
5. Coskuner, G.; Huang, H. Enhanced oil recovery in post-CHOPS cold heavy oil production with sand heavy oil reservoirs of Alberta and Saskatchewan part 2: Field piloting of cycling solvent injection. In Proceedings of the Society of Petroleum Engineers—SPE Canada Heavy Oil Conference 2020, CHOC 2020, Calgary, Canada, 15–16 September 2020; Volume 3.
6. Dusseault, M.B. *CHOPS: Cold Heavy Oil Production with Sand in the Canadian Heavy Oil Industry*; Alberta Goernment: Waterloo, Canada, 2002.
7. Shokri, A.R.; Babadagli, T. Modelling of Cold Heavy-Oil Production with Sand For Subsequent Thermal/Solvent Injection Applications. *J. Can. Pet. Technol.* **2014**, *53*, 095–108. [CrossRef]
8. Istchenko, C.M.; Gates, I.D. Well/wormhole model of cold heavy-oil production with sand. *SPE J.* **2014**, *19*, 260–269. [CrossRef]
9. Fjær, E.; Holt, R.M.; Horsrud, P.; Raaen, A.M.; Risnes, R. *Petroleum Related Rock Mechanics*; Elsevier: Amsterdam, The Netherlands, 2008.
10. Fattahpour, V.; Roostaei, M.; Mahmoudi, M.; Soroush, M.; Hosseini, S.A.; Anderson, M. Standalone sand control evaluation: Developing a large-scale high temperature sand retention test apparatus. In Proceedings of the SPE Canada Heavy Oil Conference 2020, Calgary, Canada, 15–16 September 2020.
11. Naderi, K.; Romaniuk, N.; Ozum, B. Improvement of the CHOPS process efficiency. In Proceedings of the SPE Kuwait Oil and Gas Show and Conference, Mishref, Kuwait, 11–14 October 2015.
12. Plata, M.; Bryan, J.; Kantzas, A. Experimental study of heavy oil recovery mechanisms during cyclic solvent injection processes. In Proceedings of the SPE Annual Technical Conference and Exhibition, Orlando, FL, USA, 7–10 May 2018; No. June. pp. 24–26.
13. Li, X.; Sun, X.; Yang, Z.; Gong, H.; Li, T.; Shi, X. Experimental study on chemical-assisted methane flooding for foamy oil reservoirs after primary production. *J. Pet. Sci. Eng.* **2022**, *216*, 110803. [CrossRef]
14. Luo, P.; Li, S.; Knorr, K.D.; Nakutnyy, P. A New PVT Apparatus for Automatic Measurement of Foamy Oil Generation and Stability. In Proceedings of the PE Canada Heavy Oil Technical Conference, CHOC 2018, Calgary, Canada, 13–14 March 2018; Volume 2018-Janua.
15. Maini, B. Foamy Oil Flow in Primary Production of Heavy Oil under Solution Gas Drive. In Proceedings of the Annual Technical Conference and Exhibition, Houston, TX, USA, 3–6 October 1999.
16. Shen, C.; Hamm, M.L.; Bdair, M. Improving cold heavy oil development at peace river with the understanding of foamy-oil dynamics. In Proceedings of the SPE Kuwait Oil and Gas Show and Conference, Mishref, Kuwait, 11–14 October 2015.

17. Wu, M.; Lu, X.; Yang, J.; Lin, Z.; Zeng, F. Experimental analysis of optimal viscosity for optimizing foamy oil behavior in the porous media. *Fuel* **2020**, *262*, 116602. [CrossRef]
18. Wang, H.; Torabi, F.; Zeng, F.; Xiao, H. A novel visualization approach for foamy oil non-equilibrium phase behavior study of solvent/live heavy oil systems. *Fuel* **2020**, *272*, 117648. [CrossRef]
19. Du, Z.; Zeng, F.; Chan, C. Effects of pressure decline rate on the post-CHOPS cyclic solvent injection process. In Proceedings of the Society of Petroleum Engineers—SPE Heavy Oil Conference Canada 2014, Calgary, Canada, 10 June 2014; Volume 3, pp. 1979–1996.
20. Lu, T.; Li, Z.; Fan, W.; Li, S. CO_2 huff and puff for heavy oil recovery after primary production. *Greenh. Gases Sci. Tecnol.* **2016**, *6*, 288–301. [CrossRef]
21. Yang, S.; Yang, D. Integrated characterization of wormhole network by use of a modified pressure-gradient-based (PGB) sand failure criterion and ensemble-based history matching during CHOPS processes. *J. Pet. Sci. Eng.* **2022**, *208*, 109777. [CrossRef]
22. Cartagena-Pérez, D.F.; Alzate-Espinosa, G.A.; Arbelaez-Londoño, A. Conceptual evolution and practice of sand management. *J. Pet. Sci. Eng.* **2022**, *210*, 110022. [CrossRef]
23. Jiang, L.; Liu, J.; Liu, T.; Yang, D. Characterization of Dynamic Wormhole Growth and Propagation During CHOPS Processes by Integrating Rate Transient Analysis and Pressure-Gradient-Based Sand Failure Criterion. In Proceedings of the SPE Canadian Energy Technology Conference, Calgary, Canada, 16–17 March 2022.
24. Lei, X.; Gang, Z. A novel approach for determining wormhole coverage in CHOPS wells. In Proceedings of the PE Heavy Oil Conference Canada 2012, Calgary, Canada, 12–14 June 2012; Volume 2, pp. 1531–1549.
25. Xiao, L.; Zhao, G. Integrated study of foamy oil flow and wormhole structure in CHOPS through transient pressure analysis. In Proceedings of the SPE Heavy Oil Conference Canada, Calgary, Canada, 11–13 June 2013; Volume 3, pp. 1946–1960.
26. Shokri, A.R.; Babadagli, T. Feasibility Assessment of Heavy-oil Recovery by CO_2 Injection After Cold Production with Sands: Lab-to-Field Scale Modeling Considering Non-Equilibrium Foamy Oil Behavior. *Appl. Energy* **2017**, *205*, 615–625. [CrossRef]
27. Yu, H.; Leung, J.Y. A Sand-Arch Stability Constrained Dynamic Fractal Wormhole Growth Model for Simulating Cold Heavy-Oil Production with Sand. *SPE J.* **2020**, *25*, 3440–3456. [CrossRef]
28. Oldakowski, K.; Sawatzky, R.P. Direction of wormholes growth under anisotropic stress. In Proceedings of the SPE Canada Heavy Oil Technical Conference, Calgary, Canada, 13–14 March 2018.
29. Pereira, M. A Physical Model to Assess Sand Production Processes during Cold Heavy Oil Production with Sand. Ph.D. Thesis, University of Saskatchewan, Saskatoon, Canada, 2021.
30. Meza-Díaz, B.; Sawatzky, R.; Kuru, E. Sand on Demand: A Laboratory Investigation on Improving Productivity in Horizontal Wells Under Heavy-Oil Primary Production—Part II. *SPE J.* **2012**, *17*, 1012–1028. [CrossRef]
31. Mathur, B.; Dandekar, A.Y.; Khataniar, S.; Patil, S.L. Life after CHOPS: Alaskan heavy oil perspective. In Proceedings of the SPE Western Regional Meeting Proceedings, Bakersfield, CA, USA, 23–27 April 2017; Volume 2017, pp. 914–927.
32. Chang, J.; Ivory, J.; London, M. History matches and interpretation of CHOPS performance for CSI field pilot. In Proceedings of the Society of Petroleum Engineers—SPE Canada Heavy Oil Technical Conference 2015, CHOC 2015, Calgary, Canada, 9–11 June 2015; pp. 526–544.
33. Oldakowski, K.; Sawatzky, R.P. Wormhole stability under post chops conditions. In Proceedings of the Society of Petroleum Engineers—SPE Canada Heavy Oil Technical Conference, CHOC 2018, Calgary, Canada, 13–14 March 2018; Volume 2018.
34. Mohamad-Hussein, A.; Mendoza, P.E.V.; Delbosco, P.F.; Sorgi, C.; De Gennaro, V.; Subbiah, S.K.; Ni, Q.; Serra, J.M.S.; Lakshmikantha, M.R.; Iglesias, J.A.; et al. Geomechanical modelling of cold heavy oil production with sand. *Petroleum* **2022**, *8*, 66–83. [CrossRef]
35. Shokri, A.R.; Babadagli, T. A sensitivity analysis of cyclic solvent stimulation for post-CHOPS EOR: Application on an actual field case. *SPE Econ. Manag.* **2016**, *8*, 78–89. [CrossRef]
36. Jamaloei, B.Y.; Kharrat, R.; Torabi, F. Analysis and correlations of viscous fingering in low-tension polymer flooding in heavy oil reservoirs. *Energy Fuels* **2010**, *24*, 6384–6392. [CrossRef]
37. Lin, Z. Experimental Study About Radial Viscous Fingering in Heavy Oil Reservoir. Master's Thesis, University of Regina, Regina, Canada, 2020.
38. Maas, J.G.; Springer, N.; Hebing, A.; Snippe, J.; Berg, S. Viscous fingering in CCS—A general criterion for viscous fingering in porous media. *Int. J. Greenh. Gas Control* **2024**, *132*, 104074. [CrossRef]
39. Soliman, A.A.; Aboul-Fetouh, M.E.; Gomaa, S.; Aboul-Fotouh, T.M.; Attia, A.M. Optimizing in-situ upgrading of heavy crude oil via catalytic aquathermolysis using a novel graphene oxide-copper zinc ferrite nanocomposite as a catalyst. *Sci. Rep.* **2024**, *14*, 25845. [CrossRef]
40. Soh, Y.; Rangriz-Shokri, A.; Babadagli, T. Optimization of methane use in cyclic solvent injection for heavy-oil recovery after primary production through experimental and numerical studies. *Fuel* **2018**, *214*, 457–470. [CrossRef]
41. Li, Y.; Wang, Z.; Hu, Z.; Xu, B.; Li, Y.; Pu, W.; Zhao, J. A review of in situ upgrading technology for heavy crude oil. *Petroleum* **2021**, *7*, 117–122. [CrossRef]

42. Krumrine, P.H.; Lefenfeld, M.; Romney, G.A. Investigation of post CHOPS enhanced oil recovery of alkali metal silicide technology. In Proceedings of the SPE Heavy Oil Conference Canada 2014, Calgary, Canada, 12 June 2014; Volume 3, pp. 1634–1650.
43. Du, Z.; Zeng, F.; Chan, C. An experimental study of the post-CHOPS cyclic solvent injection process. *J. Energy Resour. Technol. Trans. ASME* **2015**, *137*, 1–15. [CrossRef]
44. Bairq, Z.A.S.; Gao, H.; Huang, Y.; Zhang, H.; Liang, Z. Enhancing CO_2 desorption performance in rich MEA solution by addition of $SO_4^{2-}/ZrO_2/SiO_2$ bifunctional catalyst. *Appl. Energy* **2019**, *252*, 113440. [CrossRef]
45. Bairq, Z.; Pang, Y.; Li, J.; Hezam, A.; Tontiwachwuthikul, P.; Chen, H. Reducing energy requirements and enhancing MEA-CO_2 desorption rates in amine solutions with KIT-6 nanostructures. *Sep. Purif. Technol.* **2024**, *346*, 127536. [CrossRef]
46. Huerta, M.; Alvarez, J.M.; Jossy, E.; Forshner, K. Use of acid gas (CO_2/H_2S) for the Cyclic Solvent Injection (CSI) process for heavy oil reservoirs. In Proceedings of the Society of Petroleum Engineers—SPE Heavy Oil Conference Canada 2012, Calgary, Canada, 12–14 June 2012; Volume 2, pp. 912–921.
47. Perez, D.C.; Shokri, A.R.; Zambrano, G.; Pantov, D.; Wang, Y.; Chalaturnyk, R.; Hawkes, C. Scaled Physical Modeling of Cyclic CO_2 Injection in Unconsolidated Heavy Oil Reservoirs Using Geotechnical Centrifuge and Additive Manufacturing Technologies. In Proceedings of the SPE Canadian Energy Technology Conference and Exhibition, Calgary, Canada, 12–13 March 2024.
48. Chang, J.; Ivory, J. Field-scale simulation of cyclic solvent injection (CSI). *J. Can. Pet. Technol.* **2013**, *52*, 251–265. [CrossRef]
49. Shokri, A.R.; Babadagli, T. Field scale modeling of CHOPS and solvent/thermal based post CHOPS EOR applications considering non-equilibrium foamy oil behavior and realistic representation of wormholes. *J. Pet. Sci. Eng.* **2016**, *137*, 144–156. [CrossRef]
50. Shokri, A.R.; Babadagli, T. Laboratory Measurements and Numerical Simulation of Cyclic Solvent Stimulation with a Thermally Aided Solvent Retrieval Phase in the Presence of Wormholes after Cold Heavy Oil Production with Sand. *Energy Fuels* **2016**, *30*, 9181–9192. [CrossRef]
51. Rivero, J.A.; Coskuner, G.; Asghari, K.; Law, D.H.; Pearce, A.; Newman, R.; Birchwood, R.; Zhao, J.; Ingham, J. Modeling CHOPS Using a Coupled Flow-Geomechanics Simulator with Nonequilibrium Foamy-Oil Reactions: A Multiwell History Matching Study. In Proceedings of the SPE Annual Technical Conference and Exhibition, Florence, Italy, 20–22 September 2010.
52. Shokri, A.R.; Babadagli, T. An approach to model CHOPS (cold heavy oil production with sand) and post-CHOPS applications. In Proceedings of the SPE Annual Technical Conference and Exhibition, San Antonio, TX, USA, 8–10 October 2012; Volume 3, no. 1, pp. 2305–2316.
53. Haddad, A.S.; Gates, I. Modelling of Cold Heavy Oil Production with Sand (CHOPS) using a fluidized sand algorithm. *Fuel* **2015**, *158*, 937–947. [CrossRef]
54. Vanderheyden, B.; Jayaraman, B.; Ma, X.; Zhang, D. Multiscale Simulation of CHOPS Wormhole Networks. In Proceedings of the SPE Reservoir Simulation Symposium, Woodlands, TX, USA, 18 February 2013.
55. Ma, H.; Yu, G.; She, Y.; Gu, Y. A new hybrid production optimization algorithm for the combined CO_2-cyclic solvent injection (CO_2-CSI) and water/gas flooding in the post-CHOPS reservoirs. *J. Pet. Sci. Eng.* **2018**, *170*, 267–279. [CrossRef]
56. Zhang, M.; Du, Z.; Zeng, F.; Xu, S. Upscaling study of cyclic solvent injection process for post-chops reservoirs through numerical simulation. In Proceedings of the Society of Petroleum Engineers—SPE Heavy Oil Conference Canada 2014, Calgary, Canada, 10 June 2014; Volume 3, pp. 1651–1669.
57. Gamboa, J.J.M.; Leung, J.Y. Design of field-scale cyclic solvent injection processes for post-CHOPS applications. *Can. J. Chem. Eng.* **2019**, *97*, 123–132. [CrossRef]
58. Chang, J.; Ivory, J.; Beaulieu, G. Pressure maintenance at post-CHOPS cyclic solvent injection (CSI) well using gas injection at offset well. In Proceedings of the SPE Heavy Oil Conference, Mangaf, Kuwait, 8–10 December 2014; Volume 2, pp. 1387–1409.
59. Tang, X.; Yu, C.; Bai, Y.; Lu, H.; Mohamed, M.S. Field Trial of Nitrogen-Assisted Cyclic Steam Stimulation in Post-CHOPS Wells, Case Study in Sudan. In Proceedings of the SPE Thermal Well Integrity and Production Symposium, Banff, Canada, 30 November 2022.
60. Jia, X.; Zhu, Q.; Wang, K.; Jiao, B.; Guo, E.; Qu, T.; Wu, K.; Chen, Z. Numerical simulation of foamy-oil flow in a cyclic solvent injection process. *Fuel* **2023**, *333*, 126259. [CrossRef]
61. Layeghpour, S. Geotechnical Centrifuge Experiments to Improve Understanding of Sand Production from Heavy Oil Reservoirs. Ph.D. Thesis, University of Saskatchewan, Saskatoon, Canada, 2021.

energies

MDPI

Article

Division of Lacustrine Environment and Significance for Shale Oil Exploration: A Case Study of the Third Member of Shahejie Formation in Dongying Sag

He Zhao [1,2], Hongliang Wang [1,2,*] and Nana Mu [1,2]

[1] School of Energy Resources, China University of Geosciences, Beijing 100083, China; 3006210031@email.cugb.edu.cn (H.Z.); munn@cugb.edu.cn (N.M.)
[2] Key Laboratory of Marine Reservoir Evolution and Hydrocarbon Enrichment Mechanism, China University of Geosciences, Beijing 100083, China
* Correspondence: whliang@cugb.edu.cn

Abstract: The third member of the Shahejie Formation (Es_3) in Dongying Sag is noteworthy for its abundance of laminated shale, considerable thickness, and high organic matter content, with carbonate interbeds playing a crucial role in reservoir properties. The salinity and pH of water influence the change of sedimentary environment and the mineral composition of sediment, thereby affecting the distribution characteristics of carbonate interbeds. Based on geochemical data from 8721 samples in the Dongying Sag, this study systematically analyzed the salinity and pH characteristics. This study is the first to develop an environmental zoning framework based on aqueous medium characteristics of aqueous media, and the favorable shale oil enrichment areas in Es_3 were identified by integrating carbonate mineral content analysis. The results showed that the lower part of Es_3 is dominated by a zone with high salinity–middle pH, and middle salinity–high pH with rich carbonate. Combining the development of carbonate interbeds, it is speculated that the sweet spots in Es_3 are high salinity–middle pH and middle salinity–high pH. The favorable areas are concentrated in the lower part of Es_3, including the western and northeastern parts of the Lijin Sub-Sag and the northern gentle slope of Guangrao. It provides a novel perspective on shale oil exploration through lacustrine environmental zonation.

Keywords: aqueous medium characteristics; division of lacustrine environment; carbonate interlayer; Dongying Sag

1. Introduction

The focus of oil and gas exploration has gradually shifted to unconventional reservoirs in recent years, especially the exploration and development of shale oil. The main shale oil exploration and development areas in the world are concentrated in passive continental margin basins and rift basins formed under the effect of tension [1]. It is mainly distributed in North America, the Middle East, Western Europe, Siberia, and eastern Asia. The breakthrough in shale oil and gas exploration and development technologies, particularly the application of horizontal drilling and hydraulic fracturing, has led to a dramatic surge in U.S. shale oil production [2]. Data from the U.S. Energy Information Administration (EIA) indicate that, in 2022, U.S. shale oil output reached 378 million tons, accounting for 64% of its total crude oil production. The marine shale deposits in North America are relatively stable and continuous. The oil layer continuity is good, and it is located in the window of light oil–condensate oil. The reservoir quality is also good, with a high content of brittle minerals

and easy fracturing. The favorable area is large, and the cumulative productivity of a single well is high. Whereas China's shale oil is mainly formed in continental sedimentary basins, characterized by significant variations in total organic carbon, relatively low maturity, poorer reservoir properties, lower porosity, complex mineral composition, thinner oil layers, heavier oil quality, and lower pressure coefficients [3,4]. The exploration and development of shale oil have made some breakthroughs in Ordos, Junggar, Bohai Bay, Santanghu, Sichuan, and Qaidam Basin [5–9]. In 2024, China's first national continental shale oil demonstration zone, Xinjiang Jimsar National Continental shale Oil Demonstration Zone, achieved a cumulative output of over one million tons. The annual output of shale oil in Shengli Jiyang Shale oil National Demonstration Zone has exceeded 500,000 tons, the cumulative oil production has exceeded 1 million tons, and the daily oil production of a single well has reached 30 tons. As a typical faulted lacustrine basin in the Bohai Bay Basin, the Jiyang Depression is an important research area for shale oil. Many researchers have made a lot of discussions on the lithofacies types, reservoir space genesis, pore development, and evolution of Paleogene shale in Jiyang Depression, especially in Dongying Sag [10–12].

There is a large thickness of mudstone and a high abundance of organic matter in the low part of Es_3 and the upper part of Es_4 of the Jiyang Depression. The amount of free oil resources reached 4.1 billion tons, of which 2.3 billion tons are in Dongying Sag [13]. A large number of laminated carbonate rocks are developed in the main reservoir section. These carbonate rocks are mainly composed of calcite, which is very thin and mostly in the centimeter to millimeter level [14–18]. The kind of laminated carbonate rock in the organic-rich shale section is not unique to the Jiyang Depression. It has been found in the Araripe Basin in northeastern Brazil, the Uinta Basin in the United States, the Cankiri-Corum Basin in Turkey, the Midland Valley Basin in Scotland, the Ordos Basin, and the Santanghu Basin in China [19–22]. This has led many scholars to further study the carbonate rocks in lacustrine shale. It is generally believed that the dissolution of carbonate rocks is conducive to the self-generation and self-storage of shale oil. The original diagenetic environment of the continental sequence is closely related to the geochemical characteristics of the lake water in the basin. The salinity and pH of water directly control the chemical precipitation of the lake.

The analysis of aqueous medium characteristics is mainly applied in aspects such as water quality assessment, water resource management, and climate change research. It is less applied in the field of petroleum geology and mainly focuses on the evolution of sedimentary environments. This study is the first to develop an environmental zoning framework based on aqueous medium characteristics of aqueous media, analyzing and comparing the characteristics of each environmental zone from the organic matter content, the main trace element content, the carbonate mineral content, and other points of view. This affects the lithological composition of sediments and thereby influences the reservoir characteristics and the development of source rocks. It could predict the favorable accumulation area of shale oil in Es_3 of Dongying Sag from the macro perspective, which provides a novel perspective on shale oil exploration through lacustrine environmental zonation.

2. Materials and Methods

2.1. Geological Settings

In the northern part of Shandong Province, Dongying Sag is the area with the most abundant oil and gas in the Jiyang Depression. It covers about 5850 km^2. It faces Qingdong Sag in the east and has an over-relationship with Luxi Uplift and Guangrao Salient in the south. In the west, it is bounded by Qingcheng Salient and Linfanjia Salient, and, in the north, it reaches Binxian Salient and Chenjiazhuang Salient. In the formation and evolution of the basin, the fault activity in the north is the strongest, making Dongying Sag a typical

asymmetrical braided basin with a "steep dip angle in the north limb and gentle in the south" (Figure 1) [23].

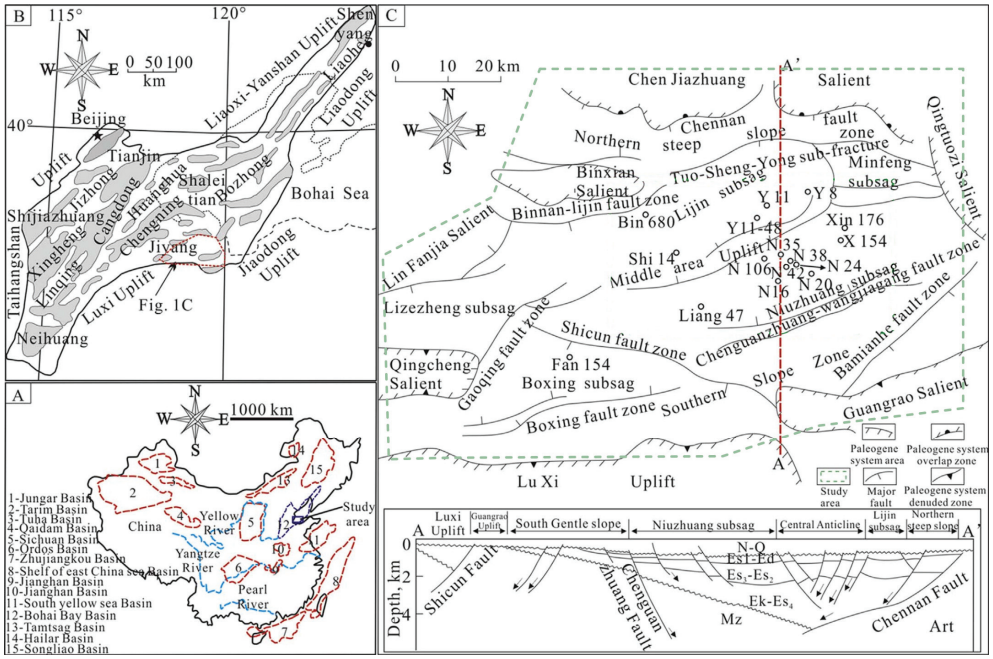

Figure 1. Geological overview of the study area. ((**A**) Location of the Bohai Bay Basin in China; (**B**) the tectonic unit division of Bohai Bay Basin; (**C**) the tectonic unit division of Dongying sag and a south-to-north structural cross-section).

The period from the middle and late deposition of Es_4 to the early deposition of Es_3 is the intense fault depression of Dongying Sag. In the middle and late stages of Es_4, the climate changed from drought to wet, accompanied by an increase in precipitation, the subsidence of the basin, the expansion of the water area, and a rise in salinity. The rapid increase in the accommodating space of the basin under the control of tectonic movement and climate. The humid climate provides sufficient moisture, causing the lake level to rise and forming a lake intrusion system. This period had a humid climate and abundant moisture. According to the results of literature research, the sedimentary period of the Shahejie Formation in the Paleogene of the Jiyang Depression was once affected by seawater or was briefly connected to the sea. In the early sedimentary stage of Es_3, the climate was wet, with the lake basin increasing and the basin fault depression enhancing. The accommodating space was larger [24–26]. The widely distributed deep water to semi-deep water environment provides favorable conditions and places for the deposition of fine-grained materials. It provides conditions for the formation of shale oil.

The main factors affecting the reservoir conditions of Paleogene shale oil in Dongying Sag include rock structure, material composition, recrystallization and dissolution of carbonate minerals, thermal evolution of organic matter, and intensity of dolomitization. The common reservoir space types of laminated shale and sandstone interlayer are mainly intergranular pores and dissolution pores, with a large pore size range and a high proportion of macropores. Most pores are filled with iron dolomite, a flake mixed-layer of illite-montmorillonite and pyrite. In the local area, due to the significant dissolution of feldspar, the pore connectivity is improved. The laminated shale rich in organic matter and carbonate minerals has the best pores and, due to its total porosity, pore connectivity, and pores conducive to the occurrence of free oil, can be regarded as a favorable lithofacies type [27]. The diagenetic environment of Es_4 in Niuzhuang Sag is controlled by aqueous medium, hydrocarbon generation, and acid expulsion. The main diagenesis includes

the dissolution of calcite, dolomite, pyrite, siderite, quartz, siliceous metasomatism, and dolomitization. The content and occurrence of inorganic minerals such as carbonates, clays, and terrigenous clasts affect the ability of shale oil reservoirs. Dissolution and recrystallization diagenesis are important ways to improve storage permeability [28]. Generally, the organic matter in the sedimentary environment is more developed in the quiet and stratified environment of lake water. The dissolution of organic acids to adjacent carbonate laminae increases reservoir space [29–31]. The effective reservoir space in the self-storage shale reservoir is the matrix gap, which mainly comes from the pores and fissures between or inside the crystals of carbonate minerals [32].

2.2. Data Collection

This study is based on data from over 270 wells in Es_3 of Dongying Sag, including core data, logging data, and geochemical data. Three shale oil exploration wells are the focus of this research, among which the thickness of Es_3 is 195 m for well FY1, 115 m for well LY1, and 62 m for well NY1. It provides a reasonable data basis for the analysis of characteristics.

2.3. Calculation Formula of Aqueous Medium Characteristics

The fitting equations in this paper are based on the author's participation in the project 'Characterization of ancient lake sedimentary water medium in the third member of Dongying Sag'.

The data are from the Shengli oil field exploration and Development Research Institute. The major elements were tested by X-ray fluorescence spectrometer (Axios Max) using the alkali-fused glass method. The trace elements were tested by an inductively coupled plasma mass spectrometer (X-Serise II) using acid melting. The systematic errors were less than 5‰.

The fitting equation of salinity by Sr/Ba is shown in Table 1 and Figure 2. By comparing logarithmic fitting, linear function fitting, and multiple function fitting, it is found that the fitting of hexagonal polynomials has the best effect. However, the discriminant effect of Sr/Ba is not obvious in the application process. We sought to improve the recognition of Sr/Ba in a sedimentary environment by the selective extraction method [33]. The sediments were soaked in hydrochloric acid, and only the strontium and barium that migrated into the sediments during the deposition process were extracted, as far as possible, so as to eliminate the interference of strontium and barium from other sources on the identification of the sedimentary environment to the greatest extent.

$$y = -0.025x^6 + 0.5532x^5 - 4.6182x^4 + 18.028x^3 - 33.74x^2 + 31.703x - 6.4797 \ (R^2 = 0.9938) \quad (1)$$

Table 1. The salinity fitting data of Well N38.

Sr/Ba	Salinity (‰)	Sr/Ba	Salinity (‰)	Sr/Ba	Salinity (‰)
0.54	3.75	0.33	0.74	4.28	17.00
0.40	1.37	0.37	1.89	3.13	15.00
0.64	3.91	4.06	15.00	7.05	19.00
0.60	3.58	2.25	9.50	6.53	18.00

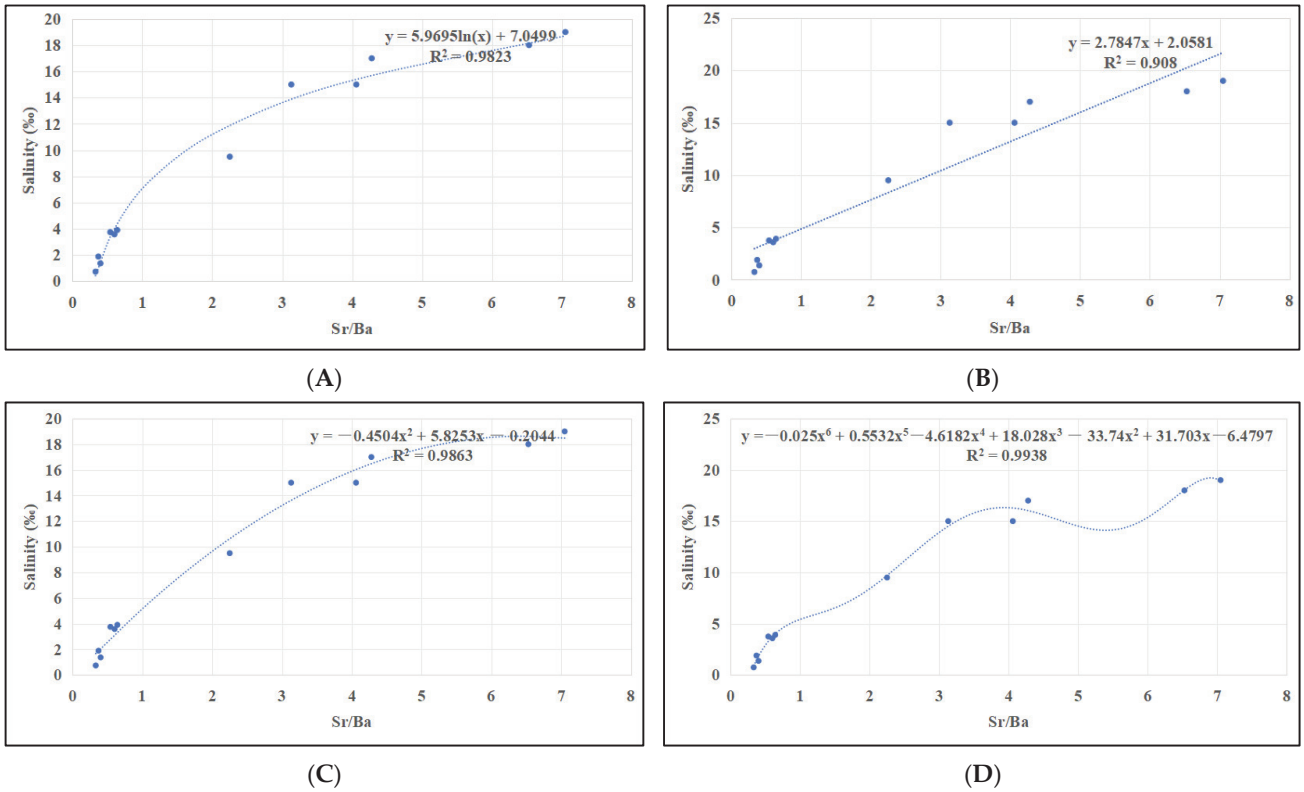

Figure 2. Correlation of salinity fitting equation. ((**A**) Exponential function; (**B**) linear function; (**C**) quadratic function; (**D**) sextic function).

The fitting equation of pH by calcium content (Table 2 and Figure 3). By comparing logarithmic fitting, linear function fitting, and multiple function fitting, it is found that cubic polynomial fitting has the best effect.

$$y = 0.0019x^3 - 0.0453x^2 + 0.3827x + 7.6933 \ (R^2 = 0.93) \quad (2)$$

Table 2. The relationship between pH and Ca% in different locations.

Location	PH	Ca (%)	Location	PH	Ca (%)
Qinghai Lake	9.11	12.00	Yellow Sea	8.40	2.09
Gahai Lake	8.93	10.50	Yellow Sea	8.18	2.29
Gahai Lake	8.83	6.50	Yellow Sea	8.50	2.37
Yellow Sea	8.54	3.71	Erhai Lake	8.08	1.21

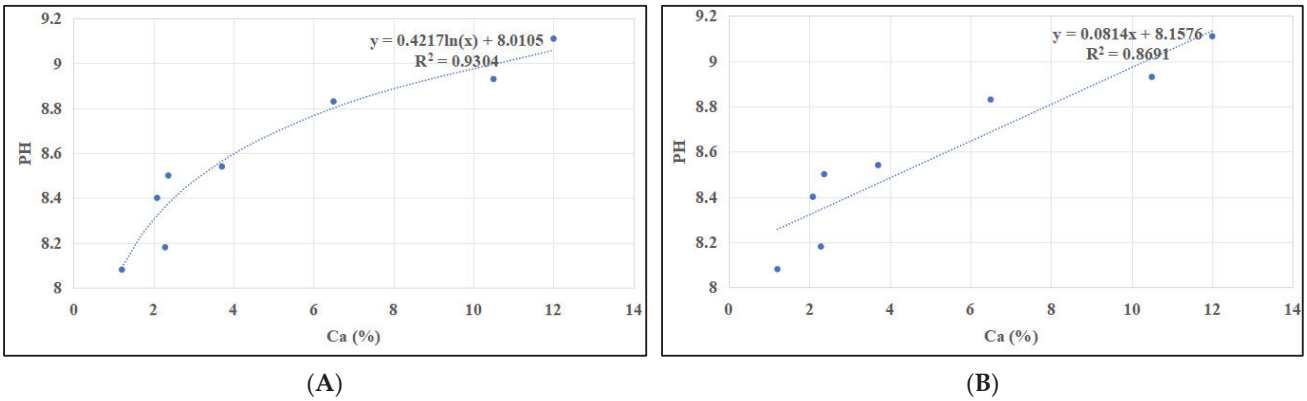

Figure 3. *Cont.*

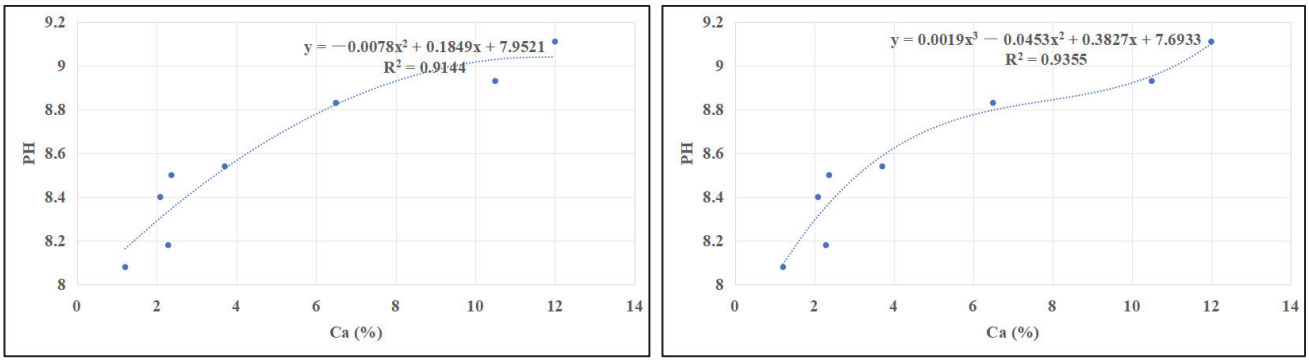

(**C**) (**D**)

Figure 3. Correlation of pH fitting equation. ((**A**) Exponential function; (**B**) linear function; (**C**) quadratic function; (**D**) cubic function).

It is found that the logging parameters with higher Pearson values are AC, CNL, and R_{25} (Table 3 and Figure 4). The fitting equation of the carbonate mineral content by the logging data is as follows:

$$y = 39.152 + 0.253 \times AC - 0.869 \times CNL + 0.094 \times R_{25} \quad (3)$$

Table 3. Pearson value of correlation between logging data and carbonate content.

Well	Samples	GR	SP	AC	DEN	R_{25}	CNL	CAL
FY1	843	0.137	−0.135	−0.225	0.019	0.413	−0.295	−0.038
NY1	517	0.132	0.020	0.035	−0.034	0.377	0.261	−0.055
LY1	762	−0.135	−0.126	−0.173	0.129	0.264	−0.306	−0.047

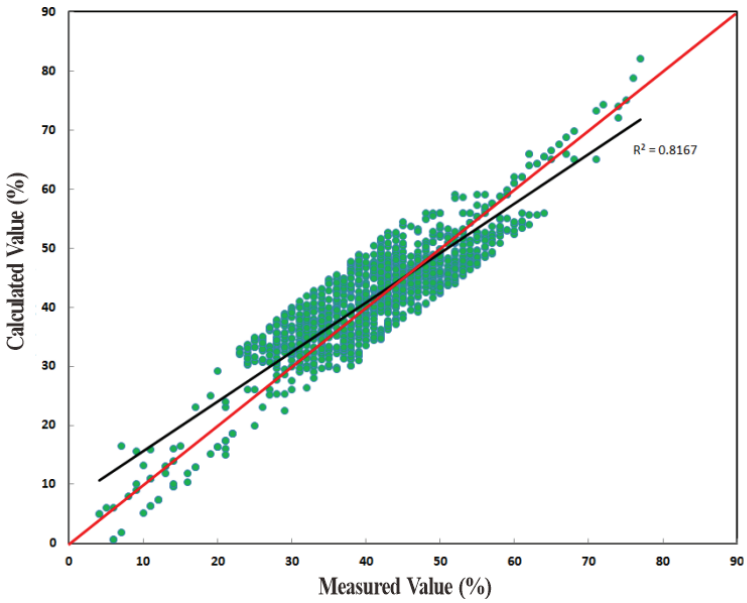

Figure 4. The accuracy test for the fitting equation of carbonate mineral content.

2.4. Analysis Method

This study combines the overlapping method in mathematical analysis, that is, one image is overlaid on another image to obtain a strong visual image. This method is often used in logging curve interpretation. Overlapping two or more different logging curves of the same scale will cause amplitude deviation due to different formation properties.

According to this phenomenon, the oil-bearing horizons and the mobility of oil and gas can be understood intuitively.

The calculation and analysis of aqueous media characteristics and the plane analysis are the basis. The overlapping treatment can visually analyze the salinity and pH of different zones. The characteristics of the partition are summarized from the perspectives of lithofacies, aqueous medium, elements, and organic matter.

The overall steps of this research are as follows: (1) collection and organization of logging data and element test data; (2) fitting calculation of water medium parameters; (3) the water medium area division is carried out by the overlapping method; (4) different zoning characteristics and reservoir evaluation.

3. Results

3.1. Basis and Scheme of Environmental Division

The salinity and pH control the chemical precipitation of the lake, and the environmental changes controlled by the aqueous medium affect the distribution characteristics of carbonate minerals.

The ratio of Sr to Ba is often used to distinguish the marine and terrestrial sedimentary environments. It has been recognized by many scholars that the ratio is larger than 1 in marine sediments and smaller than 1 in continental sediments. The salinity division values calculated by Formula (1) are 4‰ and 11‰ (Figure 5).

In the alkaline lakes, the pH value is closely related to the Ca content. Because it mainly exists in the form of strong alkali and weak acid salt ions in the water body, the pH value is small, and the water medium is rarely precipitated when it is acidic. The stronger the alkalinity is, the easier it is to precipitate. Therefore, the Ca content can be used to reflect the pH value of the water body [34]. Combined with the distribution of the Ca content in the study area, 4.5% and 8.5% near the extreme value of formula (2) are selected. Less than 4.5% is the weak acid environment, from 4.5% to 8.5% is the transitional environment, and more than 8.5% is the alkaline environment. The pH partition values calculated by Formula (2) are 8.65 and 8.85 (Figure 6).

The maximum paleo-salinity of Es_3L is 36.88‰, the minimum is 0.19‰, and the average is 6.2‰, which is most from 3‰ to 9‰. This part of the data accounts for more than 85% of the total data, and most sample points greater than 9‰ are located in the lower section of the profile. The overall pattern of Es_3L is "two low areas and one high" (Figure 5A). The maximum paleo-salinity of Es_3M is 30.09‰, the minimum is 0.05‰, and the average is 2.68‰, which is concentrated from 2‰ to 8‰. This part of the data accounts for more than 90% of the total data. The Es_3M still shows a pattern of "two low and one high" (Figure 5B). The maximum paleo-salinity of Es_3U is 17.75‰, the minimum is 0.03‰, and the average is 2.47‰, mainly from 2‰ to 6‰. This part of the data accounts for more than 85% of the total data. The low salinity area in Es_3U further expanded (Figure 5C).

The maximum pH value of Es_3L is 9.38, the minimum value is 7.66, and the average value is 8.74, which is concentrated from 8.4 to 8.9. This part of the data accounts for more than 90%. Most sample points larger than 8.9 are located in Es_3L on the profile, and the middle and high value areas are expected simultaneously. In the plane, two high-value areas are in the center and two low-value regions on both sides (Figure 6A). The maximum pH value of Es_3M is 9.21, the minimum value is 7.52, and the average value is 8.40, which is concentrated from 8.3 to 8.6. This part of the data accounts for more than 90% of the total data. On the plane of the Es_3M, the pH value along the northwest to southeast shows a banded feature of "two highs with one low" (Figure 6B). The maximum pH value of Es_3U is 9.16, the minimum value is 7.44, and the average value is 8.28, mostly from 8.1 to 8.6.

This part of the data accounts for more than 85% of the total data. Es_3U is also characterized by two highs and one low (Figure 6C).

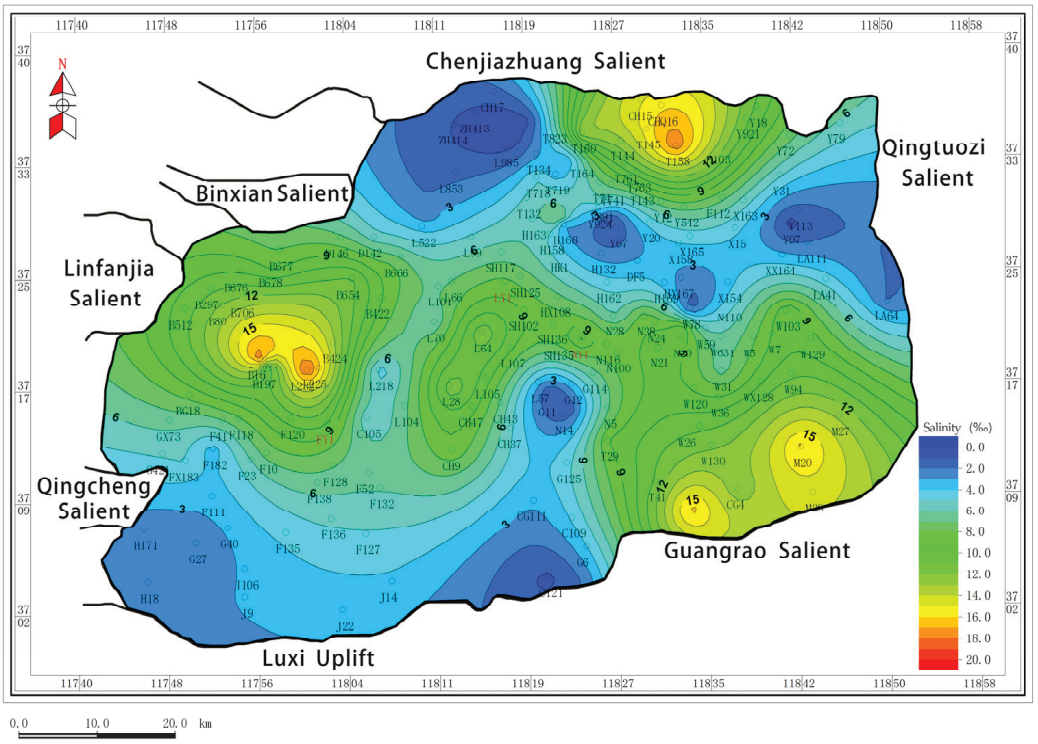

(**A**)

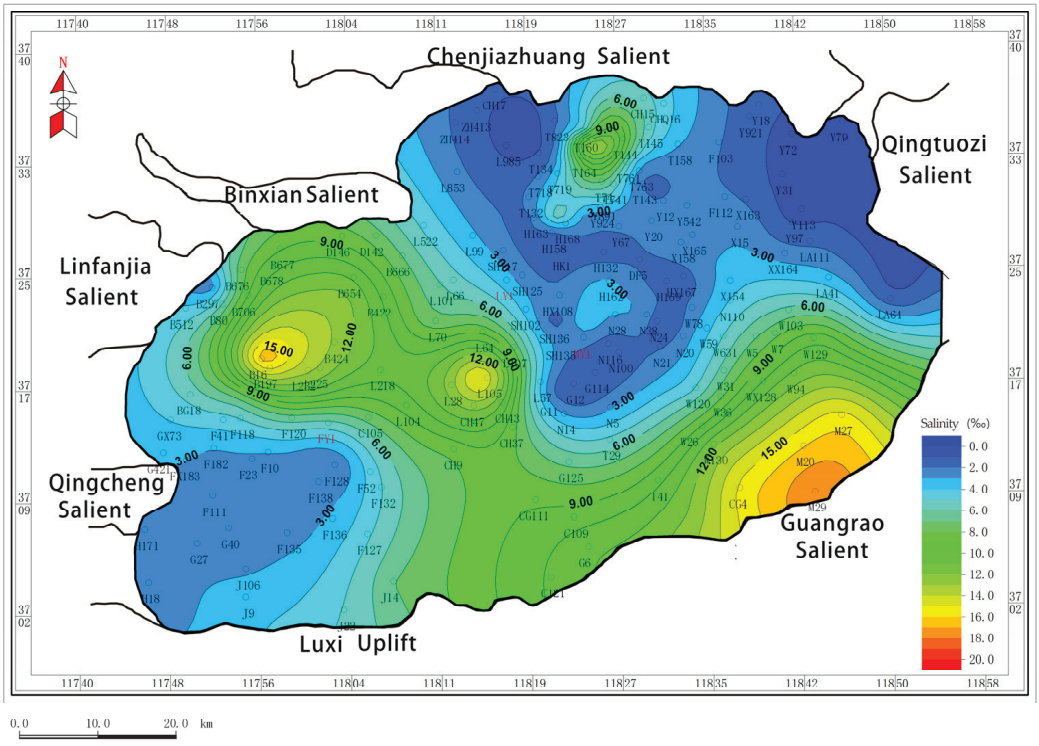

(**B**)

Figure 5. *Cont.*

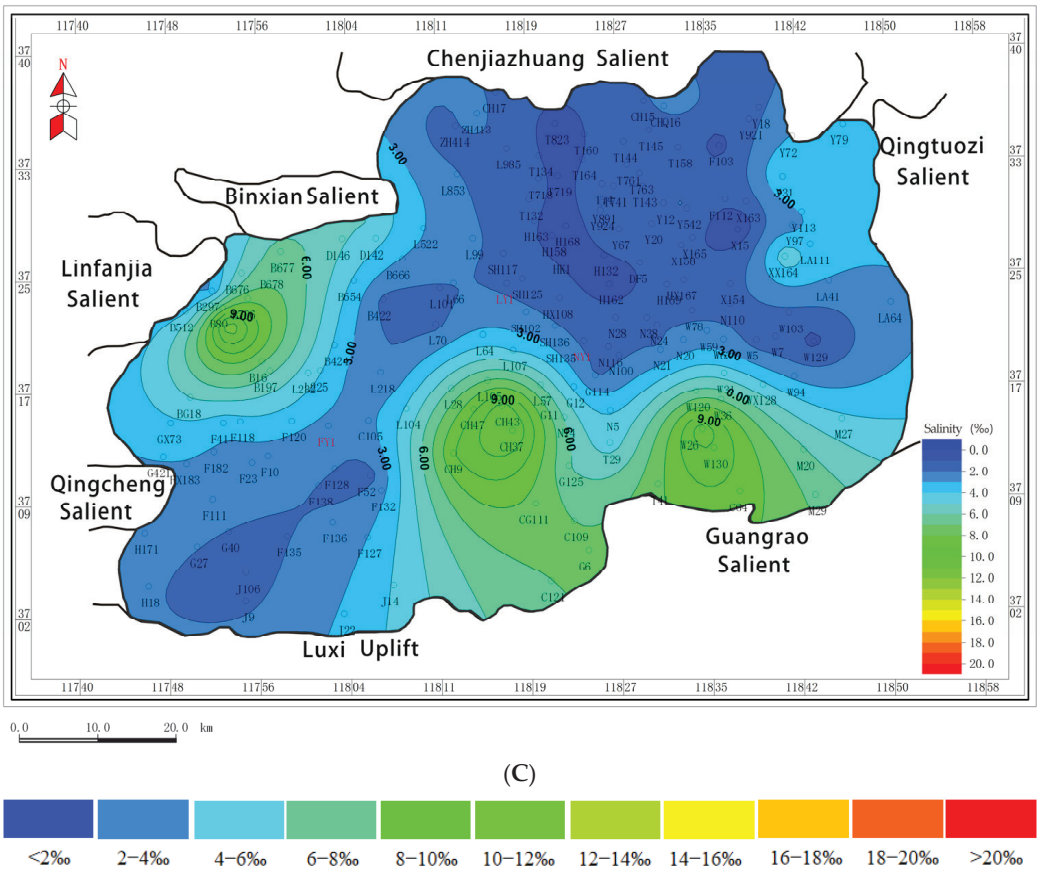

Figure 5. Salinity plane division scheme of Es_3 Dongying Sag ((**A**) Es_3L:163 wells with valid data; (**B**) Es_3M:156 wells; (**C**) Es_3U:92 wells).

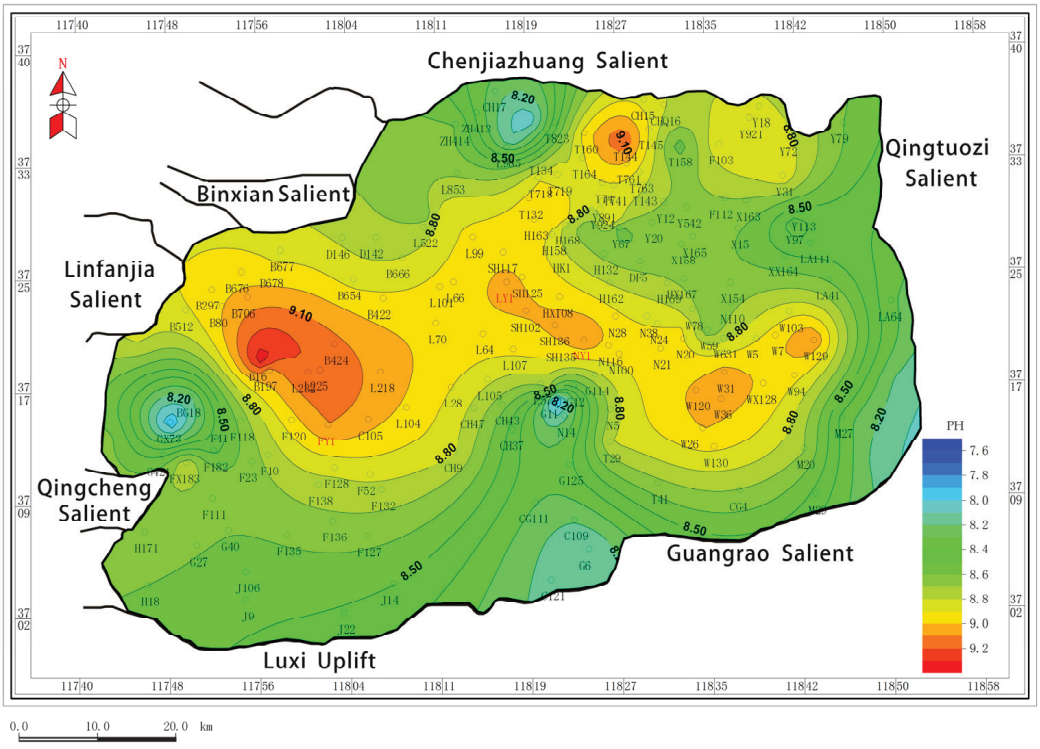

Figure 6. *Cont*.

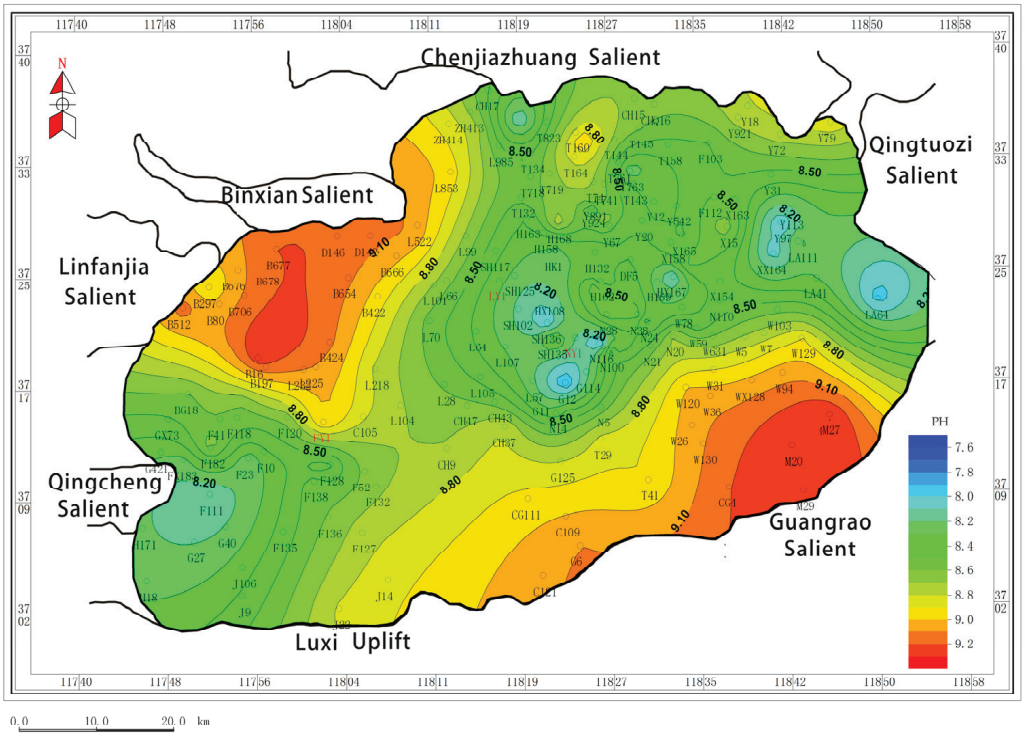

(**B**)

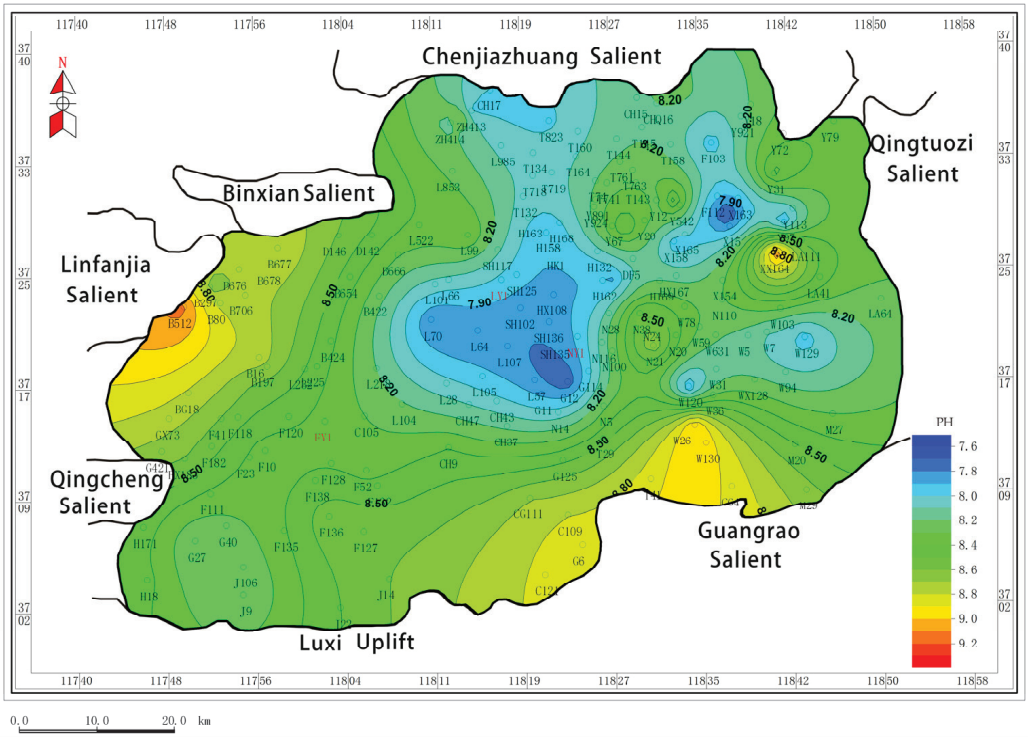

(**C**)

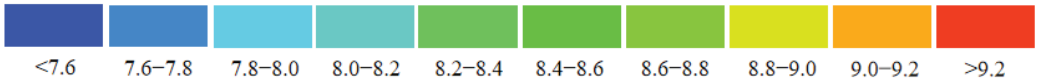

Figure 6. pH plane division scheme of Es_3 in Dongying Sag ((**A**) Es_3L; (**B**) Es_3M; (**C**) Es_3U).

According to the environmental zoning division index of the study area, the plane distribution map is drawn, and the high, middle, and low range areas are divided. The same geological period plane map is superimposed, and the study area is divided into nine regions, and the salinity and pH characteristics of different regions are analyzed intuitively.

3.2. Environmental Zone and Characteristics

There are three sub-members with different characteristics in Es_3, which are divided by the overlapping method.

In Es_3L, it shows a strip characterized by "high in the middle and low on both sides", and the environment is saline alkaline or brackish alkaline (Figure 7A). The areas with high value are distributed in a strip from the southeast of the Linfanjia Uplift to the southeast of the basin and the southern part of the Chenguanzhuang Uplift, accounting for 40% of the basin. They are surrounded by zones with medium and low value. The regions with high salinity and low pH and low salinity and high pH are rarely distributed and only exist in a small area in the north of Lijin Sub-Sag. This reflects that the water in the central area of the lake basin is salty and reductive.

In Es_3M, it shows a strip characterized by "high on both sides and low in the middle", and the environment consists of brackish water and is a neutral environment (Figure 7B). The northwest and southeast of the basin are areas with high salinity and pH values, which are specifically distributed in the Linjifan Uplift, the southeast of the Binxian Uplift, and the Chunhua areas. In the center of the basin is the middle and low value area, which extends from the southeast of Qingcheng Uplift to the northeast direction to Qingtuozi Uplift. This area is located in the slope break zone of the syngenetic fault that controls the central uplift. The fault activity results in the active flow body of the surrounding source, which reduces the pH value of the sedimentary aqueous medium.

In Es_3U, it shows the characteristics of "high on both sides and low in the middle", which is similar to Es_3M. It is a neutral to weakly acidic environment of freshwater, with a significant decrease in salinity and pH (Figure 7C). The areas with low values are significantly expanded, which are distributed in the eastern part of the sag, the south of Chenjiazhuang Uplift, the central uplift, and part of the southwest Jinjia area, accounting for nearly 80% of the basin. The high-value areas are still mainly distributed in the northwest Linfanjia Uplift, the southern margin of Chenjiazhuang Uplift, and the southeast Wangjiagang area, which is opposite to the low-value areas. It is obviously controlled by the development degree of the river delta in Es_3U. Within its influence range, the aqueous medium parameters show a low value characteristic.

3.3. Division Characteristics of Key Coring Wells

As for the key coring wells, comparing the logging data, aqueous medium data, lithology data, organic matter data, carbonate rock data, etc., could divide the environment and analyze the vertical environmental response.

The environment of Es_3L in Well NY1 is basically brackish water and alkaline, which accounts for about 80% of the total area. In the upper part of Es_3L, the range of this kind of environment becomes larger, reflecting that the salinity of the upper part is lower and lower. The Sr/Ba, Ca, and Total Organic Carbon (TOC) values of these zones are high, and the lithofacies are mainly carbonate mudstone. This is consistent with the results of previous studies. From Es_3L to Es_3M, the study area gradually developed from an "under-compensated closed lake" to a "flow-able lake" (Figure 8A). The saline alkaline condition accounts for 15% of Es_3L with high Sr/Ba, Ca, and TOC. The lithology is mainly layered mudstone. In Es_4, the basin was in the depression stage, and the lake shrank in a hot and dry climate.

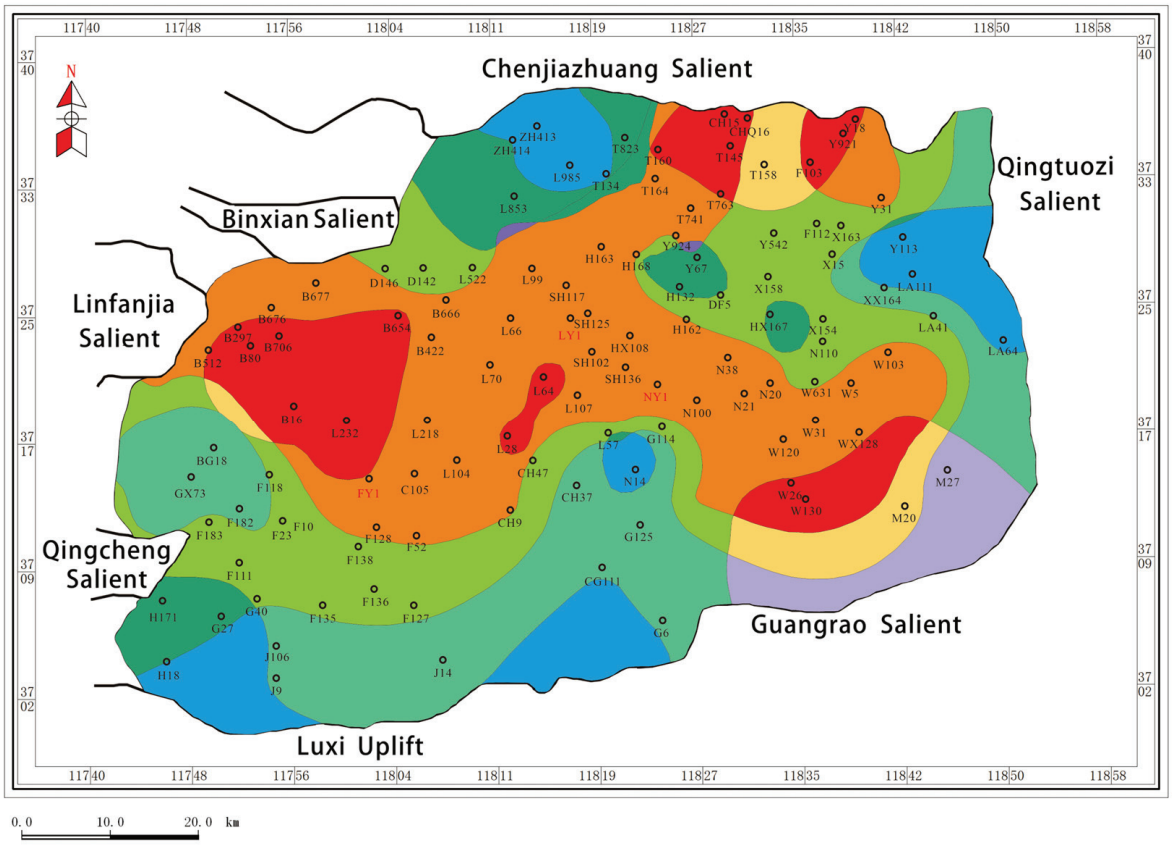

(**A**)

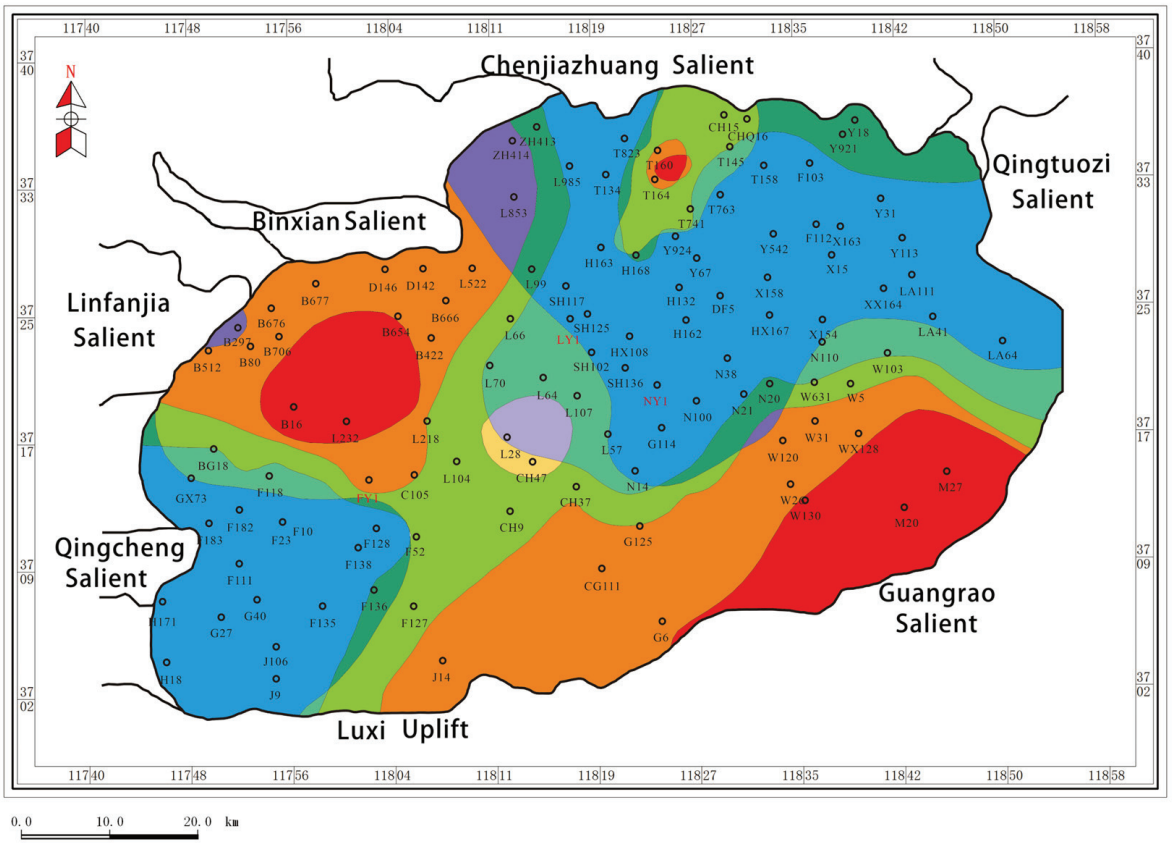

(**B**)

Figure 7. *Cont.*

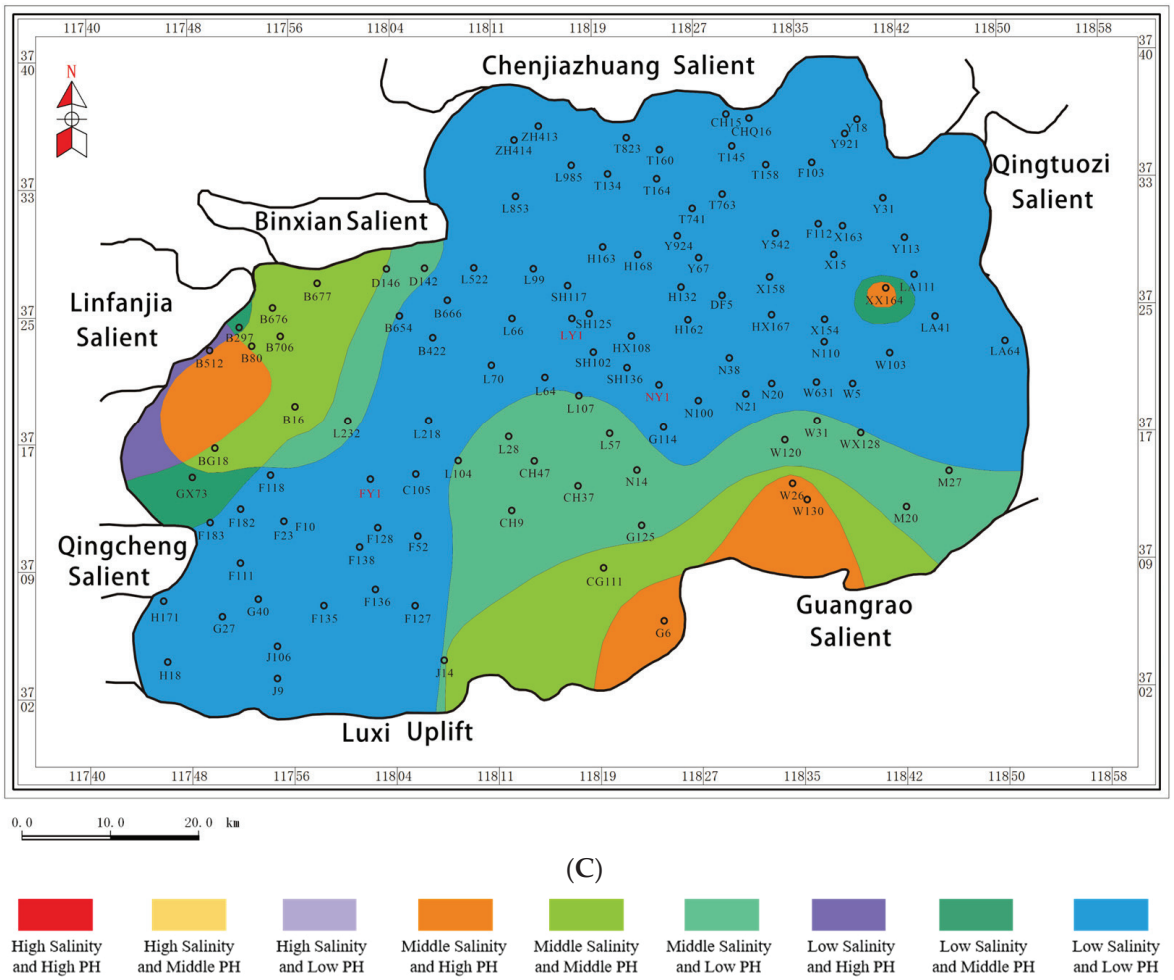

Figure 7. Environmental division plan of Es_3 ((**A**) Es_3L; (**B**) Es_3M; (**C**) Es_3U).

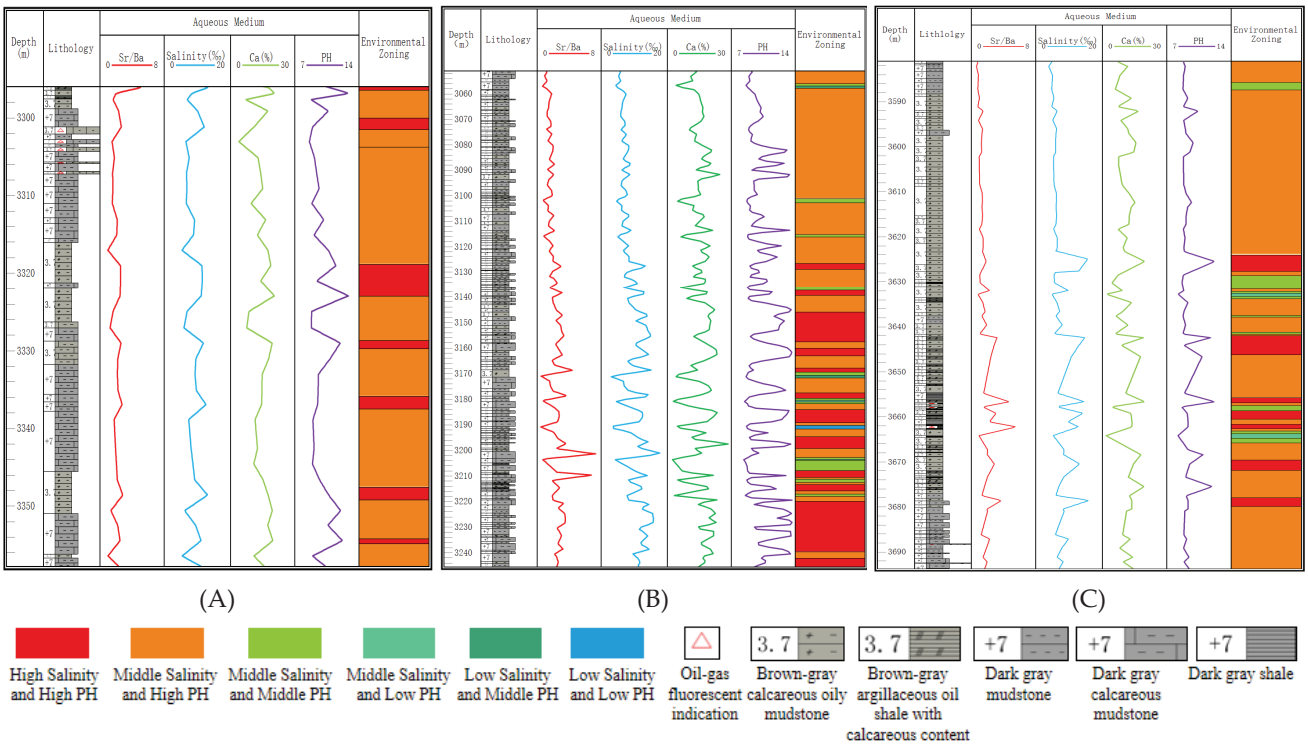

Figure 8. Environmental division of well ((**A**) NY1; (**B**) FY1; (**C**) LY1).

Less allochthonous sediment leads to higher salinity in the lake, which presents as a strongly alkaline environment. The saltwater alkaline environment in Es_3 reflects the good inheritance from Es_3L to Es_3U. In addition, the occasional moderately acidic and alkaline environment of brackish water appeared at a depth from 3302 m to 3304 m, reflecting the beginning of water dilution and an increase in allochthonous sediments.

The environment division of Es_3L in FY1 and LY1 is similar to NY1 (Figure 8B,C). There is a weakly acidic environment of brackish water in LY1. This reflects that the lake water is desalinated, and the allochthonous sediments are increased. On the other hand, it indicates that the offshore distance of LY1 is closer than NY1. Compared with the first two wells, the saline water and alkaline environment account for the largest proportion in well FY1, reflecting that well FY1 is closest to the lake center, with the strongest salinity and reducibility. There are three extra kinds of zones, including brackish water and neutral environment, fresh water and neutral environment, and fresh water and weakly acidic environment. These three zones are relatively thin in the vertical direction, accounting for about 10% of Es_3. The vertical evolution characteristics of the three key wells are fairly consistent with the plane distribution characteristics of the same period.

4. Discussion

Compared with conventional oil and gas reservoirs, the enrichment of shale oil lacks conventional cap rocks, traps, and migration processes, resulting in significant control over lithology and lithofacies. This article starts from the ash content of the third member of the Shahejie Formation and combines well logging data and geochemical testing data to analyze the distribution of carbonate reservoirs in different water medium environments.

4.1. Advantage Storage Space of Shale Oil Reservoirs

The main shale oil reservoir spaces in Es_3L of Zhanhua Sag near the research area include organic matter pores, intergranular pores, dissolution pores, structural fractures, and bedding fractures [35]. In the Jiyang Depression, the pores less than 50 nm are mainly provided by calcite dissolution pores. The pores ranging from 50 nm to 2 μm are provided by intergranular pores. The pores greater than 2 μm are provided by bedding and structural fractures (Figure 9). The larger contribution rate of porosity is intergranular pores, mainly derived from intergranular pores of clay minerals and carbonate minerals, such as calcite intergranular pores and dolomite intergranular pores.

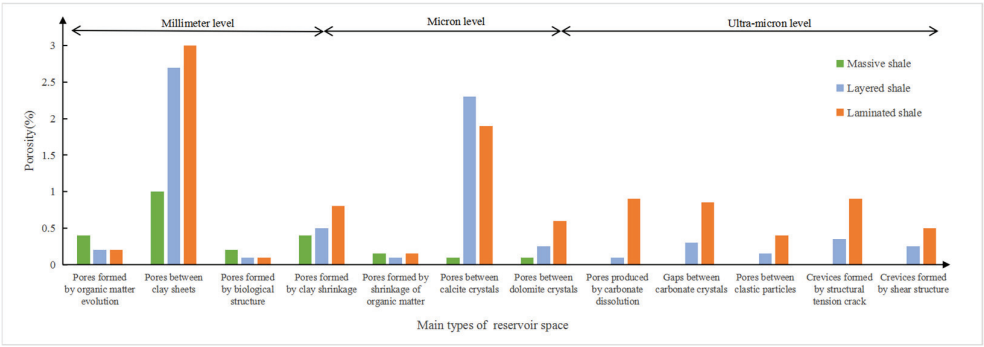

Figure 9. Contribution of main reservoir space types to porosity of Paleogene shale reservoirs in Jiyang Depression.

Organic-rich mud shale and mudstone are concentrated in Es_3. There is also a large number of laminated carbonate rocks in the form of intermediate shale. The main carbonate material is calcite, the content of which is up to 78%, and the average is 37.5%. The maximum dolomite content is 76%, and the average is 18.3%. Among them, the common

reservoir space types of laminated shale and sandstone inter-layer combination are mainly inter-granular pores and dissolution pores, with a large pore size range and high macropore proportion. The porosity of the sandstone interlayer mainly ranges from 4.7% to 21.9%, while the average porosity of the shale matrix and interlayer is 13.14% and 11.57% [36]. The carbonate mineral interlayer is an important influencing factor for the effective reservoir space in Dongying Sag, and its development is closely related to the water environment.

4.2. Prediction of Favorable Zones for Shale Oil Carbonate Reservoirs

There are many factors in the evaluation of shale oil reservoir characteristics, and the evaluation is mainly centered on oil production potential, reservoir capacity, reservoir transformation conditions, and shale oil movability. With the abundant thick-layer mudstone and source rock resources in the study area, the key factors restricting the favorable area of shale oil in the study area are reservoir properties, compressibility, and mobility. The interlayers not only produce oil themselves but also serve as important oil extraction channels for shale oil. The minerals in the interlayer are mainly carbonate minerals, which are brittle minerals and improve the compressibility of shale oil reservoirs. The development of the interlayer naturally increases the oil content, constituting an important reservoir space in the study area. This study takes carbonate rock interlayers as a bridge. The changes in the aqueous medium environment have affected the development and distribution of carbonate rock interlayers in the study area, thereby influencing the development of shale oil reservoirs.

Artificial synthesis experiments of dolomite and studies on a large number of recent dolomite sediments indicate that most dolomite forms under conditions of intense evaporation, high salinity, high Mg/Ca ratio, relatively high pH values, reducing environments, and higher temperatures [37]. Only such conditions favor the precipitation of dolomite from water by overcoming kinetic and thermodynamic barriers.

The overall environment of Es_3L is a saline-salinity alkaline environment, which is conducive to the development of carbonate rocks. It focuses on the quantitative study of the ash content of the Es_3L. According to the fitting formula, the ash content of Es_3L is calculated, and the plane distribution map is drawn (Figure 10). The value of carbonate content in Es_3L is from 11.39% to 66.25%, with an average of 36.16%. On the plane, the high-value areas with carbonate content greater than 35% are mainly distributed in the central depression zone, especially in the southeast of Linfanjia Uplift, the northeast of Lijin Sub-Sag, and the northwest of Niuzhuang Sub-Sag. The carbonate content in some wells reaches 60%.

The favorable areas of shale oil carbonate reservoirs in Es_3 follow through the environmental characteristics of the aqueous medium and, combined with the research results of the previous researchers, it is hypothesized that the favorable areas of the shale oil carbonate reservoirs in Es_3 are high salinity–high pH, high salinity–medium pH, and medium salinity–high pH, and are organic-rich and have a high carbonate content.

Based on the thick mudstone layers and high-quality source rocks in the study area (Figure 11), the abundant lamellar carbonate mineral intercalations provide sites for hydrocarbon migration and accumulation, allowing hydrocarbons to be stored during the primary migration phase. On the other hand, secondary pores formed by the dissolution of carbonate minerals are conducive to reservoir reformation. A large number of lamellar carbonate minerals are developed in the favorable areas with the carbonate content remaining above 35%, which provides a place for the migration and accumulation of hydrocarbons. The favorable reservoir areas of Es_3 are gradually reduced from the bottom to the top, and the favorable areas are concentrated in Es_3L. It is mainly distributed in the west of the Lijin Sub-Sag, which is in the intersection area of the east side of the Linfanjia Uplift and the

south side of the Binxian uplift, the northeast of the Lijin Sub-Sag, and the northern gentle slope area of Guangrao.

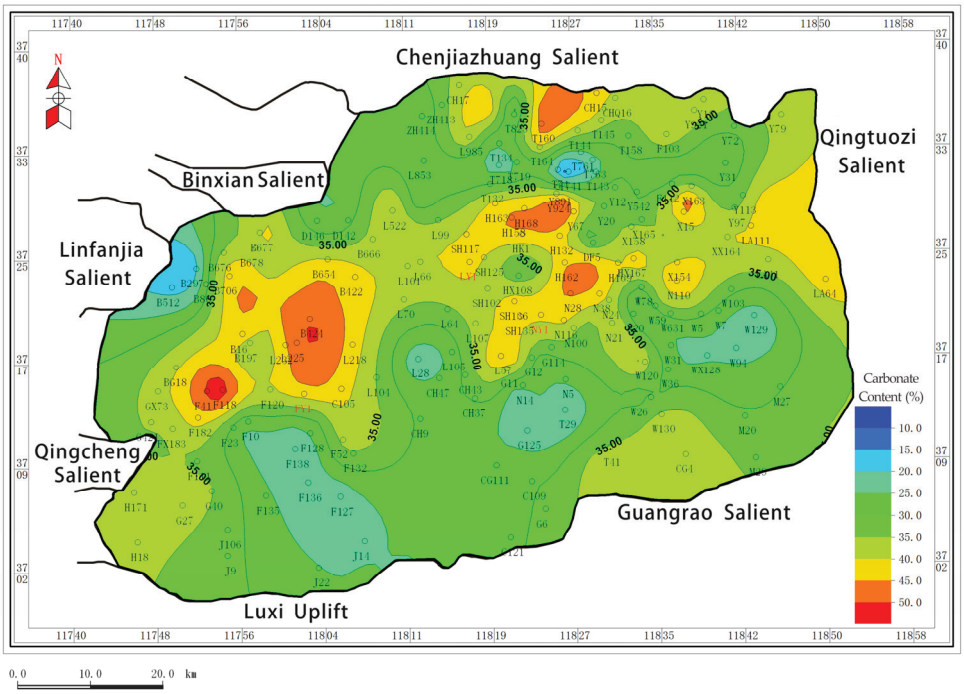

Figure 10. Characteristics of carbonate content in Es_3L.

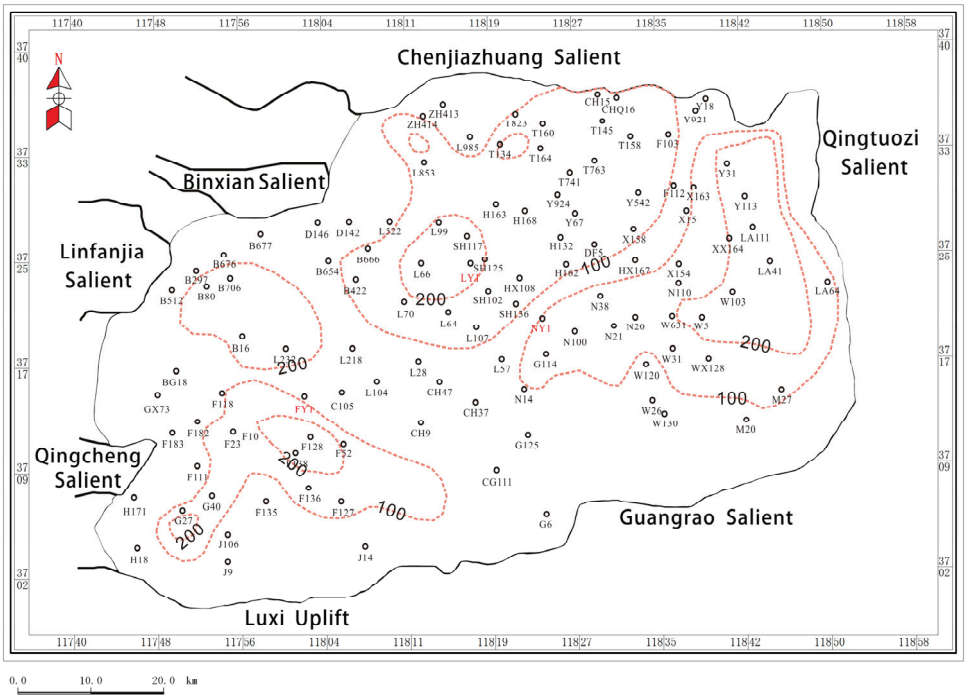

Figure 11. Mudstone thickness of Es_3.

By comparing the free resources of shale oil, it is found that the areas with higher total resource intensity are distributed in the west of Lijin Sub-Sag, while the areas with higher free resource intensity are distributed in the northeast of Lijin Sub-Sag (Figure 12) [38]. This is consistent with the predicted results, and the partitions with high salinity–high pH and high salinity–medium pH are located in the area with a good evaluation of free-phase shale resources.

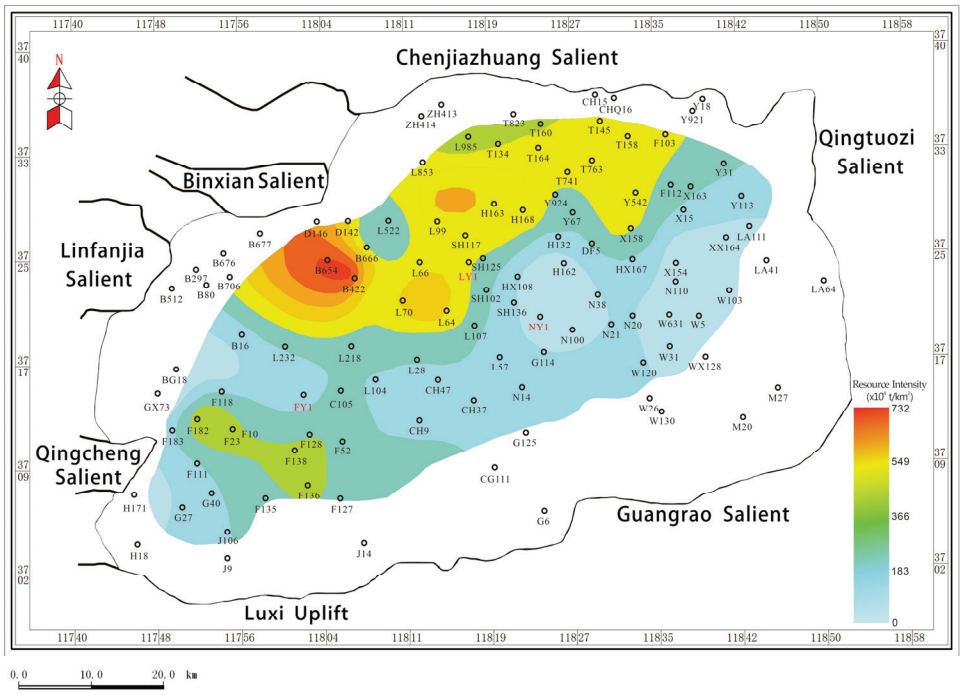

(**A**)

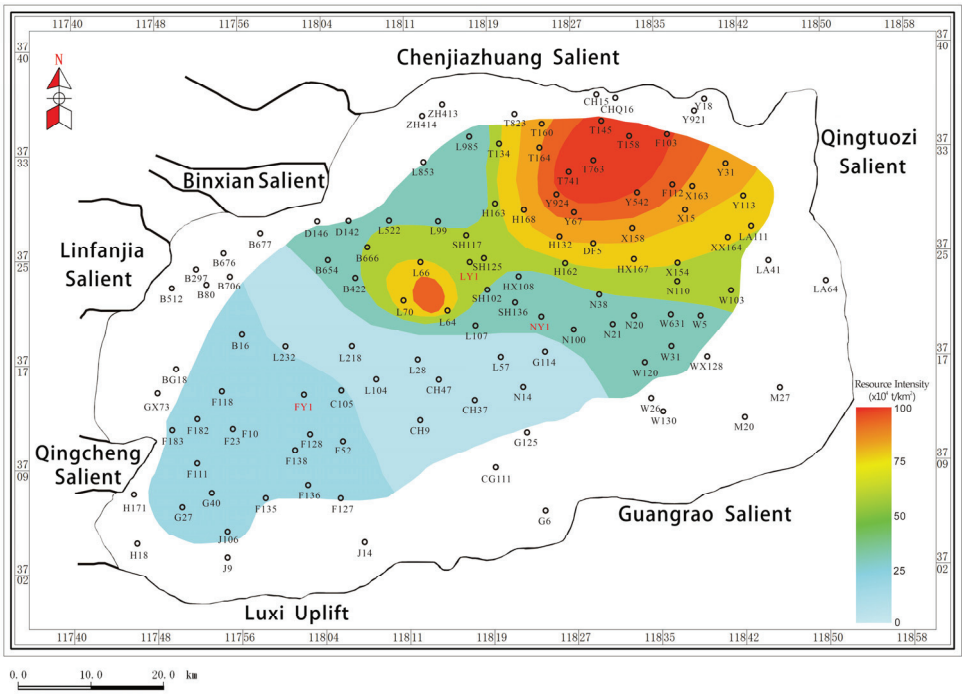

(**B**)

Figure 12. Shale oil resource intensity of Es_3L in Dongying Sag. ((**A**) Total resource intensity contour in Es_3L; (**B**) free resource intensity contour in Es_3L).

Combined with the analysis of structural location, it is predicted that the favorable areas of high salinity–high pH and high salinity–medium pH belong to the structural slope area. The enrichment of various types of shale oil in the slope area is a very valuable reserve direction for the effective exploration and development of shale oil [39].

First, the deep slope break zone with buried depth from 3200 to 3400 m in the slope area not only has the development conditions of matrix shale oil but also develops rich pre-delta turbidite sandstone interlayers, which is also a favorable environment for the development of interlayer shale oil. Secondly, the middle part of the slope area with buried

depth from 2500 m to 3200 m is the most favorable mixed area of high-quality oil shale, thin sandstone, and thin-layer carbonate rock, and it is also the area where the deformation of the basin is adjusted and the faults and fractures are widely developed. Especially in the buried depth range of from 2600 m to 3300 m, the brittle oil shale series is not only rich in authigenic oil sources but also often captures the light oil that migrates laterally from the deep depression area, which is very conducive to the formation of vertically superimposed, horizontally connected self-sourced, other-sourced, mixed-sourced high-yield fractured shale oil. Thirdly, the mid-slope zone usually has a shallower buried depth, lower drilling and completion costs, and higher natural productivity. Some wells do not even need to be fractured. Even if the productivity is not ideal, the fracturing can be slightly successful. Therefore, although the prediction of the fracture zone is difficult, the overall risk of shale oil exploration in the mid-slope zone is not high, and even the comprehensive benefits are comparable to those in the deep-lying areas.

This provides a novel perspective on shale oil exploration through lacustrine environmental zonation. The core idea is to draw on the concept of fine division of lake sedimentary systems and combine the study of the heterogeneity of shale oil reservoirs with the evolution parameters of lake environments, thereby optimizing the prediction of exploration target areas and the identification of sweet spots. The limitation of this method is that different parameters need to be selected for fitting based on the characteristics and data of different study areas, which requires a certain data foundation. The hydrodynamic conditions, paleosalinity, pH value, and biological activity in different zones vary greatly. By analyzing the correlation between different parameters and favorable reservoirs, the development characteristics of favorable reservoirs can be predicted.

5. Conclusions

1. Establishing a classification scheme for the aqueous medium environment of Es_3 is based on the salinity boundaries of 4‰ and 11‰ and pH boundaries of 8.65 and 8.85 for defining high, medium, and low levels. There are nine kinds of zones theoretically proposed by the superposition method to describe the salinity and pH.
2. Es_3L is dominated by areas with high salinity–middle pH and middle salinity–high pH, which are rich in carbonate, presenting a saline–brackish alkaline environment. The salinity and pH in Es_3M decreased, mainly in middle salinity–middle pH and low salinity–middle pH areas, which were in the brackish neutral environment. Es_3U is mainly characterized by low salinity and low pH conditions.
3. The abundant laminar carbonate mineral interbeds serve as effective reservoir spaces. The limestone content in zones with high salinity–middle pH, middle salinity–high pH, and middle salinity–high pH mostly remains above 35%, suggesting these areas as favorable for shale oil reservoirs in the Es_3 Member of the Dongying Sag. It is concentrated in the central part of Es_3L, the western and northeast parts of the Lijin Sub-Sag, and the northern gentle slope of the Guangrao. The first two environmental partitions are located in the structural slope area, which is a valuable reserve target for the exploration and development of shale oil.

Author Contributions: Conceptualization, H.Z. and H.W.; methodology, H.Z. and N.M.; writing—original draft preparation, H.Z.; writing—review and editing, H.Z., H.W. and N.M. All authors have read and agreed to the published version of the manuscript.

Funding: This research received no external funding.

Data Availability Statement: Data are contained within the article.

Acknowledgments: The completion of this paper has benefited from support and assistance from various quarters. First and foremost, I extend my heartfelt gratitude to Hongliang Wang, the corresponding author, for his invaluable guidance and advice during the research design and idea organization stages. Furthermore, I am grateful to Nana Mu for her assistance with data analysis. Discussions with them have been immensely beneficial to me. Lastly, I would like to thank the editors and reviewers of *Energies* for dedicating their valuable time to reviewing my article, as their comments and suggestions have significantly enhanced its quality. Once again, I express my sincerest thanks to all those who have helped and supported me.

Conflicts of Interest: The authors declare no conflicts of interest.

Abbreviations

The following abbreviations are used in this manuscript:

Es_3	The third member of the Shahejie Formation
Es_3L	The lower part of the third member of the Shahejie Formation
Es_3M	The middle part of the third member of the Shahejie Formation
Es_3U	The upper part of the third member of the Shahejie Formation
Es_4U	The upper part of the fourth member of the Shahejie Formation
TOC	Total Organic Carbon

References

1. Zou, C.N.; Ma, F.; Pan, S.G.; Zhang, X.S.; Wu, S.T.; Fu, G.Y.; Wang, H.J.; Yang, Z. Formation and distribution potential of global shale oil and the developments of continental shale oil theory and technology in China. *Earth Sci. Front.* **2023**, *30*, 128–142.
2. Salygin, V.; Guliev, I.; Chernysheva, N.; Sokolova, E.; Toropova, N.; Egorova, L. Global shale revolution: Successes, challenges, and prospects. *Sustainability* **2019**, *11*, 1627. [CrossRef]
3. Kuang, L.C.; Hou, L.H.; Yang, Z.; Wu, S. Key parameters and methods of lacustrine shale oil reservoir characterization. *Acta Pet. Sin.* **2021**, *42*, 1–14.
4. Zhao, X.Z.; Pu, X.G.; Jiang, W.Y.; Zhou, L.; Jin, F.; Xiao, D.; Fu, L.; Li, H. An exploration breakthrough in Paleozoic petroleum system of Huanghua Depression in Dagang Oilfield and its significance, North China. *Pet. Explor. Dev.* **2019**, *46*, 651–663. [CrossRef]
5. Fu, J.H.; Li, S.; Guo, Q.; Guo, W.; Zhou, X.; Liu, J. Enrichment condition and favorable area optimization of continental shale oil in Ordos Basin. *Acta Pet. Sin.* **2022**, *43*, 1702.
6. Sun, L.; Liu, H.; He, W.; Li, G.; Zhang, S.; Zhu, R.; Jin, X.; Meng, S.; Jiang, H. An analysis of major scientific problems and research paths of Gulong shale oil in Daging Oilfield, NE China. *Pet. Explor. Dev.* **2021**, *48*, 453–463. [CrossRef]
7. He, W.; Meng, Q.; Feng, Z.; Zhang, J.; Wang, R. In-situ accumulation theory and exploration & development practiceof Gulong shale oil in Songliao Basin. *Acta Pet. Sin.* **2022**, *43*, 1–14.
8. Li, G.; Zhu, R.; Zhang, Y.; Chen, Y.; Cui, J.; Jiang, Y.; Wu, K.; Sheng, J.; Xian, C.; Liu, H. Geological characteristics, evaluation criteria and discovery significance of Paleogene Yingxiongling shale oil in Qaidam Basin, NW China. *Pet. Explor. Dev.* **2022**, *49*, 18–31. [CrossRef]
9. Kuang, L.C.; Dong, D.; He, W.Y.; Wen, S.; Sun, S.; Li, S.X.; Qiu, Z.; Liao, X.W.; Li, Y.; Wu, J.; et al. Geological characteristics and development potential of transitional shale gas in the east margin of the Ordos Basin, NW China. *Pet. Explor. Dev.* **2020**, *47*, 435–446. [CrossRef]
10. Liu, H.M.; Wang, Y.; Yang, Y.H.; Zhang, S. Sedimentary Environment and Lithofacies of Fine-Grained Hybrid Sedimentary in Dongying Sag: A Case of Fine-Grained Sedimentary System of the Es_4. *Earth Sci.* **2020**, *45*, 3543–3555.
11. Yang, W.; Wang, X.; Ding, J.; Wang, Y. Characteristics and control factors of fine-grained sedimentary rock lithofacies in Bonan subsag. *J. China Univ. Min. Technol.* **2017**, *46*, 365–374.
12. Zhang, Q.; Zhu, X.; Li, C.; Qiao, L. Classification and quantitative characterization of microscopic pores in organic-rich shale of the Shahejie Formation in the Zhanhua Sag, Bohai Bay Basin. *Oil Gas Geol.* **2014**, *35*, 286–294.
13. Zhang, S.; Liu, H.M.; Zhang, P.F.; Li, L.J.; Liu, X.J.; Song, X.Q.; Wei, X.L.; Wang, Y.; Wang, W.Q. Geological characteristics of shale oil enrichment in Niuzhuang sag, Dongying depression. *J. China Univ. Min. Technol.* **2022**, *51*, 1138–1151.
14. Hao, Y.; Chen, F.; Zhu, J.; Zhang, S. Reservoir space of the $Es3^3$-Es_4^1 shale in Dongying Sag. *Int. J. Min. Sci. Technol.* **2014**, *24*, 425–431. [CrossRef]
15. Zhang, S.; Chen, S.; Tan, M.; Zhang, Y.; Sun, B.; Gong, W.; Hu, Z.; Hou, Z. Characterization of sedimentary microfacies of shale in the lower third sub-member of Shahejie Formation, western Dongying sag. *Acta Pet. Sin.* **2014**, *35*, 633–645.

16. Wang, Y.; Song, G.Q.; Liu, H.M.; Jiang, X.F.; Hao, X.F.; Ning, F.X.; Zhu, S.D.; Lin, L. Main control factors of enrichment characteristics of shale oil in Jiyang depression. *Pet. Geol. Recovery Effic.* **2015**, *22*, 20–25.
17. Sun, C.; Yao, S.; Li, J.; Liu, B. The Characterization of Shale Oil Reservoir in Dongying Sag. *Geol. Rev.* **2016**, *62*, 1497–1510.
18. Bai, C.Y. *The Genesis of Laminar Carbonates from Jiyang Sub-Basin and Their Implicate for Shale Oil Accumulation*; China University of Gcosciences (Beijing): Beijing, China, 2019.
19. Burton, G.R.; Woolf, K.; Sullivan, B. Lacustrine depositional environments in the Green River Formation,Uinta Basin: Expression in outcrop and wire line logs. *AAPG Bull.* **2014**, *98*, 1699–1715. [CrossRef]
20. Scherer, C.M.S.; Goldberg, K.; Bardola, T. Facies architecture and sequence stratigraphy of an early post-rift fluvial succession,Aptian Brabalha Formation,Araripe Basin,northeastern Brazil. *Sediment. Geol.* **2015**, *322*, 43–62. [CrossRef]
21. Merkel, A.; Fink, R.; Littke, R. High pressure methane sorption characteristics of lacustrine shale from the Midland Valley Basin, Scotland. *Fuel* **2016**, *182*, 361–372. [CrossRef]
22. Moradi, A.V.; Sari, A.; Akkaya, P. Paleoredox reconstruction of biturninous shales from the Miocene Hancili Formation, cankiricorum Basin, Turkey: Evaluating the role of an oxia in accumulation of organic-rich shales. *Mar. Pet. Geol.* **2016**, *78*, 136–150. [CrossRef]
23. Yang, T.; Cao, Y.; Friis, H.; Wang, Y.; Zhou, L. Diagenetic evolution and chemical changes of deep-water mudstones of Shahejie Formation in the Dongying Sag, Jiyang Depression, Eastern China. *Mar. Pet. Geol.* **2018**, *93*, 14–32. [CrossRef]
24. Sun, C.; Yao, S.; Li, J.; Liu, B. Characteristics of Mesoporous in shale oil reservoirs by Small Angle X-ray Scattering Method. *Geol. J. China Univ.* **2017**, *24*, 715–724.
25. Zou, C.; Yang, Z.; Cui, J.; Zhu, R.; Hou, L.; Tao, S.; Yuan, X.; Wu, S.; Lin, S.; Wang, L.; et al. Formation mechanism,geological characteristics and development strategy of nonmarine shale oil in China. *Pet. Explor. Dev.* **2013**, *40*, 14–26. [CrossRef]
26. Wang, G.M.; Lin, G.S. Eogene paleoclimate zone study in the Jiyang depression. Bulletin of Mineralogy. *Petrol. Geochem.* **2012**, *31*, 505–509.
27. Liu, H.M.; Zhang, S.; Bao, S.Y.; Fang, Z.; Yao, S.; Wang, Y. Geological characteristics and effectiveness of the shaleoil reservoir in Dongying sag. *Oil Gas Geol.* **2019**, *40*, 512–523.
28. Teng, J.B.; Liu, H.M.; Qiu, L.W.; Zhang, S.P.; Fang, Z.W.; Li, B.; Zhang, S.; Miao, Z.W. Characteristics and influencing factors of shale oil reservoir space in Paleogene shale of Dongying Sag. *Earth Sci.* **2022**.
29. Fang, Z.W.; Zhang, S.P.; Liu, H.M. Bedding structure characteristics and the storage controlling factors of mud-shale in Upper Es_4 to Lower Es3 Members in Jiyang Depression. *Pet. Geol. Recovery Effic.* **2019**, *26*, 101–108.
30. Wang, G.M.; Xiong, Z.H.; Zhang, J.; Fu, Y. The correspondence between the aragonite content of Palaeogene shale and the thermal evolution of source rocks in Jiyang depression. *Acta Pet. Sin.* **2017**, *38*, 855–862.
31. Wang, Y.; Liu, H.; Song, G.; Hao, X.; Zhu, D.; Zhu, D.; Ding, J.; Yang, W.; Yin, Y. Carbonate genesis and geological significance of shale hydrocarbon in lacustrine facies mud shale: A case study of source rocks in the upper sub-member of Member4 and lower sub-member of Member 3 of Shahejie Formation, Dongying sag. *Acta Pet. Sin.* **2017**, *38*, 1390–1400.
32. Kong, X.X. *Sedimentary Characteristics, Origin and Hydrocarbon Accumulation of Lacustrine Carbonate-Bearing Fine Grained Sedimentary Rocks*; China University of Gcosciences (Beijing): Beijing, China, 2020.
33. Wang, A.H.; Ye, S.Y.; Liu, J.K.; Ding, X.G.; Li, H.L.; Xu, N.C. Discrimination between Marine and Terrestrial Sedimentary Environments by the Selectively Extracted Sr/Ba Ratio: A case of sediments in the Yellow River Delta. *ACTA Sedimentolocica Sin.* **2020**, *38*, 1226–1238.
34. Chen, C.Q. *A Study on the Diagenesis of Paleogene System Based on Sequence Framework in DongYing Sag*; China University of Gcosciences (Beijing): Beijing, China, 2006.
35. Jiang, Z.; Li, T.; Gong, H.; Jiang, T.; Chang, J.; Ning, C.; Su, S.; Chen, W. Characteristics of low-mature shale reservoirs in Zhanhua sag and theirinfluence on the mobility of shale oil. *Acta Pet. Sin.* **2020**, *41*, 1587–1600.
36. Zhang, S. Shale Oil Enrichment Elements and Geological Dessert Types in Jiyang Depression. *Sci. Technol. Eng.* **2021**, *21*, 504–511.
37. Tian, J.C.; Lin, X.B.; Zhang, X.; Peng, S.; Yang, C.; Luo, S.; Xu, L. The genetic mechanism of shoal facies dolomite and its additive effect of Permian Qixia Formation in Sichuan Basin. *Acta Petrol. Sin.* **2014**, *30*, 679–686.
38. Yu, T. *Enrichment Characteristics and the Prediction of Favorable Target Areas of Shale Oil in Dongying Sag*; China University of Petroleum (East China): Qingdao, China, 2018.
39. Yu, Y.J.; Wang, H.Y.; Liu, D.X.; Zhao, Q.; Zheng, M.; Wang, S.J. Probing and Thinking on "Exploring Petroleum Inside Source Kitchen" of Continental Shale Oil Exploration—A Case Study of the First Member of Shahejie Formation in Qikou Sag, Bohai Bay Basin, China. *J. Earth Sci. Environ.* **2021**, *43*, 117–134.

MDPI AG
Grosspeteranlage 5
4052 Basel
Switzerland
Tel.: +41 61 683 77 34

Energies Editorial Office
E-mail: energies@mdpi.com
www.mdpi.com/journal/energies

Academic Open
Access Publishing

mdpi.com

ISBN 978-3-7258-5782-1